CHEMICAL REVIEWS

pubs.acs.org/CR

Review

Oxide– and Silicate–Water Interfaces and Their Roles in Technology and the Environment

José Leobardo Bañuelos, Eric Borguet,* Gordon E. Brown, Jr., Randall T. Cygan, James J. DeYoreo, Patricia M. Dove, Marie-Pierre Gaigeot, Franz M. Geiger, Julianne M. Gibbs,* Vicki H. Grassian, Anastasia G. Ilgen,* Young-Shin Jun,* Nadine Kabengi,* Lynn Katz, James D. Kubicki,* Johannes Lützenkirchen, Christine V. Putnis, Richard C. Remsing, Kevin M. Rosso, Gernot Rother, Marialore Sulpizi, Mario Villalobos, and Huichun Zhang

Cite This: *Chem. Rev.* 2023, 123, 6413–6544

Read Online

ACCESS | Metrics & More | Article Recommendations | Supporting Information

ABSTRACT: Interfacial reactions drive all elemental cycling on Earth and play pivotal roles in human activities such as agriculture, water purification, energy production and storage, environmental contaminant remediation, and nuclear waste repository management. The onset of the 21st century marked the beginning of a more detailed understanding of mineral aqueous interfaces enabled by advances in techniques that use tunable high-flux focused ultrafast laser and X-ray sources to provide near-atomic measurement resolution, as well as by nanofabrication approaches that enable transmission electron microscopy in a liquid cell. This leap into atomic- and nanometer-scale measurements has uncovered scale-dependent phenomena whose reaction thermodynamics, kinetics, and pathways deviate from previous observations made on larger systems. A second key advance is new experimental evidence for what scientists hypothesized but could not test previously, namely, interfacial chemical reactions are frequently driven by "anomalies" or "non-idealities" such as defects, nanoconfinement, and other nontypical chemical structures. Third, progress in computational chemistry has yielded new insights that allow a move beyond simple schematics, leading to a molecular model of these complex interfaces. In combination with surface-sensitive measurements, we have gained knowledge of the interfacial structure and dynamics, including the underlying solid surface and the immediately adjacent water and aqueous ions, enabling a better definition of what constitutes the oxide– and silicate–water interfaces. This critical review discusses how science progresses from understanding ideal solid–water interfaces to more realistic systems, focusing on accomplishments in the last 20 years and identifying challenges and future opportunities for the community to address. We anticipate that the next 20 years will focus on understanding and predicting dynamic transient and reactive structures over greater spatial and temporal ranges as well as systems of greater structural and chemical complexity. Closer collaborations of theoretical and experimental experts across disciplines will continue to be critical to achieving this great aspiration.

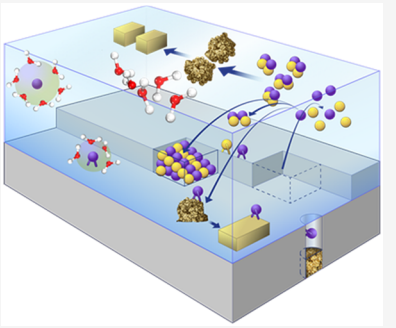

CONTENTS

Received: February 21, 2022
Published: May 15, 2023

https://doi.org/10.1021/acs.chemrev.2c00130
Chem. Rev. 2023, 123, 6413–6544

1. INTRODUCTION

1.1. Background and Progress

Chemical reactions at oxide− and silicate−water interfaces are relevant to a broad range of scientific and engineering disciplines. These include atmospheric chemistry, environmental chemistry and geochemistry, environmental engineering, heterogeneous catalysis and photocatalysis, chemical sensing, corrosion science, metallurgy and ore beneficiation, crystal growth, soil science, semiconductor manufacturing, and tribology, among others. Oxide− and silicate−water interfaces are reactive due to hydrolysis (acid−base) reactions, ligand exchange reactions, adsorption reactions, and electron transfer (redox) reactions, and they involve H_3O^+, OH^-, aqueous metal ions, and aqueous organic species and complexes among these species. The importance of these types of reactions, together with those between microorganisms and mineral surfaces, cannot be overestimated: they control the composition of our natural environment and mitigate some of the anthropogenic perturbations that are changing our planet in ways that are often unpredictable and detrimental. We discuss these processes in the section 1.2 below and how these types of interfacial chemical reactions are relevant to applications such as water treatment, agriculture, human health, and energy production and storage.

At the beginning and end of the 20th century, Irving Langmuir and Werner Stumm emphasized the broad relevance of interfacial chemical reactions:

> *"From the point of view of the chemist, the structure of the surface must be of utmost importance, for the chemical reactions in which solids take part are practically always surface reactions."*[1]
>
> *"Almost all the problems associated with understanding the processes that control the composition of our environment concern interfaces, above all, the interfaces of water with naturally occurring solids."*[2]

This review builds on *Metal Oxide Surfaces and Their Interactions with Aqueous Solutions and Microbial Organisms*, published in *Chemical Reviews* in 1999.[3] Since then, there have

https://doi.org/10.1021/acs.chemrev.2c00130
Chem. Rev. 2023, 123, 6413−6544

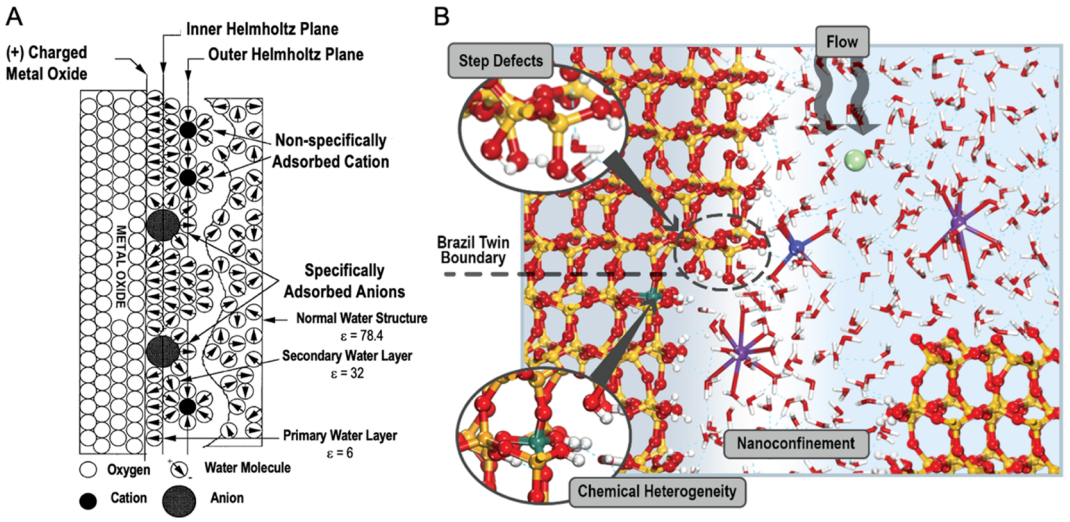

Figure 1. Our evolving understanding of metal-oxide aqueous interfaces. (A) Schematic model of the electrical double layer (EDL) at the metal oxide−aqueous solution interface reproduced from Brown et al.[3] Reproduced from ref 3. Copyright 1999 American Chemical Society. The scheme shows elements of the Gouy−Chapman−Stern model, including specifically adsorbed anions and nonspecifically adsorbed solvated cations. The metal oxide, or zero-plane, is defined by the location of surface sites, which may be protonated or deprotonated. The inner Helmholz plane, or *b*-plane, is defined by the centers of specifically adsorbed anions and cations. The outer Helmholz plane, or *d*-plane, corresponds to the beginning of the diffuse layer of ions. Estimates of the dielectric constant, ε, of water are indicated for the first and second water layers nearest the interface and for bulk water. Dipole moments are shown using the chemistry convention with the arrow pointing towards the more electronegative oxygen. (B) Atomistic model of the α-quartz (SiO_2) (101) surface with a step edge and an Fe^{3+}/H^+ substitution for Si^{4+}. Most molecular models are limited in spatial dimensions and compositional complexity. Future challenges in applying molecular-level studies of oxide−water interface chemistry to real world environmental problems (as illustrated below in Figure 2) include accounting for defects such as steps and compositional substitutions, the effects of confinement on the chemistry of adsorption (the solution at the bottom is in a 2 nm channel), flow, dissolution and precipitation, the complexity of substrates (e.g., grain−grain contacts) and solutions, and size and scale effects. Dashed line represents Brazil twinning within the crystal, insets show Fe^{3+}/H^+ substitution for Si^{4+}, and step edge and SiO^-−Na^+ interaction. (Brazil twin model courtesy of Si (Athena) Chen, The Pennsylvania State University.).

been many advances in experimental and computational methods for studying interfacial reactions. The present review discusses these advances, updates our understanding of the molecular-level processes that occur at oxide− and silicate−water interfaces, and addresses the primary knowledge gaps in this rapidly expanding research area. Two dozen scientists and engineers have co-authored this review, offering an uncommonly broad perspective on this interdisciplinary field.

One of the most important changes in our approach to molecular-level experimental studies of metal oxide surfaces is that we have addressed the "*pressure gap*" between the *ex situ* experimental methods of surface science that required an ultra-high vacuum (UHV) environment[4,5] and *in situ* methods that can make measurements on solids and aqueous solutions or gases.[6,7] We have bridged this pressure gap and studied chemical reactions at oxide− and silicate−water interfaces under *in situ* conditions, which has allowed important advances in the study of heterogeneous catalytic reactions on solid surfaces.[8,9] A complementary tool advancing our molecular-level understanding of interfacial chemical reactions is the use of quantum chemical methods, particularly density functional theory (DFT),[10] to explore oxide−water structure and dynamics,[11] surface-charging behavior,[12] and reaction mechanisms for adsorption/desorption,[13] dissolution,[14] and precipitation.[15]

Other research gaps discussed in this review include the "*chemical complexity gap*". Because many chemical reactions of interest occur on "dirty" solid surfaces, experimental methods that can handle this complexity are required.[16] This is true for the study of environmental interfacial reactions (Figure 1) that include aqueous solutions, ion complexes, natural organic matter, and microbial biofilms. Another important issue discussed here is the "*concentration gap*", where low concentration species (e.g, surface defect sites) may define the overall reactivity, while analytical signals are often dominated by more abundant species. In addition, the "*flow gap*" refers to the fact that under flow conditions at solid−water interfaces the H_2O/ion dynamics and surface reactivities differ from those observed at the static interfaces. A "*nano-size gap*" is discussed because the thermodynamics, kinetics, and reaction pathways observed for larger systems deviate when the reactive surface size reaches nanoscale, and the reactions take place under nanoconfinement (nanoparticles, nanopores).

This review is the result of a workshop on Aqueous Solution/Oxide Interfaces sponsored by the 2020 Mesilla Chemistry Workshop, Inc., held at the Hacienda de Mesilla, Mesilla, New Mexico. The goals of this workshop were to develop new ideas and approaches to bridge the knowledge gaps involving interfacial chemical processes and to develop a "roadmap" that would lead to a better understanding of the interactions between aqueous solutions and the surfaces of naturally occurring oxide-based minerals. We dedicate this review to Prof. William L. Hase (Department of Chemistry and Biochemistry, Texas Tech University), Founding President of the Mesilla Chemistry Workshop, Inc., who passed away shortly after the 2020 Mesilla Chemistry Workshop on Aqueous Solution/Oxide Interfaces.

A major challenge for the coming decade is to study complex systems under real-world conditions (flow, nanoconfinement, organic films) with the same molecular-level resolution that has been obtained for simpler systems in the past decade. Concentration ranges, longer durations, greater spatial extents,

https://doi.org/10.1021/acs.chemrev.2c00130
Chem. Rev. 2023, 123, 6413−6544

and the inclusion of heterogeneities, such as defects, must be accounted for in order to transfer knowledge from the fundamental chemical realm to macroscopic predictions. Figure 2, as an example, illustrates the problem and connections among the molecular-, nano-, micro-, macro-scales, and human health related to arsenic (As) contamination in groundwater (section 1.2.1.2.2). Complicating matters is the fact that processes can occur on time scales from femtoseconds to millennia. Thus, creating predictive models based on molecular mechanisms that can be used to optimize solutions to societal challenges requires an integrated approach including an array of experimental, analytical, computational, and theoretical methods.

We begin the review with the most fundamental aspects of mineral−water interface chemistry and then move to progressively more complex reactive interfacial systems. In section 2, we focus on oxide and silicate *surface structures* when in contact with aqueous solutions and explore the H-bonding and water structure at interfaces, charging of surfaces via protonation/deprotonation, and the structure of electrical double layer (EDL). In section 3, we focus on *surface reactivities* and introduce the added dimension of adsorbing species of various complexities (from metal cations to bacterial biofilms) and interfacial electron transfer. Building upon the interfacial structures, dynamics, and complexation reviewed in the previous sections, in section 4, we discuss *surface transformations*, including dissolution of oxides and silicates, as well as their nucleation, and precipitation and how solid surfaces mediate these processes. In section 5, we outline guidance for addressing important questions, suggest further developments, and call for an integrated research strategy that synthesizes information from a spectrum of analytical and computational techniques in collaboration with scientists and engineers working on real-world problems at the macroscopic scale. Across all sections, we aim at addressing gaps discussed above, namely chemical complexity gap (surface defects, and heterogeneities), concentration gap, flow gap, and nanosize gap.

The following section 1.2 provides a brief discussion of the critical importance of oxide−water interface chemistry, enabled by the methodological advances made in the last decade (Supporting Information (SI), section 1.1), and the challenges in transferring knowledge from molecular-level studies to macroscopic applications. These real-world problems help us to set the stage for the remainder of the review and justify the urgent need for future research in these areas.

1.2. Applications that Motivate Oxide−Water Interfacial Science and Technology

The intrinsic challenge of understanding interfacial chemistry and its relevance to health, environment, and energy is to study systems as they occur in nature. Natural systems are complex and heterogeneous across wide ranges of spatiotemporal scales. Using a reductionist approach to obtain details on simplified model systems has provided insights, but making these insights more applicable to real-world problems requires accounting for the environmental factors that have been excluded to gain detailed understanding. This accounting will require that scientists and engineers collaborate to share information among all approaches across scales and levels of complexity and that their studies are designed to interconnect. We discuss specific examples of health, environmental, or energy impacts and how understanding surface chemistry is a key to

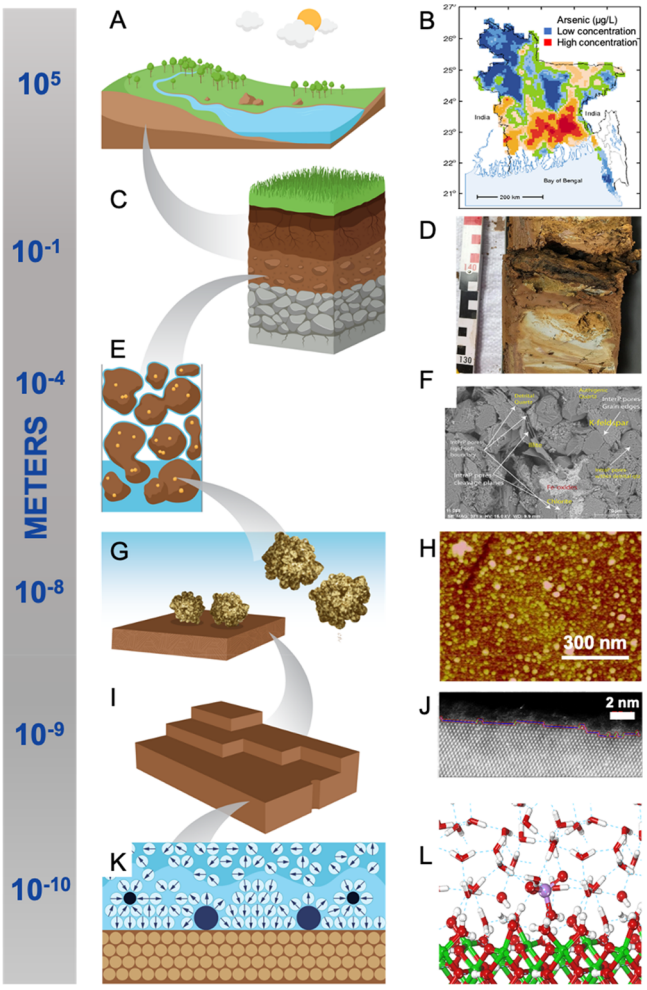

Figure 2. Multiscale impacts of oxide−water interfacial chemistry. At the global scale, oxide−water interfaces control elemental cycling and therefore impact the availability of clean water, nutritious food, and energy. (A,B) At regional scales, interfacial chemistry could result in contaminant mobilization with tragic impacts on millions of people, such as the groundwater arsenic contamination in Bangladesh. (C) On the local scale, individuals and small communities are commonly impacted when they draw their water from a well, as water quality is strongly impacted by the sediment composition at specific sites. (D) A sediment core sample from an aquifer reveals orange, arsenic-containing iron oxides.[18] (E,F) At the pore (micrometer) scale, water quality is controlled by surfaces with heterogeneous structures and multimineralic compositions, which can either adsorb or release contaminants, such as arsenic.[19] (G) The mobilization of arsenic and other contaminants can be significantly affected by new mineral formation (nucleation and growth) in bulk solution or at mineral surfaces. (H) For example, during Fe-oxy(hydr)oxides formation, arsenic can be incorporated into the newly nucleated Fe-oxy(hydr)-oxides.[20] (I) Variations of surface structures (kinks, edges, defects, confinement) at the nanoscale can have significant impacts on the extent of adsorption based on the (J) surface topography and site density of the minerals.[21] (K) Ultimately, chemical reactions at the molecular scale determine the equilibria and kinetics for these (L) surface complexation processes, such as arsenate adsorption onto Fe-oxy(hydr)oxides. Connecting the molecular, nano-, micro-, and macroscopic scales is complex due to the heterogeneities in physicochemical properties (e.g., surface sites, fluid composition, flow). Our goal is to summarize the state of the science, identify critical questions and challenges, and outline a path forward for dealing with multiscale (temporal and spatial) interfacial chemistry. (B) Modified from ref 17. (D) Adapted from ref 18. Copyright 2020

https://doi.org/10.1021/acs.chemrev.2c00130
Chem. Rev. 2023, 123, 6413−6544

Figure 2. continued

American Chemical Society. (F) Adapted with permission from ref 19. Copyright 2021 Elsevier Ltd. (G) Adapted from ref 20. Copyright 2014 American Chemical Society. (J) Adapted from ref 21. Copyright 2017 American Chemical Society. (L) Modified from ref 22 Copyright 2014 Watts, Tribe, and Kubicki.

addressing these issues. The examples below are not intended as comprehensive, but they highlight important topics that motivate detailed molecular-level research into oxide− and silicate−water interfacial chemistry.

1.2.1. Clean Water. According to the World Health Organization (WHO) "*By 2025, half of the world's population will be living in water-stressed areas*".[23] Water availability and contaminant behavior in soils, sediments, aquifers, rivers, and oceans commonly depend upon adsorption/desorption, dissolution, and precipitation—all mineral−water interface processes. Organic, inorganic, and biological components adsorb and desorb from mineral surfaces, altering the original mineral surface properties and solubilities. The presence of minerals can catalyze precipitation of other phases.[24] Detailed knowledge of the chemical principles behind these reactions is lacking for complex systems but necessary for improved models and engineering approaches to supplying clean water. For example, natural aquifer processes generally lead to water purification. Can we mimic these processes or learn from their chemical principles to handle large volumes of water filtration at low cost?

1.2.1.1. Managed Aquifer Recharge. A growing strategy for dealing with increasing water demands and uncertainties in water supplies is managed aquifer recharge (MAR).[25] Although a seemingly simple process that allows surface and treated waters to infiltrate and recharge aquifers, MAR can cause changes in soil and aquifer properties that lead, as here again exemplified for arsenic, to mobilization as well as clogging and reduced process effectiveness. First, when water recovered from MAR is used for irrigation or drinking water, one concern is that toxic metalloids, such as As, can be mobilized from subsurface reservoir systems. Injected water significantly alters the water chemistry in an aquifer during MAR, affecting As mobilization.[25] Anions in injected water (e.g., NO_3^- and Cl^-),[26] oxyanions (e.g., silicate, bicarbonate, and phosphate),[27] Fe^{3+},[28] and natural organic matter[26,29] can affect electrostatic interactions, hydrophilicity/hydrophobicity, redox condition, and aqueous and surface complexation, changing the dissolution of aquifer minerals and their consequent nucleation, aggregation, growth, and the phase transformation of secondary mineral phases. Such unintended processes in recovered water can affect the aquifer and its water quality.

Second, chemical and biological clogging[30,31] can occur during MAR. Solution and mineralogical compositional heterogeneities, combined with temperature and pressure gradients and/or ranges, complicate our understanding and control of clogging.[30,31] When recharging solutions pass through porous media, the accompanying mineral precipitation usually decreases porosities and permeabilities (Figure 3). In combination with microbiological adsorption and growth that may be induced by higher nutrient concentrations in waters used for MAR,[32] the total variety of biogeochemical effects can hinder this strategy. Our understanding of the chemical mechanisms involved is limited, and they should be studied further.[30,31]

One example that affects MAR and soil quality is the aggregation of clay particles (section 4.3). Particle aggregation can increase the porosity and permeability of soils, and aggregation can be negatively impacted by higher Na^+ or the sodium adsorption ratio (SAR, the ratio of $Na^+/(Ca^{2+} + Mg^{2+})$).[33] Current data and models alone are insufficient to predict the soil aggregation behavior for a given set of conditions.[33] The details of surface charging (section 2.3.1), ion adsorption (section 3.2), and particle repulsion (section 4.3) need molecular-level data and new theories based on this data.

A related topic is soil salinization during irrigation, which is also connected to food production (section 1.2.2). Irrigation in hot, arid regions leads to evapotranspiration from soils and plants.[35] Low concentrations of dissolved salts left behind can build up over time and negatively impact agricultural productivity (see ref 36 and refs therein). Increasing Na^+ in soils can cause charging that disperses clays (disaggregation, section 1.2.1.1). This disaggregation reduces hydraulic conductivity, enhances the chance of waterlogging, and increases organic dispersal that enhances biodegradation and leads to loss of soil organic matter (SOM) (see section 3.3).[37] Remediation is difficult and expensive, but methods such as the addition of oxide nanoparticles can ameliorate the situation (section 1.2.2).[37]

1.2.1.2. Contamination. 1.2.1.2.1. Pathogenic Microorganisms. One of the world's major health problems is the

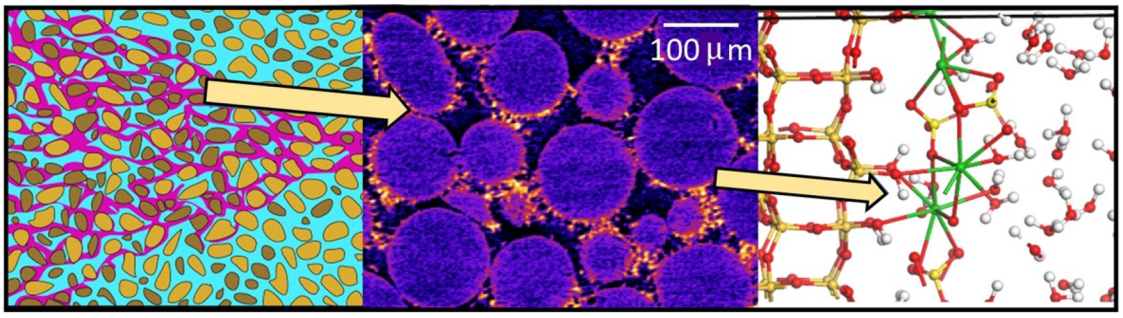

Figure 3. Flow through porous media leads to adsorption of nutrients (e.g., phosphate) and contaminants (e.g., arsenate, pathogenic bacteria), while dissolution enhances and precipitation hinders macroscopic flow. From left to right: the images depict models of flow through porous media, how the porosity and permeability change as a function of precipitation on grains, and a molecular mechanism of surface precipitation. (Left) Flow schematic reproduced from ref 34. (Middle) X-ray computed tomography data of barite precipitation courtesy of V. Starchenko, A. G. Stack, L. M. Anovitz and J. Weber (ORNL). (Right) Schematic of barite on quartz courtesy of H. D. Watts and J. D. Kubicki (UTEP).

https://doi.org/10.1021/acs.chemrev.2c00130
Chem. Rev. 2023, 123, 6413−6544

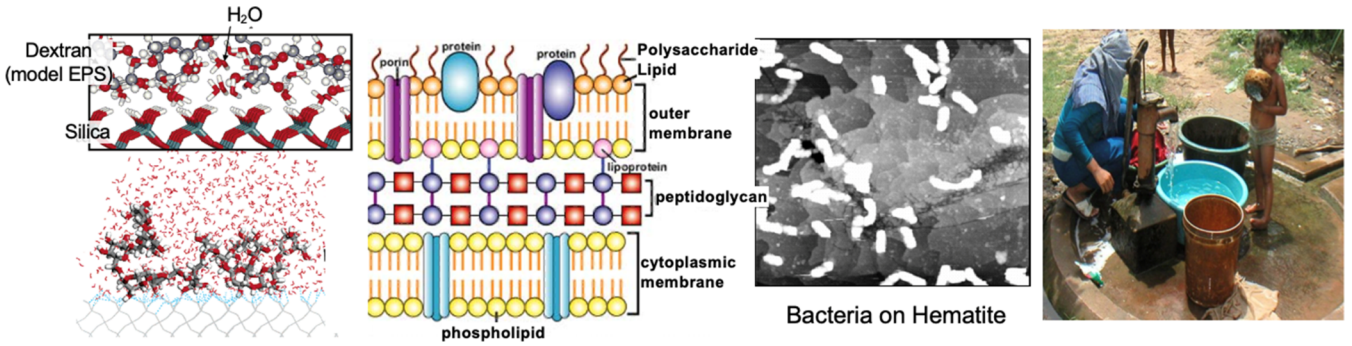

Figure 4. Bacterial−mineral interactions that impede transport of microorganisms in soils and aquifers. Extracellular polymeric substances extending from the surfaces of bacteria interact with metal oxides (commonly Fe-oxy(hydr)oxides) and filter them out of the flowing solution. This naturally-occurring phenomenon can be mimicked for low-cost water filtration systems. Left to right: Figure of model EPS interacting with silica adapted from Kwon et al.[45] Copyright 2006 American Chemical Society. Diagram of the gram-negative bacterial cell wall used with permission from Prof. G. E. Kaiser (Community College of Baltimore County, Catonsville Campus). Distributed under a CC BY 4.0 license. AFM image of Shewanella putrefaciens on hematite adapted with permission from Rosso et al.[46] Copyright 2003 Elsevier Science Ltd. Photo of villagers collecting water from a shallow well in south-east Asia, courtesy of S. Fendorf (Stanford).

contamination of drinking water by pathogenic microorganisms from animal and human waste. Without water disinfection treatment, fecally-transmitted diseases can be spread, and they are fatal mainly to the youngest and oldest in a population. As the WHO states:

> *"Globally, at least 2 billion people use a drinking water source contaminated with feces. [Contaminated] water can transmit diseases such diarrhea, cholera, dysentery, typhoid, and polio and is estimated to cause 485,000 diarrheal deaths each year."*[38]

Since the work of Omoike et al.[39] that combined attenuated total reflectance Fourier transform infrared (ATR FTIR) spectroscopy with DFT calculations, we have known that phosphoryl groups in the extracellular polymeric substances (EPS) that extend from most bacteria bond strongly to Fe-oxy(hydr)oxides such as α-FeOOH (goethite) (Figure 4). Parikh and Chorover[40] report that bacteria adhere to goethite in this manner, which explains the observations that bacterial transport is correlated with the Fe-content in sandy materials.[41,42] This reaction controls the transport and retention of *Escherichia coli* (*E. coli*) in sandy materials.[43] Work continues on Fe-oxide nanoparticles with a maximized adsorptive surface area for binding pathogenic bacteria and resulting antibacterial properties.[44]

1.2.1.2.2. Arsenic Groundwater Contamination. According to the WHO:[47]

> *"Arsenic contamination of groundwater is widespread, and there are a number of regions where arsenic contamination of drinking-water is significant. It is now recognized that at least 140 million people in 50 countries have been drinking water containing arsenic at levels above the WHO provisional guideline value of 10 μg/L."*[48]

Naturally occurring arsenic contamination is likely the greatest mass poisoning in human history. Arsenic has been geologically transported and deposited in sediments in various global locations, notably Bangladesh and Chile. Over time, the sediments have formed aquifers, which have recently been tapped as groundwater resources. Desorption[49] and dissolution (Raessler and refs therein[50]) reactions have allowed not only the release of As^{5+} but also the more soluble and toxic As^{3+} into drinking water. The speciation of As in the sediments was identified by methods such as EXAFS[51] and modeled with DFT.[52,53] Knowledge of the speciation of the source of the As has allowed avoidance of the contaminated sites, and treatment methods that mimic natural geochemical reactions have been designed based on adsorbents such as nano-ferrihydrite ($5Fe_2O_3{\cdot}9H_2O$) combined with functionalized cellulose to form composite adsorbents.[54,55] Similar approaches have been developed to deal with a variety of contaminants (Neil et al.[25] and references therein). The combination of spectroscopies with computational chemistry has been effective in obtaining surface speciation (Luo et al.[56] and references therein).

1.2.2. Food Production. The second of the United Nations Sustainable Development Goals is "Zero Hunger". According to the U.N. (https://www.un.org/sustainabledevelopment/hunger/):

> *"With more than a quarter of a billion people potentially at the brink of starvation, swift action needs to be taken to provide food and humanitarian relief to the most at-risk regions..., a profound change of the global food and agriculture system is needed if we are to nourish the more than 820 million people who are hungry and the additional 2 billion people the world will have by 2050. Increasing agricultural productivity and sustainable food production are crucial to help alleviate the perils of hunger."*

Availability of abundant, nutritious food to feed the world's projected 10 billion people will be hindered by limited water supplies, exacerbated by extended droughts and higher temperatures. Making soils more resilient to higher temperatures and drought depends upon soil−organic matter (SOM) interactions because higher SOM contents help soils retain water.[57] Dissolution of minerals allows plants to uptake nutrients that can increase productivity and drought-resistance as well.[58] Hence, agricultural productivity depends upon soil quality and nutrient availability, both of which involve mineral−water interface processes such as SOM sequestration and P cycling. Models of field-scale nutrient behavior neglect molecular-level information, but biogeochemical reactions control the bioavailability and solubility of nutrients.[59] Integrated studies involving all components and processes in soils are not common. Molecular-level studies should be integrated into larger scale studies to provide useful information to predict field-scale processes.

For example, Gardea-Torresdey and coworkers have studied the impacts of metal oxide nanoparticles on plant health and nutritional value.[60−62] Optimizing nanoparticles for adsorp-

https://doi.org/10.1021/acs.chemrev.2c00130
Chem. Rev. 2023, 123, 6413−6544

tion[63,64] or dissolution[65,66] reactions requires knowledge of the interfacial chemistry at each face of the particle as well as control of the synthesis of nanoparticle habits during nucleation.[67] Hence, improving our molecular-level information about complex nanoparticulate surface-solution chemistries will enable improving agricultural productivity by optimal time-release of nutrients and soil resilience by increasing retention of soil organic carbon.

1.2.3. Human Health: Effects of Mineral Dust Aerosols. There is a strong association between human exposure to particulate matter (PM) and increases in daily mortality.[68] Inhalation of micrometer and smaller particles is the likely cause of millions of deaths annually, through a variety of mechanisms.[69] There are numerous types of aerosol particles: secondary organics, sulfate, black/brown carbon, sea salt, and minerals. Inhalation of any of these is linked to negative health outcomes depending on exposure. Understanding the surface chemistry of the aerosols that interact with tissues is key to predicting and mitigating these negative health effects.

Oxides and silicates are emitted directly into the atmosphere through various natural processes, including volcanic eruptions and dust storms. Once in the atmosphere, the oxide and silicate components of volcanic ash and mineral dust aerosols can impact human health, Earth's climate, and the chemical balance of the atmosphere. From naturally-occurring asbestos causing cancer to silica particles leading to silicosis, the human health impacts of mineral dust aerosols are well known.[70] However, the exact surface chemistry of mineral dust aerosol and its interactions with biological systems remain poorly understood.

Mineral aerosols can also contain pathogens and toxic elements that can be inhaled or ingested together with the aerosol. The formation processes of airborne particulate matter or aerosols can create complex surface chemistries that drive the human health impacts of inhaling these particles. Recent research has shown that PM2.5 (airborne particulate matter or aerosols 2.5 microns or less in diameter) can be made up of aggregates of nanoparticles whose surface chemistries are different from those of the bulk composition of the particle.[71] In addition to providing reactive oxygen species (ROS)[72] that can synergize with carcinogens, such as polycyclic aromatic hydrocarbons (PAHs) that may be adsorbed to aerosols, these small particles can cross the blood–brain barrier[73] and affect gut microbiomes.[74] Developing methods to characterize and understand these complex interfaces is imperative for predicting and mitigating human health effects.

1.2.4. Energy. The U.S. Energy Information Agency (EIA) projects a 50% increase in total global demand for energy by 2050.[75] This growth will occur in the transportation, residential, commercial, and industrial sectors and will be dominated by needs in non-Organization for Economic Cooperation and Development (OECD) countries. Combined with the desire to achieve low- or zero-carbon dioxide emissions, a dramatic scale up in non-CO_2-emitting energy sources and/or CO_2 sequestration technologies will be necessary. Regardless of the extent to which countries decide to use wind, solar, geothermal, nuclear, and other "alternative" energy sources, detailed knowledge of mineral–water interfaces will make energy production and utilization more efficient.[76]

1.2.4.1. Critical Element Mining for the Energy Transition. Solar and wind are generally perceived as "clean" methods of generating electricity, but solar and wind energy production requires raw materials such as rare earth elements (REEs) extracted via mineral–water interface processing (Figure 5).

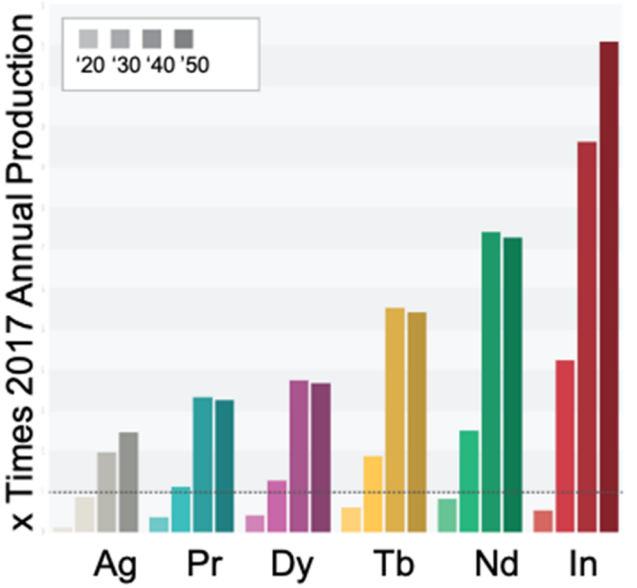

Figure 5. Global critical metal demand for wind and solar panels, between 2020 and 2050, compared with the 2017 level of annual metal production (dashed line = 2017 level). Modified from the literature.[77]

Construction of a wind turbine requires one metric ton of Nd–Fe–B alloys to produce the REE magnets used in the generator. The demand for raw materials to build solar panels and generators for wind turbines means we will have to mine efficiently and with minimal environmental impact. These extraction activities are highly dependent upon mineral–water interfaces. In addition, the demand for metals such as copper needed to build electrical vehicles and the charging infrastructure needed to replace gasoline engines and filling stations is substantial.

Supplying the dramatic increase in demand for metals means that efficient, environmentally friendly extraction techniques must be developed and employed, whether tapping new resources, utilizing mine wastes, or recycling. As near-surface deposits are exploited, deeper deposits may need to be mined, just as the quest for oil has gone deeper and deeper over the years. Biohydrometallurgy may make mine waste recovery and deep mining economically and environmentally feasible.[78] According to Levett et al.[78] "*Harnessing microbe–mineral–metal interactions may offer many opportunities to improve some mining practises and support the long-term sustainability of mining.*" In addition, mechanistic details of microbe–mineral–metal interactions may also help with stabilization of mine tailings and ecosystem restoration.[78] Sections 3.4.1.3, 3.5 and 4.3.2.6 of this review discuss such interactions at the molecular level and the challenges ahead.

1.2.4.2. Efficient Hydraulic Fracturing and Subsurface CO_2 Sequestration. In many cases, oil and gas extraction efficiencies are controlled by mineral–water interface chemistry. Hydraulic fracturing ("fracking") for oil and gas recovery requires insight into molecular-level processes at oxide–water interfaces. Even though they are present in relatively small amounts, the additives in hydraulic fracturing fluid influence

https://doi.org/10.1021/acs.chemrev.2c00130
Chem. Rev. 2023, 123, 6413–6544

the amounts and concentrations of "flowback" waters (fluids collected at the surface after injection).[79] Current fracking processes typically extract only 20% of the available gas within a shale play. Maximizing the extracted gas per well and minimizing the volume of flowback waters will decrease the environmental impacts of fracking, which has become a major global source of energy and has provided gas as an alternative fuel to coal, helping reduce U.S. CO_2 emissions dramatically.[80] For more information on the chemical and reactive transport processes associated with hydraulic fracturing of unconventional oil/gas shales, the recent review by Jew et al. is recommended.[81]

Shale wettability is a common parameter used to assess the efficiency of hydraulic fracturing. The more wettable the shale, the more complete the fracturing, and the greater the volume of natural gas that can be extracted. However, two major measures for estimating wettability, the contact angle and spontaneous imbibition, commonly provide discrepant results.[82] Siddiqui et al.[82] conclude that the mechanisms of wettability over the range of conditions encountered are not well understood and that wettability depends on the solution composition and minerals present.[83−85] Considering the enormous economic and environmental implications of hydraulic fracturing efficiency, these insights should prompt more molecular-level studies of these processes, relevant to complex real-world conditions and leading to studies at larger scales.[86,87] MD studies of water in nanopores between charged clay particles suggest novel behavior of water that fundamentally alters the way we think of mineral−water systems when a gas phase is involved.[88] Similar issues are involved with subsurface H_2 injection, storage, and retrieval.[89] This topic will be discussed in sections 5.1.2 and 5.2.2.4.4 on reactive transport modeling.

Because burning of hydrocarbon fuels generates large volumes of CO_2, geologic carbon sequestration (GCS) is an important strategy for mitigating the impacts of increasing atmospheric CO_2 concentrations and their associated climate changes. While GCS presents macro- or megascale problems, their important process mechanisms and technical solutions are often closely related to a molecular scale understanding of oxide−water interfaces.[90,91] Complex reactions among Mg- and Ca-bearing silicates[92] with aqueous solutions altered by supercritical CO_2 (sc-CO_2) determine the long-term stability of CO_2 sequestered in rocks such as shales, which have a high potential storage capacity.[93] As in hydraulic fracturing, wettability and storage capacity are influenced by the pressure, temperature, and mineralogy of the shales, which are heterogeneous within a given formation and among formations.[93] One would like the injected CO_2 to convert to HCO_3^- in solution and react with Mg^{2+} and Ca^{2+} dissolved from silicates to form $(Mg,Ca)CO_3$ minerals that are stable over geological time scales. However, this formation needs to occur without altering the physical properties of the rock to the extent that CO_2 leakage to the atmosphere occurs.[94] Because sc-CO_2 injection alters the mineralogy and pore structure of shales, the relationships among surface mineralogy, surface morphology, and adsorbed organic matter present need to be well understood (section 3.3).[56] Other host rocks include basalt[95] and sandstone,[96] where similar reactions are desired that involve dissolution of silicates and precipitation of carbonates (section 4.4). The potential for combining carbon capture and storage (CCS) with geothermal energy generation is also being discussed.[97]

1.2.4.3. Energy Storage. Energy storage is also critical to the widespread usage of variable energy sources, such as wind and solar. Electrified transportation requires efficient storage devices with high energy density that can supply high power. Batteries, the most common energy storage device, need significant technical improvement to serve many applications, and interfacial reactions are one key to this improvement.[98] Promising battery materials are the P2 layered oxides ($Na_{0.67}Mn_{1-x}M_xO_2$, where M is a transition metal), but research is needed on their interactions with aqueous electrolytes because water can induce phase transitions and degrade performance.[99] Because charging behavior is linked to surface area and habit (i.e., crystallographic orientation), control of the nucleation and growth of battery materials is a key to improving performance. Research on aqueous oriented aggregation,[100] hydrothermal synthesis,[101,102] and bacterial synthesis[103] has been successful in creating the desired material properties through more environmentally benign routes. Habit matters because the surface termination type and the presence of heteroatoms on the graphene influence Li diffusivities. Zhang et al.[104] studied graphene−hematite (α-Fe_2O_3) interfaces with DFT calculations and found that N-doped graphene/Fe-O_3-Fe-R (where R is the bulk stoichiometric stacking unit) allowed for free diffusion of Li atoms. Developing new battery materials such as $TiNb_2O_7$[105,106] will require knowledge of the growth defects present at surfaces and how these relate to the formation of surface−electrolyte interphases (SEI) at high operating voltages. Adsorption, dissolution, nucleation, growth, and bacterial interactions that occur in these systems are discussed in sections 3 and 4.

1.2.5. Climate Effects of Mineral Dust Aerosols. Oxides and silicate minerals in the atmosphere can impact the Earth's climate in several ways. For example, oxide and silicates scatter incoming solar radiation into space, causing net cooling.[107] In addition, these minerals affect the Earth's climate through cloud formation in the atmosphere because they are good cloud condensation nuclei (CCN) and ice nuclei (IN). Although not well understood, details of the interactions between nuclei surfaces and water vapor are key to understanding the ability of oxides and silicate minerals as CCN.[108] A major gap in our knowledge was expressed in a review by Tang et al.:[108]

> *"...single minerals... and authentic dust samples... may not necessarily reflect mineral dust particles found in the troposphere. After being emitted into the troposphere, mineral dust particles will undergo heterogeneous reactions and cloud processing..., forming soluble inorganic and organic materials coated on dust particles.... Therefore, heterogeneous reactivity of ambient mineral dust particles can be largely different from those used in laboratory studies."*

Aerosols are still a large source of uncertainty in current climate models, with mineral aerosols often treated in an approximate manner.[109] Providing information on mineral aerosol surfaces related to radiative effects, CCN and IN particles, and heterogeneous reactions could significantly improve predictions of future temperate and precipitation patterns.

1.2.5.1. Warming and Cooling Effects. One example of mineral aerosol surface chemistry with significant implications has been recently recognized by Klingmüller et al.[110] In addition to the implications this chemistry has for human health (section 1.2.3), these authors studied the effects of

https://doi.org/10.1021/acs.chemrev.2c00130
Chem. Rev. 2023, 123, 6413−6544

anthropogenic air pollution on the adsorption of water vapor and subsequent radiative effects. By reducing water condensation, the reflectivity of the surfaces decreases warming at the top of the atmosphere. In a similar vein, Wang et al.[111] studied the interactions of Gobi Desert dust with anthropogenic pollutants. In addition to accelerating ozone formation, the altered dust stabilized the planetary boundary layer (PBL) which limited pollutant dispersal and increased primary pollution. These complex interactions among atmospheric compounds, mineral aerosols, atmospheric dynamics, and pollutant exposures demand further study and incorporation into climate models, especially on regional scales where health impacts are affected by temperatures and atmospheric circulation.

1.2.5.2. Cloud Condensation Nuclei Effects on Precipitation. A strongly related topic is the ability of mineral aerosols to act as CCN by adsorbing water vapor and forming droplets at lower relative humidities (RH) than would occur under homogeneous nucleation conditions. For example, Zamora and Kahn[112] analyzed satellite data to investigate the effects of dust aerosols on deep convective cloud (DCC) occurrences. These authors state "*Dust... has potentially large microphysical impacts on DCCs.... However, dust effects are difficult to identify, being confounded by covarying meteorology and other factors.*" Zamora and Kahn[112] conclude that "*Dust is robustly associated with a 54% increase in DCC prevalence.*"

Arub et al.[113] highlight the need to include mineral aerosols due to their significant impacts on the hygroscopicity parameter compared to ammonium and sea salts. The association of high population areas and high mineral aerosol loads in many regions makes this a more imperative one compared to the more dominant marine aerosols that exist largely over unpopulated areas of the Earth. Molecular-level studies of these aerosol−water interactions will aid our understanding of their physicochemical properties in the atmosphere.[114] As illustrated by the numerous examples in section 1.2, cross-fertilization of the disciplines that study natural and engineered systems will bring us to a more comprehensive understanding of these complex oxide− and silicate−water interfaces. The authors of this review are convinced that knowledge transfer across spatial and temporal scales help meet challenges in providing clean water and energy, producing food for a growing population, understanding environmental impacts on human health, and predicting the effects of anthropogenic climate change on global chemical cycling.

2. THEME 1: STRUCTURE AND DYNAMICS OF SOLID−AQUEOUS INTERFACES

2.1. Introduction

In a seminal paper, Irving Langmuir (1916) concluded that "*...in general, the distances through which the surface atoms are shifted from their original positions in the solid are small compared to the average distance between atoms...*" and "*...that the abnormal surface arrangement is usually limited to the surface layer only.*" The former is true for several oxides,[115,116] while the latter is not correct based on surface X-ray scattering studies that have shown that relaxations of atoms in the surface region can extend to four or more atomic layers deep (Langmuir speculated that for "*...the case of glasses and other oxygen compounds like quartz or calcite, the surface probably consists of a lattice of oxygens*")[116,117] Over 100 years later, Langmuir's conceptual model of solid surfaces in contact with a liquid or vapor (e.g., H_2O) is generally consistent with experimental observations,[116] although a minor but necessary modification of Langmuir's idea, that the surface is terminated by a lattice of O atoms, is that the surface is terminated by hydroxo and/or aquo groups.[7] Notwithstanding recent descriptions of the structure of oxide− and silicate−water interfaces, Langmuir was prescient in his thinking about these systems at the atomic/molecular level.

In this section, we discuss the advances of our understanding in the structure of the mineral surface upon contact with water in vapor or liquid forms, and the influence of the surface on the interfacial water structure and its dynamics. Finally, the role of ions on both the oxide and the water structure, interfacial processes such as (de)protonation, and parameters related to electric double layer theory such as interfacial potentials will be discussed (Figure 6). In keeping with the theme of this review, the strong influence of confinement and surface defects on the interfacial structure and dynamics will also be addressed. From these discussions, important questions arise such as how far from a solid surface are the aqueous solution structure and dynamics impacted, and *vice versa*, how deep is the effect of an aqueous solution on the solid itself?

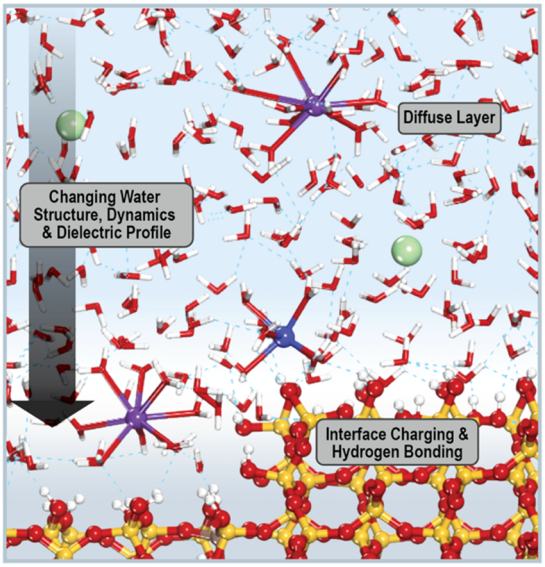

Figure 6. Schematic illustrating the interfacial structure of an oxide in contact with an aqueous salt solution. The synergistic influence of ions, surface sites, and water on one another, as well as accompanying processes such as (de)protonation and surface adsorption, lead to a highly complex environment. Different techniques can be used to access particular observables. Integration of this information, with the support of computational chemistry, is beginning to reveal the atomistic structure of the entire interfacial region and how it evolves under changing conditions.

2.2. Solid−Water Interfaces

2.2.1. Differences in the Surface and Bulk Structures of Solids. When nominally anhydrous metal oxides and silicates are exposed to water, the surface O atoms become hydroxylated,[5,7] and the hydroxide sites, XOH, can undergo protonation and deprotonation reactions.[118,119] These types of reactions are among the most important in the natural and technological worlds[3,120,121] and result in pH-dependent surface charge and potential, both of which are zero at a

https://doi.org/10.1021/acs.chemrev.2c00130
Chem. Rev. 2023, 123, 6413−6544

solid (sample)-specific pH value at the so-called point-of-zero charge (i.e., the pH_{PZC}).[122−124] (De)protonation reactions also result in the surface structures of O-based minerals undergoing relaxation or reconstruction. This is true because protonating or deprotonating one terminating O causes all of the neighboring bonds to relax. As pointed out by Brown,[125] the proton affinity of a terminating O depends on the protonation state of its neighbors. Thus, the assumption that the hydrated surfaces of this class of minerals are simple terminations of the bulk structure cannot be correct. However, until recently, this assumption was common[126] because of the lack of direct measurements of the surface structures of oxides in contact with water. Results of synchrotron-based, surface X-ray scattering studies have shown this assumption to be incorrect to various degrees based on structure determinations of hydrated oxide surfaces.[115,116,127−142]

2.2.1.1. Surface Restructuring from Vapor Phase Water. Water vapor adsorbs onto solid surfaces under ambient conditions, and accordingly the structures and compositions of oxide surfaces change in humid environments.[143−146] There have been several experimental developments in measurements of water uptake on oxide surfaces, including MgO, TiO_2, and Fe_2O_3,[7,147,148] as a function of controlled water vapor pressure allowing researchers to close the "pressure gap" described in the Introduction. One synchrotron-based technique that has been used to monitor the evolution and changes that occur in the surface structure as relative humidity (RH) increases is ambient-pressure X-ray photoelectron spectroscopy (APXPS) on a range of oxide surfaces.[149] In such studies, a clean well-ordered oxide-terminated single-crystal surface transitioned from a partially hydroxylated surface to a fully hydroxylated surface below 1% RH to a surface with adsorbed water layers 1 to 4 layers thick as the relative humidity increased. This surface evolution shows how much the structure and composition of oxide surfaces change depending on the amount of water vapor. The hydroxylation step is usually irreversible at 298 K, but the molecular water adsorption/desorption step is fully reversible.

Another important example of surface reconstruction with hydration is offered by Al-oxides which are found in the environment (e.g., α-Al_2O_3) and used in industrial applications (e.g., γ-Al_2O_3). Adsorbed water changes the interatomic spacing of the top surface plane and the layer below for single crystal α-Al_2O_3,[115] and there is a difference in water uptake for single crystal versus nanoparticle films that contain defect sites and nanoscale pores.[151] Furthermore, adsorption of organics (e.g., one monolayer of formic acid) can change the hydrophilic nature of the surface and the amount of water associated with Al-oxides.[150] The water uptake data monitored by a quartz crystal microbalance (QCM) and a cartoon representation of the change in the top most surface layer are shown in Figure 7.

2.2.1.2. Surface Restructuring from Liquid Water. An example of the relaxation/reconstruction that occurs when a metal oxide surface comes in contact with liquid water is the hydrated α-Fe_2O_3 (0001) surface. Crystal truncation rod (CTR) analysis of this surface revealed that it differs significantly from the three possible terminations of the bulk hematite structure (Figure 8) and consists of a two-domain structure, one with roughly equal numbers of hydroxyl groups coordinated by one and three $^{VI}Fe^{3+}$ and one with surface hydroxyl groups coordinated mostly by two $^{VI}Fe^{3+}$.[116]

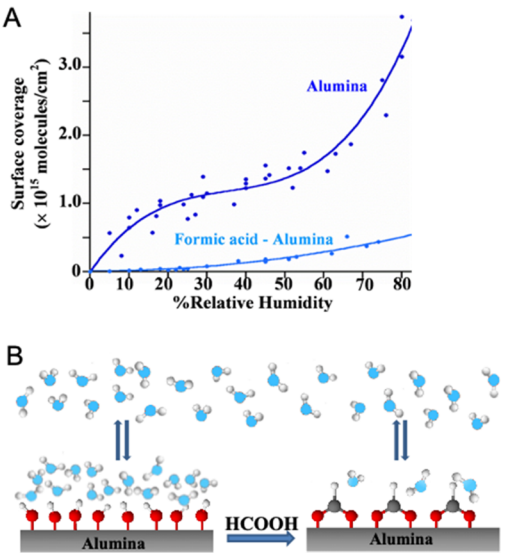

Figure 7. Adsorption of water onto hydroxylated γ-Al_2O_3 particles before and after their exposure to formic acid. (A) Calculated surface coverage by water molecules as a function of relative humidity, measured using quartz crystal microbalance technique. The dramatic decrease in water adsorption is linked to the change in the hydrophobicity of the surface following formic acid adsorption reaction. (B) A molecular-scale interpretation of surface structure and association with water for −OH-terminated vs $-O_2CH$-terminated alumina. Reproduced from ref 150. Copyright 2013 American Chemical Society.

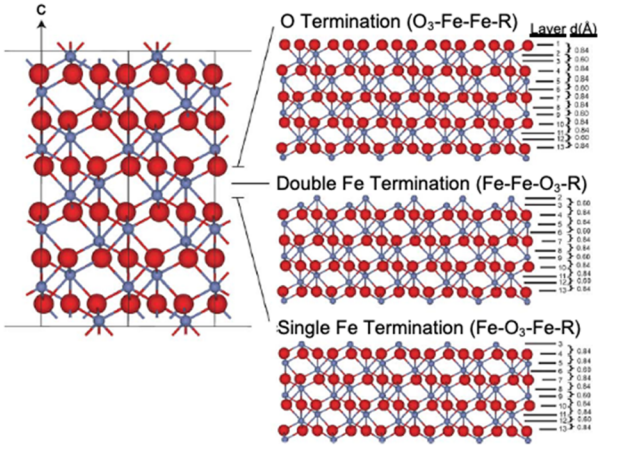

Figure 8. (left) Atomic-layer sequence of the bulk unit cell of the α-Fe_2O_3 structure along the [0001] direction. (right) Surface layer models of the three possible "clean" terminations: (top) the O-terminated surface, where O_3−Fe−Fe represents the three outermost layers of the (0001) surface, (middle) the double iron terminated (0001) surface, (bottom) the single iron terminated (0001) surface. Reproduced with permission from ref 116. Copyright 2004 Elsevier BV.

Reuter and Scheffler addressed the process of surface restructuring computationally by combining DFT with classical thermodynamics to determine the lowest energy structure of a metal-oxide surface in equilibrium with a gas phase (e.g., O_2 or H_2O).[152] This method, referred to as *ab initio* thermodynamics, expresses the surface free energy of the solid, γ, in equilibrium with a vapor in terms of the Gibbs free energy of the solid surface as a function of T and P and the number and chemical potentials of the atoms in the system. Such DFT-*ab*

https://doi.org/10.1021/acs.chemrev.2c00130
Chem. Rev. 2023, 123, 6413−6544

initio thermodynamic calculations on α-Fe_2O_3(0001) in the presence of water vapor showed the results of variations in surface energies for the different structures of hematite(0001) in equilibrium with water vapor. The $(HO)_3$-Fe-O_3-R termination was found to be the lowest energy surface in equilibrium with water vapor under the high $p(H_2O)$−low pO_2 conditions of the CTR experiments (Figure 9). $(HO)_3$−Fe−

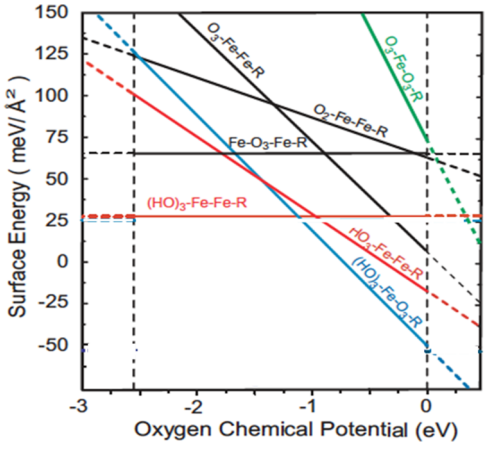

Figure 9. Surface energy vs O chemical potential for different hematite (0001) terminations. The vertical dashed line on the left is the binding energy of O in the bulk structure, and the vertical dashed line on the right corresponds to the energy of an O_2 condensate. Modified with permission from ref 116. Copyright 2004 Elsevier BV.

O_3 represents the three top layers of the (0001) surface of hydrated hematite, with each outermost OH group bonded to a single $^{VI}Fe^{3+}$ and the second-layer $^{VI}Fe^{3+}$ bonded to three O atoms in the next layer down.[116]

2.2.2. Surface Wetting. *2.2.2.1. Gas-Phase H_2O Sorption on Hydrophilic/Hydrophobic Surfaces.* The extent of water adsorption is dictated by several factors including the nature of the water−surface interactions, which depend upon the hydrophilic or hydrophobic nature of the surface, and the partial pressure of water vapor in the air. Studies of planar amorphous SiO_2 surfaces, using a Si crystal covered with its native oxide in contact with water vapor, by ATR FTIR spectroscopy have shown an evolution of the adsorbed water layer structure by monitoring the H-bonding network in the O−H stretching region.[153] Between 1 and 30% RH, the water layer has been described as a H-bonded "ice-like" network owing to the red-shifted vibrational frequencies indicating either strong H-bonding or more H-bonds per water. At intermediate % RH, this structure continues, followed by a more "liquid-like" structure (denoting a blue-shift in the OH resonance and weaker H-bonding) as more H_2O molecules adsorb onto the surface. Above 60% RH, the water layer continues to grow.[153] More recent work based on analysis of water vapor adsorption onto silica found that water in the first layer bound to surface hydroxyl groups via two H-bonds. The adsorbed structures were stabilized by H-bonds with the O and H atoms of the surface hydroxyl groups. Additional H-bonds formed between these adsorbed H_2O molecules. Onto this monolayer, additional H_2O molecules adsorbed to form the next layer.[154] Surface functionalization of silica to form a more hydrophobic surface inhibited the "ice-like" structure of adsorbed water from forming at low % RH due to the loss of surface silanol groups in the functionalized surface.[155] Changes in the bulk water contact angle due to surface functionalization were also consistent with the observed structure and thermodynamics of the adsorbed water layer on the functionalized surface in equilibrium with the vapor phase.

Studies using vibrational sum frequency generation (vSFG) have investigated water layers on amorphous fused silica,[156] finding that at low RH H_2O molecules preferentially adsorb into a weakly H-bonded state, and this H-bonded water *does not* interact with surface-bound hydroxyl groups but instead weakly interacts with surface siloxane groups. These data suggest that amorphous hydroxylated silica has a hydrophobic character even *without* functionalization, as water interaction is controlled by the site density of silanols which was also observed recently in a study using Overhauser dynamic nuclear polarization and surface force measurements.[157]

Water adsorption from the gas phase has also been described as producing "patchy surfaces,"[146] which suggests that even for single crystal oxide surfaces, there is a level of heterogeneity that can impact the structure and chemistry of these surfaces. Studies that combine experimental data with molecular simulations provide new insights into water uptake from the vapor phase onto solid surfaces including oxides and silicates.[158] In particular, the particle size and dimensionality of surface-terminated domains (nanopores) in water uptake are important, and hydrophilic mineral surfaces can adsorb water films of various thicknesses and structures. Smaller particles <1 μm can have ∼5 monolayers of water on the surface at higher relative humidity, whereas micrometer-sized particles show much thicker water films up to several thousand monolayers. Additionally, water films exhibit vibrational spectroscopic signals similar to liquid water but with a highly disrupted network of H-bonds based on the attenuation of peaks at lower wavenumber (red-shift) associated with highly coordinated water molecules.

New nanoscale insights on water adsorption on mineral surface have recently been achieved using IR nanospectroscopy along with molecular simulations.[159] Water film evolution on an individual hydrophilic mineral nanoparticle, in this case gibbsite ($Al(OH)_3$), reveals the growth to be anisotropic where edges of different crystallographic planes and defects showed preferential adsorption of water from the vapor phase. Upon cooling, thicker water films form on these mineral nanoparticles from condensation. The resulting water film that engulfs the nanoparticle is anisotropic and has a non-uniform thickness. As shown in Figure 10, the film starts on one edge of the particle surface and then spreads out. Such gas-phase water adsorption studies on hydrophilic/hydrophobic surfaces start to provide a molecular picture of these interactions when combined with MD simulations. Additionally, these studies point towards an important role for particle size, pore size and chemistry, defect sites, and inhomogeneities, all resulting in a "patchy" nature to mineral surfaces on the nanoscale.

2.2.2.2. Liquid-Phase H_2O at the Hydrophilic/Hydrophobic Surfaces. The interactions of water with oxide- and silicate-surfaces can be differentiated into metal−water, O−water, and other surface functional group−water interactions. However, for solids in contact with liquid water, water−water interactions also become important. Depending on the relative abundance of atoms and surface features, water−solid interactions and the resulting interfacial water structures and interfacial water dynamics vary widely.

https://doi.org/10.1021/acs.chemrev.2c00130
Chem. Rev. 2023, 123, 6413−6544

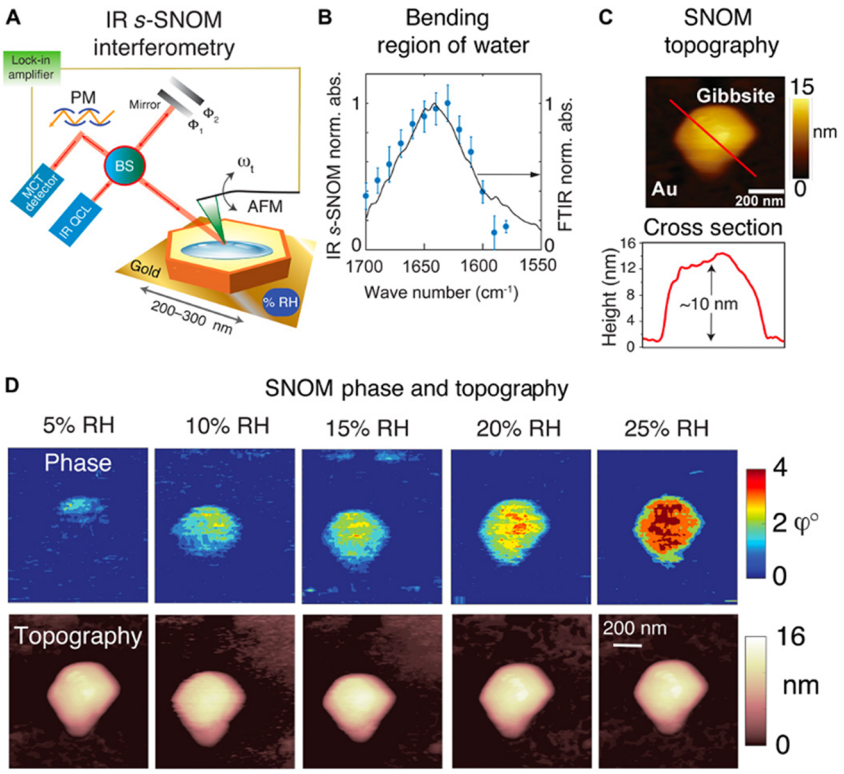

Figure 10. Anisotropic growth of water film on gibbsite $Al(OH)_3$ surface measured using IR nanospectroscopy (IR s-SNOM). (A) IR s-SNOM experimental set-up, including two-phase homodyne detection, beam splitter (BS), parabolic mirror (PM), and mercury cadmium telluride (MCT). (B) Measured IR s-SNOM absorbance (blue dots, normalized) over a gibbsite particle exposed to ambient atmosphere. SNOM phase images were used to obtain these values with the quantum cascade laser (QCL) tuned between 1580 and 1700 cm^{-1}. This SNOM-derived spectrum is compared to an analogous FTIR spectrum (black line, normalized). (C) Topography of the basal (001) gibbsite nanoparticle surface measured using SNOM, with its corresponding height cross section collected at 0% RH. (D) IR s-SNOM phase images collected with the QCL tuned at 1630 cm^{-1} and their corresponding topography images. These images illustrate anisotropic growth of water film, which initiates at one edge of the gibbsite nanoparticle. Reproduced with permission from ref 159. Copyright the Authors, some rights reserved; exclusive licensee AAAS. Distributed under a CC BY-NC 4.0 license http://creativecommons.org/licenses/by-nc/4.0/.

Water−SiO_2[136,160−162] interfaces have been studied in detail experimentally and computationally. Fluid−solid interactions control both the structure of the water adsorption layer as well as the macroscopic contact angle. For example, Si samples with a SiO_2 layer at the surface readily adsorb water, and the water contact angle can be reduced to <5° upon treating the Si sample with UV/O_3 to generate the oxide layer; such a low contact angle indicates that the surface is nearly saturated with silanol groups and is hydrophilic.[160] Indeed, the water contact angle was found to gradually reduce to 0° for a surface hydroxyl density of greater than 4.6 nm^{-2}; such low contact angles were attributed to the presence of H-bonds at the SiO_2 surface.[157] At the quartz (101) water interface, X-ray reflectivity measurements[127] and vapor adsorption measurements[154] indicate the adsorption of up to six H_2O molecules per surface hydroxyl (although at high adsorbed water to surface hydroxyl ratio, some of the adsorbed water is likely not directly associated with a silanol site but rather a bridging siloxane or coordinated water).

Similar adsorbed water structures are found for a variety of important minerals. For forsterite, MD and incoherent neutron scattering (INS) show that two H_2O molecules adsorb per Mg atom, and the oxygen in the water molecule bonds to the metal ion, and forms H-bonds to the oxygen atoms of the solid.[163] Water structures at numerous other mineral surfaces, including hematite,[164] rutile, cassiterite,[165−168] and clay surfaces,[169] have also been studied. The adsorption of water leads to formation of hydrated mineral layers with thicknesses of a few Angstroms to a few nanometers. Using fast force mapping AFM to measure the water structure between a silica AFM tip and a boehmite (010) surface, water was found to be structured up to 1 nm away from the boehmite with the largest water density appearing near surface hydroxyl sites.[170]

Although experiments indicated general similarities in the water structure at different oxide surfaces, MD simulations have shown that water on oxide surfaces can generate counterintuitive phenomena particularly with respect to water droplet formation and surface wetting. For example, Hu and Michaelides's[171] simulations revealed that a 2D water layer formed on the gibbsite plane of kaolinite owing to the underlying ability of the mineral to donate and accept hydrogen bonds. The top view of the water film reveals a six-range arrangement of water molecules that follows the surface structural motif (Figure 11B), while the side view (Figure 11A) clearly highlights the absence of options for interactions with water, i.e., additional water molecules would not be able to find a docking point (dangling bonds or lone electron pairs). Other studies[172,173] showed a similar water structure as that in Figures 11A,B for the fully-hydroxylated sapphire (0001) plane. This primary water layer that lies immediately at the surface is more or less identical to the (001) plane on kaolinite or the gibbsite basal plane. The hydrophobic character of a water film on a generic surface with strong structural similarities to the above discussed faces was also

https://doi.org/10.1021/acs.chemrev.2c00130
Chem. Rev. 2023, 123, 6413−6544

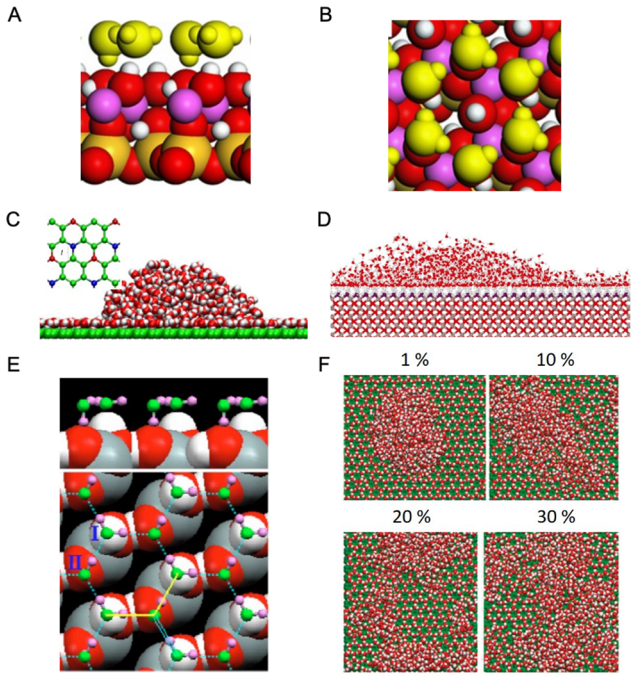

Figure 11. Hydrophobic water layers on hydrophilic surfaces. (A) Side and (B) and top view of a water film on the gibbsite plane of kaolinite.[171] (C) Water droplet on a water film that is formed on a generic surface with a hexameric structure.[174] (D) Water droplet spreading on a hydroxyl terminated sapphire (0001) plane. (E) The hydrophobic water layer on a quartz (0001) plane.[179] (F) The effect of the quantity of defects on the persistence of the hydrophobic water layer. (A,B) Adapted with permission from ref 171. Copyright 2007 Elsevier. (C) Adapted with permission from ref 174. Copyright 2009 American Physical Society. (D) Adapted from ref 175. Copyright 2011 American Chemical Society. (E) Adapted with permission from ref 179. Copyright 2006 American Physical Society. (F) Adapted from ref 182. Copyright 2011 American Chemical Society.

observed in simulations,[174] which found that beyond this primary (hydrophobic) water layer, the secondary water prefers to form a drop on the water layer instead of spreading (Figure 11C). Because the "hydrophobic" water layer has low energy, it is by no means clear that it will disappear in the presence of more water. The presence of such water films may therefore have profound consequences on interfacial properties and on interactions with solutes. The low surface energy of these kinds of secondary hydrophobic surfaces of otherwise hydrophilic surfaces may contribute to the stability of the underlying primary solid surfaces. To what extent such well-defined water films can form and affect properties on crystal planes with structures that do not allow such hexameric structures warrants further study.

In contrast, for sapphire (0001) surfaces, the computational results of Argyris et al.[175] indicate support for the view that water forms a complete first hydration layer on the hydroxylated oxide with excess water molecules forming a small droplet (Figure 11D). The formation of the first hydration layer is indicative of a pristine hydrophilic surface. Recent experiments corroborate that appropriate cleaning protocols lead to complete wetting of the sapphire (1120) and (0001) planes, with accompanying computational results suggesting these surfaces are super-hydrophilic.[176] However, other experiments have suggested that hydroxyls increase the hydrophobicity of alumina,[177,178] revealing the evolving and often conflicting state of understanding around this surface. Interestingly, in the case of the quartz (0001) surface, simulations show a hydrophobic hexameric water structure consistent with several other oxides, but they do not reveal dangling surface hydroxyls (Figure 11E),[162,179] unlike the alumina surface of kaolinite where dangling surface hydroxyls are located in the center of the adsorbed water hexamers (Figure 11A). Molecular dynamics simulations on several aqueous hydrophobic surfaces have shown the systematic formation of a well-defined 2D-H-bond network[180] of the water molecules in the layer above these surfaces.[181] While these surfaces do not have hexameric structural patterns, the distribution of H-bonded rings in this 2D-layer of water is preferentially centered on hexamers.[180]

To what extent details of the surface structure, such as lattice parameters or dipole moments, affect the structure of the water layer has been studied for generic surfaces in much detail.[182,183] For example, a hexagonal solid lattice was simulated with varying amounts of point defects, and in all cases the surface was completely covered by the primary water layer. However, increasing the density of point defects at the surface affected the spreading of a water droplet formed on the primary water film revealing that such defects changed the conformation of the primary water layer (Figure 11F).[182,183] These results suggest that surface heterogeneity can minimize the hydrophobicity of this primary water layer.

2.2.3. H-Bond Structure of Water at Mineral Surfaces.

Thus far, we have primarily considered the position of water molecules at the surface and subsequent wetting behavior when surfaces are exposed to water vapor or liquid water. For oxide or silicate surfaces submerged in water, the balance between hydrophobic and hydrophilic interactions also dictates the microscopic arrangement at the resulting solid−water interface.[157,181,184−188] The strength of these interactions as manifested in the hydrogen bonds is also important to understand, not only with respect to structure but the dynamics at oxide− and silicate−water interfaces. At the interface, one expects water to maximize water−surface H-bonds at hydrophilic surface, whereas dangling free OH groups from water are expected in hydrophobic environments where the surface H-bonding sites are insufficient or too weak. Tian and co-workers coined the term the bonded interfacial layer (BIL) to describe this water immediately adjacent to a solid that is structurally distinct from bulk-like water owing to interactions or the environment presented by the surface (Figure 12A).[189,190] As shown thus far throughout section 2, H_2O molecules have directional interactions and can form a wide variety of networks based on interactions with surface groups and other H_2O molecules leading to complex and varied BIL−water structures and dynamics.[184] The BIL−interfacial structure emerges through a competition between hydrophilic surface−water interactions and collective water−water interactions.[11,157,181,184,185,187,188] Structural, dynamic, and thermodynamic properties of interfacial water are correlated as highlighted by Monroe et al.,[184] who concluded that the surface patterns control not only the structure but the dynamics of interfacial water and that the interfacial water orientational entropy, diffusivity, and H-bonding properties are intrinsically connected.

Within the BIL, Pezzotti et al.[181] introduced the notion of vertical- and horizontal-order of the H_2O molecules at solid−water interfaces as a measure of the molecular behavior of the surface (Figure 12B). The V- and H-order descriptors directly

https://doi.org/10.1021/acs.chemrev.2c00130
Chem. Rev. 2023, 123, 6413−6544

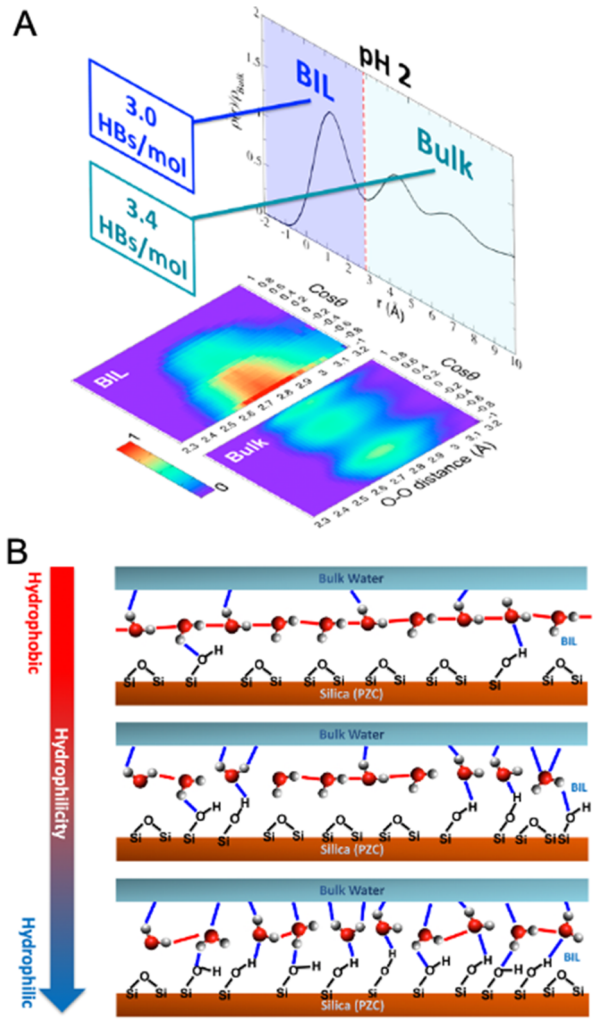

Figure 12. H-bond structure of water at solid surfaces. (A) Water density profile (r) with respect to the distance from the neutral silica surface (at the PZC of silica, pH ∼2) determined from molecular simulations. The bonded interfacial layer (BIL), the average water coordination per molecule (HBs/mol), and the angle with respect to surface normal (θ) are shown. Red−purple scale represents the probability of finding water with the corresponding angle and O−O distance. (A) Adapted from ref 11. Copyright 2020 American Chemical Society. (B) Scheme illustrating the general organization of water in the BIL of aqueous silica at the PZC with the horizontal order (H-order) shown with the red connectors and the vertical order (V-order) shown with the blue connectors. The scheme illustrates a BIL going from predominant H-order (hydrophobic, top) to predominant V-order (hydrophilic, bottom), via an intermediate balance between H- and V-orders (middle). The schemes also illustrate how the surface chemistry (silanols and siloxanes) influences the balance between H-/V-orders, and vice versa.

assess the competition between surface−water interactions and (collective) water−water interactions in the BIL. The V-order sums solid−water and BIL−water H-bonds that are formed with the subsequent bulk water or diffuse layer. The H-order measures the extent of collectivity in BIL water−water H-bonds, the ultimate H-order being the 2D-network with 1.7−2.0 H-bond/mol values revealed at the air−water interface as well as at notoriously hydrophobic surfaces like boron nitride and graphene.[180,181,191] At these interfaces, the V-order (less than 0.7 HB/mol) measures the H-bonds between BIL−water and the subsequent water layer.[180,181,191] Amorphous silica also has a large H-order with a smaller V-order that grows with increasing surface silanol density.[192] In contrast, the (0001) surface of α-quartz not only possesses a distinct horizontal order, Figure 11E, but also a highly organized V-order of BIL−water through a H-bond 5-membered ring motif that is found repeated over the surface.[162,191] For both amorphous silica and quartz surfaces at the pH_{PZC}, the BIL is composed of one water layer at the direct surface, roughly 3 Å thick.[190,191,193−195]

Similar molecular structural characterizations have been obtained for Al- and Ti-oxide aqueous interfaces.[196−204] Taking the example of α-Al_2O_3, there is a diversity of surface morphologies with the (0001) facet being rather planar with a high density of aluminols, while other facets such as the $(11\bar{2}0)$ or $(1\bar{1}02)$ have highly-corrugated surface morphologies made of channels with separate layers of outer- and inner-aluminols that dictate the water accessibility to the surface sites and competitive aluminol−aluminol intrasurface interactions that modulate the balance of BIL−water V-/H-orders. While the BIL−water H-order of the collective 2D H-bonding network prevails at the (0001) α-alumina aqueous interface,[181] a V-order has been identified at, e.g., the $(11\bar{2}0)$ aqueous interface.[205] Understanding the BIL−water at the (0001) alumina aqueous interface has been challenging and elusive for experiments and simulations:[132,181,196,206] the basic pK_a of the aluminols at the (0001) α-alumina aqueous facet[207] leads to only $^1/_3$ of AlOHs being H-bonded to BIL−water,[181] which in itself explains the appearance of the collective H-order of the 2D H-bonding network in the BIL as a consequence of maximizing water−water interactions.

2.2.4. Dynamics (Vibration, Rotation, Diffusion) of H_2O at a Hydrophilic/Hydrophobic Surface. At an interface, many properties of water, especially those depending on H-bonding, are expected to be modified. Yet vibrational sum frequency generation (vSFG) experiments on the vibrational relaxation of the OH stretch at the SiO_2−water interface were consistent with bulk-like behavior.[208] However, later this observation was suggested to be likely due to an artefact of the vSFG response that samples bulk-like water in the presence of an interfacial electric field,[209] a hypothesis that was tested in experiments where the lifetime increased to $T_1 \sim 600$ fs with added electrolyte (Figure 13).[210] The rationale for

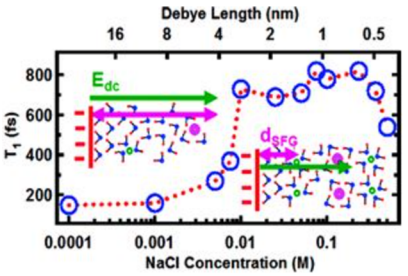

Figure 13. Impact of NaCl concentration on the observed OH stretch vibrational relaxation dynamics at SiO_2 water interfaces. Adapted from ref 211. Copyright 2020 American Chemical Society.

slower interface vibrational relaxation compared to the bulk ($T_1 \sim 250$ fs) was a reduced number of H-bonding partners at the interface compared to the bulk aqueous environment. The influence of H-bonding on vibrational relaxation was tested in an experiment that probed the OH stretch of HOD diluted in D_2O at the silica surface, revealing that the more strongly H-bonded the sampled species are, the faster the rate at which

https://doi.org/10.1021/acs.chemrev.2c00130
Chem. Rev. 2023, 123, 6413−6544

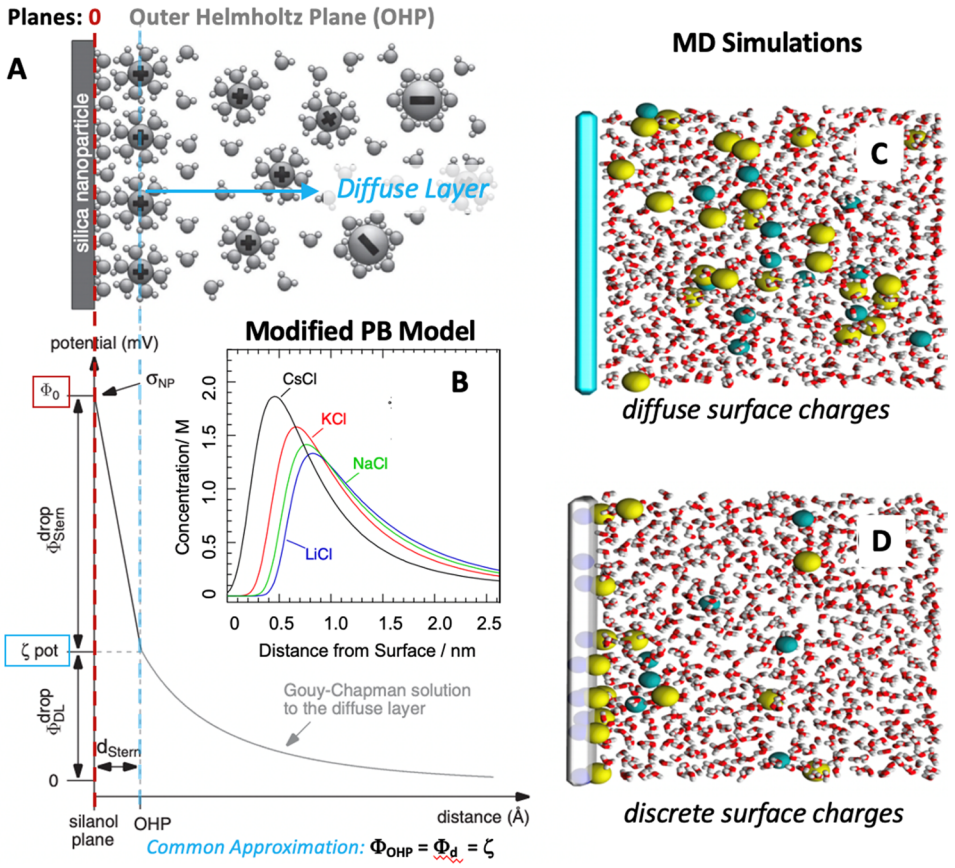

Figure 14. The electrical double layer. (A) Schematic of the electrical double layer at a charged silica surface and the corresponding changes in potential as a function of distance from the surface. Modified with permission from ref 223. Copyright 2016 Wiley-VCH. The surface oxygen sites of silica mark the 0-plane, which corresponds to the surface potential Φ_0, while the ions are shown at the outer Helmholtz plane (OHP). The potential at the OHP (Φ_{OHP}) is often approximated by the measurable ζ potential (B). Simulations of the ion distribution at a charged silica surface as a function of distance using a modified Poisson−Boltzmann model that incorporates hydration repulsion.[224] (B) Adapted from ref 224. Copyright 2015 American Chemical Society. (C) Classical MD simulation of aqueous sodium chloride solution at a carbon surface with a diffuse negative surface charge.[225] (C) Adapted from ref 225. Copyright 2014 American Chemical Society. (D) MD simulation of an aqueous sodium chloride solution at a carbon surface with discrete surface charge.[225] (D) Adapted from ref 225. Copyright 2014 American Chemical Society.

vibrational energy transfers.[210] The impact of ions was to accelerate the vibrational relaxation by reorienting water H-bonds from out-of-plane (towards the SiO_2 surface) to in-plane resulting in a H-bonding environment more similar to the hydrophobic air-water interface.[211]

To determine the effect of water orientation on vibrational relaxation at interfaces, the dynamics of water at positively and negatively charged Al_2O_3 surfaces (pH 4 and 10) were probed with the expectation that reversing the charge of the solid should change the direction of the dipole moment of water. (Although recent work has suggested the IEP of the (0001) facet of alumina is at pH 4.)[212] Surprisingly, no difference in dynamics was observed. Rather, the OH stretch lifetime was found to be faster ($T_1 \sim 100$ fs) at the aqueous Al_2O_3 interfaces than in bulk water and barely impacted by the presence of ions,[205] be they cations,[213] or anions,[214] as well as the nature of the Al_2O_3 surface, e.g., (0001) vs $(11\bar{2}0)$.[215] The difference in water dynamics observed for silica compared to alumina surfaces in aqueous solutions suggests that the higher density of surface hydroxyls on Al_2O_3 ($\sim 15/nm^2$) vs SiO_2 ($\sim 5/nm^2$) led to the faster dynamics, likely related to an increased density of H-bonded states and a red-shift in the OH stretch SFG spectra. This may be related to the correlation between the higher density of vibrational states at lower frequencies in the OH stretch region of the spectrum seen for bulk ice vs water, and the faster OH vibrational relaxation of bulk ice vs water.

The diffusion of water is critical but little is known about this process at oxide− and silicate−water interfaces from either a computational or experimental perspective under geochemically relevant conditions, although studies of water confined at surfaces of SiO_2[216] and TiO_2,[217] have been reported. While there have been investigations, computational and experimental, of H-bond dynamics at air−water interfaces,[218] there are few reported on oxide or silicate surfaces.[165] A computational study found shorter H-bond lifetimes at the aqueous−hematite (0001) interface.[219] Several MD studies address the variation of water diffusion rates near oxide surfaces. Holmboe and Bourg[220] and Greathouse et al.[221] have both demonstrated the variation of the diffusion rate for water and Na^+ across smectite nanopores, while Churakov[222] examined water and Cs^+ at or near the surface. Nevertheless, more is required to aid in our understanding of diffusion and H-bond dynamics at oxide− and silicate−water interfaces and address the current knowledge gap.

https://doi.org/10.1021/acs.chemrev.2c00130
Chem. Rev. 2023, 123, 6413−6544

2.3. Solid−Electrolyte Interfaces: Including Adsorbate (Ion) Structure and Dynamics

2.3.1. Electric Double Layer (EDL) Model Review. EDL models are widely used to describe charged surfaces in contact with an electrolyte solution. Depending on the pH, (oxyhydr)-oxides of Si, Fe, Mn, Al, and Ti behave as amphoteric acids, as they can either take up or release H^+, making the surface positively or negatively charged, respectively. The total surface charge is neutral at the pH_{PZC}. As the pH is increased or decreased away from the pH_{PZC}, a net surface charge results from deprotonation or protonation, respectively, which, in turn, are compensated by the accumulation of ions bearing the opposite charge with respect to the surface, building up the EDL. The EDL that develops at the interface between a solid surface and the surrounding aqueous solution is a complex environment that controls the chemical reactions taking place.[3]

EDL theory has its origins in the work of Helmholtz in the 1850s as an explanation of the behavior of aqueous solutions near charged electrodes. Over time, theories have evolved based on the work of Gouy and Chapman to describe water and aqueous ion structures in terms of the electrostatic potential from the surface with a varying capacitance dependent upon charge and solution ionic strength (I). Later, Stern combined concepts from Helmholtz and Gouy−Chapman, generating a condensed ion layer near the surface and the diffuse layer of enriched counter ions that decayed some distance from the surface. Grahame integrated both specific and nonspecific adsorption within the Stern layer (at the inner and outer Helmholtz plane, respectively), and the modern notion of the EDL was born.[226] The resulting molecular schematic of the EDL is shown in Figure 14A with the corresponding decay profile of the potential away from the charged surface.

The influence of ion identity has been introduced in various ways into EDL models based on hydration volume and whether an ion binds specifically (with concomitant dehydration, chemisorption, inner-sphere adsorption) or nonspecifically (maintaining its hydration sphere, physisorption, outer-sphere adsorption) to a surface. As the thickness of the Stern layer, and in turn the capacitance, depend on these different modes of ion binding, as well as the ionic radii and the presence of surface hydration layers, the inner layer capacitance was determined by Sverjensky for a wide variety of mineral oxides and ions by regression of surface charge data from a variety of studies under a range of pH and concentrations to compile a comprehensive list of proposed EDL structures based on a triple layer model that separates the Stern layer into two layers with different capacitances.[227] This triple layer model, which involves site binding and is one example, and surface complexation models (SCMs) for describing the EDL as described in section 2.3.5. In contrast to empirical or semi-empirical models such as SCMs, others have utilized a variety of modified Poisson−Boltzmann models that incorporate parameters such as ion volume, polarizability (including the corresponding dielectric decrement caused by hydrated ions),[228] and repulsive non-electrostatic hydration forces[224] to simulate the interfacial structure as a function of oxide and cation identity, which often results in the emergence of the expected Stern and diffuse layers in the simulation (Figure 14B).[224]

Beyond the continuum models, MD simulations may provide a more detailed description of the EDL including steric effects, ion specificity, changes in the surface morphology, and, depending on the level of description, polarization and charge transfer effects.[10] Classical molecular dynamics simulations (CMD), where the forces acting on the atoms are calculated from empirical potentials, have the advantage of a relatively low computational cost, which permits treating systems of 100 000s of atoms for 100s of nanoseconds. Accordingly, CMD simulations can describe ion equilibrium behavior for a relatively dilute system corresponding to Debye lengths on the order of 10s or 100s of nanometers. On the other hand, "*ab initio*" molecular dynamics (AIMD) simulations, that explicitly include the electronic structure, permit an accurate description of the Stern layer, taking into account ion specificity, polarization, charge transfer, and reactivity that cannot be easily incorporated in the force field approach. The AIMD drawback is the limited size of the systems (up to few thousand atoms for 10s of nanoseconds) which can be currently treated with modern computational resources. However, such a limitation is overcome by the use of machine learning (ML) that extends the "*ab initio*" level of accuracy to system sizes typically used within force field-based CMD calculations. A recent example for a mineral oxide is the development and use of a ML potential for the titania−water interface.[229−232]

An important aspect for mineral oxides and silicates is that, unlike the case of metals or semiconductors where the overall charge is delocalized, the surface charge may be highly localized and heterogeneous.[233] As such, the complexity of the surface structure calls into question the utility of the simple mean-field view of the EDL based on ensemble values such as the capacitance, surface charge density, and surface or Stern layer potential. CMD simulations of a charged surface in contact with different alkali chloride solutions found that the structure of ions and water near the surface changed significantly when discrete rather than diffuse surface charges were incorporated into the simulation (Figure 14C,D).[225] Also, for the CaF_2−water interface, a recent study combining AIMD simulations and interface selective vibrational spectroscopy pointed out the impact of localized charges on the water structure and dynamics at the interface.[234] Additionally, the relative position of ions with respect to the surface, an indicator of ion affinity, often differs depending on the model used. For example, the Poisson−Boltzmann model that incorporated hydration repulsion interactions predicted that Cs^+ resided closer to the surface than Na^+,[224] whereas MD simulations reached the opposite conclusion.[225] However, we note that one challenge in comparing both theoretical and experimental studies is differences in the conditions they are simulating or measuring, respectively, which varied in these two instances in terms of not only salt concentration but also of surface charge density. As will be discussed, recent experiments and simulations suggest that relative trends in the ion affinity for a mineral oxide can vary with pH and the extent of surface deprotonation.[235−237]

Several techniques can be used to provide estimates for the fundamental surface charge density based on charged sites at the mineral surface and its dependence on pH. One of them is potentiometric acid−base titrations, where the equilibrium pH value of the colloid dispersion is measured as a function of the added volume of titrant, namely a strong acid or strong base, and compared with a reference that does not contain the colloid.[238−240] The microscopic interpretation of the values obtained for the charge density is, however, not straightforward, as the release of protons cannot be distinguished from

https://doi.org/10.1021/acs.chemrev.2c00130
Chem. Rev. 2023, 123, 6413−6544

the binding of hydroxide and vice versa.[241] Additionally, potentiometric techniques are not suitable for large planar samples with small surface area to volume ratios, which can complicate the interpretation of nonlinear optical or X-ray spectroscopy measurements carried out on larger samples as the fundamental surface charge density is not explicitly known.

Another important parameter related to EDL theory that can be determined experimentally is the zeta potential (ζ) (see section 2.3.3.1.3). In the presence of millimolar concentration of ions, this potential is often used to approximate the potential at the start of the diffuse layer, sometimes referred to as the Stern layer or diffuse layer potential (Φ_d, Figure 14).[223,242] Such an approximation is challenging, as the location of the slip plane where this ζ potential arises is generally not known in the experiments, making it difficult to relate to classical EDL models. However, atomistic simulations[243] including non-equilibrium molecular dynamics simulations[200,244] have revealed the position of this slip plane to be approximately 15−20 Å from the charged surface. The ζ potential unlike potentiometric measurements that report on the fundamental surface charge density can be measured on both colloidal and planar samples.[245] Yet knowledge of both the fundamental surface charge density and the ζ potential are generally required to provide information about the composition of the Stern layer.[242] Furthermore, simulations suggest that even in the presence of a neutral surface, different extents of binding or distance of approach of cations versus anions in solution can result in a non-zero ζ potential as a result of the uneven distribution of cations and anions in the direction normal to the surface,[244] making complementary knowledge of the fundamental surface charge density helpful in interpreting ζ potential measurements.

Valuable information on the structure and net order of water in the EDL at the oxide− and silicate−water interface can also be obtained from second harmonic generation (SHG) and SFG spectroscopy.[237,246−253] X-ray techniques that can resolve the position of ions in regions near the surface also provide molecular information about the EDL structure, which will also be discussed below. Overall, a new understanding regarding the EDL is emerging that goes beyond primitive ions models in which Cl^- is not like I^-, for instance, or Na^+ is not the same as Cs^+. Likewise, the relative permittivity in the diffuse layer is probably well approximated with water's bulk value, but the Stern layer's permittivity, thickness, and capacitance are still underdetermined and can currently only be employed as rough estimates,[254] similar to the sketch from the previous review[3] (Figure 1A). Spatial variations of these properties are generally accounted for as mean field approximations, but how good such approximations are is just now becoming clear: nonlinear optical, electrical impedance, and X-ray spectroscopic experiments indicate the mean field (Gouy−Chapman−Stern) model can underestimate the total potential drop across the silica−water interface by up to 80−90% percent at high ionic strength and around 50 percent at low ionic strength.[253]

2.3.2. Structural Measurements and Theories. Numerous experimental studies explore the structure and dynamics of oxides and silicates in the presence of "simple" aqueous ions such as alkali halides. Wherever possible, we focus on the most recent examples that have benefited from advances in computational power, synchrotron light sources, laser technology, and AFM capabilities.

2.3.2.1. Crystalline Solids. Ion-specific effects at oxide− and silicate−water interfaces are often predicted based the ability of either the ion or the oxide to structure water (related to the law of matching water affinities[255] by Collins). Ions causing a similar effect on the structure of water as the oxide surface are easily adsorbed, whereas ions that affect water structure differently than the oxide surface tend not to adsorb as strongly. This model accurately predicts that small highly hydrated cations such as Li^+ and Na^+ adsorb more strongly to metal oxides such as α-Fe_2O_3, α-Al_2O_3, α-TiO_2, and ZnO, as these oxides are considered "structure-promoting", whereas metal oxides such as α-SiO_2, V_2O_5, MoO_3, and WO_3 are considered "structure-breaking", adsorbing Cs^+ preferentially over Na^+. However, sample preparation and treatment may result in a regular adsorption sequence;[256] altering the surface charge density by changing the pH has also affected the preferred adsorbing ion sequence of the same oxide.[235−237] Additionally, the behavior of simple monovalent electrolytes depends on the facet of a given solid.[257]

Measuring the structure of the EDL at oxide− and silicate−water interfaces and its changes as a function of sorbent type and crystallographic orientation, solute type and concentration, and solution variables such as pH and I, is a challenging objective. Synchrotron long-period X-ray standing wave-fluorescence yield spectroscopy[258,259] has been used to probe the vertical distribution of atoms at a number of different types of interfaces, including oxide− and silicate−water interfaces,[142,260] and mineral surfaces coated with microbial biofilms or thin organic films.[261−269] Similarly, synchrotron XRR measurements and resonant anomalous XRR have proven useful at exploring the EDL structure at oxide and silicate surfaces.[127,133,270,271] In one example, synchrotron XRR measurements were combined with MD simulations to identify the structure of the muscovite mica/aqueous interface.[128] The authors observed that the ions formed inner-sphere complexes at two different sites on mica: a cavity site and a "triad" site, so-called because of the interaction with three surface O atoms. The larger cations preferred the cavity sites, whereas Li^+ and Na^+ preferred the triad site, but in all instances inner-sphere complex formation dominated over outer-sphere complex formation. The authors proposed that the site preference of the ion was determined by its preferred coordination number. The data also revealed water ordering out to ∼1 nm from the surface, on the order of one Debye length based on the salt concentration in the model.

Nonlinear optical techniques including SFG have been utilized to monitor crystalline oxides such as alumina and rutile.[272] Some of these studies will be discussed later in the section discussing surface heterogeneity and defects (vide infra).

2.3.2.2. Amorphous Solids. Amorphous planar substrates are ill-suited for certain types of measurements such as X-ray spectroscopies owing to the symmetry within the plane of the surface. However, one marked exception is synchrotron-based AP-XPS using "tender" X-ray energies (1−5 keV).[273−275] Although *in situ* AP-XPS provides useful information about surface chemical reaction products under more realistic conditions than conventional *ex situ* XPS studies carried out under UHV conditions, AP-XPS cannot be used by itself to quantitatively investigate interfaces in an element-specific and chemical-state-specific way with subnanometer resolution of the z-position of a chemical element above a solid−water interface. Nemšák et al.[276] got around this limitation utilizing X-ray standing waves to excite photoelectrons, a technique known as standing wave ambient pressure photoelectron

https://doi.org/10.1021/acs.chemrev.2c00130
Chem. Rev. 2023, 123, 6413−6544

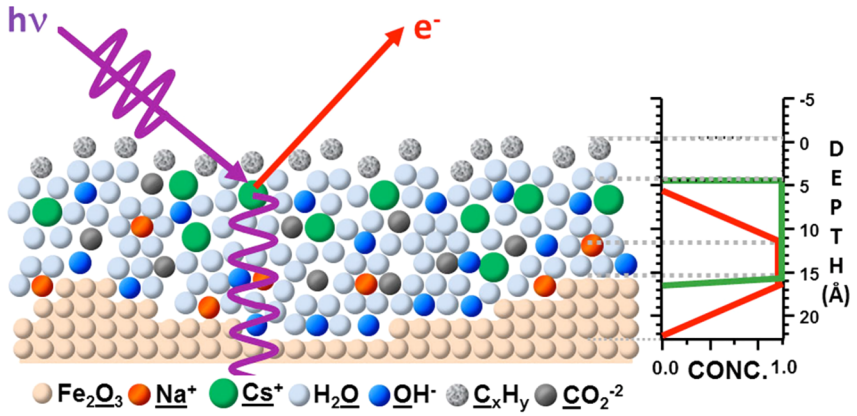

Figure 15. SWAPPS: Standing wave ambient pressure photoelectron spectroscopy of hydrated mixed NaOH and CsOH layers on nanocrystalline or amorphous α-Fe_2O_3. SWAPPS of films deposited on a Si−Mo multilayer mirror showing the vertical positions (depth in Å) of Na^+ and Cs^+ ions as a function of their concentrations.[276] The Na^+ penetrates within the surface region of the α-Fe_2O_3, whereas the Cs^+ only resides in one region of the interface. Image courtesy of the Fadley Group (UC Davis).

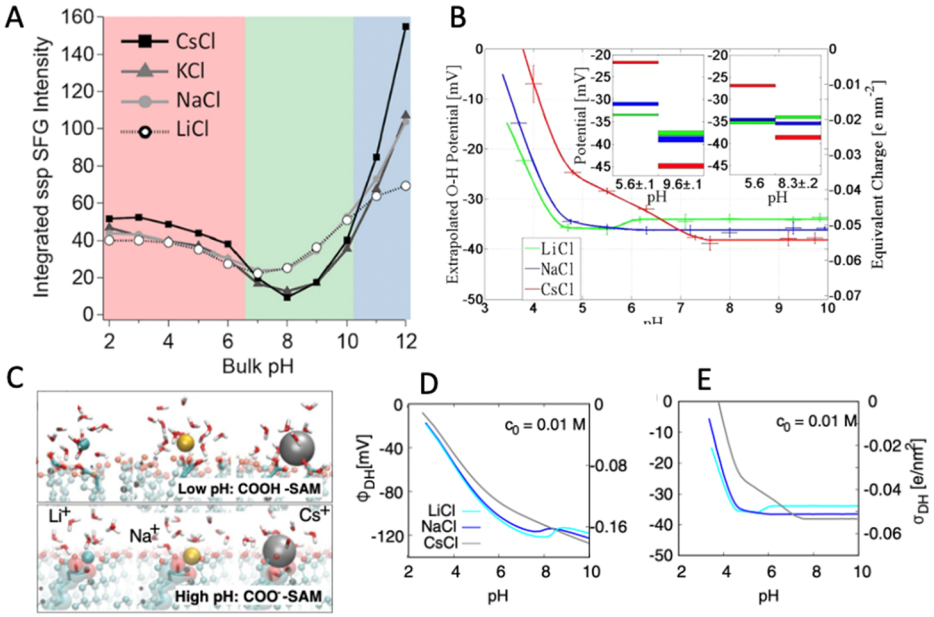

Figure 16. pH-Dependence of ion affinity for surfaces. (A) Integrated SFG intensities at the silica−aqueous interface as a function of pH with 500 mM alkali chloride solutions.[237] The integrated intensity is proportional to the amount of ordered water at the interface, which at this high salt concentration should be within a nanometer of the surface. (B) Extrapolated outer Helmholtz (O−H) potentials from AFM force measurements between silica surfaces in the presence of 31 mM alkali chlorides. The inset shows replicates on different samples.[235] (C) MD simulation of alkali ions interacting with a carboxylic acid-terminated self-assembled monolayer (SAM) at low pH, corresponding to primarily neutral COOH sites, and high pH, corresponding to more COO^- sites. (D) Modified PB calculation of the outer Helmholtz potential (left axis) and net surface charge density (right axis) as a function of pH for the COOH-terminated SAM. (E) Experimental measurements of the outer Helmholtz potential and net surface charge density for a silica surface under the same salt concentration as those calculated in D (0.01 M salt). Both surfaces exhibit this trend reversal with pH, suggesting all surfaces dominated by weak acid sites should exhibit such behavior. (A) Adapted from ref 237. Copyright 2017 American Chemical Society. (B) Adapted from ref 235. Copyright 2013 American Chemical Society. (C−E) Reproduced with permission from ref 236. Copyright 2016 Elsevier Ltd.

spectroscopy (SWAPPS) on a thin layer of nanocrystalline or amorphous hematite (α-Fe_2O_3) (~37 Å thick) grown by reactive magnetron sputtering in a UHV chamber (Figure 15). By combining experimental results with theoretical photoemission calculations to derive quantitative information on the relative depths of Cs^+, Na^+, and other chemical elements in the EDL, with sub-nm accuracy, as well as the concentrations of each chemical component present, including water vapor at a RH of ~8%. They observed that Na^+ approached the hematite surface more closely than Cs^+. Such preferential adsorption of Na^+ over Cs^+ has also been reported for α-TiO_2, α-Al_2O_3,[277] and α-Fe_2O_3 surfaces.[278,279] Other recent explorations of ion interactions at silica−water interfaces at constant pH have also revealed information about the ion position within the EDL structure for "simple" alkali chlorides using standing-wave X-ray spectroscopy on a native oxide layer on silicon coupled with complementary MD simulations.[280]

To probe both the Stern and diffuse layers, particularly when the latter is large extending nanometers or more from the surface, SFG and SHG are ideal as these second-order techniques are sensitive to noncentrosymmetric assemblies. Within the BIL or Stern layer, water has a net orientation

https://doi.org/10.1021/acs.chemrev.2c00130
Chem. Rev. 2023, 123, 6413−6544

owing to H-bonding with the oxide surface as well as asymmetric ion solvation, while interactions between electrostatic fields arising from charged surfaces order water within the diffuse layer.[246,281] The distance from the surface to the end of the diffuse layer is typically approximated as four times the Debye length, a parameter inversely related to the ionic strength owing to enhanced screening of the surface field with increasing ion concentration.[281]

Using vSFG, several groups have explored the effect of added salt on the interfacial water structure at the silica−water interface at pH above the pH_{PZC}.[247,252,281,282] The impact of ions on the vibrational relaxation of interfacial water, increasing or decreasing the rate in a manner that depends on the surface charge, have also been noted.[11,209,211] For both monovalent and divalent salts, the overall intensity of the interfacial water vSFG signal (proportional to the amount of water with net order at the interface) decayed with increasing ion concentration. However, divalent ions such as Ca^{2+} at high concentrations (∼2 M) were shown to completely disrupt the amount of ordered interfacial water, which was not observed for the monovalent ions even at higher concentrations (e.g., Li^+).[283] The ion identity was found to impact the amount of signal, which suggested either different screening behavior or specific adsorption at the interface. Complementary to these experiments is SHG, which has suggested that the ion identity and concentration impact the relative distribution of acidic sites on silica surface as well as their apparent acidity constants.[248,284,285] More recently, the impact of ion identity on the net amount of ordered water within the Stern layer and within the diffuse layer has also been explored with heterodyne-detected SHG revealing ion specific effects.[251]

Another benefit of nonlinear optical experiments on planar substrates is that conditions can be used where colloidal samples are less stable or undergo significant dissolution due to their higher exposed surface areas, which impacts many colloidal measurements owing to the sensitivity of analysis on the specific surface area. For example, Borguet and co-workers varied the pH from pH 2 to 12 (a pH typically unexplored in colloidal systems) for the planar silica−aqueous interface and found that the impact of NaCl on the relative signal of ordered water was highly pH dependent.[252] At both low and high pH, the addition of salt had little effect on the interfacial water structure, but at intermediate pH the differences in signal between pH-adjusted water free of additional NaCl and solutions containing 0.1 M NaCl were significant; the authors correlated these pH where the interfacial water structure was very sensitive to the presence of ions with previous work on the impact of ions on the dissolution rate of silica, which similarly observed that the addition of alkali chlorides impacted dissolution mostly around neutral pH.[286,287] More recently, the trend in alkali chloride behavior with respect to the SFG signal intensity at the silica−water interface around neutral pH from $Li^+ \sim Na^+ > K^+ > Cs^+$ (the Hofmeister series) to $Cs^+ > K^+ \sim Na^+ > Li^+$ (the reverse Hofmeister series) above pH 10.5 (Figure 16A).[237] This suggested the nature of the EDL structure and the relative behavior of ions depend on the surface charge density of the underlying oxide, also observed previously utilizing other techniques such as surface force measurements for silica (Figure 16B)[235] as well as in studies on TiO_2 and SnO_2.[256,288] Variability in ion trends have also been shown for similar pH based on different silica samples, suggesting that the surface porosity or the presence of gel layers also impacts ion specificity.[289]

The sensitivity of vSFG and SHG to the systems where inversion symmetry is broken can make it challenging to deconvolute where in the interfacial region the signal arises. Recently, strategies have been explored for separating the signal arising from water at the surface vs that further away in the diffuse layer by taking advantage of signal interference that occurs in the latter when the diffuse layer penetration depth is of the same magnitude as the coherence length of the SFG or SHG light.[250,251,290] One implementation of this strategy has used phase-sensitive SFG at the silica−water interface, which allows the orientation of the waters to be resolved, and the contributions from different populations at the surface and in the diffuse layer to be separated. Using this approach, the difference in the imaginary spectra (the imaginary component of the SFG electric field) was measured at pH 12 with increasing amounts of salt, allowing the authors to resolve the SFG behavior of water immediately at the charged silica interface.[291] The resulting Stern layer spectra were similar for both H_2O and HOD aqueous systems, indicating strong hydrogen-bonding for the OH of water that was donating a H-bond to the surface while the other OH within the molecule was effectively decoupled, providing much weaker signal at higher wavenumber for this H-bond oriented away from the surface. More recent work at lower pH, pH 5.6, monitored the evolution of the surface water (the bonded interfacial layer-BIL) by separating the contribution of the diffuse layer from the total imaginary spectra.[246] At very low salt concentrations, where a Stern layer is yet to form, the BIL structure exhibited a significant amount of ordered water, which looked similar to that observed near the pH_{PZC} (pH 2) with the dominant feature stemming from water accepting H-bonds from the silanol-rich surface. This similarity suggested that the BIL water structure is correlated with silica reactivity, as the tendency of silica to avoid aggregation has been observed both near the pH_{PZC} (pH 2) and at low ionic strengths (requiring near neutral pH).[289] One possible origin of the stability is the steric repulsion of neighboring particles under conditions that facilitate highly ordered BIL water. As salt is added, leading to disruption of the BIL, particle−particle interactions are less sterically hindered.

Surface force measurements have also explored the impact of ions and pH on interactions between oxide surfaces.[292] Sivan and co-workers used AFM measurements to map the force between two silica surfaces in alkali chloride solutions, which exhibited pH-dependence in the relative force trend for the examined ions.[235] For example, the extrapolated outer Helmholtz potentials determined from the measurements exhibited the lowest force for Cs^+ at low pH consistent with Cs^+ forming a closer interaction with the silica surface, followed by Na^+ and Li^+ (Figure 16B). Above pH 8, the trend was reversed. The authors proposed that the weakly hydrated silanol sites that dominated at low pH had stronger interactions with the weakly hydrated Cs^+. However, upon deprotonation the resulting siloxide attracted more hydration waters, which expelled the Cs^+ and instead led to greater interactions with the strongly hydrated Li^+.

MD-DFT studies and a modified PB model observed similar changes in ion affinity with pH for another weak acid: carboxylic acid-terminated self-assembled monolayers.[236] The authors' simulations supported that the weakly hydrated Cs^+ had the closest approach to the neutral COOH group but that

https://doi.org/10.1021/acs.chemrev.2c00130
Chem. Rev. 2023, 123, 6413−6544

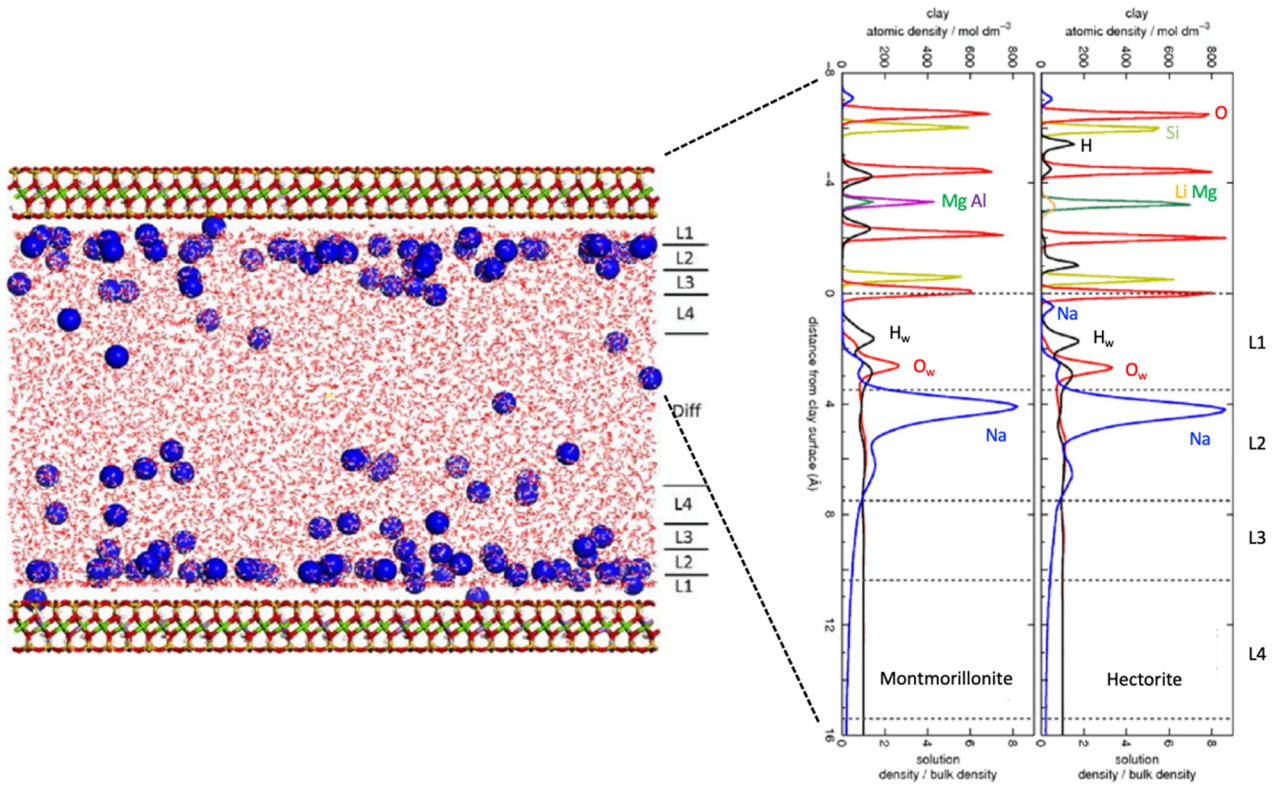

Figure 17. Interfacial structures of montmorillonite and hectorite nanopores. Snapshot of the simulation supercell for hectorite and atomic density profiles representing MD-equilibrated interfacial structures for montmorillonite and hectorite nanopores. Blue spheres in hectorite model represent Na ions; clay layers in the model are indicated by bonded atoms of the octahedral (Mg–Li–O) and tetrahedral (Si–O) sheets. Labels for aqueous layers are indicated as L1 to L4 and diffuse (Diff).[221] Adapted from ref 221. Copyright 2015 American Chemical Society.

the trend was reversed with deprotonation (Figure 16C). They proposed that this mechanism for reversal in ion affinity with changing surface charge density was likely general for other mineral oxides and weak acid monolayers (Figure 16D,E). Subsequently, vSFG studies have confirmed this pH dependent reversal in ion trend at carboxylic acid-terminated films.[293] Finally, force measurements have identified the significant impact of surface roughness on interactions between oxide surfaces.[294] Recent MD simulations found that certain silica surface structures that yielded sterically hindered sites could lead to a higher adsorption affinity of Na^+ versus Ca^{2+}, suggesting ion affinity and mode of binding should also be sensitive to surface roughness.[295]

Another approach to exploring the EDL structure on amorphous silica utilized internal reflection ellipsometry at the silica interface in the presence of Na^+ or Ca^{2+} chlorides at low and high pH.[296,297] The authors were able to interpret the data in terms of ion adsorption, with Ca^{2+} showing a higher affinity for silica, using a modified PB model coupled with a triple layer SCM, but they noted that their experimental observable could not distinguish whether overcharging occurred under their conditions.[296]

2.3.2.3. Coupled and Decoupled Dynamics in the Stern and Diffuse Layers. As mentioned previously, the two basic components of the most established and commonly used EDL models are the Stern and the diffuse layers. The textbook picture is static and suggests that processes in each region occur simultaneously. Yet, one may ask whether a sudden reduction in the ionic strength of an aqueous solution in contact with an oxide changes the ion concentrations in the Stern and the diffuse layers in synchronicity, or if one responds before the other. Time-resolved X-ray reflectivity measurements have shown Rb^+ exchange kinetics to depend on the distance from the solid–liquid interface, at least over the first few nm.[298] Related to this emerging view is the well-documented and yet still enigmatic phenomenon of hysteretic acid–base chemistry at charged solid–water interfaces,[299] which can maintain a pH 3-like condition at the interface for hours while the bulk solution pH is 10.[300] These findings present the opportunity to consider whether the various parts of the EDL are decoupled from one another under certain conditions. The various regions may then present quite different environments to incoming or outgoing ions. As a result, various parts of the EDL shown in Figure 14A may need to be viewed as acting separately from one another under certain dynamically changing bulk conditions (pH, *I*, solutes).

2.3.2.4. Nanoparticles/Nanoconfined Interfaces/Porous Systems. As we have shown above, water can change the surface structure of the solid, while surfaces define the structure of water/solution above them. The EDL can extend up to several nm, therefore in some narrow nanopores there could be no "bulk" solution present. The effect of overlapping EDLs from the opposing surfaces on both the solution structure and surface structure is an active area of research.

When a reactive surface reaches the nanoscale size range as, for example, happens for nanoparticles, interlayers of clay minerals, fluids inside geologic nanopores, and nanoscale water films, chemical properties deviate significantly from those observed for larger systems.[301−304] The properties of pore-confined water under unsaturated conditions are controlled by adsorption on surfaces and pore condensation. Adsorption of water in narrow pores, for instance, in porous SiO_2 MCM-41

https://doi.org/10.1021/acs.chemrev.2c00130
Chem. Rev. 2023, 123, 6413−6544

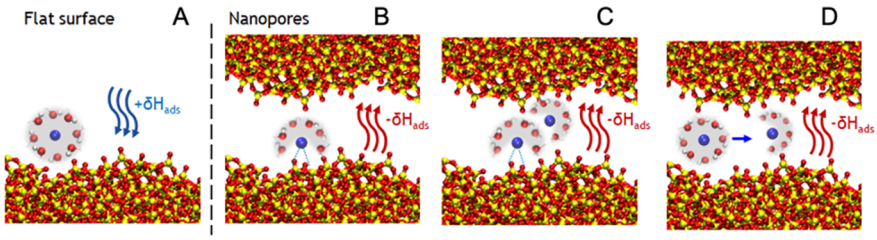

Figure 18. Lanthanide adsorption on surfaces and in pores. Proposed lanthanide (III) adsorption mechanisms which can result in an endothermic (+δH) or an exothermic (−δH) signal. (A) Lanthanide adsorption as an outer-sphere complex on unconfined SiO_2 surface. (B) Lanthanide adsorption as an inner-sphere complex on nanoconfined SiO_2 surface. (C) Lanthanide adsorption as an inner-sphere dimer complex on nanoconfined SiO_2 surface. (D) Decrease in ΔG_{hydr} under nanoconfinement, making dehydration reaction less energetically costly. Modified from ref 335. Copyright 2021 Royal Society of Chemistry.

with pore diameters of 1 to 4 nm, leads to the formation of approximately one adsorbed H_2O layer with a density that scales linearly with surface hydroxyl site density. In these nanopores, low surface hydroxyl densities lead to reduced densities of adsorbed H_2O,[305] as opposed to a large (101) surface of quartz, where the density of adsorbed H_2O is approximately equal to bulk H_2O density.[127] The thickness of the adsorbed water layer in nanopores is controlled through the inverse relationship between pore condensation pressure and pore size given by the Kelvin equation. In MCM-41 with 1.2−1.7 nm pores, the H_2O layer thickness at $P/P_0 \approx 0.65$ is ∼0.2 to 0.4 nm, whereas it is ∼0.6 nm in CPG-75 with 13 nm pore diameters;[154] for comparison, the adsorbed water layer at the unconfined quartz (101) surface is ∼1.1 nm at $P/P_0 = 1$.[127]

The importance of dimensionality must also be considered in confined systems.[306] Recent advances in nanoporous material synthesis and synchrotron-based probes allowed for quantitative descriptions of nanoconfinement effects on interfacial chemistry. Inside small water-filled nanopores, the ratio of interfacial to bulk water is large, and therefore the changes in H-bonding structures and decreased rotational freedom of surface-associated H_2O molecules lead to decreases in the mean dielectric response, density, surface tension, and freezing temperature of confined H_2O.[305,307−313] The lower mean dielectric response of nanoconfined water causes a decrease in the solvation energy of dissolved ions increasing equilibrium constants for homogeneous[314] and heterogeneous[304,315−317] complexation reactions. Selected experimental and computational advances in understanding the structures and reactivities of nanoconfined solid−water interfaces are discussed below.

2.3.2.4.1. Computational. Greathouse *et al.* used MD simulations to evaluate the structure and dynamics of water and solutes confined within clay mineral interlayers of hectorite and montmorillonite.[221] These phyllosilicates have charged layers comprised of tetrahedral−octahedral−tetrahedral sheets. Hectorite is characterized by $Mg_{2.5}Li_{0.5}$ occupancy in its octahedral sheet, whereas montmorillonite has $Al_{1.5}Mg_{0.5}$ (with a vacancy) for its octahedral sheet. Figure 17 shows the equilibrated simulation cell for the ∼6 nm nanopore in hectorite. Large-scale all-atom MD simulations, involving atomic trajectories for approximately 50 000 atoms run for 50 ns, utilized the CLAYFF interatomic potentials.[220,318−320] Molecular simulations involving clay mineral models have been shown to be accurate in evaluating structure and dynamics of bulk, aqueous, and interfacial systems.[318,321−323] Figure 17 also provides the atomic density profiles for hectorite and montmorillonite simulations, which both indicate a dominant outer-sphere adsorption peak for Na^+ at approximately 4 Å from the surface oxygen plane of the clay. Hectorite exhibits an extra Na^+ adsorption peak near the siloxane surface associated with an inner-sphere complex involving tightly bound Na^+ interacting with the hexagonal siloxane ring structure of the basal surface. A comparison of H profiles for the two clay structures shows the difference in orientations of hydroxyl groups near the interface, due to an octahedral vacancy associated with montmorillonite, and resulting in enhanced inner-sphere Na^+ adsorption for the hectorite simulation. Additionally, diffusion coefficients for water and Na^+, calculated for each water layer at the interface, show reduced transport rates close to the surface, and increase two to three times and approach bulk diffusion values: 3×10^{-9} m^2/s for water and 1.3×10^{-9} m^2/s for Na^+ in the diffuse central region of the nanopore.[324] These results collectively demonstrate the utility of an atomic model of nanopore structure and dynamics, which can inform and guide experimental, spectroscopic, and macroscopic measurements.

Many other molecular simulation studies have contributed insights to the structure and dynamics of clay−water interfaces and nanopores.[220,318,319,325−332] Much of this effort is related to understanding model interfacial systems for environmental investigations and to advance chemical and nuclear waste remediation and repository technologies.

2.3.2.4.2. Experimental. Experimental investigations into nanoconfinement-driven effects on interfacial chemistry indicate that energetics, kinetics, and products of the nanoconfined systems differ from unconfined counterparts. Wu and Navrotsky showed that ΔH of small molecule interactions with nanoporous SiO_2 surfaces becomes more negative with decreasing pore size and increasing density of Si−OH functional groups, with ΔH of immersion for NaCl rising from −8 to −11 kJ/mol when pore diameter is decreased from 16 to 3 nm; this trend is consistent for water, ethanol, triethylamine, NaCl, and $NaHCO_3$.[333] Similarly, Knight *et al.* showed that ΔH of H_2O desorption from nanoporous SiO_2 increases from 2 to 6 kJ/mol when pore diameter in SiO_2 is decreased from 8 to 2 nm.[334] The ΔH of adsorption for Cu^{2+}, Nd^{3+}, Tb^{3+}, and Lu^{3+} changes dramatically for nanoconfined SiO_2−H_2O interfaces: ion adsorption is *endothermic* for free and *exothermic* for nanoconfined (4 and 7 nm pores) SiO_2 surfaces.[304,335] Mechanistically, these observed changes in ΔH are explained by (i) lower energetic cost of partial dehydration of hydrated ions under nanoconfinement, which is a necessary step for the formation of inner-sphere surface complexes detected experimentally, and (ii) increased polymerization reactions on nanoconfined surfaces, with Cu^{2+}, Nd^{3+}, Tb^{3+}, and

https://doi.org/10.1021/acs.chemrev.2c00130
Chem. Rev. 2023, 123, 6413−6544

Lu^{3+} forming a larger proportion of polynuclear species under nanoconfinement (Figure 18).[304,335]

Analogous nanoconfinement-driven increases in inner-sphere surface complexation and changes in the local coordination environment of adsorbed species have been reported for Na^+ and Ca^{2+} ion exchange reactions in the nanopores of several zeolite minerals[316] and for trace levels of Zn^{2+} in amorphous SiO_2 nanopores.[317] Figure 19 shows SEM

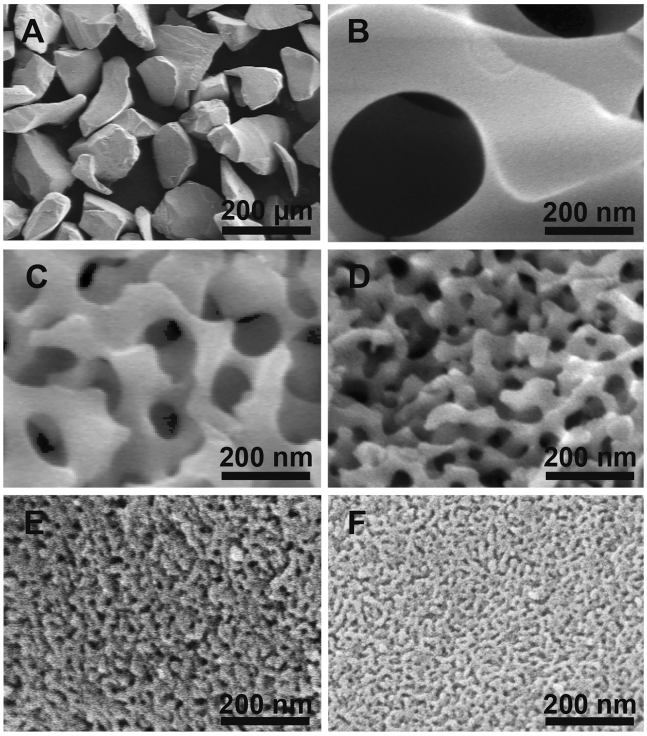

Figure 19. Scanning electron microscopy (SEM) images of experimental substrates: (A) amorphous silica controlled pore glass (CPG) particles, and surfaces of porous particles with different average pore sizes (B) CPG3000 (328 nm), (C) CPG1000, (D) CPG500, (E) CPG120, and (F) CPG75. Reproduced with permission from ref 317. Copyright 2016 Elsevier Ltd.

images of the nanoporous silica samples used in this latter study, ranging in average pore diameter from 328 (CPG3000) to 10 nm (CPG75). Zn^{2+} surface coverages ranged from 0.12 to 3.6 μmoles m^{-2}. As pore sizes decrease in the nanoscale size regime of nanoporous silica, tetrahedrally coordinated inner-sphere, monodentate Zn^{2+} adsorption complexes dominate over octahedrally coordinated Zn^{2+} adsorption complexes on am-SiO_2 nanopore surfaces (Figure 20).

As opposed to nanopores, where interfacial reactivity is defined by the properties of nanoconfined water, reactivity, and stability of nanoparticles are determined by the balance between interfacial (surface enthalpy) and bulk (free energy of formation) energies. This leads to apparent crossovers in thermodynamic stability fields, and metastable phases, becoming stable at the nanoscale, a phenomenon consistently observed for Fe-, Al-, and Ti-oxides.[301] For iron oxides, for example, when particles reach 60 nm or less, goethite (α-FeOOH) becomes more stable than hematite (α-Fe_2O_3), and for particles of 12 nm and less, lepidocrocite (γ-FeOOH) becomes more stable than hematite.[301] The size-dependent thermodynamic properties of nanoparticles lead to size-dependent reactivity trends, which define the fate and

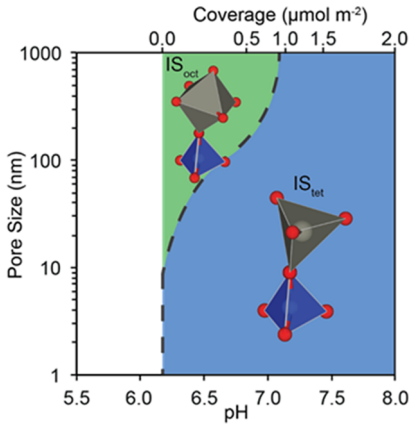

Figure 20. Predominance diagram of Zn^{2+} surface complexes with respect to pH and pore size. Positions of lines, curves, and shaded regions are specific to the chemical conditions of experiments and would shift as a function of aqueous Zn^{2+} concentration and amount of available substrate surface area. Green regions and IS_{oct} refer to inner-sphere monodentate Zn^{2+} complexes in octahedral coordination with surface oxygen atoms on am-SiO_2. Blue regions and IS_{tet} refer to inner-sphere monodentate Zn^{2+} complexes in tetrahedral coordination with surface oxygen atoms on am-SiO_2. Superimposed structures depict possible molecular-level geometries. Reproduced with permission from ref 317. Copyright 2016 Elsevier Ltd.

transport of chemical species and biogeochemical cycling in the environment.[303]

The large surface areas and curvature associated with nanoparticles enhances their response to interactions with water.[336] The adsorption of water onto nanoparticle surfaces can decrease their surface energies, stabilizing nanoparticulate phases, as has been shown for SnO_2.[337] These complex phenomena impact the stability of colloidal suspensions, contaminant transport, and the development of macroscopic geological features such as river deltas. Additionally, acid−base surface properties of oxide nanoparticles are amplified in the presence of ions, which will be further discussed in section 3. Adding salts, such as NaCl that fully dissociates and does not affect bulk solution pH, can drive a pH change in an aqueous suspension of oxide particles. This is typically explained to be a consequence of ion driven deprotonation above the point of zero charge of surface hydroxyl groups that leaves behind negatively charged surface groups that complex with salt cations,[241] driving changes in interfacial water structure.[338,339]

2.3.2.5. Spatial and Structural Heterogeneities of Surfaces and Interfaces. There are a number of features that provide heterogeneity on oxide surfaces. Broadly speaking, these surfaces are covered with bound hydroxyl groups and bridging oxygen species. For example, SiO_2 has SiOH groups and siloxane bridges (Si−O−Si), which have reportedly hydrophilic and hydrophobic character, respectively;[157] although some debate exists about the nature of water wetting and hydrogen bonding to SiO_2 surfaces,[340] there is evidence that the adsorption of H_2O from the vapor phase on oxide surfaces is spatially heterogeneous, occurring first at the siloxane bridges.[156] Furthermore, the SiOH groups are not all identical: they can be in plane or out of plane of the surface, and the silanols can be either geminal or isolated. Surface preparation impacts the silanol speciation.[341] Crystalline materials can be cut to expose specific crystallographic facets, e.g., Al_2O_3 (0001) and Al_2O_3 (1120) that results in distinct roughness, density, and types of surface hydroxyl groups. Finally, surfaces are not

https://doi.org/10.1021/acs.chemrev.2c00130
Chem. Rev. 2023, 123, 6413−6544

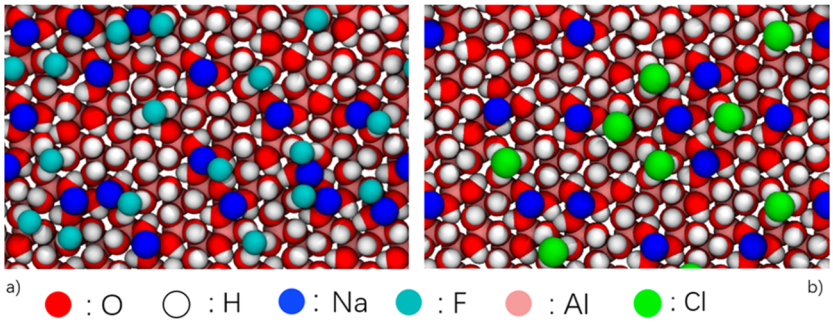

Figure 21. Sodium halide adsorption at alumina(0001)/water interfaces. Snapshot of (a) NaF and (b) NaCl adsorption near the α-alumina(0001)/water interface. Water molecules are omitted for clarity. Pink, red, white, blue, dark-green, and light-green spheres represent aluminum, oxygen, hydrogen, sodium, fluorine, and chlorine atoms, respectively. In both simulations, most Na^+ ions are triply coordinated by the surface, and halides can form H-bonds with hydroxyl groups of the surface, which reorient to accommodate the solvation of the adsorbed ions. Reproduced from ref 198. Copyright 2019 American Chemical Society.

perfect and there are many kinds of defects (steps, kinks, point defects, line defects, etc.).

Once exposed to an aqueous environment, further heterogeneity can develop on the surface. For example, hydroxyl groups can ionize to form positively charged (e.g., $SiOH_2^+$ and $Si(OH^+)$[342−344] or negatively charged (e.g., SiO^-)[342,344,345] sites depending on the bulk aqueous pH and electrolyte composition. Experiments by Gibbs and co-workers illustrate differences in the acid−base equilibria of the distinct SiOH species at silica−water interface[248,285] that are also supported by the computational studies by Gaigeot, Sulpizi, and co-workers.[162,207] Experiments to determine the acidity of individual hydroxyl groups on In_2O_3, as well as ZrO_2 and TiO_2 have been performed in UHV,[346] opening up the perspective for similar studies in aqueous environments and eventually the investigation of hydroxyls at defect sites, steps, and near impurities. The situation is complicated by the adsorption of aqueous species, e.g., cations, to the interface that can lead to deprotonation,[241] charge reversal,[213,249] and reorientation of surface bound hydroxyls (Figure 21).[198]

Many of the properties that characterize a surface, e.g., the IEP and surface potential, are determined by measurements that average over this heterogeneity (see section 2.3.3.1. for a more in-depth discussion of what constitutes the surface potential). Therefore, probes that provide spatially-resolved quantification are desirable. SHG microscopy has revealed heterogeneity via quantifying water orientation.[347] In principle, this nonlinear microscopy allows *in situ* imaging of heterogeneity on the sub-300 nm lateral length scale without exogenous labels. However, heterogeneity on surfaces is expected on much smaller length scales. For example, the surface charge dependence of vSFG and SHG suggests in-plane interfacial heterogeneity of the spatial sampling of vSFG and SHG, coupled with a depth dependence of the response that complicates the interpretation of the complex interfacial environment. Using the vSFG of a reporter molecule (SCN^-), Borguet et al. have revealed that the surface potential of the Al_2O_3 (0001) surface in aqueous solution is heterogeneous and provided an estimate of the potential at AlO^-, AlOH, and $AlOH_2^+$ sites that may be simultaneously present, of −154, 0, and +308 mV, respectively.[233]

Surfaces are also dynamic and therefore can be seen as heterogeneous in time. The rapid making and breaking of interfacial H-bonds, the adsorption and desorption of diverse species, and the acid−base equilibria that characterize surface bound hydroxyl groups are fundamentally dynamic processes, leading to time-dependency in the chemical composition and environment of a particular surface site. This has been addressed by MD simulations. On longer time scales, hysteresis of surface behavior likely reflects additional heterogeneity.[285,348]

2.3.3. Interfacial Potential Measurements. *2.3.3.1. Defining Different Potentials and Their Experimental Influence. 2.3.3.1.1. The Total Surface Potential.* The total surface potential at oxide−water interfaces contains contributions that arise from electrical charges via the Coulomb potential, aligned water molecules in the form of dipole potentials, and other contributions to the electrostatic potential (Figure 7A,B). Depending on the ionic strength, the relative contributions of these components can vary. Consider the dipole potential due to water: Kelvin probe studies at air:surfactant:water interfaces[349] show it to be on the order of several 100s mV, therefore the adsorbing ions of the same charge sign must do work to reach the solid surface in addition to the Coulomb contribution. For oppositely charged ions, the attractive forces can be considerable. For a net charge density around 0.01 C m^{-2}, typical for amorphous SiO_2 in 1 mM NaCl at pH 6,[350] this latter contribution is in the few to tens of mV range, indicating dipole potentials can have an outsized (albeit short-ranged) role. To what extent the dipoles that generate the high potentials at the air−water interface continue to prevail for buried surfaces is open to discussion. For measurements on single crystals, the same variation in humidity on a silica sample amplified the measured potential,[351] while an increase in humidity was shown to have no effect in Kelvin probe measurements for alumina. Dipole potentials are even more important at the pH_{pzc}, where the Coulomb potential vanishes, making it difficult to predict the dipolar alignment of interfacial water molecules. Under dilute conditions, dipole potentials add to the sizable Coulomb potential that oxides can exhibit above and below the pH_{pzc}. Yet, the classical colloid chemistry textbook by Hunter[352] discusses dipole contributions as negligible compared to contributions due to charges. Kelvin probe measurements are currently challenging to carry out at oxide− and silicate−water interfaces due to their insulator character, so information on the magnitude of the dipole potential comes mainly from atomistic computer simulations.[243,349,353] Such simulations indicate that measurements of the ζ-potential are not sensitive to the dipole potential,[243] emphasizing the need to experimentally elucidate the relative contributions to the total surface potential at the insulator surfaces in contact with aqueous solutions.

https://doi.org/10.1021/acs.chemrev.2c00130
Chem. Rev. 2023, 123, 6413−6544

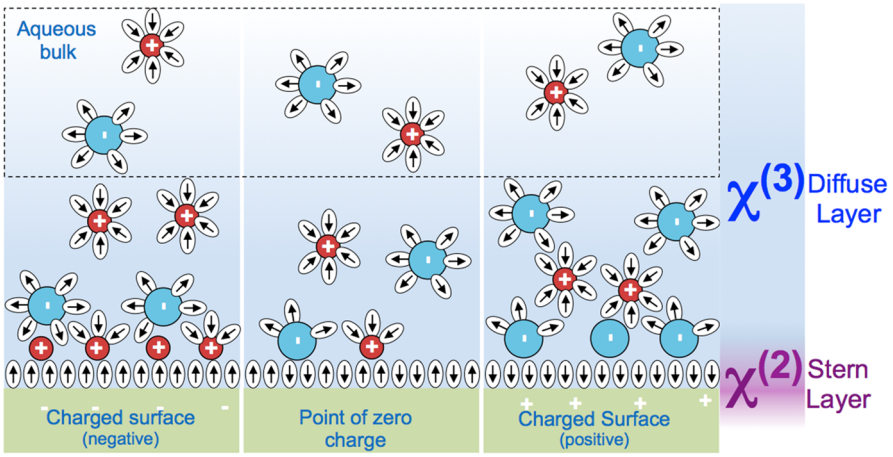

Figure 22. Simplified textbook cartoon of a surface transitioning through the point of zero charge. Dipoles of strongly coordinated water molecules are shown along with ions and charges. (Note: Dipole are illustrated using the definition prevalent in chemistry, where dipole moments are seen to result from the difference in electronegativity between two chemically bonded atoms and point toward the most electronegative atom the chemist's vision of electron flow. The physics definition would have the dipole point in the opposite directions, from the negative to the positive.) The ion concentration is constant at 1 cation and 1 anion in the bulk slab. $\chi^{(2)}$ and $\chi^{(3)}$ are the nonlinear susceptibilities that contribute to both SHG and SFG measurements and form a basis for understanding structure and electrostatic in the Stern and the diffuse layers.

2.3.3.1.2. Direct Measurements of Interfacial Potential. The most frequently applied approach to interfacial potential involves ζ measurements,[352] as reviewed by Delgado et al.,[245] while measurements of the surface potential are scarce. Various approaches for planar surfaces[354,355] and for particles are discussed below.[254,356]

Simultaneous measurements of the total surface potential and interfacial structure are possible using optical means in the form of nonresonant heterodyne-detected SHG. This nonresonant signal is understood to originate from the instantaneous response of the electrons bound to the interfacial species to the incident optical fields. The photons generated at the interface interfere with the photons generated in the diffuse layer over a distance that roughly corresponds to the Debye screening length, at least in the commonly used reflection geometries.[246,250] The SHG amplitude and phase determined by this technique yield the total interfacial potential, which contains the Coulomb, dipole, quadrupole, and all other contributions to the potential at the interface.[357] It serves as a prime experimental benchmark for computational studies of charged surfaces and provides the upper boundary of other estimates of interfacial electrostatics (dipole potential, Gouy−Chapman−Stern potential, ζ, etc.). The technique also yields the second-order susceptibility of the surface, $\chi_s^{(2)}$, which is a fundamental structural property of matter in noncentrosymmetric environments.[358] It is a measure of how the electrons are distributed in a noncentrosymmetric medium (an interface) and $\chi_s^{(2)}$ is given by the number, N_i, of a given interfacial species, i, multiplied by the orientational average of the hyperpolarizability, $\alpha^{(2)}$.[359−361] At an oxide−water interface, these are the interfacial hydroxyl groups, the interfacial water molecules and metal oxy(hydroxide) surface sites, and the adsorbed ions. To relate the sign of and magnitude of $\chi_s^{(2)}$ to net orientation and order, consider as an example an array of two water molecules having their dipoles pointed up (hydrogens pointed towards the negatively charged surface, Figure 22) which would correspond to a positive $\chi_s^{(2)}$ value. In contrast, two waters oppositely aligned would result in a $\chi_s^{(2)}$ value of zero. Two water dipoles pointing down (hydrogens pointed away from the positively charged surface, Figure 22) would yield a negative $\chi_s^{(2)}$ value. Surface silanol groups (neutral, protonated, and deprotonated) and counterions also contribute to $\chi_s^{(2)}$, according to their abundance.

These three scenarios of aligned water dipoles at the surface are shown in Figure 22 for an oxide transitioning through the PZC. The cartoons are highly idealized, with dipolar alignment only affected by the interfacial charge which competes with the energetics needed to establish the interfacial H-bonding network. The adsorbed ions also contribute with their own individual hyperpolarizabilities to the resulting signal. Potentiometric measurements and calculations with surface complexation models have established that cations and anions influence charge densities at charged surfaces via their adsorption affinities.[237,362−365] Important properties such as the pH_{PZC} will in general be sensitive to electrolyte identity as well. Pourbaix diagrams[366] and thermodynamic calculations[367] can guide an understanding of bulk speciation, against which measurements of interfacial ion speciation can then be compared. HD-SHG delivers the necessary sensitivity to probe ion specificity in terms of $\chi^{(2)}$, as demonstrated recently for RbCl, NaCl, and NaI, showing I^- with a 4× larger $\chi^{(2)}$ than Cl^-, reflecting the differences in these ions' polarizabilities.[251] Likewise, Mg^{2+} at the silica/water interfaces produces a much smaller $\chi_s^{(2)}$ than Na^+.[368] The $\chi_s^{(2)}$ values are positive for fused silica in contact with 0.5 and 0.05 M NaCl for all pH values between pH 2 and 12, which is consistent with the classic work of Duval et al.[342] showing that the surface consists of >80 percent molecular SiOH groups at all these pH values. In other words, the amphoteric character of fused silica only involves about 5−15 percent of protonated or deprotonated (SiO^-) surface sites, while the remainder are neutral. (The identity of the protonated sites remains unclear as to whether it constitutes protonated bridging siloxanes or silanolium sites given the current computation and experimental evidence.)

Such a level of microscopic insights from experiments can then be compared to atomistic simulations of ions at charged surfaces[114,180,190,195,369,370] to determine which molecular structures resemble the experimental results. Key advances are then expected if one combines second harmonic amplitude and phase measurements with simultaneous measurements of ζ

https://doi.org/10.1021/acs.chemrev.2c00130
Chem. Rev. 2023, 123, 6413−6544

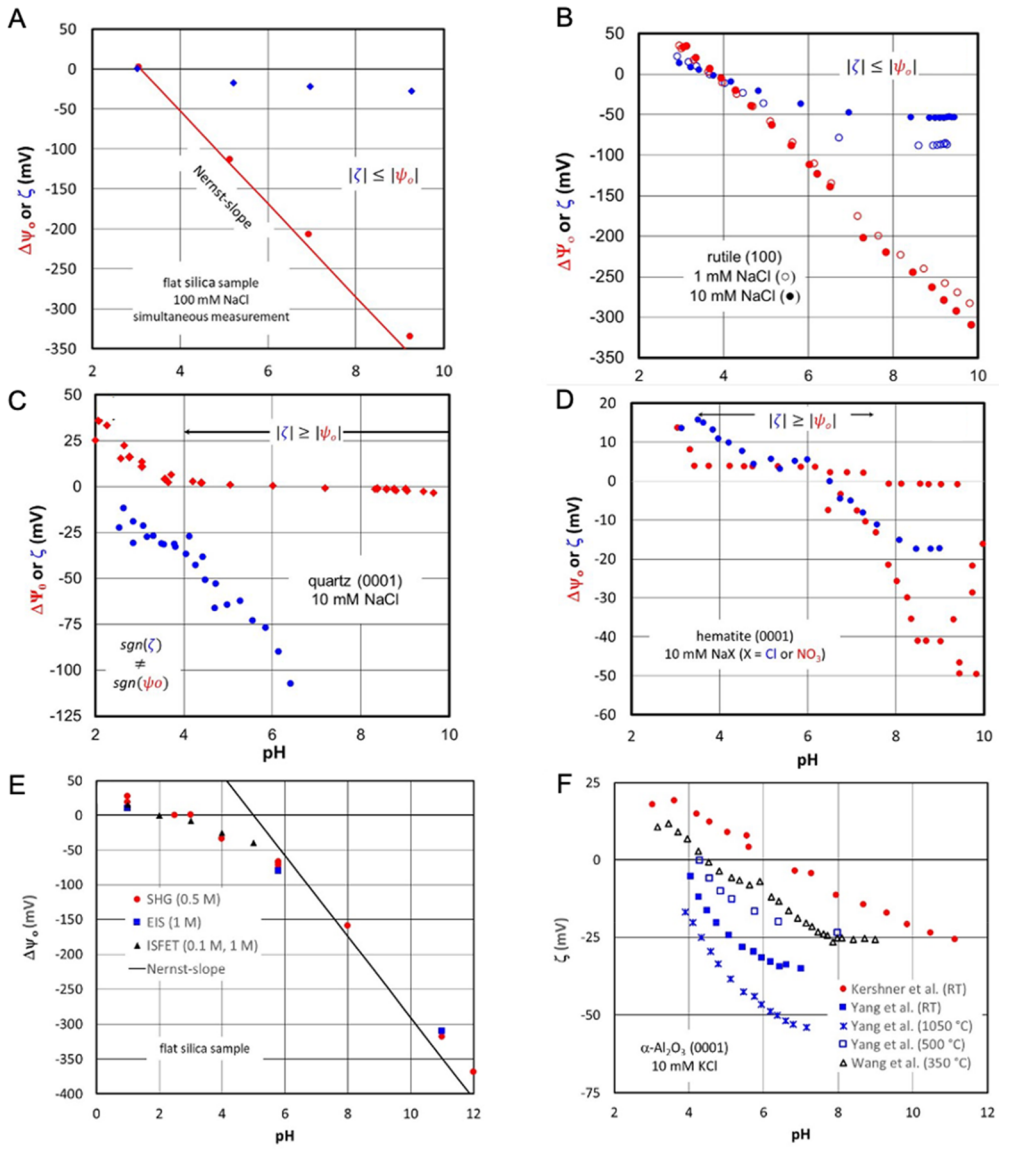

Figure 23. Simultaneous measurements of potentials. (A) Surface (ISFET) and zeta (streaming) potentials for flat silica surfaces;[372] the straight line corresponds to the Nernst slope. (B,C) Measured surface potential (single crystal electrode) and zeta potential (streaming current) for rutile(100) and quartz(0001) faces.[377] (D) Measured surface potential (single crystal electrode)[379] and zeta potential (streaming current)[382] for hematite(0001) faces. Ψ_o is the surface potential, and ζ is the zeta potential. (E) Comparison of reported surface potentials for flat silica samples as obtained by various methods. SHG, second harmonic generation in 0.5 M NaCl;[383] EIS, electric impedance spectroscopy in 1 M NaCl;[384] ISFET, ion-sensitive field-effect transistor in 0.1 and 1 M $NaNO_3$.[385] (F) Comparison of reported zeta potentials from streaming potential/current measurements for (0001) cut of sapphire single crystals in 10 mM KCl by Kershner et al.,[386] Yang et al.[387] and Wang et al.[382] The data labeled RT were only treated at room temperature, while the temperatures indicated correspond to heating steps during the crystal preparation.

so that contributions by the dipole, quadrupole, and other potentials can be further investigated. First steps in that direction have already been made by simultaneous measurements of SHG intensity and streaming potentials,[371] which is encouraging.

2.3.3.1.3. Surface Potential versus Zeta Potential. It is important to distinguish the different specific electrostatic potentials that can be assigned in the EDL. The potential that is the origin of the double layers on oxide surfaces is the surface potential, which, within the idealizing picture, is assigned to the plane of the surface functional groups (the 0-plane, Figure 14a). This potential is often denoted Φ_0 or Ψ_o and is referred to as the inner potential in surface complexation models. It is commonly assumed that titratable charge at the 0-plane is caused by the protonation and deprotonation of the surface functional groups. The electrical charge and (if applicable) additional contributions, e.g., from dipoles and higher-order moments, generate the (total) surface potential. The term surface potential is also sometimes applied to the diffuse layer potential, when a given study is not interested in the processes within the Stern layer. For example, the diffuse layer potential, as obtained from the evaluation of force distance curves, is sometimes called the surface potential.[372] This is often the case for DLVO type investigations when the diffuse layer potential is relevant and the innermost interfacial potential does not need to be probed.[373]

In the classical picture of the EDL, the diffuse layer potential (Ψ_d or Φ_d) is close to the measurable ζ. Yet Ψ_d is, by definition, situated at the head-end of the diffuse layer, while ζ is an experimentally determined parameter situated at the slip-

https://doi.org/10.1021/acs.chemrev.2c00130
Chem. Rev. 2023, 123, 6413−6544

plane, the location of which might be displaced towards an unknown position within the diffuse layer, leading ζ to be smaller in magnitude than Ψ_d (see section 2.3.1). When $|\Psi_d| > |\zeta|$, the magnitude of the diffuse layer charge density would accordingly be larger than that of the electrokinetic charge density ($|\sigma_d| > |\sigma_{ek}|$). It would be helpful if authors clearly stated their assumptions relating Ψ_d and ζ (and the corresponding surface charge densities) to limit confusion, but this is not always the case. Besides the difference mentioned above, σ_d and σ_{ek} need to be distinguished from the basic charge density (fundamental surface charge density) that can be obtained from potentiometric acid−base titrations on oxide minerals. This fundamental charge density, σ_H, is exclusively generated by adsorption or desorption of protons (which cannot be distinguished from desorption and adsorption of hydroxide ions, respectively). If it is assumed that any interaction with proton and hydroxide occurs at the idealized plane of the surface hydroxyls of the oxide surface (i.e., $\sigma_H = \sigma_{o,H}$) and that no other ions contribute charge to this plane, then within the classical picture the fundamental surface charge density corresponds to the surface charge density in this plane (i.e., $\sigma_o = \sigma_H$). However, this classical picture has been challenged in more recent work,[374] where specific adsorption of hydroxide ions was assumed beyond the plane of surface hydroxyls (i.e., $\sigma_H \neq \sigma_{o,H}$). These hydroxide ions would contribute to the results of potentiometric acid base titrations, thereby making it impossible to assign individual contributions to a given idealized plane of adsorption based on the titration data.

The fundamental surface charge density (at the plane of the surface potential) may not only arise from H^+ sorption or desorption. Contributions from inner-sphere surface complexes have to be included. In turn for the H^+-related charge, if H^+ reactions in the other parts of the double layer occur, the assignment of the measured titratable charge to the plane of the surface potential is erroneous. As is the case for the surface potential, the proton related charge density has to be related to some reference value to go from measured differences to absolute values, whereas the determination of ζ yields absolute values. Measurement of ζ for both colloids and flat samples is routine. The determination of the more fundamental surface potential is limited to few laboratories and therefore data remain scarce.

Nernstian behavior of surface potentials of oxides has been previously used to calculate the surface potential using the equation $\Psi_o = \ln(10) \times RT/F \times (pH_{pzc} - pH)$, where pH_{pzc} is the pH of zero surface potential. As shown, Nernstian behavior corresponds at 25°C to a change of −59.16 mV per pH unit.[375] More direct measurements of the surface potential for various oxides have been published at different pH with respect to the pH_{pzc}, for example, utilizing ion-sensitive field-effect transistors (ISFETs) for planar surfaces[376] or particle systems.[356] All of these measurements reported Nernstian, or near-Nernstian surface potential vs pH behavior, suggesting that Nernstian approaches to estimate the surface potential from the pH_{pzc} were valid. Moreover, these studies were also consistent with the classical EDL model, in which the interfacial potential in absolute value decays linearly within the Stern layer from the surface to the head end of the diffuse layer and subsequently decays further towards the bulk of solution, where it vanishes (Figure 14b). Yet one problem related to the measurement of the surface potential is that only differences can be measured. Typically, some pH_{PZC} is then taken to mark an absolute value.

Surface potential measurements have become available for oxide surfaces, with crystal face specificity in many cases.[355] Although, as mentioned above, surface potential measurements in relation to surface complexation models or concomitant ζ measurements for some oxide minerals had previously shown the expected behavior within the classical EDL picture with measured surface potential typically showing near-Nernst slopes,[354,356] the more recent measurements on some systems clearly challenge this picture. As shown in Figure 23, the simultaneous measurements by Bousse et al.[372] on silica surfaces (Figure 23A) show the magnitude of ζ (or the streaming potential) to be far less compared to the surface potential, which indicates a near-Nernstian slope. Recent measurements on particles have corroborated these results.[223] Likewise, the rutile(100) surface (Figure 23B)[377] shows this classical behavior and the expected ionic strength (I) dependence, with little effect of NaCl concentration on surface potential, but decreasing magnitude of ζ with increasing NaCl.[253]

Unlike these examples, many cases have emerged where the conventional picture of the EDL cannot explain the observations.[377] As an example, Figure 23C shows such data for quartz (0001) as observed with identical samples within a collaboration[378] and for hematite(0001) from separate studies (Figure 23D).[379] Here, the surface potential does not show the Nernstian behavior, which in the case of the hematite(0001) is not expected based on the a popular and successful SCM the Charge-Distribution Multisite Complexation (CD-MUSIC) model.[380,381] More importantly, in the two cases, the surface potential can be lower in magnitude than the ζ for a given I of monovalent electrolyte, which is at odds with the classical picture of the EDL, see potential profile in Figure 14. To explain the discrepancies within a classical EDL picture, contributions from within the slip plane are required from lectrolyte ions, water molecules, or impurities. Seemingly inert surfaces (as characterized by the surface potential plateau, which is set to zero mV) have been frequently observed in single crystal electrode measurements.[377] The general situation is far from clear in this respect, as is apparent from Figure 23. In particular the two SiO_2 systems (Figure 23A,C) tell different stories. Another aspect concerns the I-dependence of the surface potential, which is expected to be small. Unlike for ζ, where the increase in magnitude with decreasing level of inert electrolyte is established and observed (e.g., Figure 23B), the observations for the surface potential appear to be more diverse with the single crystal electrodes.

Surface potentials have also been obtained by other approaches. Thus, Figure 23E compares results from three methods between 0.1 and 1 M sodium salts with very good agreement. Figure 23F shows a similar comparison for zeta-potentials measured for the (0001) facet of α-Al_2O_3 in 0.01 M KCl by streaming current/potential approaches. The measured ζ-potentials for the samples exposed to higher temperatures (350 and 500 °C) agree fairly well but differ significantly for samples that were not annealed (Figure 23F, RT samples). Also, the two data sets for these nonannealed samples differ from each other. Similar discrepancies for nominally identical surfaces have been reported for this crystal plane in NaCl solutions, and the influences of sample origin, treatment, and other factors have been discussed.[212]

The measured surface potentials should, in the future, be subject to rigorous re-evaluation and related to the results from nonlinear optical data to come to a consensus between

https://doi.org/10.1021/acs.chemrev.2c00130
Chem. Rev. 2023, 123, 6413−6544

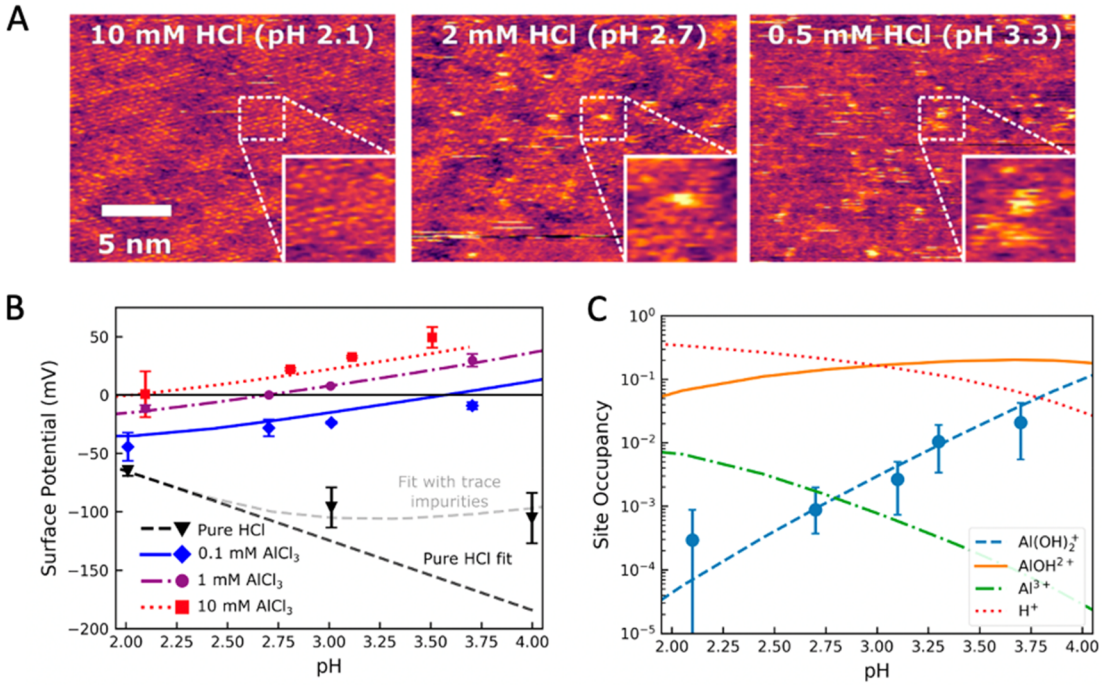

Figure 24. (A) High-resolution AFM images of the mica−aqueous interface with increasing pH in the presence of 1 mM $AlCl_3$. (B) Zeta potentials determined from streaming potential measurements as a function of pH in the presence of various initial concentrations of $AlCl_3$. (C) Results from a fit of the experimental measurables with a triple layer model. The predicted speciation results were corroborated by AIMD calculations. Reproduced from ref 391. Copyright 2020 American Chemical Society.

methods but also and maybe more importantly to understand to what extent the classical picture of the EDL needs revision and what is causing the differences between systems. Combined measurements should be preferable because they limit ambiguity with respect to the sample properties or treatment (Figure 23A and as further discussed in section 2.3.4).

2.3.3.2. Overcharging or Charge Reversal Phenomena. An interesting phenomenon observed for oxide surfaces in contact with aqueous ions is overcharging, where counterion accumulation within the Stern layer overcompensates the charge of the surface such that a negative oxide surface can result in a positive ζ.[388] Overcharging has been observed directly in force measurements[389] and indirectly by potentiometric experiments coupled with ion adsorption experiments where, based on charge balance, an oxide at pH above its pH_{PZC} can yield a net positive charge. However, the most common evidence of overcharging is electrokinetic data that measure ζ, which is often used as an approximation for the potential at the outer Helmholtz plane. When this potential becomes zero (an isoelectric point) at pH far above the pH_{pzc} and then changes sign, it indicates that the system is exhibiting overcharging owing to the composition of the Stern layer.

There are two general conditions where overcharging, or charge reversal, from a negative ζ to a positive ζ, is observed. The first involves increasing the ion concentration of divalent or trivalent ions while maintaining a constant pH of the system at a pH above the pH_{pzc} of the oxide. This has been attributed to specific adsorption of the cations to surface sites, although it can also be explained by quantum mechanical models that consider ion−ion and ion−site correlations.[388] The other condition involves increasing the pH while maintaining constant ion concentration. The latter experiment is particularly interesting as it reveals instances where the ζ becomes more positive with increasing pH, unexpectedly for an oxide surface. To understand how the structure of the EDL changes under such conditions, researchers utilized vSFG at the silica−water interface in the presence of Ca^{2+} as the pH was increased from pH 6 to 12.[249] Near the isoelectric point at pH 10.5, they observed a minimum in the SFG signal from water in the OH stretching region while also observing the growth from pH 9 until the isoelectric point (∼pH 10.5) of a peak at 3650 cm^{-1} that was attributed to $Ca(OH)^+$. Divalent ion adsorption at the $Al_2O_3(0001)$−water interface was also proposed to lead to charge reversal at pH 10 based on SFG observations.[213]

Other recent studies have utilized different techniques to monitor overcharging of oxide−aqueous interfaces using other techniques besides vSFG. For example, XPS was used to examine ion speciation at the silica−aqueous interface under conditions of overcharging albeit *ex situ*;[390] for a number of divalent transition metal ions at pHs where the ζ was positive, an increase in hydrolyzed cations (cation−hydroxide complexes) were observed on the silica surfaces. In another example, high-resolution AFM, in combination with streaming potential measurements, for the mica−water interface has been utilized to correlate the speciation of adsorbed Al^{3+} with ζ as the pH was raised, causing the potential to reverse from negative to positive (Figure 24).[391] More recently, X-ray reflectivity measurements combined with simulations revealed overcharging by RbI on muscovite mica with increasing RbI concentration at ∼pH 6.[392] The authors attributed overcharging to the positional organization of ions in an alternating layered structure of cations and anions rather than surface complexation. Such structures had not been predicted by ion−ion correlation models revealing the need for experimental evaluation of the EDL to inform new theoretical models.[392,393]

https://doi.org/10.1021/acs.chemrev.2c00130
Chem. Rev. 2023, 123, 6413−6544

2.3.3.3. Acidity Constants. A major mechanism of charging oxide surfaces involves the (de)protonation of surface hydroxyl sites. Knowing the acid dissociation constant K_a (or pK_a) of these sites is useful for predicting the pH-dependence of their H^+-related surface charge density. Moreover, to predict surface reactivity of oxide and silicate surfaces in terms of their composition and orientation, their acidity constants can be used.[118,239,394,395] These acidity constants can also be used to estimate the pristine pH_{PZC} values, considered a characteristic of a reactive surface and accessible via macroscopic measurements. Recent developments may raise expectations that pK_a constants of individual surface sites may become accessible via direct measurements.[346] Estimates of surface pK_a constants have been classically obtained as so-called intrinsic constants by fitting a certain thermodynamic model to a set of experimental data, often potentiometric titrations that yield H^+-related surface charge density as a function of pH. An apparent pK_a can be extracted from the data for the specific experimental conditions and may then be related to the intrinsic pK_a of the surface by a thermodynamic model that accounts for the difference in surface conditions compared with the bulk, for example, the surface H^+ concentration versus the bulk H^+ concentration. The surface and bulk values may differ by many log units. Unfortunately, fitting results depend on the chosen thermodynamic model.

Various attempts have been made to estimate pH_{PZC} and pK_a values for oxides.[124,380,396−398] The first models considered the surfaces in terms of the bulk solid and generic surface groups, while later ones included distinct crystal planes with their specific surface groups. In the final development, the H-bonding of the surface functional groups was explicitly included. However, one should not be blinded by the success of such models. For example, first attempts to obtain the crystal plane specific charging behavior of goethite using the bond valence model[380] ignored the relevance of H-bonding between surface hydroxyls and adsorbed water and used a wrong surface morphology. When the wrong assumptions concerning the exposed crystal planes were corrected, the original model no longer reproduced the experimental pH_{PZC} value. This was only achieved with the correct crystal planes once H-bonding was included making the model more complex. One property affecting fitted surface complexation constants, the surface site parameter involves higher complexity than the assumption of a planar, smooth surface even on well-defined goethite particles.[399] The roughness at small scales severely affects surface site densities, and thus stability constants should be reviewed based on the present information with respect to the ability to reproduce experimental pH_{PZC} values. Nanoconfinement adds to the problems because traditional models do not account for overlapping EDLs, e.g., in narrow pores, and this will impact acidity of surface sites.

On unconfined samples, multiple distinct pK_a constants for nominally the same type of surface site (e.g., −SiOH sites in the case of silica) have been observed. For example, for silica, potentiometric, and ζ measurements of colloidal samples have led to reported pK_a values in the range of 4 to 7. In general, at pH > 8 silica dissolution has to be accounted for because dissolution affects potentiometric titrations to obtain the H^+-related charge density at pH values where dissolved silicic acid releases a H^+. To what extent dissolution in particular under flow directly affects charging properties is an ongoing debate.[400,401] Experiments on planar substrates under higher pH conditions using planar silica samples have indicated that a second type of silanol site with a relatively high apparent pK_a is present (pK_a ∼7−10).[248,284,285,402] The presence of two types of silanol sites has also been reported for colloidal samples.[403,404]

Quantifying the pK_a values (the intrinsic constant) of individual sites remains challenging as it requires knowledge of other parameters such as the surface pH, which in turn requires knowledge of the total surface potential, which is not trivial to decipher. The apparent pK_a depends on the local environment comprising the electrostatic potential, building up across the double layer, and the localized charges on the surface (e.g., due to other titratable species) and in the EDL in the form of cations/anions.[285] The microscopic picture, provided by theoretical and computational models, may therefore be of great help to interpret the results of pH-dependent or salt-dependent experiments such as vSFG that are influenced in complicated ways by the various interfacial potentials, surface charge, and surface site densities.

Quantitative interpretation has been based on semi-empirical surface complexation models (SCM)[380,398] and bond valence models,[125] where the acidity constants depend on the undersaturated valence of the O bond. One concern with the use of such bond valence models is that they are incredibly sensitive to small changes in the M−O bond length or the valence distribution in H-bonds.[379] For example, varying the bond length from an average Fe−O distance in the bulk of goethite to reported values for relaxation of Fe−O distances at the surface of hematite results in changes of the K_a of the singly coordinated group by 8 log units. Electrostatic charging behavior of the (110) surface of rutile was measured by SHG as a function of pH in Fitts et al.,[405] who used the relaxation of surface bonds to allow for a fitting of the observed pH_{PZC}. There is also agreement between CD-MUSIC estimates for surface groups and AIMD simulations, for example, for gibbsite.[406] A notable exception is the deprotonation of the doubly coordinated group on the basal plane,[406] which also was reported for the same group on hematite.[407] CD-MUSIC type models are routinely utilized in combination with a Gouy−Chapman−Stern type EDL model.[408] Recent progress in applying these models to ferrihydrite has shown that molecular level based surface complexation models do have the potential to be applied to real-world systems.[409−413] Some of the considerations and challenges of using SCM models to accurately determine site pK_a will be discussed in section 2.3.5.

Intrinsic pK_a values can also be calculated with DFT-MD simulations.[162,192,414−417] The latest simulations have pointed out how the intrinsic pK_a is strongly dependent on the local environment and have tried to rationalize the effects of ions on the pK_a of the surface groups (e.g., the silanols[416]). In most of these simulations, PZC conditions are considered, therefore neglecting the EDL contribution, which was considered to be beyond the size limitations of DFT-MD. However, such a picture has been recently changing with the explicit introduction of ions at the oxide− and silicate−water interfaces. For example, the recent development of the constant electric displacement Hamiltonian[418] has been extended also to the oxide−water interface in the presence of salt (e.g., TiO_2(110)−NaCl electrolyte interface).[419] Using finite-field DFT-MD, the pH-dependence of the Stern layer (Helmholtz) capacitance was identified as arising from stronger structural fluctuations of the interfacial water with increasing pH. Yet even with these advances, the pK_a of only one site can be explored in the simulation. As computational

https://doi.org/10.1021/acs.chemrev.2c00130
Chem. Rev. 2023, 123, 6413−6544

power grows, larger simulations can be explored, allowing the pK_a of sites to be determined in the presence of charged sites that have already been deprotonated. Such explorations will be critical to understanding cooperative deprotonation processes on oxide and silicate surfaces.

Regarding the bimodal SHG response of the silica−water interface,[402] simulations have been able to capture the expected two pK_a values associated with bimodal character, but no systematic attribution of pK_as based on vicinal or geminal silanols could be found.[162,192,414] Instead, the local environment of the silanol(s) at the surface (e.g., inter-hydroxyl H-bonding, presence of neighboring siloxanes, strained zones, silanol coverage of patches, and stability of the conjugated base, were all found to influence the pK_a values. For instance, two Q^2 geminals at the surface of amorphous silica were found with opposite chemistries, one being acidic and the other basic because of the local surface morphology (concave/convex zones) and immediate Si−OH and Si−O−Si surface chemical surroundings; a substantial H-bond network that can be formed by the SiO^- conjugate base and defines the silanol pK_a value.

For quartz, DFT-MD/AIMD studies indicated that the bimodal pK_a behavior of the surface silanols arises from the hexameric arrangement of acidic Si-OHs that are oriented out-of-the-plane forming strong donor H-bonds with BIL−water (vertical H-bonds) and basic Si-OHs that are oriented in-plane (horizontal) and simultaneously donate H-bonds to neighboring acidic SiOHs (horizontal H-bonds) and accept H-bonds from BIL−water (vertical H-bonds). The high density of hydrophilic sites (9.6 SiOH/nm^2), the bimodal character of their pK_a, and the crystalline and repetitive topology and planar morphology of the quartz surface favor the vertical order of BIL−water and hence favor a crystalline-type of structural organization of BIL−water.

2.3.4. Combined Experimental Approaches. Models and interpretations relying on one experimental approach may lead to erroneous conclusions. In aqueous speciation studies, coupling of macroscopic investigations (e.g., titrations) with spectroscopic experiments, for example NMR, and simultaneously fitting data to a speciation model[420] yields models that directly include the molecular-level information. Similar combinations can be found concerning mineral surfaces,[137] including anion adsorption (combination of ATR-FTIR or EXAFS, uptake data, and theory)[421,422] or radionuclide uptake (TRLFS coupled to uptake data, EXAFS, and theory).

Some examples of combined experimental approaches that utilize the same or similar mineral samples are electrokinetic measurements combined with linear and nonlinear optical spectroscopies like SHG and vSFG.[246,249,338] Potentiometric experiments have also been utilized with SHG scattering to correlate surface charge density and the interfacial potential of SiO_2 particles.[241] Vibrational SFG has been combined with streaming current or streaming potential measurements using similar planar silica samples and identical salt solutions, allowing the signal intensities to be related to changes in ζ.[246,249] XPS measurements that used a synchrotron light source incident on a liquid jet to introduce the colloidal silica sample have been performed on Ludox silica suspensions at temperatures below 10 °C in combination with otentiometric and electrokinetic room-temperature experiments performed at room temperature.[223,254] This combination allowed the surface potential to be measured separately from the outer Helmholtz potential using the results from XPS and ζ determination, respectively. From this information and the surface charge density, the Stern layer thickness was obtained as a function of salt concentration[223] and ion identity for the alkali chloride series.[254] Finally, nonlinear optical methods have also been combined and performed on the same type of planar silica to yield information about the different sensitivities of non-resonant SHG and vSFG to the amount of ordered water at the interface as well as the contribution of the underlying silica surface (Figure 25).[423] To improve confidence that the sample

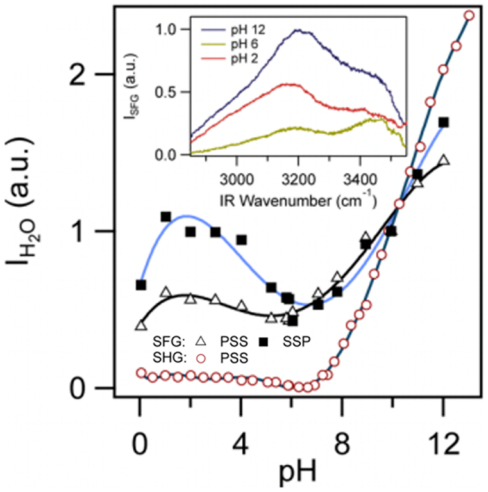

Figure 25. A comparison of nonresonant SHG and vibrational SFG intensities at the silica−water interface at various pH in the presence of 100 mM NaCl. These experiments were performed on the same type of silica sample from the same supplier using the same experimental conditions. These results highlight that nonresonant SHG and SFG report on different features of the interface despite their general dependence on the interfacial water structure. Adapted from ref 423. Copyright 2019 American Chemical Society.

behavior is consistent across the different techniques, simultaneous measurements might be preferable because it is not always trivial to assure that sequential surface preparation yields identical specimens. To this end, SHG has been measured simultaneously with streaming potential experiments to correlate the SHG signal and the ζ of the interface (Figure 26).[371]

2.3.5. Surface Complexation Modeling. Surface complexation models (SCMs) are widely used to generate a molecular interpretation of the interface from a variety of experimental observables. Generally, these models consider the different equilibrium constants that determine the interfacial structure such as the surface pK_a, the ion adsorption equilibrium constants, the magnitude of which can suggest a mode of binding and ion speciation equilibrium constants. The first issue SCMs deal with is the "charging" of the mineral−water interface based on the pH dependent protonation and deprotonation of O atoms at the surface. Hence, potentiometric titrations are conducted and pK_as of presumed surface sites are estimated. However, most of this work has been carried out on powdered samples and authors report a pH_{PZC} or IEP of a solid without regard to the crystallographic orientation. Because each crystal facet may have different surface sites with varying pK_as, these experiments are limited to average values, and the samples with different prevalence of distinct crystallographic orientations would have significantly

https://doi.org/10.1021/acs.chemrev.2c00130
Chem. Rev. 2023, 123, 6413−6544

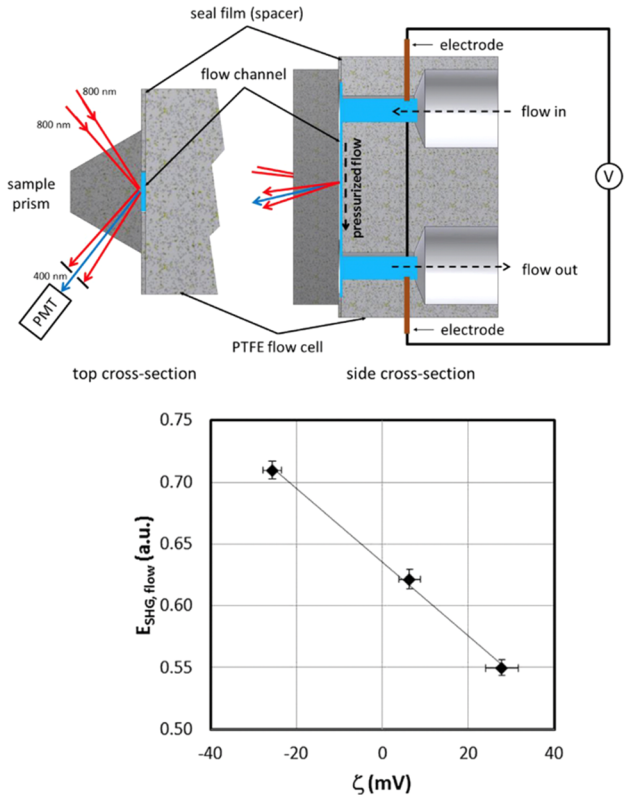

Figure 26. The simultaneous measurement of SHG and streaming potential. (top) Experimental set-up. (bottom) The ζ calculated from the streaming potential measurements and the corresponding SHG electric field. Reproduced with permission from ref 371. Copyright 2018 Elsevier.

different average pK_as (for an example on α-FeOOH (goethite), see Villalobos *et al.*[424]).

Each crystallographic orientation therefore needs to be treated explicitly to consider the types and densities of sites and how they may react rather than treating an oxide or silicate as if it had only one type of charged surface. This is handled more appropriately in some models (e.g., CD-MUSIC[425]), but not all SCMs consider that a given solid will have various habits with surfaces of various properties. To illustrate this point, we will focus on the (110) surface of rutile because there are numerous experimental and modeling results for this surface.

Once a surface charge is determined, the structure of the solid−water interface is defined by the charge within the EDL, where water dipoles are oriented. The charged surface and solution structure then generate a ζ potential that diminishes in strength away from the surface. Thus, a region between the charged surface and bulk aqueous solution is created that is often ascribed a Stern layer capacitance that can be used as an adjustable parameter when fitting adsorption isotherm data in SCM framework (section 3.2.1). The CD-MUSIC model has bridged the macroscopic modeling of surface charging and adsorption isotherms by relating pK_as (or proton affinities) to surface bond lengths and H-bonding of surface sites based on the Pauling bond valence concept.[426]

Much of the theory and application of SCMs to oxide and silicate interfacial chemistry occurred before recent spectroscopic techniques and molecular simulations were available to test the assumptions upon which EDL theory was built. For instance, in the EDL concept, surface charges resulting from (de)protonation control the structure of H_2Os in the interfacial region, but Boily and Song[427] have demonstrated that H-bonding energetics can be a controlling factor and that this H-bonding depends on curvature of nanoparticles. Properties such as curvature (which becomes relevant with radii below 5 nm) and roughness are ignored in most SCM models, so adding these terms to predictive models is imperative if we are to model surface chemistry in real-world systems where these factors are ubiquitous. The concept of a distributed surface charge has led to a picture where H_2O molecules orient their dipoles according to the average charge, but molecular simulations indicate that H_2O orientations are based on the relative strengths of various H-bond types (Figure 27, left panel). The ions adsorbed in the EDL also orient H_2Os especially for cations where M^+-OH_2 bonding in the first solvation sphere of inner- and outer-sphere adsorbed species controls H_2Os (Figure 27, right panel).

Another issue is that the role of so-called "background electrolytes" has been assumed to be negligible in most SCM studies. When one looks for the effects of changing aqueous salt compositions, however, such as NaCl and $NaNO_3$, it becomes apparent that they can alter the IEP and ξ potential[430] via surface interactions and ion pairing.[413] As stated in Kosmulski:[430]

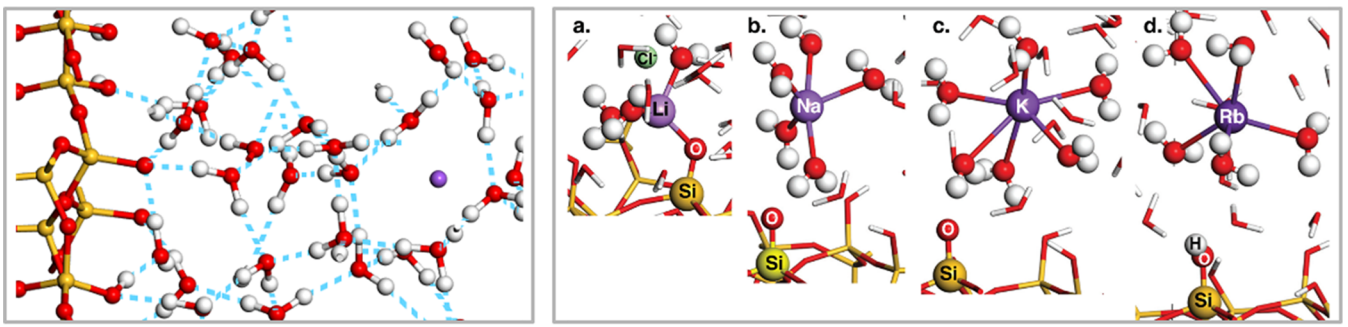

Figure 27. Hydrogen bonding, and impact of ions, at quartz−water interfaces. (left) Quartz (101) surface SiO^- with three strong H-bonds to nearby H_2O. Note that the dipoles of these H_2Os are not aligned perpendicular to the charged surface (image based on data from DelloStritto *et al.*[428]). (right) Geometry optimized group I cations ions at the quartz (101) surface showing (a) Li^+ bonded inner-sphere (IS) to the surface through a SiO^- on the surface, (b,c) Na^+ and K^+ outer-sphere (OS) to SiO^- on the surface, and (d) Rb^+ OS to SiOH on the surface. (right) Reproduced from ref 429. Copyright 2022 American Chemical Society.

https://doi.org/10.1021/acs.chemrev.2c00130
Chem. Rev. 2023, 123, 6413−6544

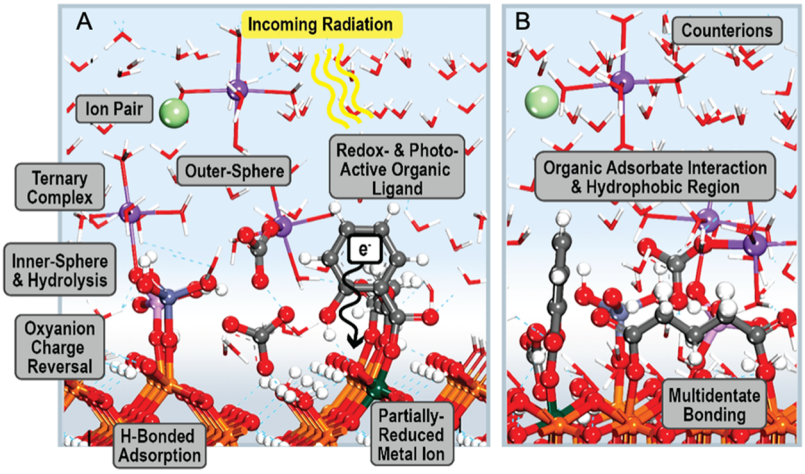

Figure 28. Schematic illustrating the types of sorbates and reactions at the interface. (A) The EDL as discussed in section 2 with various types of adsorbates and sorption mechanisms represented complicating the surface structure and water interactions. Sorbates can compete for sites or form ion pairs and ternary surface complexes. Redox reactions on surfaces such as goethite (α-FeOOH) shown here often catalyzed by light can be precursors to dissolution reaction discussed in section 4. (B) Adsorption of organic compounds can lead to hydrophobic region on previously hydrophilic surfaces. Longer chain organics can form multiple bonds to a surface and connect multiple particles by binding to more than one surface.

> *"In studies by electrophoresis, and especially by electro-osmosis and streaming potential, where the solid-to-liquid ratios are low, minor amounts... of surface active ions are capable of shifting the IEP by several pH units and even of reversal of sign of electrokinetic potential to positive (cations) or to negative (anions) over the entire pH range."*

This will be especially important in studies of colloidal aggregation. Mendez and Hiemstra,[413] citing the work of Bompoti and Boily,[431,432] emphasized this issue for the environmentally important colloid ferrihydrite (Fh):

> *"This obstructs for Fh a fully independent calibration of the parameters of the SCM, because the determination of the affinity constants is inversely correlated with the SSA."*

The molecular nature of this effect was observed by Tuladhar et al.,[11] who found that inner-sphere ions changed the H-bonding at silica−water interfaces. These authors observed a major change not accounted for in SCMs that is the switch from surface-water H-bonding to intrasurface H-bonding. Such a switch had been predicted based on DFT-MD simulations of quartz−solution interfaces by Kubicki et al.,[343] who suggested that this switch may explain why silica dissolves more rapidly in salt solutions compared to distilled water.[433]

The specific-surface area (SSA) is generally used to estimate the adsorption capacity of aqueous species onto surfaces, but reactive site densities and affinity constants are not always proportional to SSA because the crystallographic orientation and percentages of defect sites may change with particle size[399,413,424] as mentioned above. Thus, it is the total concentration of reactive sites that should be included in models to upscale to macroscopic behavior. Adding to this is the complication that surfaces can evolve with time, especially in poorly crystalline phases, which is not incorporated into current SCMs. Mendez and Hiemstra[413] used phosphate adsorption over time onto ferrihydrite to study this phenomenon. Because poorly crystalline phases are often the most reactive and influence sorbate behavior,[434] these kinetics must be included for long-term predictability we desire.

Bompoti et al. have used a CD-MUSIC approach applied on chromate adsorption to ferrihydrite and goethite to generate a self-consistent model.[435] They learned:

(a) "There is no single set of parameter values that describes such diverse data sets when modeled independently.

(b) Parameter differences among the data sets are mainly due to different amounts of total sites, i.e., surface area and surface coverages, rather than structural differences between the iron (oxy)hydroxides.

(c) Unified equilibrium constants can be extracted if total site dependencies are taken into account."

These results indicate that it is site-specific chemistry, rather than surface charge and Stern layer capacitance values that controls H^+-transfer reactions and ion adsorption, otherwise a set of unified equilibrium constants could not be derived for ferrihydrite and goethite with their different surfaces. This helps explain why molecular cluster models are able to model surface complexes.[13]

In the following section 3, we will further explore how the EDL structures at oxide− and silicate−water interfaces affect the adsorption of (in)organic species and interfacial electron transfer processes.

3. THEME 2: ADSORPTION AND REACTIONS AT INTERFACES

3.1. Introduction

3.1.1. Applications and Challenges. Adsorption/desorption, electron transfer, and heterogeneous nucleation reactions (Figure 28) occur at oxide− and silicate−water interfaces during groundwater flow that transports contaminants, subsurface storage of CO_2 and nuclear waste, and resource extraction from reservoirs. Detailed knowledge of the molecular mechanisms involved in these reactions will allow for the development of predictive models of these processes. Significant strides have been made by combining experiments to determine the thermodynamics and kinetics of solution−surface reactions with spectroscopy and molecular simulations,[436] but most work in this arena has focused on single phases and one or two adsorbates in simple, low ionic strength solutions that do not reflect natural systems completely.

Figure 28 illustrates the multiple types of sorbates found on mineral surfaces and the multiple mechanisms by which they

https://doi.org/10.1021/acs.chemrev.2c00130
Chem. Rev. 2023, 123, 6413−6544

interact. Adding to the already complex picture of the EDL as water and surface structures adapt to one another, sorbates directly influence H_2O orientations and dynamics as well as alter surface bonding and H-bonding. Surface charges and hydrophobicity/hydrophilicity can switch signs due to sorbates. Depending on the sorption thermodynamics and desorption rates, these reactions may be irreversible and surfaces can remain altered from the original state as particles move through streams and the atmosphere. Deciphering the complex chemistry of all these possibilities is a key to addressing the myriad significant challenges addressed in section 1.

The major difficulty in obtaining experimental data of complex, environmentally relevant systems are detection limits and interferences from nontarget species in spectroscopic techniques. Detection limits characteristic of most spectroscopic measurements require experimental concentrations orders of magnitude higher than found in the systems of interest. Additionally, to minimize interferences and matrix effects, background electrolytes are typically dilute (under 1 g L^{-1}) whereas groundwater may have salt concentrations up to 400 g L^{-1}.[437] A parallel problem is the heterogeneous nature of the studied surfaces. Defects are often more reactive but occur at low concentrations on a surface so signals from these minority sites are swamped when working at high concentrations and surface coverages. These issues are particularly pervasive in molecular simulation studies where model size limitations and use of ideal surfaces are common.

This section will discuss recent advances in molecular science of sorption and reactivity at oxide−water interfaces, challenges ahead, and strategies for overcoming the obstacles that hinder progress in understanding and application of fundamental scientific knowledge to societally-relevant environmental problems.

3.2. Inorganic Sorbates

3.2.1. Adsorption Isotherms and Surface Complex Speciation. Adsorption isotherms originate from the classical gas adsorption studies. Popular equations are the Langmuir, Freundlich, or Brunauer−Emmet−Teller (BET) isotherms. Uptake of a target solute from a defined solution at constant T often follows one of the above equations. Therefore, it is logical that these equations have been applied to the adsorption of solutes from aqueous solution on mineral surfaces. Because the isotherm parameters for different pH values in otherwise identical solutions are different, surface complexation models (SCMs, section 2.3.5) should be used instead. The parameters of empirical isotherms inferred for a given pH and salt level include all contributions from electrostatic effects and from variation in solution speciation.

Unlike the conditional models (see Limousin et al.[438] for a review), the SCM approach handles competitive effects in both solution and at the surface. SCMs also simulate co-operative effects such as ternary complexes or promotive electrostatics if the required parameters have been determined. For surfaces and solutions, the major challenge is to obtain comprehensive thermodynamic databases ideally linked to mechanistic, atomic-level knowledge.

Still, isotherm data are useful but, in many cases, difficult to obtain. For instance, the pH must be constant, but addition of the adsorbing target solute will change the pH, and this variation depends on the solute-to-sorbent ratio and on the target pH itself. Auto-titrator systems or manual additions of acid and/or base can correct this obstacle but may lead to overshoot and result in conditions favoring target solute adsorption. Because desorption is sometimes hampered, overshooting can obscure trends.

Reliable isotherm data can give indications about mechanisms, in particular when the transition from a typical single-layer (Langmuir-type) adsorption via an intermediate Freundlich-regime to a multilayer (BET-type) behavior occurs. An example is shown in Figure 29. As a first important feature, the

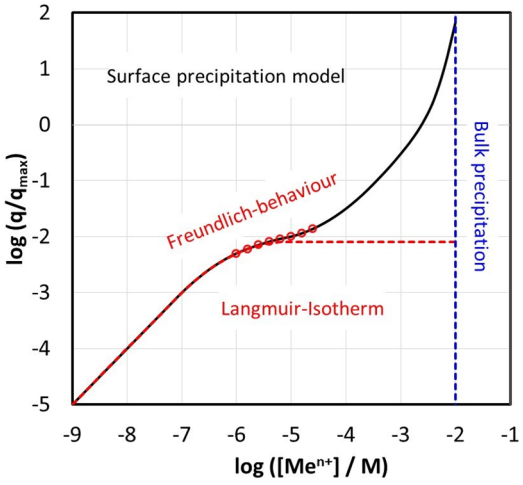

Figure 29. Uptake behavior for a metal ion with charge n^+ on an oxide surface as a function of metal concentration at constant pH and background electrolyte concentration within the surface precipitation model according to Farley et al.[439] The black full line shows the surface precipitation isotherm. The red-dotted line shows the contribution from a Langmuir isotherm-type behavior. The concentration range with open circles indicates Freundlich-type behavior. The vertical, blue-dotted line shows the limit of bulk precipitation. The symbol q is the adsorbed amount of Me (a cation of charge n^+), and q_{max} represents the amount of surface sites. Reproduced with permission from ref 439. Copyright 1985 Elsevier.

Langmuir isotherm is not plateauing at the amount of surface sites available (q_{max}). This may be observed if not all sites are adsorbing the solutes and/or if the electrostatic term impedes full coverage and/or if multidentate surface complexes form. Therefore, it is not advisible to infer site densities from macroscopic uptake curves.

As an example, maximum uptake calculated at various pH values is compared to the expected denticity of a surface complexation and the site density. Figure 30a shows though for goethite that for strongly adsorbing arsenate <20% of the sites available for arsenate binding are consumed. Moreover, Figure 30A shows that the isotherms differ for the two pH values, and this would result in two different "apparent" site densities. Even the relative contributions from the two relevant surface species differ. This shows the advantage of using SCMs, although they require knowledge about the bare surface in detail, and this may not be easily obtained (see section 3.3.3). Concerning site densities, it had originally been attempted to obtain surface site densities from plateauing charging curves[239,394] because no alternatives were available and such plateaus were actually observed. Yet, it is difficult to exclude the possibility that these plateaus are apparent.[440] Figure 30B shows that <15% of the surface sites (as estimated by crystallography and particle morphology) can be protonated within 8 pH units and at high salt levels. For lower salt levels

https://doi.org/10.1021/acs.chemrev.2c00130
Chem. Rev. 2023, 123, 6413−6544

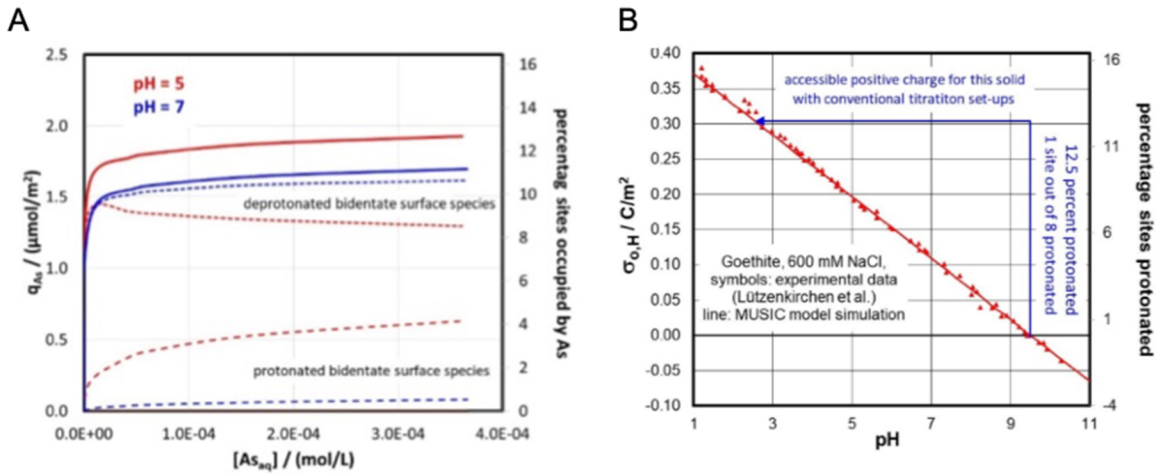

Figure 30. Adsorption of arsenate on goethite. (A) Isotherms for arsenate (As) on goethite (0.2 g/L, 100 m^2/g) at constant pH in 10 mM $NaNO_3$ solution (inert atmosphere), calculated using parameters from ref 443 at pH 5 (red) and pH 7 (blue). Full lines correspond to the overall uptake (i.e., sum of all surface complexes), and dotted lines show the contributions from the relevant surface species (the monodentate species has no contribution for these conditions). The left *y*-axis shows the percentage of sites that is occupied by As or the surface species. (B) Titratable surface charge of goethite as a function of pH for 600 mM NaCl; symbols are experimental data,[440] and the full line is a simulation using the MUSIC model.[440]

and the typically accessible pH range, it can be estimated that at most 1 out of 8 sites can be protonated. Thus, discussion about the effect of next neighbor protonation on pK_a values is probably obsolete.

Although not useful for inferring coverage or mechanism in general, the shape of isotherms can be used to gain insight. For example, the onset of surface precipitation can be inferred at sufficiently high concentrations (Figure 29) (see section 4 for details about heterogeneous nucleation and growth). Furthermore, at the lower concentration range (or solute to surface area ratio), isotherms can give indications about defects. In the absence of defects, a linear isotherm with a constant distribution coefficient for surfaces is expected and the adsorption process leaves sufficient surface area for uptake without lateral effects or significant changes of the mean-field surface potential. Few studies are available that cover the very broad range that is environmentally relevant.

In two such studies covering an extremely large concentration range, a conditional isotherm model required three kinds of sites for Np adsorption on goethite,[441] whereas for Pu adsorption to goethite between 10^{-17} M and 10^{-8} M, linear isotherms were observed.[442] At higher concentrations, particulate Pu was found, so that an adsorption model no longer applies. The Np case suggests the presence of 0.002% high-affinity sites (likely defects), whereas the most abundant site made up 99.6%. The example shows that for the environmental case Np retention would be on the less abundant sites. Comparing the Np isotherm data to the existing mechanistic goethite models would allow for obtaining more reliable information.

Instead of using generic types of sites as in the conditional isotherms, surface complexation reactions can be written using true surface sites (including defect sites) and spectroscopically defined bonding mechanisms. As an illustration of the latter such equations are given for the example of arsenate adsorption on goethite[443] (corresponding to the example of Figure 30A).

$$1{\equiv}FeOH^{-1/2} + 2H^+ + AsO_4^{-3} \leftrightarrow {\equiv}FeO_2AsO_2OH^{-1.5} + H_2O \quad (1)$$

$$2{\equiv}FeOH^{-1/2} + 2H^+ + AsO_4^{-3} \leftrightarrow {\equiv}(FeO)_2AsO_2^{-2} + 2H_2O \quad (2)$$

$$2{\equiv}FeOH^{-1/2} + 3H^+ + AsO_4^{-3} \leftrightarrow {\equiv}(FeO)_2AsOOH^{-1} + 2H_2O \quad (3)$$

In this case, one monodentate and two bidentate surface complexes were used in line with spectroscopic results.[444−447] Similar examples for arsenate or other anions[448,449] or cations[404,450] support the success of these approaches, even for saturated salt solutions. One unsolved problem is the treatment of multidentate surface complexes.[451−453] The multidentate treatment can be treated by simply putting the denticity as the exponent in the mass-law equation for the involved surface functional group. This generates a solid−liquid ratio dependence of the stability constant for the formation of the multidentate species, if molar concentrations are used in the calculations (i.e., no fractions, no normalizations). Alternatively, it is possible to consider the involved functional groups as already being assembled on the surface (i.e., very much as for solutes exposing two functional groups, like oxalate), which results in an exponent of unity in the mass law equation. This does not require any corrections if the solid−liquid ratio varies.

In essence, the treatment can be summarized by differences in writing like $2{\equiv}FeOH^{-1/2}$ as in the above eqs 2 and 3 or as $({\equiv}FeOH^{-1/2})_2$. Both variants will fail at high coverage because the thermodynamic treatment does not consider how the sites are occupied, i.e., whether or not site assemblies continue to be available for multidentate complexes. Moreover, it can be reasoned that the exponent should depend on the options of the adsorbing solute to form further bonds (once the first has formed). Thus, for example, for a central ${\equiv}FeOH^{-1/2}$ site that coordinates with an adsorbing solute (assuming it has more than one exactly identical ${\equiv}FeOH^{-1/2}$ sites that would be

https://doi.org/10.1021/acs.chemrev.2c00130
Chem. Rev. 2023, 123, 6413−6544

Table 1. Crystalline Reactive Surface Site Densities on the Two Predominant Faces of Goethite[432,454−456,461] and Total Calculations for Two Goethites of Different BET-SSA

Face	Surface site type	Site Density (sites/nm^2)	SSA (m^2/g)	Surface site type	Site Density (sites/nm^2)
{101}	≡FeOH	3.03	**>80** (16% {210})	≡FeOH	3.68
	≡Fe_2OH	0		≡Fe_2OH	0.51
	≡Fe_3OH	3.03		≡Fe_3OH	2.60
{210}	≡FeOH	7.5	**43** (36% {210})	≡FeOH	4.68
	≡Fe_2OH	3.75		≡Fe_2OH	1.26
	≡Fe_3OH	0		≡Fe_3OH	1.92

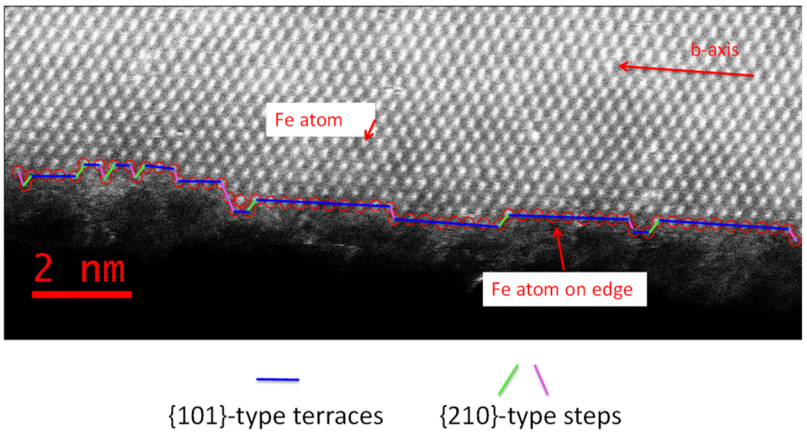

Figure 31. STEM HAADF image of a 42 m^2/g (BET) goethite showing the Fe atom positions at the {101} crystal edge looking down the C-axis.[399] The steps and kinks are identified as {210} crystal faces alternating with the otherwise dominant {101} crystal face. Adapted from ref 399. Copyright 2017 American Chemical Society.

available for forming the second bond), one could argue that the exponent four should take this into account for both options. While such an alternative approach is not being used, it is also clear that the above described situation with four identical sites around the central site already is a highly idealized situation. On goethite, this would require a crystal plane that only has one kind of site. This is not the case for any of the relevant faces of goethite. Instead, the detailed configuration of the different groups differs among the crystal planes, and the situations can become extremely complex.

3.2.2. Reactive Site Densities for Surface Proton Charging and Ion Adsorption. Primary surface charging on metal (hydr)oxides in aqueous media occurs through protonation and deprotonation reactions to satisfy the charge imbalance arising from the dangling bonds of the surface >OH/>O groups [which will be referred to here as surface sites (SS)] exposed to the aqueous phase. Please see section 2.3.3 for an in-depth discussion of this behavior and the description of the variable surface proton charge both in magnitude and in sign as a direct function of the aqueous H^+ concentration.

One of the most challenging physical parameters required for an accurate thermodynamic description of ionic adsorption phenomena on metal (hydr)oxides and silicates is the reactive surface site density, n_s (/nm^2), whether an "average" >OH SS is considered or the specific crystallographic SS with singly- (SC), doubly- (DC), and/or triply-coordinated (TC) O atoms to the central metal atom are accounted for independently. In models that consider two consecutive pK_a values, the value of this n_s parameter is left either for optimization or is taken from the maxima of adsorption isotherms under highly favorable electrostatic conditions. In models that consider one pK_a value for each type of surface group, SC, and TC SS in Fe^{3+}− oxides (and of those of other octahedrally structured trivalent metals, such as Al) are the only SS reactive to protonation/deprotonation reactions in most of the aqueous pH range. However, for example, in goethite (α-FeOOH), certain TC SS are considered nonreactive because of their H-bonding configuration[432,454−456] (Table 1). SC SS are recognized to be reactive towards ion adsorption, but it is unclear whether DC or TC SS also participate. Some SCMs have had to make use of DC SS,[457,458] but others have not.[408,435,459,460]

Regardless of the reactivity of each type of SS, calculation of their accurate n_s may prove a highly challenging aspect for the description of proton/ion adsorption. Even though the crystallographic values for the different faces of the adsorbent mineral particles may prove to be straightforward,[461] determination of the actual crystal face contributions (CFCs) may not be that simple. Recent work with a suite of high-resolution electron microscopy techniques [most notably scanning transmission electron microscopy using high-angle annular dark-field imaging (STEM HAADF)] has revealed that crystal faces, even on ideal single mineral crystals, are not completely smooth but contain contributions from other faces as steps or kinks (Figure 31).[399,462] These other faces may show widely different n_s of the different SS. The CFCs depend on the crystal morphology and on the degree of roughness (defects) of each surface present. However, a complex relationship exists between these characteristics and the size of the crystals because of imperfect growth (at relatively larger sizes) or via surface strains as particles become smaller (towards the nanometer range). This CFC relationship with

https://doi.org/10.1021/acs.chemrev.2c00130
Chem. Rev. 2023, 123, 6413−6544

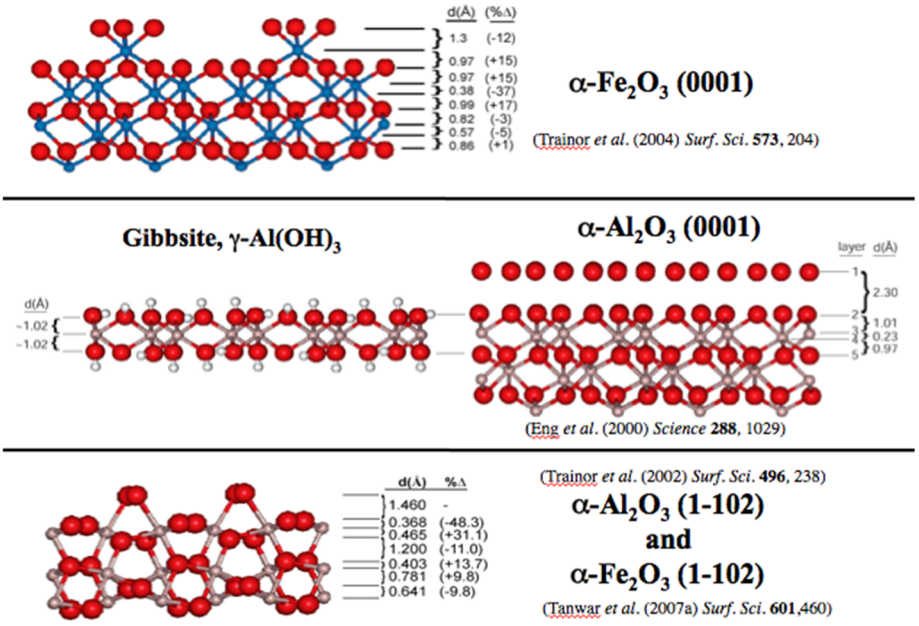

Figure 32. CTR X-ray diffractions studies of the hydrated surfaces of Al- and Fe-oxides. (top) Projection of the α-Fe_2O_3 structure showing a cross section of the CTR-derived structure of the (0001) hydrated surface. (middle) Projections of the γ-$Al(OH)_3$ and α-Al_2O_3 structures showing a cross section of the (0001) surfaces of gibbsite and hydrated corundum from CTR analysis. (bottom) Projection of the α-Al_2O_3 and α-Fe_2O_3 structures showing a cross section of the CTR-derived structure of the hydrated (1-102) surfaces. Large red spheres are oxygen, and small silver spheres are Al. %Δ is the percent atomic layer relaxation from the ideal lattice spacing. Adapted with permission from ref 476. Copyright 2012 European Association for Geochemistry.

particle size has become one of the most difficult issues to resolve in order to determine accurate values of n_s because the techniques required are not easily available and the procedures are highly time-consuming. However, they are necessary because the resulting n_s values may be widely variable (Table 1). Currently, by studying a series of goethite preparations of different SSA values ranging from ca. 40 m^2/g to 100 m^2/g, as determined by BET, the goal is to formulate a function of CFCs in relation to BET-SSA to predict the CFCs values for any other goethite preparation. This would have to be done for every metal oxide independently because it is suspected that this is a common phenomenon for real metal oxide surfaces, so far partly quantified only for synthetic goethite and rutile.[399,462] A further complication comes from the different degrees of particle aggregations with individual particle sizes as a result of drying procedures to perform the BET-SSA determination, because this blocks surface area that otherwise would be available under aqueous suspension conditions. To estimate degrees of aggregation, cryo-TEM techniques have proven useful when compared to TEM of heat-dried goethite samples.[399]

Another set of metal oxides requires a much more complicated description of their sorption behavior than those arising only from reactive external n_s, because their internal structures are imperfect and allow sorbates to bind to highly reactive sites that are available inside these structures. This is the case of layered phylomanganates, such as birnessites (δ-MnO_2), that show three sources of electrostatic charge: cation-vacant layer sites with no Mn^{4+}, variable Mn^{3+} replacements of Mn^{4+} layer sites, and pH-variable H^+ charge at the particle edges and perhaps at the internal vacancies. The first two are a source of negative charge, and thus of high affinities for cation binding, and the latter is variable, so it may bind anions or cations, depending on pH. The total n_s becomes difficult to compute as a function of surface area (even if it is internal) because of their different natures and because the internal reactive sites are randomly distributed. Current studies have focused on the differences in reactivity between internal and external (particle edges) sites.[463]

The large differences in cationic metal affinities for internal vacant sites of birnessites have been studied, and, for example, Pb(II) has been found to bind with similar affinity to internal (vacant) sites as to external (edge) sites[464,465] in contrast to most other heavy metal cations, which bind much more strongly onto vacant sites within the structure.[466,467] Attempts at modeling the adsorption behavior of Pb^{2+} on birnessites, which binds with similar affinity to internal (vacant) sites as to external (edge) sites[464,465] and of other divalent metals have been made.[468]

3.2.3. Adsorption Investigations on Individual Crystal Faces. The structure and reactivity of hydrated α-Al_2O_3 and α-Fe_2O_3 surfaces have been the subjects of a number of studies,[132,469−472] including a synchrotron-based XPS study of their interaction with water,[5] and GI-XAFS spectroscopy studies of their reactivities with respect to aqueous Pb^{2+} ions.[473−475] The XPS study showed that the reactivity of α-Fe_2O_3(0001) with respect to water is significantly greater than that of α-Al_2O_3(0001). The GI-XAFS spectroscopy studies showed that Pb^{2+} forms dominantly inner-sphere adsorption complexes on α-Fe_2O_3(0001), α-Fe_2O_3(1-102), and α-Al_2O_3(1-102) but dominantly outer-sphere adsorption complexes on hydrated α-Al_2O_3(0001),[473] indicating a lower reactivity of hydrated α-Al_2O_3(0001) to aqueous Pb^{2+}. These studies suggest that differences in the structure of the hydrated α-Al_2O_3(0001) relative to hydrated α-Al_2O_3(1-102), α-Fe_2O_3(0001), and α-Fe_2O_3(1-102) could be the reason for these differences in reactivity. There is also experimental

https://doi.org/10.1021/acs.chemrev.2c00130
Chem. Rev. 2023, 123, 6413−6544

evidence that two faces of a given substrate may exhibit differences in ion specificity.[257]

To test this hypothesis, CTR X-ray diffractions studies of the hydrated surfaces of α-Al_2O_3(0001),[115] α-Al_2O_3 (1-102),[142] α-Fe_2O_3(0001),[116] and α-Fe_2O_3(1-102)[140] were carried out to determine if the hydrated surface structures of these isostructural metal oxides are also isostructural and to understand why α-Al_2O_3(0001) has a lower reactivity with respect to water and aqueous Pb^{2+} ions than the other three surfaces. The CTR diffraction results for hydrated α-Al_2O_3 (0001)[115] showed that this surface is terminated dominantly by doubly-coordinated OH groups and closely resembles the (0001) termination of gibbsite (γ-$Al(OH)_3$) (Figure 32). These doubly-coordinated surface hydroxo groups are stable over a broad pH range[477] and would be valence oversaturated if they formed strong surface complexes with Pb^{2+}.[478] CTR X-ray diffraction of hydrated α-Fe_2O_3 (0001) revealed two surface structural nanodomains: one dominated by two-coordinated hydroxo groups and one dominated by one- and three-coordinated hydroxo groups. Trainor et al.[116] suggested that the two-domain structure of hydrated α-Fe_2O_3(0001) is metastable and undergoes slow dissolution kinetics.

These findings provide a reasonable structural explanation for the lower reactivity of hydrated α-Al_2O_3(0001) to water and aqueous Pb^{2+} ions relative to hydrated α-Fe_2O_3(0001). It also provides a structural foundation for understanding the H^+-dependent charging behavior of hematite particles, as the different surface structural sites will have significantly different pK_a values.[381] In contrast to hydrated α-Al_2O_3(0001), hydrated α-Al_2O_3(1-102) has about equal proportions of one, two-, and three-coordinated O atoms.[142] The α-Fe_2O_3 (1-102) surface also has about equal proportions of one-, two-, and three-coordinated OH groups. These observed differences in structure of the hydrated (0001) and (1-102) alumina and hematite surfaces help explain their differences in reactivity to water and metal ions in solution. DFT calculations on hydrated α-Fe_2O_3 and α-Al_2O_3 surfaces[470−472,479] have shown that the higher reactivity of the former can be attributed mainly to the empty *d*-states of the surface Fe atoms that exhibit a first peak at ∼1 eV above the Fermi level and act as very strong Lewis acid sites. In comparison, the empty *p*-states of Al in the hydrated α-Al_2O_3 surface, which are ∼5 eV above the Fermi level, much less reactive to potential adsorbates.

3.2.4. Dynamics of Water, Sorbates, and Surfaces. Papers on the dynamics of water at oxide interfaces utilizing techniques such as QENS and NMR have shown that interfacial water behavior varies significantly from that of bulk water in terms of dissociation, H-bonding, rotations, and diffusion[165,480] (section 2.2.4). Furthermore, X-ray scattering[481] and ATR-FTIR[482] have documented adsorption and desorption rates while characterizing the nature of the sorbates as outer-sphere and various inner-sphere configurations. Molecular simulations can complement these observations by verifying structures, thermodynamics, and kinetics.[13]

An example that combines NMR and MD simulations is Xue et al.,[483] who studied adsorption dynamics of amino acids onto gel-supported TiO_2 nanoparticles. Because NMR peak widths are a function of molecular reorientations, Xue et al.[483] used dark-state exchange saturation transfer (DEST) to monitor amino acid adsorption via NMR line broadening. They found that arginine, lysine, aspartic acid, leucine, and alanine all adsorb onto TiO_2 and observed exchange between a free (i.e., solution) and two bound states. Similar to other studies, the authors concluded that the main mechanism of adsorption was via the polar groups of the molecules, but interactions of the nonpolar components may play a role as well. Metadynamics with classical methods were performed to complement the NMR analyses to predict the thermodynamics and mechanisms of adsorption. Overall, the adsorption could be modeled as outer-sphere species exchanging with two inner-sphere configurations, which was similar to results for phenol adsorption onto CeO_2.[484] These types of insights are useful for understanding the connections among the dynamics of the surfaces, interfacial water, and adsorbates, which will lead to a clearer picture of reaction dynamics (section 4). More research of this type on other minerals, sorbates, and complex conditions will be required to apply these insights to real-world problems.

3.2.5. Thermodynamics of Sorption Reactions. Experimental methods for deriving thermodynamic parameters involve conducting T-dependent studies of sorption isotherms.[485,486] These isotherm-derived values remained inconsistent, predominantly due to different assumptions regarding the underlying equilibria and shortcomings related to how electrostatic contributions are handled as discussed above (section 3.2.1). SCMs have also been used indirectly to derive thermodynamic parameters. Both adsorption isotherms and edges are useful to fit for equilibrium constants.[487]

More recently, calorimetric techniques that allow for direct measurement of ΔH during solute adsorption from an aqueous phase unto a powdered sample, in either batch or flow mode, have been increasingly utilized. For instance, systematic work utilizing *operando* flow microcalorimetry measured the energetics of ions exchange and adsorption reactions on rutile, quartz, corundum, and nanohematite particles, as well as mesoporous silicas and zeolites. Studies have included alkali metal and alkali earth cations,[488,489] transition metal cations,[490] and oxyanions.[491,492] These calorimetric studies highlighted the role that hydration thermodynamics and properties play in determining the net sign of the energetics. Others have also established a strong relationship between the adsorption free energy and the speciation of cations at interfaces using X-ray reflectivity and MD approaches.[128,270] In addition to hydration, cation hydrolysis was found to affect the selective sorption of cations by lowering their overall dehydration energies and favoring bond formations.[490] On zeolites[316] and mesoporous silicas,[304,335] the authors found that surface complexation reactions become exothermic under nanoconfinement, while they exhibit endothermic behavior on analogous unconfined surfaces.

Calorimetric measurements do not resolve molecular configurations and interactions that underpin them. Measurements are obtained from powdered samples and hence are averaged over crystallographic surfaces, reactive sites and defects (step corners, regular terraces, etc.), and bonding configurations (denticities and speciation). Thus, the energetic heterogeneity of various surface sites is not well captured. This is particularly pertinent for disordered and defect-rich minerals, such as ferrihydrite. Therefore, there is a need for atomic-molecular details of the interfacial ion, water, and surface functional group configurations to better interpret calorimetric measurements. These details can be provided by other in-depth spectroscopic and molecular simulations.

Adsorption energies have been calculated by DFT on molecular clusters, but these could overestimate the ΔE, especially when the model surface charges are higher than

https://doi.org/10.1021/acs.chemrev.2c00130
Chem. Rev. 2023, 123, 6413−6544

actual surface charge densities.[493] More recently, periodic models have been used to obtain structures and energetics,[494−496] but these commonly used ideally flat periodic surfaces that do not capture edge and corner defects that may be preferred sites of adsorption. The use of nanoparticle models[497] has increased the realism of the model and allowed the investigation of adsorption at different sites. However, without experimental verification, the virtual experiments come with a significant degree of uncertainty regarding the realism of the models and the accuracy of the calculations. DFT simulations are limited in size and duration, and larger spatial and longer temporal scale classical MD simulations are necessary to access the range of pH and ionic strengths. A challenge for the computation is to predict enthalpies of adsorption that reproduce observed experimental values.

Efforts to reconcile experimental and theoretical thermodynamic parameters have been scarce. Linking observed thermodynamics and reaction rates with molecular-level bonding and reaction mechanisms will produce models that deal with longer spatial and temporal scales. The significance of connecting fundamental thermodynamic parameters of sorption with molecular-level structure of the interface lies in the ability to predict macroscopic behavior based on surface reactivity. Then, equilibrium and kinetic information at the molecular scale can be used to model macroscopic reactive transport (sections 5.1.2 and 5.2.2.4.4).

3.2.6. Kinetics of Adsorption Reactions. Kinetic studies are used to infer reaction mechanisms, useful in the geochemical context of oxide− and silicate−water interactions.[498,499] Kinetic studies at oxide− and silicate−water interfaces have involved isotope exchange techniques mostly in relation to weathering.[31,500,501] In the context of interfacial (de)protonation and cation/anion adsorption reactions, pressure-jump experiments have been used to infer rate constants,.[499,502−505] The adsorbate concentration is typically in the millimolar range, and the method records changes in conductivity following a pressure change. The data is interpreted to derive a mechanistic rate law and includes one or two reaction steps with the appropriate rate constants for adsorption and desorption. These can be related to independently-determined equilibrium constants. As an example, two-step scenarios for the adsorption of cations in some of the published work were inferred involving the initial formation of outer-sphere surface complexes and subsequent release of water as the rate-limiting step resulting in the formation of an inner-sphere surface complex as the equilibrium product.[505]

Another technique to study kinetics of interfacial reactions involves flow-through experiments with an ATR-FTIR cell.[506−510] The sorbent of interest is coated on the ATR crystal and equilibrated with a solution of defined composition that is pumped through the flow-cell. Subsequently, a solute is added into the otherwise identical solution and the uptake of the solute (usually an anion or organic molecule that shows IR bands in the wavenumber range that can be detected) can be followed with time in the spectra. The resulting data on sorption of contaminants from solution can be used to infer rates and compare to batch uptake results.[506] Apart from rate laws, the ATR-FTIR cell technique yields the spectroscopic signature of the adsorbing solute and potential variations in surface speciation. As the pressure-jump technique, sufficiently high-solute concentrations are required and solutes with characteristic bands in the relevant wavenumber range that ideally do not overlap with the omnipresent water bands. Using D_2O can help avoid such complications. Such ATR-FTIR experiments are also useful for *in situ* studies of competitive adsorption effects.[511]

QEXAFS[512] has evolved significantly over the last two decades, with distinct beamlines[513,514] that allow kinetic experiments with sub-second time resolution.[515] This is a significant advancement with respect to the early QEXAFS measurements[512] in terms of time resolution, and in conjunction with the improvements concerning concentrations, much will be learned from experiments carried out at such beamlines. Prominent examples include redox chemistry discussed in detail in section 3.4.2.[516]

Combining kinetic experiments with the different methods will be useful in linking rate laws inferred from macroscopic results (as in the pressure-jump experiments) to spectroscopic observations from ATR-FTIR or QEXAFS. Due to the concentration ranges required for the various methods, the role of surface defects is difficult to access. One way to circumvent this current restriction could be to synthesize solids with systematic variation of defects.[517,518]

For environmental applications, the desorption process (caused by decrease or the absence of the solute of interest in the solution and/or due to the presence of solutes competing for adsorption sites) is also relevant. Notably, desorption of "strongly" adsorbed solutes is typically slow, and in some cases adsorption reactions were considered irreversible. Such irreversible adsorption is a safeguard for radionuclides in the near-field of a nuclear waste repository and has led to the point of view that research in this field should now focus on the weakly binding radionuclides.[519,520] The irreversible adsorption is sometimes explained by binding to stronger sites that may include surface defects.[521] Alternatively, spectroscopic data suggest multidentate binding for many inner-sphere surface complexes.[451] The requirement that all bonds in such multidentate surface complexes have to be broken for desorption to occur could also explain sluggish desorption.

The combination of kinetic and equilibrium studies with spectroscopic measurements on well-defined mineral surfaces should help to link the various methods and modeling approaches and lead to enhanced mechanistic understanding or result in new questions. The understanding of the slow desorption process remains crucial because the slow remobilization of strongly adsorbed radionuclides for example can only be used in safety analysis if the observed irreversibility or the sluggish desorption is mechanistically understood.

In myriad adsorption studies, the kinetic experiments only involve the adsorption step and the data are modeled predominantly using a pseudo-second-order rate law.[522] Although kinetic modeling involving speciation schemes exists,[523−525] little has been done to interpret such data based on speciation models, maybe also for lack of easily accessible codes that would allow such modeling.

3.3. Organic Sorbates

3.3.1. Surface Effects. Organic sorbates exhibit similar thermodynamics and kinetics as inorganic sorbates because many of the compounds of interest are negatively-charged organic acids (carboxyl, phosphoryl groups) that are electrostatically attracted to positively-charged surface sites. Exchange reactions with OH or OH_2 surface groups are determined by the free energy of adsorption from solution to surface complex

https://doi.org/10.1021/acs.chemrev.2c00130
Chem. Rev. 2023, 123, 6413−6544

ΔG_{ads}, but organic adsorption commonly has other associated effects that are not typical for inorganic sorbates. More extensive van der Waals and H-bonding interactions can be significant, especially for higher molecular weight compounds. Organic acids such as acetic acid can flip the nature of a surface from hydrophilic to hydrophobic as the carboxylate group binds to the surface and the methyl group is oriented towards solution. These effects are particularly pronounced for natural organic matter (NOM) such as fulvic and humic acids. For example, Cheng et al.[526] examined water behavior at α-FeOOH (goethite) interfaces as a function of Leonardite humic acid (LHA) content and found changes in hydrophilicity and formation of gel-like layers. These authors conclude:

> *"Together with the molecular-level description provided in this work, this relationship should guide efforts in predicting water availability, and thereby occurrences of water-driven geochemical processes in terrestrial environments..."*

which is critical for water absorption and retention in soils, especially in arid climates and under conditions of increasing temperatures and/or drought. This chemistry is also important in petroleum geosystems as documented by Yuan et al.,[527] who studied mineral and oil degradation in oil−water−feldspar (alkali and alkaline earth aluminosilicates) mixtures and found:

> *"in the oil−water transition zone of a reservoir, oil degradation via thermal cracking and oxidative decomposition may dominate the oil degradation and may lead to the generation of secondary pores with leaching of minerals by the generated CO_2 and organic acids."*

Thus, changes in petroleum chemistry and reservoir physical characteristics are influenced by complex molecular-level reactions.

3.3.2. Adsorption and Charge Transfer. In addition to the site- and surface-specific controls on reactivity[528,529] for adsorbing inorganic ions, the pK_as of organic acids can change due to complexation with solid surfaces. This phenomenon has been known for decades in aqueous solutions[530] and can cause bond formation between phenolic groups with high pK_as and surface cations.[449,531,532] This is due to the bonds that form with the carboxylate such as COO-Fe^{3+}, the lower dielectric response of water in the interfacial regions, and electron-sharing between organic ligands and higher oxidation state metals, especially when aromatics such as salicylic acid are the sorbates (Figure 33). Adsorption of electron-donating organic ligands can be effective in increasing metal solubilities and dissolution rates through ligand-promoted dissolution[533] (see section 4) and the lowering of charge on Fe^{3+}, which makes this ion more similar to Fe^{2+}, which has higher solubility.[14] This effect will be more significant when the organic ligand binds to a defect corner site that has fewer bonds to the bulk. Nanoparticles such as ferrihydrite will be highly susceptible because of their relatively high ratio of corner and edge sites (see section 4.3.2.4).

3.3.3. Adsorption and Speciation. *3.3.3.1. Adsorbate Interactions.* Since Templeton et al.,[261] the importance and complexity of organic adsorption onto oxide and silicate surfaces has been recognized. Plant exudates and decaying plant matter contribute to subsurface organics, but the dominant components in soils are generally microbes and their necromass (see section 3.5). These organics may affect adsorption of inorganic components such as nutrients and contaminants by preventing diffusion or adsorbing species to the reactive oxide and silicate surfaces; however, they can also

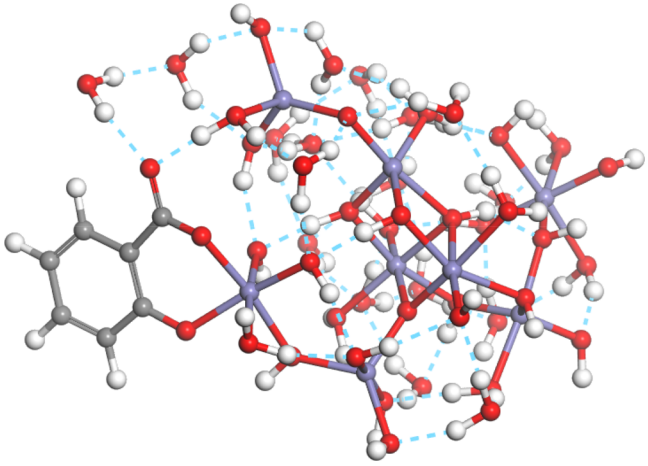

Figure 33. Salicylate bonding to Fe^{3+} on a model corner site of the goethite (010) surface allows for delocalization of electrons in the aromatic ring and partial reduction of the Fe^{3+}. Reduction towards the Fe^{2+} state increases Fe solubility (unpublished results). C = gray, H = white, O = red, Fe = purple, dashed blue line = H-bonds (Kubicki, J. D., unpublished results).

be relatively permeable and allow adsorption onto mineral surfaces to occur.[261] This is because organic polymers such as extracellular polymeric substances (EPS) are composed of polysaccharides that create relatively open gels upon adsorption onto minerals.[45,534] These biofilm layers have important implications for soil moisture adsorption and water runoff,[535] as they form long-lasting soil crusts. The wettability of soils is a critical factor in plant growth and agricultural productivity, so characterizing this property[536] and influencing soils for water uptake is a necessary step in increasing food production in increasingly warm and dry climates. Complicating the problem further is the fact that the order and kinetics of adsorption control interfacial properties in many instances. Shakiba et al.[537] demonstrated that irreversible adsorption could coat TiO_2 nanoparticles and allow for multilayer adsorption of other organic compounds. In addition to systems where solids are the matrix for water flow (e.g., water treatment, soils, aquifers), solid suspensions (e.g., particles in rivers and the oceans), especially of nanoparticles,[303] are also influenced by organic adsorption onto oxides and silicates. For example, extracellular polymeric substances can influence the stability and composition of aggregates by adsorption and alteration of the solid particle surface properties.[538] For further discussion of biotic compound adsorption and its effects, see section 3.5. This section discusses simpler organic compounds and features they exhibit that are less common for inorganic sorbates (section 3.2).

Sit et al.[539] performed a study in which both deoxyadenosine monophosphate (dAMP) and phosphate were adsorbed onto hematite to examine the roles of site competition and sorbate interactions. Using ATR-FTIR and two-dimensional correlation spectroscopy (2DCOS), the authors identified the mechanism of dAMP adsorption via the phosphoryl head group (see also Fry et al.[540] for an NMR study on the related Al_2O_3 system) and the synergistic interactions among co-adsorbates. Two major factors play a role. First, adsorption of a charged species such as PO_4^{3-} will reduce the electrostatic attraction of a positively-charged surface and decrease the thermodynamic driving force for further adsorption of anions. Second, van der Waals and H-bonding interactions between

https://doi.org/10.1021/acs.chemrev.2c00130
Chem. Rev. 2023, 123, 6413−6544

the tail groups of molecules such as dAMP may lower the ΔG_{ads} as well as they alter the interfacial water structure. Sit et al.[539] demonstrated that a linear combination of two adsorbates alone does not explain the observed spectra. They concluded that different modes of adsorption occurred for phosphate when dAMP was present, which may be due to their interactions (see section 3.5.2. Figure 40). Modeling these types of interactions would be a worthwhile endeavor to help interpret the adsorption and spectral data.

3.3.3.2. Quantification of Adsorption onto Specific Surfaces. Facet-dependent adsorption is critical for organic adsorbates as with inorganic species.[424,528,541] Any time an adsorbate has the possibility for multidentate bonding, consideration of surface structure is crucial in determining surface complexation mechanisms. Organic compounds are more complicated, compared to inorganic species, due to the common existence of tails and hydrophobic regions on organic compounds, so we highlight examples of these issues.

An important example is phenylarsonic acid ($C_6H_5AsO(OH)_2$), which was studied for its facet-dependent adsorption onto hematite by Cao et al.[542] Hematite is a good choice for this type of study because it is relatively straightforward to synthesize reactive, high surface area nanoparticles of various habits. Cao et al.[542] synthesized hematite nanocubes and nanoplatelets to adsorb phenylarsonic acid which they studied with EXAFS, ATR-FTIR, and DFT. They found that adsorption was favored on the (012) over the (001) even though both surfaces formed inner-sphere complexes. Phenylarsonic acid forms monodentate mononuclear complexes on the (001) surface and bidentate bridging on the (012) surface. Similar results were obtained by Yang et al.[64] for adsorption of ciprofloxacin onto goethite (see section 3.3.3.5 as well) by performing 2D-COS analysis of ATR-FTIR spectra to determine that the (021) surface has a higher adsorption capacity than the (110) surface. The fact that so many studies have been performed, assessing adsorption capacities and mechanisms without examination of the relative surface areas of each crystal face present means that using these data to create predictive models is extremely challenging; to overcome this challenge, we need to determine the type of surface-reactive group responsible for bonding and quantify the surface concentrations of these groups (see section 2.3.5).

Another approach has been to use AFM to obtain the binding energy to specific facets. Zhai and Wang[543] performed such a study using alginate on amorphous Fe_xO_y and hematite. These authors determined that ΔG_{ads} of binding were most favorable for the amorphous Fe_xO_y followed by hematite (10-10), (11-20), and (0001) surfaces. Such observations apply to complex NOM as well. For example, Shen et al.[63] observed Suwannee River humic and fulvic acid adsorption onto anatase and hematite nanocrystals with two habits for each phase. Zhai and Wang[543] discovered that <3 kDa components exhibited facet-dependent adsorption onto both phases, which they attributed to the simple carboxylic acids. In this case, higher molecular weight components were favored on the hematite (001) via hydrophobic interactions. Thus, depending on the habit of a given substrate, organic adsorption behavior can vary widely and affect the surface properties of the particles with significant organic loadings.

3.3.3.3. H-Bonding and Hydrophilicity/Hydrophobicity. Although the roles of sorbates and surface properties are necessary for describing and predicting adsorption phenomena, the dynamics of water including H-bond dynamics and translational/vibrational water diffusivity are of equal importance to understanding adsorption of organic solutes onto surfaces. Hydrophilicity and hydrophobicity of surfaces are indicators for adsorption of organic solutes to interfaces, and typical indices of these properties are provided by macroscopic measures such as contact angle, nonpolar solvent accessible surface area, or by group-specific parameters such as octanol–water partition coefficients. However, these macroscopic indices fail to capture the complex dynamics of water–water and water–solute interactions that determine interfacial water structure.[544] Molecular level studies on silica surfaces have probed the origins of both hydrophilic and hydrophobic moieties.[157,545] For example, silica is typically considered to be hydrophilic due to weakly H-bonded surface OH groups.[341] Using phase-resolved vSFG in conjunction with MD simulations, molecular hydrophobic sites have been identified and associated with weakly H-bonded water hydroxyl groups that bind to O atoms of siloxane bridges.[340] In a study comparing the CLAYFF force field to the INTERFACE force field, the results highlighted the layered structure of interfacial water at silica surfaces and suggested that for hydrophobic surfaces, surface-induced orientation is short-range, whereas for the hydrophilic surface the molecular orientation perturbations are more long-range, ∼ >3 Å.[546] Changes in the density of hydrophobic groups correlated with measured contact angles. Monroe and Shell[547] demonstrated that hydration water orientational entropy, diffusivity, and H-bonding properties are intrinsically connected and that surface patterns control the dynamics of hydration water primarily due to the directional interactions of water molecules and the wide range of networks that can form with neighboring surface groups and water molecules. For example, cristobalite (SiO_2) surfaces with intermediate hydrophilicity patterned to maximize water diffusivity exhibited water diffusivities similar to a surface with reduced hydrophilic coverage but having randomly generated surfaces.[547]

The impacts of water dynamics are also evident for hydrophobic organic solutes. Around small hydrophobic solutes, water can maintain its H-bond network at the cost of an entropic penalty due to restricting configuration space.[548,549] A study of linear alcohols suggests that T and hydrophobic chain length impact the structure of their hydrophobic hydration shells relative to the bulk.[550] At low T, hydration shells with tetrahedral order and few weak H-bonds exhibited more hydrophobic character, but this structure disappeared with increased T and chain length. Similar evidence for a more tetrahedrally-ordered hydration shell that diminishes with T has been observed for methane in water.[551] A balance of solute–water and water–water interactions was shown to isolate solute molecules from each other at concentrations where water molecules can complete hydration shells for solutes.

Surface–water dynamics and solute–water dynamics have an impact on solute adsorption to surfaces. For example, sorption of atrazine to silica surfaces has been attributed to interactions with silanol groups and/or surface water, but the weak interactions allow for rapid displacement during desorption.[552] The importance of water monolayers for H-bond dominated adsorption has been demonstrated for benzoic acid and ibuprofen.[553] A recent study examining solute–surface affinity to model hydroxyl terminated self-assembled monolayers highlighted the fact that many small, charge neutral solutes show affinity for hydroxylated surfaces

https://doi.org/10.1021/acs.chemrev.2c00130
Chem. Rev. 2023, 123, 6413–6544

and direct attractive solute−surface interactions dominate this affinity.[554] Taken together, these studies highlight the power of combined spectroscopic and molecular dynamic simulation tools for characterizing the impact of water dynamics on molecular hydrophobicity and adsorption onto hydroxylated surfaces.[181,554]

3.3.3.4. Thermodynamics of Organic Adsorption Reactions. The thermodynamics governing the adsorption of organic ligands on surfaces are more complex than those for simple inorganic sorbates (section 3.3.1). The reasons are thoroughly discussed throughout section 3.3. These include a bigger role of electrostatic interactions, i.e., H-bonding and van der Waals, complex structures with hydrophobic and hydrophilic domains that can attach at multiples sites, and complex chemistries because many organic molecules, namely those with high molecular weight, will possess several functional groups with different pK_as as well as their own IEPs. Equally important is the need to account for conformational changes that occur during adsorption. Therefore, it is expected that many different types of molecular interactions will contribute to the total energies of organic adsorption and that it would be challenging to tease them apart. Some authors have chosen to assert that the contributions from some of these components would be relatively small and instead looked to identify dominant forces.[555] Despite a recognition that capturing the role of organics, particularly the interactions of inorganics and organics ligand at interfaces, is an important component of representing natural complexity and scaling up our predictions to more realistic systems (section 1.1), investigations on the thermodynamics of organics adsorption to metal oxides remain limited and have not caught up to the advances made in the spectroscopic arena.

Experimental thermodynamics investigations report exothermic ΔH_{ads} and negative ΔG_{ads} when derived. For example, using Calvet-type differential microcalorimetry, Gu et al.[556] studied the adsorption of natural organic matter isolated from a wetland pool on commercially available hematite powder and measured a heat of adsorption equivalent to about −125 to 320 kJ per mol of carboxyl/hydroxyl functional groups of NOM adsorbed. Benoit et al.[557] studied the adsorption of organic ligands (e.g., aromatic acids, monochlorophenols, and aliphatic acids) on Al-oxides by ITC and reported exothermic adsorption enthalpies for all ligands considered. Similarly, the adsorption of pyrocatechol and oxalate, as proxies for NOM, on hematite nanoparticles was exothermic and significantly larger than the ΔH_{ads} of As on the same solid under similar experimental conditions.[492,558]

Although these measurements are useful in assessing comparative affinities and favorability, they can become more challenging to interpret, particularly for larger polymeric substances where steric crowding and conformational changes come into play as surface coverage increases. In fact, "simple" organics such as catechol will exhibit a concentration-dependent adsorption as shown by Lin et al.[559] on ZnO quantum dots. Steric crowding has also been reported to result in less favorable enthalpies in studies of nitroaromatic compounds adsorption on clay surfaces[555] as molecules are forced into less than optimal configurations at higher coverages. The impact of conformational changes or steric packing was also reported.[45] The authors found that the conformation of adsorbed dextran (proxy for EPS) continuously changed on an alumina surface but remained constant on a silica surface. In the area of polymer adsorption from aqueous solution to solid surfaces the self-consistent-field (SCF or Scheutjents−Fleer) model has been used to analyse the kinetics of adsorption with respect to confirmation changes.[560,561]

The literature suggests that ΔH is the driving force for the adsorption of organics on solids. This is most likely because we lack a good to measure or even calculate ΔS_{ads}, and therefore its contributions to the overall thermodynamics are not well elucidated. Nevertheless, in cases where conformational changes are expected, one could argue that capturing changes in ΔS is imperative. For instance, through the application of the solvation and electrostatic (SE) model, Sahai[562] highlighted the importance of ΔS_{ads} as they posited that changes in ΔS_{ads} could explain why some minerals, such as quartz and other crystalline polymorphs, are cytotoxic and others, e.g., amorphous silica, rutile, anatase (TiO_2), and hematite, are less harmful to biomembranes. The author modeled the initial interaction of the quaternary ammonium component of a phospholipid (PL) with different oxides surface and found that when $\Delta S_{ads} < 0$, the PL conformation is changed significantly upon interaction with the oxide and the biomembrane is ruptured. This was the case for quartz. In the case of favorable entropy, i.e. $\Delta S_{ads} > 0$, the PL structure will change less and the oxide, e.g., amorphous silica, Al_2O_3, and TiO_2, exhibits less membranolytic ability. This occurred even though ΔG_{ads} of the TMA was favorable (<0) on all oxides.

3.3.3.5. Kinetics of Organic Adsorption Reactions. Adsorption kinetics depends upon diffusion from the bulk solution to the surface and often surface diffusion and transformations from outer-sphere to inner-sphere, monodentate to bidentate, and exchange with surface species of the bulk solid. Reactions can be either transport-controlled or surface-controlled depending on the nature of the surface, the sorbate, solution conditions, and flow rate. For simple (i.e., nonpolymeric) sorbates, the rate-limiting step is commonly assumed to be the outer-sphere to inner-sphere step because aqueous diffusion is relatively rapid for ions and formation of outer-sphere species does not require a bond-breaking event. To form an inner-sphere species, de-solvation of the ion necessitates removal of one or more M^+-OH_2 bonds or A^-−H_2O H-bonds which can be a significant energy barrier. Additionally, to form an inner-sphere surface complex, a bond on the surface is usually broken (typically MO-H, M−OH or $M-OH_2$), which is an additional energy penalty. Hence, the nature of the surface leaving group is critical for adsorption reaction rates, with $M-OH_2$ being a much better leaving group because these bonds are much weaker than the corresponding M−OH bonds.

An example can be found in Soldoozy et al.,[13] who compared inorganic arsenate (iAs) and dimethylarsinate (DMA) adsorption onto α-Fe_2O_3 (hematite) via ATR-FTIR complemented with DFT calculations of IR spectra and reaction pathways. Initial faster rates of adsorption were more sensitive to aqueous As concentrations than the slower adsorption rates consistent with diffusion limiting the aqueous to outer-sphere transformation. The inner-sphere adsorption ΔE_a were +4 to +11 kJ/mol, indicative of a mechanism in which strong bonds are not broken. This observation led to the conclusion that defect Fe^{3+}-(OH_2) sites were the reactant species in these reactions because these were the only moieties that resulted in DFT model ΔE_a values similar to experiment. Inorganic As (iAs) adsorption was faster than DMA, and iAs desorption was slower than DMA. ATR-FTIR and DFT results

https://doi.org/10.1021/acs.chemrev.2c00130
Chem. Rev. 2023, 123, 6413−6544

were consistent with bidentate bridging mechanisms dominating the surface complexes for both iAs and DMA. All three species are likely to be present, however. Note that the DFT calculations in this case were performed using simple molecular clusters rather than periodic hematite surfaces. This can contribute to inaccuracy, but the general experimental-computational agreement may also be indicative of short-range bonding dominating the adsorption reaction thermodynamics, kinetics, and speciation.[492]

Flow rate can influence kinetics of adsorption, as the slow step between outer-sphere and inner-sphere species may be disrupted.[563] Zhou et al. studied ciprofloxacin (CIP, a model antibiotic compound) under constant flow and flow-interrupted conditions and observed significant differences in behavior. Similar to Soldoozy et al.,[13] CIP forms bidentate surface complexes on hematite nanoparticles although a bidentate, mononuclear complex was invoked in this case with one carboxylate and one carbonyl O atom bonding to the same surface Fe atom.[564] Interruption of flow allowed for oxidation of the CIP adsorbed onto the hematite nanoparticles which was interpreted as an outer- to inner-sphere transformation during the no-flow conditions. Similar changes in flow rates are common as water travels through natural media such as soils and aquifers, but there have been few molecular-level studies including this important factor. Zhou et al.[563] states:

> *"Failure to take into consideration redox mechanisms coupled to water flow in natural porous media may introduce a bias in the characterization of affected environments leading to misevaluation of ecotoxicity. Therefore, predicting the mobility of parents and daughter compounds in groundwater and subsurface environments is crucial for assessing potential genotoxic effects and human health risks."*

Over- or under-estimation of ecotoxicity is a common issue because laboratory assessments typically only consider the parent compound and not the intermediate products resulting from environmental reactions. For example, benzo[*a*]pyrene (B[a]P) is considered one of the most carcinogenic of the polycyclic aromatic hydrocarbons (PAHs), but it is B[a]P that forms adducts with DNA and leads to mutation and cancer.[565]

3.3.3.6. Competitive Inorganic and Organic Adsorption Reactions. Another phenomenon that contributes to the complexity of the interfacial region is competitive adsorption. Many real-world solutions are mixtures of various components, and these aqueous components do not interact with surfaces in a linear manner. In a relatively simple solutions of Na^+, Rb^+, and Sr^{2+} interacting with the nearly atomically flat (001) surface of muscovite mica ($KAl_2(F,OH)_2(SiO_2)_6$), nonclassical behavior has been detected by Lee et al.[271] via *in situ* RAXR experiments. Nearly equivalent distributions of IS and OS species were observed for $Sr(NO_3)_2$ solutions, but addition of Na^+ or Rb^+ to the solution shifted the predominant Sr^{2+} species to OS. The data were not well fit by a classical competitive adsorption model. The authors suggested that Sr^{2+} ΔG_{ads} became more positive in the presence of Na^+ and Rb^+ due to both site-specific and non-site-specific interactions mediated in part by the lateral distribution of the Al^{3+} for Si^{4+} substitutions that create negative sites on the muscovite(001) surface. Similar chemistry has been seen for sulfate adsorption onto hematite by Schmidt et al.[482]

Considering that simple ions on relatively flat surfaces have nonclassical behavior, it is not surprising that adsorption of more complex species onto surfaces with greater heterogeneity would lead to nonlinear effects. Many naturally-occurring organic acids contain deprotonated carboxylate groups that bind to metal ions on surfaces, and these acids can have significant variations in molecular weight from low (e.g., oxalate, salicylate) to high (humic acids). Thus, the larger size of these adsorbates causes steric effects upon adsorption, sorbate−sorbate interactions that can be positive or negative, changes in the hydrophilicity/hydrophobicity of the surface, and provide specific sites for adsorption of other ions such as Ca^{2+} bonding to remaining COO^- groups not bonded to the surface. One example is a study by Fleury et al.[566] that examined competitive sorption of the metals Cu^{2+}, Zn^{2+}, Cd^{2+}, and Pb^{2+} onto hematite as a function of fulvic acid (FA) concentration. The FA/hematite ratio, *r*, influenced both the type of FA molecules and the sorption of the metals. As might be expected, higher *r* values led to greater adsorption of aromatics from solution, but varying *r* also affected the adsorption of the metals to differing degrees. These complexities exist in nature and properties such as *r* vary dramatically from site to site and on centimeter scales within a given site. Principles to predict adsorption and transport must include these complexities. Another example is adsorption of oxalate at boehmite− and corundum−water interfaces, which elucidates dynamic speciation of oxalate with four distinct species identified by IR spectroscopy (aqueous oxalate, outer-sphere adsorbed oxalate, inner-sphere adsorbed oxalate, and aqueous Al^{3+}-oxalate species).[567] The abundance of each species is defined by the pH and surface coverage: at low surface coverages, inner-sphere mononuclear bidentate oxalate adsorbed at a 5-membered Al^{3+} sites is predominant, in agreement with IR spectroscopy measurements and DFT calculations.[567]

3.3.3.7. Hysteresis in Organic Adsorption Reactions. For higher molecular weight polymeric adsorbates (e.g., proteins, lipids, cellulose, lignin), conformations can change upon adsorption and influence sorption of other ions or allow diffusion and adsorption.[45,568] Covalent, ionic, H-bonding, and van der Waals forces play a significant role where polar groups are present in organic polymers with COO^- groups as a common initial bond-former. Relaxation of the less polar sections of the polymers then interact with the surface and release H_2O molecules solvating the surface, which leads to an entropically favorable state. Wu et al.[568] studied ascorbic, citric, and humic acids as well as bovine serum albumin (BSA) adsorption and desorption onto nanoparticles coated with TiO_2 (Note: The phase of TiO_2 was not characterized, and the method of coating likely leads to amorphous or poorly crystalline TiO_2 rather than rutile or anatase.). The simpler ascorbic and citric acids demonstrated greater reversibility (less desorption hysteresis) than the humic acid and BSA. Changing humic acid conformations were documented via QCM experiments in which the frequency dissipation increased with time. This is indicative of a more densely packed and lower hydration surface coating as seen in classical MD simulations of dextrans on SiO_2 and Al_2O_3 surfaces.[45] Another phenomenon that may occur is multidentate attachment of organic compounds with multiple COO^- or other polar groups.[569,570] Wu et al.[568] also investigated the order of adsorption, which will be a critical factor in natural environments as surfaces are exposed to constantly changing conditions that will result in a complex surface coating. Modeling these complexities is essential for predicting surface

https://doi.org/10.1021/acs.chemrev.2c00130
Chem. Rev. 2023, 123, 6413−6544

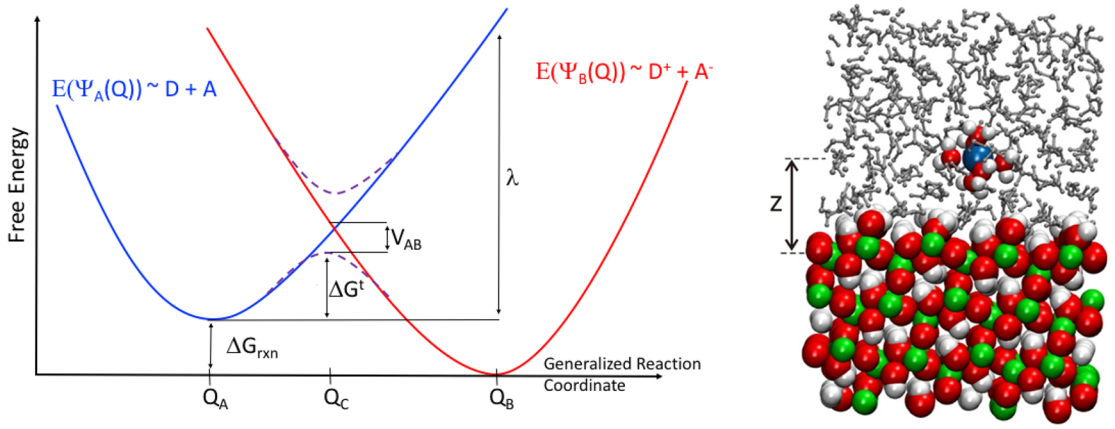

Figure 34. Free energy of an ET system. (left) Illustration of ET diabatic states (solid curves) and their splitting to produce adiabatic states (dashed curves), (right) example implementation using molecular dynamics simulations with umbrella sampling to compute the ET diabatic states and ET kinetics between an adsorbed Fe^{2+} hexaaquo ion and Fe^{3+} cations comprising the (110) surface of goethite. Adapted from ref 605. Copyright 2015 American Chemical Society.

reactions such as contaminant adsorption and radiative effects in the atmosphere.

Once one considers aggregates that occur in soils and aquifers, the possibility of sequestration in pores can lead to extreme hysteresis (irreversibility) in adsorption/desorption reactions. Individual minerals may exhibit porosity such as etch pits, but aggregates of fine-grained minerals can form extensive pore networks varying in diameter from nanometers to millimeters. One recent study that examined these effects focused on the important contaminants per- and polyfluoroalkyl substances (PFAS; Xiao et al.[571]). The authors found that

> *"Sorption of zwitterionic PFAS... displayed concentration-dependent hysteresis in soils with a low SOM content... electrostatic interactions with negatively charged soil constituents and the hydrophobic effect were found to be major sorption driving forces for cationic/zwitterionic PFAS at low and high concentrations, respectively."*

Xiao et al.[571] used DFT to calculate the maximum electrostatic potential of the PFAS and were able to use this parameter to predict sorption of ionic PFAS successfully. Hence, in order to predict long-term behavior of contaminants and the associated bioavailability, one must understand the molecular mechanisms controlling the macroscopic behavior in complex systems rather than in binary systems with one sorbent and one sorbate.

Organic ligands form complexes with the ions of interest in solution, altering adsorption mechanisms and measured adsorption isotherms. For example, overall surface uptake of trivalent lanthanides (Ln^{3+}) onto natural soils is defined by the organic ligands complexing with Ln^{3+} ions in solution.[572] Macroscopic Ln^{3+} adsorption can be fit equally well with Langmuir and Freundlich isotherm models; the maximum surface coverage correlates with the K_β constants for the Ln^{3+}–organic acid complex, with adsorption decreasing as K_β constant increases in the order: citric acid > malic acid > tartaric acid > acetic acid.[572] Similar observations were made for the adsorption of Cu^{2+} onto nanoparticulate hydroxyapatite ($Ca_{10}(PO_4)_6(OH)_2$). With increasing K_β constants between Cu^{2+} and organic acids, the overall adsorption decreases and the adsorption data is best fit to the Dubinin–Radushkevich isotherm model.[573]

3.4. Redox Processes

Interfaces play a critical role as facilitators of redox reactions, either directly in the case of redox-active mineral solids or indirectly by providing support for redox-active metals or organics. The central underlying process is electron transfer (ET), which can follow a wide range of mechanistic pathways including abiotic and biotic, homogeneous and heterogeneous, spontaneous and photochemically mediated. In natural waters, many biogeochemical processes directly depend on the ET rate. These include the cycling of redox-sensitive metals such as Fe and Mn,[574,575] the respiration of dissimilatory metal-reducing bacteria[576] and the related role of electron shuttle molecules,[577,578] the reductive dissolution of metal oxide minerals,[579] and the fate and transport of contaminant metals, organic solvents, and pesticides.[580,581] ET reactions that are intrinsically slow despite being thermodynamically favorable are often key to understanding overall process rates. Rates of such processes can be strongly influenced by interfacial structure and dynamics[582] and may comprise a basis for specific adaptations in biological organisms to increase ET efficiency.[583]

3.4.1. Kinetics and Mechanisms. The foundation for understanding and predicting ET kinetics and mechanisms is Marcus–Hush theory, led by seminal papers by Marcus[584,585] and continually further developed, tested, and refined by numerous others.[586−588] Applications to aquatic geochemical systems date back to Wehrli.[589] Development of accurate quantum mechanical methods and adaptation of these methods to compute Marcus theory quantities from first-principles, such as for metal aquo ion redox reactions,[574,590] and furthermore adapted to semiconducting mineral–water interfaces[591−593] and biogeochemical redox reactions has started from this.[594−597] Modern planewave DFT codes contain algorithms to directly compute Marcus theory quantities such as the electronic coupling.[102,598,599] Other computational advances such as various approaches to rare event sampling have helped advance our ability to simulate ET processes in increasingly complex systems with high accuracy.[600,601] Likewise, on the experimental front, the increasing availability of highly time-resolved pump-probe synchrotron X-ray absorption spectroscopies have enabled interfacial ET kinetics for geochemical systems to be directly measured.[602]

https://doi.org/10.1021/acs.chemrev.2c00130
Chem. Rev. 2023, 123, 6413−6544

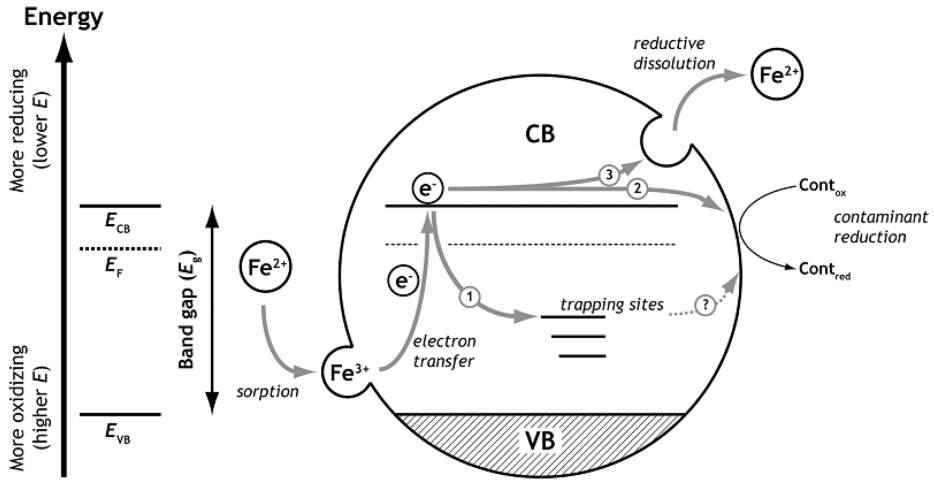

Figure 35. Conceptual schematic representation of the redox-driven conveyor belt mechanism. Reproduced from ref 663. Copyright 2011 American Chemical Society.

Molecular simulation studies on larger more complex geochemical redox interfaces with quantum mechanical accuracy are essential. Exciting new developments in interface-sensitive, time-resolved SFG spectroscopy[603] and 2D-IR spectroscopy[604] have the potential to directly map the nuclear reaction coordinate for redox processes at ultrafast time scales. The increasing availability of X-ray free electron laser beamlines for X-ray (or optical) pump/X-ray probe studies, as well as the X-ray scattering technique of X-ray photon correlation spectroscopy (XPCS) hold the potential to directly probe the dynamics of water at interfaces associated with ET processes.

3.4.1.1. Marcus Theory and Its Extensions. The free energy for a single ET event between a donor and an acceptor (e.g., $D + A \rightarrow D^+ + A^-$) can be described as occurring along a generalized nuclear reaction coordinate (Q) between two equilibrium configurations (initial Q_A and final Q_B) possessing two different electronic configurations (Figure 34). The ET system can be described as having two electronic states $\Psi_A(Q)$ and $\Psi_B(Q)$, along with their associated energies $E(\Psi_A(Q))$ and $E(\Psi_B(Q))$, which are functions of the atomic position. This is referred to as a Franck−Condon process, which indicates that the movement or relaxation of electrons is essentially instantaneous compared to the nuclear motion. The ET driving force is contained in ΔG_{rxn}, the free energy difference between respective minima in $E(\Psi_A(Q))$ and $E(\Psi_B(Q))$. The transition state configuration (Q_C) of main concern is the lowest energy at which $E(\Psi_A(Q)) = E(\Psi_B(Q))$, a configuration that can be considered a distortion in the positions of the atoms within the donor−acceptor complex that makes the donor−acceptor ET states (e.g., orbitals) degenerate. This distortion energy relates to the forces between atoms in the ET encounter complex as well as the energy to repolarize the surrounding medium towards the charge distribution of the ET products state, quantities that are captured in the ET reorganization energy λ, which is the energy cost to distort $[D + A]$ into the equilibrium nuclear configuration of $[D^+ + A^-]$ without moving the electron.

The electronic coupling matrix element, V_{AB}, between the two states at Q_C along with the kinetic energy of the atoms, determines the mechanism of ET (Figure 34). The magnitude of the coupling becomes exponentially weaker with increasing ET distance, such as in outer-sphere ET complexes, but can be strongly enhanced by superexchange interactions through bridging ligands, such as possible in inner-sphere ET complexes. For $V_{AB} \geq k_B T$ and small atomic kinetic energies, the ET reaction evolves adiabatically along double-well ground state potential energy surface (e.g., the Born−Oppenheimer approximation). This reflects relatively strong electronic interaction between the donor and acceptor, such as in many inner-sphere ET complexes,[606] small polaron transport in metal oxides,[591,607] and soliton transport in conduction polymers.[598] When $V_{AB} \ll kT$, the energy separation between the two states at Q_C becomes small and the Born−Oppenheimer approximation breaks down. In weak-coupling cases, the ET reaction is often described from a semiclassical viewpoint where the possible transitions between state Ψ_A and Ψ_B may only occur in the finite region where the curves are close to one another. First, the system evolves along the ground state from Q_A to Q_C, where there is a finite probability that the system stays on Ψ_A or conversely jumps to Ψ_B, after which the system either progresses along the adiabatic curve to the ET products state Q_B or it continues evolving up Ψ_B while maintaining in its initial [D···A] bonding. Examples of this type of ET in the weak coupling limit include a variety of outer-sphere reactions,[574] charge transfer between ions in solution, and small polaron transport in mixed oxides and low-Fe clays near the percolation limit. It is often termed as being (microscopically) non-adiabatic, or simply diabatic, and its rate can be modeled by Marcus theory and extensions, diabatic methods, and coupled quantum electron−nuclear dynamics methods (see section 3.7).

3.4.1.2. Extension to Interfaces. Aspects of ET kinetics that change upon going from redox systems in homogeneous solution to heterogeneous ET at mineral−water interfaces can be understood in the same framework of Marcus−Hush (Figure 34). In contrast, to encounter complex formation in solution, often treated as a 3D collision theory problem with electrostatics, the rate of encounter complex formation at interfaces becomes a quasi-2D adsorption/desorption kinetics problem, which is subject to familiar interfacial chemistry issues of pH-dependent surface charge and speciation of ET donor/acceptor ions, and the composition, structure, and dynamics in the electrical double layer.

At interfaces, the reorganization energy now has contributions both from repolarization in first few solvent layers near

https://doi.org/10.1021/acs.chemrev.2c00130
Chem. Rev. 2023, 123, 6413−6544

the interface as well as distortion of the mineral surface groups and lattice surrounding the ET donor/acceptor pair spanning the interface. In the case where the mineral is redox-active and part of the ET pair, the electronic structure at the mineral surface is important to take into consideration. This aspect is often treated with a semiconductor model of the mineral surface to describe the energies of valence and conduction band edges participating in the ET process (Figure 35).

In addition to contributions from a single mineral surface, confining aqueous solutions between two mineral surfaces can lead to deviations from Marcus theory. In the birnessite phase of MnO_2, the interlayer consists of concentrated solutions of water and cations (to balance the negative charge of the MnO_2 sheets). Water molecules H-bond to the oxide sheets and interact with other waters, mainly through dipole−dipole interactions. A competition between water−water dipole−dipole interactions and water−ion dipole−charge interactions arises, and this competition frustrates interlayer water molecules and enhances solvent fluctuations relevant to ET. These enhanced solvent fluctuations lead to nonparabolic free energy surfaces and lower the barrier to ET, increasing ET rates beyond expectations from Marcus theory.[608−610] Further increasing frustration by decreasing interlayer distances increases reaction rates,[610] and these concepts have been exploited to enhance birnessite-catalyzed water oxidation.[611−613] Similar effects have been found for ET in nickel−iron oxyhydroxides[611,614] and may also play a role in the interlayer chemistry of zirconium phosphates[615] and in the development of energy technologies.[616,617] We note that confinement effects on ET do not universally enhance ET rates. Confinement within disordered carbon electrodes leads to deviations from Marcus theory that decrease ET rates due to changes in ion coordination structure.[618]

3.4.1.3. Complex Interfaces. Because realistic mineral−water interfaces in natural environments typically are defective, impure, and are often coated with a variety of organic and biologic sorbates, including at times microbial biofilms (section 3.5), interfacial redox reactivity can be strongly modified. In practice, it remains impossible to fully account for the interplay of these complex components on redox mechanisms and kinetics. Some progress has been made in evaluating effects at the molecular-level concerning ET reactions at the interface between metal reducing microbes and low-index surfaces of metal oxide minerals such as hematite. To a first approximation, because ET rates decrease by about an order of magnitude with each Ångstrom increase in separation distance between donor and acceptor, intervening components that are electronically decoupled from the donor−acceptor pair tend to decrease ET rates simply by acting as intervening spacers.[606,619] For example, the efficacy of ET to metal oxide mineral surfaces by redox-active heme cofactors in bacterial outer-membrane cytochromes has been shown to depend strongly on separation distance, which in turn is controlled by the details of macromolecular protein structure, docking orientation, and the atomic details of surface structure that define the ET gap.[591,594−597,620−623] Here, important effects include terminal heme solvent exposure, protein surface electrostatics, the redox potential gradient between the terminal heme and the Fermi level of the metal oxide, and intervening water and ions. The additional complexity of intervening bacterial structures such as exopolysaccharide remains poorly understood, with possible effects ranging between inert spacer to an electronically coupled bridge mediator of the interfacial ET process.[624,625] Bacterial extracellular ET can also be mediated by redox-active organic shuttle molecules or biogenic exudates that bypass direct enzymatic ET at interfaces.[577,626]

3.4.1.4. Oxidative Reaction with Fe- and Mn-Oxides. Oxidative reactions of Fe- and Mn-oxides define the fate and transport of organic and inorganic contaminants[627−630] and the global geochemical cycles of many major elements, such as C, N, O, P, and S.[631] Fe- and Mn-oxides usually co-exist in complex mixtures with clay minerals, other metal oxides, natural organic matter, and dissolved species, such as simple ions and organic and inorganic ligands, some of which are redox-active. Therefore, the oxidative reactions on Fe- and Mn-oxide surfaces depend on the environmental matrices.

3.4.1.4.1. Oxidation of Organic and Inorganic Solutes by Mn and Fe Oxides. The standard redox potentials (Eh^0) for the half-reactions of $Mn^{(3+/4+)}/Mn^{2+}$ and Fe^{3+}/Fe^{2+} redox couples make them strong oxidants towards organic and inorganic solutes. For example, the standard redox potential is 1.23 V for $MnO_2/Mn^{2+}_{(aq)}$[632] or between 0.768−1.067 V for Fe^{3+}-oxides/$Fe^{2+}_{(aq)}$.[633] The bulk of literature on the oxidative reaction of Fe- and Mn-oxides is on the oxidation kinetics and mechanisms of organic solutes, such as phenols and anilines,[627] and inorganic solutes, such as As^{3+}[634] and Cr^{3+},[635] as summarized below. Different from earlier work that focuses on simple organics,[627,632,636−638] more recent work examines diverse emerging contaminants from pesticides, fire retardants, to pharmaceutical and personal care products.[630,639−643] Additional work investigates phase transformation of the Mn oxides or surface complex formation during reaction.[634,644,645] The same surface-associated reaction mechanism was reported for all of the above systems:[630]

$$>Mn^{4+} + ArXH \rightleftharpoons (>Mn^{4+},\ ArXH) \quad (4)$$

$$(>Mn^{4+},\ ArXH) \rightleftharpoons (>Mn^{3+},\ ArX^{\bullet}) + H^{+} \quad (5)$$

$$(>Mn^{3+},\ ArX^{\bullet}) \rightleftharpoons >Mn^{3+} + ArX^{\bullet} \quad (6)$$

$$>2Mn^{3+} \rightleftharpoons >MnO_2 + >Mn^{2+} \quad (7)$$

$$ArX^{\bullet} \rightleftharpoons \text{products} \quad (8)$$

where ">" indicates surface bound, Ar is short for aromatic ring, and the parentheses suggest reaction intermediates. Either the first (adsorption) or the second (one-electron transfer) elementary reaction steps is believed to be the rate-limiting step. After the electron-transfer reaction, the Mn oxide has a higher than initial Mn^{3+} content in the structure,[644] while the generated Mn^{2+} ions accumulate at the oxide surface followed by a release to the solution once the surface has been saturated.[630] Both structural Mn^{2+} and adsorbed Mn^{2+} suppress the oxidative reactivity for they lower the redox potential of the oxide/Mn^{2+} couple.[630,635] Because radicals are involved as the reaction intermediates for organic solutes, a range of oxidation products have been reported by following the formation of radical intermediates.[639−641,643,646] More details regarding how organic solutes are oxidized by Mn oxides are provided in another review.[627] For inorganic solutes, their oxidation by Mn oxides also proceeds by initial surface complex formation followed by electron transfer.[634,635,647,648] A similar mechanism has been established for oxidation of organic and inorganic solutes by Fe-oxides, but the reaction

https://doi.org/10.1021/acs.chemrev.2c00130
Chem. Rev. 2023, 123, 6413−6544

kinetics with Fe-oxides are slower owing to their lower redox potentials.[642,649−651]

3.4.1.4.2. Oxidative Reactivity of Mn Oxides in Complex Mixtures. Oxidative reactions of Mn- and Fe-oxides are surface-mediated; therefore, anything that affects the surface chemistry is expected to affect their redox activity. Indeed, metal ions such as Ca^{2+}, Ni^{2+}, Cr^{3+}, and Cu^{2+} can inhibit the reactivity through adsorption on the oxide surface.[639] Inorganic and organic ligands also inhibit Mn-oxide reactivity via either competitive adsorption and/or complexation to block surface sites or reductive dissolution to provide Mn^{2+}.[629] Natural organic matter of a small quantity is also known to strongly complex with Mn^{2+}, therefore facilitating Mn^{2+} removal from the surface, which mitigates the inhibitory effect of the Mn^{2+} on MnO_2 reactivity.[652,653] Metal oxides including Al, Fe, Si, and Ti oxides often inhibit Mn-oxide reactivity through one or a combination of the following mechanisms:

(1) heteroaggregation between oxide particles

(2) surface complexation of the dissolved ions with Mn oxide surfaces

(3) competitive adsorption of the oxide surfaces toward the solute[654−656]

Upon the addition of natural organic matter or small organic ligands to mixtures of Mn- and Fe- or Al-oxides, the oxidative reactivity of the Mn-oxide is often enhanced as compared to when no organic ligands are present. This has been attributed to enhanced homoaggregation within the Fe- or Al-oxide, which in turn mitigates the inhibitory effect of its heteroaggregation with the Mn-oxide.[655,656] Interestingly, in ternary mixtures of Al_2O_3, MnO_2, and natural organic matter, dissolution of Al_2O_3 is largely suppressed so the impact of soluble Al^{3+} ions becomes minimal.[656]

Regarding Fe-oxides, the effects of metal ions and ligands on their oxidative reactivity are reportedly similar to those on Mn-oxides.[629] However, different from the above mechanisms for binary oxide mixtures containing MnO_2, in binary mixtures of Al- and Fe-oxides at pH 3, the Al_2O_3 strongly inhibits the oxidative reactivity through adsorbing dissolved Fe^{3+},[657] pointing to the complexity of multicomponent mixtures and the need to continuously examine them.

3.4.1.5. Reductive Reaction with Surface-Associated Fe^{2+}-Fe^{3+}-Oxides. In the presence of both Fe^{2+}- and Fe^{3+}-oxides, sorbed Fe^{2+} forms on the oxide surfaces and becomes a strong reductant for a wide range of organic and inorganic solutes.[629] Sorbed Fe^{2+} can induce transformation of amorphous Fe^{3+} to more thermodynamically stable crystalline Fe^{3+}-oxides.[658,659] The involved ET mechanism in the above processes has evolved from the traditional static view of the reduction ability of the so-called "surface-complexed Fe^{2+}" being much better than that of aqueous Fe^{2+}, owing to the much lower reduction potential of the former,[660,661] to a recent dynamic view based on the proposed redox-driven conveyor belt model,[582,662] as detailed in the figure below.

The reactivity of sorbed Fe^{2+} strongly depends on reaction conditions such as the pH, amount of sorbed Fe^{2+}, underlying Fe^{3+}-oxide structure, formation of reactive intermediates such as $Fe(OH)_{2(s)}$, particle size, aggregation state, exposed facets, and surface defects.[664] For instance, more sorbed Fe^{2+} often leads to higher reactivity.[661] Readers are referred to a recent review article for details on the reactivity of sorbed Fe^{2+} in simple model systems containing different Fe^{3+}-oxides or clay minerals.[664] In more complex mixtures containing other compositions, metal ions such as Co^{2+}, Ni^{2+}, and Zn^{2+} inhibit the reactivity of sorbed Fe^{2+} by limiting Fe^{2+} adsorption.[665] NOM can either promote or inhibit sorbed Fe^{2+} reactivity. The promotion effect is mainly attributable to NOM that has been reduced biotically or abiotically which can then reduce iron oxide surfaces to form additional sorbed Fe^{2+},[666] whereas the inhibition effect is due to NOM complexing with Fe^{2+}, blocking Fe^{2+} adsorption, and/or blocking ET.[667] Moreover, formation of ternary surface complexes of Fe^{2+}, Fe-oxide, and NOM could be a minor contributor to the lower sorbed Fe^{2+} reactivity.[668] Upon mixing of SiO_2 with sorbed Fe^{2+}, dissolved silicate ions play a major role in inhibiting the reductive reactivity of sorbed Fe^{2+}.[669] Upon mixing of TiO_2 with sorbed Fe^{2+}, however, the reactivity of sorbed Fe^{2+} is enhanced. Although the mechanism for this enhancement is not well understood yet, the authors proposed a similar redox-driven conveyor-belt mechanism where interparticle ET occurs from the conduction band of TiO_2 to that of the Fe- oxide.[669]

Future work on model systems with increasing complexity is necessary before we can even begin to decipher reaction kinetics and mechanisms in the environment. Toward this goal, advanced experimental and computational tools are vital. In addition, the redox chemistry of Fe- and Mn-oxides is essential in the Fe/Mn cycle as well as in many biogeochemical cycles;[627,664] therefore, examining the involvement of Fe and Mn redox chemistry in these cycles will enable us to better understand their roles in carbon sequestration, climate change, and nutrients, among others.

3.4.1.6. Clay Minerals and Redox. Clay minerals are an example of challenging environmental surfaces because they often form solid solutions with permanent structural charge and contain impurities and defect sites. Standard redox potential of clay minerals depends on their composition and layer charge, as well as redox history,[670] making predicting Eh^0 value for clay mineral structures difficult. Adding to the challenge, there are two distinct types of reactive surfaces: edge sites with pH-dependent charge, and permanently charged basal surfaces outside and inside nanoconfined interlayers.[671] Controversy remains about electron transfer mechanisms to and from clay mineral structures, namely, do electrons hop through the basal surfaces, or through the edge sites?

Here we discuss progress in understanding ET reactions involving Fe residing in clay mineral structures (Figure 36), where it can substitute for Al^{3+} in the octahedral lattice sites.[671] Spectroscopic studies on both Fe-rich[673] and Fe-poor[674]

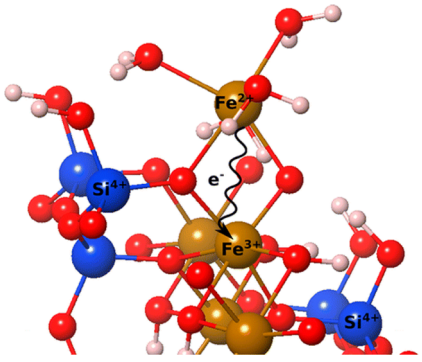

Figure 36. Electron transfer from Fe^{2+} adsorbed at the edge site to Fe^{3+} in the structure of an Fe-containing clay mineral.[672] Adapted from ref 672. Copyright 2013 American Chemical Society.

https://doi.org/10.1021/acs.chemrev.2c00130
Chem. Rev. 2023, 123, 6413−6544

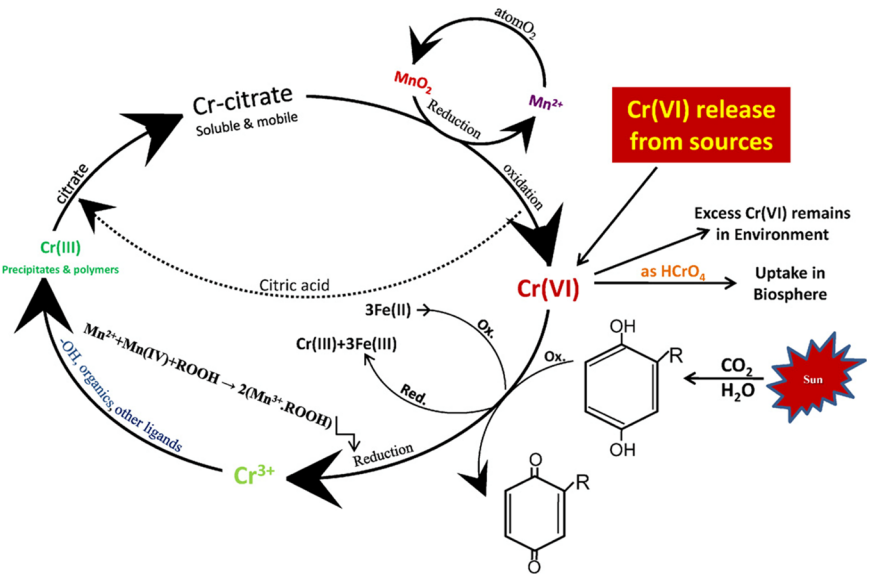

Figure 37. Potential abiotic redox cycles of chromium in the presence of Fe- and Mn-bearing minerals and organic ligands. Adapted with permission from ref 691. Copyright 2013 Elsevier BV.

Table 2. Redox Reactions of CrO_4^{2-} with $Fe^{2+}_{(aq)}$ and Fe^{2+}-Bearing Minerals Resulting in the Reduction of CrO_4^{2-} and the ΔG (in kJ mol^{-1}) of the Reactions (after Fendorf et al.[690])

reaction	$\Delta G°$ (pH 7)
$Fe^{2+}(aq) + 1/3HCrO_4^- + 8/3H_2O \leftrightarrow 4/3[Cr^{3+}_{0.25}Fe^{3+}_{0.75}](OH)_3(s) + 5/3H^+$	−417
$FeCO_3(s) + 1/3HCrO_4^-HCrO_4 + 8/3H_2O \leftrightarrow 4/3[Cr^{3+}_{0.25}Fe^{3+}_{0.75}](OH)_3(s) + 2/3H^+ + 1/3HCO_3^-$	−256
$[Fe^{2+}_4Fe^{3+}_2(OH)_{12}][SO_4\cdot 3H_2O](s) + 4/3HCrO_4^- + 5/3H_2O \leftrightarrow 16/3[Cr^{3+}_{0.25}Fe^{3+}_{0.75}](OH)_3(s) + 2/3H^+ + SO_4^{2-} + 2Fe^{3+}(OH)_3(s)$	− 1706
$Fe^{2+}Fe^{3+}_2O_4 + 1/3HCrO_4^- + 14/3H_2O + 1/3H^+ + \leftrightarrow 4/3[Cr^{3+}_{0.25}Fe^{3+}_{0.75}](OH)_3(s) + 2Fe(OH)_3(s)$	−167

swelling clay minerals reported that ET from adsorbed Fe^{2+} to Fe^{3+} in the octahedral sheet takes place through both edge sites and through basal surfaces. Other spectroscopic work implies that for electron transfer to take place from an adsorbed arsenic As^{3+}, specific Fe^{2+}−O-Fe^{3+} reactive moiety must be available, which could only form at an edge site.[675] Additionally, DFT calculations predict that ET from adsorbed Fe^{2+} to Fe^{3+} in the octahedral sheet could only happen through an edge site, with no evidence for ET complexes forming at the basal surfaces.[672] The previously proposed redox-driven conduction mechanism for Fe-oxides may also be at play during the ET and subsequent Fe atom exchange between adsorbed Fe^{2+} and Fe-bearing clay minerals,[676] during which electron delocalization in clay structures is significant.[677] The ET routes associated with clay mineral structures must be resolved in the future. This is important because of the vast abundance of clay minerals and their ability to mediate Fe (and likely other elements) redox activity in various environments.

We know of no experimental techniques capable of probing ET processes at clay mineral edge- vs basal surfaces. A promising advance which may be possible in the coming years is further improvement in *in situ* TEM and EELS spectroscopy, which could combine near-atomic resolution with spectroscopic measurements of adsorbed species oxidation states.

3.4.1.7. An Example of Complex Abiotic and Biotic Redox Chemistry at Interfaces: Comparison of Rates of Cr^{6+} Reduction to Cr^{3+}. Redox reactions play a major role in controlling the toxicity and bioavailability of redox-sensitive environmental contaminants, particularly the oxyanions of chromium,[437,678−680] arsenic,[681,682] and selenium.[683−686] The environmental impacts of these oxyanions and other redox-sensitive contaminants depend on the valence state of the metal ion and the affinity of these aqueous species for various sorbents, among other variables. This section focuses on the abiotic and biotic pathways of Cr^{6+} to Cr^{3+} reduction and the kinetics of these redox reactions for various common reductants.

Figure 37 illustrates various abiotic Cr reduction/oxidation pathways in the presence of Fe- and Mn-bearing minerals and organic ligands. Fe-bearing biogenic minerals formed by the microbial reduction of Fe-(oxyhydr)oxides have been identified.[576,687−689] These biogenic Fe^{2+}-bearing phases can reduce Cr^{6+} to Cr^{3+} species in subsurface environments (Table 2).[690]

Kinetic factors will dictate the dominant pathways for redox-sensitive contaminant reduction. Here we use CrO_4^{2-} and $HCrO_4^-$ to illustrate the rates of potential reduction pathways. Included in this rate comparison are measured reduction rates of chromate by various species including $Fe^{2+}_{(aq)}$,[692] S^{2-}_{aq},[693]

https://doi.org/10.1021/acs.chemrev.2c00130
Chem. Rev. 2023, 123, 6413−6544

Fe^{3+}-catalyzed reduction of chromate by oxalate,[694] TiO_2-catalyzed reduction by mandelic acid,[695] and surface reactions with magnetite,[696] siderite, and hydroxy green rust.[697] Fendorf et al.[690] included only the reduction rate for *Desulfovibrio vulgaris* as a function of pH because it has one of the fastest published reduction rates for pure cultures of anaerobic bacteria.[698]

The cumulative rates for bacterial reduction of chromate in combination with reaction rates calculated for abiotic reduction show that abiotic pathways are more than 100× faster than measured biotic rates. The dominant reductant of chromate at pH > 5.5 is $Fe^{2+}_{(aq)}$; at pH < 5.5, $S^{2-}_{(aq)}$ is the dominant reductant. The abiotic reduction pathways are more dominant than biotic reduction pathways for Cr^{6+} reduction to Cr^{3+} in anaerobic environments. However, the generation of reductant pools (e.g., ferrous iron or ferrous sulfide) depends on microbial activity, as Fe^{3+} and SO_4^{2-} reduction occurs via dissimilatory reduction pathways.[698,699] In determining the mechanism of chromate or other contaminant reduction, one must consider the microbial selection of terminal electron acceptor(s) and the resulting concentration of competing chemical reductants such as Fe^{2+} or S^{2-}. Direct biological pathways do not appear to contribute appreciably to chromate reduction in anaerobic environments; however, they may play a critical role in Cr^{6+} reduction to Cr^{3+} in aerated environments, where reduced constituents other than organic matter are at a minimum.[690] Although either pathway ultimately leads to Cr^{6+} reduction, the resulting products and rates of reduction may differ significantly. For example, enzymatic reduction of chromate may result in soluble Cr^{3+}-organic complexes that may remain stable for extended periods of time.[700−702]

3.4.2. Photocatalysis. Photo-induced biogeochemical reactions can play a commanding role in the photic zone of natural aquatic systems. Solar radiation can stimulate charge transfer reactions across mineral−water interfaces by several mechanisms. Direct photoabsorption by common semiconducting metal oxide nanoparticles produces reactive charge carriers by promoting valence band electrons to the conduction band, leaving positively charged holes in the valence band. If these charge carriers have sufficiently long lifetimes near the oxide surface, either by direct excitation or having reached it through diffusion, charge transfer with adsorbates can occur resulting in photocatalyzed chemical reactions. Alternatively, many natural organic adsorbates contain chromophoric groups that can likewise be photoexcited, causing charge transfer to mineral substrates, and certain phototrophic bacteria can couple absorption of light energy to biogeochemical charge transfer with mineral substrates. Because these photocatalyzed interfacial charge transfer reactions often change the valence state of metal cations, they are often coupled to mineral dissolution or precipitation.

In order for photocatalysis by direct band gap excitation to occur, the energy difference between the valence and conduction bands (the band gap) and the positions of the band edges must be appropriate for the reaction of interest.[703] For example, Fe-oxides play important roles in natural photochemical processes. In addition, Fe_2O_3 and TiO_2 have also gained significance in photocatalytic applications such as water splitting, motivating substantial investigation into their interfaces with water for renewable energy applications. Because of this widespread importance and the breadth of investigations into their water−oxide interfaces, we will focus on Fe- and Ti-oxides as examples. However, there are many other oxides, including but not limited to $SrTiO_3$, $FeTiO_3$, $BaTiO_3$, SnO_2, MnO_2, WO_3, and ZnO, as well as many sulfides of Fe, Mn, Cu, Co, Ni, As, and Zn that are also photoactive and have been studied in the context of natural and/or artificial photocatalytic systems.

3.4.2.1. Overview of Interfacial Photocatalytic Processes in the Environment. Photocatalysis plays a number of important roles in environmental processes. Mineral nanoparticles are ubiquitous at the Earth's near-surface[303,704−706] and their capacity for light harvesting is profound. A key class of photoactive materials is semiconducting metal oxides, most of which naturally occur in nanophases that, because of their chemical stability, are highly persistent. Dissolution of metal oxides and Fe-oxides in particular, discussed further in section 4.3, can be induced by photoreduction. Such photoreductive dissolution readily occurs under marine conditions (e.g., in seawater) and is enhanced by the presence of adsorbed natural organic matter, leading to important photochemical fluxes of redox active species such as Cu, Fe,[707−709] and Mn.[703,710] For example, aeolian dust transport and subsequent photoreductive dissolution is an important source of aqueous Fe, which is a limiting factor on phytoplankton growth over much of the ocean.[711,712] Siffert and Sulzberger showed that photoreductive dissolution of hematite is active in the near-ultraviolet (UV) portion of the solar spectrum (λ < 400 nm), particularly in the presence of common organic acids acting as photosensitizers.[711] However, it is noteworthy that actual interfacial photoreduction pathways to $Fe^{2+}_{(aq)}$ remain uncertain because the competition between direct band gap excitation versus photoexcitation of adsorbed organics is poorly understood. The lack of comprehensive knowledge about the mechanistic pathways of photoexcitation processes at particle interfaces leaves major ambiguities in quantifying the roles of intrinsic photoexcitation efficiency versus those of extrinsic effects.

An increasing number of studies are emerging that specifically examine photocatalyzed reactions between adsorbed organics and metal oxide surfaces. Photoexcitation of adsorbed organic molecules can inject excess charge into the metal oxide, creating the electrons/holes necessary for the mineral surface to catalyze chemical reactions. To improve understanding of the charge transfer mechanism and consequences, recent studies have been taking advantage of well characterized adsorbed organic dye molecules to act both as photosensitizers and reactants with transient intermediates. For example, methylene blue adsorbed on hematite nanoparticles can undergo photocatalytic degradation in the presence of hydrogen peroxide.[713] Photoexcitation of methylene blue injects hot electrons into hematite and reduces a fraction of the surface iron to Fe^{2+}, which subsequently reacts with hydrogen peroxide, yielding the strong oxidant $OH^{\bullet}$ that decomposes the adsorbed dye. The main degradation pathway is thus the photo-induced Fenton reaction that is triggered after photoinduced injection of charge to hematite. Moreover, the rate of degradation depends on the specific crystal facet at which chemistry is occurring. For methylene blue on hematite, photodegradation on the (001) surface is nearly 15 times faster than on the (012) surface,[713] rhodamine B also undergoes facet-dependent photocatalytic degradation on hematite in a similar fashion.[714]

The coupling of light energy to charge transfer reactions at metal oxide interfaces can also be mediated by microorganisms in the photic zone. An example of this biologically mediated

https://doi.org/10.1021/acs.chemrev.2c00130
Chem. Rev. 2023, 123, 6413−6544

photocatalytic process was shown for the mixed-valent magnetite, using co-cultures of dissimilatory Fe-reducing bacteria that in the dark convert Fe^{3+} in magnetite to Fe^{2+}, which then when illuminated provides a source of Fe^{2+} that is accessed by photoferrotrophic Fe-oxidizing bacteria.[715] The two very different Fe-dependent organisms were thus shown to cooperatively use magnetite as a sort of battery for reversibly storing and then releasing electron equivalents with diurnal cycles of daylight exposure. The redox cycling caused by these bacteria may represent a biophotocatalytic pathway for iron mineralization on global scales such as in the creation of banded iron formations in ancient sediments. Understanding and controlling photocatalytic chemistry at bacteria−mineral interfaces can also be used to address important demands in biotechnology and energy sciences, including bioelectronics, bioenergy generation, and biofuel cells.

3.4.2.2. Theoretical Treatment of Excited States in Solids and Adsorbates. Theoretical and computational approaches to photocatalysis necessarily involve modeling excited states. Because of this necessity of describing excitations, one must either move beyond ground state DFT, such as with using the GW[716,717] or Bethe-Salpeter[718,719] methods, or employ ground state DFT in clever ways.[703,720] To model the excitation of organic adsorbates, wave function-based approaches, such as coupled cluster and multiconfigurational self-consistent field theory methods, can also be employed. However, their application is typically limited to a few molecules at most due to computational expense. Recent developments in coupled cluster theory for periodic systems have enabled the use of wave function methods for metal oxides.[721,722]

If we are only concerned with the events following excitation, particularly the behavior of the excess electron or hole, ground state DFT can be used to model mineral surfaces with a net charge. These approaches have been used with great success to describe how the electron or hole distorts the oxide lattice within its vicinity to form a polaron.[723−725] These approaches have been used to examine the influence of polaron formation on the structure of interfacial water and adsorbates on TiO_2.[726−729] The expense of ab initio models still limits the use of DFT-based methods to small system sizes and short time scales. However, the information provided from *ab initio* calculations has been used to develop multiscale models of electron transport across goethite nanoparticles in solution,[730] providing a strategy for overcoming some of these issues. Additional recent developments in mixed quantum-classical simulations could also be used to reach larger length and time scales needed to describe polarons at oxide−water interfaces.[731]

Charge transfer between a mineral surface and an adsorbate typically requires quantum mechanical models, although Marcus theory-based approaches can often be used for simple adsorbates, like monatomic ions. Successful modeling of photoactivated electron transfer processes has been enabled by developments in nonadiabatic dynamics simulations.[732−736] These simulations have been used to quantify electron transfer on sensitized oxide surfaces, mainly TiO_2, and are able to include thermal fluctuations, vibronic effects and quantum coherence, and solvent effects.[734,737,738] Extending these approaches to additional oxide interfaces can shed light on a variety of photochemical processes.

3.5. Biogeochemical Interfaces

3.5.1. Biological Components. Biological components are present in water−mineral systems. These biological components include a variety of different macromolecular species, such as proteins, amino acids, DNA, RNA, nucleotides, lipids, and EPS, just to name a few. There is great interest in understanding the adsorption of these components on the surfaces of oxides, silicates, and other minerals from fundamental aspects and applications,[739] as well as understanding many of the environmental aspects discussed here. Different experimental techniques, such as ATR-FTIR spectroscopy[39,740−742] or QCM, can provide insights into the adsorption process.[743] In particular, vibrational spectroscopy can assess the binding and structure of these biological components at the oxide− and silicate−water interfaces. This can be done at different pH values and temperatures to provide insights into phase transitions of macromolecular biological species and their interactions with oxide−water and silicate−water interfaces. Several examples of adsorption studies of proteins, amino acids, and nucleotides on such surfaces are described below.

Figure 38 shows ATR-FTIR spectra of BSA on TiO_2 particle surfaces at three pH values.[744] The most striking observations

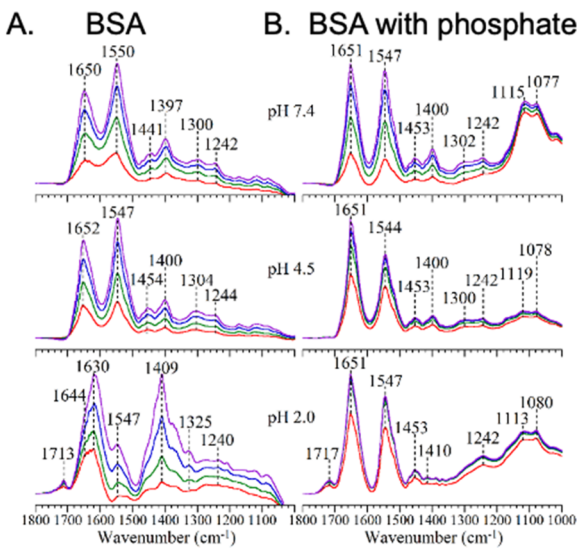

Figure 38. Normalized ATR-FTIR spectra of 1 mg/mL BSA adsorption as a function of time on TiO_2(22 nm) (A) without phosphate at pH 7.4 (top), pH 4.5 (middle), and pH 2.0 (bottom), (B) with phosphate at pH 7.4 (top), pH 4.5 (middle), and pH 2.0 (bottom). Spectra are shown for four different time points: 10, 30, 60, and 90 min (red, green, blue, and purple colored spectra, respectively). Reproduced from ref 744. Copyright 2017 American Chemical Society.

from these spectra are the changes in the amide I and II absorption bands with pH, which are the two major bands of the protein infrared spectrum. Secondary structure analysis of these bands is done by curve fitting the amide I band (between 1600 and 1700 cm^{-1}). Within the broad, amide I band, peak fitting associated with secondary structural elements, including α-helices and β-sheets, were determined. This analysis shows that at low pH the protein structure denatures considerably on the surface, much more than changes in protein structure in solution alone. Similar studies on amorphous SiO_2 particles show that although the protein structure changes upon

https://doi.org/10.1021/acs.chemrev.2c00130
Chem. Rev. 2023, 123, 6413−6544

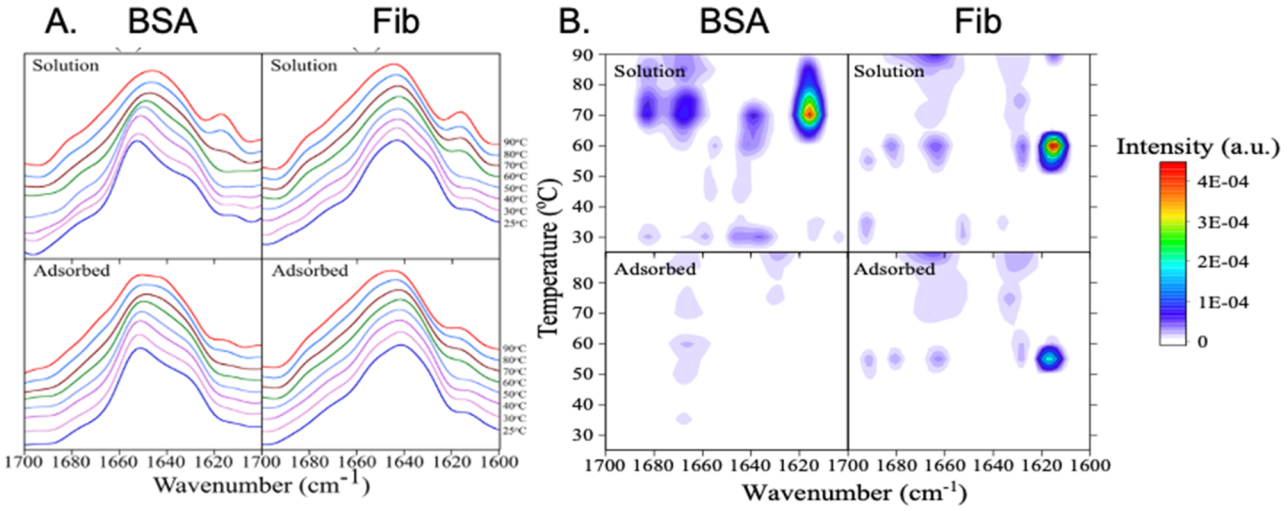

Figure 39. Changes in BSA structure as a function of temperature. (A) Normalized ATR-FTIR spectra over a temperature range of 25−90 °C for solution phase BSA and Fib (top) and adsorbed BSA and Fib on TiO_2 (bottom). (B) Autocorrelation moving window 2-dimensional correlation map of the amide I band shown in A relating temperature to spectral intensity changes for solution phase BSA and Fib (top) and adsorbed BSA and Fib on TiO_2 (bottom). The color bar intensity (a.u.) value represents the extent of spectral variation due to the external perturbation, i.e., temperature. Reproduced with permission from Sit et al.[747] Copyright 2019 Elsevier Ltd.

adsorption compared to in the solution phase, the larger changes seen for TiO_2 adsorption, especially at low pH, are not seen for BSA adsorption on SiO_2.[745,746] The results of these experiments demonstrate several important points. The first is that protein secondary structure changes upon surface adsorption and that the extent of that change depends on the interaction with the underlying surface. The second is that protein secondary structure changes also depend on pH and that changes can be greater than that seen in solution phase.

Changes in protein structure depend on pH, surface coverage, and temperature. Quantitative understanding of how these changes occur as a function of T on oxide particle surfaces is limited. Sit et al.[747] investigated phase transitions of protein secondary structure as a function of T for two proteins adsorbed onto TiO_2 surfaces (Figure 39). 2D-COS analysis was used as a guide for establishing secondary structural changes as a function of solution phase temperature for two different plasma proteins, BSA and Fib. The protein with the greatest structural changes upon adsorption, BSA, did not show any further transformations as a function of T (Figure 39).

Peptide and amino acid adsorption can provide insights into adsorption processes of proteins on oxide and silicate surfaces.[748,749] Analyzing the pH-dependent adsorption of amino acids can provide a better understanding of protein−surface interactions *in vivo* and different environmental and biological milieu. Protein adsorption is highly dependent on the affinity between exterior amino acid residues and the NP surface, and therefore investigating the adsorption of individual amino acids or small peptides can provide insight into protein adsorption. A recent study of the adsorption of α-amino acids onto TiO_2 as a function of solution pH showed that depending on the predominant speciation and TiO_2 surface charge, adsorption involves a combination of carboxylate and amine group interactions.[749] Differences in surface affinity were due to the different speciation of the functional groups as a function of solution pH within the amino acids and the TiO_2 surface charge at each pH. Differences in surface speciation were attributed to solution pH as well as the impact of the surface and a surface-induced deprotonation of the amine group and proton transfer to the carboxylate. Combining these results with that of specific proteins and their exterior residues can provide insights into the mechanisms of surface adsorption and secondary structural changes at different pH and for different surfaces. Experiments involving hydrogen-deuterium exchange (H/DX) do provide insights into the residues and moieties within a larger macromolecule, such as a protein, that may be interacting with the surface.[750,751]

Besides proteins, deoxyribonucleic acids (DNA) are also of interest in the environment. Spectroscopic, kinetic, and quantitative adsorption measurements show that DNA and EPS can adsorb onto the surface of goethite.[39,752] Analyses of the spectroscopic data shows that the structure of surface adsorbed DNA retains a B-form, suggesting the DNA helix adsorbs on goethite without degradation or changes to the secondary helical structure. This suggestion is interesting, given that the data also demonstrated strong interactions between DNA and goethite with inner-sphere coordination between the backbone phosphate groups of DNA and the goethite surface. This adsorption mechanism is confirmed for nucleotide adsorption on hematite surfaces.[539] The IR spectra show large changes in the phosphate vibrational frequencies compared to the solution phase, and no other vibrational modes show these changes. Furthermore, the adsorption behavior of dAMP on hematite nanoparticle surfaces was interrogated as a function of solution pH. The results show that fewer nucleotides adsorb at higher pH. The pH dependence provides insights into the adsorption process and the importance of electrostatic interactions. The adsorption of EPS onto soil minerals has been shown to depend on electrolyte concentration, thus highlighting the importance of electrostatics in some cases.[742]

These studies on the surface adsorption of different biological components on oxide and silicate surfaces provide important insights on how these interfaces behave in the environment. However, the role of surface defects on the surface adsorption of these larger biological macromolecular species is poorly understood, the exact detailed nature of the

https://doi.org/10.1021/acs.chemrev.2c00130
Chem. Rev. 2023, 123, 6413−6544

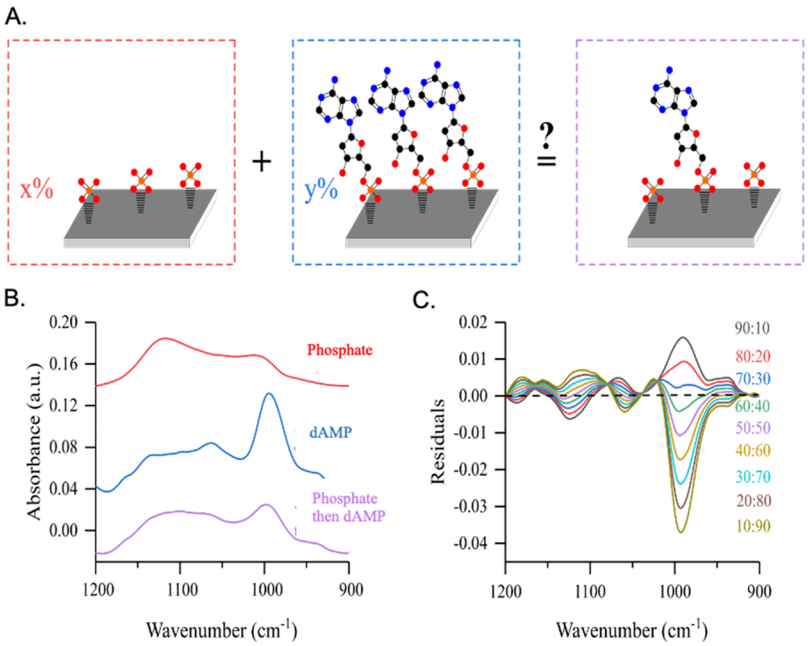

Figure 40. Linear convolution of adsorbed species on α-Fe_2O_3. (A) Representative cartoon emphasizing the possible percent absorbance intensity of a saturated adsorbed phosphate surface spectrum (red dashed box) added to a percent of saturated adsorbed dAMP surface spectrum (blue dashed box) to yield the spectral absorbance intensity of a multicomponent surface composed of dAMP and phosphate (purple dashed boxed). (B) The spectra used for the linear convolution at pH 5. (C) The residuals of the experimental spectrum compared to the linear convolution at various percent combinations where the absorbance ratios correspond to % PO_4:% dAMP. The dotted line represents a perfect overlay of the linear convolution to experimental spectra. Because these cannot be fit using a linear combination, these results suggest synergistic interactions between adsorbed phosphate and dAMP. Reproduced from ref 539. Copyright 2020 American Chemical Society.

surface protein interaction is also difficult to glean. In addition to adsorption studies, MD simulations can provide insights into the details of the surface interactions.[753] Future studies that combine structural analysis using spectroscopic probes, H/DX mass spectrometry, and MD simulations have the potential to provide unique insights into the adsorption of biomolecules on oxide surfaces.

3.5.2. Adsorbate Interaction Effects and the Impact of Inorganic Sorbates on Organic and Biological Sorbates. Most laboratory studies on surface adsorption and reactivity on oxide− and silicate−water interfaces are on binary systems. Experiments often focus on a single adsorbate under varying environmental conditions of pH and ionic strength. For example, Situm et al.[492] showed the important role of organics on the surface of hematite and the impact these had on the kinetics of adsorption as well as the fate of As compounds. Kim and Doudrick[103] investigated the impact of oxalate, a simple model for dissolved organic carbon, on the adsorption of BSA protein on catalytic and food grade titanium dioxide. Shakiba et al.[537] showed that interactions between NOM and proteins controlled adsorption onto TiO_2 surfaces in complex environmental media. Recently, Grassian and co-workers have begun to investigate the impact of the co-adsorption of phosphate with different biological components. This work seeks to better understand possible synergistic effects between adsorbates that lead to different behavior than expected based on a simple linear combination of the two adsorbates alone.[539,744] Phosphate is often present in the environment and biological systems as well as in different cell media and in simulated biological fluids.[740,741,754,755]

Xu and Grassian[744] showed that pre-adsorbed phosphate on TiO_2 decreases the degree of structural changes of BSA protein adsorption at all pHs evaluated, but most important is the finding that at low pH in the presence of adsorbed phosphate, there is much less denatured protein present. dAMP adsorption on hematite surfaces occurs through the phosphate moiety within the nucleotide, as discussed above. When phosphate is first adsorbed onto the hematite surface, less dAMP can adsorb, presumably due to site-blocking by inorganic phosphate, which occupies the same binding sites as dAMP. Although there is a displacement of some of the adsorbed phosphate by dAMP as a function of time, additional spectral analyses show that there are synergistic effects between the inorganic phosphate and the phosphate in the nucleotide (Figure 40). Other studies have shown the impact of adsorbed phosphate on two antibiotic contaminants, including tetracycline.[756]

3.5.3. Bacteria on Mineral Interfaces. Bacterial adhesion on mineral surfaces plays a role in a number of biogeochemical processes, including biosorption, microbial catalyzed oxidation/reduction processes, mineral formation and transformation, and biodegradation.[631,757−760] The interactions between bacteria and surfaces depend on structural properties (e.g., microtopography, composition), chemical functional groups, surface charge, the hydrophobicity of both the bacteria and the surface, and the presence of EPS.[761−764] Bacteria adsorb to surfaces in a series of steps: (1) transport to the surface, (2) initial attachment via van der Waals forces, electrostatic forces, and hydrophobic interactions, (3) irreversible attachment of the cells via exo-polysaccharides and/or specific ligands that employ covalent and H-bonding, hydrophobic interactions, and ET between the cell and the surface, and (4) microcolony or biofilm growth that often involves quorum sensing.[765−768] Models describing initial bacterial attachment or adhesion are typically based on thermodynamics or DLVO theory, and AFM is often employed to measure the adhesion forces.[769,770]

https://doi.org/10.1021/acs.chemrev.2c00130
Chem. Rev. 2023, 123, 6413−6544

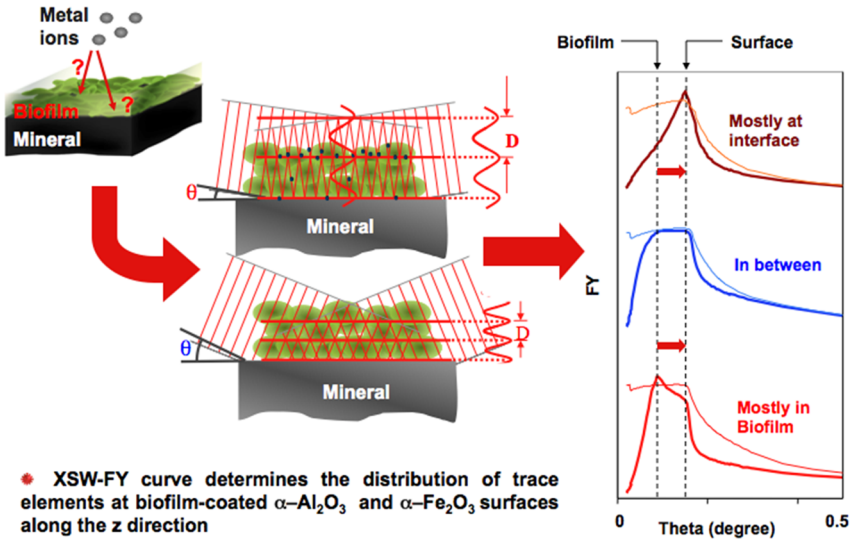

Figure 41. Application of LP-XSW-FY spectroscopy to studies of Pb^{2+} partitioning between *Burkholderia cepacia* biofilm coatings and oriented single crystal substrates. (left) Schematic illustration of the generation of X-ray standing waves by reflection of X-rays at grazing incidence off a mirror-like single-crystal mineral surface coated by a biofilm, showing the effect of changing the incidence angle on the spacing between the antinodes of the X-ray standing waves. (right) Examples of Pb^{2+} Lα X-ray fluorescent yield (FY) data (heavy lines) for three different scenarios: (top) Pb^{2+} is dominantly at the interface between the biofilm coating and the mineral substrate; (middle) Pb^{2+} is distributed roughly evening between the mineral surface and the overlying biofilm coating; (bottom) Pb^{2+} is dominantly in the biofilm coating. Modified from ref 261. Copyright 2001 National Academy of Sciences.

DLVO theory describes the balance between Lifshitz–van der Waals interactions and electrostatic forces, and it can account for observed ionic strength interactions between bacteria and surfaces. However, in some cases, extended DLVO theories, which include Lewis acid–base hydrophobic interactions, repulsive hydration terms, and steric interactions, provide a better description of bacterial attachment.[771−773]

The contribution of bacterial surface functional groups to adhesion has also been investigated. For *Shewanella putrefaciens*, formation of inner-sphere coordinative bonds to hematite surface sites has been identified using FTIR during initial attachment, but cell wall protein and carboxyl groups played a more important role over longer time periods.[774] Similar findings with respect to the importance of P-OFe bonds were found for a wider range of species with additional outer- and inner-sphere (monodentate) sorption of carboxyl groups.[39,40] In contrast, no P-OFe bonds or other bonds were identified for adsorption of *Bacillus subtilis* to kaolinite or montmorillonite, and removal of the EPS reduced bacterial adhesion on the clay minerals and increased adhesion on goethite.[761] Finally, bacterial attachment to minerals has been shown to impact adsorption of trace contaminants. For example, competition between As oxyanions and bacterial phosphate and carboxylate groups for Fe^{3+}-(oxyhydr)oxide surface sites led to reduced As^{3+} and As^{5+} adsorption and As^{5+} desorption.[775] These studies reveal the complexity of microbial attachment to mineral surfaces but also highlight the significant progress that has been made over the past two decades to isolate mechanisms of bacterial attachment and their impact on geochemical processes.

3.5.4. How Biofilms Affect Surface Reactivity. Microorganisms, including fungi, such as lichen, and NOM, such as fulvic and humic acids, are common in aquatic systems and soils and often coat mineral and rock surfaces, modifying the rates and mechanisms of chemical and physical mineral weathering. These species play major roles in such interfacial chemical processes as mineral disaggregation, hydration and hydrolysis reactions, dissolution, ET reactions, and secondary mineral formation.[776,777] Consequently, they have an enormous impact on humans and the critical zone by affecting water quality, climate, the rate of chemical weathering of minerals and soil formation, agricultural soil fertility, the bioavailability of environmental contaminants, and the distribution of mineral resources in Earth's crust.[776] They also add to the complexity of sorption reactions at oxide– and silicate–water interfaces, which makes molecular-level processes at mineral/aqueous solution/NOM/microbial biofilm interfaces more difficult to study experimentally.

Microbial organisms commonly occur in consortia known as biofilms, with the bacteria embedded in a hydrated matrix of EPS that adheres to surfaces.[778−782] The functional groups of microbial cell surfaces, EPS and dissolved metabolic byproducts excreted by microbial organisms, and NOM compete with reactive sites on mineral surfaces for hydrated metal–cation and oxyanion complexes. Such biofilms form microenvironments in which aqueous chemical conditions (e.g., pH and redox potential) differ from those of the host geomedium (e.g., groundwater). Bacterial and EPS surfaces have a high affinity for metal cations even at low pH, and uptake is enhanced at neutral pH.[783−788] Metal cation sorption data and FTIR spectroscopy indicate a distribution of metal binding sites consisting mostly of carboxyl and phosphoryl functional groups.[789−793] Initial binding of metal cations may occur on reactive sites within the bacterial cell wall,[792,794] where the adsorption of metal ions is rapid and reversible.[787,795] The adsorbed metal ions may then act as nucleation sites in the formation of silicates, carbonates, phosphates, sulfides, and organometallic complexes containing the metal cation or oxyanion.[263,264,783,788,796−800] Here we address the following questions about mineral coatings. How does a biofilm or NOM coating affect the reactivity of the underlying mineral surface, and how do the many carboxyl, phosphoryl, and phenolic and

https://doi.org/10.1021/acs.chemrev.2c00130
Chem. Rev. 2023, 123, 6413−6544

alcoholic hydroxyl functional groups in the biofilm coating compete for cations, such as $Pb^{2+}_{(aq)}$ and $Zn^{2+}_{(aq)}$, or oxyanions, such as selenite (SeO_3^{2-}), with reactive sites on the mineral surface? A synchrotron X-ray-based method that can be used to address these questions is long period X-ray standing wave fluorescence yield (LP-XSW-FY) spectroscopy; the basic physics of this application of LP-XSW-FY spectroscopy are shown in Figure 41.[261] In one of the first such studies, Templeton et al. examined the partitioning of $Pb^{2+}_{(aq)}$ between *Burkholderia cepacia* biofilm coatings and oriented α-Al_2O_3 and α-Fe_2O_3 single crystal substrates.[261] *B. cepacia* is a Gram-negative bacterium common in soils.

As shown in Figure 41, when the maximum of the X-ray fluorescence yield (FY) of a sorbed element occurs at the critical angle of the mineral substrate, the fluorescing element occurs dominantly at the mineral surface, whereas when the FY maximum occurs at a lower angle Θ, the fluorescing element occurs dominantly in the biofilm. At pH 6, an ionic strength of 0.005 M, an aqueous Pb concentration of 1 μM, and a 3-hour reaction time, the FY intensity for the α-Al_2O_3(1-102) and α-FeO_3(0001) surfaces peaks at the critical angles of the two substrates (~160 mdeg and 185 mdeg, respectively, at 14 keV), indicating that Pb^{2+} is located primarily at the corundum or hematite surfaces at this concentration. With increasing Pb concentration, one of the two FY peaks occurs at the critical angle of each substrate, while the FY peak occurs at ~60 mdeg for the α-Al_2O_3(1-102)-coated surface and at about 85 mdeg for the α-Fe_2O_3(0001)-coated surface. The growing FY intensity at the lower incidence angles with increasing Pb concentration indicates that Pb^{2+} is also binding to sites in the *B. cepacia* biofilm coating (Figure 42). At all Pb concentrations

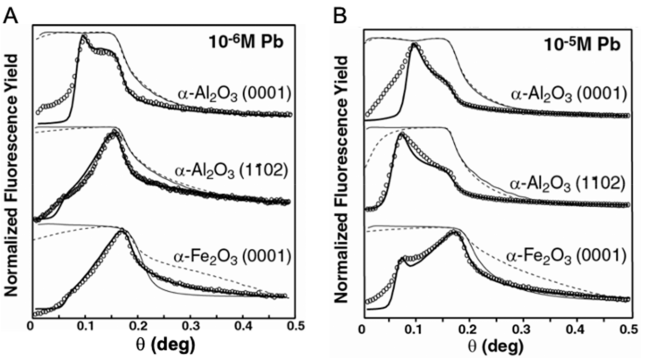

Figure 42. LP-XSW-FY spectroscopy studies of Pb^{2+}partitioning between *Burkholderia cepacia*biofilm coatings and oriented single crystal substrates. Measured (dashed) and modeled (light line) reflectivity (Log I_0/I_1) profiles and Pb Lα FY profiles (circles) with model fits (heavy line) for α-Al_2O_3(0001), α-Al_2O_3(1-102), and α-Fe_2O_3(0001) surfaces at (A) 10^{-6} M and (B) 10^{-5} M [Pb] at pH 6 after 3 h of reaction. Modified from ref 261. Copyright 2001 National Academy of Sciences.

studied, the FY-data show that Pb^{2+} binds primarily to functional groups in the biofilm on the α-Al_2O_3(0001) surface. This study also shows that Pb^{2+} binds initially to reactive sites on α-Al_2O_3(1-102) and α-Fe_2O_3(0001) even with a biofilm coating that covers essentially the entire mineral surface, as confirmed by other microscopic studies such as atomic force microscopy and confocal laser scanning microscopy. The order of reactivity of these biofilm-coated surfaces for $Pb^{2+}_{(aq)}$ [α-Fe_2O_3(0001) > α-Al_2O_3(1-102) ≫ α-Al_2O_3(0001)] is the same as that observed in uptake and EXAFS studies of Pb^{2+} sorption on biofilm-free alumina and hematite surfaces.[473,474,478] These results are also consistent with the findings of Brydie et al.[801,802]

LP-XSW-FY spectroscopy studies of Pb^{2+} partitioning between *Shewenella oneidensis* MR-1 biofilm coatings and metal-oxide substrates show that the biofilms do not block all reactive sites on the alumina and hematite surfaces and that sites on the α-Al_2O_3(1-102) and α-Fe_2O_3(0001) surfaces "outcompete" functional groups in the biofilm (including the EPS exudate) at low Pb concentrations (Figure 43).[265,269] Similar results were found for Elliot soil humic acid (ESHA) coatings on these metal oxide surfaces.[266] As mentioned earlier, a reaction time of 3 h was used by Templeton et al.[261] In the study by Wang et al.[266] of Pb(II) partitioning onto ESHA-coated α-Al_2O_3(1-102) surfaces, the reaction time was varied from 3 h to 7 days and resulted in 11.4% Pb^{2+} at the surface after 3 h and a steady state of ~58% Pb after 72 h.[266] This finding suggests that an ESHA coating on the α-Al_2O_3(1-102) surface results in slower reaction kinetics. Presumably, slower reaction kinetics would also be found for biofilm-coated metal oxide surfaces, although this hypothesis has not yet been tested.

The results of these studies suggest that NOM or biofilm coatings change the adsorption kinetics of mineral surfaces.[803] However, they are not consistent with the suggestion that NOM coatings block reactive sites on mineral surfaces.[804] These studies also show that biofilms can transform redox-sensitive elements like Se into less toxic and less mobile forms,[262] and they can lead to enhanced sequestration via adsorption of reduced forms of these elements. Biomineralization was also found to result in the formation of a highly insoluble form of Pb on cell membranes in *B. cepacia* biofilms.[263]

In the following section 4, we will further explore how the adsorption of (in)organic species and interfacial ET processes affect surface transformations, including dissolution, nucleation, and growth of solid phases and oriented particle attachment.

4. THEME 3: DISSOLUTION, NUCLEATION, AND GROWTH

4.1. Introduction

Dissolution of mineral surfaces, also referred to as chemical weathering, results from interactions with aqueous solutions, NOM, and microorganisms, and it profoundly affects the distribution of chemical elements in the Earth's crust. Chemical weathering of continents forms soils and releases chemical species into rivers and groundwater, which leads to their redistribution, including deposition in the oceans. Emerging questions related to mineral dissolution and growth are closely relevant to weathering systems in the critical zone (defined as biogeochemical systems extending from the tops of the trees to the bottom of the groundwater), where conditions can be far from equilibrium. By recognizing the multiple interconnected processes involved in dissolution, nucleation, and growth phenomena, scientists can develop a new understanding of the physical basis for why some settings exhibit "anomalously" slow (or high) weathering rates and unexpected reactivities.

In engineered systems, describing solid crystallization requires a quantitative framework that correctly captures the underlying physics by linking atomistic details to ensemble

https://doi.org/10.1021/acs.chemrev.2c00130
Chem. Rev. 2023, 123, 6413−6544

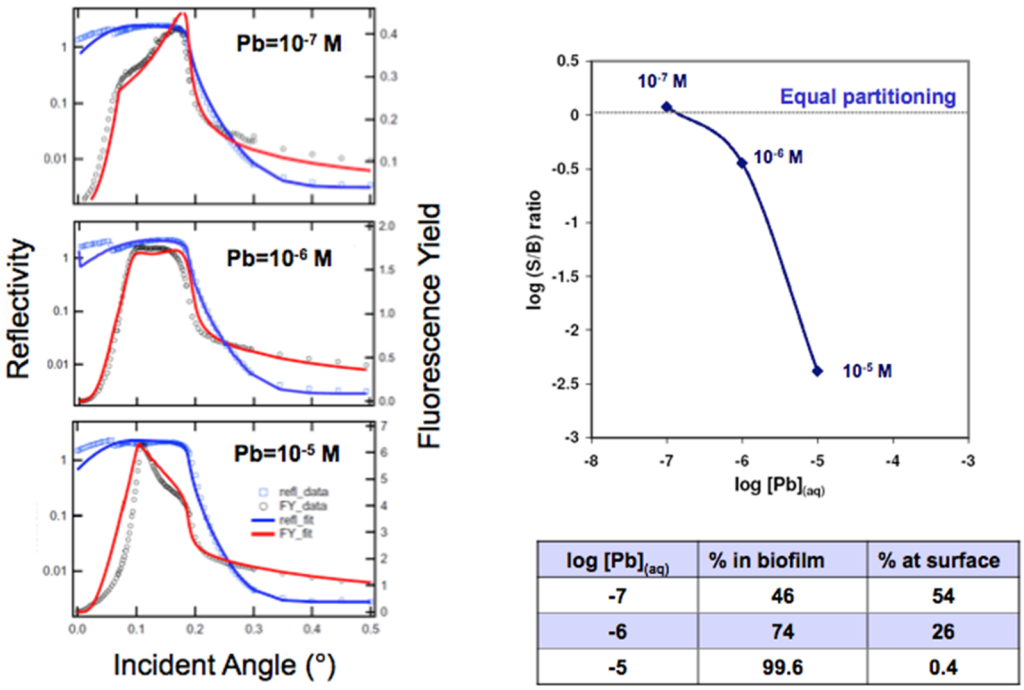

log [Pb](aq)	% in biofilm	% at surface
-7	46	54
-6	74	26
-5	99.6	0.4

Figure 43. LP-XSW-FY spectroscopy studies of Pb^{2+} partitioning between *Shewenella oneidensis* MR-1 biofilm coatings and metal-oxide substrates. (left) LP-XSW-FY spectra (open circles), fits (red line), and X-ray reflectivity data (open squares) and fits for Pb^{2+} at different lead concentrations on a *Shewanella oneidensis* MR-1 biofilm-coated α-Fe_2O_3(0001) substrate. (right) Plot of log Pb^{2+} concentrations in the biofilm coating relative to Pb^{2+} concentrations on α-Fe_2O_3(0001) as a function of log aqueous Pb and the % Pb^{2+} in the biofilm and on α-Fe_2O_3(0001) at different Pb concentrations. Adapted with permission from ref 265. Copyright 2016 Elsevier Ltd.

outcomes. In particular, knowledge gaps become apparent when observed crystallization pathways cannot be adequately described by classical models of nucleation and growth. A more accurate predictive framework will improve the science of material synthesis by taking the longstanding paradigm of structure-function relationships, understanding where atoms must be placed to obtain a desired function, and extending it to process−structure relationships, understanding how to get the atoms where they need to go to obtain desired structure. This knowledge is key to predictive materials synthesis, particularly for those materials that cannot be synthesized along pathways envisioned in classical models. Moreover, the exquisite control exhibited by organisms over all the processes of crystallization, from the location of nuclei to the orientation, phase, morphology, and 3D organization of the resulting crystals, serves as an inspiration for precision materials synthesis and process design.

In section 4, we illustrate the importance of dissolution and precipitation reactions and discuss mechanisms and theoretical models capturing the dissolution of oxide and silicate minerals (Figure 44). We introduce and evaluate the current understanding of the nucleation and growth of large crystals, as well as of nanoscale metal oxide crystallites. Then we highlight recently recognized underappreciated impacts on dissolution, precipitation, nucleation, particle attachment, and crystal growth arising from nontrivial environmental conditions. This recognition serves as a basis for discussing current challenges and future opportunities in section 5.

4.2. Importance of Dissolution, Nucleation, And Growth in Natural and Engineered Environments

4.2.1. Climate Impacts. Cloud formation in the atmosphere is governed by heterogeneous nucleation processes. CCN and ice nucleating particles drive cloud formation in the atmosphere, and these particles often involve mineral phases, including oxide and silicate minerals.[805] Mineral aerosols contribute to the Earth's albedo and radiative forcing (RF) via cloud formation and by reflecting solar radiation into space.[806] The presence of mineral aerosols in the atmosphere has offset temperature increases driven by increases in CO_2 and other greenhouse gases.[806] Mineral aerosols are a significant component of the total global aerosol mass, especially in arid terrestrial regions,[807,808] and contribute to the uncertainty in climate models. As stated in the IPCC AR5 report on clouds and aerosols,[808]

> *"...aerosols dominate the uncertainty in the total anthropogenic RF. Furthermore, our inability to better quantify non-greenhouse gas RFs, and primarily those that result from aerosol−cloud interactions, underlie difficulties in constraining climate sensitivity from observations..."*

The sources of mineral aerosols are soils, in which complex biogeochemical reactions[809] can alter the surface compositions with adsorbed compounds.[810] Because aerosol radiative effects are surface-chemistry dependent, alteration of a mineral surface by organics or oxyanions (e.g., CO_3^{2-} and NO_3^-) will significantly change its RF with respect to both long-wavelength (IR) and short-wavelength (visible and UV) radiation.[811] In addition, surface chemistry changes can lead to charge reversal as pristine positively charged oxide surfaces take up anions (section 2.3.3.2). On well-defined substrates, surface charge properties affect ice nucleation.[812−815] Additionally, the role of defects in ice nucleation (IN) for K-feldspar particles has been recently recognized, with defects acting as preferred ice-nucleation sites.[816] However, this is an example where the experimental substrate does not realistically represent the complexity of real-world mineral aerosols. Hydrophilic surfaces can become hydrophobic with adsorption

https://doi.org/10.1021/acs.chemrev.2c00130
Chem. Rev. 2023, 123, 6413−6544

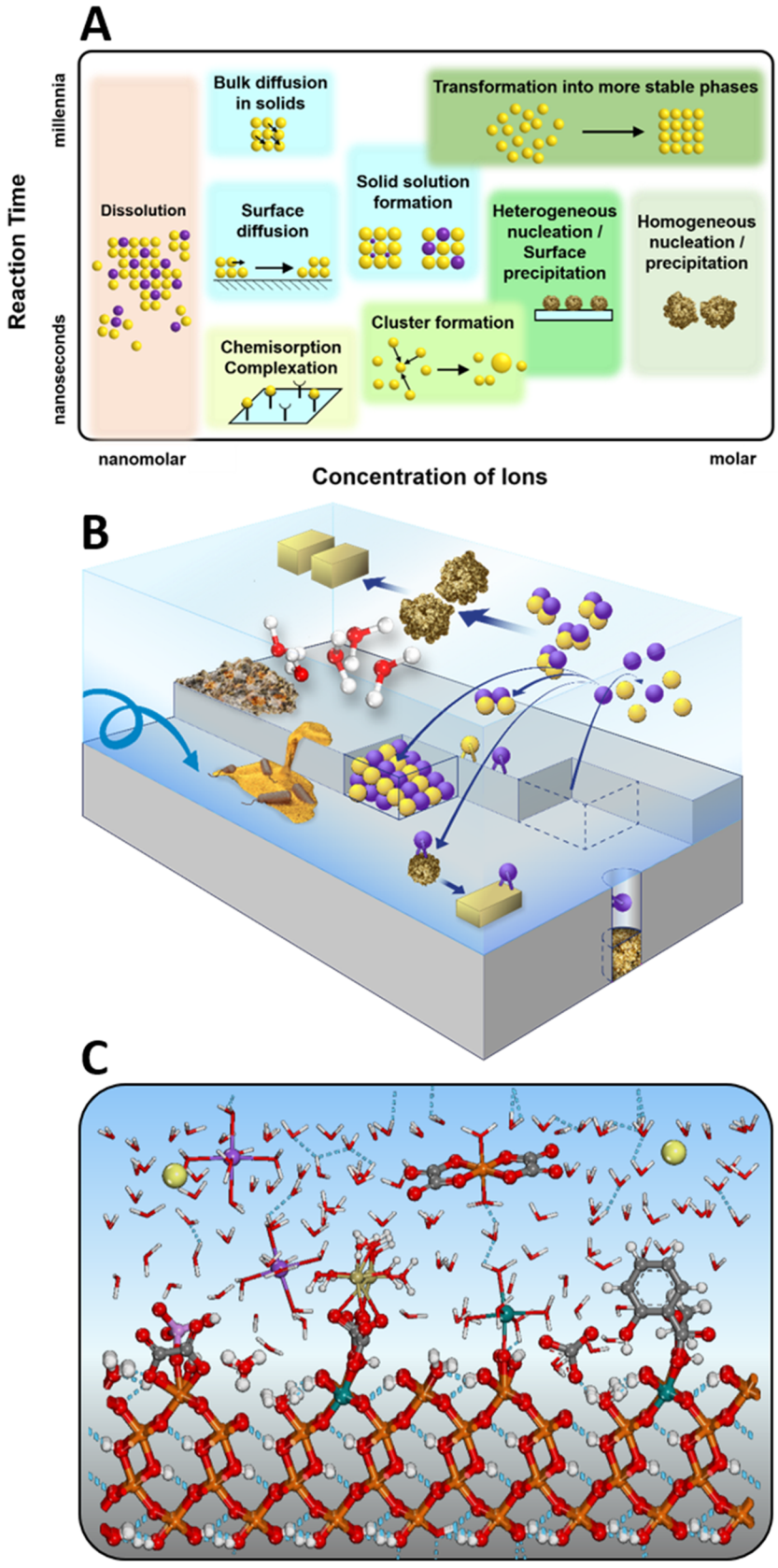

Figure 44. Dissolution and precipitation (nucleation and growth) processes discussed in section 4. (A) The wide range of time scales and relevant concentrations where dissolution and precipitation processes are observed. (B) Dynamic chemical transformations and phenomena playing out on an oxide surface, not to scale (left to right): local flow fields affecting dissolution and precipitation; local compositional/mineralogical/morphological heterogeneities; the presence of biofilms and organic molecules; water structure dictated by the surface and solution chemistry; homogeneous complexation, nucleation, aggregation reactions, and crystallization; ion-by-ion attachment and epitaxial growth; adsorption reactions; surface-mediated crystallization reactions, including heterogeneous nucleation and growth; adsorption and nucleation under

https://doi.org/10.1021/acs.chemrev.2c00130
Chem. Rev. 2023, 123, 6413−6544

Figure 44. continued

nanoconfinement; and coupled dissolution−precipitation reactions. (C) Complex local interfacial structure of goethite in the presence of inorganic and organic molecules, where coupled processes can lead to unexpected reactivity trends. Light yellow, anions; purple, cations; teal, Fe(II); orange, Fe(III); gray, C; red, O; white, H; golden yellow, $CaCO_3$ nucleation precursors. (C) image was drawn with Materials Studio 2016 (Accelrys Inc., San Diego CA).

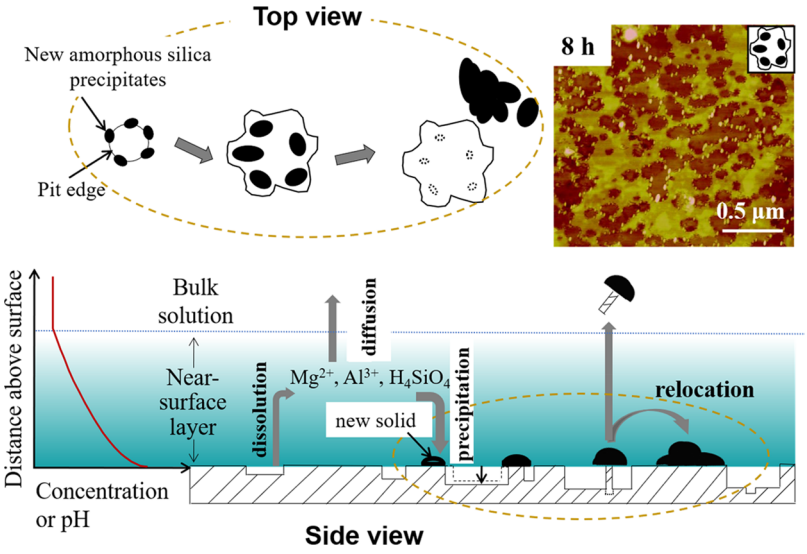

Figure 45. Schematic of proposed reaction pathways for dissolution and precipitation on a phlogopite surface under geologic CO_2 sequestration conditions. The top view, not to scale, shows the evolution of silica particles formed on the edges of a dissolution pit. The inset AFM image shows nanoscale amorphous silica particles formed close to edges of phlogopite dissolution pits after 8 h reaction with 1 M NaCl under 102 atm of CO_2 and at 368 K. Reproduced from ref 824. Copyright 2010 American Chemical Society.

of compounds (section 3.3.1), such as acetate, where the carboxylate group replaces surface OH^-, leaving a methyl group on the surface.[150] If more extensive patches of organic matter from microbial or soil humic acids bind to soil particles before they become aerosols (section 3.3), then the changes to surface reactivity will be more apparent. Changes in surface chemistry alter the extent to which mineral aerosols act as CCN and IN, but for the most part, this surface chemistry is poorly accounted for in current climate models.[817] Additional complications arise because larger particles may be aggregates of smaller particles,[818] and the adsorbates play a role in particle aggregation.

Other global climate impacts include dissolution/precipitation reactions of mineral phases in ocean water. For example, ocean acidification due to higher levels of CO_2 will increase the dissolution of carbonate-containing shells.[819] Iron fertilization occurs when Fe-oxy(hydr)oxides provide bioavailable Fe to marine life, and mineral aerosols play an important role in this nutrient cycling process as well.[820−822]

4.2.2. Subsurface Engineering Processes. Subsurface formations have attracted increasing interest with growing societal demands for energy, natural resources, and waste storage. Subsurface engineering operations include geologic CO_2 sequestration (GCS), conventional and unconventional oil and gas recovery, geothermal energy production, mining, and chemo- and radiotoxic waste disposal (section 1.2.4). Such subsurface engineering operations are conducted at ∼1−3 km depths, where the physicochemical conditions differ from those in near-surface environments. At such depths, due to lithostatic and geothermal gradients, temperatures and pressures are elevated, and diagenetic and compaction processes can lead to highly saline brines and reducing conditions and the prevalence of nanoconfined chemical environments. In particular, during GCS, sedimentary rocks (usually sandstone, consisting of feldspars and quartz) and caprocks (e.g., shales rich in aluminosilicate clays) undergo alteration by CO_2-acidified brines,[91,823] releasing metal ions and eventually forming carbonate minerals.

While mineral carbonation on a reservoir scale can take from several years to hundreds of years, interestingly, Shao et al. found that nanoscale secondary amorphous silica can form on phlogopite ($KMg_3Si_3AlO_{10}(F,OH)_2$) surfaces within 8 h (Figure 45). These nanoscale SiO_2 particles preferentially form close to dissolution pits and edges, and they can relocate and aggregate quickly.[824] During GCS, the coupled dissolution of aluminosilicate and the nucleation/aggregation/growth of newly formed secondary nanoparticles can alter rock permeability when these phases accumulate at the pore throats. Kate and Gokhale found that 22−81% of the total pore volume of sandstones from several geological formations had pore radii smaller than 100 nm, and 2−36% of the total pore volume had pore radii smaller than 10 nm.[825] These small sizes suggest that, if newly formed amorphous SiO_2 nanoparticles grew or accumulated at the pore throats, they would decrease pore connectivity and permeability and consequently hinder further transport of CO_2. Thus, the size, shape, locations, and phases of new solids are important for understanding permeability changes in subsurface environments.

4.2.3. Nutrient Cycling. Nutrient availability, storage, and transport are inexorably linked to mineral dissolution and precipitation reactions. Ultimately, these processes occur at molecular-scale interfaces, and mineral dissolution/precipitation mechanisms impact the transport of nutrients to and from living matter (section 1.2.2). Phosphorus bioavailability is

https://doi.org/10.1021/acs.chemrev.2c00130
Chem. Rev. 2023, 123, 6413−6544

essential to the growth of plants, and with the need to feed an increasing human population, the way in which P is made available in common agricultural practices[826] warrants revision. Global P reserves mined from phosphate rock will be depleted in 50−100 years, with peak production expected around 2030.[827]

A promising strategy for phosphate recovery is precipitation of struvite ($MgNH_4PO_4$) and associated compounds from wastewater streams.[828,829] The nucleation and growth kinetics of struvite[830] and molecular-scale *in situ* AFM studies have shown the details of how hexametaphosphate, polyphosphate type 45, and phytic acid inhibit nucleation due to their affinity for all principal struvite crystal facets.[831] Struvite formation is closely related to ionic composition, temperature, pH, and ion speciation.[832] In addition to struvite, hydroxyapatite-nucleated calcium alginate hydrogels have been used for effective recovery of phosphate,[833,834] which can be utilized as fertilizer, enabling a circular economy for the phosphorous chemistry. In this process, *in situ* nucleation of calcium phosphate (hydroxyapatite) in hydrogels decreased the energy barriers to subsequent calcium phosphate nucleation.

As biogeochemical cycles become increasingly interrelated with societal needs, the interfaces among these facets warrant meticulous inspection. The integration of experimental and theoretical approaches to elucidate the atomic- and molecular-scale behavior of the interacting systems will enable the incorporation of these findings into macroscopic models, greatly strengthening long-term predictions of nutrient cycling.

4.2.4. Water Treatment. Water treatment has employed coagulative precipitation to remove turbidity since the early part of the 20th century. To be effective, the solid nucleation and growth must occur within minutes, and particles must reach sizes sufficient for entrapment of colloidal particles and gravity settling separation within a similarly short time. Alum ($Al_2(SO_4)_3{\cdot}18H_2O$) and ferric chloride ($FeCl_3{\cdot}6H_2O$) are two of the most common coagulants that produce amorphous Al- and Fe-hydroxides. Using MD simulations, Zhang et al.[835] reported that nucleation of Fe-oxyhydroxide particles proceeds via cluster aggregation rather than monomer addition. The use of fast data-acquisition spectroscopic and scattering tools enabled a clearer picture of the nucleation process for ferrihydrite: μ-oxo dimers undergo structural reconfiguration into transient dihydroxo dimers, which rapidly condense to oligomers and then ferrihydrite.[836]

Although extensive research has focused on identifying inner- vs outer-sphere and mono- vs bidentate surface complexes associated with oxyanion adsorption to precipitated Al or Fe amorphous and crystalline phases (section 3.2.3),[837] until recently, less attention has been paid to understanding the role of these species in nucleation and particle growth. For example, Neil et al.[838] utilized GISAXS and studied heterogeneous Fe-hydroxide nucleation and growth on quartz substrates for systems containing arsenate and phosphate anions at pH = 3.6 ± 0.2. Systems containing these oxyanions had more growth, but a system containing only Fe^{3+} had the most nucleation events on quartz surfaces. *Ex situ* analyses of homogeneously and heterogeneously formed precipitates indicated that precipitates in the arsenate system had the highest water content and that oxyanions can bridge Fe-hydroxide polymeric embryos to form a structure similar to ferric arsenate or ferric phosphate. EXAFS spectroscopy has also been employed to develop a nucleation and growth model that involves Fe^{3+} bridging of PO_4/Fe^{3+} clusters.[839] Similarly, on-line photodispersion analysis[840] showed that the floc growth rate increased with increasing sulfate concentration and that the growth rate of Fe-hydroxide was greater than that of Al-hydroxide.

Particle nucleation and growth are affected by the presence of other surfaces. Anions (e.g., F^- and Cl^-) or oxyanions can either enhance or decrease particle growth,[445,448,841−843] while NOM drastically changes the size, charge, and morphology of particles.[844,845] As a result of these interactions, enhanced coagulation triggered by higher doses of Al or Fe is now a common treatment for removing NOM,[846] as well as for adsorbing oxyanions, such as As.[847] By utilizing in situ GISAXS and complementary *ex situ* techniques, Neil et al.[848] found unique fractal aggregation behaviors in a system containing NOM and precipitating Fe(III) (hydr)oxide nanoparticles. Furthermore, the coexistence of arsenic and NOM showed two distinct particle size ranges: larger particles dominated by arsenic effects and smaller particles dominated by NOM effects. The results of these studies suggest that in multi-component natural waters, complexation with NOM, and aggregation can occur simultaneously during adsorption, nucleation, and growth and can affect the composition of amorphous phases.

4.2.5. Mineral Fouling of Membranes. Membrane performance depends on the water or solvent's permeability, the selectivity for rejecting undesired solutes, and the membrane's stability. Hence, current membrane research focuses on maximizing permeability-selectivity, performing solute-specific separations, and preventing membrane fouling.[849−852] Membrane fouling, the precipitation of sparingly soluble phases in solution, at membrane surfaces, and within porous membranes— contributes to flux declines, reduces membrane lifespan, and increases energy demands.[853,854] Other important scalants (fouling phases) affecting water purification membranes are $CaCO_3$ and $CaSO_4$,[855] followed by Si- and Fe-oxides.[856] Fe-(hydr)oxides were the major inorganic scalants on a full-scale reverse osmosis membrane module taken from a seawater desalination plant performing coagulation pre-treatment with $FeCl_3$.[857] Local effects at the interface (e.g., concentration, polarization) can lead to supersaturation with respect to inorganic scalants near membrane surfaces, especially in highly contaminated waters, which are of great interest to future water reuse and resource recovery. These include seawater, industrial wastewater, and unconventional water resources such as produced waters.[858,859] Membrane hydrophobicity/hydrophilicity can affect scaling via surface-induced nucleation and attachment of crystals forming in solution,[664,853,855] while membrane surface charge and functionality can attract/repel scaling species.[860] For example, in a study of functionalized polyamide membranes, the initial silica layer formation during heterogeneous nucleation was controlled predominantly through electrostatic repulsion rather than changes in interfacial energy or competitive adsorption.[861] In addition, membrane surface morphologies, not just chemistries, can define the nucleation of scalants.[855]

Synergistic interactions such as silica scaling on pre-formed NOM fouling layers:[862] combined protein−silica[863] or iron-polysaccharide fouling,[864] and co-precipitation of iron hydroxide and gypsum[865] can intensify scaling, making it irreversible. Thus, there is an urgent need to develop a fundamental understanding of nucleation and growth of scales on membrane surfaces. Such a fully developed understanding can guide the development of water treatment to selectively

https://doi.org/10.1021/acs.chemrev.2c00130
Chem. Rev. 2023, 123, 6413−6544

remove fouling/scaling species or prevent their formation altogether.

4.2.6. Nuclear Waste Management. Light actinide contaminants (Th, Pa, U, Np, Pu, Am, and Cm) are associated with anthropogenic activities, such as the mining and milling of uranium ores, generation of nuclear energy, storage of legacy waste from nuclear reactors, and manufacturing and testing of nuclear weapons.[866] As a result of these activities, large quantities of high-level nuclear waste are stored in temporary repositories in most countries with nuclear capabilities. To develop a widely accepted plan for managing nuclear waste and remediating actinide-contaminated sites, the speciation of light actinides must be understood at the molecular level. This understanding must encompass a range of geochemical conditions, including those in nuclear waste storage tanks and cannisters, nuclear waste repositories, and actinide-contaminated soils, sediments, and groundwater. It is also vital to understand the types of geochemical processes that affect different actinide species, including the sorption/desorption of actinides at mineral/water and NOM/water interfaces (section 3), ET reactions that have a major impact on the stability and solubility of redox-sensitive actinide species, and the dissolution and precipitation of actinide-containing minerals and amorphous phases that release and/or sequester actinides.

The oxidation state of actinides primarily determines their fate and environmental mobility. Although Th, Am, and Cm exist in only one oxidation state (Th^{4+}, Am^{3+}, and Cm^{3+}), U, Np, and Pu can exist in multiple oxidation states, depending on E_h and pH. For example, U can occur as 3+, 4+, 5+, and 6+ oxidation states, with 4+ and 6+ being the most common. U^{4+} is commonly present in the nearly insoluble mineral uraninite (UO_2), whereas UO_2^{2+} (uranyl) can occur in over 360 crystal structures (e.g., schoepite [$UO_3 \cdot 1.2H_2O$]) and uranophane group minerals, such as sodium boltwoodite [$Na(UO_2)(SiO_3OH) \cdot 1.5H_2O$], as well as in many pH-dependent aqueous species.[866] In the presence of soil bacteria, mobile U^{6+} can be reduced to sparingly soluble U^{4+} in a variety of species other than uraninite, including molecular complexes bound to biomass.[867] During *in situ* bioremediation, the stability of U^{4+} solids in the contaminated subsurface environments can be limited by reoxidation to more mobile UO_2^{2+} species in the presence of Mn-(oxyhydr)oxides.[868]

There have been many studies of the speciation of redox-sensitive U, Np, and Pu in actinide-contaminated soils and high-level nuclear waste currently stored in underground tanks, such as those at Hanford, WA. See Maher et al.[866] for a review of these studies, which include U.S. DOE field sites at Hanford, Washington, Rifle, Colorado, Oak Ridge National Laboratory, Tennessee, Fernald, Ohio, Fry Canyon, Utah, and Rocky Flats, Colorado. For example, detailed studies of the speciation of U in contaminated plumes in vadose zone soils at Hanford, Washington, showed that Na-boltwoodite is one of the major uranyl-containing precipitates in microcracks in quartz and plagioclase feldspar grains.[869,870] This finding indicates that U is in a relatively stable form. At shallow depths, U precipitates as metatorbernite [$Cu(UO_2PO_4)_2 \cdot 8H_2O$] and cuprosklodowskite [$Cu(UO_2)_2(SiO_4)(H_3O)_2 \cdot 2H_2O$], which are also relatively stable.[870]

Studies by Wan et al.[871,872] of a U-containing contaminant plume confirmed the importance of aqueous uranylcarbonato complexes [$UO_2(CO_3)_3^{4-}$] within the plume body and $Ca_2UO_2(CO_3)_3$ in the plume front in facilitating U transport to the groundwater aquifer. This study also highlighted the importance of colloids of variable compositions, which can transport U in plumes. In addition, Kersting and Zavarin[873] and Kersting[874] showed that low levels of Pu can migrate over kilometer scales in association with clay and zeolite colloidal particles (10−100 nm). A review of colloid-facilitated transport of tetravalent actinides in field experiments and real-world scenarios is given by Zanker and Henning.[875]

4.2.7. Materials Science. From the perspective of developing new materials for sustainable energy, water resources, and information technologies, the highest importance lies in transforming the design and synthesis of hierarchical nanostructures, such as multiphase or highly branched nanoparticles,[876−879] nanoparticle superlattices,[880] layered 2D materials,[881] and mesoporous crystals,[882,883] which exhibit controls over transport of matter and energy not available in bulk solids or compact nanomaterials. For example, dense liquid and amorphous precursors offer the potential for forming moldable crystalline materials akin to biomineral structures produced in nature.[884,885] Branched nanowires can have short electron mean-free paths,[879] large photon absorption cross sections,[876] and complex patterns of optical scattering,[886] which can improve photovoltaic and photocatalytic efficiency; porous framework solids and 3D networks of 2D materials can provide high catalytic activity and molecule-specific separation.[882,883] In addition, great strides in synthesis could be achieved if we understood the design elements of the protein scaffolds that guide the earliest stages of mineralization and of the soluble proteins that help orchestrate the events transforming precursors into crystalline products and guiding the evolution of crystal shape.[811,887−907] Thus, developing a quantitative framework describing crystallization processes would advance the translation of transformative materials science to disruptive technologies.

Considering the aforementioned importance of dissolution, nucleation, growth, crystallization, and aggregation in many fields, in the following section, we will discuss these processes in more detail.

4.3. Dissolution

Mineral weathering is a crucial part of the global biogeochemical cycling of elements, with consequences for the critical zone, including climate.[908] These interfacial reactions, combined with economic motivations to understand fluid−rock interactions deeper in the Earth's crust, have motivated dissolution studies for many decades. Researchers have sought to establish the physical basis for mineral dissolution and build quantitative kinetic models that explain the history of Earth environments over geological time scales as well as provide predictive models to assess the future behavior and properties of Earth systems. However, this has proven challenging because predictive relationships that incorporate reliable thermodynamic variables over a range of undersaturation and temperature are still elusive.[468] Significant experimental efforts have provided considerable insight (e.g., Luttge et al. and references therein[909]), yet, their data, even for a single mineral under experimental conditions, show apparent inconsistencies that could not be explained by the mostly empirical rate laws.[909]

4.3.1. Dissolution Rate. To develop quantitative models for dissolution rates in diverse Earth environments and engineered systems, expressions have been derived to link mineral dissolution to the solution saturation state and mineral

https://doi.org/10.1021/acs.chemrev.2c00130
Chem. Rev. 2023, 123, 6413−6544

surface properties.[909−911] These approaches use assumptions from transition state theory (TST), introduced in the 1930s,[912] and the principle of detailed balancing (PDB) to postulate that the dependence of dissolution rate on driving force obeys the form:

$$\gamma_{dis} = k_+\left[1 - \exp\left(\frac{\Delta G}{RT}\right)\right] \quad (9)$$

where ΔG is the free energy change for the overall dissolution reaction and R is the gas constant. The rate of reaction in eq 9 is widely rewritten to a more convenient form that gives the dependence of rate upon solution chemistry:

$$\gamma_{dis} = k_+\left[1 - \left(\frac{IAP}{K_{sp}}\right)\right] \quad (10)$$

where K_{sp} is the mineral solubility product at standard state conditions and IAP is the ion activity product or reaction quotient. By using eqs 9 and 10, these approaches begin with the assumption that the PDB can be applied across the full range of chemical driving force from near to far-from-equilibrium conditions.[913,914] However, the original PDB requires that all elementary steps in a dissolution or growth reaction be near equilibrium, except for a single, slow rate-determining step. To apply this approach to diverse geological settings, it was further assumed that the dissolution process is independent of undersaturation across the full range of chemical driving force. Moreover, nonequilibrium surface defects were thought to not have a significant role in the dissolution/growth kinetics,[915] although nonequilibrium defects are common (Figure 46).[916] This concept also caused most dissolution data to be collected over far-from-equilibrium conditions, although near-equilibrium conditions are common in the environment. Moreover, dissolution rates and mechanisms can differ significantly when near- vs far-from-equilibrium conditions are compared.[917−919]

At far-from-equilibrium conditions, experimental data on dissolution rates disagree with eq 9 or 10 predictions. To address this problem, eqs 9 or 10 were modified into two types of power-law expressions that are still widely applied.[649,914,920,921] A constant, n, was introduced to the exponential term such that

$$\gamma_{dis} = k_+\left[1 - \exp\left(\frac{n\Delta G}{RT}\right)\right] \quad (11)$$

or

$$\gamma_{dis} = k_+\left[1 - \left(\frac{IAP}{K_{sp}}\right)^n\right] \quad (12)$$

where n is not necessarily equal to 1.0.[920−922] In this form, the dissolution rate becomes constant as the degree of undersaturation increases at far-from-equilibrium conditions. The approach was rationalized with PDB because eq 11 reduces to the expected linear form at near-equilibrium conditions, where $n\Delta G < RT$.[915] Equations 9 and 10 became widely invoked with the assumption that the dissolution rates of diverse mineral−water systems were independent of driving force at far-from-equilibrium conditions.[923,924]

A second inconsistency was revealed when additional experiments showed that the dissolution rates of some mineral−water systems have an exponential dependence

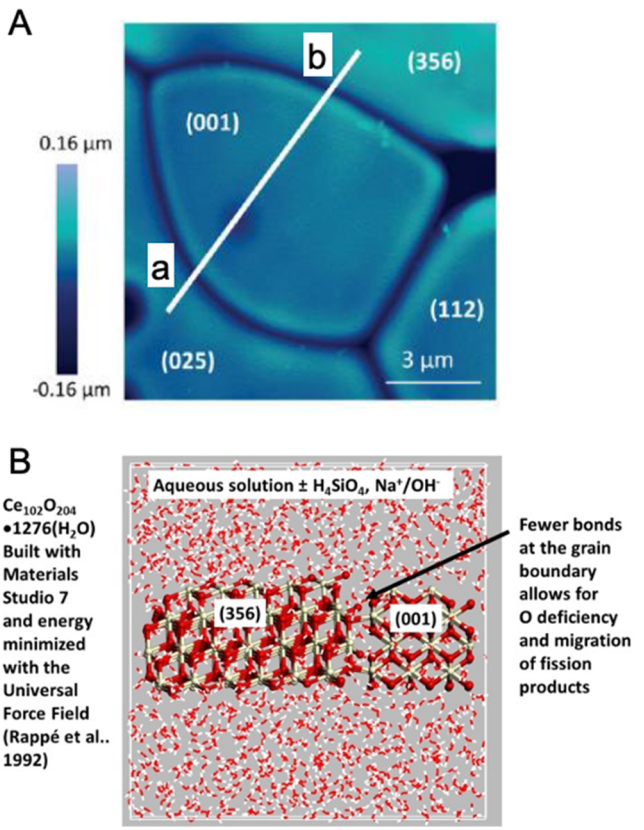

Figure 46. (A) AFM image and cross sections of CeO_2 grains, with grain boundaries of low (a) and high (b) misorientation angles.[916] (B) A model of a CeO_2 grain boundary with exposed (001) and (356) faces models the site of enhanced dissolution, in Corkhill et al.[916] Incompatible elements will concentrate within grain boundaries. Image B was drawn with Materials Studio 2016 (Accelrys Inc., San Diego CA). Adapted from ref 916. Copyright 2014 American Chemical Society.

upon driving force, without any evidence of a plateau.[924−927] To address this issue, an exponent was added to the entire driving force term, so that eqs 9 and 10 became generalized to the form

$$\gamma_{dis} = k_+\left[1 - \exp\left(\frac{\Delta G}{RT}\right)\right]^n \quad (13a)$$

or

$$\gamma_{dis} = k_+\left[1 - \left(\frac{IAP}{K_{sp}}\right)\right]^n \quad (13b)$$

The most widely accepted explanation for this nonlinear rate law called upon surface defects as affecting dissolution.[925,928] This realization acknowledged that the wide variations in the reaction orders found for eqs 13a or 13b were not understood and that complex surface phenomena must have a role.[428,909,911,929]

4.3.2. Dissolution Mechanisms. *4.3.2.1. Hydrolysis.* Metal oxides and silicates are networks of M−O−M bonds, and the aqueous species of the cations in these networks are typically monomers or small oligomers with varying degrees of coordination with H_2O or OH^-. Consequently, dissolution mechanisms entail hydrolysis of the M−O−M networks to break up the solid into smaller soluble units. In general, the

https://doi.org/10.1021/acs.chemrev.2c00130
Chem. Rev. 2023, 123, 6413−6544

weaker the M−O bond, the higher the proton affinity allowing protonation of the M−O−M linkage and initiating hydrolysis under acidic conditions. For basic solutions, OH^-(aq) groups can directly form bonds with surface M atoms, which leads to breakage of M−O−M linkages. In either case, the weaker the M−O bond, the lower the activation energy barrier to dissolution.

The molecular level mechanisms of how hydrolysis plays out to dissolve metal oxides and silicates are unclear. Although hydrolysis of Si−O−Si linkages has been modeled for over 30 years, computational chemistry has not provided a reaction pathway consistent with the observed rates, activation energies, and changes in rate constant with salt type and concentration. Most modeling work has presumed a direct H^+-transfer from H_2O or H_3O^+ in solution to the O in the M−O−M linkage. However, DFT-MD simulations of quartz−water interfaces predict that H-bonding to the bridging O (O_{br}) in the M−O−M linkage is very weak at best, so the probability of H^+-transfer occurring directly from H_2O or H_3O^+ is extremely small.[930] Instead, intrasurface H-bonds between SiOH groups and O_{br} may form that could allow for H^+-transfer. The percentages of these types of H-bonds increase with the salt content of the model solution,[11] which may explain the observed increase in silica dissolution rate constants as salts are added, while the activation energy remains remarkably constant.[433]

4.3.2.2. Effects of Cations. Although extensive "bulk" dissolution rate studies have yielded considerable early insight, the community has recognized the inherent empirical nature of the aforementioned "rate laws". There is an ongoing need for a molecular picture that can explain the differences in experimental data sets for the same mineral−water system. The apparent earlier reported inconsistencies were compounded by experimental measurements that showed the major solutes in natural waters (Ca^{2+}, Mg^{2+}, Na^+, or K^+) have little effect on the dissolution rate of silicate minerals[922] but increase the dissolution rate of quartz up to 100 times (Figure 47).[931,932]

Several studies noted the potential contribution of etch pits,[929] but these insights were interpreted using TST models without resolving ongoing inconsistencies. Building upon these insights, Dove et al.[933] conducted a quantitative study that examined the morphology of quartz surfaces during congruent dissolution for a broad span of undersaturated conditions and electrolyte concentrations[933,934] and in the absence of secondary precipitates forming on the quartz surface.

As seen in Figure 48, surface structures evolved with an increasing degree of undersaturation or addition of electrolytes, which shows the dissolution rate trends, are correlated with the predominant surface morphology, with a transition from simple step retreat to the opening of defects (postulated to be dislocations or impurities) then to nucleating 2-D vacancy islands at composition impurities or homogeneous sites across the entire surface.

The changes in the predominant microscopic dissolution process can be understood in the context of crystal growth processes and the energy barrier to ion detachment and attachment. Crystal growth theory considers the probability of ion attachment at step edges versus dislocation defects versus growth by nucleation of two-dimensional adatom islands, either at impurity defects or homogeneously across the surface (Figure 49). With increasing supersaturation, the dominant crystal growth process transitions from ion attachment at step edges to nucleation-driven crystal growth. Not surprisingly, the

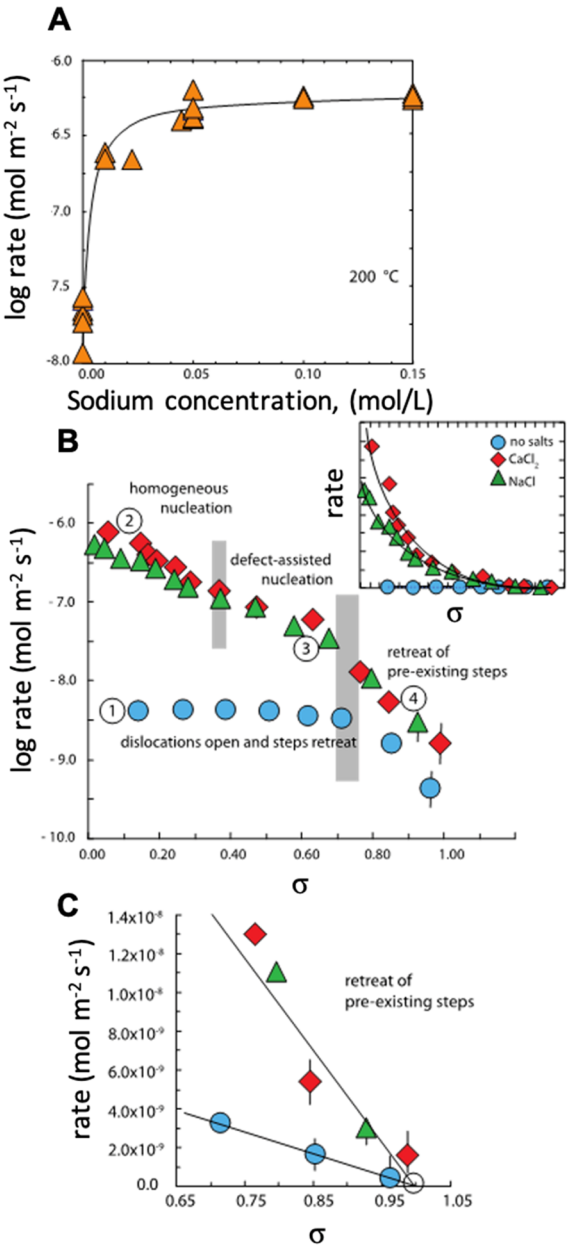

Figure 47. (A) Experimental measurements show the dissolution rate of quartz (mol H_4SiO_4 m^{-2} s^{-1}) is dependent upon NaCl concentration, with increases up to 1.5 orders of magnitude. Reproduced with permission from ref 931. Copyright 1990 Elsevier Ltd. (B) Electrolytes modify the dissolution rate's dependence on the degree of undersaturation (σ = IAP/K_{sp}). Blue circles, distilled-deionized water; red diamonds, 0.0167 M $CaCl_2$; green triangles, 0.05M NaCl. Gray zones show the undersaturation range where the dominant dissolution mechanism undergoes a transition. Inset uses a linear ordinate to better illustrate the exponential dependence of rate on driving force when salts are introduced. (C) Expanded view of rate dependence on σ at near-equilibrium conditions, showing linear dependence predicted by PDB. In this region, the widely accepted first-order rate dependence is fit to the data by forcing rate to zero at σ = 1.0, as denoted by open symbols. (B,C) Reproduced with permission from ref 933. Copyright 2005 National Academy of Sciences.

principles that describe congruent dissolution processes are similar to those used in crystal growth models, and rates are quantified using primary parameters: supersaturation σ, the

https://doi.org/10.1021/acs.chemrev.2c00130
Chem. Rev. 2023, 123, 6413−6544

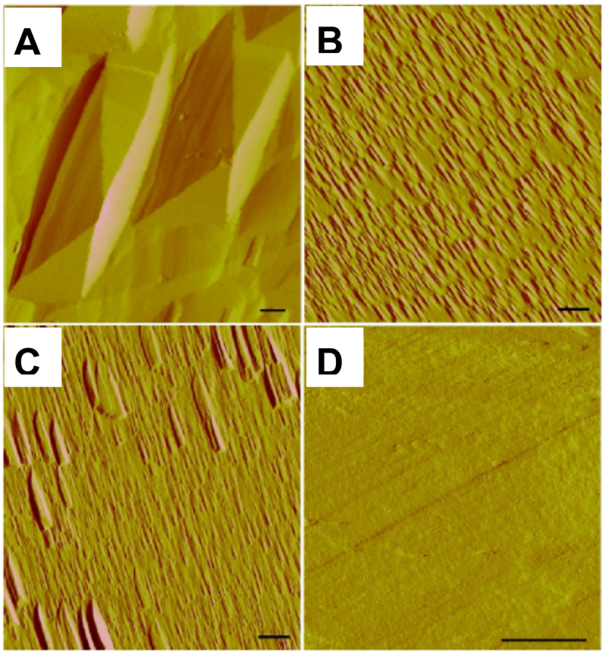

Figure 48. AFM images of (100) quartz surfaces exposed to different solution chemistries for equivalent extents of reaction show the different dissolution processes that are active across driving force and solution chemistry (scale bar: 1 mm in all images). (A) For $\sigma = 0.10$ in H_2O, surfaces are dominated by large etch pits with sloping sides that converge at dislocation sources. Pits are separated by relatively flat regions on the surface. (B) Where $\sigma = 0.10$ for a solution of 0.0167 M $CaCl_2$, surfaces show a high density of small pits with flat bottoms and with flanks that are 25% steeper than measured for pits in (A). (C) At the intermediate driving force of $\sigma = 0.65$ in 0.0167 M $CaCl_2$, mixed larger and smaller flat bottomed pits forms across the surface. (D) For a driving force of $\sigma = 0.90$ in 0.0167 M $CaCl_2$, surfaces present only straight-edged steps, with no evidence of pitting. Adapted from ref 933. Copyright 2005 National Academy of Sciences.

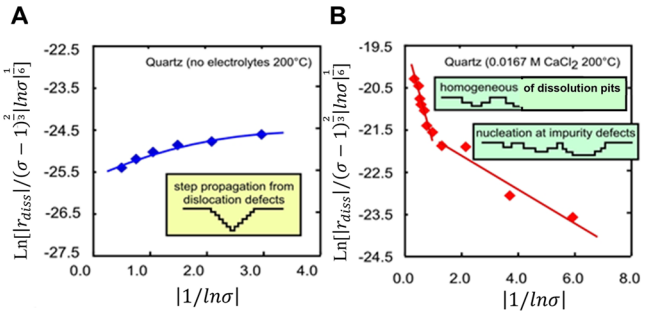

Figure 50. Process-specific models describe the dependence of dissolution rate (r_{diss}) on (inverse) undersaturation for measured rates of quartz and reported rates of aluminosilicate dissolution. Adapted from ref 933. Copyright 2005 National Academy of Sciences. (A) Dislocation model predicts the behavior of quartz dissolution rate in the absence of electrolytes. (B) In contrast, dependence of quartz dissolution rate on undersaturation in 0.0167 M $CaCl_2$ solutions is predicted by the nucleation model.

interfacial free energy barrier to forming an etch pit at a dislocation (or forming a vacancy island) α, the step kinetic coefficient β, and temperature T.[935,936]

This mechanistic model for dissolution without secondary precipitation predicts the behavior of the crystalline polymorph of SiO_2, and the changes with undersaturation from step retreat to defect-driven and homogeneous etch pit formation (Figure 50).[933] This model reveals the "salt effect", which can explain the complex dependence of the dissolution rate on the chemical driving force for the major weathering aluminosilicates, feldspar ($KAlSi_3O_8$) and kaolinite ($Al_2Si_2O_5(OH)_4$), when the ratio of the total dissolved Al:Si is stoichiometric with their composition. These studies of materials that undergo congruent dissolution provide a physical basis by which the formalisms of crystal nucleation and step growth can be coupled to dissolution. That is, analogous to growth, dissolution occurs when "solutes" are released to solution at a rate that is controlled by overcoming energy barriers to "corrosion". This model does not imply the energy barriers to growth and dissolution processes are equivalent or symmetric about the chemical driving force. Energetic and kinetic factors, including the role of water in the dehydration and hydration steps, likely present process-specific barriers.

4.3.2.3. Ligand-Promoted Dissolution. The effects of ligands on metal oxides' solubility and dissolution rates have been known since the seminal work of Stumm and coworkers (e.g., Stumm and references therein).[937] In particular, Fe can be the limiting nutrient in marine environments, despite the fact that large amounts of Fe in the form of mineral dusts are blown into the oceans from continents (ref 938 and section 4.2.1). To become bioavailable, the mineral dusts must be dissolved. On the other hand, interactions of marine organic C compounds with Fe-(oxyhydr)oxides may inhibit conversion to more crystalline and less soluble Fe-oxides.[938]

One mechanism to increase the solubility of Fe^{3+} solid phases is by creating Fe^{3+}–ligand complexes that are more soluble than the Fe^{3+} ion alone. Thus, Fe-oxy(hydr)oxide dissolution can be substantially promoted by the addition of other ligands and Fe^{2+}. For example, synergistic effects with factors of 2 to 10 on the dissolution rates of Fe-oxides have been reported between different ligands, e.g., among organic

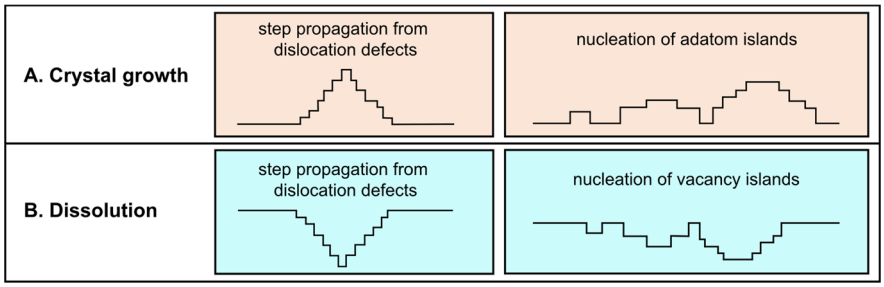

Figure 49. Illustrative physical models for (A) classical crystal growth by formation and propagation of steps across a surface, and (B) the reverse process of dissolution by opening etch pits and step retreat. Adapted from ref 933. Copyright 2005 National Academy of Sciences.

https://doi.org/10.1021/acs.chemrev.2c00130
Chem. Rev. 2023, 123, 6413−6544

acids and siderophores. One of the ligands, such as oxalate, adsorbs strongly on the oxide surface and promotes dissolution, and the other, such as siderophores, complexes strongly with the Fe^{3+} in the dissolved Fe^{3+}−oxalate complex, which frees the oxalate for continuous adsorption-dissolution.[939] The addition of a small amount of Fe^{2+} has a major effect, by factors of 10 to 100, on promoting Fe-oxy(hydr)-oxide dissolution, and the dissolution rate increases linearly with adsorbed Fe^{2+} concentration. This promotion effect was initially explained by Fe^{3+}-L^{-} complexes being stronger reductants than Fe^{2+} alone, and/or by ligand surface bridging that facilitates electron transfer from the Fe^{2+} to the surface Fe^{3+}.[14,940] Recently, a conveyor belt mechanism (section 3.4.1.5), in which sorbed Fe^{2+} injects electrons into the conduction band of the mineral that reduces Fe^{3+} at another location, has been invoked to rationalize the synergistic effect because ligand-assisted detachment of Fe^{2+} is more favorable than that of Fe^{3+}.[582,662]

However, there is still much to be understood about the molecular mechanisms of these interactions. For example, Torres et al.[941] ascribed dissolution-enhancement of olivine ($(Fe,Mg)SiO_4$) by the siderophore DFO-B to adsorption and "*...removal of an oxidized surface coating that forms during dissolution of olivine at circumneutral pH in the presence of O_2 and the absence of organic ligands.*" These authors cite Cheah et al.[942] as evidence that the rate of goethite dissolution is proportional to adsorbed DFO-B, but the adsorption isotherms indicate that DFO-B adsorption decreases by approximately 50% as the oxalate concentration increases above 70 μM. Cheah et al.[942] showed that the increase in rate with oxalate concentration does not occur until [oxalate] >70 μM. Consequently, DFO-B adsorption cannot be enhancing the dissolution rate of goethite. When one considers that high Fe-siderophore binding constants are the result of the six Fe−O bonds that can form in solution, it is improbable that more than two of these bonds could form to a Fe atom on a mineral surface. Even when a siderophore does adsorb to a Fe-bearing mineral surface, there is no explanation as to why this should mobilize the Fe away from the surface. These assumptions are likely based on the hypothesis that protonation of surface M−OH groups and ligand bonding to surface atoms "polarize and weaken" the remaining bonds to the mineral (Stumm and references therein).[937] A key finding in Wang et al.[943] is stated as "*The correlation of rate coefficients with stability constants suggests that the binding strength of the ligand to* Fe in solution [emphasis added] *is related to the rate-limiting step in ligand-promoted dissolution.*" If surface complexation were controlling dissolution rather than making the ΔG of dissolution more favorable, the weaker adsorbing siderophores would not control the rate coefficients. The need for molecular-level data is cited by Wang et al.:[943] "*Deeper interpretation of this correlation is hampered by the unknown surface speciation of the adsorbed ligand in general and the coordinative environment of the precursor of the rate-determining step in particular.*"

DFT calculations predict the opposite is generally true.[14,944] Instead, an alternative hypothesis is that the ΔG of dissolution is lowered by the presence of ligands, such as oxalate and DFO-B, and that this more negative ΔG of dissolution enhances the dissolution rate because the reverse reaction (attachment) is less favorable. This is an example of where molecular mechanisms, thermodynamics, and macroscopic rates need to be assessed simultaneously to achieve an accurate picture of the interfacial chemistry. Future experimental work to assess the accuracy of the DFT predictions regarding the strength of metal bonds to the bulk crystal after surface ligand complexation could determine which hypothesis is correct.

4.3.2.4. Reductive and Oxidative Dissolution. Similar to ligand-promoted dissolution, reductive and oxidative dissolution are important for marine biochemistry,[945] mineral extraction and mine waste remediation,[78] soil biogeochemistry,[946] and water quality.[736,947] The general principle of redox-mediated dissolution and precipitation is based on the change in solubility of many elements with variable oxidation state. For example, Fe^{2+} is much more soluble than Fe^{3+}, so reduction leads to dissolution of Fe-oxides, and UO_2^{2+} (i.e., U^{6+}) is more soluble than U^{4+} (e.g., UO_2, uraninite), so oxidation causes dissolution. Interfacial redox reactions have been discussed in detail in section 3.4.1.2, so here we focus on examples of reductive dissolution coupled with ligand-promoted dissolution. This type of reaction is used by organisms to acquire Fe and hence is critical in the environment and for food production. This chemistry is often enhanced in the presence of light, as is discussed in section 4.7.10.

During reductive dissolution, Fe^{3+}-oxy(hydr)oxides can undergo recrystallization, e.g., from ferrihydrite to lepidocrocite and then to goethite, and become more resistant to dissolution.[948] During this process, the reduction potential of the Fe^{2+}−Fe^{3+} oxide mixture decreases over time.[949] With an increasing amount of Fe^{3+} dissolved from Fe^{3+}-containing clay minerals in the presence of Fe^{2+}, the reduction potential of the system increases, so the corresponding reduction ability keeps decreasing.[949] Smaller particles can undergo Fe^{2+}-catalyzed reductive dissolution more easily because they tend to be better hydrated and have higher solubility.[950] Facets also strongly influence the dissolution rate. For example, hematite (001) facets are more favorable than (012) in reductive dissolution because the bidentate mononuclear Fe−ascorbate complexes that form on the (001) facets are better positioned to undergo interfacial charge transfer than the monodentate mononuclear configurations on the (012) facets.[529]

Reductive dissolution of Fe^{3+}-(hydr)oxides is also affected by co-existing species. For example, soluble Al^{3+} ions adsorb to goethite surfaces and inhibit reductive dissolution by hydroquinone.[649] Under oxic conditions, ascorbate itself cannot reduce goethite to a detectable level because the generated surface Fe^{2+} undergoes facile oxidation by aqueous O_2.[943] With the addition of different ligands, reductive dissolution rates could increase, decrease, or remain unchanged, depending on the solution conditions, including pH, the nature of the ligand, and the type of Fe^{3+} oxides.[943,951] At least four mechanisms could explain the ligand effects: (1) competitive adsorption of the reductant and the ligand, (2) favorable generation of surface Fe^{2+}, which could affect the oxide structure, (3) the complexation of surface Fe^{2+} by the ligand, and (4) some ligands are radical scavengers that inhibit reaction between the radical and surface Fe^{2+}.[943]

Fe^{3+}-oxide dissolution can noticeably impact the reactivity of oxides. For example, under acidic conditions, the dissolved Fe^{3+} from goethite contributes to the fate of contaminants,[649] and the reductive dissolution of Fe^{3+} oxides can lead to the release of elements associated with the oxides. For Cu-, Co-, and Mn-substituted goethite and hematite or Fe^{3+}−As^{5+} co-precipitates, the Fe^{2+}-facilitated reductive dissolution of these oxides is accompanied by the release of Cu, Co, and Mn to solution, while the released As^{5+} is largely retained in solid

https://doi.org/10.1021/acs.chemrev.2c00130
Chem. Rev. 2023, 123, 6413−6544

phases as amorphous $Fe_3(AsO_4)_2$.[952,953] The release of trace elements from the corresponding substituted Fe-oxides can be hindered by the incorporation of Al in the oxides.[954] The speculated reasons include Al or Zn physically blocking Fe sites or directing electron flow, forming a coating during the oxide dissolution, or inhibiting bulk electron conduction.[954,955]

The issues of ligand and siderophore adsorption coupled with reductive dissolution of goethite are discussed in Wang et al.,[943] who examined the synergistic effects of ascorbic acid with the siderophores DFO-B and *N*,*N*′-di(2-hydroxylbenzyl)-ethylenediamine-*N*,*N*′-diacetic acid (HBED). Based on their data, Wang et al.[943] proposed possible mechanisms for the reductive/ligand-promoted dissolution enhancement, but they could not distinguish among these individual mechanisms. Kubicki et al.[14] examined potential synergistic effects of reductive dissolution (via Fe^{2+}) and ligand-promoted (via oxalate) dissolution in the goethite−Fe^{2+}−oxalate system. DFT calculations were consistent with the observed delocalization of an adsorbed Fe^{2+} onto goethite,[956] except in the case where a Fe atom had a single Fe−O−Fe to the model goethite. In this case, approximately 0.5 e^- reduced the charge of the corner site so that bonding one or two oxalate ligands would be possible and detachment from the surface would be more likely due to weaker bonds attaching the surface Fe atom to the bulk. As shown in this example, combined thermodynamics, kinetics, spectroscopic, and molecular modeling studies would be useful in more definitively addressing the details of this important biogeochemical reaction.

Reductive dissolution of $Mn^{3+/4+}$ oxides has also been widely studied since the 1980s. Readers are referred to a recent review by Huang and Zhang[629] for more details regarding the reaction kinetics, mechanisms, and the impact of reaction matrices.[629] While much progress has been made in understanding the dissolution kinetics and mechanisms of Fe- and Mn-(hydr)-oxides, the complexity of environmental conditions prevents quantitatively extrapolating results obtained from simple model systems to environmental matrices.

Mn-oxides can strongly oxidize both cations and anions, which makes their complete description even more challenging (section 3.4.1.4). As a result, their structures may be modified though Mn reduction. For example, when Mn^{2+}, Fe^{2+}, or Tl^+ are added, the layered structure of birnessite (δ-$Mn^{IV}O_2$) may be reduced to a Mn^{III} oxide,[957] partly dissolve and delaminate,[958,959] change its layer symmetry,[960] or change to a tunneled Mn oxide.[961,962] The size of the resulting tunnels depends on the redox kinetics cycling.[963] This cycling occurs with nanoparticulate birnessite, which may oxidize species that are stable under oxygenated conditions (such as Tl^+), suggesting higher oxidation potentials than oxygen, and therefore the possibility to oxidize water.[962] Current related active research areas include both water oxidation[964,965] by birnessite and the electrochemical properties for processes such as water splitting to produce H_2.

4.3.2.5. Defect-Controlled Dissolution. Defect sites on surfaces are likely to have lower values of activation energy, ΔE_a, for dissolution. Hence, planar defects (e.g., twinning, such as Brazil twinning in quartz Figure 1) and point defects (e.g., elemental substitution) exposed on the surface may be foci for dissolution. Another set of under-studied "defect" sites for dissolution is grain boundaries (Figure 46). At grain-to-grain contacts, both structural distortions from mismatch of the adjacent crystal structures and compositional defects may concentrate and allow dissolution rates an order of magnitude greater than for the planar surface.[916] To date, most simulations of mineral dissolution have modeled planar surfaces and steps as the sites for hydrolysis, so a better coordination of simulation studies with experiments examining dissolution and surface defects is needed to obtain realistic dissolution rates and mechanisms for oxides and silicates. To properly model defects and their propagation at varied concentrations, accurate reactive force fields and/or tight-binding DFT models must be developed (sections 5.2.2.4).

4.3.2.6. Biologically-Induced Dissolution. The above discussions on ligand-promoted, reductive/oxidative, and defect-controlled dissolution all apply to biologically-induced dissolution of minerals. This section will focus on unique features that plants, microorganisms, and biological systems exhibit to obtain macro- and micronutrients. In addition to macronutrients, such as N, P, K, and Ca, plants require elements such as Mn for photosynthesis[966,967] and Si for stalk strength and water retention (Li et al. and references therein; section 1.2.2).[968] Thus, highly insoluble elements must be extracted to sustain life, so organisms have devised strategies to continually pump these elements out of minerals in a manner that is not strictly controlled by chemical equilibrium or steady-state conditions as reactants are produced to meet the organisms' demands.

In addition to using Le Châtellier's principle to continually produce reactants that drive dissolution and element extraction, microenvironments are created in the rhizosphere that alter chemical conditions to favor mineral dissolution. Fungi are critical in this regard, and an excellent example of this effect is discussed in Gerrits et al.[969] By contrasting the wild-type with the melanin-deficient mutant (Δ*Kppks*), these authors studied the impact of *Knufia petricol*o A95 on olivine ($Mg_{1.86}Fe_{0.19}SiO_4$) dissolution and explored the role of fungal attachment in creating microenvironments. Their data demonstrated that differences in EPS, such as the pullulan content between the wild-type and mutant, affect ion attachment and olivine dissolution rates. Furthermore, the biofilm within the EPS creates an environment where reuse of siderophores, lower O_2 concentrations, and lower pHs all contribute to enhancing olivine dissolution. Consequently, molecular-level details within these microenvironments must be elucidated to predict long-term macroscopic behavior or design systems to maximize dissolution for sustainable nutrient cycling and effective mineral carbonation (e.g., Rim et al. and references therein).[970]

Another vital issue is the dissolution of minerals in lungs and the gastrointestinal tract as biological fluids react with inhaled particles, negatively impacting human health (see Sattler et al., 2020, and section 1.2.3).[971] The scope of this topic is so extensive that it warrants its own review volume,[972] so here we discuss only key points and refer the readers to the abundant literature on the topic. First, a major concern is the generation of reactive oxygen species (ROS), such as *OH and $*O_2^-$. The availability of Fe^{2+} and the solubility of the solid phase are key factors because Fenton chemistry helps to create the ROS that lead to cell or DNA damage.[973] Higher body temperatures, lower pH, and the presence of complexing ligands contribute to the dissolution of inhaled mineral dust.[974] Other elements, such as U[975] and Pb,[976] can also be released, and they have their own complex impacts on health.[977] Because the potential for reactions and negative impacts can be increased when the phases of interest are in the form of nanoparticulates,[73,978,979]

https://doi.org/10.1021/acs.chemrev.2c00130
Chem. Rev. 2023, 123, 6413−6544

the effects of each mineral should be assessed as a function of size, phase, and surface chemistry.

4.3.3. Effects of Crystallography on Dissolution. *4.3.3.1. Dissolution of Silica.* The dissolution mechanism of amorphous silica is elusive because noncrystalline solids lack the long-range structural order that allows the terrace, ledge, and kink-based models to be applied.[933,980] Thus, describing dissolution probabilities requires statistical approaches to variations in Si−O−Si bond lengths and angles in solids. The absence of a regular structure implies that the surfaces of amorphous phases are atomically rough, so repeated release of H_4SiO_4 to solution leaves the surface free energy of the solid unchanged. Consequently, the dissolution rates of amorphous phases should scale linearly with increasing driving force (undersaturation) through the higher probability of detaching silica tetrahedra from the surface. However, dissolution rate measurements[981] of such amorphous SiO_2 polymorphs as fused quartz glass, synthetic colloids, and biological amorphous silicas reveal a paradox. While rates measured in solutions that lack electrolytes show the expected linear dependence on undersaturation, in contrast, in $CaCl_2$ electrolyte solutions, the dissolution rates of vitreous silica under conditions of intermediate to high undersaturation exhibit an exponential dependence on driving force, as seen for quartz (Figure 51).

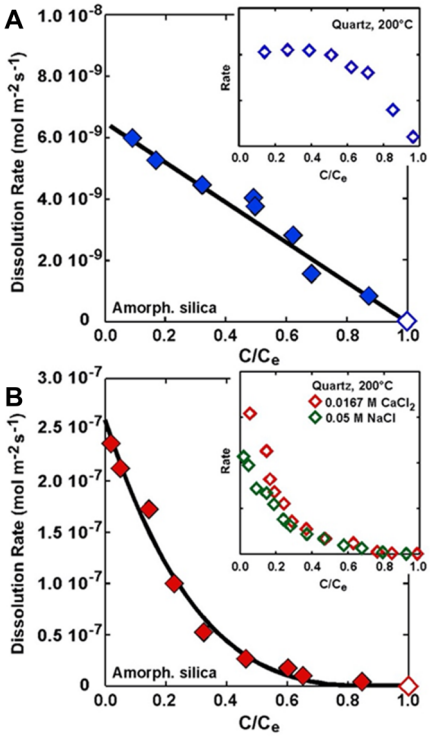

Figure 51. Measured rates of vitreous silica dissolution versus undersaturation, C/C_e, show two different trends, where C and C_e are measured and equilibrium concentrations of $H_4SiO_4^\circ$, respectively. (A) In the absence of electrolytes, the rates show a linear dependence on chemical driving force, as expected for an amorphous material. (B) Solutions of NaCl or $CaCl_2{\cdot}6H_2O$ at 150 °C induce 100× faster dissolution rates at high undersaturations because a pit nucleation-dominated process predominates. The measurements show exponential dependence upon the degree of undersaturation, just as was determined for a crystalline polymorph, quartz, at 200 °C. Adapted from ref 981. Copyright 2008 National Academy of Sciences.

To explain this enigma, Dove et al.[981] showed that silica polymorphs present common types of surface-bonded silica groups to solution with differing degrees of polymerization. Whether amorphous or crystalline, low-pressure silicas share the silica tetrahedron as a fundamental polymeric unit. Thus, silica tetrahedra on quartz surfaces have distinct bonding coordinations at terraces and steps[982] that roughly correlate with degree of polymerization at the amorphous silica−water interface. There are variations in the Si−O−Si bond angles,[983] but both surfaces present two sites for reaction with water, called Q^2 and Q^3.[984] The Q^2 groups are bonded to two bridging oxygens at a step edge on the (100) surface of quartz (Figure 52). The Q^3 groups that comprise a terrace have a higher coordination to the mineral structure through binding to three bridging oxygens and thus have fewer degrees of freedom.

4.3.3.2. Dissolution of Feldspars. Feldspars are the most abundant rock-forming minerals in the Earth's crust. The dissolution kinetics of feldspars are closely related to their crystallography (Figure 53A). All feldspars are tectosilicates and share similar "mirrored crankshaft-chain" frameworks of polymerized Si and Al tetrahedra (Figure 53B). Each Al or Si is bonded to four oxygens, and each oxygen is shared with another tetrahedron, which forms T−O−T linkages (tetrahedral sites (T) and oxygen atoms (O)). The Al content (Al/Si ratio) of feldspar determines the average T−O bond length. Thus, T−O−T bond lengths (the average distance between T sites and O) and Al/Si ordering in feldspars define their dissolution behavior. Yang et al. examined the role of T−O−T bond length and Al/Si ordering in feldspar dissolution.[985−987] The dissolution rates of feldspars were found to be a linear function of the average T−O bond length, a relationship which is applicable from the pure end member of anorthite (Al/Si = 1) to the pure end-member of albite (Al/Si = 1/3), and even extendable to quartz (Al/Si = 0).

In addition to the T−O bond length, the Al/Si ordering in feldspars can control their dissolution rates. Each Al or Si has four closest neighbor T sites. All four neighbors of Al must be Si because Al−O−Al linkage formation is not energetically favored. However, the neighbors of Si can be Al or Si. For different numbers of Si neighbors, Si sites are categorized as Si_I, Si_{II}, Si_{III}, and Si_{IV} (1, 2, 3, and 4 Si neighbors, respectively, Figure 53B). The fractions of these four configurations are determined by the Al/Si ordering, affecting the dissolution kinetics. First, because Al−O−Si linkages are weaker than Si−O−Si linkages, the four configurations have different dissolution rates (i.e., dissolution is fastest in Si_I), and the overall dissolution rate of Si is the combination of all four rates. Second, the hydrolysis of Si−O−Si linkages is weakly affected by protons, while the hydrolysis of Al−O−Si linkages can be promoted by proton. Hence, with different numbers of Al−O−Si linkages, the Si_I, Si_{II}, Si_{III}, and Si_{IV} have different pH dependencies (Figure 53B).[987] In feldspar dissolution, the relatively faster release of Al than Si can be correlated with crystallographic information from high resolution XRD and FTIR spectroscopy (Figure 53C). The correlation can explain how feldspar crystallography (i.e., T−O bond length and Al/Si ordering) can result in the incongruency of feldspar dissolution, as shown in Figure 53C,D.[986] These results provide a valuable perspective on feldspar dissolution, which links the crystallography and the dissolution kinetics in environmental systems and offers useful insight into dissolution of engineered materials under extreme conditions.

https://doi.org/10.1021/acs.chemrev.2c00130
Chem. Rev. 2023, 123, 6413−6544

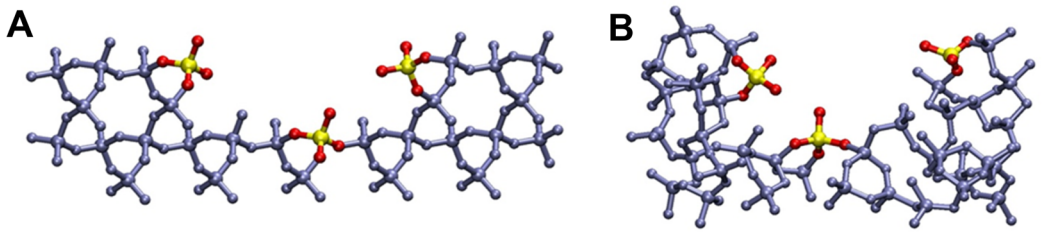

Figure 52. (A) Quartz and (B) amorphous silica surfaces present Q^2 and Q^3 tetrahedra with two and three coordinations to the surface, respectively. Adapted from ref 981. Copyright 2008 National Academy of Sciences. The physical model holds that amorphous surfaces are repeatedly atomically roughened at a length scale that is the average distance over which Q^2 groups must be removed to get back to a Q^3-enriched SiO_2 surface.

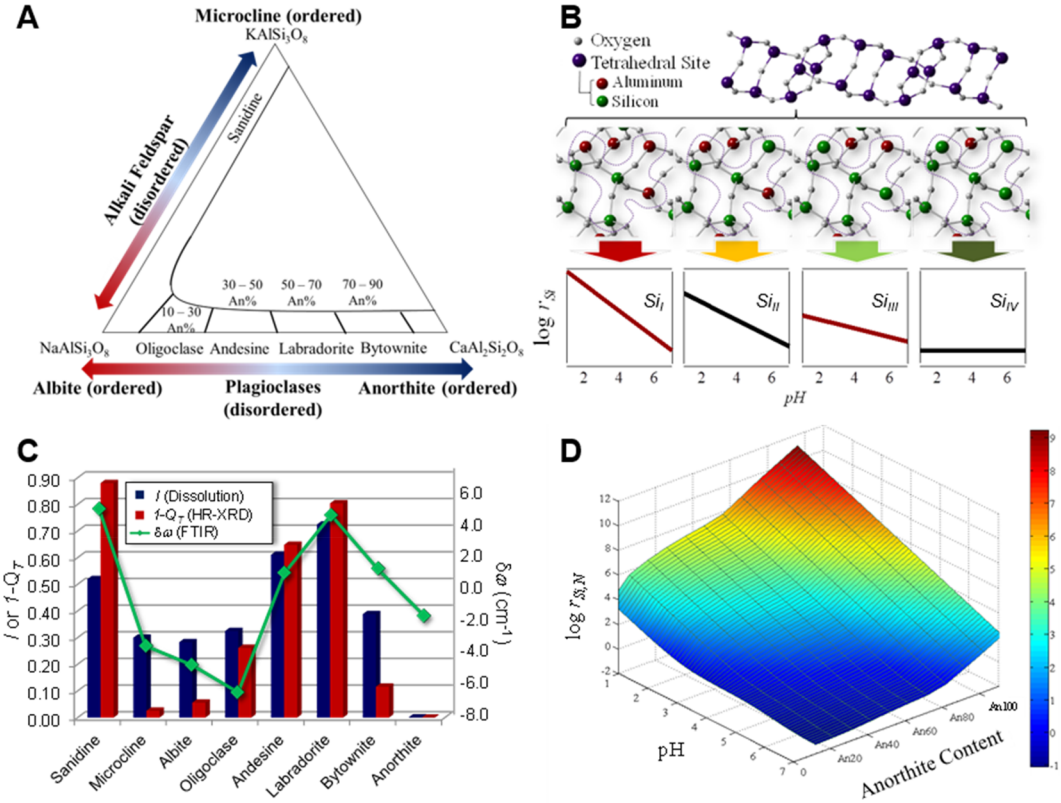

Figure 53. Effect of crystallography on feldspar dissolution. (A) The feldspar group. (B) The "crankshaft chain" structure in feldspar's framework and illustrations of the pH dependence of the release of different types of Si atoms. Reproduced with permission from ref 987. Copyright 2014 Elsevier Ltd. (C) Results from feldspar dissolution experiments (I), structure refinements based on synchrotron X-ray diffraction ($1 - Q_T$, where Q_T represents the distribution of Al between two different types of tetrahedral sites. $Q_T = 0$ if completely ordered, and $Q_T = 1$ if Al is randomly distributed), and data from Fourier transform infrared (FTIR) spectroscopy analyses ($\delta\omega$ is the displacement of the peak at 650 cm^{-1}, which is proportional to the square of the difference in Al/Si ordering). Here, the dissolution incongruence is shown as I, where $I = 0$ means congruent and $I = 1$ if $r_{Si}/r_{Al} = 0$. It is obtained from water chemistry experiments and correlates closely with the pattern of the variation in the degree of Al/Si ordering for the feldspar specimens. The Al/Si ordering varies with anorthite contents, as shown in C. Reproduced with permission from ref 986. Copyrights 2014 Elsevier Ltd. (D) pH dependence of plagioclase dissolution (r_{si}) at various anorthite contents. Reproduced with permission from ref 987. Copyright 2014 Elsevier Ltd.

4.4. Mineral Precipitation. Dissolution provides precursor molecules needed for the formation of new solid phases. Often, solid formation processes are referred to as "precipitation" for simplicity, without clear distinction of nucleation from growth phenomena. This simplification occurs because it has been challenging to experimentally detect nucleation *in situ* in real-time. In the last two decades, however, significant advances in mineral nucleation and growth research have been made, enabled by new X-ray, electron, and laser analytical capabilities. Here, we highlight the current state of knowledge of nucleation and growth as two explicit steps in the formation of solid phases from solutions.

4.4.1. Classical and Nonclassical Nucleation. Nucleation of solid nanoparticles from a supersaturated liquid solution is important in nanomaterial synthesis, dendrite formation in Li-metal batteries, biomineralization, pipeline operation, and rock alteration.[833,988] Solid nucleation can occur both in bulk solution (homogeneous nucleation) and on a substrate surface (heterogeneous nucleation).[989,990] In the environment, nucleation occurs ubiquitously, providing excellent reactive sites for

https://doi.org/10.1021/acs.chemrev.2c00130
Chem. Rev. 2023, 123, 6413−6544

trace ions or organic compounds and significantly contributing to biogeochemical cycles.

Classical nucleation theory, developed by Gibbs in the 1800s, describes nucleation as based on two principles: (1) A free energy barrier to nucleation (ΔG_{nuc}) is created by surface tension at the solid−liquid interface. Because the free energy of nucleation consists of bulk free energy and surface energy (Figure 54A), the positive surface free energy impedes nucleation. When the nucleating cluster size becomes bigger than the critical size, clusters can exceed the chemical driving force and grow spontaneously. (2) Inherent thermal fluctuations of the system can allow nucleation clusters to overcome this energy barrier so that individual ions and molecules can be added.[989,991,992] Based on these principles, we expect that fluctuations will allow overcoming the energy barrier, and that the nucleation rate will be exponentially related to supersaturation (σ) and interfacial energy (α). These predictions enable quantitative description of the nucleation process. However, nucleation can include much more complex processes and may not be the simple sequential addition of ions and molecules. For these complexities, the nonclassical nucleation theory (Figure 54B) describes the addition of complexes, such as multi-ion complexes and oligomers, and the pathway through transient metastable states of dense liquids, amorphous solids, and crystalline polymorphs.[990,991]

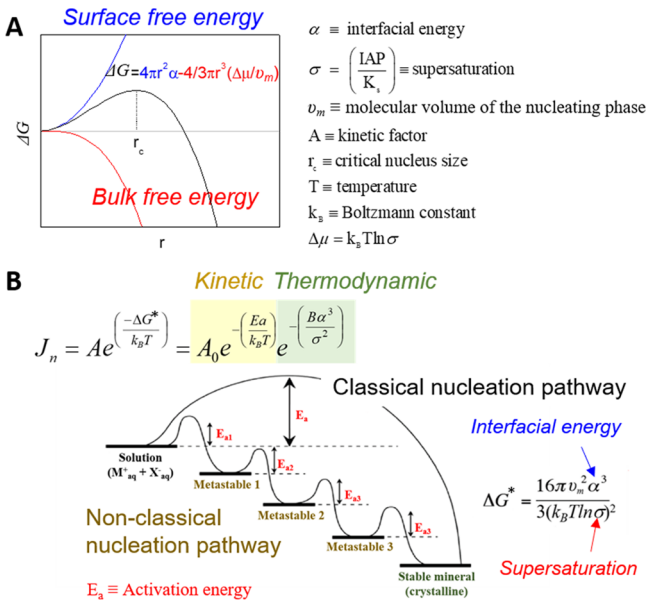

Figure 54. (A) Energy landscape of classical nucleation theory: the bulk and surface terms are related as functions of cluster size, creating a free energy barrier. (B) Energy landscape of nonclassical nucleation theory.

Nonclassical nucleation theory explains the interplay of the free energy landscape and kinetic factors (e.g., ion pairing, dehydration barriers, cluster sticking coefficients, and structure-directing factors) that can drive mineral nucleation and growth.[993] Thus, nonclassical nucleation theory presents a more complex free energy landscape than the classical nucleation theory (Figure 55). Deviations from classical pathways can be expected for two main reasons. First, they arise from complexities in the free energy landscape that create metastable structures offering lower barrier pathways to the final stable state (Figure 54B and 56B,C). These metastable structures can be true bulk phases on a phase diagram that are more stable than the solution but less stable than the final solid (Figures 54B and 56B). Alternatively, they can be configurations that represent local minima, which are less stable than the solution itself (Figure 55C), and thus can only exist transiently and microscopically, but provide an environment in which the stable configuration appears more readily than in the bulk.

Specifically, for metal oxides, Figure 56 illustrates both classical and nonclassical nucleation theoretic views of the formation of Fe- and Al-oxides (FeO_x/AlO_x).[995] Based on classical nucleation theory, ferrihydrite can form directly (top), via unstable and metastable crystalline nuclei. In nonclassical nucleation (blue box), there are multiple overlapping pathways for forming stable associated states. In the initial stages of hydrolysis and condensation, amorphous intermediates form and transform to ferrihydrite-like domains (middle). Alternatively, isolated, stable oligomers can form separately and subsequently grow and aggregate (bottom). The different reactions can cross, blending nonclassical pathways that have different process kinetics. Specific environmental conditions, such as pH, T, concentration, and/or the presence of additives, determine the corresponding kinetics.

4.4.1.1. Quantitative Description of Nucleation. Nuclei can form in solution, with the water−nucleus interfacial energy as the controlling factor. However, nuclei formation on a substrate surface is more thermodynamically-favorable due to the low effective interfacial energy (Figure 57).[915,990,996]

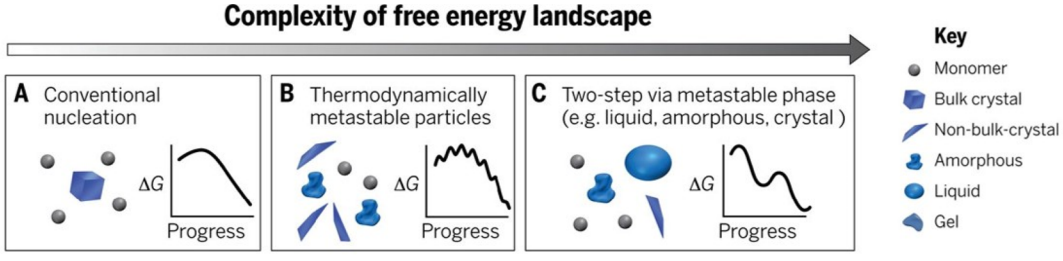

Figure 55. Crystallization by a wide variety of pathways. The possible pathways by which monomers form a stable bulk crystal, and the physical mechanisms that give rise to them, can have thermodynamic origins (A−C). (A) Classical monomer-by-monomer addition. (B) Aggregation of metastable particles, such as liquid, amorphous, or poorly crystalline particles. Although not shown, the free energy landscape graphed in (B) can also result from aggregation by oriented (and nearly oriented) attachment of metastable nanocrystals. (C) Crystallization via the formation of a metastable bulk phase, such as a liquid or solid polymorph. B and C illustrate the nonclassical nucleation pathway. Reproduced with permission from ref 994. Copyright 2015 American Association for the Advancement of Science.

https://doi.org/10.1021/acs.chemrev.2c00130
Chem. Rev. 2023, 123, 6413−6544

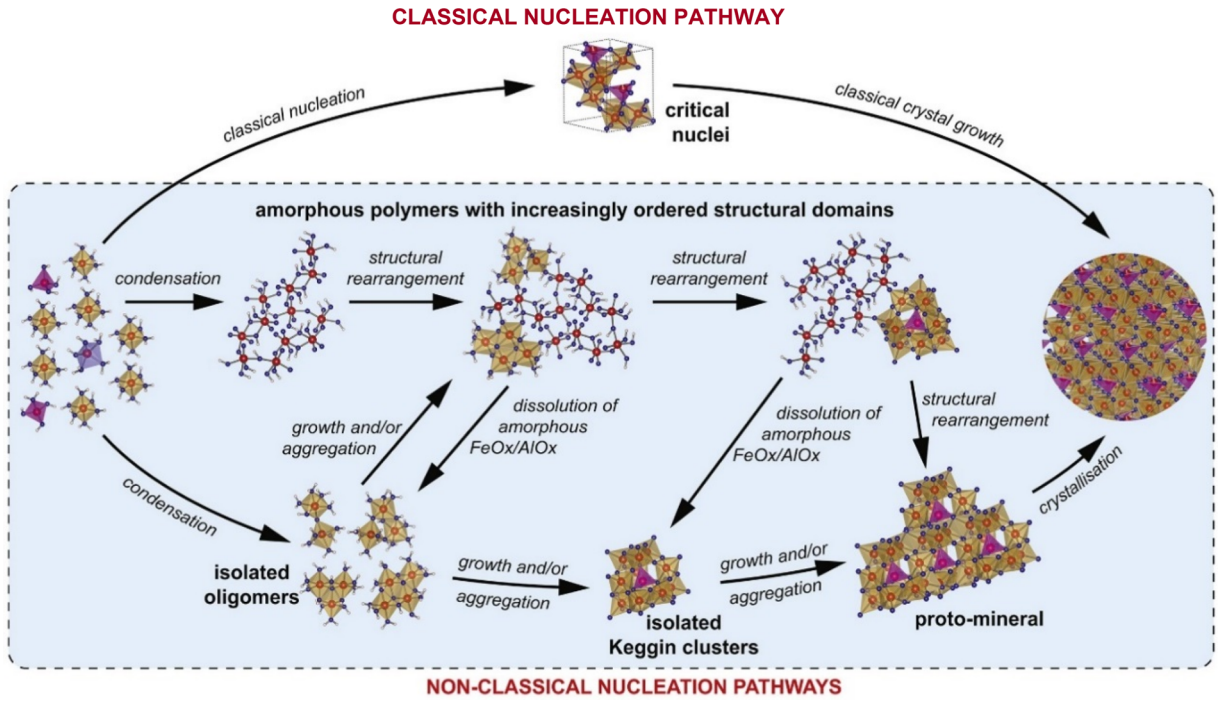

Figure 56. Schematic of the broad conceptual framework of distinct pathways to ferrihydrite. This concept is transferable to the formation mechanisms of other FeO_x and AlO_x, in principle. Reproduced with permission from ref 995. Copyright 2020 Elsevier.

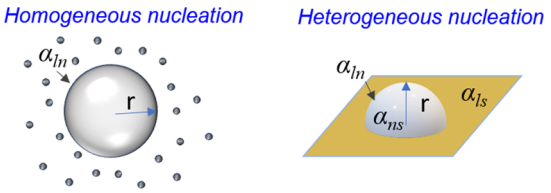

Figure 57. (left) Formation of a spherical nucleus of radius r from a solution leads to the free energy changes shown in Figure 54A. (right) Heterogeneous formation of a hemispherical nucleus on a foreign substrate.

In classical nucleation theory, the nucleation rate can be expressed by eq 14:[915,997,998]

$$J = J_0 \exp\left(-\frac{\Delta G^*}{k_B T}\right) = J_0 \exp\left\{-\frac{16\pi v_m^2 \alpha^3}{3k_B^3 T^3 \left[\ln\left(\frac{IAP}{K_{sp}}\right)\right]^2}\right\} \quad (14)$$

where J_0 is a kinetic factor related to the efficiency of building blocks diffusing and attaching to an existing nucleus, and ΔG^* is the thermodynamic barrier generated by the combination of the bulk reaction free energy and surface energies. ΔG^* is $\frac{16\pi v_m^2 \alpha^3}{3k_B^2 T^2 \left[\ln\left(\frac{IAP}{K_{sp}}\right)\right]^2}$, where v_m is the molecular volume of the nucleating phase, α is the interfacial energy, k_B is the Boltzmann constant (1.38×10^{-23} J K^{-1}), T is temperature (K), IAP is the ion activity product, and K_{sp} is the solubility product of the nucleating phase. For homogeneous nucleation, $16\pi/3$ is a geometric factor from the mathematical derivation of the nucleation rate, assuming spherical nuclei with an interfacial energy with the liquid phase of α_{ln} (subscript l for liquid and n for nucleus).[999] Any information about the geometry of the heterogeneously formed nuclei is included in α, which becomes the effective interfacial energy for the heterogeneous nucleation case.[998] An effective interfacial energy, α, for heterogeneous nucleation is a complex function of the nucleus geometry, including the nucleus shape and the contact angle of the nuclei on the substrate, and the interfacial energies among the liquid, nucleus, and substrate (i.e., $\alpha = \alpha$ (nucleus geometry, α_{ln}, α_{ls}, α_{ns}), in which the subscripts l, n, and s denote liquid, nucleus, and substrate, respectively) (Figure 57).

To quantitatively describe the nucleation process, eq 14 was derived based on an imaginary pathway in which nuclei continuously evolve by adding monomers one at a time (classical nucleation theory). Despite the discovery of more realistic pathways (nonclassical nucleation theory),[906,1000,1001] eq 14 has been successful to experimentally observed nucleation rates under various conditions.[901,903,1000,1002−1005] The effective interfacial energy of heterogeneous nucleation can be obtained by regression of nucleation rates as a function of supersaturation, according to the logarithmic form of eq 14:[1003,1004]

$$\ln(J) = \ln(J_0) - \frac{16\pi v_m^2 \alpha^3}{3k_B^3 T^3 \left[\ln\left(\frac{IAP}{K_{sp}}\right)\right]^2} \quad (15)$$

By fixing the nuclei and substrate materials, the kinetic factors (J_0) under various conditions can also be obtained from the intercept of the linear regression on the $\ln(J)$ using eq 16:

$$\ln(J) = \ln(J_0) - \frac{B \cdot \alpha^3}{\left[\ln\left(\frac{IAP}{K_{sp}}\right)\right]^2} \quad (16)$$

where B is calculated from the known values of v_m, k_B, and T, and $B \cdot \alpha^3$ is the slope obtained from linear regression of $\ln J$

https://doi.org/10.1021/acs.chemrev.2c00130
Chem. Rev. 2023, 123, 6413−6544

over $1/[\ln(\mathrm{IAP}/K_{sp})]^2$. In this calculation, J_0 can be assumed constant for a given aqueous condition, and α can be calculated for that aqueous condition. The calculated effective interfacial energy, α, is $\left(\frac{B\cdot 3k_B{}^3T^3}{16\pi v_m{}^2}\right)^{1/3}$. Next, J_0 in eq 15 is attributed to the kinetics of the system and can be expanded into $A\exp\left(-\frac{E_a}{k_BT}\right)$,[997,1002,1006,1007] where A is a pre-exponential kinetic factor related to ion diffusion and nuclei surface properties, and E_a is the apparent activation energy ($J\cdot\mathrm{mol}^{-1}$) and, therefore, is the kinetic energy barrier. Then, eq 14 becomes

$$J = A\cdot\exp\left(-\frac{E_a}{k_BT}\right)\cdot\exp\left(-\frac{\Delta G^*}{k_BT}\right) \tag{17}$$

With eq 17 and experimentally obtained nucleation rates at different temperatures, the value of E_a can be obtained from the relationship between $\ln(J)$ and $1/T$, and this will provide the values of $E_a + \Delta G^*$. After substituting ideal gas constant R for k_B and calculating ΔG^*, the values of E_a can be obtained:

$$\ln(J) = \ln(A) - \frac{E_a + \Delta G^*}{RT} \tag{18}$$

Surprisingly little is known concerning the kinetic parameter, J_0; hence most previous studies have assumed a constant J_0 term.[903,1002,1003] Very recently, using a calibration method based on nucleation rate results from GISAXS and AFM experiments,[1008] Wu et al.[1009] estimated the kinetic factors A and J_0 of poorly crystalline iron (hydr)oxide nanoparticles on quartz. With E_a obtained from the fitting method (32.8 ± 1.8 kJ/mol), J_0 was $10^{14.4\pm0.3}$ nuclei/m^2·min at 25°C,[1009] which falls in the range of reported values for other mineral nucleation processes on quartz surfaces at room temperature, including $10^{13.5\pm0.7}$ nuclei/m^2·min for silica and $10^{16.1\pm1.0}$ nuclei/m^2·min for $CaCO_3$.[1008,1010]

When one attempts to employ nonclassical nucleation theory to achieve a detailed understanding of kinetic pathways and transient metastable phases and polymorphs, it emerges that currently no clear quantitative description provides this realistic view. So far, only a few attempts have been made on the nonclassical nucleation pathway, while still using the main framework of classical nucleation theory's quantitative description. Habraken et al. used *in situ* X-ray scattering and AFM to study hydroxyapatite nucleation on collagen surfaces. They found precursor nanometer-sized units of Ca−phosphate crystallization that were Ca−triphosphate complexes. Considering the aggregation of amorphous Ca−phosphate precursor complexes during apatite formation, they thought that excess free energy ($\Delta G_{Ex} = 4\pi r^2\alpha_{complex}$) could be eliminated by prenucleation cluster aggregation and could decrease the magnitude of the free-energy barrier, as shown in eq 19.[1011]

$$\Delta G^* = \frac{16f\pi v_m{}^2\alpha^3}{3(k_BT\ln\sigma)^2}\left(1 + \frac{4v_m\alpha}{rk_BT\ln\sigma}\eta\right)^{-2}, \quad \eta = \frac{\alpha_{complex}}{\alpha} \tag{19}$$

Similarly, for homogeneous magnetite (Fe_3O_4) nucleation, Baumgartner et al. considered the aggregation of cluster precursors in forming the amorphous and crystalline bulk phases.[1000] While such modified equations can capture the presence of amorphous precursor complexes as an umbrella term for ΔG_{Ex}[1011] or the primary particle energy contribution,[1000] currently, they can be used only to understand the trend of the nucleation energy barrier and not to specifically predict the reactions.

Kim et al.[833] revised classical nucleation theory to quantitatively describe plate-like Ca−phosphate nuclei formation in confined collagen fibrils and delineate the contributions of extrafibrillar nucleation and intrafibrillar nucleation.[833] These fibrils have narrow channel-like gap regions ($40 \times 30 \times 2$ nm^3)[1012−1015] that provide nucleation sites with a lower energy barrier: the confined space effectively reduces the surface free energy, ΔG_s, by minimizing the effective surface area of nuclei. The modified nucleation energy barrier for the plate-like confined space is expressed as[833]

$$\Delta G^* = \frac{hv_m\alpha^2}{k_BT\ln\sigma}, \quad h = \text{height} \tag{20}$$

To successfully describe nonclassical nucleation pathways in quantitative ways, we will need to fully characterize the phase identities and extents of the potentially mixed transient metastable phases over time. In addition, the temporal evolution of interfacial energy changes should be monitored as a function of changing nucleus sizes.

4.4.1.2. Challenges in Measurements of Nucleation in Situ. Because newly formed nanoparticles at solid−water interfaces are often amorphous and hydrated, accurate evaluation of nucleation kinetics requires time-resolved *in situ* experimental techniques. Previous nanoscale observations relied on snapshot images of these nanoparticles, which could have undergone significant alteration in their physicochemical properties during sample preparation prior to imaging. While recent advances in *in situ* microscopic analysis can resolve some challenges,[1016−1018] these studies are still limited to aqueous environments within a narrow-slit observation chamber or those held at cryogenic conditions. These challenges, therefore, prevent us from fully exploring the *in situ* nucleation kinetics of metal (hydr)oxides. Specifically, probing heterogeneous nucleation of nanoparticles on substrates during their initial stage is extremely challenging.[989]

Four recent developments allow *in situ* observation of nucleation at relevant spatiotemporal scales. First, liquid-cell TEM enables *in situ* imaging with nanometer-scale spatial resolution in time increments of fractions of a second. Nielsen *et al.* used a dual-inlet flow stage to observe homogeneous $CaCO_3$ nucleation and found a range of nucleation pathways under identical or similar solution conditions, with nucleation often taking multiple pathways within a single experiment.[1017] Second, atomic electron tomography (AET) can determine the 3D atomic structure of homogeneously nucleated materials without the assumption of crystallinity and with high temporal resolution (μs/each image).[1019] Third, *in situ* fluid-cell AFM can be used to observe heterogeneous nucleation and growth.[996,1011] Fourth, an *in situ* experimental setup developed by Jun *et al.*[989,1020] uses simultaneous SAXS and GISAXS to quantify homogeneous and heterogeneous nucleation and growth, respectively. This approach can provide the nucleus size, shape, and nucleation rates in real time for different water chemistries and substrates.

4.4.2. Nonclassical Crystallization. 4.4.2.1. Crystallization by Particle Attachment (CPA). Crystallization mechanisms often diverge from this classical picture in both the nucleation and the growth stages. Many research efforts have revealed poorly understood, diverse crystallization pathways that

https://doi.org/10.1021/acs.chemrev.2c00130
Chem. Rev. 2023, 123, 6413−6544

involve so called "nonclassical" processes, generally consisting of multistage pathways and relying on CPA.[14] The impacts of CPA on solid structure and properties are extensive because these pathways offer the potential for capturing intermediate states not otherwise accessible and the resulting crystals often exhibit complex, hierarchical morphologies with novel properties (Figure 58).

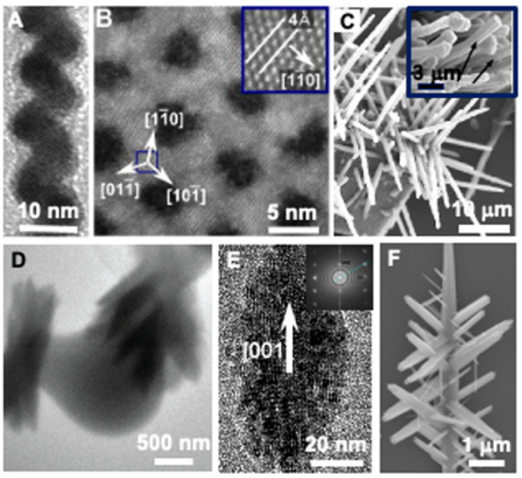

Figure 58. Hierarchical crystallization pathways lead to novel architectures. (A,B) PbSe nanowire (A)[1021] and honeycomb structure sheet (B)[1022] formed by particle assembly. (A) Reproduced from ref 1021. Copyright 2005 American Chemical Society. (B) Adapted with permission from ref 1022. Copyright 2014 American Association for the Advancement of Science. (C) Calcite pillars growing epitaxially on calcite rhomb via dense liquid phase (DLP).[1023] (D) Aragonite bundles forming from $CaCO_3$ DLP droplet. (D) Adapted with permission from ref 1017. Copyright 2014 American Association for the Advancement of Science. (E) Spindle-shaped mesocrystal formed by interface-drive nucleation and subsequent particle attachment. (E) Adapted with permission from ref 919. Copyright 2021 The Authors, under exclusive licence to Springer Nature Limited. (F) Branched rutile nanowire where branches start by attachment and transformation of anatase nanoparticles. (F) Adapted from ref 877. Copyright 2013 American Chemical Society.

Such deviations from classical crystallization pathways occur for two main reasons: First, complexities in the free energy landscape can create metastable structures, as discussed in section 4.4.1. Second, dynamic effects can create an assembly of precritical clusters and postcritical particles that subsequently interact and assemble to either form highly branched structures or coarsen to form compact single crystals. Alternatively, these effects can create a kinetically trapped metastable or bulk phase (or particles) in a microscopically unstable phase, or in a globally unstable state. While we now know such pathways can exist for both thermodynamic and kinetic reasons, the challenge is to predict which systems follow which pathway, and why.

4.4.2.2. Multistep Nucleation Processes. Advanced imaging, spectroscopy, and computational methods have improved our understanding of how multistep nucleation occurs in a variety of systems (Figure 59). Atomic resolution TEM studies applied to nucleation metals (Au, γ-Fe, and Re) forming in vacuum[1024,1025] revealed that the onset of nucleation consists of amorphous cluster nucleation overcoming one free energy barrier; this is followed by crystallization overcoming a second free energy barrier, where the amorphous phase exhibits one critical size and the crystalline phase exhibits a larger critical size. The nucleation of each phase follows the classical picture, but the results prove a long-expected phenomenon of crossover in phase stability with particle size, which arises from the inverse correlation between surface energies and bulk phase stability. This phenomenon leads to an inherent two-step nucleation process not captured by classical nucleation theory. Other studies detailed the formation and transformation of microscopic transient structures that consist of atomically-controlled clusters of inorganic semiconductors,[1026] micellular units of sequence defined polymers,[1027] and dense liquid droplets of proteins.[1028−1030] A number of studies have documented the development of complex structural units that drive nucleation through their assembly.[1011,1031−1034] These cases blur the line between nucleation and particle assembly, with the assembly of preformed units becoming the mechanism for overcoming the critical size, rather than merely a feature of postnucleation growth. Computational studies on zeolite systems showed that oligomerization marks the earliest stages and highlighted the role of water dissociation in creating reactive sites for further oligomerization,[1031] adding key insights to the long-established role of amorphous precursors in zeolite nucleation.[1035] Moreover, when zeolite crystals are present, amorphous or dense liquid precursors can be the main material source for mineral growth.[1036]

The role of water in nonclassical pathways was further illuminated by studies on Mg:$CaCO_3$[907] and the protein ferritin,[1037] showing that the development of crystal order is a gradual process associated with the loss of water and an increase in coordination number with neighbors in the lattice within an initially hydrated amorphous precursor. Other work showed that, at a sufficiently high driving force, the first phase is a dense liquid for both Au[1038] and $CaCO_3$,[885,1039,1040] where the latter case once again reflects a high-water content that must be eliminated to form the amorphous phase and subsequent crystals.

Other atomically-resolved AFM measurements and molecular simulations revealed the dramatic impact that surface charge (or potential) and interfacial structure has on local speciation[128,391] and subsequent nucleation.[919,1041,1042] For example, the inherent surface charge of muscovite mica in $AlCl_3$ solutions promotes aluminum hydrolysis at the interface, so that hydrolyzed species ($Al(OH)_2^+$ and $AlOH^{2+}$) become predominant over unhydrolyzed species (Al^{3+}) by orders of magnitude, while in bulk solutions the abundance of these species is reversed.[391] As a consequence, monolayer films of gibbsite ($Al(OH)_3$) form on mica surfaces even when the solution is undersaturated. In addition, hematite formation in the presence of oxalate showed that new nanoparticles nucleated in the interfacial region 2 nm away from the surface of existing particles, in contrast with simulations that predicted gradients in Fe^{3+} concentrations with maxima 1 nm away from the surface.[919] Although the chemical potential of the solution relative to the crystal in the bulk solution is presumably the same, the difference in solution structure near the interface suggests that the interfacial energy or the solubility is different locally.

4.4.2.3. Post Nucleation Growth by Particle Assembly. The terrace-ledge-kink model for post nucleation crystal growth, first introduced by Sir Charles Frank more than 70 years ago, was a stunning achievement in imaginative thinking, as no methods previously existed to indicate there are atomic steps on surfaces. The addition of the screw dislocation sources

https://doi.org/10.1021/acs.chemrev.2c00130
Chem. Rev. 2023, 123, 6413−6544

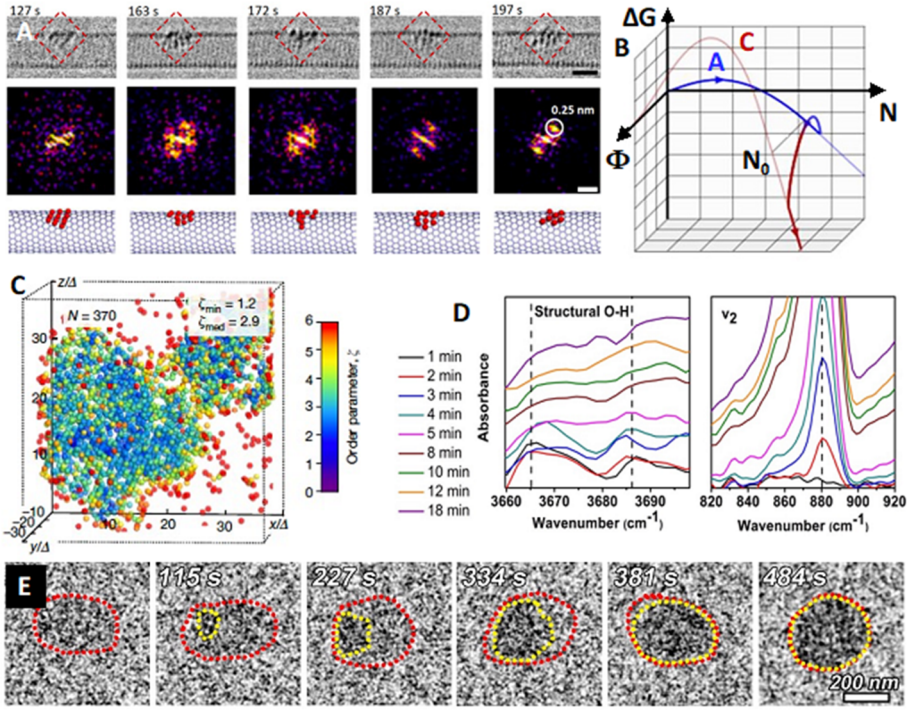

Figure 59. Recent microscopy studies have shed light on multistage nucleation pathways. (A) Reproduced with permission from ref 1024. Copyright 2020 Springer Nature. Portion of Au nucleation pathways in a carbon nanotube, showing transition from amorphous to crystalline structure due to (B) crossover in phase stability with size, leading to two nucleation barriers. (B) Reproduced with permission from ref 1025. Copyright 2020 Springer Nature Limited. (C) Nucleation of ferritin crystal, showing a gradual increase in order (and coordination) simultaneously throughout the particle. (C) Reproduced with permission from ref 1037. Copyright 2020, The Authors, under exclusive license to Springer Nature Ltd. (D, E)[907] Nucleation of calcite, marked by the rise of the ν_2 IR peak (D) and the spread of high contrast (E) accompanied by loss of structural water (D). (D,E) Adapted from ref 907. Copyright 2020 National Academy of Sciences.

of steps and the 2D nucleation of islands, introduced by Burton, Cabrera, and Frank, explained crystallization in a world of monomers and faceted crystalline interfaces. This picture began to unravel with the discovery by Ocana et al. in 1995 that Fe_2O_3 nanocrystals aggregated into larger single crystals by attaching on the same crystallographic facets with co-alignment or "oriented attachment" (OA).[1043] This OA behavior was subsequently observed for TiO_2 by Penn and Banfield.[1044,1045] OA leads to remarkable morphological outcomes, including the formation of tetrapods,[878] chains,[1021,1045,1046] sheets,[1022,1047] highly branched nanowires,[877] and self-similar 3D mesocrystals (Figure 58).[919] Song et al. showed that OA coupled with strain relaxation is even responsible for the growth of the commonly observed five-fold twin structures of noble metal nanoparticles.[1048] OA and, more generally, particle-mediated growth of single crystals, has now been widely observed in semiconductors,[877,1021,1022,1049] metals,[1048,1050,1051] silicates,[1036,1052] oxides,[877,919,1000,1044,1046,1053−1059] carbonates,[1055,1060] fluorides,[1061] organic compounds,[1062] peptides,[1063] and proteins.[1032] Many styles of particle-mediated growth that result in single crystal products have been observed since the first report of OA, including: (1) attachment with crystallographic coalignment prior to coalescence,[1016,1046,1064] (2) attachment with some degree of misalignment, followed by relaxation through atomistic processes into a coaligned state,[1016,1048] (3) attachment of metastable particles of a nanoscopic phase onto crystals of the bulk phase, followed by transformation,[877,1000,1065,1066] and (4) a special class of no. 3 in which the nanoscopic phase is amorphous.[1036,1055,1060]

OA reflects an interplay of the solution structure, forces, and resultant motion (Figure 60), in which the crystal surface

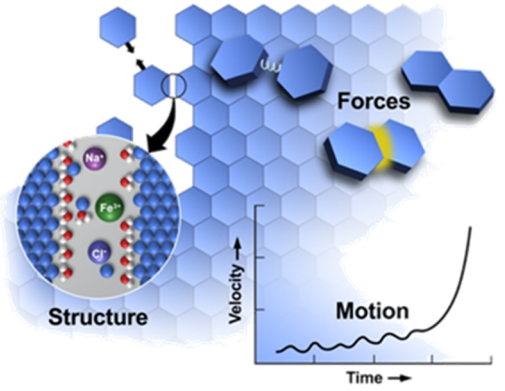

Figure 60. OA is a mesoscale response to forces defined by molecular details of the interfacial region. These details create forces that drive particle motion. As particles move, the local structure and corresponding forces evolve, taking particles from a regime of long-range to short-range interactions that lead to alignment and attachment. Reproduced with permission from ref 994. Copyright 2015 American Association for the Advancement of Science.

imposes structure on the near-surface solution that leads to a set of interparticle forces, including hydration barriers, van der Waals forces modified by the solution structure-dependent dielectric constant, and electrostatic forces.[994,1054,1059] Early views of the driving force for OA centered on minimization of surface energy.[1067,1068] However, this thermodynamic perspec-

https://doi.org/10.1021/acs.chemrev.2c00130
Chem. Rev. 2023, 123, 6413−6544

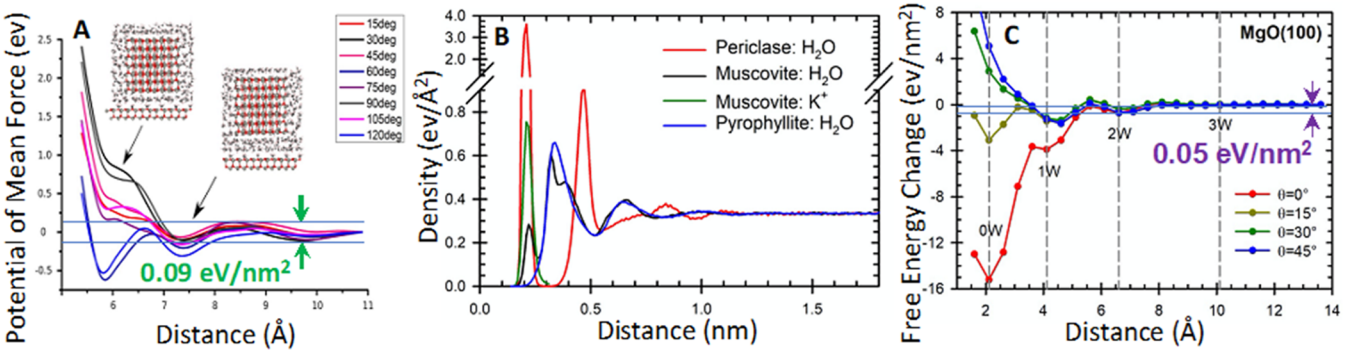

Figure 61. Simulations predict a dependence of interparticle potentials on relative orientation driven by hydration structure, which is strongly impacted by surface hydrophobicity.[1072,1074] (A) Potential of mean force vs distance between ZnO surfaces, showing minima that correspond to integer numbers of water layers and barriers between minima equivalent to ~40 k_BT for a 10 nm^2 contact area.[1074] (B) Effect of hydrophobicity on water density, with periclase (MgO) being most hydrophilic and pyrophyllite most hydrophobic. (C) Free energy vs distance between MgO surfaces for the water structure in (B), showing strong orientation dependence and sizeable barriers. Figure (A) adapted from ref 1074, Copyright 2017 Nature Springer, and Figures (B) and (C) adapted from ref 1072. Copyright 2020 American Chemical Society.

tive can work only if particle dynamics allow systems to explore all potential orientations and if attachment events are reversible. As it happens, neither statement is true, and, moreover, attachment on any pair of matched faces will reduce the surface energy of the system. Consequently, face selectivity must be controlled by particle interaction dynamics and attachment kinetics.[1058] A second early perspective has its origins in DLVO theory, in which van der Waals attraction and electrostatic repulsion create an overall attractive potential with a secondary minimum in which particles reside long enough to rotate into alignment before overcoming the final (electrostatic) barrier to attachment.[1054] This general picture found support in a pair of studies. The first, based on cryo-TEM, showed that nanoparticles of goethite were organized into multi-micrometer rod-shaped arrays of particles that were aligned but not yet attached.[1046] The second, based on *in situ* liquid phase TEM (LP-TEM), showed particles diffusing to close proximity, hovering at this distance while they rotated into alignment, and then jumping into contact with a slight misalignment that healed by elimination of dislocations.[1016]

With advances in cryo-TEM and the advent of LP-TEM, mechanistic studies of OA have come to the fore. Investigations have utilized AFM-based methods with custom-made, oriented single-crystal tips to measure the dependence of crystal−crystal binding on relative crystal orientations.[1069−1075] Measurements on rutile TiO_2 (001)[1073,1075] and ZnO (0001)[1074] yielded rupture forces that displayed the orientational symmetry expected for each crystal symmetry: 6-fold for ZnO and 4-fold for TiO_2. However, the results with muscovite mica[1069] were less clear in this regard, with a weak dependence on orientation and numerous maxima and minima and a dependence on ionic strength that decreased rapidly to a minimum (at 10 mM for NaCl) before rising to a maximum (at 30 mM for NaCl) before decaying again with further increases. Recent simulations of the electrostatic interactions between charged proteins and muscovite mica revealed a complex solvent response that creates a unique directionality within a very small range of separation. Moreover, this directionality can flip its sign simply by changing an electrolyte from NaCl to KCl. These complexities, likely manifest in the DFS data for the mica system, highlight the important role of interfacial structure.[1076]

New key contributions have come from molecular simulations, which have investigated the solution structure between approaching particles and the resulting interaction potentials that drive particles together or keep them apart, as well as attachment mechanisms. One of the most confounding results to emerge from such simulations is the near-universal prediction from MD simulations of large barriers to attachment that arise from the hydration structure created by the interaction of the crystal surface with the surrounding solution (Figure 61).[1057,1072,1074] Calculations done for MgO,[1072] ZnO,[1074] gibbsite (γ-$AlOH)_3$),[1077] muscovite (KAl_2-$(AlSi_3O_{10})(OH)_2$),[128,1072] pyrophylite ($Al_2Si_4O_{10}(OH)_2$),[1072] TiO_2,[1078] graphene,[1079] and boehmite (AlOOH)[1070] all predict layering of water with a layer spacing of about 3 Å discernable to about three layers (Figure 61B). This result is not surprising and is consistent with X-ray reflectivity studies on many crystal−water interfaces, but these simulations also predict that the resulting potential-of-mean-force between two approaching like-crystal surfaces exhibits minima in free energy at each integral number of water layers that are separated by barriers on the order of 10−20 k_BT per nm^2 of contact area (Figure 61B,C). While a small barrier seems necessary to obtain OA by creating a secondary minimum where particles can reside long enough to coalign before attachment, as observed in the case of goethite, these barriers seem prohibitively large. For particles of a few nm or more in size, the barrier to attachment is more than 100 k_BT. Given that the attachment attempt frequency is determined by diffusive translational and rotational motion, not atomic vibrations, the attachment rates should be miniscule. Nonetheless, many of these systems undergo OA. Based on simulations in water vapor sufficient to saturate the surface of TiO_2 crystals, Raju *et al.*[1057] attributed the face-specific attachment to the ability of certain faces to dissociate the adsorbed water, but how that mechanism would overcome barriers associated with elimination of intervening water layers in bulk water is unclear. Moreover, TiO_2 is distinct in its ability to drive such chemistry, exhibiting photocatalyzed facet-dependent H_2O splitting.[1080]

Two studies offered mechanisms to overcome such barriers. For the case of hematite (Fe_2O_3) growing in supersaturated solution containing Na-oxalate, Zhu *et al.*[919] showed that oxalate ligands adsorb to the hematite particles and create interfacial gradients in aqueous speciation that both drive new particles to nucleate 2 nm away from existing ones and create a

https://doi.org/10.1021/acs.chemrev.2c00130
Chem. Rev. 2023, 123, 6413−6544

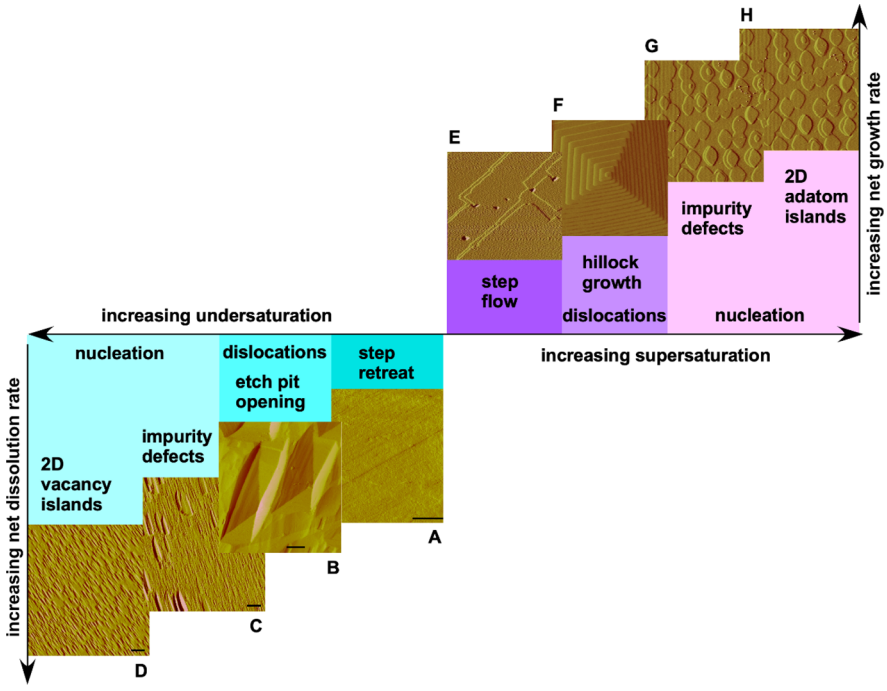

Figure 62. AFM images of quartz (100) and calcite (104) surfaces produced from different solution chemistries illustrate dissolution and growth as reversed processes.[934] Quartz surfaces produced after equivalent extents of reaction show the different dissolution processes that occur across driving force and solution chemistry. Scale bars = 1 micrometer: (A) At a low driving force of σ = 0.90 in 0.0167 M $CaCl_2$, surfaces show only straight edged steps with no evidence of pitting. (B) When σ = 0.10 in H_2O, surfaces are dominated by large etch pits with sloping sides that converge at a dislocation source. Pits are separated by relatively flat regions on the surface. (C) At an intermediate driving force of σ = 0.65 in a salt solution of 0.0167 M $CaCl_2$, a mixture of larger and smaller flat bottom pits forms across the surface. (D) When σ = 0.10 and the solution contains 0.0167 M $CaCl_2$, the surface is covered with a high density of small pits with flat bottoms and with flanks 25% steeper than those measured for pits in the previous image. The *growth* of calcite occurs as equivalent inverse processes whereby (E) step propagation occurs at near-equilibrium conditions with (F) a transition to sufficient chemical potential to initiate new steps at dislocation defects and thus generate growth hillocks. (G,H) At higher driving force, surface nucleation processes dominate net rate.

purely attractive potential for their subsequent attachment. This mechanism has the added consequence that assemblages of coaligned particles are formed with a shape that reflects differences in nucleation rates along distinct crystallographic directions. Thus, the random nucleation and diffusion process that dominates in many OA systems is replaced by a deterministic process that gives rise to self-similar hierarchical mesocrystals in this system (Figure 58e).

A second system that avoids solvent-induced barriers is ZnO, where the presence of a permanent electric dipole produces a strong long-range attractive interaction that drives particles towards one another, beginning at distances beyond 5 nm, well beyond the distance at which simulations predict van der Waals attraction or ion correlation forces operate, with no observable barrier to attachment.[1070] While such a scenario might be expected to lead to misoriented attachment, as explained above, the torque arising from the dipole−dipole interactions rotates the particles into alignment by the time particles are within ∼5 nm, thus avoiding misalignment at the point of contact. This result suggests that, even in polarizable materials that lack a permanent dipole, we may be able to drive OA using applied electric fields, coupled with translational and rotational particle mobilities.

Three additional complexities influence the solution structure, the interplay of forces and torques, and the coupling to particle mobility that leads to attachment: (1) the shapes of the particles, which impacts the rate of diffusive particle−particle encounters relative to that of rotation into alignment,[1081] (2) hydrodynamic forces/torques and solution properties, like dielectric permittivity and viscosity, that are dramatically different near particle surfaces than in the bulk,[312,1082,1083] and (3) the presence of surface-adsorbed ligands, which can drive the initial assembly of particles into a superlattice, and then either remain intact to inhibit particle−particle contact, leaving the particles in an assembled but unattached state,[1084,1085] or be eliminated, resulting in particle fusion to form a single crystal, often with mesocrystalline morphology.[1047,1086] Finally, a number of studies reported OA of primary particles of a nanoscopic phase, which convert to the bulk phase upon attachment to the stable bulk phase crystal, despite the fact that the nanoscopic phase has a different stoichiometry or hydration state than the stable bulk phase.[877,1000,1055,1065] One can expect the situation to be further complicated in cases where the surface potential evolves with particle size. Although these individual factors have been identified and considered for individual cases, defining a generalizable picture that accounts for the impact of complexities in particle and solution characteristics, especially the physical properties of the interfacial solution layer and role of surface potential and adsorbed ligands, remains a major challenge.

4.5. Coupling of Dissolution and Precipitation and Simultaneous Reactions. Coupled dissolution and precipitation processes can be understood as a continuum extending from relatively simple congruent reactions that can be modeled using concepts from nucleation theory (section 4.3) to exceedingly complex incongruent reactions. While all of these reactions are governed by kinetic and thermodynamic

https://doi.org/10.1021/acs.chemrev.2c00130
Chem. Rev. 2023, 123, 6413−6544

principles, incongruent reactions are most widespread in Earth environments. To elucidate these coupled processes, recent *in situ* studies discussed myriad factors that influence these types of reactions, including metastable intermediate phases and the roles of local interfacial solution chemistry and mineral structure.

4.5.1. Simple Congruent Systems. The process-based kinetic model for dissolution of quartz and calcite (section 4.3.1) shows that *dissolution*, without secondary products or potentially at short time scales before the onset of secondary product formation, can be understood through the lens of mechanistic nucleation theory developed for mineral *growth*. That is, dissolution and growth can be conceptualized as reciprocal microscopic processes under some conditions. In Figure 62 (left side), the high-resolution AFM images show changes in mineral surface structure that occur with an increasing degree of undersaturation or addition of electrolytes. For quartz and calcite, the predominant structures transition from simple step retreat to opening of defects (postulated to be dislocations or impurities), to nucleating two-dimensional vacancy islands (i.e., pits) at impurities or homogeneous sites across the entire surface.

By coupling the formalisms of nucleation and step-growth to dissolution, the rate of solute release to solution is controlled by the energy barrier to "corrosion" at dislocation defects or at impurities or homogeneous sites. Although dissolution and growth reactions can be modeled as reversed processes, their rates are not expected to be numerically equivalent. For example, hydration processes associated with mineral surface hydrolysis are dissimilar from the desolvation that occurs prior to ion attachment nucleating 2-D vacancy islands.

In electrolyte solutions, the dissolution rate becomes dominated by the detachment of the higher coordinated groups. This detachment increases surface free energy, and the detachment probability scales exponentially with driving force. By defining a statistical volume of the reacting unit, the classical polynuclear theory explains the dependence of dissolution on chemical potential, while also quantifying the surface energy of amorphous silica in the absence and presence of solutes. The polynuclear model also predicts the kinetic behavior reported for biogenic and colloidal silicas and predicts both the growth and dissolution rates of colloidal silica, as shown in Figure 51. This physical picture is analogous to the degree of polymerization, and thus interfacial energy, associated with step edges, defects, and layers. Hence, a plausible mechanism-based model should be formally identical to the polynuclear theory originally developed for crystal growth. In principle, such knowledge can be applicable to many materials with diverse compositions and structural orders that dissolve congruently when the reacting units are defined by the energy of the constituent species.

4.5.2. Complex Dynamic Systems. Field and laboratory observations document the widespread occurrence of multistep mineral dissolution and reprecipitation and new phase formation.[1087,1088] These processes are remarkably complex and challenging to decipher because the predominant reaction processes are strongly dependent on the fluid composition at the mineral−fluid interface as well as the structural details of that interface, including surface roughness, porosity, and confinement. Thus, mineral dissolution and growth are interrelated dynamic processes, continuously changing in response to the evolving fluid composition, so that a coupling of dissolution and precipitation occurs at the reactive interface.[996,1089,1090] The concomitant formation of porosity in the reacting mineral is an essential feature that allows the progression of the reaction interface within the mineral by providing a pathway for fluid access into an impermeable solid.[1089,1091]

For more complex minerals, dissolution of a parent mineral results in a solute composition that is generally supersaturated with respect to a number of phases whose precipitation will be spatially and temporally coupled to the dissolution of the parent phase.[996] Cardew and Davey[1092] referred to this scenario as "solvent-mediated phase transformations". The role of water is central to coupling dissolution and precipitation reactions. The structure of water molecules at charged mineral surfaces is the subject of current research[272] to define how water molecules are oriented and organized at a surface, and how that changes the surface characteristics and properties of the solid phase.[1093] Water hydrolyses the unsatisfied surface bonds, solvates the ions, and produces a solution at the interface. We can, therefore, define an IAP within the interfacial solution and hence a supersaturation with respect to any other solid phase that may be more stable.

Although historically the thermodynamics and kinetics of mineral dissolution and precipitation have been investigated separately, there is increasing evidence that coupling between dissolution and precipitation controls the dynamics of the Earth's lithosphere.[1087,1088,1094,1095] Potential reactions are dependent on the fluid compositions at the mineral−fluid interface, which in turn is controlled by local dissolution occurring preferentially at highly reactive sites, such as etch pit edges and steps.[1096] The resulting fluid compositions at the mineral−fluid boundary will vary across the mineral surface. Dissolution and precipitation are interrelated dynamic processes, continuously changing in response to the heterogeneously changing fluid composition across a mineral−fluid interface. The feedback mechanisms involved in this scenario present interesting and important information for the understanding of Earth processes as well as enabling conditions to be determined for the control of crystal growth through replacement reactions.[303] In general, crystal growth resulting from these coupled processes does not follow a traditional classical crystal growth model, instead it is dominated by the formation of nanoparticles at the reaction interface.[1097]

Real-time *in situ* analytical methods have enabled us to define and clarify many processes occurring at a reacting mineral surface. Phase-shift interferometry has been used to define dissolution at mineral surfaces.[909,1089] Similarly, AFM has enabled reactions to be followed in time sequences so that reactions can be directly observed at the nanoscale.[996,1090,1097−1099] Recent advances in AFM have visualized the nature of the mineral−water interface as atoms and ions can be directly seen moving in response to changing fluid conditions.[1093] Using these methods, reactions are no longer hypothetical: direct evidence is presented.[996,1100] These findings and the example below suggest a frontier opportunity to deploy computational models and machine learning approaches to build comprehensive models that describe dissolution and dissolution−reprecipitation in these systems.

4.5.2.1. CO_2 Sequestration by Mineral Carbonation. GCS can be a good example of coupled dissolution and precipitation of minerals. A GCS project led by the CarbFix program is underway at the Hellisheiði geothermal power plant in Iceland, where gases released from Reykjavik energy production are pumped in solution down into the basaltic rocks. Field test

https://doi.org/10.1021/acs.chemrev.2c00130
Chem. Rev. 2023, 123, 6413−6544

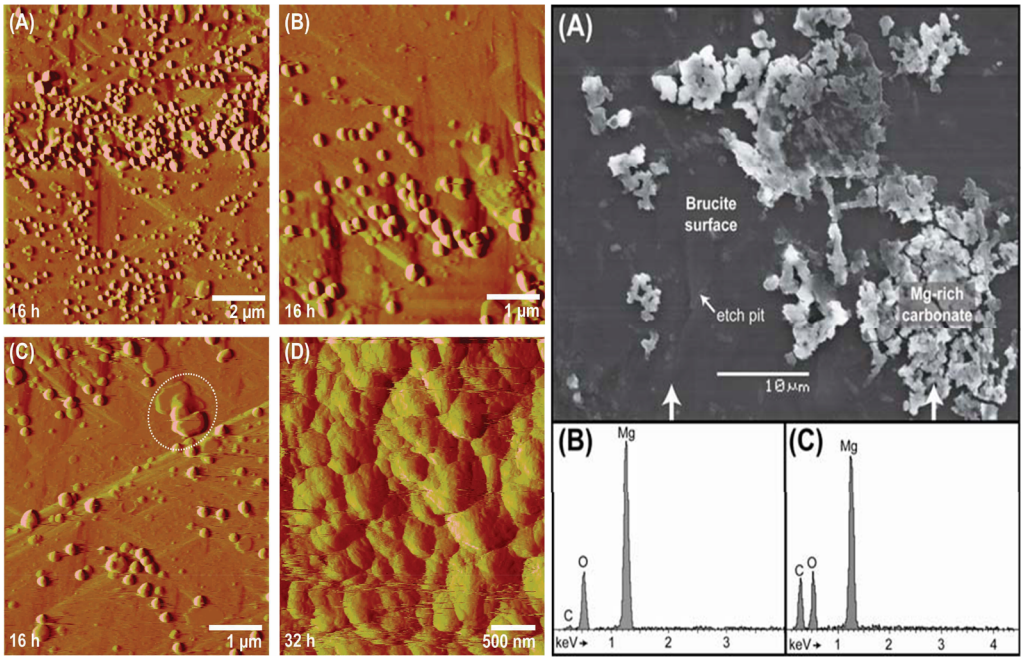

Figure 63. Left side images: (A–D) AFM deflection images show the characteristic triangular dissolution etch pits formed on a brucite ($Mg(OH)_2$) surface, together with the immediate formation of nanoparticles after exposure to carbonated water. Particles predominantly form in positions of higher dissolution, such as deep etch pits and step edges. The nanoparticles then merge and coalesce to form larger particles (circled in C and enlarged in D), identified by Raman spectroscopy as a hydrated Mg-carbonate phase, probably dypingite $Mg_5(CO_3)_4(OH)_2{\cdot}5H_2O$. CO_2 has been captured into a new stable carbonate phase. Right side images: (A) SEM image and (B,C) corresponding EDX spectra, positions marked by arrows. Reproduced from ref 1102. Copyright 2012 American Chemical Society.

results show that through the release of cations from dissolution of the parent basalt rock, CO_2 is being sequestered into new carbonate minerals.[1101] Using AFM, Hövelmann et al.[1102] have shown how brucite ($Mg(OH)_2$) can dissolve and simultaneously reprecipitate a Mg-carbonate phase in the form of nanoparticles on the brucite surface, as shown seen in Figure 63. Di Lorenzo et al.[1103] used the carbonation of wollastonite ($CaSiO_3$) as a model GCS system for silicate minerals to test natural and biomimetic catalysts for enhanced CO_2 sequestration, given that most silicate rock-forming minerals are slow to react at ambient temperatures. Their results show that dissolution is the rate-limiting step for wollastonite carbonation. Amorphous silica and calcite were formed on mineral surfaces by wollastonite dissolution coupled with crystal growth through the formation and aggregation of nanoparticles.

4.6. Biomineralization. In a process referred to as biomineralization, many living organisms orchestrate mineral dissolution, nucleation, crystallization, and phase transformation events to create materials required for their life.[887,889,890,896] Biomineralization occurs in terrestrial and aquatic environments (including physiological fluids) and is a major factor in regulating the biogeochemical character of the planet. Our oxygen-rich atmosphere developed during the Precambrian through interactions of microbial systems with the iron-rich minerals of early Earth.[1104] In addition, microbial metabolism induces formation and transformation of Fe-oxides, and these interactions contribute significantly to the global Fe cycle.[1105,1106] Biomineralization also occurs in the oceans on such a large scale that it influences many aspects of seawater chemistry and results in large-scale carbon sequestration in the form of carbonate sediments. Moreover, major classes of tissues, such as bones and teeth, are formed in animals and humans through biomineralization.[833,889,890,895,902,1107−1114]

What sets biomineralization apart from abiotic mineral formation and dissolution processes is the involvement of an organic matrix that promotes, inhibits, or otherwise directs these processes through an interplay of thermodynamic and kinetic factors (Figure 64).[1115] Whether that matrix is insoluble and provides a scaffold for mineral formation or is soluble and acts to shape mineral products or drive dissolution, it manipulates energetic controls over ion transfer and phase transformation through processes that are inherently interfacial (Figure 64B,C).[833,997] Although few, if any, examples exist for which there is a clear understanding of the physicochemical mechanisms by which bioorganic matrices alter free energy landscapes and kinetic barriers to exert such controls, *in vitro* studies point towards a number of possibilities, ranging from the purely physical, such as the effects of confinement on mineral phase, shape, and orientation,[833,1116−1122] to chemically-defined processes, including the complexation of ions by highly charged macromolecules, stabilization of hydrated amorphous phases by both proteins and ions,[1109] and stereochemical effects that combine lattice matching with chemical reactivity to guide nucleation or modify crystal habits. In addition, living organisms can cause pulsed bioelectricity to trigger biomineralization,[1108] and repeated mechanical loading induced by their movements can also facilitate the transport of precursor molecules into confined spaces of organic matrices and direct biomineralization in specific locations with desired functionalities.[1107]

Overlying these energetic controls and of equal or greater importance are the biological controls that create the local physicochemical environment for biomineralization. The biological machinery of the cell, such as membrane proteins,

https://doi.org/10.1021/acs.chemrev.2c00130
Chem. Rev. 2023, 123, 6413−6544

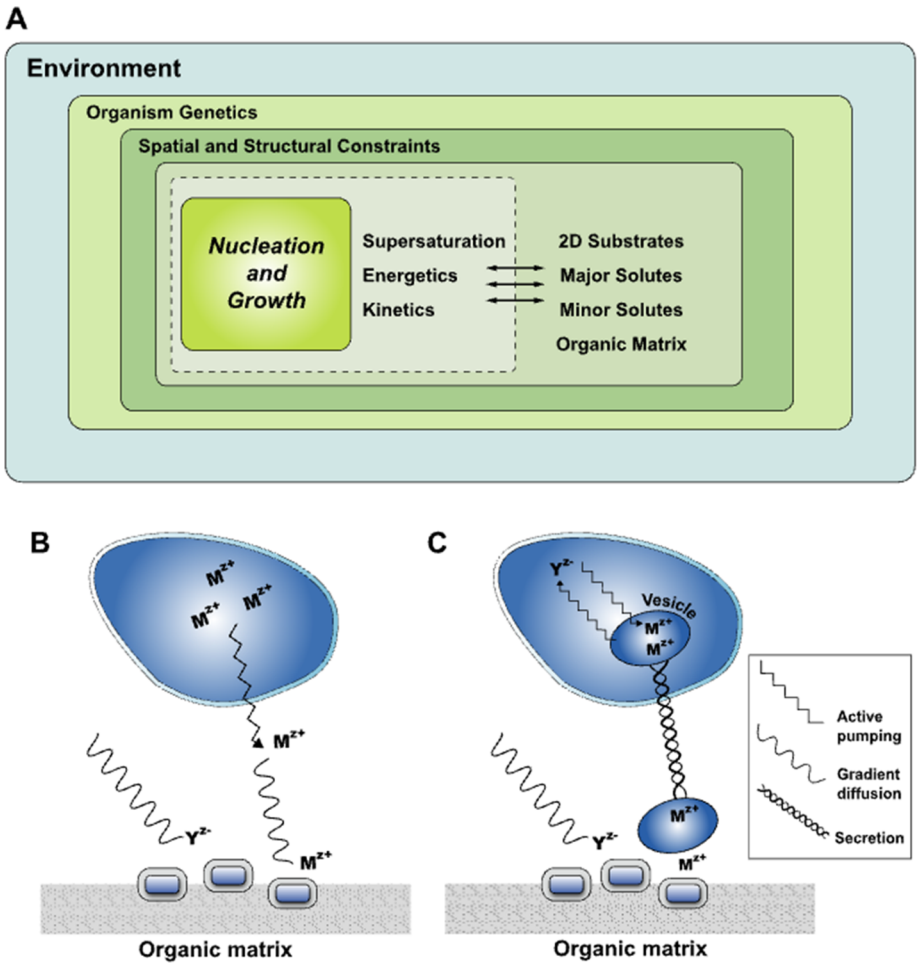

Figure 64. Biomineralization. (A) An understanding of biomineralization processes and the composition and morphological signatures contained in the final products is subject to many layers of control from environmental conditions, biological instructions, and the principles of crystal growth within an organic matrix. (B) Controlled biomineralization via extracellular processes involves pumping cations across a cell membrane and their movement by diffusion through extracellular fluids to the site of mineralization. (C) Aqueous ions are concentrated intracellularly into a vesicle compartment that is subsequently secreted. This compartment degrades at the site of mineralization to release cations for biomineral formation.[890]

vesicles, and ion pumps, bring together the bioorganic matrices, reactants, and/or precursor phases. Working in concert and modulated by responses to environmental conditions, these physiochemical systems produce the mineral architectures or selective dissolution and transformation processes characteristic of biomineralizing organisms (Figure 64C). A detailed understanding of these underlying biological controls exists for few, if any, biomineralizing organisms. Thus, a number of frontier themes are emerging from research aimed at elucidating the details of biomineralization processes and pathways. From the perspective of interfacial science, major challenges include the sequestration of ions in vesicular spaces at concentrations and under conditions that generate amorphous precursor phases, which are then transported to the sites of crystallization during coral[1123] and sea urchin formation,[1124] mechanistic controls of macromolecule chemistry and conformation at a specific time and location, and the roles of solvation water associated with macromolecules and spectator ions in modulating nucleation and particle-particle interactions.[994,1125,1126]

4.7. Underappreciated Impacts of Environmental Conditions on Dissolution and Precipitation. *4.7.1. Chemical, Physical, and Biological Complexity, Simulated Biological Fluids, and Usage of Mesocosm.* Capturing environmentally relevant chemical, physical, and biological complexities in laboratory studies of oxide−water and silicate−water interfaces is difficult. Equally difficult is understanding and experimentally accessing the details of these interfaces in the environment. One way to bridge this complexity gap is to use "controlled" mesocosm experiments, which have been successfully performed for quantifying the effects of physical and chemical stressors in mining-contaminant streams,[1127] of nanomaterials in water systems,[1128] and even mineral particles on ocean−atmosphere environments.[1129] A great deal can be learned from these studies, including the environmental fate of micro- and nanoscale oxide and silicate minerals in aqueous systems.

The use of simulated fluids is another approach to capturing the chemical complexity of environmental and biological systems in laboratory studies.[822,1130] Simulated biological fluids and various environmentally relevant media have been used to investigate metal dissolution from metal and metal oxides.[755,822,1130] These simulated fluids contain different metal cations, oxyanions, and organic compounds, and, importantly, the pH of the solution differs with the biological and environmental media being simulated. In these different media, the surface composition is changed by surface protonation and adsorption reactions.[741] For example, Fe-

https://doi.org/10.1021/acs.chemrev.2c00130
Chem. Rev. 2023, 123, 6413−6544

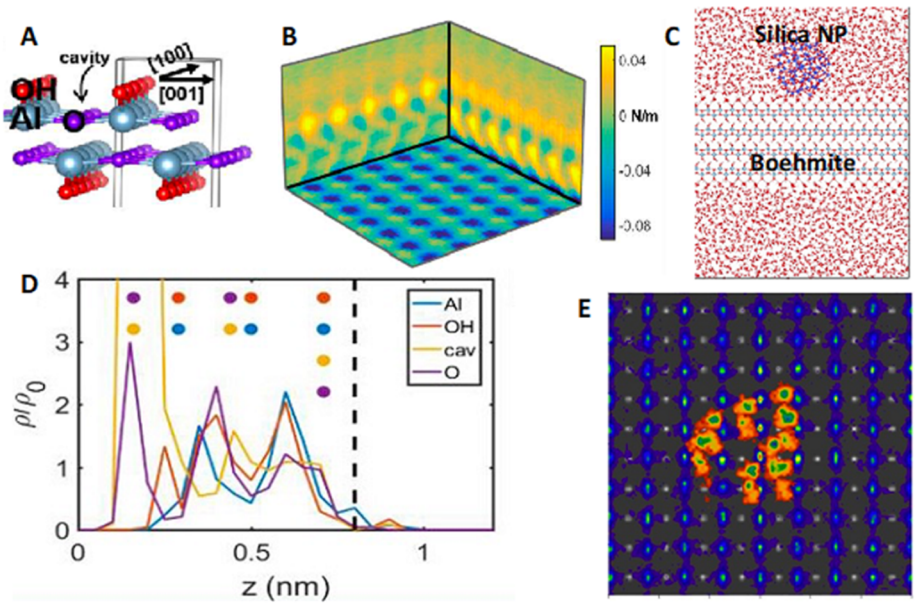

Figure 65. FFM provides atomic level maps of solvent structure that can be interpreted in terms of tip−solvent interactions via MD.[170] (A) Boehmite structure. (B) FFM map of force gradient in three orthogonal planes above surface of (A). (C) Simulation cell of silica particle representing AFM tip above boehmite in pure water. (D) Predicted water density (relative to bulk) vs height above the distinct atomic sites. Dots indicate locations of peaks in (A). (E) Pattern of H_2O (blue) and oxygens of OH (gray) in first hydration layer, as well as silanols on tip (orange/green) that H-bond to H_2O molecules in first hydration layer, thereby defining the observed hydration structure. Adapted from ref 170. Copyright 2021 American Chemical Society.

oxide particles of different sizes selectively adsorb antimicrobial proteins and peptides when placed in culture medium containing a variety of different components.[754]

4.7.2. Solid Solutions, Including Complexity of Mineral Phases, Layered Double Hydroxides, and Phase Transformation. Minerals can remove contaminants of concern from solution and retard their environmental transport. In many cases, sorption processes are responsible for the uptake and immobilization of metal ions. However, when contaminants or solutes become structurally incorporated into a bulk phase, they can be immobilized in the environment until the phase undergoes transformation or dissolution. These solid solutions can be classified as substitutional, interstitial, or omissional, depending respectively on whether solutes reside in one or more regularly occupied crystallographic sites, whether they are located in interstices between normal lattice sites or whether unoccupied structural vacancies are created.[1131] Concentrations of metal ions in equilibrium with solid solutions are often lower than their pure (hydr)oxide counterparts. For example, compared to $PbO{\cdot}nH_2O$ scales, the lower equilibrium Pb^{2+} activity associated with $Pb_3(CO_3)_2(OH)_2$ or $Pb_5(PO_4)_3(OH)$ prevents the release of lead from scales in water distribution system pipes into drinking water.[1132−1135] However, recent evidence from water distribution scales suggests that solid solutions of calcite ($Ca_xPb_{1-x}CO_3$) and apatite [$Ca_xPb_{5-x}(PO_4)_3(OH; Cl; F)$] may control Pb solubility in some systems rather than the pure mineral phases.[1136,1137] Scant thermodynamic data and a limited understanding of the nucleation, growth, and dissolution of solid solutions hinder our ability to predict how the changing chemistry of feed water can result in Pb release in water distribution systems.

Pb^{2+} can also be immobilized within vacant sites within layered minerals. For example, as a class of minerals, layered Mn-oxides show highly reactive vacant sites within their structures and can strongly bind and preferentially immobilize certain metal cations such as Pb^{2+} (section 3.2.2). Additionally, they are highly oxidizing agents and thus, structural Mn^{4+} can reduce to Mn^{3+} and Mn^{2+}, which leads to different types of phase transformations depending on the conditions and types of reductants (section 4.3.2.4). Such transformations can have significant implications for immobilization and release of trace metals.

Layered double hydroxides (LDHs), which can be considered as solid solutions, have applications across a wide range of fields, including materials science, catalysis, biomedical science, and enviromental chemistry.[1138−1146] Uptake of metal ions in LDHs formed from the dissolution of clay minerals and Al-oxides has been studied for over two decades.[1144,1147−1153] LDHs have the general formula $[M_{1-x}^{2+}M_x^{3+}(OH)_2]^{x+}[A^{n-}]_{x/n}{\cdot}mH_2O$, where M^{2+} are divalent cations (e.g., Mg^{2+}, Fe^{2+}, Zn^{2+}, and Ni^{2+}), M^{3+} are trivalent cations (e.g., Al^{3+}, Fe^{3+}, and Cr^{3+}), and A^{n-} are anions of valence n. The LDH structure contains edge sharing, octahedrally-coordinated metal ions (i.e., M^{2+} and M^{3+}) that form brucite-like layers. The interlayer anions balance the net positive charge: they can range from inorganic oxyanions such as carbonate, nitrate, sulfate, or silicate to organic anions and are randomly located in the interlayer region along with water molecules. The layers are held together by H-bonding between hydroxide groups, anions, and water molecules.[1154−1156]

Recent work on LDH has emphasized growth mechanisms and the impact of solution chemistry.[1149,1157,1158] In natural systems, the formation of LDH phases had been shown to be driven by dissolution of Al-containing sorbents (e.g., clay minerals and oxides) followed by reprecipitation of the LDH for minerals such as kaolinite and pyrophyllite, where the LDH grows heteroepitaxially from the surface.[1159−1162] In addition, the stability and sorption capacity of these phases is affected by the particular anion used to balance charge in the interlayer

https://doi.org/10.1021/acs.chemrev.2c00130
Chem. Rev. 2023, 123, 6413−6544

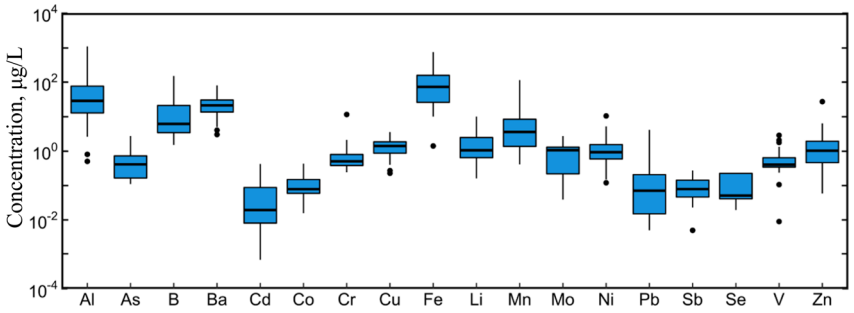

Figure 66. Concentrations of dissolved (<2 µg/L) trace elements in river waters. The data is based on the information in Gaillardet et al.[1184]

and the presence of other solutes.[1156,1163,1164] The presence of Si has been implicated in inhibiting the formation of crystalline LDH phases, whereas Si-free systems have produced LDH nanocrystals.[1162,1165] High humic acid coatings on kaolinite inhibited Ni LDH formation in favor of $Ni(OH)_2(s)$; in contrast to the LDH phase, the resulting hydroxide phase was not resistant to proton-promoted dissolution.[1166] While much progress has been made in understanding metal uptake on and the stability of LDH phases, we need a better understanding of LDH phase formation and their growth to design more efficient materials for their diverse applications.

Fe-(hydr)oxides can undergo phase transformation from poorly amorphous oxides to more stable, crystalline oxides or can recrystallize as more stable forms. These processes are particularly catalyzed in the presence of aqueous Fe^{2+}[659] and have been interpreted based on the conveyor belt mechanism (section 3.4.1.5). Future efforts on elucidating iron oxide phase transformation will advance our ability to accurately quantify phase transformation extent, improve our understanding of the thermodynamic driving forces and reaction mechanisms at the molecular scale, and assist us in translating laboratory studies to complex environmental systems.

4.7.3. Impacts of Interfacial Structures on Dissolution and Precipitation. Studies of crystallization demonstrated the importance of the interfacial solution structure in defining chemical speciation, the driving force for nucleation, and the attractive and repulsive forces for particle assembly. Solvent orientation and the hydration properties of solutes at solid–water interfaces also are important in determining dissolution.[286] As discussed in sections 2.2.3, 2.2.4, and 2.3.2, researchers have used surface vibrational spectroscopic methods like SFG to demonstrate relationships between solution pH-surface properties and water orientation at SiO_2–H_2O interfaces,[11,253,1167,1168] while the information about the ion distribution at surfaces has been obtained from a combination of MD simulations[170] and X-ray or neutron scattering.[298,392,1036]

The ability to probe interfacial structure, particularly between two mineral surfaces, has been augmented by AFM-based 3D fast force mapping (FFM), which provides a 3D image of a solution's structure at the atomic scale, as seen by an AFM tip interacting with the surface (Figure 65).[170,1079,1093,1169−1174] The data consist of a 3D map of the force gradient along the vertical distance, df/dz seen by the tip as it approaches and retracts from the surface. Initial studies were carried out on the interface of water with the surface of muscovite mica,[1169] followed by studies of calcite,[1175] graphene, and other 2D materials,[1079] and boehmite (AlOOH).[170] The impact of electrolytes on water structure above muscovite and graphite were also investigated in these studies.

4.7.4. Chemical Disequilibria by Transport Limitation. The chemistry of oxide–water interfaces can change with the flow rate of the solution. In some natural and engineered systems where the solutions are static or slow moving, this is not a problem. In other systems, however, such as a flow through porous media or where suspended colloids are transported, it may be an issue. From the experimental viewpoint, static and flow-through experiments may not be directly comparable, which could explain disagreements in the literature. Expanded efforts are needed to quantify the effects of solution flow and perform experiments and simulations under realistic flow conditions.

For example, Schaefer et al.[1176] showed that the SFG signal from fused silica–solution interfaces in CO_2-equilibrated water varies with the NaCl concentration and time. Although the observations were interpreted as autocatalytic silica dissolution, with the species $Si(OH)_3(OH_2)^+$ generating charge-screening at the interface, the $Si(OH)_3(OH_2)^+$ aqueous species has not been shown to exist at any pH. If it is stable, it is likely so only under very low pH conditions (i.e., <0).[1177] Thus, while the observation of changing interfacial structure is real, it must still be explained by a chemistry other than the unlikely dissolution of nearly insoluble fused silica.

Fluid flow can also affect adsorption and dissolution/nucleation kinetics, which in turn influence the redox rates of aqueous compounds. For example, Zhou et al.[563] performed column flow-through studies in which the antibiotic ciprofloxacin (CIP) interacted with a hematite (α-Fe_2O_3) powder. Flow interruption led to adsorption and oxidation of the CIP. These authors concluded that the no-flow conditions allowed for the conversion of the outer-sphere to inner-sphere adsorption, which then allowed for ET between the CIP and Fe^{3+} of the hematite (section 3.3.2). Furthermore, different flow rates can affect mineral dissolution kinetics when the systems are controlled by fluid transport.[1178,1179] They can also control the nucleation kinetics of minerals by affecting the induction times before the nucleation rate becomes a constant.[1004]

4.7.5. Environmentally Relevant Solute Concentrations. The presence of spectator ions and complexing ligands have significant impacts on dissolution and precipitation, the formation and stability of oxide minerals, and the release and sequestration of trace metals from solids.[1180−1183] These are typical concentrations of dissolved trace elements in rivers (Figure 66).[1184] A mechanistic understanding of the geochemical processes operative under these low concentrations is often challenging because of the typical ~ mg/L detection limits of spectroscopic and microscopic instrumentation.

https://doi.org/10.1021/acs.chemrev.2c00130
Chem. Rev. 2023, 123, 6413−6544

Additionally, redox active species are commonly transient and thus difficult to detect. For example, the lowest concentration employed in spectroscopic experiments examining the interaction of Fe^{2+} with phosphate on Fe-oxide surfaces was reported as 0.1 mM (3.1 mg/L total P).[1185] Therefore, quantifying the role of the species with low concentrations in dissolution and precipitation processes can be challenging, especially for analysis of nanoparticles and for ligand- and redox-driven processes.[1186,1187]

Nevertheless, mechanisms of dissolution within environmentally relevant and ultralow concentration ranges have been identified for a number of systems, especially Fe-oxides.[1188] In near surface environments, where Fe^{3+} is predominantly present as oxides, oxy(hydroxides), and clay minerals, dissolved Fe concentrations are typically low (e.g., <1 nM).[1189] Fe reaction mechanisms, especially oxidation, at these low Fe concentrations have been successfully studied,[1190−1192] and over the past several decades, improved isotope techniques, such as multicollector inductively coupled plasma mass spectrometry (MC−ICP−MS), have advanced our understanding of the low concentrations of ions.[1193]

As discussed in section 4.3.2.3, the strong complexing ability of biologically produced siderophore ligands provides mechanisms for satisfying an organism's Fe requirements from Fe minerals or aqueous Fe^{3+} complexes.[1193] Siderophores are typically present at low concentrations in natural systems (10^{-7} to 10^{-10} M) and can promote Fe-oxide dissolution either by a direct surface-controlled mechanism or by facilitating H^+-promoted or ligand-promoted dissolution mechanisms.[1194] However, as with proton-promoted dissolution of Fe^{3+} minerals, ligand-controlled dissolution of Fe^{3+} is typically slow in environmentally relevant aerobic conditions at circumneutral to alkaline pH.[1195]

Recent studies have also demonstrated sub-micromolar Fe^{2+} (as low as 0.2 μmolar) catalyzed dissolution of lepidocrocite under anoxic, circumneutral pH conditions that is initiated by adsorption of Fe^{2+}-EDTA (50 μmolar EDTA), followed by formation of ternary Fe^{2+} −Fe^{3+} surface complexes, ET to the surface Fe^{3+} sites, and detachment of Fe^{3+}-EDTA.[1196] Diffusion-based electron shuttling that reduces spatially distant metal oxides also provides a mechanism for organisms to generate bioavailable Fe via Fe^{3+} dissolution. For example, microrganisms such as *Shewanella* can endogenously produce electron shuttling molecules, such as flavins, that can reduce soluble and insoluble Fe^{3+} to Fe^{2+} and can form Fe-complexes.[1197] Recent evidence for this mechanism has also been observed with Mn-oxide (i.e., birnessite), in which reduced flavins produced during lactate oxidation within *Shewanella oneidensis* MR-1 reduced birnessite (Mn^{4+}) to Mn^{2+} to form rhodochrosite ($MnCO_3$).[1198] These studies highlight the importance of identifying mechanisms by which ultra-low concentrations or biogenically produced species impact mineral dissolution and new phase formation.

4.7.6. Extreme pH. Dissolution and precipitation processes can also occur under extreme pH conditions. For example, at the Hanford, Washington, and at the Savannah River site, Georgia, in the United States, legacy nuclear wastes have been stored in the extremely caustic environment.[1199,1200] At Hanford, an estimated 56 million gallons of extremely caustic multiphasic wastes, comprised of supernatant liquid, sludges, and saltcake solids, are stored in 177 underground tanks awaiting processing and disposal.[1201] Containing 170 million curies of radioactivity and 240 000 tons of complex chemicals, these wastes resulted from the different reprocessing techniques used during plutonium production for the U.S. weapons program from 1943 to 1989.[1202,1203] They are rich in NaOH and Al, introduced to maintain a high pH and sequester fluoride, respectively, to prolong the life of the aging steel tanks.[1204] Processing these complex mixtures requires retrieval, mobilization, and chemical manipulation of Al-oxy(hydr)-oxides, such as gibbsite and boehmite, prior to vitrification.

Understanding the mechanisms and kinetics of dissolution and reprecipitation of Al-oxy(hydr)oxides in these highly alkaline conditions has been advanced recently by fundamental laboratory and computational modeling studies. In contrast to acidic conditions, where Al speciates as octahedral aquo ions that readily oligomerize into various polyoxo clusters, at high pH (Al^{3+} > 1 M and pH >14), the tetrahedrally-coordinated aluminate oxyanion monomer ($Al(OH)_4^-$) dominates. Thus, at high pH, the dissolution/precipitation of gibbsite and boehmite are mediated by Al coordination changes between six and four.[1205−1210] At temperatures above 120 °C, gibbsite converts to boehmite by dissolution−reprecipitation, entailing multiple coordination change events enhanced at step edges.[1211−1214] As alkalinity increases to a molar concentration level, water activity decreases and competition for waters of solvation increasingly promotes the influence of ion pairing on metal speciation and oligomerization.[1215−1219] The unique conditions at high pH also enable complex synergistic interactions between the surfaces of Al-oxy(hydr)oxides and condensation of other metals such as Cr^{3+}.[1220,1221] Here, multinuclear Cr oxyhydroxides condense on boehmite surfaces by a structural templating effect (Figure 67).[1220] and these

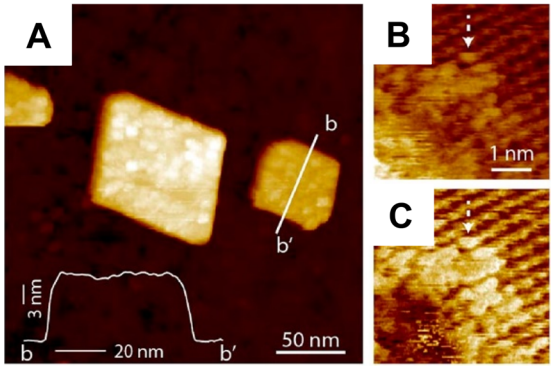

Figure 67. AFM images showing Cr(III) oxyhydroxide clusters on boehmite (010) surfaces formed after 3 h in Cr(III) = 50 mg/L at pH 13 at room temperature: (A) low-resolution topographic image, and (B,C) high-resolution phase and topographic images, respectively. The line profile along bb′ is inserted in the lower left corner of (A). Reproduced from ref 1220. Copyright 2019 American Chemical Society.

sparsely coated Cr could strongly modify the reactivity (in particular, dissolution) of the underlying boehmite substrate.[1221] These collective findings highlight the important interfacial chemistry that can arise at mineral−water interfaces at the limit of high alkalinity and low water activity.

In contrast to the highly alkaline conditions of the legacy nuclear waste example, the unusually low pH of acid mine drainage represents another extreme of dissolution and precipitation processes. Acid mine drainage refers to the wastewater or runoff produced when sulfide-bearing minerals such as pyrite, chalcopyrite, and pyrrhotite are oxidized in areas

https://doi.org/10.1021/acs.chemrev.2c00130
Chem. Rev. 2023, 123, 6413−6544

where the surrounding soils or host rock provide insufficient pH buffer capacities. The resulting low pH of these waters, typically between pH 2 and 4, creates a highly reactive environment in which mineral weathering and subsequent formation of secondary Fe- or/and Al-containing (hydr)oxide phases take place. The formation of secondary mineral phases depends on the water chemistry, including the concentrations of Fe^{2+}, sulfate, arsenic, phosphate, silica, and organic acid, and the pH.[1222,1223] This all varies with the geology of the mining region, and the microbiology within the system.[1224] For example, at high sulfate and pH values below 2.8, crystalline jarosite [$KFe_3(SO_4)_2(OH)_6$] is typically the dominant Fe^{3+} phase, which can sequester both contaminant cations and anions within its internal structure.[1225−1230] As pH increases, schwertmannite, ferrihydrite, and goethite can form.[1231,1232]

4.7.7. High Salinity. The effects of salinity on mineral solubility have received considerable attention over the past decade. A better understanding of saline water chemistry is critical for sustainable engineered practices during alternative water source utilization, water reuse, resource recovery, and minimal and zero liquid discharge. Predicting the solubility and fate of major ions (Na^+, K^+, Ca^{2+}, Ba^{2+}, Mg^{2+}, Cl^-, SO_4^{2-}, and PO_4^{3-}) and minor elements (e.g., B, Ra, U, As, Se, Fe, Zn, Si, and Cd) in complex, high salinity waters is challenging. For example, in 2017, the United States generated 3.88×10^9 m^3 of produced water, geologic formation water that is produced during oil and gas extraction, with salinities ranging from less than 2000 to nearly 400 000 mg/L TDS.[1233] During unconventional oil and gas recovery operations, the salinity of the hydraulic fracturing fluids plays a key role in shale reactivity and mineral precipitation/dissolution, with subsequent effects on wettability, hydraulic conductivity, and the generation of mineral fines.[84,1234] The complexity of treating or discharging high salinity waters that also contain contaminants is the largest impediment to beneficial water reuse.

At the nanoscale, salinity can affect the heterogeneous nucleation of minerals. For example, by using *in situ* GISAXS and AFM, Li and Jun[1235] studied the effects of aqueous salinity (from 0.15 to 0.85 M NaCl) on thermodynamic and kinetic factors in the nucleation of $CaCO_3$ on quartz under different supersaturations ($IAP/K_{sp(calcite)} = 10^{1.40}-10^{2.00}$).[1235] The effective interfacial energy (α) dropped from 48 to 35 mJ/m^2, owing to decreased water−$CaCO_3$ and $CaCO_3$−quartz interfacial energies. This decreased α induced faster $CaCO_3$ nucleation. However, at high salinity, the kinetic factor J_0 was reduced by ∼13 times. In particular, at higher salinity, the electrostatic attraction between $CaCO_3$ and quartz is lower, and the ion diffusivity decreases. Hence, the impingement rate of $CaCO_3$ monomers onto the quartz surface would be slower at high salinity, and thus the kinetic factor for nucleation would be reduced. Therefore, a more accurate description of $CaCO_3$ nucleation should account for both thermodynamic and kinetic factors. The findings highlight the importance of salinity in nucleation thermodynamics and the kinetics of mineral phases abundant in GCS, resource recovery, desalination membranes, and contaminated environments.

Regardless of the particular crystal or amorphous phase, a major challenge to understanding precipitation in high salinity waters is to obtain the thermodynamic parameters of the minerals. In many cases, the difficulties result from the lack of experimental data under concurrent extreme ionic strength, temperature, and pressure, and they are compounded by the need to select an appropriate model for activity corrections.[1236] For highly saline waters over 1 or 2 M, the Pitzer activity formulation is typically recommended.[1237] However, there are still limitations when using the Pitzer activity model; for example, the model does not specifically include ion pair formation (e.g., $NaSO_4^-$). Interactions of ion pairs with functional groups at interfaces, especially in membrane pores, cannot be accurately captured without incorporating the species specifically. Further complicating attempts to predict solubility in these complex systems are interactions involving scale inhibitors, including the impacts of the isolated and combined effects of silica, Ca^{2+}, Mg^{2+}, and Fe^{2+}.[1238] These challenges highlight the necessity for increased understanding of ion interactions to predict solubility behavior and understand the role of background ions on nucleation processes in highly saline waters.

4.7.8. Highly Confined Spaces. When water is confined inside nanoscale pores or in thin films, its dielectric constant, density, surface tension, and freezing temperature decrease. The nanoconfinement-driven alterations in the structure, dynamics, and thermodynamics of water[311,312] decrease the free energies of solvation for ions and clusters, making them less negative, and therefore, change the energy landscape for nucleation and growth reactions inside water-filled nanopores. Additionally, steric constraints define what solid phases can form inside nanopores, because for crystal growth to proceed, the nucleus must reach its critical size, a size that is often close to the nanoscale dimension of the pore. Therefore, thermodynamically stable phases cannot form in nanopores when the pore size is near or below the critical nucleus size, in which case less stable phases are observed. For example, ice with cubic structure is rarely found in nature; however, it is the stable solid phase when water freezes inside alumina nanopores (anodic aluminum oxide, AAO) with diameters at or less than 35 nm.[1239] Suzuki *et al.*[1239] propose that cubic ice is stabilized inside <35 nm pores because it has a smaller critical nucleus size than hexagonal ice. Also, ice nucleation mechanisms differ for different pore diameters: in <35 nm pores, cubic ice inside alumina channels nucleates homogeneously, starting in the middle of the pore, while in larger pores, hexagonal ice grows heterogeneously, initiating at the pore walls.[1239]

The confinement-dependent growth of organic compounds has been studied in detail (see the review by Jiang and Ward, 2014). These studies show that by confining nucleation and growth reactions in nanopores that are near the critical nucleus size, less stable organic polymorphs can be grown in controlled-pore glasses, porous AAO membranes, and other nanoporous matrices. Additionally, crystal growth in nanopores depends on their geometry: for example, in aligned cylindrical nanochannels, crystal habit can be controlled because nanocrystals orient themselves so that the fastest growing facet advances along the longest dimension of the nanochannel.[1240,1241]

Some studies have found that precipitation inside nanopores can be suppressed.[1242] In controlled pore glasses where both macropores and nanopores are present, $CaCO_3$ preferentially formed inside macropores but not inside examined nanopores (8 and 32 nm diameters). Following surface functionalization with an anhydride-terminated self-assembled monolayer, $CaCO_3$ began to precipitate inside the nanopores as well.[1242] This change is attributed to potentially increased ion diffusion inside the functionalized pores, and it points to the critical role that surface chemistry plays during crystal nucleation and growth inside nanoconfined domains. An important physical

https://doi.org/10.1021/acs.chemrev.2c00130
Chem. Rev. 2023, 123, 6413−6544

distinction of nanoconfined systems is that the supersaturation state decreases measurably following the precipitation reaction due to limited volume of aqueous phase inside the nanoconfined spaces. Therefore, a higher degree of supersaturation is required to sustain nucleation in progressively smaller pores or droplets, such as those found in biomineralization scenarios.[1243,1244]

This system will be even more complicated if the pH in the nanopore space is different from that in the bulk solution.[1245] Zhu et al. found that in negatively charged 3 nm silica nanopores, anion concentrations were enhanced, whereas cation concentrations were suppressed. The effects of these opposite surface propensities of ions became stronger at high salinity, causing electroneutrality breakdown in the nanopores. Additional protons may then compensate for the excess of anions, inducing a significant pH decrease. Compared to the bulk solution pH, the pH in the nanopores was lowered by as much as two units.[1245]

While the nucleation energy barrier is higher in nanopores than in unconfined spaces, if complexing ligands or nucleation inhibitors exist in solution, the free energy landscape can be significantly altered. Kim et al. showed that during Ca-phosphate biomineralization in nanoconfined collagen matrices, the complexing ligands can increase the apparent solubility of the nucleating phase in solution and the interfacial energies between nuclei and mineralization fluids. In contrast, the confined nanospaces can lower the energy barrier by reducing the reactive surface area of nuclei, decreasing the surface energy penalty and thus forming nanoparticles in the nanoconfined domain.[833]

Intriguing observations for the reactivity of confined mineral surfaces terminated by thin water films have been reported. For example, during forsterite Mg_2SiO_4 carbonation reactions in thin water films, the formation of magnesite $MgCO_3$ is limited until the water layer thickness reaches 1.5 monolayers.[1246] Once the water layer is thick enough for carbonation reactions to proceed, micrometer-scale magnesite precipitates form on surfaces with only nm-scale water films.[1247] These studies also indicate that the activation energy for $MgCO_3$ formation depends on the thickness of the water film: in water films limited to ~1 nm (5 H_2O monolayers), $MgCO_3$ precipitation has anomalously low activation energy (36 ± 6 kJ mol^{-1}). When the H_2O thickness is decreased from 0.92 to 0.64 nm, the apparent activation energy for carbonation reaction is doubled.[1248]

4.7.9. Surface Reactivity in Systems with Low Activity of Water. During GCS, deep groundwaters can dissolve in the injected supercritical $scCO_2$ phase. The resulting water-bearing $scCO_2$ can react with Ca-, Mg-, and Fe-bearing silicates, dissolving them and forming carbonates and amorphous silica.[1249−1267] Shao et al. reported that when phlogopite contacted $scCO_2$−$H_2O(g)$, the resulting formation of dissolution pits and secondary mineral phases significantly changed the surface morphology. Compared to phlogopite in contact with $scCO_2$−$H_2O(l)$, the dissolution pits in $scCO_2$−$H_2O(g)$ were deeper, suggesting faster dissolution. In addition, after 1 week of reaction in the $scCO_2$−$H_2O(g)$ system, the bottom of the phlogopite pits was covered by secondary mineral coatings, and isolated nanoscale precipitates simultaneously formed on both the unaltered surface and the new layer.[1264] Notably, the formation of surface coatings on phlogopite occurred less than a week after CO_2 injection. These surface coatings could change the wettability of the pre-existing rock and thus alter fluid transport during GCS.

The system pressure and the pressure history also affect mineral carbonation in GCS. Min et al. studied wollastonite carbonation in water-bearing $scCO_2$ at 35, 60, and 93 °C, 25−125 bar, and $0-140 \times S_w$, where S_w represents 100% water saturation in $scCO_2$.[1268] Figure 68A shows that the extent of reaction increased significantly with increasing pressure. The results differ from the findings of Whitfield et al. in that the kinetics of wollastonite carbonation are independent of pressure,[1267] and they depend on whether the mineral was in contact with only water vapor[1268] or additionally in contact with liquid water.[1267] There are several possible explanations

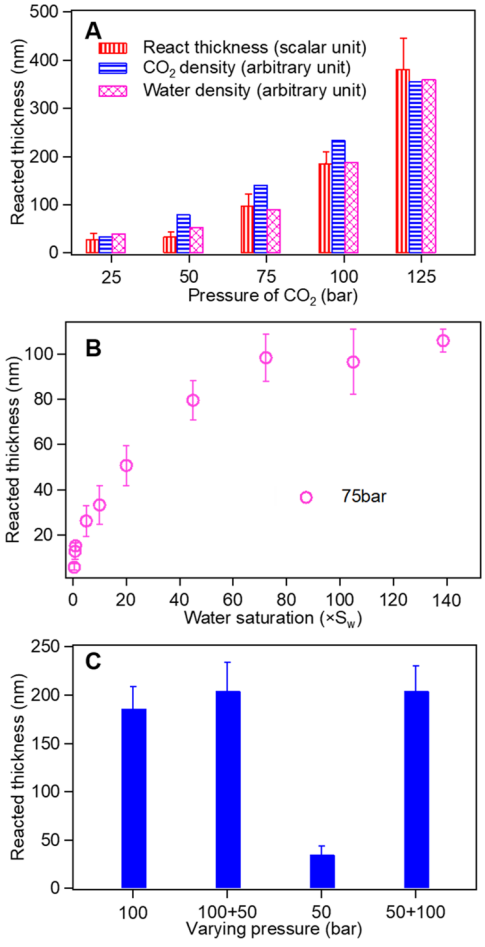

Figure 68. (A) Reacted thicknesses of wollastonite particles with a volumetric mean size of 3.8 μm, after 40 h at $140 \times S_w$, 60 °C, and different pressures of CO_2. The density scales for CO_2 and water at different pressures are not shown. The reacted thicknesses show the same trend as the densities of CO_2 and water. (B) Reacted thicknesses of wollastonite particles with a volumetric mean size of 3.8 μm after 40 h at different water saturation percentages, 60 °C, and 75 bar CO_2. The reacted thicknesses reached a plateau beyond $75 \times S_w$. (C) The reacted thicknesses of wollastonite particles with a volumetric mean size of 3.8 μm after 40 h at varying pressures, 60 °C, and $140 \times S_w$. The reacted thicknesses are similar for the control sample reacted only at 100 bar and the sample reacted at 50 bar after an initial reaction at 100 bar. The sample reacted at 100 bar after initial reaction at 50 bar had a larger reacted thickness than the sample reacted only at 50 bar and was similar to the sample reacted only at 100 bar. Reproduced with permission from ref 1268 Copyright 2018 Elsevier BV.

https://doi.org/10.1021/acs.chemrev.2c00130
Chem. Rev. 2023, 123, 6413−6544

for the higher reaction extent with higher pressure. First, Figure 68A shows that the thickness of the reaction front is proportional to the density of CO_2. With higher pressure, CO_2 can diffuse deeper below wollastonite surfaces. Second, pressure can also change the water density in the water-bearing $scCO_2$. As seen in Figure 68B, at 75 bar, a plateau is reached after 75 × S_w. In comparison, at 100 bar, 20 × S_w is sufficient to establish a plateau, suggesting that a lower pressure reaction needs more water, which is attributed to the lower water density. Third, under different pressures of CO_2, mineral surfaces might exhibit different extents of hydrophilicity, as shown by Saraji et al.[1269] Min et al. investigated the effects of pressure history on wollastonite dissolution at 60°C with 140 × S_w. As Figure 68C shows, a sample initially reacted at 100 bar for 20 h did not react further in a less reactive condition at 50 bar. However, a sample initially reacted at 50 bar for 20 h reacted even further at 100 bar. Interestingly, the final reacted thickness was the same for a sample reacted only at 100 bar for 40 h, suggesting that product layers produced at different pressures have the same permeability to water-bearing $scCO_2$.[1268]

4.7.10. Photochemically-Induced Oxidation and Consequent Precipitation of Oxides. The solubilities of materials are strongly dependent on their oxidation state. Photochemical redox reactions can quickly oxidize soluble ions and trigger fast precipitation. For example, $Mn^{2+}_{(aq)}$ oxidation has an estimated half-life of 200 to 300 days in abiotic systems,[1270] and studies have reported only the abiotic inorganic oxidation from $Mn^{2+}_{(aq)}$ to Mn^{3+}.[1271] Thus, until recently, bacteria-mediated Mn oxidation was thought to be the biggest contributor to Mn oxidation in natural systems because of the fast Mn oxidation and the formation of MnO_2.[1272−1275] Consequently, an abiotic inorganic process has not been considered as a prominent oxidation pathway to Mn^{4+}. However, Jung et al.[1276,1277] reported the fast photochemically-assisted oxidation of $Mn^{2+}_{(aq)}$ in the presence of nitrate in the absence of microorganisms or organic matter and the consequential formation of δ-MnO_2 nanosheets within a few hours. The nitrate photolysis generates superoxide radicals ($O_2^{\bullet-}$) that trigger fast oxidation of $Mn^{2+}_{(aq)}$ to Mn^{4+} via two steps, each of which transfers one electron, with Mn^{3+} as an intermediate. The Mn^{4+} oxide formation rate was comparable to or even higher than biologically mediated Mn^{4+} oxide formation. In the presence of halide ions, such as bromide and chloride, the oxidation of $Mn^{2+}_{(aq)}$ into Mn^{4+} was facilitated by newly formed reactive halogen species and promoted δ-MnO_2 formation.[1278,1279] These findings bring to our attention the importance of the photochemically-assisted abiotic pathway (e.g., via the generation of reactive radical species) for redox-active metal oxidation and formation of oxide nanoparticle formation in natural and engineered systems.

5. FUTURE DIRECTIONS

5.1. Critical Research Questions and Problems

This section summarizes pressing research questions, asks how and why current theoretical frameworks are lacking and outlines a roadmap for advancing our knowledge of solid−water interfaces and their inherent complexities.

5.1.1. Classical Theories and Their Limitations. *5.1.1.1. Theories Related to Interfacial Structure and Dynamics. 5.1.1.1.1. EDL Theory.* For over a century, electric double layer models have been used to describe the ion concentration profile and the decaying potential at charged surfaces.[1280] Yet, questions remain as to whether these mean-field models can fully capture the structure and reactivity of interfaces on a molecular level. As discussed in section 2.3.1, mineral oxides generate localized charged sites through deprotonation, protonation, or substitution reactions.[225] Classical MD simulations accounting for the localization of the surface charge found stronger interactions and more accumulation of cations near the surface than they did for a delocalized charge.[225] More recent simulations that calculate the potential-of-mean-force have addressed the question of which ions drive adsorption on neutral surfaces.[198] Still, questions about how ions affect the interfacial structure, chemical potential, water dielectric properties, and van der Waals forces remain. Furthermore, the impacts of nano-confinement, heterogeneity, surface curvature, and particle−particle interactions on EDL structure are unsettled.

Another persistent question is how thick is the interface? Spectroscopic measurements and MD simulations observe three layers (1 nm) of ordered water away from the solid surface, with or without added salt (refs 137, 165, 196, 198, 213, 215, 930, and 1281−1283), but the interfacial potential based on the EDL and the Debye−Hückel theory extends nanometers or micrometerss away from the surface at high and low ionic strength, respectively. We note that classical and DFT-MD simulation dimensions are commonly <10 nm and may not capture longer range effects. Spectral evidence suggests that water exhibits a small amount of net order or polarization induced by the electric field far from the surface at low ionic strength and distances of 100s of nanometers.[246,1284,1285] Whether this observation disagrees with the simulations is unclear. Only a small net orientation of water would be required to generate a substantial nonlinear optical experimental signal, given the large amount of water within the volume defined by the signal coherence length and the Debye length; as simulations only sample small volumes, this signal may be lost. Ideally, one would compare experimental observables with traditional mean-field models to determine whether such simulations reveal the expected decay profile in potentials, ion distribution, and water orientation.

Finally, the interactions of charged species with charged surfaces often behave in a manner that is not described by classical EDL models. As discussed in section 2.3.3.2, overcharging or charge reversal within the EDL has been observed, particularly in the presence of multivalent ions. A concentration of charges in the Stern layer that over-compensates for the charge density of the oxide surface cannot be explained by classic mean-field models; however, models have been put forth that explain overcharging based on the affinity of surface sites for cations (specific adsorption models) versus models that invoke ion−ion or ion−site correlations as the driving force for overcharging.[388] The experimental signatures of the different mechanisms of overcharging have been proposed, which should allow the theory and simulations to be refined to account for the different mechanisms.[249,392] To date, no unified theory has described the impacts of surface potentials on interfacial structure, surface speciation, and water dynamics, and how these further impact the adsorption dynamics, the stability of adsorbates, mineral dissolution, and nucleation. In all cases, advances in experiment, computation, and theory are required to allow us to determine the evolution of the potential, surface charge, ion distribution, and water structure across the EDL.

https://doi.org/10.1021/acs.chemrev.2c00130
Chem. Rev. 2023, 123, 6413−6544

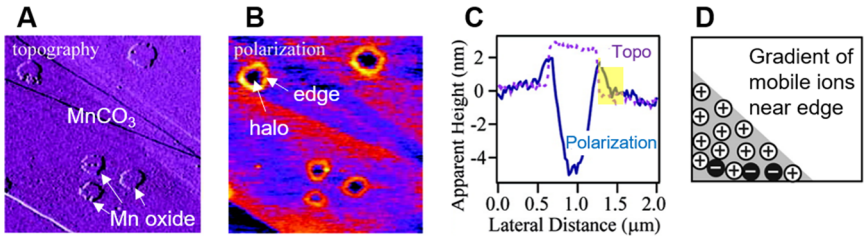

Figure 69. Edge polarization effects are apparent in these dc electric-force microscopy images of Mn oxide on a $MnCO_3$ surface at 75% relative humidity. Imaging mode: (A) contact, (B) negative dc (note edges), and (C) height profiles of *a*–*b*. (D) schematic of mobile ion concentration gradient shown in the yellow box in (C). Reproduced from ref 1292. Copyright 2008 American Chemical Society.

5.1.1.1.2. Theories of van der Waals and Other Short-Range Forces Defined by Water Structure. van der Waals forces arise from dynamic electron correlations and are especially important in solid–water interfacial systems.[1286,1287] Readers are referred to detailed reviews.[1288,1289] We note nontrivial environmental conditions, where predicting water structure, van der Waals, and other short-range forces presents challenges. For instance, as discussed in section 2.3.2.3, nanoconfined surfaces are examples of nontrivial solid–water interfaces, including water-filled nanopores, nanotubes, thin water films, and (within nanoscale spaces) the region in between two particles approaching each other prior to OA. Nanoconfinement can decrease H_2O density by as much as 20% compared to bulk H_2O,[307,334] and dramatically lower dielectric permittivity, from 78 (bulk H_2O) to ~2.[312] Although the mean H_2O density decreases under nanoconfinement, the apparent H_2O viscosity can increase at the same time, in particular for hydrophilic surfaces where H_2O's slip length at a surface, a distance relative to the wall where the tangential velocity vanishes,[1290] determines the effective H_2O viscosity.[1291] How the interplay between decreasing H_2O density and changing apparent near-surface H_2O viscosity affects surface protonation, surface complexation, redox reactions, OA, and particle nucleation and aggregation is unknown. Furthermore, in nanoconfined spaces (e.g., a few nanometers), polarization can strongly affect and even control the structure of the local aqueous environments.[1245]

Theories incorporating van der Waals and other short-range forces offer complex explanations for the processes of coupled dissolution and nucleation of minerals. For example, nanostructures on mineral surfaces, newly formed via nucleation, growth, and aggregation, alter the electrical properties of mineral surfaces, affecting reactions with charged species. Using electric-force microscopy, Kendall et al. found that the electrical properties of heterogeneously-formed manganese oxide nanostructures on a $MnCO_3$ substrate change as a function of water activity (e.g., relative humidity).[1292] At low RH, the surface potential contribution is important, while the polarization of mobile ions becomes the major component at high RH (RH >52%) (Figure 69). The heterogeneity of surface chemistry created by Mn oxide formation on $MnCO_3$ resulted in reduced ion mobility compared to that from bare $MnCO_3$, and it generated the highest ion polarization on the edge of a Mn oxide nanostructure, creating electrical heterogeneity.

At present, the outstanding research questions related to theories of van der Waals and other short-range forces defined by water structure include the following:

- How does water at nanoconfined surfaces slip as a function of hydrophobicity, surface functional groups, humidity, and salt content?
- How do changes in dielectric properties at an interface alter van der Waals forces, and how does this van der Waals force anisotropy further lead to torques during particle attachment?
- How do both dielectric profiles and van der Waals forces dynamically evolve as particles come together, and what is the impact of fluctuating dipoles? How can we measure these coupled phenomena separately?
- What are the energy barriers associated with the flipping of interfacial water molecules due to overcharging or charge reversal?

5.1.1.1.3. Thermodynamics of Solid–Water Interfaces. The most outstanding research question regarding thermodynamics at solid–water interfaces is this: *How does the solid-solution interface alter the thermodynamic properties related to solubility, interfacial energies, electron transfer, and stability of certain chemical species?* The energetics of interfacial reactions often cannot be explained by the current thermodynamic framework, especially for nanoconfined surfaces.[316,333,335] The current lack of a satisfactory explanation raises a question: *Are the common reference states, such as 1 M concentration of solute, still applicable to surfaces and nanoconfined domains?* Current simulations often struggle to connect with experimental observations, because they do not capture all the parameters and complexities that allow us to link the chemical potential of a chemical moiety/species in bulk materials to the chemical potential of the same chemical moiety at an interface (see more discussion in section 5.1.4).

Limitations in current thermodynamic frameworks become apparent for solid surfaces in contact with high salinity electrolytes or in ultra-high or ultra-low pH solutions (section 4.7). Researchers ask: *Can chemical potentials for interfacial and aqueous species in high salinity electrolytes be predicted using current theories?* The answer is often "*No*", because activity correction coefficients are empirical in nature, and even the databases for the empirical models are far from comprehensive. Similarly, nanoconfined surfaces often show unexpected reactivities due to changes in the thermodynamic properties of nanoconfined H_2O. We need to update thermodynamic approaches to be able to predict the thermodynamic properties of nanoconfined chemical species and chemical species in high salinity environments, where the activity of H_2O is low. Confinement in nanopores can cause local separation between anion- and cation-enriched regions due to the ion-specific surface interactions, which defines local fluid chemistry in nanopores. Zhu et al. (2022) found that anions have a high propensity to concentrate near the surface inside 3 nm silica

https://doi.org/10.1021/acs.chemrev.2c00130
Chem. Rev. 2023, 123, 6413–6544

nanopores, while cation transport into the nanopore is suppressed. This difference causes a local breakdown in electroneutrality, decreasing the pH within nanopores. One force driving this phenomenon is the polarization in nanopores, which increases concentrations of anions, but not cations. The impacts of nanoconfinement on the pH are even more significant in high salinity systems.[1245] Although the distinctive differences between the local pH and that in bulk solution affect ion adsorption, dissolution, and nucleation in nanopores, our understanding of these effects is still in its infancy.

Future research should develop consistent quantum mechanics-based correction coefficients to account for interfacial effects on fundamental thermodynamic properties: the free energies of hydration, deprotonation, complexation, electron transfer, and other interfacial reactions. Ultimately, we hope to develop a unified thermodynamic model of the surface with a common set of standard conditions (reference states for high salinity, low/high pH, low/high T and P, and nanoconfinement).

5.1.1.1.4. DLVO Theory. According to the classical DLVO theory, the overall interaction energies between two particles are determined from the sum of two forces, i.e., electrostatic repulsive forces and van der Waals attractive forces. To accurately calculate the energies, we need to have the surfaces well characterized to obtain particle information, including particle size, surface charge, and surface roughness.[294] This characterization may not be possible when it comes to mixed-phase particles or coated surfaces, when water structure is not homogeneous around particles, or in the presence of co-solutes, all conditions that can affect local surface structures and make accurate representation nearly impossible. In addition, other forces must be considered in complex systems. For example, in the presence of NOM, particle surfaces are coated with large NOM molecules, which, in addition to changing surface charge status, can introduce steric hindrance between two particles. A modified DLVO theory attempted to consider the impact of steric hindrance on particle interaction energies;[1293] however, the thickness of the adsorbed NOM layer is required for the calculation.[656,1293] This thickness is not easily obtainable, given the diversity in and heterogeneity of the types of NOM. There is even less information regarding biopolymers, microorganisms, etc. Furthermore, the surface potential and structure can evolve with prenucleation cluster development, solid nucleation, and crystal growth. They can reciprocally affect solid nucleation and crystal growth by changing the driving force of prenucleation cluster aggregation and particle−particle interactions and attachment. In the following section, we provide more discussion about the impact of surface potential and interfacial structure on solid nucleation and growth.

5.1.1.2. Classical and Nonclassical Theories for Nucleation, Growth, and Dissolution of Solids. 5.1.1.2.1. Quantitative Descriptions of Nonclassical Pathways of Nucleation. As shown in section 4.4.1, classical nucleation theory provides a quantitative description for capturing the thermodynamic aspects of nucleation. Many recent studies have pointed out that nucleation involves multiple kinetic steps in a complex energetic landscape. Although such nonclassical nucleation theory can provide details about kinetic pathways and describe transient metastable phases and polymorphs, no clear quantitative description captures this realistic view. There have been attempts to embrace the nonclassical nucleation pathway while using the main framework of classical nucleation theory's quantitative description.[833,1011] A new framework that describes the nonclassical pathway of the nucleation will be an important future direction.

To capture nucleation and dissolution, computation techniques such as MD and Monte Carlo (MC) have been used.[1294,1295] These high atomic resolution techniques allow us to study nucleation and dissolution, but the energy barriers associated with the nucleation can be much larger than the energy scale sampled by MD and MC simulations. For this reason, observing a nucleation event with MD and MC is hard within a typical molecular simulation time scale.[1296] Thus, over the last decades, many enhanced sampling techniques, such as metadynamics, have been used to describe the energetics of nucleation and cluster structures.[1296−1298] A more detailed introduction to metadynamics on homogenous nucleation is available in a review by Giberti et al.[1296] Advancing such enhanced sampling techniques will assist our understanding of solid dissolution and heterogeneous nucleation reactions.

In addition, recent advances in understanding the dynamics, formation energies, and structure of prenucleation clusters have sharpened our awareness of several knowledge gaps largely driven by the role of the hydration−dehydration reactions, chemical transformations, and phase evolution that accompany nucleation, as well as the impact of surface potential,[1108] whether inherent or applied, on the development of nuclei associated with system complexity. In the case of nonclassical nucleation pathways, the complexities relate to the chemical transformations and phase evolution that accompany nucleation. In particular, research is needed to answer these questions:

- How do crystalline phases emerge along nucleation pathways that start from dense liquid phases (DLP)/amorphous phases and that are accompanied by an evolution in chemical composition as solidification and crystallization proceed, and how is water eliminated from the DLP in this process?

- How does surface potential impact interfacial structure, surface speciation, and the formation dynamics and stability of nuclei?

5.1.1.2.2. Quantitative Descriptions of Growth by Particle Attachment. Recent developments in understanding the forces and response dynamics leading to CPA have defined new knowledge gaps associated with complexities in the structural features of the solid−liquid interfaces that underlie interparticle potentials. These complexities center on heterogeneities and anisotropies in particle and solution properties. The following findings highlight the need to understand how particle and solution properties deviate from the time-averaged predictions for ideal, charge-neutral, flat surface interparticle potentials, and response dynamics: (1) the near-universal prediction of large hydration barriers, (2) the fact that dipolar interactions can overwhelm other terms in the potential, (3) the finding that H-bond formation can facilitate the elimination of water and is a natural consequence of hydroxylation reactions. In particular, research is needed to answer the following questions:

- How do the complexities of a particle system impact CPA? These complexities include pH-dependent surface potential, interfacial solution structure and the resulting unique interfacial solution properties, anisotropies in

https://doi.org/10.1021/acs.chemrev.2c00130
Chem. Rev. 2023, 123, 6413−6544

particle shape and solvent dielectric constant, and stoichiometric variations of particles.

- How does the presence of surface-bound organic ligands and solution electrolytes impact the interfacial solution structure, the resultant dielectric and transport properties, and interparticle forces to enhance or hinder CPA?

5.1.1.2.3. Roles of Nucleus and Interfacial Solution Structure and Chemistry in Nucleation. Despite numerous insights provided by computational work, surface X-ray scattering and diffraction, and surface vibrational spectroscopy, the nature of the solution structure between mineral surfaces separated by nanometers remains largely undescribed. Although data and simulations exist for solutions in contact with a free surface for a small set of minerals, such as mica, rutile, and quartz, investigations of what happens as surfaces approach one another have barely begun. Here, 3-D FFM combined with molecular simulations offers an opportunity to gain new understanding. Besides the evolution of solution structure as surfaces approach, key unknowns include the dependence of solution structure on electrolyte type and strength, the effects of surface ligands, particle shapes, and surface curvature and defects (e.g., steps, kinks, vacancies, and impurities) on solution structure. Even with robust efforts in surface X-ray scattering and diffraction, vibrational spectroscopy, and 3-D FFM, understanding how hydration barriers are eliminated will depend on molecular simulations for the foreseeable future, because the time scale for water dynamics is orders of magnitude beyond that of the measurements that sample the time-averaged structure. Developing a time-resolved *in situ* experimental technique that can overcome this limitation is a challenge with promise.

5.1.1.2.4. Coupled Dissolution and Crystal Precipitation: Defining Reaction Pathways. Real-time nanoscale imaging of mineral surface reactions has given insights into the mechanisms of crystal growth and dissolution.[996,1090,1096,1097] Together with advanced analytical tools to define compositions and structures at the atomic and nanoscale levels, we have a clearer view of the mechanisms governing crystallization and potential reaction pathways, either classical crystal nucleation and growth or nanoparticle-mediated nonclassical growth, with the knowledge that both of these pathways may not be mutually exclusive. Isotope tracing of these fluid reactions also clarifies the actual mechanisms. Given that minerals start to dissolve in undersaturated aqueous solutions, subsequent reactions will be controlled by the dynamic changes in the interfacial mineral−fluid composition. From these initial reactions, subsequent larger-scale effects of these reactions can be better understood, but nanoscale observations need to be better linked to larger-scale data. One of the next challenges is relating these nanoscale observations and measurements by up-scaling to the micro- and millimeter scales.

Defining the reaction pathways that lead to the addition or removal of ions from steps and terraces is not an easy task. Progress has occurred in atomic- and nanoscale speciation analysis, but work remains to be done because observables range from molecular to micrometer-scale. Different growth regimes occur, depending on the fluid composition at the mineral−fluid interfacial boundary layer. If a solution is supersaturated with a phase, then that phase may precipitate in a classical pathway of monomer attachment to active kink sites, such as step edges, resulting in island and spiral growth producing advancing steps that spread and cover the growing crystal as a new growth layer. However, if the solution is slightly saturated or undersaturated with any phase, then dissolution is accompanied by precipitation (nucleation and growth) of nanoparticles along active dissolving sites, such as step edges or etch pit sites. Following the laws of thermodynamics, this process implies that the interfacial fluid has become supersaturated with another phase. These nanoparticles usually merge and eventually spread over the substrate surface. Their identification is hampered by the fact that these initial particles are usually disordered. Also, if the solution contains other impurities in contact with a dissolving surface, the released ions may allow the interfacial fluid to become supersaturated with respect to another phase, which may then precipitate.[1096] This phenomenon also happens in scenarios observed in AFM images, such as the precipitation of a Ca-phosphate (apatite) when a PO_4-rich solution is passed over a calcite surface.[65,1299] To identify the relevant species, regular or surface enhanced Raman spectroscopy, IR spectroscopy, and surface-sensitive analytical techniques such as grazing incidence synchrotron-based X-ray analysis can be utilized. More detailed discussion about these techniques is available in the SI.

5.1.1.2.5. Confinement Effects on Dissolution and Precipitation. Future work on precipitation under nanoconfinement needs to focus on decoupling steric effects from thermodynamic and kinetic effects. Experimental data from Stack et al.[1242] and Miller et al.[1300] reveal important deviations in both the kinetics and thermodynamics of precipitation reactions in nanoconfined pores and films. Classical crystal growth theory successfully predicts the suppression of nucleation and growth in nanopores that are at or below the critical nucleus size. However, experiments indicate that suppression may also take place in pores that are larger than critical nuclei, because nanoconfinement-driven changes to the H-bonding and solvation structure around ions[1301] determine the formation of inner-sphere adsorption complexes and polynuclear species inside nanopores.[304,335] Theory predicts that free energy of ion solvation decreases (becomes less negative) when the dielectric constant of water decreases inside nanopores and near surfaces; hence, ions have a lower barrier for the formation of dimer and other polynuclear species.[335] Therefore, based on thermodynamics alone, if the pore is large enough to accommodate a critical nucleus, precipitation inside the pore will be enhanced; nonetheless, the opposite is frequently observed. Furthermore, the local pH of nanopores can be significantly different from that of the bulk solution, drastically altering the driving forces of nucleation and dissolution.[1245] Taking all these aspects into account, there is a critical need for new predictive theories of nucleation and growth in nanoscale domains. Ideally, to accurately capture local chemistries in nanoconfined spaces, these theories will encompass both nanoconfinement-driven changes to thermodynamic and kinetic parameters as well as new experimental and computational approaches. In addition, research into the effects of nanoconfinement on solid dissolution is still in its infancy, presenting a fruitful research topic for future experiments and modeling.

5.1.2. Connecting Nanoscale Findings to Larger Scale Predictive Models. Nanoscale thermodynamics and kinetics deviate from known bulk scale phenomena. More accurate representations are needed to describe the relations among nanostructure, dynamics, and reactivity in complex geochemical phenomena at the macroscale, using surface

https://doi.org/10.1021/acs.chemrev.2c00130
Chem. Rev. 2023, 123, 6413−6544

complexation or reactive transport modeling. Thus, the nanoscale represents a bridge connecting the atomic scale to the macroscale.[1302] To cross the nanobridge (address *"nano-size" gap*), we need to understand how surface and adsorbate-induced long-range order and collective motions affect the thermophysical properties of the solid−water interface (section 5.1.1). Moreover, as the complexity of experimental approaches increases to meet the demand of mesocosm experiments and beyond, advanced computation and machine learning tools must be enlisted to understand geoscience problems over wide spatiotemporal scales (section 5.2).

As an example, to obtain the PZC of the (110) surface of rutile, Fitts et al.[405] connected molecular-level measurements, DFT calculations, and surface complexation modeling, using SHG spectroscopy to detect changes in surface potential as a function of pH and salt content. DFT calculations supplied estimates of the surface Ti−O and H-bonding, which are key parameters in the MUlti-SIte Complexation[398] model. The agreement between the model and the SHG-determined PZC were within experimental uncertainty, which demonstrated the connection of molecular-level parameters to observed acid−base behavior of surfaces and the need to determine sample and face-specific PZCs for minerals rather than using averaged values from powder experiments.

The structures and processes encountered in studying coupled processes in fine-grained sedimentary rocks have been reviewed by Ilgen et al., who described complexity over length scales that cover ∼15 orders of magnitude.[437] In the nanopores of geologic materials, such as diatomaceous matter, nanoconfinement affects fluid and ion adsorptive behavior and reactivity.[1245,1303] These nanoconfinement-driven changes of interfacial reactions affect reservoir-scale transport of water, nutrients, and contaminants, both on land and in the subsurface.

Experimentally obtained nucleation information, such as nucleation rates, activation energies, and interfacial energies, are important in scaling up nanoscale observations of chemical reactions to larger scale predictions. Recently, Li et al. incorporated experimentally-obtained kinetic and thermodynamic information about calcium carbonate nucleation into a reactive transport model code, CrunchTope,[1304] and improved the modeling of the evolution of the $Ca(OH)_2$-depleted zone and the surface dissolution zone at supercritical CO_2-brine-cement interfaces. This is the first work that incorporates nucleation information into a reactive transport model, successfully scaling up molecular scale reactions into a larger prediction. Furthermore, this new combination of experimental and modeling work successfully incorporates the pore-size controlled nucleation in nanoscale confined spaces and the higher solubility of materials in nanopore spaces than in unconfined spaces.

Transferring molecular-scale data (e.g., K_{eq} and k) into macroscale reactive transport codes is complicated because this data is usually collected on chemically pure systems with a limited number of components. Real-world environments, however, have complicated aqueous chemistries and solution conditions (e.g., pH, I, $[CO_2]$, T, and P),[1305−1307] and they can have three phases, including fluid-gas-solid interfaces[1308,1309] with spatiotemporal variations in compositions of all phases. Typically, these factors are not included in experiments conducted to obtain thermodynamic and kinetic parameters, so the applicability of laboratory values must be skeptically regarded. In addition, the porous nature of soils and sedimentary rocks means that seemingly simple concepts—such as surface area—are no longer related to BET or geometric surfaces in a straightforward manner.[1307] Reactive transport modelers are forced to extrapolate the values of parameters such as dissolution rate constants from conditions far from real systems of interest. Furthermore, the pore size distribution and its network influence variations in flow rates, and these parameters are rarely evaluated for their effects on solid dissolution and precipitation in molecular-scale experiments. Although estimating surface areas based on imaging of porous media can provide a more useful assessment of reactive surface areas,[1307] the resolution so far is limited to ≈0.3 μm, which is sufficient for sandy materials but not for clay-dominated sediments such as shales. Reactivity as a function of pore and pore opening sizes can also significantly impact the accuracy of model results.[1310] Hence, connecting thermodynamic and kinetic parameters with realistic reactive surface areas will be key to advancing predictive modeling capabilities, because porosity and permeability can be controlled by precipitation of phases such as SiO_2.[1307] We can expect continued advances in computational approaches that integrate multiscale phenomena to help interpret complex experimental results and accurately predict broad spatiotemporal behavior rooted in dissolution and precipitation phenomena of mineral−water interfaces. These advances will position scientists and engineers across disciplines to gain valuable insights on major challenges in the coming decades.

5.1.3. Rigorous Methodologies for Incorporating Complexity into Study Design. Disagreement among experimental observations and theories describing interface structure and reactivity are often reported for nanoconfined surfaces with high surface-to-fluid ratios and for complex and highly concentrated solutions containing electrolyte and/or organic compounds, where cooperative and coupled interactions can lead to unexpected behaviors. One of the key questions is *How do surface and solution complexity—including deviations from an atomically flat surface, anisotropies in particle shape, and solvent dielectric properties, surface reactivity, adsorbed electrolytes and organics, nanoconfinement, and solvent fluctuations—impact interfacial structure, surface speciation, interparticle forces, and particle attachment dynamics?*

New methodologies are needed to examine solid−water interfaces relevant to real-world conditions.[1311] Current interface studies are designed on reductionist approaches by utilizing either "the cleanest possible system", with simple and dilute background electrolytes and a few reactive species, or "samples collected in the field", characterized by complex solution chemistries, multi-mineralic compositions, and organic and inorganic surface coatings. These studies on real-world samples provide crucial information about reaction products and speciation in these systems,[1311] but they are often too complex to tease out the discrete chemical mechanisms and pathways of interfacial reactions. Additionally, field studies capture the final or steady-state conditions of the system, but provide limited information on intermediate reaction steps and pathways. To bridge the gap between clean systems and field investigations, we must be able to say *how simple systems can more accurately capture complex processes that are operative in the environment.*

The issue of surface "cleanliness" (*complexity gap*) is sometimes ignored in interfacial chemistry studies. Adventitious carbon, common on solid surfaces, affects both physical

https://doi.org/10.1021/acs.chemrev.2c00130
Chem. Rev. 2023, 123, 6413−6544

and chemical properties,[1312] raising the question of *what is the impact of the adventitious carbon on experimental results?*

Furthermore, in the soil and aqueous environments, microbial biofilms often grow on solid surfaces. Laboratory investigations have shown that when a reactive surface is covered with microbial biofilm, ions can still diffuse through the biofilm and bind to the surface; however, the kinetics of adsorption reactions are affected unpredictably.[261] These observations have led to the following new research questions:

- How do we incorporate the dynamic processes that impact adsorption, solubility, nucleation, and reactivity in the presence of biofilms and complex organic compounds?
- How do surface-bound organic ligands and electrolytes affect interfacial solution structures and the resultant dielectric and transport properties and interparticle forces?

Multidisciplinary investigations of interfacial reactions form a new field, where microbes and complex organics can be used as interfacial reactivity probes to identify dynamics and pathways of interfacial reactions.

Complex heterogeneities at the molecular- to continuum-scales need to be resolved. In particular, lateral surface heterogeneity at a molecular level arises from an underlying lattice structure with localized electron densities defined by the crystal lattice or local electronic structure characteristic for amorphous solids. We do not know how this imprinted-by-the-interface pattern affects the distribution and dynamics of ions, or what that means for the interfacial structure and behavior of interfaces. At the nanoscale, variations in composition, surface roughness, and curvature (e.g., surfaces of nanoparticles and nanopores) affect local charge distribution and charge densities, and this can change which solid phases are forming in the localized domains.[1292] At micron- to millimeter-scales, the heterogeneity of surfaces leads to variation of reactivity; in particular, dissolution is often intricately coupled to precipitation reactions (section 4.5). These unexplained observations show that in undersaturated solutions, precipitation on the solid surface can take place. In fact, in complicated heterogeneous systems, dissolution and precipitation are not two independent processes, as they are coupled at interfaces. This leads to the question: *What are the driving forces for these coupled dissolution−precipitation reactions, and are their rates interdependent?*

These complexities must be addressed to answer the questions:

- Can reactive transport models be developed that more accurately capture interfacial processes, including dissolution/reprecipitation, aggregation, biofilm formation/growth, while also accounting for mineral heterogeneity, nanoconfinement, and local hydrodynamics?
- Can we create a more complete understanding of the kinetically-coupled phenomena that occur at interfaces, including surface restructuring, dissolution/precipitation, etc.?
- How can we measure and predict the local chemistry and surface potential evolution at solid−water interfaces to better describe the coupled processes?

5.1.4. Connection between Theory, Computation, and Experiment. Although enormous progress has been made in the last 20 years, the remaining disconnects among theory, computation, and experiment make a comprehensive molecular model of many interfacial phenomena elusive. Thus, it is necessary to use a combination of theory, experimentation, and computation to characterize these complex, dynamic systems. A strategic approach can employ a set of benchmarking systems (e.g., agreed upon minerals, probe molecules, surface preparation, and experimental conditions, etc.) that can be studied across platforms to critically evaluate the basis of the underlying assumptions embedded in the theories and models. For example, extracting the z-dependent evolution (where z is the distance from the solid surface) of the hydrogen-bonding structure and orientation of water and other non-centrosymmetric interfacial species has allowed for comparisons between simulations and experiments. While overall *qualitative* agreement between experiment and CMD modeling in these systems has been achieved, there is often a lack of *quantitative* agreement about surface speciation, reaction energetics, and kinetics. It is necessary to improve accuracy while simulating the chemical identity and density of charged surface sites as well as aqueous ion speciation and comparing them to experimental data. Furthermore, we need to provide computational validation of experimental observables that are proposed to identify interfacial species. For example, some researchers attribute the presence of a peak at 3650 cm^{-1} in the SFG spectrum of the silica−water interface to surface silanols, while other work[341] includes computations that suggest this spectral feature arises from water molecules.[340] Based on peak-fitting of O 1s binding energies in XPS, surface silanolium charged sites ($-SiOH_2^+$) have also been posited,[342] but DFT calculations indicate that the proton affinities of O atoms in SiOH and SiOSi sites on silica surfaces are equivalent.[344,1313] If these XPS assignments are incorrect or incomplete, then the molecular picture of the interface needs to be readdressed with respect to these interfacial species.

Direct comparisons of experimentally-consistent simulations with classic EDL theories such as the Guoy−Chapman−Stern model are required to address a critical outstanding question: *How accurate are mean-field models in capturing interfacial structure?* These models are the most commonly used to interpret interfacial phenomena, and they form the basis of many predictive models based on surface complexation. Extracting parameters from simulations that relate to these models, such as the z-dependent interfacial potentials (including dipole potentials), ion work functions, and z-dependent ion concentrations, will allow for straightforward comparisons. Improving these EDL models should directly translate to improved surface complexation modeling, although it might require a significant rebuilding of the models from first principles.

Finally, current and future researchers should consider the following questions as they design collaborative explorations of interfacial phenomena.

- What improvements can be made in computational models that will allow us to guide, interpret, and validate experiments that are conducted over longer time scales and in more complex systems than currently employed in simulations?
- What common computational and experimental benchmark system would allow us to develop theories that address the complexity of interfacial water dynamics, adsorption/desorption, and precipitation/dissolution processes, as well as complicating factors like flow and multi-mineralic system compositions?

https://doi.org/10.1021/acs.chemrev.2c00130
Chem. Rev. 2023, 123, 6413−6544

- What is the added value in simulating more realistic systems (e.g., pH, pressure, temperature, and ionic strength)?

Substantial advances in experimental and computational power will be needed as discussed below. To reach the goal of creating predictive models that capture interfacial processes, a deliberate combination of experimental, analytical, and computational approaches will be critical, as will the development of new models that improve classic theories based on insights from these combined experimental/computational studies.

5.2. Developments in Analytical and Computational Methods That Will Enable Advances

5.2.1. Advanced Analytical Characterization Tools for in Situ Nanoscale Kinetics. Developing techniques to probe oxide− and silicate−water interfacial phenomena *in situ* is a step toward the study of realistic systems. The structural, dynamical, and chemical heterogeneity of interfaces require that experimental techniques provide nanoscale resolution and chemical specificity. Bringing real-world chemical complexity to the laboratory and implementing mobile versions of techniques into the environment can provide unprecedented new insights into oxide− and silicate−water interfaces. In cases where this is not yet possible, mesocosm experiments are critical to bridging the complexity gap. Closer integration of analytical and computational methods is key to helping interpret increasingly complex experimental results.

The complex phenomena explored in oxide− and silicate−water interface research occur on wide spatiotemporal scales. The nanoscale represents a critical domain for bridging experimental and theoretical knowledge uncovered by atomic scale approaches and macroscopic, field-scale geochemical research. Advances in X-ray and neutron scattering techniques, scanning probe technologies, and electron/ion/optical microscopies continue to improve their ability to offer real-time monitoring of interfacial processes via an expanding suite of *in situ* environments. Below we highlight a number of experimental methods that will enable new insights into studies of oxide− and silicate−water interfaces. While the following discussion summarizes recent advances, it is not intended to encompass all advanced analytical techniques. More detailed discussion is available in the SI.

5.2.1.1. Upgrades of Storage Ring and Free Electron Laser-Based Synchrotron Light Sources in the U.S. Synchrotron radiation sources have played major roles in atomic- and molecular-level studies of solid surfaces and their interaction with water, other liquids, and gases. For example, much of our current knowledge of the EDL comes from synchrotron X-ray-based scattering and spectroscopy studies: see sections 2.3.2, 2.3.3.1, and 2.3.3.2.[258,273,274,276]

Upgrades to existing synchrotron facilities, which will involve replacement of the electron storage rings with next-generation magnet technology known as multibend achromats,[1314] will result in significant gains in brightness, which in turn will result in X-ray beams that are micrometer to submicrometer (∼10 nm) in diameter. These advances will allow new classes of spatial- and time-resolved studies of real environments *operando*, such as the electrochemistry occurring in batteries or the chemistry occurring at solid−aqueous solution interfaces as a function of solution variables such as pH, Eh, and ionic strength. The gains in X-ray beam coherence will result in higher spatial resolution measurements, whereas the gains in brightness will allow ultrafast measurements. This combination will allow *operando* studies of realistic rather than simple systems. For example, *in situ* nucleation of nanoparticle formation and phase transformation can be probed by GISAXS or transmission mode SAXS and WAXS with a higher spatiotemporal resolution.[989] The improved high-resolution and real-time *in situ* data can provide the measurement statistics necessary to decipher elusive pathways of classical and nonclassical nucleation, growth, and crystallization of solids in fluids and at interfaces (see sections 4.4 and 5.1 for more detailed discussion). The gains in brightness will allow more rapid interrogation of individual biological cells, illuminating how they interact with drugs and how elements are distributed around grain boundaries in polycrystalline materials, which in turn will lead to understanding their mechanical properties.

Next-generation synchrotron radiation will allow ultrafast spectroscopic measurements on the order of a few hundred femtoseconds, of catalytic reactions, stimulated by femtosecond laser pulses. With an expected 10^6 X-ray pulses per second with femtosecond widths, rings under construction will permit ultrafast spectroscopy and X-ray scattering experiments that will yield new knowledge about chemical reaction mechanisms. For example, at the Linac Coherent Light Source (LCLS),[1315] new methods such as serial femtosecond crystallography (SFX) can follow structural changes on time scales of picoseconds. The fluctuations of diffraction peaks describe the dynamic responses of materials' X-ray reflectivity, with preserved phase information.

One concern about higher brightness synchrotron radiation sources is the possibility of beam damage to samples. One recent example of beam damage is the study of GaAs/In0.2 Ga0.8 As/GaAs core−shell nanowires using nanoprobe XRD.[1316] Nanowires exposed to high brightness X-ray beams under ambient conditions were found to have severe optical and morphological damage. Under a He atmosphere, the damage was reduced. These authors concluded that the beam damage was caused by oxidation processes from beam-induced ozone reactions in ambient air. Beam damage could also potentially cause dehydration reactions of hydrous solids or oxidation/reduction of redox-sensitive elements such as Cr, Fe, As, and Se. An important scientific challenge is how to minimize beam interactions with samples and beam-induced reactions caused by the higher brightness of the synchrotron radiation source. Future efforts should address this challenge and confirm the findings with results from complementary experimental and modeling approaches.

5.2.1.2. Neutron Spin Echo-Based Methods. NSE experiments were briefly described earlier in this review. Further progress in NSE techniques has been realized by the development of Modulation of Intensity with Zero Effort (MIEZE) spectroscopy and Neutron Resonance Spin Echo (NRSE) (Franz et al. and references therein).[1389] These techniques allow measurements of picosecond to nanosecond dynamics for the nanostructure range typically observed using small-angle scattering (1−200 nm). In longitudinal NRSE, a range 1 fs to 20 ns is achievable. Benchmarking MIEZE measurements of water show the seven order-of-magnitude (0.01 to 1000 ps) dynamic range of the technique.[1389] One advantage of these approaches includes continuous coverage over a broad range of dynamics in one measurement, compared to other techniques that require careful merging of dynamic information from several instrument configurations.

https://doi.org/10.1021/acs.chemrev.2c00130
Chem. Rev. 2023, 123, 6413−6544

Additionally, $S(q,\tau)$ information is obtained directly and does not require a Fourier transform from the frequency domain.

5.2.1.3. Nonlinear Optics. Nonlinear optics is at a point where experimentally determined estimates of nonresonant and resonant $\chi^{(2)}$ values and $\Phi(0)_{tot}$, the total interfacial potential drop across mineral−water interfaces, can serve as benchmarks for testing theory. As a fundamental structural property of noncentrosymmetric matter, $\chi^{(2)}$ encodes for the distribution of charges and nuclei in space and is thereby directly accessible through atomistic simulations, as is $\Phi(0)_{tot}$. The latter can also serve as a benchmark for mean-field theories that go beyond the "standard" (the Gouy−Chapman−Stern model), because the total interfacial potential includes the Coulombic, dipolar, and multipolar contributions to the potential, including the dipolar potential from net-aligned water molecules. Moreover, measurements should be sensitive to ion-specific effects on interfacial structure and electrostatics and manifest themselves in both non-resonant and resonant $\chi^{(2)}$ values and $\Phi(0)_{tot}$, making these parameters good candidates for developing models that go beyond primitive ion assumptions. Lastly, relative permittivity and capacitance estimates for the interfacial region provided by theory can also be constrained by the experimentally determined $\Phi(0)_{tot}$ values.

Moving from purely spectroscopic forms of nonlinear optics to imaging opens the door for pursuing spatially- and temporally-resolved dynamic changes at oxide and silicate−water interfaces. The time resolution in raster-free widefield illumination is in the subsecond range, and the spatial resolution in nonlinear optical microscopy is about half the signal wavelength, a few 100 nm. However, as a coherent method, SHG and SFG imaging have been shown by Roke and co-workers[1317] and Baldelli and co-workers,[1318] respectively, to be sensitive to submicrometer-scale regions. Modifications such as structured illumination[1319] offer opportunities to further improve the resolution. As in any vibrational spectroscopy, water's "strong absorber" problem needs to be overcome to obtain maps of the $\mathrm{Im}(\chi^{(2)})$ of interfacial water molecules after correction for the $\chi^{(3)}\Phi_{0,\,tot}$ contribution from the diffuse layer. Heterodyne-detected nonlinear optical microscopy, both for second harmonic as well as vSFG, will need to be developed to realize such an experiment, and maintaining stable optical phases will be important in this regard. Once achieved, such approaches will offer direct, spatially resolved views, in real time, of how the strength of the interfacial H-bond network evolves in response to an external stimulus, such as a change in pH or electrolyte concentration.

5.2.1.4. Transmission Electron and Scanning Electron Microscopy (TEM and SEM). TEM and SEM are no longer limited to high-vacuum sample environments and no longer require special sample coatings. Environmental TEM (E-TEM), which introduces a gas into the TEM sample chamber,[1320,1321] is becoming a standard technique at several large facilities, many of which allow access to a larger community of scientists worldwide. E-TEM is routinely used to investigate mineral substrates under a humid atmosphere.[1322,1323] Moreover, by lowering the temperature below the dew point, the formation of liquid water and ice films on mineral substrates can be directly imaged.[1324]

The advent of *in situ* liquid phase TEM (LP-TEM) and SEM (LP-SEM) in microfabricated silicon/silicon nitride cells and sandwiched graphene films has enabled direct observation of mineral particles in solution, including their nucleation, growth, interaction dynamics, aggregation, and fusion.[1321,1325−1328] Commercial microfabricated TEM cells can include capabilities for fluid flow,[1326,1328−1330] mixing of reagents,[1017] heating to near 100 °C,[919,1331] and the application of electric fields.[1332−1337] *In situ* LP-TEM and -SEM have led to numerous important discoveries about the behavior of mineral systems in aqueous electrolytes. For example, a recent study by Zhu et al.[919] provided an explanation for the formation of self-similar hematite mesocrystals from ferrihydrite suspensions, which has significant consequences for understanding the structural and chemical heterogeneity at mineral−water interfaces. The authors found that when Na-oxalate was added to ferrihydrite suspensions that were heated to 80°C, isolated hematite particles rarely appeared in the solution, but once formed, interfacial gradients at the oxalate-covered surfaces drove hematite particles to repeatedly nucleate about 2 nm from those surfaces, to which they then attach, thereby generating the mesocrystals.

5.2.2. Computational. *5.2.2.1. Quantum Computing.* Although not yet fully practical, quantum computers are beginning to show promise in expanding computational chemistry methods.[1338] The electronic structure of a H_2 molecule was first calculated in 2016 using a programmable array of superconducting qubits,[1339] and this feat was soon followed by similar calculations of metal hydrides.[1340] Of particular interest to environmental chemists and geochemists, especially those investigating oxide−water interactions, is the ground-state electronic structure of a water molecule that was recently determined using a quantum computer using trapped ions as the qubits.[1341] Prognosticators of advances in computer technology indicate that quantum computational supremacy is near,[1342] and this prediction bodes well for future computational studies of aqueous interfacial structures and reactivities. How soon practical quantum computers, and the associated quantum algorithms, will be developed to investigate complex oxide− and silicate−water systems remains to be seen, but we suspect that the computational tools 20 years from now will certainly perform beyond our expectations.

5.2.2.2. Nuclear Quantum Effects. Nuclear quantum effects are often neglected in classical and DFT simulations, but they can be critical in processes such as photo-induced proton transfer and proton-coupled electron transfers (PCET) that occur on the surfaces of oxide catalysts and natural minerals[1343] (see also section 3.4). By following the nuclear-electronic orbital (NEO) approach, significant advances in overcoming the Born−Oppenheimer approximation for electrons and positrons have been made for problems such as transition states, reaction paths, and thermodynamics,[1344] as well as proton affinities.[1345] Recent efforts to develop a multicomponent unitary coupled cluster method have shown promise for simple systems, although incorporating these techniques into complex systems will require further research.[1346] The development and deployment of quantum computers should speed up progress in this area.[1346]

5.2.2.3. Methods for Modeling Nonadiabatic Electron-Transfer (ET) Dynamics. ET can be modeled by a variety of standard molecular modeling techniques, including *ab initio* molecular dynamics, when $\Delta G^{t} \approx kT$, as well as by Eyring−Polanyi transition state theory and extensions, reactive flux methods, rare event methods, and discrepancy techniques when $\Delta G^{t} \gg kT$. Because many metal oxide minerals are wide band gap semiconductors, electron transport often needs to be

https://doi.org/10.1021/acs.chemrev.2c00130
Chem. Rev. 2023, 123, 6413−6544

treated as mediated by thermally activated hopping of charge carriers self-trapped as mid-gap states, such as by small polaron hopping.[591,724,725] Ideally, to accurately portray metal ion adsorption and interfacial/bulk ET with a realistic description of structure, hydration, and defects requires use of periodic cells and large system sizes.

Moving beyond DFT for estimating the ET rates and reaction energetics has recently become tractable with the implementation of new algorithms that enable wavefunctions that can describe localized diabatic electronic states (e.g., constrained DFT) and computation of the electronic coupling matrix element in computational chemistry software, such as NWChem[102] and CP2K.[1347] Emerging methods hold promise for higher accuracy for modeling ET by moving beyond first-quantized, many-body methods, such as MCSCF and CASSCF, into second-quantized methods consistent with higher level theories, such as select configuration interaction (CI), coupled cluster methods, Møller−Plesset perturbation theories, and Greens function theories. Although historically prohibitively expensive, new implementations for plane-wave basis sets will enable the advantages of second-quantized Hamiltonians in accurately calculating excited states and the thermochemistry for ET. This advance is particularly important because many oxide− and silicate−water interfaces of interest are strongly correlated systems.

Mixed quantum-classical methods can enable modeling of ET in larger, more complex systems than those that can be treated with the methods discussed above. Ring polymer MD simulations of an electron in a classical environment can produce accurate ET rates, including the effects of quantum tunneling, and their extension to nonadiabatic dynamics can describe Marcus' inverted regime.[1348−1351] A recent extension of these path integral-based methods to charge carriers in solids can model ET, polarons, and trap states.[731] Similarly, combining quantum master equations with classical models of the environment surrounding an electron is a promising route to efficient and accurate computation of ET rates.[1352] Further development of these quantum-classical approaches promises to enable modeling ET in increasingly complex systems on large spatial and temporal scales.

The above techniques focus on equilibrium systems, but many important interfacial redox processes, and interfacial chemistry more broadly, occur out of equilibrium, for example, in the presence of thermal gradients or flow. Driving the system out of equilibrium can drastically increase its complexity: thermal gradients in hydrothermal vents can enhance reactivity and favor metastable products.[1353] Similarly, flowing a solution over a surface can alter the interfacial structure and chemistry (*"flow gap"*).[347,400,401] Generalizations of ET theories to nonequilibrium steady states are beginning to emerge for simple models,[1354,1355] and their generalization and application to water−oxide interfaces should provide important insights into interfacial processes under real-world conditions.

5.2.2.4. Extending Spatial and Temporal Scales. Given the incomplete knowledge of the physicochemical processes that occur at mineral−water interfaces and the extent to which such processes control key phenomena, the scientific benefits gained by investigating interfacial chemistry with atomistic simulations have been transformative. Two main issues have limited the application of molecular simulations to this class of problems:

(1) The wide range of spatial and temporal scales intrinsic to these problems.

(2) The need for an accurate treatment of chemical reaction mechanisms and charge-transfer, balanced with realistically screened long-ranged electrostatic interactions.

Three developments will overcome these limitations and allow for atomistic simulations that overlap the spatial and temporal scales of reactive transport models (see section 4.7.6). These developments are machine learning-based interatomic potentials, exascale computing, and tight-binding DFT (DFTB). The following sections will extend our discussion of exascale computing-enabled interatomic potential (section 5.2.2.4.1) and DFTB (section 5.2.2.4.2). Then, we will introduce approaches to assess larger scale reactive processes, such as surface complexation modeling (section 5.2.2.4.3) and reactive transport modeling (section 5.2.2.4.4)

5.2.2.4.1. Machine Learning Applications. Building upon the growth in data collection, storage capabilities, and computing power, machine learning modeling has become a powerful tool for revealing hidden patterns or building predictive correlations that challenge conventional analytical methods.[1356] The self-learning ability of machine learning algorithms to make predictions or decisions (output or outcome) is based on a sufficient amount of data, known as "training data". Researchers in the field of environmental science and geochemistry have started taking advantage of this exciting tool. For example, recent work has relied on different machine learning algorithms, such as a deep neural network or a convolutional neural network, to develop predictive models for estimating the redox reaction rate constants for a wide range of organic compounds reacting with either hydroxyl radicals or a soluble Fe^{2+}−ligand complex. Readers are referred to a recent feature article by Zhong et al. for many more applications of machine learning in the field of environmental science and engineering.[1357]

Machine learning has only begun to be applied to model oxide−water interfaces.[435] As a first step, data could be compiled into a large dataset of known surfaces and corresponding surface complexes. Then, machine learning models could be developed to link those surface features (inputs) to these complexes (output) so that we can predict the formation of certain surface complexes once we know the corresponding surface features. Regarding dissolution kinetics, machine learning models can be built to connect different surface features (input) and their dissolution kinetics under different reaction conditions. Once the models are calibrated and validated, the dissolution kinetics may be predicted based on their key features. Another potential application is analysing different X-ray spectra, or any other microscopic images or spectra, that are not easily attainable and require extensive expertise. With machine learning algorithms, predictive models can be developed to link surface features to their respective spectra/images, or vice versa, and predictions can be made with respect to the desired features/spectra without the need for experimental approaches.

In addition, investigating systems and processes of interest in the molecular level demands lengths and time inaccessible to conventional electronic structure methods with state-of-the-art computer resources. Machine-learning interatomic potentials[1358] can be systematic and scalable (e.g., FitSNAP3[1359−1361]). Development of an exascale computing-enabled interatomic potentials capable of simulating 10^7

https://doi.org/10.1021/acs.chemrev.2c00130
Chem. Rev. 2023, 123, 6413−6544

atoms for time scales on the order of milliseconds would provide a paradigm-shifting capability that would allow researchers to address challenges in relating molecular simulations to chemical observables.

Current examples of combining computational chemistry and machine learning include work on anatase (TiO_2) and H_2O. For example, Andrade et al.[1362] extended the spatiotemporal scales of DFT-MD simulations using a deep neural network (DNN) approach to model the potential energy surface (PES). The DNN was trained via an active learning iterative scheme to determine the state of H_2O on the surface by modeling H^+-transfers at the interface. These authors observed a "solvent-assisted concerted proton transfer" to form a pair of short-lived hydroxyl groups on the TiO_2 surface, similar to that modeled for TiO_2 rutile and SnO_2 cassiterite (110) surfaces.[199] Studies combining DFT and SFG to benchmark the accuracy of models are a key component of this approach, ensuring the simulations are realistic.[203] Performing similar studies on TiO_2 nanoparticles and their aggregation behavior would yield a predictive model of crystal growth.[1363] A similar approach was used to create a model of amorphous TiO_2[229] that will be invaluable for understanding poorly crystalline, metastable nanoparticles in the environment.[1364] Machine learning techniques can improve the modeling of molecular and transition-state energies,[1365,1366] proton potentials,[1367] energy levels,[1367] and solvation environments,[1368] but, to our knowledge, these approaches have not been applied to oxide−water interface systems.

Despite the potential of machine learning tools, their applications face limitations and challenges, for which collaborating with data/computer scientists and learning "best practices" in machine learning are viable options. Also, a given prediction application typically lacks well-curated datasets, which requires experts to conduct comprehensive literature reviews and compile high-quality databases based on their domain knowledge. Here, the complex nature of different interfaces, the limited amount of data available for "clean" surfaces, and the much less data available for "complex" surfaces will likely prevent immediately developing machine learning models. Therefore, before any models can be set up, researchers will have to combine machine learning and experimental approaches to actively develop appropriate datasets. Finally, a machine learning algorithm is a "black box", so proper model interpretation is necessary to ensure that calibrated machine learning models are built on sound physical science. For more information on how to develop proper machine learning models, readers are referred to a recent feature article.[1357]

5.2.2.4.2. Tight Binding DFT. DFTB makes approximations to DFT calculations and balances a simulation's size, length, and accuracy while including reactivity. DFTB is 2−3 orders of magnitude faster than DFT and provides detailed electronic structures (lacking in CMD) by solving Kohn−Sham equations using a parameterized Hamiltonian.[1369−1371] DFTB allows for computation of energy gradients on systems of over 10^6 atoms,[1372,1373] and its methods can be parameterized to reproduce experimental water structures[1374] and reaction barriers,[1375] and used with rare-event methods.[1376,1377] Recent work has successfully modeled the defect structures of the quartz(101) surface.[1378]

5.2.2.4.3. Surface Complexation Modeling. SCMs have the potential to incorporate molecular-level information into predictive tools that describe macroscopic adsorption behavior. The development of these models has already benefitted from prior advances in spectroscopic, microscopic, and computational tools, such as XAS and FTIR spectroscopy, AFM, STM, and MD simulations. Nevertheless, accurate prediction of adsorption phenomena in natural and engineered systems requires a greater shift in model parameterization, from multiparameter optimization approaches to independent molecular-level parameter estimation based on surface structure, morphology, and reactivity. Using STEM, work on direct measurements of crystal face contributions has begun for goethite and rutile (cf. section 3.2.2), which are converted to independently obtained reactive surface site densities that may be incorporated into SCMs. Another example of a crucial parameter for any mineral surface is the surface potential. Recent advances using tools such as ambient jet (or near ambient pressure) XPS have been used to determine the surface potentials of silica nanoparticles in various background electrolytes, as well as the location of the shear plane and the capacitance of the Stern layer.[254]

As a further example, the model inherent value for specific capacitance of the Stern layer(s) depends on the relative ε of the Stern layer(s) and its thickness. The availability of both parameters from independent experimental or theoretical investigations will constrain their values and also shed light on the validity of the models. The thickness of the Stern layer is related to the number of water molecules bound in this layer. Nonlinear optical (NLO) measurements may in principle yield information on the amount of bound water and the net dipole orientation. Moreover, contributions from water orientation to the electric field at an interface can be obtained, and this can in principle be used in CD-MUSIC type approaches and be related to advanced chemical calculations. Coupling with additional methods, such as direct surface potential measurements (or application of external electric fields), can show to what extent the net dipole is affected. Another issue is whether the ε of the interfaces changes with the electric field strength (which is affected by the pH). The field strength affects water orientation and the amount of water. In this sense, available NLO measurements do suggest that the amount of oriented/bound water, and thus the "thickness" of the Stern layer, varies. Such variations would cause changes in the capacitance values, currently assumed to be constant. These issues can probably be addressed soon: with experiment-based data on such variations, new models can be formulated, and existing models can be further refined.

The water dipole orientation in current models is perpendicular to the surface, but angles deviating from the surface normal are probably the rule rather than the exception. As another example, outer-sphere surface complexation constants can now be determined from molecular simulations. These constants and the position of the outer-sphere complex are other fitting parameters that are inherently difficult to constrain by macroscopic data. Furthermore, the optimization process for binding constants is often correlated to capacitance. Overall, only a combination of methods will provide a comprehensive picture of mineral specific EDLs.

Finally, to predict proton affinities at surfaces, these new data will compel the field to revise or develop new model formulations (e.g., refined MUSIC equations) based on more detailed crystallographic data of the bulk solids. It is possible to use experimentally determined bond distances or values from simulations to obtain a more relevant MUSIC equation,[405] and simulations constrain assumptions of H-bonding.[12,1379] Simu-

https://doi.org/10.1021/acs.chemrev.2c00130
Chem. Rev. 2023, 123, 6413−6544

lations might make the use of the MUSIC equation obsolete because one can obtain the pK_a value of a given regular site and of defect sites directly.[162,414] Although there is usually good agreement between the MUSIC equation and such simulations, in some cases, the pK_a values from simulations have shown huge differences between hematite,[407] and gibbsite basal planes.[406] Overall, there are promising opportunities to obtain independent parameter values for surface complexation models from various sources. These opportunities will challenge the validity of the assumptions inherent in the models and show that mineral−water interfaces are far more complex than these models currently have to portray.

Ultimately, the multicomponent character and the physicochemical heterogeneities of real-world systems will impose limits on surface complexation models. Multiple surfaces (potentially of varying mineral composition) competing for solutes, the role of defects, surface blockage, effects of dissolution/reprecipitation, and ternary surface complexes remain challenging from all points of view. Still, insights from fundamental studies characterizing these systems continue to drive the evolution of these models.

5.2.2.4.4. Reactive Transport Modeling. With advances in computational power, the power and possibilities of nonreactive and reactive transport calculations have also significantly advanced.[1380] Many different reactive transport codes are available, and major geochemical software also includes simpler hydrodynamic options.[1381] Of course, many of the developed codes are tailored to the specific purpose of a project or require details of the planned calculations.

In this context, reactive transport in the sense of pollutant migration can be handled by standard codes such as PHREEQC for laboratory systems or with simplification of natural complexity for environmental settings. The challenge is to describe the transport of pollutants of interest and variations in pH. As an example, with pH fronts in a column, which may be caused by the adsorption phenomena themselves, describing the transport of pollutants with pH-dependent uptake behavior may become a formidable task, even for laboratory systems. One problem concerns the uncertainty of the exposed surface area of material in the column,[1307] even if the porous medium behaves ideally. Another critical issue concerns the assumption of local equilibrium, because it is known that desorption may be sluggish with strongly adsorbing solutes. Kinetic parameters appear to be largely missing in this context, and even the slow desorption is not properly understood. In such applications, chemical feedbacks are the main challenge, such as the pH effect mentioned above.

The simulation of dissolution/precipitation within a porous medium poses another challenge in reactive transport modeling.[1382] Variations in solution composition can be caused by chemical and physical feedbacks, such as increasing porosity[1383] or pore clogging.[1384] Yet another challenge lies in the connection of reactive transport processes with heat-flow and mechanical phenomena.[1385] Two reviews[1386,1387] provide more detailed discussion about reactive transport modeling, and future perspectives on reactive transport modeling have been discussed in view of the history of this modeling technique.[1388]

6. SUMMARY

Oxide− and silicate−water interfaces are central to environmental processes, such as global elemental cycling, the transport of contaminants and nutrients, nucleation of clouds by mineral dust, and health impacts of inhaled particulate matter. Oxide− and silicate−water interfaces are also widely used in industry for water purification, catalysis, diagnostics, and drug delivery, yet much about their detailed chemistry under relevant conditions remains unknown. The challenge is four-fold. First, interfacial chemistry evolves in complex ways because it is dynamically coupled to the composition of both the solid and the aqueous phase and yet is distinct from either. Second, the number of atoms present at the surface is small compared to the number of atoms that compose the bulk (either solid or the liquid) phases, complicating the deconvolution of surface analytical signals from the bulk response. Third, real-world interfaces are inherently heterogeneous, down to the nanoscale, making it difficult to distinguish different types of surface sites with their corresponding reactivities or to create predictive models that capture this complexity. Lastly, interfacial processes span femtosecond to millennial time scales, necessitating a breadth of experimental, analytical, and theoretical approaches.

These challenges lead researchers to use "average" properties to understand the structure of the oxide−water interface, measurements of surface acidity or surface potentials reported for related colloids or powders. Similarly, modelers use mean field approximations to predict how minerals impact environmental transport processes. Only rarely are interfacial systems explored using more advanced techniques to ascertain information about continuously evolving reactant binding, transient species, or phase transformations at the interface. This oversimplified approach limits our ability to predict the interfacial structure and, therefore, the reactivity in realistic, more complex environments.

We see a need for collaboration among scientists and engineers with expertise that includes chemistry, materials science, and environmental science. Diverse researchers, working in teams, are necessary to generate breakthroughs while combining experimental, analytical, and computational approaches that can lead to predictive models for complex real-world systems. Incomplete and over-simplified descriptions of interfacial structures and dynamics ultimately limit our ability to tailor and control natural and engineered systems involving oxide− and silicate−water interfaces, such as catalysis, water purification, containment of contaminant plumes, radioactive waste disposal, and the capture, utilization, and storage of CO_2. This lack of knowledge lies at a fundamental molecular level, and accordingly it impacts all fields where oxide−water interfaces play a role.

In this review, we have illustrated how a molecular foundation will allow us to create solutions for clean water, improved agriculture, better health, renewable energy, and a sustainable climate. The urgency of these grand challenges demands immediate investment in multidisciplinary collaborations that leverage recent computational and experimental advances.

ASSOCIATED CONTENT

Supporting Information

The Supporting Information is available free of charge at https://pubs.acs.org/doi/10.1021/acs.chemrev.2c00130.

Overview of techniques for probing oxide and silicate aqueous interfaces Note: The descriptors of crystal faces have been used as in the original work, so that the very

https://doi.org/10.1021/acs.chemrev.2c00130
Chem. Rev. 2023, 123, 6413−6544

same crystal face may appear with different notations. (PDF)

AUTHOR INFORMATION

Corresponding Authors

Julianne M. Gibbs − *Department of Chemistry, University of Alberta, Edmonton, Alberta T6G 2G2, Canada;* orcid.org/0000-0001-5819-2306; Email: julianne.gibbs@ualberta.ca

Eric Borguet − *Department of Chemistry, Temple University, Philadelphia, Pennsylvania 19122, United States;* orcid.org/0000-0003-0593-952X; Email: eborguet@temple.edu

Anastasia G. Ilgen − *Geochemistry Department, Sandia National Laboratories, Albuquerque, New Mexico 87185, United States;* orcid.org/0000-0001-7876-9387; Email: agilgen@sandia.gov

Young-Shin Jun − *Department of Energy, Environmental & Chemical Engineering, Washington University in St. Louis, St. Louis, Missouri 63130, United States;* orcid.org/0000-0003-4648-2984; Email: ysjun@wustl.edu

Nadine Kabengi − *Department of Geosciences, Georgia State University, Atlanta, Georgia 30303, United States;* orcid.org/0000-0002-1901-0992; Email: kabengi@gsu.edu

James D. Kubicki − *Department of Earth, Environmental & Resource Sciences, The University of Texas at El Paso, El Paso, Texas 79968, United States;* orcid.org/0000-0002-9277-9044; Email: jdkubicki@utep.edu

Authors

José Leobardo Bañuelos − *Department of Physics, The University of Texas at El Paso, El Paso, Texas 79968, United States;* orcid.org/0000-0003-4644-526X

Gordon E. Brown, Jr. − *Department of Earth and Planetary Sciences, The Stanford Doerr School of Sustainability, Stanford University, Stanford, California 94305, United States*

Randall T. Cygan − *Department of Soil and Crop Sciences, Texas A&M University, College Station, Texas 77843, United States;* orcid.org/0000-0003-1262-6177

James J. DeYoreo − *Physical Sciences Division, Pacific Northwest National Laboratory, Richland, Washington 99354, United States;* orcid.org/0000-0002-9194-6699

Patricia M. Dove − *Department of Geosciences, Department of Chemistry, Department of Materials Science and Engineering, Virginia Tech, Blacksburg, Virginia 24060, United States*

Marie-Pierre Gaigeot − *Université Paris-Saclay, Univ Evry, CNRS, LAMBE UMR8587, 91025 Evry-Courcouronnes, France;* orcid.org/0000-0002-3409-5824

Franz M. Geiger − *Department of Chemistry, Northwestern University, Evanston, Illinois 60208, United States;* orcid.org/0000-0001-8569-4045

Vicki H. Grassian − *Department of Chemistry and Biochemistry, University of California, San Diego, California 92093, United States;* orcid.org/0000-0001-5052-0045

Lynn Katz − *Department of Civil, Architectural and Environmental Engineering, The University of Texas at Austin, Austin, Texas 78712, United States*

Johannes Lützenkirchen − *Karlsruher Institut für Technologie (KIT), Institut für Nukleare Entsorgung—INE, Eggenstein-Leopoldshafen 76344, Germany;* orcid.org/0000-0002-0611-2746

Christine V. Putnis − *Institute for Mineralogy, University of Münster, Münster D-48149, Germany*

Richard C. Remsing − *Department of Chemistry and Chemical Biology, Rutgers University, Piscataway, New Jersey 08854, United States;* orcid.org/0000-0002-0922-4882

Kevin M. Rosso − *Physical Sciences Division, Pacific Northwest National Laboratory, Richland, Washington 99354, United States;* orcid.org/0000-0002-8474-7720

Gernot Rother − *Chemical Sciences Division, Oak Ridge National Laboratory, Oak Ridge, Tennessee 37831, United States;* orcid.org/0000-0003-4921-6294

Marialore Sulpizi − *Department of Physics, Ruhr Universität Bochum, NB6, 65, 44780 Bochum, Germany;* orcid.org/0000-0002-7810-3224

Mario Villalobos − *Departamento de Ciencias Ambientales y del Suelo, LANGEM, Instituto De Geología, Universidad Nacional Autónoma de México, Mexico City 04510, Mexico;* orcid.org/0000-0003-2820-848X

Huichun Zhang − *Department of Civil and Environmental Engineering, Case Western Reserve University, Cleveland, Ohio 44106, United States;* orcid.org/0000-0002-5683-5117

Complete contact information is available at: https://pubs.acs.org/10.1021/acs.chemrev.2c00130

Notes

The authors declare no competing financial interest.

Biographies

José Leobardo Bañuelos received his Ph.D. in Physics from New Mexico State University in 2010. He was a postdoc within the Fluid Interface Reactions, Structure and Transport Center and Geochemistry and Interfacial Sciences Group, both led by David J. Wesolowski at Oak Ridge National Laboratory. In 2014, he became a member of the Large Scale Structures Group at the Rutherford Appleton Laboratory's ISIS pulsed neutron and muon facility (UK). Since 2016, he has been a Professor in the Physics Department at The University of Texas at El Paso. Dr. Bañuelos is interested in how confinement and interfaces affect the nanoscale structure, dynamics, and reactivity of complex fluids. He uses x-ray and neutron scattering techniques to further our understanding of molecular liquids, mineral precipitation/dissolution, reactive separations and catalysis, and energy storage. He enjoys collaborations to integrate experimental findings with theoretical and computational approaches.

Eric Borguet is the inaugural Hazel Tomlinson Professor of Chemistry at Temple University in Philadelphia, PA, where his research focuses on chemical and physical processes at surfaces, interfaces, and in confined environments using ultrafast nonlinear spectroscopy and other techniques. Eric has mentored more than 30 graduate students, over 100 undergraduate researchers, and 19 post-doctoral fellows, leading to over 150 peer reviewed publications, more than 300 invited talks, and 270 contributed presentations. He was born in Dublin, Ireland, where he spent his formative years. He is a graduate of the Université de Paris-Sud (XI-Orsay). He obtained his Ph.D. in Physical Chemistry at the University of Pennsylvania and completed his post-doctoral training at Columbia University.

Gordon E. Brown, Jr. is the D. W. Kirby Professor Emeritus in the School of Earth, Energy & Environmental Sciences at Stanford University, where he served on the faculty for 48 years. He completed B.S. degrees in Chemistry and Geology at Millsaps College (1965),

https://doi.org/10.1021/acs.chemrev.2c00130
Chem. Rev. 2023, 123, 6413−6544

and M.S. (1968) and Ph.D. (1970) degrees in Crystallography/Mineralogy at Virginia Tech with Gerald V. Gibbs. He completed postdoctoral study with Charles T. Prewitt and James J. Papike in the Department of Earth and Space Sciences at Stony Brook University (1970−1971), where he carried out X-ray crystallographic studies of the returned Lunar samples from the Apollo 12 and 14 missions and developed high-temperature single-crystal X-ray diffraction methods. Following two years on the faculty in the Department of Geological and Geophysical Sciences at Princeton University (1971−1973), he moved to Stanford University. Over the past 43 years, he has been an active user of synchrotron radiation sources such as the Stanford Synchrotron Radiation Lightsource (SSRL) at the SLAC National Accelerator Laboratory, where he served on the Photon Science faculty for 25 years. His research interests include the surface chemistry at metal oxide−aqueous solution interfaces, environmental chemistry/geochemistry of heavy metals and actinides, environmental transformations of natural, incidental, and manufactured nanoparticles, geological sequestration of CO_2, and the chemistry of hydraulic fracturing of unconventional oil/gas shales.

Randall T. Cygan earned his Ph.D. in Geochemistry and Mineralogy in 1983 from Pennsylvania State University. He recently retired as Senior Scientist from Sandia National Laboratories, where he worked for over 30 years. His research interests are varied, including investigations of mineral equilibria, chemical kinetics, adsorption and dissolution of minerals, interfacial behavior of materials, shock metamorphism, and atomistic modeling of minerals, materials, and geochemical processes. He currently holds an adjunct position at Texas A&M University.

James J. De Yoreo is a Battelle Fellow at Pacific Northwest National Laboratory (PNNL) and an Affiliate Professor of Materials Science and Engineering at the University of Washington. He received his Ph.D. in Physics from Cornell University in 1985. Following postdoctoral work at Princeton University, he became a member of the technical staff at Lawrence Livermore National Laboratory in 1989, where he held numerous positions. He joined Lawrence Berkeley National Laboratory in 2007, where he served as Interim Director of the Molecular Foundry before moving to PNNL in 2012. De Yoreo's research focuses on crystallization and self-assembly in inorganic, biomolecular, and biomineral systems.

Patricia M. Dove, "Trish", is the C. P. Miles Professor of Science and University Distinguished Professor at Virginia Tech in the Department of Geosciences. She is also a Faculty Affiliate in the Department of Chemistry and the Macromolecules and Interfaces Institute. Dove earned B.S. and M.S. degrees at Virginia Tech and then completed a Ph.D. at Princeton University (1991), followed by an NSF Postdoctoral Fellowship at Stanford University (1991−1993). Following seven years on the faculty at Georgia Tech as an assistant and tenured Associate Professor (1993−2000), Dove relocated to Virginia Tech in 2000. Dove is recognized with the F. W. Clarke Medal, Dana Medal, Thomas Jefferson Medal of Natural Sciences, and is a two-time recipient of the U.S. DOE Best University Research Award. She is a Fellow of the American Geophysical Union, Mineralogical Society of America, Geochemical Society, and the European Association of Geochemists. Dove is a member of the National Academy of Sciences (NAS) and currently serves as the Chair of Class I (Physical Sciences). She is also a member of the DOE Council for the Division of Chemical Sciences, Geosciences, and Energy Biosciences. Her research interests include mineral−water interactions in studies of silica and calcium carbonate reactions during biological mineralization and the geochemistry of subsurface and aquatic environments.

Marie-Pierre Gaigeot is a physicist by training, and she received her Ph.D. in Computational and Theoretical Chemistry in 1997. She joined the University of Paris 6 in France (now Sorbonne University) as Assistant Professor in 1999 and was appointed Professor at the University of Evry val d'Essonne−University Paris Saclay in 2007. Her research has contributed to the emergence of ab initio molecular dynamics simulations in theoretical spectroscopy for gas phase molecules and clusters, liquids, and inhomogeneous interfaces between solids and liquids. Her current research implements novel developments that couple algorithmic graph theory with theoretical computational chemistry, especially for the structural and spectroscopic characterization of aqueous solid interfaces. To date, she has published 125 papers and 4 book chapters, she is/has been member of journal editorial boards including PCCP, JCP, *Spectrochimica Acta*, and *Philosophical Transactions A*, and she is subject Editor for *Proceedings A* of the Royal Society of Chemistry. She is FRSC Fellow of the Royal Society of Chemistry, Overseas Fellow of Churchill College−UK, and has been a Junior Member of the French Excellence Center IUF Institut Universitaire de France.

Franz M. Geiger is currently the Charles E. and Emma H. Morrison Professor of Chemistry at Northwestern University, where his work involves experiments and computations to study the special role that surfaces and interfaces play in the world. He is the recipient of the 2021 ACS Nobel Laureate Signature Award (as preceptor, with Paul Ohno), the 2017 Friedrich Wilhelm Bessel Prize of the Alexander von Humboldt (AvH) Foundation, and the 2016 Faculty Diversity Award from Northwestern University's Graduate School. He is a Fellow of the Alfred P. Sloan Foundation, the American Association for the Advancement of Science (AAAS), and the Royal Society of Chemistry (RSC), and serves as Senior Editor at the *Journal of Physical Chemistry*.

Julianne M. Gibbs is a Professor in the Department of Chemistry at the University of Alberta. Gibbs earned a B.A. in Chemistry from Arizona State University in 2000 and her Ph.D. at Northwestern University in 2006, working in materials chemistry. She then held a Dreyfus Postdoctoral Fellowship in environmental chemistry at Northwestern University. Since beginning her independent career in 2008 at the University of Alberta, a major focus of her group has been the application of second-order nonlinear optical methods to see the effect of pH and ions on the interfacial structure of aqueous mineral oxides. She is a Fellow of the Alfred P. Sloan Foundation.

Vicki H. Grassian is a Distinguished Professor and Chair of the Department of Chemistry & Biochemistry at the University of California San Diego. She is currently the Chair of the Department of Chemistry and Biochemistry and Co-Director of the Center for Aerosol Impacts on Chemistry of the Environment. Prior to joining the faculty at UC San Diego, she was the F. Wendell Miller Professor of Chemistry at the University of Iowa. She received her Ph.D. from the University of California Berkeley, M.S. from Rensselaer Polytechnic Institute and B.S. from the University at Albany (SUNY). Her research focuses on the chemistry and impacts of environmental interfaces such as geochemical and mineral surfaces present in soil and in air as mineral dust aerosol. She has received many awards and accolades during her academic career including two ACS National Awards for Surface Chemistry (2021) and Creative Advances in Environ. Sci. Technol. (2012).

Anastasia G. Ilgen is a Principal Member of Technical Staff at Sandia National Laboratories. She earned her Ph.D. in Environ. Chem. from the University of Alaska Fairbanks in 2010, and completed her Postdoctoral Training there in 2012. She joined Geochemistry Department at Sandia National Laboratories in 2012. She is an

https://doi.org/10.1021/acs.chemrev.2c00130
Chem. Rev. 2023, 123, 6413−6544

experimental geochemist, specializing in chemical reactions at solid–water interfaces. Her notable discoveries include identifying chemical reactions within crack tips, which can slow down or speed up fracturing of crystalline phases. Her innovative work on cation adsorption in silica nanopores led to new understanding of how nanoconfinement changes pathways, products, and thermodynamics of adsorption reactions.

Young-Shin Jun is a Professor of Energy, Environmental and Chemical Engineering at Washington University in St. Louis. She received her Ph.D. degree (2005) in Environmental Chemistry from Harvard University, Massachusetts, and conducted postdoctoral research (2005–2007) at the University of California—Berkeley/Lawrence Berkeley National Laboratory, California. She investigates chemical reactions in energy-related subsurface systems and water quality. Additionally, based on nanoscale interfacial chemistry and solid nucleation, her research group seeks new techniques and materials for more sustainable energy and environmental systems. Jun received a 2011 U.S. National Science Foundation CAREER award and was named a 2015 Kavli Fellow by the U.S. National Academy of Sciences, a 2016 Frontier of Engineering Fellow by the U.S. National Academy of Engineering, a 2018 RSC Fellow, and a 2019 Fellow of the American Chemical Society.

Nadine Kabengi is an Associate Professor in the Department of Geosciences at Georgia State University and associate Dean of The Graduate School there. She earned her Ph.D. in Soil Physical Chemistry from the University of Florida in 2004. She is an experimental geochemist, specializing in measuring the energetics and thermodynamic properties of reactions at solid–fluid interfaces. She has built a one-of-a-kind *operando* flow microcalorimeter set up, allowing for precise quantification of the heats in a *in situ* flow-through system. She is the recipient of the prestigious U.S. Department of Energy—Office of Basic Energy Sciences—Faculty Career Development (CAREER) program award in 2014 for her work on furthering thermodynamics measurements of interfacial reactions.

Lynn Katz is the Hussein M. Alharthy Centennial Chair in Civil Engineering in the Department of Civil, Architectural and Environmental Engineering and the Director of the Center for Water in the Environment at the University of Texas at Austin. She received her Ph.D. in Environmental Engineering from the University of Michigan in 1993. Her research has focused on understanding the role of sorption processes (adsorption, absorption, and precipitation) on contaminant fate and transport in natural and engineered systems including: (1) development of modeling approaches to predict contaminant sorption at surface/water interfaces and (2) development of novel treatment processes for targeted solute removal.

James D. Kubicki received his Ph.D. in Geochemistry from Yale University in 1990. He worked as a postdoctoral fellow for the Carnegie Institution of Washington, Caltech, and the U.S. Navy before joining the faculty at Penn State in 1998. He was a Professor in Geosciences at Penn State before becoming Chair of Earth, Environmental & Resource Sciences at The University of Texas at El Paso in 2015.

Johannes Lützenkirchen studied Chemical Engineering at Karlsruhe University (TU), now KIT. After receiving a Ph.D. in Physical Chemistry for the Environment from Strasbourg University, he moved to Umeå University for a post-doctoral stay. Prior to moving back to KIT, Johannes spent a year with Colenco Power Engineering, where he made first contact with Nuclear Waste Storage. His interests are in mineral water interactions and, in particular, surface complexation modeling. In 2006, he edited a book on this topic. Current experimental priorities are streaming current/potential and force distance curves, as well as column experiments, all with the aim of applying mechanistic models to simulate the data.

Christine V. Putnis is a Professor in the Institute for Mineralogy, University of Münster, Germany, where she has led an atomic force microscopy laboratory for the past 20 years, resulting in many international publications. Previously, Christine graduated with a B.Sc. in Geology from Newcastle University, Australia, followed by a research associate position in the Department of Earth Sciences at the University of Cambridge, UK. She is the mother of six children and is married to the mineralogist/Earth scientist Andrew Putnis. Christine's research centers on mineral–fluid reactions at the nanoscale related to coupled dissolution–precipitation processes and the formation of nanoparticles.

Richard C. Remsing received his B.S. in Chemistry from the University of the Sciences in Philadelphia in 2008 and his Ph.D. in Chemical Physics from the University of Maryland in 2013. He then worked as a postdoctoral fellow at the University of Pennsylvania and Temple University before joining Rutgers University as an Assistant Professor in the Department of Chemistry and Chemical Biology. His research interests include the theory and simulation of molecular systems relevant to renewable and sustainable energy, geochemistry, astrobiology, and materials science.

Kevin M. Rosso is a Laboratory Fellow and the Associate Director of the Physical Sciences Division for Geochemistry at Pacific Northwest National Laboratory (PNNL). Rosso earned his B.S. degree from Cal Poly Pomona (1992) and M.S. and Ph.D. degrees from Virginia Tech (1994, 1998). Since then, he has been a staff scientist at PNNL, where he now leads the Geochemistry Group comprised of about 40 scientists, post-doctoral fellows, and visiting students. He also leads the U.S. Department of Energy's Basic Energy Sciences Geosciences program at PNNL. Rosso was an Associate Editor for *American Mineralogist* (2004–2006), for *Geochimica et Cosmochimica Acta* (2008–2011), and currently serves on the Editorial Board of *ACS Earth and Space Chemistry* and on the Strategic Advisory Board for *Applied Geochemistry*. He has held honorary visiting professorships at the University of Manchester, the University of Grenoble, and the University of New South Wales. He is a life fellow of the Mineralogical Society of America (MSA), the Geochemical Society, and the European Association of Geochemistry (EAG). Rosso won the MSA Award in 2004, the Mineralogical Society's Hallimond Lectureship in 2016, and the EAG's Stumm Medal in 2020. He regularly serves on panels for the U.S. Department of Energy and for the U.S. National Academy of Sciences. His research focuses on understanding and predicting rates of electron transfer reactions in geochemical systems involving aqueous ions, mineral surfaces, organics, and bacteria.

Gernot Rother received his Ph.D. in Physical Chemistry for his studies on pore fluids from Technical University Berlin in 2002. He applied neutron scattering to the study of polymers and confined fluids in his postdoctoral work and has been a Staff Scientist at Oak Ridge National Laboratory since 2007. His research interests are in the atomic, molecular, and nanoscale structures of fluids, interfaces, and composition–structure–function relationships in natural and engineered porous materials.

Marialore Sulpizi graduated in Physics at the University of Rome, La Sapienza. She received her Ph.D. in Physics of Condensed Matter from the International School for Advanced Studies in Trieste in 2001. She was a postdoctoral fellow in the Chemistry Department of ETH Zurich and subsequently at Cambridge University before joining the University of Mainz, first as a junior Professor and then apl Professor. In March 2022, she joined the Ruhr Universität Bochum as

https://doi.org/10.1021/acs.chemrev.2c00130
Chem. Rev. 2023, 123, 6413–6544

the new chair in Physics of Electrified Interfaces. She has contributed to the understanding of several aspects of solid/liquid interfaces, including their structure, dynamics, reactivity, and vibrational spectroscopy.

Mario Villalobos is a Professor in Environmental Molecular Geochemistry at the National University of Mexico (UNAM). He received his B.S. degree in Chemistry (1987) at the same university and won a fellowship from the Dutch government to do a Master's degree (1989) in Soil Chemistry at Wageningen University. Later he received his Ph.D. (2000) in Environmental Engineering and Science from Stanford University, and was a Postdoctoral fellow at UC Berkeley, with Professor Sposito. He is currently Associate Editor of the journal *Geochimica et Cosmochimica Acta*, and head of the Soil and Environmental Sciences Department at the Geology Institute at UNAM.

Huichun Zhang is the Frank H. Neff Professor in the Department of Civil and Environmental Engineering at Case Western Reserve University (U.S.). She received her B.S. (1994) and M.S. (1997) in Environmental Chemistry from Nanjing University (China), and Ph.D. (2004) in Environmental Engineering from Georgia Institute of Technology (US). Her major research interests include interfacial reduction−oxidation processes in complex mixtures and the fate and transformation of emerging organic contaminants in natural and engineered environments. Her recent research areas also include predictive modeling for contaminant reactivity and sorption using both classical models and machine learning tools.

ACKNOWLEDGMENTS

P.M.D. acknowledges the U.S. DOE Office of Basic Energy Sciences (OBES), Division of Chemical Sciences, Geosciences and Biosciences through award DE FG02-00ER15112. V.H.G. was supported by the Army Research Office/Army Research Laboratory via grant #W911NF-19-1-0078 to the University of California, San Diego (VHG). Any errors and opinions are not those of the Army Research Office or Department of Defense and are attributable solely to the author(s). A.G.I. was supported by the U.S. Department of Energy, Office of Science, Office of Basic Energy Sciences, Chemical Sciences, Geosciences, and Biosciences Division under Field Work Proposal number 21-015452 at Sandia National Laboratories. Sandia National Laboratories is a multimission laboratory managed and operated by National Technology and Engineering Solutions of Sandia LLC, a wholly owned subsidiary of Honeywell International Inc., for the U.S. Department of Energy's National Nuclear Security Administration under contract DE-NA-0003525. We would like to acknowledge Eric Lundin at Sandia for help creating and editing graphics included in this manuscript. This paper describes objective technical results and analysis. Any subjective views or opinions that might be expressed in the paper do not necessarily represent the views of the U.S. Department of Energy or the United States Government. Y.-S.J. is grateful for the support received from the U.S. National Science Foundation's Environmental Chemical Sciences program (CHE-1905077), the American Chemical Society's Petroleum Research Fund (62756-ND5), and the U.S. Department of Energy Office of Science (DE-SC0023390). N.K. acknowledges support from the U.S. Department of Energy, Office of Science, Office of Basic Energy Sciences, Chemical Sciences, Geosciences, and Biosciences Division (Geosciences Program) under award number DE-SC0012186. K.M.R. acknowledges support from the U.S. Department of Energy, Office of Basic Energy Sciences, Chemical Sciences, Geosciences, and Biosciences Division through its Geosciences program at Pacific Northwest National Laboratory (FWP #56674). G.R. was supported by the U.S. Department of Energy, Office of Science, Office of Basic Energy Sciences, Chemical Sciences, Geosciences and Biosciences Division. M.V. acknowledges the financial support of CONACyT through project 2016-CB 283416, as well as to the LANGEM, Geology Institute, UNAM. M.S. acknowledges funding by the Deutsche Forschungsgemeinschaft (DFG, German Research Foundation) under Germany's Excellence Strategy-EXC 2033-390677874-RESOLV. We all appreciate Prof. James C. Ballard's careful review of the entire article and acknowledge the McKelvey School of Engineering at Washington University in St. Louis for editorial support. We also thank Gabrial Goldner (Georgia State University) for her immense help with cataloguing, organizing, and inserting the many references into the manuscript. We also gratefully acknowledge Drs. Louise Criscenti and Kevin Leung at Sandia for technical review of this manuscript prior to submission and Andrea Heacock-Reyes at Sandia for copy editing portions in this manuscript.

DEDICATION

We dedicate this review to Prof. William L. Hase (Department of Chemistry and Biochemistry, Texas Tech University), Founding President of the Mesilla Chemistry Workshop, Inc., who passed away shortly after the 2020 Mesilla Chemistry Workshop on Aqueous Solution/Oxide Interfaces.

ABBREVIATIONS AND SYMBOLS

Symbols

α = interfacial energy
$\alpha^{(2)}$ = hyperpolarizability
r_{diss} = dissolution rate
$\Delta\mu$ = chemical potential, equal to $k_B T \ln \sigma$
σ = supersaturation (degree of saturation = IAP/K_{sp})
σ_H = proton related surface charge density
σ_o = surface charge density in the plane of the inner surface potential
$\sigma_{o,H}$ = proton related surface charge density in the plane of the inner surface potential
υ_m = molecular volume of the nucleating phase
ϖ = angular frequency (no definition in text)
λ = electron transfer reorganization energy
ζ = zeta potential
$\chi^{(2)}$ = second-order susceptibility
$\chi^{(3)}$ = third-order susceptibility
Ψ_d or Φ_d = diffuse layer potential
Ψ_o or Φ_0 = inner surface potential
Φ_{OHP} = potential at the outer Helmholtz plane
A = Arrhenius pre-exponential kinetic factor
a_{CL} = condensate−liquid interface
a_{SC} = substrate−condensate interface
a_{SL} = substrate−liquid interface
a_{eff} = effective interfacial energy
df/dz = force gradient
ΔE_a = activation energy
ΔG = Gibbs free energy change
ΔG^* = thermodynamic barrier
ΔG_{nuc} = thermodynamic barrier to nucleation
I = ionic strength
IAP = ion activity product

https://doi.org/10.1021/acs.chemrev.2c00130
Chem. Rev. 2023, 123, 6413−6544

k = rate constant
k_B = Boltzmann constant
K_{sp} = solubility product
J = nucleation rate
J_0 = kinetic factor
pH_o = pH of zero surface potential
pK_a = −log acidity constant
Q = the reaction quotient
Q_C = transition state configuration
r_c = critical nucleus size
R = the universal gas constant
T = temperature
V_{AB} = electronic coupling matrix element

Properties, Materials, and Processes

AAO = anodic aluminum oxide
am-SiO_2 = amorphous silica
BIL = bonded interfacial layer
BM = bidentate mononuclear complex
BSA = bovine serum albumin
CCN = cloud condensation nuclei
CCS = carbon capture and storage
CFC = crystal face contribution
CIP = ciprofloxacin
CPA = crystallization by particle attachment
dAMP = deoxyadenosine monophosphate
DCC = deep convective cloud
DFO-B = desferroxamine-B
DL = diffuse layer
DLP = dense liquid phase
DMA = dimethyl arsenate
EDL = electrical double layer
EPS = extracellular polymeric substances
ET = electron transfer
ETM = electron-transporting materials
FA = fulvic acid
GCS = geologic CO_2 sequestration
IN = ice nuclei
MM = monodentate mononuclear
I = ionic strength
IAP = ion activity product
IEP = isoelectric point
iAs = inorganic arsenate
LDH = layered double hydroxide
NOM = natural organic matter
OA = oriented attachment
OHP = outer Helmholtz plane
PBL = planetary boundary layer
PDB = principle of detailed balancing
PFAS = polyfluoroalkyl substances
pH_{PZC} = pH at the point of zero charge
PM = particulate matter
PSC = perovskite solar cell
PTE = potentially toxic elements
PZC = point-of-zero charge
Q^2 = $(SiO_4)^{4-}$ group bonded to two bridging oxygens
Q^3 = $(SiO_4)^{4-}$ group bonded to three bridging oxygens
RH = relative humidity
REE = rare earth element
RF = radiative forcing
R_g = radius of gyration
ROS = reactive oxygen species
SAL = surface alteration layer
SAM = self-assembled monolayer
$scCO_2$ = supercritical carbon dioxide
SS, SC, DC, TC = surface sites, singly-, doubly-, and triply-coordinated
TDS = total dissolved solids
TST = transition state theory

Techniques and Equations

2DCOS = two-dimensional correlation spectroscopy
AET = atom electron tomography
AFM = atomic force microscopy
AIMD = *ab initio* molecular dynamics
APT = atom probe tomography
APXPS = ambient pressure X-ray photoelectron spectroscopy
ATR FTIR = attenuated total reflectance Fourier transform infrared
BET = Brunauer−Emmett−Teller surface area measurement
CD-MUSIC = charge distribution multisite complexation
CLAYFF = a classical force field for mineral−water systems
CMD = classical molecular dynamics
CNT = classical nucleation theory
CT = computed tomography
CTR = crystal truncation rod
cwODNP NMR = continuous wave Overhauser effect dynamic nuclear polarization nuclear magnetic resonance spectroscopy
DFS = dynamic force spectroscopy
DFT = density functional theory
DLVO = Derjaguin−Landau−Verwey−Overbeek
DOSY NMR = diffusion-ordered nuclear magnetic resonance spectroscopy
EFC = eutectic freeze crystallization
EXAFS = extended X-ray adsorption fine structure
FFM = fast force mapping
FTIR = Fourier transform infrared
FT-ICR-MS = Fourier transform ion cyclotron resonance mass spectrometry
GGA = generalized-gradient approximation
GISAXS = grazing-incidence small angle X-ray scattering
GI-XAFS = grazing-incidence X-ray absorption fine structure spectroscopy
H/DX = hydrogen−deuterium exchange
HPRO = high pressure reverse osmosis
INS = inelastic neutron scattering
INTERFACE = a classical force field for mineral−water systems
IR = infrared
ISFETs = ion-sensitive field-effect transistors
LEED = low-energy electron diffraction
LP-XSW-FY = long-period X-ray standing wave fluorescence yield
MAR = managed aquifer recharge
MC = Monte Carlo
MC-ICP-MS = multicollector inductively coupled plasma mass spectrometry
MD = molecular dynamics
ML = machine learning
MLL = multilayer Laue lenses
MO = molecular orbital
MUSIC = multisite complexation
NLO = nonlinear optics

https://doi.org/10.1021/acs.chemrev.2c00130
Chem. Rev. 2023, 123, 6413−6544

NMR = nuclear magnetic resonance
NSE = neutron spin echo
OARO = osmotically assisted reverse osmosis
PDB = principle of detailed balancing
PFG NMR = pulsed-field gradient nuclear magnetic resonance
PSI = phase shift interferometry
QCM = quartz crystal microbalance
QENS = quasielastic neutron scattering
QEXAFS = quick extended X-ray adsorption fine structure
RAXR = resonant anomalous X-ray reflectivity
RS = Robinson−Stokes equation
SAXS = small-angle X-ray scattering
SCAN = strongly constrained and appropriately normed
SCM = surface complexation model
SEM = scanning electron microscopy
SFG = sum frequency generation
SHG = second harmonic generation
SIT = specific ion interaction theory
SNOM = scanning near-field optical microscope
STA = solvent tip approximation
STEM HAADF = scanning transmission electron microscopy using high-angle annular dark-field imaging
SWAPPS = standing wave ambient pressure photoelectron spectroscopy
SWAT = soil and water assessment tool
TEM = transmission electron microscopy
TOF SIMS = time-of-flight secondary-ion mass spectrometry
TRLFS = time-resolved laser-induced fluorescence spectroscopy
TST = transition state theory
UHV = ultra-high vacuum
VSI = vertical scanning interferometry
XPS = X-ray photoelectron spectroscopy
XPCS = X-ray photon correlation spectroscopy
XRF = X-ray fluorescence
XANES = X-ray adsorption near-edge spectroscopy
XRR = X-ray reflectivity

REFERENCES

(1) Langmuir, I. The Constitution and Fundamental Properties of Solids and Liquids. Part I. Solids. *J. Am. Chem. Soc.* **1916**, *38* (11), 2221−2295.
(2) Stumm, W. *Chemistry of the Solid−Water Interface: Processes at the Mineral−Water and Particle−Water Interface in Natural Systems*; Wiley, 1992; 448 pp.
(3) Brown, G. E.; Henrich, V. E.; Casey, W. H.; Clark, D. L.; Eggleston, C.; Felmy, A.; Goodman, D. W.; Grätzel, M.; Maciel, G.; McCarthy, M. I.; et al. Metal Oxide Surfaces and Their Interactions with Aqueous Solutions and Microbial Organisms. *Chem. Rev.* **1999**, *99*, 77−174.
(4) Kendelewicz, T.; Liu, P.; Doyle, C. S.; Brown, G. E.; Nelson, E. J.; Chambers, S. A. X-Ray Absorption and Photoemission Study of The Adsorption of Aqueous Cr(VI) on Single Crystal Hematite and Magnetite Surfaces. *Surf. Sci.* **1999**, *424*, 219−231.
(5) Liu, P.; Kendelewicz, T.; Brown, G. E.; Nelson, E. J.; Chambers, S. A. Reaction of Water Vapor with a-Al2O3(0001) and α-Fe2O3(0001) Surfaces: Synchrotron X-Ray Photoemission Studies and Thermodynamic Calculations. *Surf. Sci.* **1998**, *417* (1), 53−65.
(6) Bluhm, H.; Andersson, K.; Araki, T.; Benzerara, K.; Brown, G. E.; Dynes, J. J.; Ghosal, S.; Gilles, M. K.; Hansen, H. C.; Hemminger, J. C.; et al. Soft X-Ray Microscopy and Spectroscopy at the Molecular Environmental Science Beamline at the Advanced Light Source. *J. Electron Spectrosc.* **2006**, *150* (2), 86−104.
(7) Yamamoto, S.; Kendelewicz, T.; Newberg, J. T.; Ketteler, G.; Starr, D. E.; Mysak, E. R.; Andersson, K. J.; Ogasawara, H.; Bluhm, H.; Salmeron, M.; et al. Water Adsorption on α-Fe2O3 (**0001**) at Near Ambient Conditions. *J. Phys. Chem. C* **2010**, *114* (5), 2256−2266.
(8) Friebel, D.; Louie, M. W.; Bajdich, M.; Sanwald, K. E.; Cai, Y.; Wise, A. M.; Cheng, M.-J.; Sokaras, D.; Weng, T.-C.; Alonso-Mori, R.; et al. Identification of Highly Active Fe Sites in (Ni,Fe)OOH for Electrocatalytic Water Splitting. *J. Am. Chem. Soc.* **2015**, *137* (3), 1305−1313.
(9) Huang, Z.; He, D.; Deng, W.; Jin, G.; Li, K.; Luo, Y. Illustrating New Understanding of Adsorbed Water on Silica for Inducing Tetrahedral Cobalt(II) for Propane Dehydrogenation. *Nat. Commun.* **2023**, *14* (1), 100.
(10) Wang, R.; Klein, M. L.; Carnevale, V.; Borguet, E. Investigations of Water/Oxide Interfaces by Molecular Dynamics Simulations. *WIREs Comput. Mol. Sci.* **2021**, *11* (6), No. e1537.
(11) Tuladhar, A.; Dewan, S.; Pezzotti, S.; Brigiano, F. S.; Creazzo, F.; Gaigeot, M. P.; Borguet, E. Ions Tune Interfacial Water Structure and Modulate Hydrophobic Interactions at Silica Surfaces. *J. Am. Chem. Soc.* **2020**, *142* (15), 6991−7000.
(12) Ridley, M. K.; Machesky, M. L.; Kubicki, J. D. Anatase Nanoparticle Surface Reactivity in NaCl Media: A CD-MUSIC Model Interpretation of Combined Experimental and Density Functional Theory Studies. *Langmuir* **2013**, *29* (27), 8572−8583.
(13) Soldoozy, S.; Trinh, A.; Kubicki, J. D.; Al-Abadleh, H. A. In Situ and Real-Time ATR-FTIR Temperature-Dependent Adsorption Kinetics Coupled with DFT Calculations of Dimethylarsinate and Arsenate on Hematite Nanoparticles. *Langmuir* **2020**, *36* (16), 4299−4307.
(14) Kubicki, J. D.; Tunega, D.; Kraemer, S. A Density Functional Theory Investigation of Oxalate and Fe(II) Adsorption onto the (010) Goethite Surface with Implications for Ligand- and Reduction-Promoted Dissolution. *Chem. Geol.* **2017**, *464*, 14−22.
(15) Stubbs, J. E.; Legg, B. A.; Lee, S. S.; Dera, P.; De Yoreo, J. J.; Fenter, P.; Eng, P. J. Epitaxial Growth of Gibbsite Sheets on the Basal Surface of Muscovite Mica. *J. Phys. Chem. C* **2019**, *123* (45), 27615−27627.
(16) Hayes, K. F.; Roe, A. L.; Brown, G. E.; Hodgson, K. O.; Leckie, J. O.; Parks, G. A. In Situ X-ray Absorption Study of Surface Complexes: Selenium Oxyanions on α-FeOOH. *Science* **1987**, *238* (4828), 783−786.
(17) Kinniburgh, D. G.; Smedley, P. L. *Arsenic Contamination of Groundwater in Bangladesh; Summary*; BGS Technical Report WC/00/19; British Geological Survey, Department for International Development, 2001; Vol. *1*
(18) *SciTechDaily*; "Arsenic Contamination in Groundwater Influenced by Natural Organic Matter"; American Chemical Society, Ed., 2020.
(19) Abdlmutalib, A.; Abdullatif, O.; Alqubalee, A.; Gonzalez, L.; Humphrey, J. Effects of Lithofacies on Pore System Evolution of Storm-Wave Silt-Rich Fine-Grained Sediments. Early Silurian Qusaiba Member (Qaliba Formation), NW Saudi Arabia. *Marine and Petroleum Geology* **2021**, *128*, 105048.
(20) Neil, C. W.; Lee, B.; Jun, Y.-S. Different Arsenate and Phosphate Incorporation Effects on the Nucleation and Growth of Iron(III) (Hydr)oxides on Quartz. *Environ. Sci. Technol.* **2014**, *48* (20), 11883−11891.
(21) Livi, K. J. T.; Villalobos, M.; Leary, R.; Varela, M.; Barnard, J.; Villacis-Garcia, M.; Zanella, R.; Goodridge, A.; Midgley, P. Crystal Face Distributions and Surface Site Densities of Two Synthetic Goethites: Implications for Adsorption Capacities as a Function of Particle Size. *Langmuir* **2017**, *33* (36), 8924−8932.
(22) Watts, H. D.; Tribe, L.; Kubicki, J. D. Arsenic Adsorption onto Minerals: Connecting Experimental Observations with Density Functional Theory Calculations. *Minerals* **2014**, *4* (2), 208−240.
(23) *UNESCO World Water Assessment Programme, The United Nations World Water Development Report 2018*; United Nations Educational, Scientific and Cultural Organization, New York, 2018.

https://doi.org/10.1021/acs.chemrev.2c00130
Chem. Rev. 2023, 123, 6413−6544

(24) Wan, B.; Yang, P.; Jung, H.; Zhu, M. Q.; Diaz, J. M.; Tang, Y. Z. Iron Oxides Catalyze the Hydrolysis of Polyphosphate and Precipitation of Calcium Phosphate Minerals. *Geochim. Cosmochim. Acta* **2021**, *305*, 49−65.
(25) Neil, C. W.; Yang, J.; Jun, Y. S. Arsenic Mobilization and Attenuation by Mineral−Water Interactions: Implications for Managed Aquifer Recharge. *J. Environ. Monit.* **2012**, *14*, 1772−1788.
(26) Neil, C. W.; Yang, Y. J.; Schupp, D.; Jun, Y. S. Water Chemistry Impacts on Arsenic Mobilization from Arsenopyrite Dissolution and Secondary Mineral Precipitation: Implications for Managed Aquifer Recharge. *Environ. Sci. Technol.* **2014**, *48* (8), 4395−4405.
(27) Wu, X.; Burnell, S.; Neil, C. W.; Kim, D.; Zhang, L.; Jung, H.; Jun, Y.-S. Effects of Phosphate, Silicate, and Bicarbonate on Arsenopyrite Dissolution and Secondary Mineral Precipitation. *ACS Earth Space Chem.* **2020**, *4* (4), 515−525.
(28) Neil, C. W.; Jun, Y. S. Fe^{3+} Addition Promotes Arsenopyrite Dissolution and Iron(III) (Hydr)oxide Formation and Phase Transformation. *Environ. Sci. Technol. Lett.* **2016**, *3* (1), 30−35.
(29) Wu, X.; Bowers, B.; Kim, D.; Lee, B.; Jun, Y.-S. Dissolved Organic Matter Affects Arsenic Mobility and Iron(III) (hydr)oxide Formation: Implications for Managed Aquifer Recharge. *Environ. Sci. Technol.* **2019**, *53* (24), 14357−14367.
(30) Zhang, H.; Xu, Y.; Kanyerere, T. A Review of the Managed Aquifer Recharge: Historical Development, Current Situation and Perspectives. *Phys. Chem. Earth* **2020**, *118-119*, 102887.
(31) Zhu, C.; Rimstidt, J. D.; Zhang, Y.; Kang, J.; Schott, J.; Yuan, H. Decoupling Feldspar Dissolution and Precipitation Rates at Near-Equilibrium with Si Isotope Tracers: Implications for Modeling Silicate Weathering. *Geochim. Cosmochim. Acta* **2020**, *271*, 132−153.
(32) Ofori, S.; Puskacova, A.; Ruzickova, I.; Wanner, J. Treated Wastewater Reuse for Irrigation: Pros and Cons. *Sci. Total Environ.* **2021**, *760*, 144026.
(33) Abdalrahman, G. A. M.; Lai, S. H.; Snounu, I.; Kumar, P.; Sefelnasr, A.; Sherif, M.; El-shafie, A. Review on Wastewater Treatment Ponds Clogging Under Artificial Recharge: Impacting Factors and Future Modelling. *J. Water Process Eng.* **2021**, *40*, 101848.
(34) Freeze, A.; Cherry, J. *Groundwater*; Prentice-Hall, 1979.
(35) Zarai, B.; Walter, C.; Michot, D.; Montoroi, J. P.; Hachicha, M. Soil Salinization Monitoring Method Evolution at Various Spatial and Temporal Scales in Arid Context: A Review. *Arabian J. Geosci.* **2021**, *14*, 283.
(36) Singh, A. Soil Salinization Management for Sustainable Development: A Review. *J. Environ. Manage.* **2021**, *277*, 111383.
(37) Ondrasek, G.; Rengel, Z. Environmental Salinization Processes: Detection, Implications & Solutions. *Sci. Total Environ.* **2021**, *754*, 142432.
(38) WHO Fact Sheet on Infertility. *Global Reproductive Health* **2021**; *6*, e52.
(39) Omoike, A.; Chorover, J.; Kwon, K. D.; Kubicki, J. D. Adhesion of Bacterial Exopolymers to Alpha-Feooh: Inner-Sphere Complexation of Phosphodiester Groups. *Langmuir* **2004**, *20* (25), 11108−11114.
(40) Parikh, S. J.; Chorover, J. ATR-FTIR Spectroscopy Reveals Bond Formation During Bacterial Adhesion to Iron Oxide. *Langmuir* **2006**, *22* (20), 8492−8500.
(41) Ryan, J. N.; Elimelech, M.; Ard, R. A.; Harvey, R. W.; Johnson, P. R. Bacteriophage PRD1 and Silica Colloid Transport and Recovery in an Iron Oxide-Coated Sand Aquifer. *Environ. Sci. Technol.* **1999**, *33* (1), 63−73.
(42) Scholl, M. A.; Harvey, R. W. Laboratory Investigations on the Role of Sediment Surface and Groundwater Chemistry in Transport of Bacteria Through a Contaminated Sandy Aquifer. *Environ. Sci. Technol.* **1992**, *26* (7), 1410−1417.
(43) Liu, Z. D.; Li, J. Y.; Hong, Z. N.; Xu, R. K. Effect of Fe/Al Hydroxides on Transport and Retention of Escherichia coli in Saturated Sand Media. *Geomicrobiol. J.* **2017**, *34* (10), 881−888.
(44) Mehrabi, M.; Ghasemi, M. F.; Rasti, B.; Falahati, M.; Mirzaie, A.; Hasan, A. Nanoporous Iron Oxide Nanoparticle: Hydrothermal Fabrication, Human Serum Albumin Interaction and Potential Antibacterial Effects. *J. Biomol. Struct. Dyn.* **2021**, *39* (7), 2595−2606.
(45) Kwon, K. D.; Green, H.; Bjoorn, P.; Kubicki, J. D. Model Bacterial Extracellular Polysaccharide Adsorption onto Silica and Alumina: Quartz Crystal Microbalance with Dissipation Monitoring of Dextran Adsorption. *Environ. Sci. Technol.* **2006**, *40* (24), 7739−7744.
(46) Rosso, K. M.; Zachara, J. M.; Fredrickson, J. K.; Gorby, Y. A.; Smith, S. C. Nonlocal Bacterial Electron Transfer to Hematite Surfaces. *Geochim. Cosmochim. Acta* **2003**, *67*, 1081−1087.
(47) WHO Fact Sheet on Infertility. *Global Reproductive Health*, **2021**, *6*, e52.
(48) Ravenscroft, P.; Brammer, H.; Richards, K. *Arsenic Pollution: A Global Synthesis*; Wiley-Blackwell, 2009.
(49) Polizzotto, M. L.; Harvey, C. F.; Li, G. C.; Badruzzman, B.; Ali, A.; Newville, M.; Sutton, S.; Fendorf, S. Solid-phases and Desorption Processes of Arsenic Within Bangladesh Sediments. *Chem. Geol.* **2006**, *228* (1-3), 97−111.
(50) Raessler, M. The Arsenic Contamination of Drinking and Groundwaters in Bangladesh: Featuring Biogeochemical Aspects and Implications on Public Health. *Arch. Environ. Con. Tox.* **2018**, *75* (1), 1−7.
(51) Waychunas, G.; Trainor, T.; Eng, P.; Catalano, J.; Brown, G.; Davis, J.; Rogers, J.; Bargar, J. Surface Complexation Studied Via Combined Grazing-Incidence EXAFS and Surface Diffraction: Arsenate on Hematite (0001) and (10-12). *Anal. Bioanal. Chem.* **2005**, *383* (1), 12−27.
(52) Kubicki, J. D. In *Advances in Arsenic Research: Integration of Experimental and Observational Studies and Implications for Mitigation*; ACS Symposium Series, Vol. 915; O'Day, P. A., Vlassopoulos, D., Meng, Z., Benning, L. G., Eds.; American Chemical Society, 2005; Vol. *915*.
(53) Bargar, J. R.; Kubicki, J. D.; Reitmeyer, R.; Davis, J. A. ATR-FTIR Spectroscopic Characterization of Coexisting Carbonate Surface Complexes on Hematite. *Geochim. Cosmochim. Acta* **2005**, *69* (6), 1527.
(54) Mukherjee, S.; Kumar, A. A.; Sudhakar, C.; Kumar, R.; Ahuja, T.; Mondal, B.; Srikrishnarka, P.; Philip, L.; Pradeep, T. Sustainable and Affordable Composites Built Using Microstructures Performing Better than Nanostructures for Arsenic Removal. *ACS Sustain. Chem. Eng.* **2019**, *7* (3), 3222−3233.
(55) Sudhakar, C.; Kumar, A. A.; Bhuin, R. G.; Sen Gupta, S. S.; Natarajan, G.; Pradeep, T. Species-Specific Uptake of Arsenic on Confined Metastable 2-Line Ferrihydrite: A Combined Raman-X-Ray Photoelectron Spectroscopy Investigation of the Adsorption Mechanism. *ACS Sustain. Chem. Eng.* **2018**, *6* (8), 9990−10000.
(56) Luo, J. M.; Yu, D. Y.; Hristovski, K. D.; Fu, K. X.; Shen, Y. W.; Westerhoff, P.; Crittenden, J. C. Critical Review of Advances in Engineering Nanomaterial Adsorbents for Metal Removal and Recovery from Water: Mechanism Identification and Engineering Design. *Environ. Sci. Technol.* **2021**, *55* (8), 4287−4304.
(57) Altieri, M. A.; Nicholls, C. I.; Henao, A.; Lana, M. A. Agroecology and the Design of Climate Change-Resilient Farming Systems. *Agron. Sustain. Dev.* **2015**, *35* (3), 869−890.
(58) Lavinsky, A. O.; Detmann, K. C.; Reis, J. V.; Avila, R. T.; Sanglard, M. L.; Pereira, L. F.; Sanglard, L.; Rodrigues, F. A.; Araujo, W. L.; DaMatta, F. M. Silicon Improves Rice Grain Yield and Photosynthesis Specifically when Supplied During the Reproductive Growth Stage. *J. Plant Physiol.* **2016**, *206*, 125−132.
(59) Coskun, D.; Deshmukh, R.; Shivaraj, S. M.; Isenring, P.; Bélanger, R. R. Lsi2: A Black Box in Plant Silicon Transport. *Plant Soil* **2021**, *466* (1), 1−20.
(60) Ye, Y. Q.; Medina-Velo, I. A.; Cota-Ruiz, K.; Moreno-Olivas, F.; Gardea-Torresdey, J. L. Can Abiotic Stresses in Plants be Alleviated by Manganese Nanoparticles or Compounds? *Ecotox. Environ. Safe.* **2019**, *184*, 109671.
(61) Dimkpa, C. O.; Andrews, J.; Fugice, J.; Singh, U.; Bindraban, P. S.; Elmer, W. H.; Gardea-Torresdey, J. L.; White, J. C. Facile Coating of Urea with Low-Dose ZnO Nanoparticles Promotes Wheat

https://doi.org/10.1021/acs.chemrev.2c00130
Chem. Rev. 2023, 123, 6413−6544

Performance and Enhances Zn Uptake Under Drought Stress. *Front. Plant Sci.* **2020**, *11*, 108.
(62) Adisa, I. O.; Rawat, S.; Pullagurala, V. L. R.; Dimkpa, C. O.; Elmer, W. H.; White, J. C.; Hernandez-Viezcas, J. A.; Peralta-Videa, J. R.; Gardea-Torresdey, J. L. Nutritional Status of Tomato (Solanum lycopersicum) Fruit Grown in Fusarium-Infested Soil: Impact of Cerium Oxide Nanoparticles. *J. Agr. Food Chem.* **2020**, *68* (7), 1986−1997.
(63) Shen, Z. L.; Zhang, Z. H.; Li, T.; Yao, Q. Q.; Zhang, T.; Chen, W. Facet-Dependent Adsorption and Fractionation of Natural Organic Matter on Crystalline Metal Oxide Nanoparticles. *Environ. Sci. Technol.* **2020**, *54* (14), 8622−8631.
(64) Yang, M.; Ren, X. H.; Hu, L. X.; Zhou, H. H.; Guo, W. L. Insights into the Facet-Dependent Adsorption of Antibiotic Ciprofloxacin On Goethite. *Environ. Sci. Pollut. R.* **2021**, *28* (9), 11486−11497.
(65) Wang, L.; Putnis, C. V. Dissolution and Precipitation Dynamics at Environmental Mineral Interfaces Imaged by In Situ Atomic Force Microscopy. *Acc. Chem. Res.* **2020**, *53* (6), 1196−1205.
(66) Hu, S. W.; Wu, Y. D.; Li, F. B.; Shi, Z. Q.; Ma, C.; Liu, T. X. Fulvic Acid-Mediated Interfacial Reactions on Exposed Hematite Facets During Dissimilatory Iron Reduction. *Langmuir* **2021**, *37* (20), 6139−6150.
(67) Adair, J. H.; Suvaci, E. Morphological Control of Particles. *Curr. Opin. Colloid In.* **2000**, *5* (1-2), 160−167.
(68) Liu, C.; Chen, R.; Sera, F.; Vicedo-Cabrera, A. M.; Guo, Y. M.; Tong, S. L.; Coelho, M.; Saldiva, P. H. N.; Lavigne, E.; Matus, P.; et al. Ambient Particulate Air Pollution and Daily Mortality in 652 Cities. *New Engl. J. Med.* **2019**, *381* (8), 705−715.
(69) Burnett, R.; Chen, H.; Szyszkowicz, M.; Fann, N.; Hubbell, B.; Pope, C. A.; Apte, J. S.; Brauer, M.; Cohen, A.; Weichenthal, S.; et al. Global Estimates of Mortality Associated with Long-Term Exposure to Outdoor Fine Particulate Matter. *Proc. Natl. Acad. Sci. U.S.A.* **2018**, *115* (38), 9592−9597.
(70) Guthrie, G. B. T., Mossman, E., Eds.; *Health Effects of Mineral Dust*; Mineralogical Society of America. 1993; Vol. *28*, 584 pp.
(71) Li, W. J.; Shao, L. Y.; Zhang, D. Z.; Ro, C. U.; Hu, M.; Bi, X. H.; Geng, H.; Matsuki, A.; Niu, H. Y.; Chen, J. M. A Review of Single Aerosol Particle Studies in the Atmosphere of East Asia: Morphology, Mixing State, Source, and Heterogeneous Reactions. *J. Clean. Prod.* **2016**, *112*, 1330−1349.
(72) Fubini, B.; Hubbard, A. Reactive Oxygen Species (ROS) and Reactive Nitrogen Species (RNS) Generation by Silica in Inflammation and Fibrosis. *Free Radic. Biol. Med.* **2003**, *34* (12), 1507−1516.
(73) Maher, B. A.; Ahmed, I. A. M.; Karloukovski, V.; MacLaren, D. A.; Foulds, P. G.; Allsop, D.; Mann, D. M. A.; Torres-Jardon, R.; Calderon-Garciduenas, L. Magnetite Pollution Nanoparticles in the Human Brain. *Proc. Natl. Acad. Sci. U.S.A.* **2016**, *113* (39), 10797−10801.
(74) Li, R. S.; Yang, J. P.; Saffari, A.; Jacobs, J.; Baek, K. I.; Hough, G.; Larauche, M. H.; Ma, J. G.; Jen, N.; Moussaoui, N. Ambient Ultrafine Particle Ingestion Alters Gut Microbiota in Association with Increased Atherogenic Lipid Metabolites. *Sci. Rep.* **2017**, *7*, 42906.
(75) *USIEA International Energy Outlook 2019 with Projections to 2050*; U.S. Department of Energy, 2019.
(76) Barry, E.; Burns, R.; Chen, W.; De Hoe, G. X.; De Oca, J. M. M.; de Pablo, J. J.; Dombrowski, J.; Elam, J. W.; Felts, A. M.; Galli, G.; et al. Advanced Materials for Energy-Water Systems: The Central Role of Water/Solid Interfaces in Adsorption, Reactivity, and Transport. *Chem. Rev.* **2021**, *121* (15), 9450−9501.
(77) van Exter, P.; Bosch, S.; Schipper, B.; Sprecher, B.; Kleijn, R. *Metal Demand for Renewable Electricity Generation in The Netherlands: Navigating a Complex Supply Chain*; Report for Springtij Forum; Colophon, 2018.
(78) Levett, A.; Gleeson, S. A.; Kallmeyer, J. From Exploration to Remediation: A Microbial Perspective for Innovation in Mining. *Earth Sci. Rev.* **2021**, *216*, 103563.
(79) Manz, K. E.; Palomino, A. M.; Cyr, H.; Carter, K. E. Shale Particle Interactions with Organic and Inorganic Hydraulic Fracturing Additives. *Appl. Geochem.* **2021**, *127*, 104901.
(80) Kotchen, M. J.; Mansur, E. T. Reassessing the Contribution of Natural Gas to US CO_2 Emission Reductions Since 2007. *Nat. Commun.* **2016**, *7*, 10648.
(81) Jew, A. D.; Druhan, J. L.; Ihme, M.; Kovscek, A. R.; Battiato, I.; Kaszuba, J. P.; Bargar, J. R.; Brown, G. E. Chemical and Reactive Transport Processes Associated with Hydraulic Fracturing of Unconventional Oil/Gas Shales. *Chem. Rev.* **2022**, *122* (9), 9198−9263.
(82) Siddiqui, M. A. Q.; Chen, X.; Iglauer, S.; Roshan, H. A Multiscale Study on Shale Wettability: Spontaneous Imbibition Versus Contact Angle. *Water Resour. Res.* **2019**, *55* (6), 5012−5032.
(83) Zhang, L.; Kim, D.; Jun, Y.-S. The Effects of Phosphonate-Based Scale Inhibitor on Brine-Biotite Interactions Under Subsurface Conditions. *Environ. Sci. Technol.* **2018**, *52* (10), 6042−6049.
(84) Zhang, L.; Kim, Y.; Jung, H.; Wan, J.; Jun, Y.-S. Effects of Salinity-Induced Chemical Reactions on Biotite Wettability Changes Under Geologic CO2 Sequestration Conditions. *Environ. Sci. Technol. Lett.* **2016**, *3* (3), 92−97.
(85) Zhang, L.; Zhu, Y.; Wu, X.; Jun, Y.-S. Effects of Sulfate on Biotite Interfacial Reactions Under High Temperature and High CO_2 Pressure. *Phys. Chem. Chem. Phys.* **2019**, *21* (12), 6381−6390.
(86) Lu, J. M.; Mickler, P. J.; Nicot, J. P.; Choi, W.; Esch, W. L.; Darvari, R. Geochemical Interactions of Shale and Brine in Autoclave Experiments-Understanding Mineral Reactions During Hydraulic Fracturing of Marcellus And Eagle Ford Shales. *AAPG Bull.* **2017**, *101* (10), 1567−1598.
(87) Pearce, J. K.; Turner, L.; Pandey, D. Experimental and Predicted Geochemical Shale-Water Reactions: Roseneath and Murteree Shales Of The Cooper Basin. *Int. J. Coal Geol.* **2018**, *187*, 30−44.
(88) Hao, Y. Z.; Jia, X. T.; Lu, Z. W.; Lu, D. T.; Li, P. C. Water Film or Water Bridge? Influence of Self-Generated Electric Field on Coexisting Patterns of Water and Methane in Clay Nanopores. *J. Phys. Chem. C* **2019**, *123* (36), 22656−22664.
(89) Yekta, A. E.; Manceau, J. C.; Gaboreau, S.; Pichavant, M.; Audigane, P. Determination of Hydrogen-Water Relative Permeability and Capillary Pressure in Sandstone: Application to Underground Hydrogen Injection in Sedimentary Formations. *Transp. Porous Media* **2018**, *122* (2), 333−356.
(90) Jun, Y. S.; Giammar, D. E.; Werth, C. J.; Dzombak, D. A. Environmental and Geochemical Aspects of Geologic Carbon Sequestration: A Special Issue. *Environ. Sci. Technol.* **2013**, *47* (1), 1−2.
(91) Jun, Y. S.; Zhang, L.; Min, Y.; Li, Q. Nanoscale Chemical Processes Affecting Storage Capacities and Seals during Geologic CO_2 Sequestration. *Acc. Chem. Res.* **2017**, *50* (7), 1521−1529.
(92) Monasterio-Guillot, L.; Fernandez-Martinez, A.; Ruiz-Agudo, E.; Rodriguez-Navarro, C. Carbonation of Calcium-Magnesium Pyroxenes: Physical-Chemical Controls and Effects of Reaction-Driven Fracturing. *Geochim. Cosmochim. Acta* **2021**, *304*, 258−280.
(93) Fatah, A.; Bennour, Z.; Ben Mahmud, H.; Gholami, R.; Hossain, M. M. A Review on the Influence of CO_2/Shale Interaction on Shale Properties: Implications of CCS in Shales. *Energies* **2020**, *13*, 3200.
(94) DePaolo, D. J.; Cole, D. R. In *Geochemistry of Geologic CO_2 Sequestration*; DePaolo, D. J.; Cole, D. R.; Navrotsky, A.; Bourg, I. C., Eds.; Mineralogical Society of America, 2013; Vol. *77*.
(95) Kumar, A.; Shrivastava, J. P. Secondary Silicates as a Barrier to Carbon Capture and Storage in Deccan Basalt. *Acta Geol. Sin.* **2020**, *94* (3), 861−876.
(96) Rosenqvist, J.; Kilpatrick, A. D.; Yardley, B. W.; Rochelle, C. A. Alkali Feldspar Dissolution in Response to Injection of Carbon Dioxide. *Appl. Geochem.* **2019**, *109*, 104419.
(97) Wu, Y.; Li, P. The Potential of Coupled Carbon Storage and Geothermal Extraction in a CO2-Enhanced Geothermal System: A Review. *Geotherm. Energy* **2020**, *8*, 19.

https://doi.org/10.1021/acs.chemrev.2c00130
Chem. Rev. 2023, 123, 6413−6544

(98) Grey, C. P.; Hall, D. S. Prospects for Lithium-Ion Batteries and Beyond: A 2030 Vision. *Nat. Commun.* **2020**, *11*, 6279.
(99) Boyd, S.; Dhall, R.; LeBeau, J. M.; Augustyn, V. Charge Storage Mechanism and Degradation of P2-Type Sodium Transition Metal Oxides in Aqueous Electrolytes. *J. Mater. Chem. A* **2018**, *6* (44), 22266−22276.
(100) McBean, C. L.; Wang, L.; Moronta, D.; Scida, A.; Li, L. Y.; Takeuchi, E. S.; Takeuchi, K. J.; Marschilok, A. C.; Wong, S. S. Examining the Role of Anisotropic Morphology: Comparison of Free-Standing Magnetite Nanorods versus Spherical Magnetite Nanoparticles for Electrochemical Lithium-Ion Storage. *ACS Appl. Energy Mater.* **2019**, *2* (7), 4801−4812.
(101) Zhao, H. L.; Song, Z. F.; Gao, H. X.; Li, B. Q.; Hu, T.; Liu, F. Q.; Sohn, H. Y. The Structure-Directing Role of Graphene in Composites with Porous Feooh Nanorods for Li Ion Batteries. *RSC Adv.* **2020**, *10* (68), 41403−41409.
(102) Aprà, E.; Bylaska, E. J.; de Jong, W. A.; Govind, N.; Kowalski, K.; Straatsma, T. P.; Valiev, M.; van Dam, H. J. J.; Alexeev, Y.; Anchell, J.; et al. NWChem: Past, Present, and future. *J. Chem. Phys.* **2020**, *152* (18), 184102.
(103) Kim, J.; Doudrick, K. Emerging Investigator Series: Protein Adsorption and Transformation on Catalytic and Food-Grade Tio2 Nanoparticles in the Presence of Dissolved Organic Carbon. *Environ. Sci. Nano* **2019**, *6* (6), 1688−1703.
(104) Zhang, Q.; Han, P. D.; Mei, J. Interfacial Design on Graphene-Hematite Heterostructures for Enhancing Adsorption and Diffusion Towards Superior Lithium Storage. *Nanomaterials* **2021**, *11*, 81.
(105) Griffith, K. J.; Harada, Y.; Egusa, S.; Ribas, R. M.; Monteiro, R. S.; Von Dreele, R. B.; Cheetham, A. K.; Cava, R. J.; Grey, C. P.; Goodenough, J. B. Titanium Niobium Oxide: from Discovery to Application in Fast-Charging Lithium-Ion Batteries. *Chem. Mater.* **2021**, *33* (1), 4−18.
(106) Kim, Y.; Jacquet, Q.; Griffith, K. J.; Lee, J.; Dey, S.; Rinkel, B. L. D.; Grey, C. P. High Rate Lithium Ion Battery with Niobium Tungsten Oxide Anode. *J. Electrochem. Soc.* **2021**, *168*, 010525.
(107) Nousiainen, T.; Kandler, K. Light Scattering by Atmospheric Mineral Dust Particles. In *Light Scattering Reviews 9: Light Scattering and Radiative Transfer*; Kokhanovsky, A. A., Ed.; Springer: Berlin, Heidelberg, 2015; pp 3−52.
(108) Tang, M. J.; Huang, X.; Lu, K. D.; Ge, M. F.; Li, Y. J.; Cheng, P.; Zhu, T.; Ding, A. J.; Zhang, Y. H.; Gligorovski, S.; et al. Heterogeneous Reactions of Mineral Dust Aerosol: Implications for Tropospheric Oxidation Capacity. *Atmos. Chem. Phys.* **2017**, *17* (19), 11727−11777.
(109) Zaveri, R. A.; Easter, R. C.; Singh, B.; Wang, H. L.; Lu, Z.; Tilmes, S.; Emmons, L. K.; Vitt, F.; Zhang, R. D.; Liu, X. H. Development and Evaluation of Chemistry-Aerosol-Climate Model CAM5-Chem-MAM7-MOSAIC: Global Atmospheric Distribution and Radiative Effects of Nitrate Aerosol. *J. Adv. Model. Earth Syst.* **2021**, *13*, e2020MS002346.
(110) Klingmuller, K.; Karydis, V. A.; Bacer, S.; Stenchikov, G. L.; Lelieveld, J. Weaker Cooling by Aerosols Due to Dust-Pollution Interactions. *Atmos. Chem. Phys.* **2020**, *20* (23), 15285−15295.
(111) Wang, Z. L.; Huang, X.; Wang, N.; Xu, J. W.; Ding, A. J. Aerosol-Radiation Interactions of Dust Storm Deteriorate Particle and Ozone Pollution in East China. *J. Geophys. Res. Atmos.* **2020**, *125*, e2020JD033601.
(112) Zamora, L. M.; Kahn, R. A. Saharan Dust Aerosols Change Deep Convective Cloud Prevalence, Possibly by Inhibiting Marine New Particle Formation. *J. Clim.* **2020**, *33* (21), 9467−9480.
(113) Arub, Z.; Singh, G.; Habib, G.; Sunder Raman, R. Highly Significant Impact of Mineral Dust on Aerosol Hygroscopicity at New Delhi. *Atmos. Environ.* **2021**, *254*, 118375.
(114) Reddy, S. K.; Thiraux, R.; Wellen Rudd, B. A.; Lin, L.; Adel, T.; Joutsuka, T.; Geiger, F. M.; Allen, H. C.; Morita, A.; Paesani, F. Bulk Contributions Modulate the Sum-Frequency Generation Spectra of Water on Model Sea-Spray Aerosols. *Chem.* **2018**, *4* (7), 1629−1644.
(115) Eng, P. J.; Trainor, T. P.; Brown, G. E.; Waychunas, G. A.; Newville, M.; Sutton, S. R.; Rivers, M. L. Structure of the Hydrated α-Al2O3 (0001) Surface. *Science* **2000**, *288* (5468), 1029−1033.
(116) Trainor, T. P.; Chaka, A. M.; Eng, P. J.; Newville, M.; Waychunas, G. A.; Catalano, J. G.; Brown, G. E. Structure and Reactivity of the Hydrated Hematite (0001) Surface. *Surf. Sci.* **2004**, *573* (2), 204−224.
(117) Bracco, J. N.; Lee, S. S.; Stubbs, J. E.; Eng, P. J.; Heberling, F.; Fenter, P.; Stack, A. G. Hydration Structure of the Barite (001)-Water Interface: Comparison of X-ray Reflectivity with Molecular Dynamics Simulations. *J. Phys. Chem. C* **2017**, *121* (22), 12236−12248.
(118) Stumm, W.; Huang, C.; Jenkins, S. Specific Chemical Interaction Affecting the Stability of Dispersed Systems. *Croat. Chem. Acta* **1970**, *42*, 223−245.
(119) Schindler, P. W.; Fürst, B.; Dick, R.; Wolf, P. U. Ligand Properties of Surface Silanol Groups. I. Surface Complex Formation with Fe3+, Cu2+, Cd2+, and Pb2+. *J. Colloid Interface Sci.* **1976**, *55* (2), 469−475.
(120) Stumm, W.; Wehrli, B.; Wieland, E. Surface Complexation and its Impact on Geochemical Kinetics. *Croat. Chem. Acta* **1987**, *60*, 429−456.
(121) Brown, G. E. How Minerals React with Water. *Science* **2001**, *294* (5540), 67−69.
(122) Parks, G. A. The Isoelectric Points of Solid Oxides, Solid Hydroxides, and Aqueous Hydroxo Complex Systems. *Chem. Rev.* **1965**, *65* (2), 177−198.
(123) Parks, G. A. Aqueous Surface Chemistry of Oxides and Complex Oxide Minerals. In *Equilibrium Concepts in Natural Water Systems*; Advances in Chemistry; American Chemical Society, 1967; Vol. *67*, pp 121−160.
(124) Sverjensky, D. A. Zero-Point-of-Charge Prediction from Crystal Chemistry and Solvation Theory. *Geochim. Cosmochim. Acta* **1994**, *58* (14), 3123−3129.
(125) Brown, I. D. Recent Developments in the Methods and Applications of the Bond Valence Model. *Chem. Rev.* **2009**, *109* (12), 6858−6919.
(126) Koretsky, C. M.; Sverjensky, D. A.; Sahai, N. A Model of Surface Site Types on Oxide and Silicate Minerals Based on Crystal Chemistry: Implications for Site Types and Densities, Multi-Site Adsorption, Surface Infrared Spectroscopy, and Dissolution Kinetics. *Am. J. Sci.* **1998**, *298* (5), 349−438.
(127) Bellucci, F.; Lee, S. S.; Kubicki, J. D.; Bandura, A.; Zhang, Z.; Wesolowski, D. J.; Fenter, P. Rb+ Adsorption at the Quartz(101) - Aqueous Interface: Comparison of Resonant Anomalous X-Ray Reflectivity With Ab Initio Calculations. *J. Phys. Chem. C* **2015**, *119* (9), 4778−4788.
(128) Bourg, I. C.; Lee, S. S.; Fenter, P.; Tournassat, C. Stern Layer Structure and Energetics at Mica-Water Interfaces. *J. Phys. Chem. C* **2017**, *121* (17), 9402−9412.
(129) Catalano, J. G.; Fenter, P.; Park, C. Water Ordering and Surface Relaxations at the Hematite (1 1 0)-Water Interface. *Geochim. Cosmochim. Acta* **2009**, *73* (8), 2242−2251.
(130) Fenter, P.; Teng, H.; Geissbühler, P.; Hanchar, J. M.; Nagy, K. L.; Sturchio, N. C. Atomic-Scale Structure of the Orthoclase (001)-Water Interface Measured with High-Resolution X-Ray Reflectivity. *Geochim. Cosmochim. Acta* **2000**, *64* (21), 3663−3673.
(131) Fenter, P.; Cheng, L.; Park, C.; Zhang, Z.; Sturchio, N. C. Structure of the Orthoclase (001)- and (010)-Water Interfaces by High-Resolution X-Ray Reflectivity. *Geochim. Cosmochim. Acta* **2003**, *67* (22), 4267−4275.
(132) Harmon, K. J.; Chen, Y.; Bylaska, E. J.; Catalano, J. G.; Bedzyk, M. J.; Weare, J. H.; Fenter, P. Insights on the Alumina-Water Interface Structure by Direct Comparison of Density Functional Simulations with X-ray Reflectivity. *J. Phys. Chem. C* **2018**, *122* (47), 26934−26944.
(133) Lee, S. S.; Fenter, P.; Nagy, K. L.; Sturchio, N. C. Monovalent Ion Adsorption at the Muscovite (001)-Solution Interface: Relationships Among Ion Coverage and Speciation, Interfacial Water

https://doi.org/10.1021/acs.chemrev.2c00130
Chem. Rev. 2023, 123, 6413−6544

Structure, and Substrate Relaxation. *Langmuir* **2012**, *28* (23), 8637−8650.
(134) Park, C.; Fenter, P.; Zhang, Z.; Cheng, L.; Sturchio, N. C. Structure of the Fluorapatite (100)-Water Interface by High-Resolution X-Ray Reflectivity. *Am. Mineral.* **2004**, *89* (11-12), 1647−1654.
(135) Schlegel, M. L.; Nagy, K. L.; Fenter, P.; Sturchio, N. C. Structures of Quartz (1010)- and (1011)-Water Interfaces Determined by X-Ray Reflectivity and Atomic Force Microscopy of Natural Growth Surfaces. *Geochim. Cosmochim. Acta* **2002**, *66* (17), 3037−3054.
(136) Skelton, A. A.; Fenter, P.; Kubicki, J. D.; Wesolowski, D. J.; Cummings, P. T. Simulations of the Quartz(10$\bar{1}$1)/Water Interface: A Comparison of Classical Force Fields, Ab Initio Molecular Dynamics, and X-Ray Reflectivity Experiments. *J. Phys. Chem. C* **2011**, *115* (5), 2076−2088.
(137) Zhang, Z.; Fenter, P.; Cheng, L.; Sturchio, N. C.; Bedzyk, M. J.; Předota, M.; Bandura, A.; Kubicki, J. D.; Lvov, S. N.; Cummings, P. T.; et al. Ion Adsorption at the Rutile-Water Interface: Linking Molecular and Macroscopic Properties. *Langmuir* **2004**, *20* (12), 4954−4969.
(138) Petitto, S. C.; Tanwar, K. S.; Ghose, S. K.; Eng, P. J.; Trainor, T. P. Surface Structure of Magnetite (111) Under Hydrated Conditions by Crystal Truncation Rod Diffraction. *Surf. Sci.* **2010**, *604* (13-14), 1082−1093.
(139) Tanwar, K. S.; Catalano, J. G.; Petitto, S. C.; Ghose, S. K.; Eng, P. J.; Trainor, T. P. Hydrated α-Fe_2O_3(1$\bar{1}$02) Surface Structure: Role of Surface Preparation. *Surf. Sci.* **2007**, *601* (12), L59−L64.
(140) Tanwar, K. S.; Lo, C. S.; Eng, P. J.; Catalano, J. G.; Walko, D. A.; Brown, G. E.; Waychunas, G. A.; Chaka, A. M.; Trainor, T. P. Surface Diffraction Study of the Hydrated Hematite (1$\bar{1}$02) Surface. *Surf. Sci.* **2007**, *601* (2), 460−474.
(141) Ghose, S. K.; Waychunas, G. A.; Trainor, T. P.; Eng, P. J. Hydrated Goethite (α-FeOOH) (1 0 0) Interface Structure: Ordered Water and Surface Functional Groups. *Geochim. Cosmochim. Acta* **2010**, *74* (7), 1943−1953.
(142) Trainor, T. P.; Eng, P. J.; Brown, G. E.; Robinson, I. K.; De Santis, M. Crystal Truncation Rod Diffraction Study of the α-Al₂O₃ (1$\bar{1}$02) Surface. *Surf. Sci.* **2002**, *496*, 238−250.
(143) Al-Abadleh, H. A.; Grassian, V. H. Oxide Surfaces as Environmental Interfaces. *Surf. Sci. Rep.* **2003**, *52* (3), 63−161.
(144) Al-Abadleh, H. A.; Al-Hosney, H. A.; Grassian, V. H. Oxide and Carbonate Surfaces as Environmental Interfaces: The Importance of Water in Surface Composition and Surface Reactivity. *J. Mol. Catal. A: Chem.* **2005**, *228* (1), 47−54.
(145) Grassian, V. H. Surface Science of Complex Environmental Interfaces: Oxide and Carbonate Surfaces in Dynamic Equilibrium with Water Vapor. *Surf. Sci.* **2008**, *602* (18), 2955−2962.
(146) Rubasinghege, G.; Grassian, V. H. Role(s) of Adsorbed Water in the Surface Chemistry of Environmental Interfaces. *Chem. Commun.* **2013**, *49* (30), 3071−3094.
(147) Newberg, J. T.; Starr, D. E.; Yamamoto, S.; Kaya, S.; Kendelewicz, T.; Mysak, E. R.; Porsgaard, S.; Salmeron, M. B.; Brown, G. E.; Nilsson, A.; et al. Formation of Hydroxyl and Water Layers on MgO Films Studied with Ambient Pressure XPS. *Surf. Sci.* **2011**, *605* (1), 89−94.
(148) Ketteler, G.; Yamamoto, S.; Bluhm, H.; Andersson, K.; Starr, D. E.; Ogletree, D. F.; Ogasawara, H.; Nilsson, A.; Salmeron, M. The Nature of Water Nucleation Sites on TiO2(110) Surfaces Revealed by Ambient Pressure X-ray Photoelectron Spectroscopy. *J. Phys. Chem. C* **2007**, *111* (23), 8278−8282.
(149) Ogletree, D. F.; Bluhm, H.; Hebenstreit, E. D.; Salmeron, M. Photoelectron Spectroscopy Under Ambient Pressure and Temperature Conditions. *Nucl. Instrum. Methods Phys. Res., Sect. A* **2009**, *601* (1), 151−160.
(150) Rubasinghege, G.; Ogden, S.; Baltrusaitis, J.; Grassian, V. H. Heterogeneous Uptake and Adsorption of Gas-Phase Formic Acid on Oxide and Clay Particle Surfaces: The Roles of Surface Hydroxyl Groups and Adsorbed Water in Formic Acid Adsorption and the Impact of Formic Acid Adsorption on Water Uptake. *J. Phys. Chem. A* **2013**, *117* (44), 11316−11327.
(151) Al-Abadleh, H. A.; Grassian, V. H. FT-IR Study of Water Adsorption on Aluminum Oxide Surfaces. *Langmuir* **2003**, *19* (2), 341−347.
(152) Reuter, K.; Scheffler, M. Composition, Structure, and Stability of RuO2(110) as a Function of Oxygen Pressure. *Phys. Rev. B: Condens. Matter* **2001**, *65*, 035406.
(153) Asay, D. B.; Kim, S. H. Evolution of the Adsorbed Water Layer Structure on Silicon Oxide at Room Temperature. *J. Phys. Chem. B* **2005**, *109* (35), 16760−16763.
(154) Rother, G.; Gautam, S.; Liu, T.; Cole, D. R.; Busch, A.; Stack, A. G. Molecular Structure of Adsorbed Water Phases in Silica Nanopores. *J. Phys. Chem. C* **2022**, *126* (5), 2885−2895.
(155) Asay, D. B.; Barnette, A. L.; Kim, S. H. Effects of Surface Chemistry on Structure and Thermodynamics of Water Layers at Solid-Vapor Interfaces. *J. Phys. Chem. C* **2009**, *113* (6), 2128−2133.
(156) Isaienko, O.; Borguet, E. Hydrophobicity of Hydroxylated Amorphous Fused Silica Surfaces. *Langmuir* **2013**, *29* (25), 7885−7895.
(157) Schrader, A. M.; Monroe, J. I.; Sheil, R.; Dobbs, H. A.; Keller, T. J.; Li, Y.; Jain, S.; Shell, M. S.; Israelachvili, J. N.; Han, S. Surface Chemical Heterogeneity Modulates Silica Surface Hydration. *Proc. Natl. Acad. Sci. U.S.A.* **2018**, *115* (12), 2890−2895.
(158) Yeşilbaş, M.; Boily, J.-F. Particle Size Controls on Water Adsorption and Condensation Regimes at Mineral Surfaces. *Sci. Rep.* **2016**, *6*, 32136.
(159) Yalcin, S. E.; Legg, B. A.; Yeşilbaş, M.; Malvankar, N. S.; Boily, J. F. Direct Observation of Anisotropic Growth of Water Films on Minerals Driven by Defects and Surface Tension. *Sci. Adv.* **2020**, *6*, eaaz9708.
(160) Chen, L.; He, X.; Liu, H.; Qian, L.; Kim, S. H. Water Adsorption on Hydrophilic and Hydrophobic Surfaces of Silicon. *J. Phys. Chem. C* **2018**, *122* (21), 11385−11391.
(161) Sun, E. W. H.; Bourg, I. C. Molecular Dynamics Simulations of Mineral Surface Wettability by Water Versus CO2: Thin Films, Contact Angles, and Capillary Pressure in a Silica Nanopore. *J. Phys. Chem. C* **2020**, *124* (46), 25382−25395.
(162) Sulpizi, M.; Gaigeot, M.-P.; Sprik, M. The Silica-Water Interface: How the Silanols Determine the Surface Acidity and Modulate the Water Properties. *J. Chem. Theory Comput.* **2012**, *8* (3), 1037−1047.
(163) Liu, T.; Gautam, S. S.; Daemen, L. L.; Kolesnikov, A. I.; Anovitz, L. M.; Hartl, M.; Cole, D. R. Vibrational Behavior of Water Adsorbed on Forsterite (Mg2SiO4) Surfaces. *ACS Earth Space Chem.* **2020**, *4* (7), 1050−1063.
(164) Kerisit, S. Water Structure at Hematite-Water Interfaces. *Geochim. Cosmochim. Acta* **2011**, *75* (8), 2043−2061.
(165) Mamontov, E.; Vlcek, L.; Wesolowski, D. J.; Cummings, P. T.; Wang, W.; Anovitz, L. M.; Rosenqvist, J.; Brown, C. M.; Garcia Sakai, V. Dynamics and Structure of Hydration Water on Rutile and Cassiterite Nanopowders Studied by Quasielastic Neutron Scattering and Molecular Dynamics Simulations. *J. Phys. Chem. C* **2007**, *111* (11), 4328−4341.
(166) Vlcek, L.; Zhang, Z.; Machesky, M. L.; Fenter, P.; Rosenqvist, J.; Wesolowski, D. J.; Anovitz, L. M.; Predota, M.; Cummings, P. T. Electric Double Layer at Metal Oxide Surfaces: Static Properties of the Cassiterite-Water Interface. *Langmuir* **2007**, *23* (9), 4925−4937.
(167) Mamontov, E.; Vlcek, L.; Wesolowski, D. J.; Cummings, P. T.; Rosenqvist, J.; Wang, W.; Cole, D. R.; Anovitz, L. M.; Gasparovic, G. Suppression of the Dynamic Transition in Surface Water at Low Hydration Levels: A Study of Water on Rutile. *Phys. Rev. E* **2009**, *79*, 051504.
(168) Wang, H.-W.; DelloStritto, M. J.; Kumar, N.; Kolesnikov, A. I.; Kent, P. R. C.; Kubicki, J. D.; Wesolowski, D. J.; Sofo, J. O. Vibrational Density of States of Strongly H-Bonded Interfacial Water: Insights from Inelastic Neutron Scattering and Theory. *J. Phys. Chem. C* **2014**, *118* (20), 10805−10813.

https://doi.org/10.1021/acs.chemrev.2c00130
Chem. Rev. 2023, 123, 6413−6544

(169) Hatch, C. D.; Wiese, J. S.; Crane, C. C.; Harris, K. J.; Kloss, H. G.; Baltrusaitis, J. Water Adsorption on Clay Minerals as a Function of Relative Humidity: Application of BET and Freundlich Adsorption Models. *Langmuir* **2012**, *28* (3), 1790−1803.
(170) Nakouzi, E.; Stack, A. G.; Kerisit, S.; Legg, B. A.; Mundy, C. J.; Schenter, G. K.; Chun, J.; De Yoreo, J. J. Moving Beyond the Solvent-Tip Approximation to Determine Site-Specific Variations of Interfacial Water Structure Through 3D Force Microscopy. *J. Phys. Chem. C* **2021**, *125* (2), 1282−1291.
(171) Hu, X. L.; Michaelides, A. Ice Formation on Kaolinite: Lattice Match or Amphoterism? *Surf. Sci.* **2007**, *601* (23), 5378−5381.
(172) Ranea, V. A.; Carmichael, I.; Schneider, W. F. DFT Investigation of Intermediate Steps in the Hydrolysis of α-Al2O3(0001). *J. Phys. Chem. C* **2009**, *113* (6), 2149−2158.
(173) Thissen, P.; Grundmeier, G.; Wippermann, S.; Schmidt, W. G. Water Adsorption On The α -Al2O3 (0001) Surface. *Phys. Rev. B* **2009**, *80* (24), 245403.
(174) Wang, C.; Lu, H.; Wang, Z.; Xiu, P.; Zhou, B.; Zuo, G.; Wan, R.; Hu, J.; Fang, H. Stable Liquid Water Droplet on a Water Monolayer Formed at Room Temperature on Ionic Model Substrates. *Phys. Rev. Lett.* **2009**, *103* (13), 137801.
(175) Argyris, D.; Ho, T.; Cole, D. R.; Striolo, A. Molecular Dynamics Studies of Interfacial Water at the Alumina Surface. *J. Phys. Chem. C* **2011**, *115* (5), 2038−2046.
(176) Wang, R.; Zou, Y.; Remsing, R. C.; Ross, N. O.; Klein, M. L.; Carnevale, V.; Borguet, E. Superhydrophilicity of α-alumina Surfaces Results from Tight Binding of Interfacial Waters to Specific Aluminols. *J. Colloid Interface Sci.* **2022**, *628*, 943−954.
(177) Lützenkirchen, J.; Zimmermann, R.; Preočanin, T.; Filby, A.; Kupcik, T.; Küttner, D.; Abdelmonem, A.; Schild, D.; Rabung, T.; Plaschke, M.; et al. An Attempt to Explain Bimodal Behaviour of the Sapphire C-Plane Electrolyte Interface. *Adv. Colloid Interface Sci.* **2010**, *157* (1), 61−74.
(178) Gentleman, M. M.; Ruud, J. A. Role of Hydroxyls in Oxide Wettability. *Langmuir* **2010**, *26* (3), 1408−1411.
(179) Yang, J.; Wang, E. G. Water Adsorption on Hydroxylated α-Quartz (0001) Surfaces: From Monomer to Flat Bilayer. *Phys. Rev. B* **2006**, *73* (3), 035406.
(180) Pezzotti, S.; Galimberti, D. R.; Gaigeot, M.-P. 2D H-Bond Network as the Topmost Skin to the Air-Water Interface. *J. Phys. Chem. Lett.* **2017**, *8* (13), 3133−3141.
(181) Pezzotti, S.; Serva, A.; Sebastiani, F.; Brigiano, F. S.; Galimberti, D. R.; Potier, L.; Alfarano, S.; Schwaab, G.; Havenith, M.; Gaigeot, M.-P. Molecular Fingerprints of Hydrophobicity at Aqueous Interfaces from Theory and Vibrational Spectroscopies. *J. Phys. Chem. Lett.* **2021**, *12* (15), 3827−3836.
(182) Wang, C.; Zhou, B.; Xiu, P.; Fang, H. Effect of Surface Morphology on the Ordered Water Layer at Room Temperature. *J. Phys. Chem. C* **2011**, *115* (7), 3018−3024.
(183) Wang, C.; Li, J.; Fang, H. Ordered Water Monolayer at Room Temperature. *Rendiconti Lincei* **2011**, *22* (1), 5−16.
(184) Monroe, J.; Barry, M.; DeStefano, A.; Aydogan Gokturk, P.; Jiao, S.; Robinson-Brown, D.; Webber, T.; Crumlin, E.; Han, S. H.; Shell, M. S. Water Structure and Properties at Hydrophilic and Hydrophobic Surfaces. *Annu. Rev. Chem. Biomol. Eng.* **2020**, *11*, 523−557.
(185) Giovambattista, N.; Rossky, P. J.; Debenedetti, P. G. Effect of Temperature on the Structure and Phase Behavior of Water Confined by Hydrophobic, Hydrophilic, and Heterogeneous Surfaces. *J. Phys. Chem. B* **2009**, *113* (42), 13723−13734.
(186) Giovambattista, N.; Debenedetti, P. G.; Rossky, P. J. Hydration Behavior under Confinement by Nanoscale Surfaces with Patterned Hydrophobicity and Hydrophilicity. *J. Phys. Chem. C* **2007**, *111* (3), 1323−1332.
(187) Shin, S.; Willard, A. P. Characterizing Hydration Properties Based on the Orientational Structure of Interfacial Water Molecules. *J. Chem. Theory Comput.* **2018**, *14* (2), 461−465.
(188) Xi, E.; Venkateshwaran, V.; Li, L.; Rego, N.; Patel, A. J.; Garde, S. Hydrophobicity of Proteins and Nanostructured Solutes is Governed by Topographical and Chemical Context. *Proc. Natl. Acad. Sci. U.S.A.* **2017**, *114* (51), 13345.
(189) Wen, Y.-C.; Zha, S.; Liu, X.; Yang, S.; Guo, P.; Shi, G.; Fang, H.; Shen, Y. R.; Tian, C. Unveiling Microscopic Structures of Charged Water Interfaces by Surface-Specific Vibrational Spectroscopy. *Phys. Rev. Lett.* **2016**, *116* (1), 016101.
(190) Pezzotti, S.; Galimberti, D. R.; Shen, Y. R.; Gaigeot, M.-P. Structural Definition of the BIL and DL: A New Universal Methodology to Rationalize Non-Linear: χ (2)(ω) SFG Signals at Charged Interfaces, Including χ (3)(ω) Contributions. *Phys. Chem. Chem. Phys.* **2018**, *20* (7), 5190−5199.
(191) Pezzotti, S.; Galimberti, D. R.; Gaigeot, M. P. Deconvolution of BIL-SFG and DL-SFG Spectroscopic Signals Reveals Order/Disorder of Water at the Elusive Aqueous Silica Interface. *Phys. Chem. Chem. Phys.* **2019**, *21* (40), 22188−22202.
(192) Pfeiffer-Laplaud, M.; Costa, D.; Tielens, F.; Gaigeot, M. P.; Sulpizi, M. Bimodal Acidity at the Amorphous Silica/Water Interface. *J. Phys. Chem. C* **2015**, *119* (49), 27354−27362.
(193) Smirnov, K. S. Structure and Sum-Frequency Generation Spectra of Water on Neutral Hydroxylated Silica Surfaces. *Phys. Chem. Chem. Phys.* **2021**, *23* (11), 6929−6949.
(194) Kroutil, O.; Chval, Z.; Skelton, A. A.; Předota, M. Computer Simulations of Quartz (101)-Water Interface over a Range of pH Values. *J. Phys. Chem. C* **2015**, *119* (17), 9274−9286.
(195) Joutsuka, T.; Hirano, T.; Sprik, M.; Morita, A. Effect of Third-Order Susceptibility in Sum Frequency Generation Spectroscopy: Molecular Dynamics Study in Liquid Water. *Phys. Chem. Chem. Phys.* **2018**, *20*, 3040−3053.
(196) DelloStritto, M.; Piontek, S. M.; Klein, M. L.; Borguet, E. Relating Interfacial Order to Sum Frequency Generation with Ab Initio Simulations of the Aqueous Al2O3(0001) and (11(2)over-bar0) Interfaces. *J. Phys. Chem. C* **2018**, *122* (37), 21284−21294.
(197) DelloStritto, M. J.; Piontek, S. M.; Klein, M. L.; Borguet, E. Effect of Functional and Electron Correlation on the Structure and Spectroscopy of the Al2O3(001)-H2O Interface. *J. Phys. Chem. Lett.* **2019**, *10* (9), 2031−2036.
(198) Wang, R.; DelloStritto, M.; Remsing, R. C.; Carnevale, V.; Klein, M. L.; Borguet, E. Sodium Halide Adsorption and Water Structure at the α-Alumina(0001)/Water Interface. *J. Phys. Chem. C* **2019**, *123* (25), 15618−15628.
(199) Kumar, N.; Kent, P. R. C.; Bandura, A. V.; Kubicki, J. D.; Wesolowski, D. J.; Cole, D. R.; Sofo, J. O. Faster Proton Transfer Dynamics of Water On Sno2 Compared to TiO2. *J. Chem. Phys.* **2011**, *134*, 044706.
(200) Biriukov, D.; Kroutil, O.; Predota, M. Modeling of Solid-Liquid Interfaces Using Scaled Charges: Rutile (110) surfaces. *Phys. Chem. Chem. Phys.* **2018**, *20* (37), 23954−23966.
(201) Liu, L.-M.; Zhang, C.; Thornton, G.; Michaelides, A. Structure and Dynamics of Liquid Water on Rutile TiO_2 (110). *Phys. Rev. B* **2010**, *82* (16), 161415.
(202) Huang, P.; Pham, T. A.; Galli, G.; Schwegler, E. Alumina-(0001)/Water Interface: Structural Properties and Infrared Spectra from First-Principles Molecular Dynamics Simulations. *J. Phys. Chem. C* **2014**, *118* (17), 8944−8951.
(203) Calegari Andrade, M. F.; Ko, H. Y.; Car, R.; Selloni, A. Structure, Polarization, and Sum Frequency Generation Spectrum of Interfacial Water on Anatase TiO2. *J. Phys. Chem. Lett.* **2018**, *9*, 6716−6721.
(204) Hosseinpour, S.; Tang, F.; Wang, F.; Livingstone, R. A.; Schlegel, S. J.; Ohto, T.; Bonn, M.; Nagata, Y.; Backus, E. H. G. Chemisorbed and Physisorbed Water at the TiO2/Water Interface. *J. Phys. Chem. Lett.* **2017**, *8* (10), 2195−2199.
(205) Tuladhar, A.; Dewan, S.; Kubicki, J. D.; Borguet, E. Spectroscopy and Ultrafast Vibrational Dynamics of Strongly Hydrogen Bonded OH Species at the α-Al2O3(112-0)/H2O Interface. *J. Phys. Chem. C* **2016**, *120* (29), 16153−16161.
(206) Melani, G.; Nagata, Y.; Saalfrank, P. Vibrational Energy Relaxation of Interfacial OH on a Water-Covered α-Al2O3(0001)

https://doi.org/10.1021/acs.chemrev.2c00130
Chem. Rev. 2023, 123, 6413−6544

Surface: A Non-Equilibrium Ab Initio Molecular Dynamics Study. *Phys. Chem. Chem. Phys.* **2021**, *23* (13), 7714−7723.
(207) Gaigeot, M.-P.; Sprik, M.; Sulpizi, M. Oxide/water Interfaces: How the Surface Chemistry Modifies Interfacial Water Properties. *J. Phys.: Condens. Matter* **2012**, *24* (12), 124106.
(208) McGuire, J. A.; Shen, Y. R. Ultrafast Vibrational Dynamics at Water Interfaces. *Science* **2006**, *313* (5795), 1945−1948.
(209) Eftekhari-Bafrooei, A.; Borguet, E. Effect Of Surface Charge on the Vibrational Dynamics Of Interfacial Water. *J. Am. Chem. Soc.* **2009**, *131* (34), 12034−12035.
(210) Eftekhari-Bafrooei, A.; Borguet, E. Effect of Hydrogen-Bond Strength on the Vibrational Relaxation of Interfacial Water. *J. Am. Chem. Soc.* **2010**, *132* (11), 3756−3761.
(211) Eftekhari-Bafrooei, A.; Borguet, E. Effect of Electric Fields on the Ultrafast Vibrational Relaxation of Water at a Charged Solid-Liquid Interface as Probed by Vibrational Sum Frequency Generation. *J. Phys. Chem. Lett.* **2011**, *2* (12), 1353−1358.
(212) Lützenkirchen, J.; Franks, G. V.; Plaschke, M.; Zimmermann, R.; Heberling, F.; Abdelmonem, A.; Darbha, G. K.; Schild, D.; Filby, A.; Eng, P.; et al. The Surface Chemistry of Sapphire-C: A Literature Review and a Study on Various Factors Influencing its IEP. *Adv. Colloid Interface Sci.* **2018**, *251*, 1−25.
(213) Piontek, S. M.; Tuladhar, A.; Marshall, T.; Borguet, E. Monovalent and Divalent Cations at the α-Al2O3(0001)/Water Interface: How Cation Identity Affects Interfacial Ordering and Vibrational Dynamics. *J. Phys. Chem. C* **2019**, *123* (30), 18315−18324.
(214) Tuladhar, A.; Piontek, S. M.; Frazer, L.; Borguet, E. Effect of Halide Anions on the Structure and Dynamics of Water Next to an Alumina (0001) Surface. *J. Phys. Chem. C* **2018**, *122* (24), 12819−12830.
(215) Tuladhar, A.; Piontek, S. M.; Borguet, E. Insights on Interfacial Structure, Dynamics, and Proton Transfer from Ultrafast Vibrational Sum Frequency Generation Spectroscopy of the Alumina(0001)/Water Interface. *J. Phys. Chem. C* **2017**, *121* (9), 5168−5177.
(216) Lee, D.; Ahn, G.; Ryu, S. Two-Dimensional Water Diffusion at a Graphene-Silica Interface. *J. Am. Chem. Soc.* **2014**, *136* (18), 6634−6642.
(217) Agosta, L.; Dzugutov, M.; Hermansson, K. Supercooled Liquid-Like Dynamics in Water Near a Fully Hydrated Titania Surface: Decoupling of Rotational and Translational Diffusion. *J. Chem. Phys.* **2021**, *154* (9), 094708.
(218) Ni, Y.; Gruenbaum, S. M.; Skinner, J. L. Slow Hydrogen-Bond Switching Dynamics at the Water Surface Revealed by Theoretical Two-Dimensional Sum-Frequency Spectroscopy. *Proc. Natl. Acad. Sci. U.S.A.* **2013**, *110* (6), 1992−1998.
(219) von Rudorff, G. F.; Jakobsen, R.; Rosso, K. M.; Blumberger, J. Fast Interconversion of Hydrogen Bonding at the Hematite (001)-Liquid Water Interface. *J. Phys. Chem. Lett.* **2016**, *7* (7), 1155−1160.
(220) Holmboe, M.; Bourg, I. C. Molecular Dynamics Simulations of Water and Sodium Diffusion in Smectite Interlayer Nanopores as a Function of Pore Size and Temperature. *J. Phys. Chem. C* **2014**, *118* (2), 1001−1013.
(221) Greathouse, J. A.; Hart, D. B.; Bowers, G. M.; Kirkpatrick, R. J.; Cygan, R. T. Molecular Simulation of Structure and Diffusion at Smectite-Water Interfaces: Using Expanded Clay Interlayers as Model Nanopores. *J. Phys. Chem. C* **2015**, *119* (30), 17126−17136.
(222) Churakov, S. V. Mobility of Na and Cs on Montmorillonite Surface Under Partially Saturated Conditions. *Environ. Sci. Technol.* **2013**, *47* (17), 9816−9823.
(223) Brown, M. A.; Goel, A.; Abbas, Z. Effect of Electrolyte Concentration on the Stern Layer Thickness at a Charged Interface. *Angew. Chem. Int. Ed.* **2016**, *55* (11), 3790−3794.
(224) Brown, M. A.; Bossa, G. V.; May, S. Emergence of a Stern Layer from the Incorporation of Hydration Interactions into the Gouy-Chapman Model of the Electrical Double Layer. *Langmuir* **2015**, *31* (42), 11477−11483.
(225) Dewan, S.; Carnevale, V.; Bankura, A.; Eftekhari-Bafrooei, A.; Fiorin, G.; Klein, M. L.; Borguet, E. Structure of Water at Charged Interfaces: A Molecular Dynamics Study. *Langmuir* **2014**, *30* (27), 8056−8065.
(226) Crothers, A. R.; Li, C.; Radke, C. J. A Grahame Triple-Layer Model Unifies Mica Monovalent Ion Exchange, Zeta Potential, and Surface Forces. *Adv. Colloid Interface Sci.* **2021**, *288*, 102335.
(227) Sverjensky, D. Interpretation and Prediction of Triple-Layer Model Capacitances and the Structure of the Oxide-Electrolyte-Water Interface. *Geochim. Cosmochim. Acta* **2001**, *65*, 3643−3655.
(228) Nakayama, Y.; Andelman, D. Differential Capacitance of the Electric Double Layer: The Interplay Between Ion Finite Size and Dielectric Decrement. *J. Chem. Phys.* **2015**, *142* (4), 044706.
(229) Calegari Andrade, M. F.; Selloni, A. Structure of Disordered TiO2 Phases from Ab Initio Based Deep Neural Network Simulations. *Phys. Rev. Mater.* **2020**, *4*, 113803.
(230) Eckhoff, M.; Behler, J. Insights into Lithium Manganese Oxide-Water Interfaces Using Machine Learning Potentials. *J. Chem. Phys.* **2021**, *155* (24), 244703.
(231) Hellström, M.; Quaranta, V.; Behler, J. One-Dimensional Vs. Two-Dimensional Proton Transport Processes at Solid-Liquid Zinc-Oxide-Water Interfaces. *Chem. Sci.* **2019**, *10* (4), 1232−1243.
(232) Quaranta, V.; Behler, J.; Hellström, M. Structure and Dynamics of the Liquid-Water/Zinc-Oxide Interface from Machine Learning Potential Simulations. *J. Phys. Chem. C* **2019**, *123* (2), 1293−1304.
(233) Piontek, S. M.; DelloStritto, M.; Mandal, B.; Marshall, T.; Klein, M. L.; Borguet, E. Probing Heterogeneous Charge Distributions at the α-Al2O3(0001)/H2O Interface. *J. Am. Chem. Soc.* **2020**, *142* (28), 12096−12105.
(234) Lesnicki, D.; Zhang, Z.; Bonn, M.; Sulpizi, M.; Backus, E. H. G. Surface Charges at the CaF_2/Water Interface Allow Very Fast Intermolecular Vibrational-Energy Transfer. *Angew. Chem. Int. Ed.* **2020**, *59* (31), 13116−13121.
(235) Morag, J.; Dishon, M.; Sivan, U. The Governing Role of Surface Hydration in Ion Specific Adsorption to Silica: An AFM-Based Account of the Hofmeister Universality and its Reversal. *Langmuir* **2013**, *29* (21), 6317−6322.
(236) Schwierz, N.; Horinek, D.; Sivan, U.; Netz, R. R. Reversed Hofmeister Series:The Rule Rather than the Exception. *Curr. Opin. Colloid In.* **2016**, *23*, 10−18.
(237) DeWalt-Kerian, E. L.; Kim, S.; Azam, M. S.; Zeng, H.; Liu, Q.; Gibbs, J. M. pH-Dependent Inversion of Hofmeister Trends in the Water Structure of the Electrical Double Layer. *J. Phys. Chem. Lett.* **2017**, *8* (13), 2855−2861.
(238) Lutzenkirchen, J.; Preocanin, T.; Kovacevic, D.; Tomisic, V.; Lovgren, L.; Kallay, N. Potentiometric Titrations as a Tool for Surface Charge Determination. *Croat. Chem. Acta* **2012**, *85*, 391.
(239) Schindler, P.; Kamber, H. R. Die Acidität von Silanolgruppen. Vorläufige Mitteillung. *Helv. Chim. Acta* **1968**, *51* (7), 1781−1786.
(240) Sjöberg, S.; Lövgren, L. The Application of Potentiometric Techniques to Study Complexation Reactions at the Mineral/Water Interface. *Aquat. Sci.* **1993**, *55* (4), 324−335.
(241) Campen, R. K.; Pymer, A. K.; Nihonyanagi, S.; Borguet, E. Linking Surface Potential and Deprotonation in Nanoporous Silica: Second Harmonic Generation and Acid/Base Titration. *J. Phys. Chem. C* **2010**, *114* (43), 18465−18473.
(242) Lyklema, J. Colloidal Models. A Bit of History. *J. Colloid Interface Sci.* **2015**, *446*, 308−316.
(243) Bonthuis, D. J.; Horinek, D.; Bocquet, L.; Netz, R. R. Electrohydraulic Power Conversion in Planar Nanochannels. *Phys. Rev. Lett.* **2009**, *103*, 144503.
(244) Předota, M.; Machesky, M. L.; Wesolowski, D. J. Molecular Origins of the Zeta Potential. *Langmuir* **2016**, *32* (40), 10189−10198.
(245) Delgado, A. V.; González-Caballero, F.; Hunter, R. J.; Koopal, L. K.; Lyklema, J. Measurement and Interpretation of Electrokinetic Phenomena. *J. Colloid Interface Sci.* **2007**, *309* (2), 194−224.

https://doi.org/10.1021/acs.chemrev.2c00130
Chem. Rev. 2023, 123, 6413−6544

(246) Rehl, B.; Gibbs, J. M. Role of Ions on the Surface-Bound Water Structure at the Silica/Water Interface: Identifying the Spectral Signature of Stability. *J. Phys. Chem. Lett.* **2021**, *12* (11), 2854−2864.
(247) Darlington, A. M.; Jarisz, T. A.; DeWalt-Kerian, E. L.; Roy, S.; Kim, S.; Azam, M. S.; Hore, D. K.; Gibbs, J. M. Separating the pH-Dependent Behavior of Water in the Stern and Diffuse Layers with Varying Salt Concentration. *J. Phys. Chem. C* **2017**, *121* (37), 20229−20241.
(248) Azam, M. S.; Weeraman, C. N.; Gibbs-Davis, J. M. Specific Cation Effects on the Bimodal Acid-Base Behavior of the Silica/Water Interface. *J. Phys. Chem. Lett.* **2012**, *3* (10), 1269−1274.
(249) Rashwan, M.; Rehl, B.; Sthoer, A.; Darlington, A. M.; Azam, M. S.; Zeng, H.; Liu, Q.; Tyrode, E.; Gibbs, J. M. Structure of the Silica/Divalent Electrolyte Interface: Molecular Insight into Charge Inversion with Increasing pH. *J. Phys. Chem. C* **2020**, *124* (49), 26973−26981.
(250) Ohno, P. E.; Chang, H.; Spencer, A. P.; Liu, Y. D. L.; Boamah, M. D.; Wang, H. F.; Geiger, F. M. Beyond the Gouy-Chapman Model with Heterodyne-Detected Second Harmonic Generation. *J. Phys. Chem. Lett.* **2019**, *10* (10), 2328−2334.
(251) Boamah, M. D.; Ohno, P. E.; Lozier, E.; Van Ardenne, J.; Geiger, F. M. Specifics about Specific Ion Adsorption from Heterodyne-Detected Second Harmonic Generation. *J. Phys. Chem. B* **2019**, *123* (27), 5848−5856.
(252) Dewan, S.; Yeganeh, M. S.; Borguet, E. Experimental Correlation Between Interfacial Water Structure and Mineral Reactivity. *J. Phys. Chem. Lett.* **2013**, *4* (11), 1977−1982.
(253) Rehl, B.; Ma, E.; Parshotam, S.; DeWalt-Kerian, E. L.; Liu, T.; Geiger, F. M.; Gibbs, J. M. Water Structure in the Electrical Double Layer and the Contributions to the Total Interfacial Potential at Different Surface Charge Densities. *J. Am. Chem. Soc.* **2022**, *144* (36), 16338−16349.
(254) Brown, M. A.; Abbas, Z.; Kleibert, A.; Green, R. G.; Goel, A.; May, S.; Squires, T. M. Determination of Surface Potential and Electrical Double-layer Structure at the Aqueous Electrolyte-nanoparticle Interface. *Phys. Rev. X* **2016**, *6*, 011007.
(255) Collins, K. D. The Behavior of Ions in Water is Controlled by their Water Affinity. *Q. Rev. Biophys.* **2019**, *52*, No. e11.
(256) Dumont, F.; Warlus, J.; Watillon, A. Influence of the Point of Zero Charge of Titanium Dioxide Hydrosols on the Ionic Adsorption Sequences. *J. Colloid Interface Sci.* **1990**, *138* (2), 543−554.
(257) Lützenkirchen, J. Specific Ion Effects at Two Single-Crystal Planes of Sapphire. *Langmuir* **2013**, *29* (25), 7726−7734.
(258) Bedzyk, M. J.; Cheng, L. X-ray Standing Wave Studies of Minerals and Mineral Surfaces: Principles and Applications. *Rev. Mineral. Geochem.* **2002**, *49*, 221.
(259) Trainor, T. P.; Templeton, A. S.; Eng, P. J. Structure and Reactivity of Environmental Interfaces: Application of Grazing Angle X-ray Spectroscopy and Long-Period X-ray Standing Waves. *J. Electron Spectrosc.* **2006**, *150* (2), 66−85.
(260) Levard, C.; Michel, F. M.; Wang, Y.; Choi, Y.; Eng, P.; Brown, G. E., Jr. Probing Ag Nanoparticle Surface Oxidation in Contact with (In)organics: An X-ray Scattering and Fluorescence Yield Approach. *J. Synchotron Radiat.* **2011**, *18* (6), 871−878.
(261) Templeton, A. S.; Trainor, T. P.; Traina, S. J.; Spormann, A. M.; Brown, G. E. Pb(II) Distributions at Biofilm-Metal Oxide Interfaces. *Proc. Natl. Acad. Sci. U.S.A.* **2001**, *98*, 11897−11902.
(262) Templeton, A. S.; Trainor, T. P.; Spormann, A. M.; Brown, G. E. Selenium Speciation and Partitioning Within Burkholderia Cepacia Biofilms Formed on α-Al_2O_3 Surfaces. *Geochim. Cosmochim. Acta* **2003**, *67*, 3547−3557.
(263) Templeton, A. S.; Trainor, T. P.; Spormann, A. M.; Newville, M.; Sutton, S. R.; Dohnalkova, A.; Gorby, Y.; Brown, G. E. Sorption Versus Biomineralization of Pb(II) Within Burkholderia Cepacia Biofilms. *Environ. Sci. Technol.* **2003**, *37*, 300−307.
(264) Templeton, A. S.; Spormann, A. M.; Brown, G. E. Speciation of Pb(II) Sorbed by Burkholderia Cepacia/Goethite Composites. *Environ. Sci. Technol.* **2003**, *37*, 2166−2172.
(265) Wang, Y.; Gélabert, A.; Michel, F. M. M.; Choi, Y.; Gescher, J.; Ona-Nguema, G.; Eng, P. J.; Bargar, J. R.; Farges, F.; Spormann, A. M.; Brown, G. E. Effect of Biofilm Coatings at Metal-Oxide/Water Interfaces I: Pb(II) and Zn(II) Partitioning and Speciation at Shewanella Oneidensis/Metal-Oxide/Water Interfaces. *Geochim. Cosmochim. Acta* **2016**, *188*, 368−392.
(266) Wang, Y.; Michel, F. M.; Choi, Y.; Eng, P. J.; Levard, C.; Siebner, H.; Gu, B.; Bargar, J.; Brown, G. E. Pb, Cu, and Zn Distributions at Humic Acid-Coated Metal-Oxide Surfaces. *Geochim. Cosmochim. Acta* **2016**, *188*, 407−423.
(267) Templeton, A. S.; Ostergren, J. D.; Trainor, T. P.; Foster, A. L.; Traina, S. J.; Spormann, A.; Brown, G. E., Jr. XAFS and XSW Study of the Distribution of Pb(II) Sorbed to Biofilms on [Alpha]-Al_2O_3 and [Alpha]-FeOOH Surfaces. *J. Synchotron Radiat.* **1999**, *6* (3), 642−644.
(268) Yoon, T. H.; Trainor, T. P.; Eng, P. J.; Bargar, J. R.; Brown, G. E. Trace Metal Ion Partitioning at Polymer Film-Metal Oxide Interfaces: Long-Period X-ray Standing Wave Study. *Langmuir* **2005**, *21* (10), 4503−4511.
(269) Wang, Y.; Gélabert, A.; Michel, F. M.; Choi, Y.; Eng, P. J. E.; Spormann, A. M.; Brown, G. E. Effect of Biofilm Coatings at Metal-Oxide/Water Interfaces II: Competitive Sorption Between Pb(II) and Zn(II) at Shewanella Oneidensis/Metal-Oxide/Water Interfaces. *Geochim. Cosmochim. Acta* **2016**, *188*, 393−406.
(270) Lee, S. S.; Fenter, P.; Nagy, K. L.; Sturchio, N. C. Changes in Adsorption Free Energy and Speciation During Competitive Adsorption between Monovalent Cations at the Muscovite (001)-Water Interface. *Geochim. Cosmochim. Acta* **2013**, *123*, 416−426.
(271) Lee, S. S.; Park, C.; Sturchio, N. C.; Fenter, P. Nonclassical Behavior in Competitive Ion Adsorption at a Charged Solid-Water Interface. *J. Phys. Chem. Lett.* **2020**, *11* (10), 4029−4035.
(272) Gonella, G.; Backus, E. H. G.; Nagata, Y.; Bonthuis, D. J.; Loche, P.; Schlaich, A.; Netz, R. R.; Kühnle, A.; McCrum, I. T.; Koper, M. T. M.; et al. Water at Charged Interfaces. *Nat. Rev. Chem.* **2021**, *5* (7), 466−485.
(273) Axnanda, S.; Crumlin, E. J.; Mao, B.; Rani, S.; Chang, R.; Karlsson, P. G.; Edwards, M. O. M.; Lundqvist, M.; Moberg, R.; Ross, P. Using "Tender" X-ray Ambient Pressure X-Ray Photoelectron Spectroscopy as a Direct Probe of Solid-Liquid Interface. *Sci. Rep.* **2015**, *5*, 9788.
(274) Favaro, M.; Jeong, B.; Ross, P. N.; Yano, J.; Hussain, Z.; Liu, Z.; Crumlin, E. J. Unravelling the Electrochemical Double Layer by Direct Probing of the Solid/Liquid Interface. *Nat. Commun.* **2016**, *7*, 12695.
(275) Starr, D. E.; Liu, Z.; Hävecker, M.; Knop-Gericke, A.; Bluhm, H. Investigation of Solid/Vapor Interfaces Using Ambient Pressure X-ray Photoelectron Spectroscopy. *Chem. Soc. Rev.* **2013**, *42* (13), 5833−5857.
(276) Nemšák, S.; Shavorskiy, A.; Karslioglu, O.; Zegkinoglou, I.; Rattanachata, A.; Conlon, C. S.; Keqi, A.; Greene, P. K.; Burks, E. C.; Salmassi, F.; et al. Concentration and Chemical-State Profiles at Heterogeneous Interfaces with Sub-nm Accuracy from Standing-Wave Ambient-Pressure Photoemission. *Nat. Commun.* **2014**, *5* (1), 5441.
(277) Johnson, S. B.; Scales, P. J.; Healy, T. W. The Binding of Monovalent Electrolyte Ions on α-Alumina. I. Electroacoustic Studies at High Electrolyte Concentrations. *Langmuir* **1999**, *15* (8), 2836−2843.
(278) Amhamdi, H.; Dumont, F.; Buess-Herman, C. Effect of Urea on the Stability of Ferric Oxide Hydrosols. *Colloids Surf. A Physicochem. Eng. Asp.* **1997**, *125* (1), 1−3.
(279) Siebentritt, M.; Volovitch, P.; Ogle, K.; Lefevre, G. Surface potential of hematite particles in high concentration electrolytes: Electroacoustic measurements and suspension stability. *Colloids Surf. A Physicochem. Eng. Asp.* **2014**, *443*, 338−344.
(280) Malloggi, F.; Jabrallah, S. b.; Girard, L.; Siboulet, B.; Wang, K.; Fontaine, P.; Daillant, J. X-ray Standing Waves and Molecular Dynamics Studies of Ion Surface Interactions in Water at a Charged Silica Interface. *J. Phys. Chem. C* **2019**, *123* (50), 30294−30304.

https://doi.org/10.1021/acs.chemrev.2c00130
Chem. Rev. 2023, 123, 6413−6544

(281) Jena, K. C.; Covert, P. A.; Hore, D. K. The Effect of Salt on the Water Structure at a Charged Solid Surface: Differentiating Second- and Third-order Nonlinear Contributions. *J. Phys. Chem. Lett.* **2011**, *2* (9), 1056−1061.
(282) Covert, P. A.; Jena, K. C.; Hore, D. K. Throwing Salt into the Mix: Altering Interfacial Water Structure by Electrolyte Addition. *J. Phys. Chem. Lett.* **2014**, *5* (1), 143−148.
(283) Lovering, K. A.; Bertram, A. K.; Chou, K. C. New Information on the Ion-Identity-Dependent Structure of Stern Layer Revealed by Sum Frequency Generation Vibrational Spectroscopy. *J. Phys. Chem. C* **2016**, *120* (32), 18099−18104.
(284) Azam, M. S.; Darlington, A.; Gibbs-Davis, J. M. The Influence of Concentration on Specific Ion Effects at the Silica/Water Interface. *J. Phys.: Condens. Matter* **2014**, *26*, 244107.
(285) Darlington, A. M.; Gibbs-Davis, J. M. Bimodal or Trimodal? The Influence of Starting pH on Site Identity and Distribution at the Low Salt Aqueous/Silica Interface. *J. Phys. Chem. C* **2015**, *119* (29), 16560−16567.
(286) Dove, P. M. The Dissolution Kinetics of Quartz in Sodium Chloride Solutions at 25° to 300°C. *Am. J. Sci.* **1994**, *294* (6), 665−712.
(287) Dove, P. M.; Nix, C. J. The Influence of the Alkaline Earth Cations, Magnesium, Calcium, and Barium on the Dissolution Kinetics of Quartz. *Geochim. Cosmochim. Acta* **1997**, *61* (16), 3329−3340.
(288) Dumont, F.; Contreras, S.; Diaz y Alonso, M. Estabilidad De Hidrosoles De Estano en Presencia De Iones Monovalentes. *Ann. Quim.* **1990**, *91*, 635−640.
(289) Iler, R. K. *The Chemistry of Silica: Solubility, Polymerization, Colloid and Surface Properties and Biochemistry of Silica*; John Wiley and Sons, 1979.
(290) Hore, D. K.; Tyrode, E. Probing Charged Aqueous Interfaces Near Critical Angles: Effect of Varying Coherence Length. *J. Phys. Chem. C* **2019**, *123* (27), 16911−16920.
(291) Urashima, S.-h.; Myalitsin, A.; Nihonyanagi, S.; Tahara, T. The Topmost Water Structure at a Charged Silica/Aqueous Interface Revealed by Heterodyne-Detected Vibrational Sum Frequency Generation Spectroscopy. *J. Phys. Chem. Lett.* **2018**, *9* (14), 4109−4114.
(292) Smith, A. M.; Borkovec, M.; Trefalt, G. Forces Between Solid Surfaces in Aqueous Electrolyte Solutions. *Adv. Colloid Interface Sci.* **2020**, *275*, 102078.
(293) Sthoer, A.; Hladílková, J.; Lund, M.; Tyrode, E. Molecular Insight into Carboxylic Acid-Alkali Metal Cations Interactions: Reversed Affinities and Ion-Pair Formation Revealed by Non-Linear Optics and Simulations. *Phys. Chem. Chem. Phys.* **2019**, *21* (21), 11329−11344.
(294) Eom, N.; Parsons, D. F.; Craig, V. S. J. Roughness in Surface Force Measurements: Extension of DLVO Theory to Describe the Forces Between Hafnia Surfaces. *J. Phys. Chem. B* **2017**, *121* (26), 6442−6453.
(295) Döpke, M. F.; Lützenkirchen, J.; Moultos, O. A.; Siboulet, B.; Dufrêche, J.-F.; Padding, J. T.; Hartkamp, R. Preferential Adsorption in Mixed Electrolytes Confined by Charged Amorphous Silica. *J. Phys. Chem. C* **2019**, *123* (27), 16711−16720.
(296) Wang, L.; Zhao, C.; Duits, M. H. G.; Mugele, F.; Siretanu, I. Detection of Ion Adsorption at Solid-Liquid Interfaces Using Internal Reflection Ellipsometry. *Sens. Actuators, B* **2015**, *210*, 649−655.
(297) Porus, M.; Labbez, C.; Maroni, P.; Borkovec, M. Adsorption of Monovalent and Divalent Cations on Planar Water-Silica Interfaces Studied by Optical Reflectivity and Monte Carlo Simulations. *J. Chem. Phys.* **2011**, *135* (6), 064701.
(298) Lee, S. S.; Fenter, P.; Nagy, K. L.; Sturchio, N. C. Real-Time Observation of Cation Exchange Kinetics and Dynamics at the Muscovite-Water Interface. *Nat. Commun.* **2017**, *8*, 15826−15826.
(299) Onoda, G. Y.; De Bruyn, P. L. Proton Adsorption at the Ferric Oxide/Aqueous Solution Interface: I. A Kinetic Study of Adsorption. *Surf. Sci.* **1966**, *4* (1), 48−63.
(300) Gibbs-Davis, J. M.; Kruk, J. J.; Konek, C. T.; Scheidt, K. A.; Geiger, F. M. Jammed Acid-Base Reactions at Interfaces. *J. Am. Chem. Soc.* **2008**, *130* (46), 15444−15447.
(301) Navrotsky, A.; Mazeina, L.; Majzlan, J. Size-Driven Structural and Thermodynamic Complexity in Iron Oxides. *Science* **2008**, *319* (5870), 1635−1638.
(302) Wang, Y. Nanogeochemistry: Nanostructures, Emergent Properties and Their Control on Geochemical Reactions and Mass Transfers. *Chem. Geol.* **2014**, *378-379*, 1−23.
(303) Hochella, M. F.; Mogk, D. W.; Ranville, J.; Allen, I. C.; Luther, G. W.; Marr, L. C.; McGrail, B. P.; Murayama, M.; Qafoku, N. P.; Rosso, K. M. Natural, Incidental, and Engineered Nanomaterials and Their Impacts on the Earth System. *Science* **2019**, *363* (6434), eaau8299.
(304) Knight, A. W.; Ilani-Kashkouli, P.; Harvey, J. A.; Greathouse, J. A.; Ho, T. A.; Kabengi, N.; Ilgen, A. G. Interfacial Reactions of Cu(ii) Adsorption and Hydrolysis Driven by Nano-Scale Confinement. *Environ. Sci. Nano* **2020**, *7* (1), 68−80.
(305) Rother, G.; Stack, A. G.; Gautam, S.; Liu, T.; Cole, D. R.; Busch, A. Water Uptake by Silica Nanopores: Impacts of Surface Hydrophilicity and Pore Size. *J. Phys. Chem. C* **2020**, *124* (28), 15188−15194.
(306) Wilson, K. G. Renormalization Group and Critical Phenomena. I. Renormalization Group and the Kadanoff Scaling Picture. *Phys. Rev. B* **1971**, *4* (9), 3174−3183.
(307) Takei, T.; Mukasa, K.; Kofuji, M.; Fuji, M.; Watanabe, T.; Chikazawa, M.; Kanazawa, T. Changes in Density and Surface Tension of Water in Silica Pores. *Colloid Polym. Sci.* **2000**, *278* (5), 475−480.
(308) Coudert, F. X.; Vuilleumier, R.; Boutin, A. Dipole Moment, Hydrogen Bonding and IR Spectrum of Confined Water. *ChemPhysChem* **2006**, *7* (12), 2464−2467.
(309) Singh, S.; Houston, J.; Van Swol, F.; Brinker, C. J. Superhydrophobicity: Drying Transition of Confined Water. *Nature* **2006**, *442* (7102), 526−526.
(310) Findenegg, G. H.; Jähnert, S.; Akcakayiran, D.; Schreiber, A. Freezing and Melting of Water Confined in Silica Nanopores. *ChemPhysChem* **2008**, *9* (18), 2651−2659.
(311) Le Caër, S.; Pin, S.; Esnouf, S.; Raffy, Q.; Renault, J. P.; Brubach, J. B.; Creff, G.; Roy, P. A Trapped Water Network in Nanoporous Material: The Role of Interfaces. *Phys. Chem. Chem. Phys.* **2011**, *13* (39), 17658−17666.
(312) Fumagalli, L.; Esfandiar, A.; Fabregas, R.; Hu, S.; Ares, P.; Janardanan, A.; Yang, Q.; Radha, B.; Taniguchi, T.; Watanabe, K.; et al. Anomalously Low Dielectric Constant of Confined Water. *Science* **2018**, *360* (6395), 1339−1342.
(313) Breynaert, E.; Houlleberghs, M.; Radhakrishnan, S.; Grübel, G.; Taulelle, F.; Martens, J. A. Water as a Tuneable Solvent: A Perspective. *Chem. Soc. Rev.* **2020**, *49* (9), 2557−2569.
(314) Kalluri, R. K.; Konatham, D.; Striolo, A. Aqueous NaCl Solutions Within Charged Carbon-Slit Pores: Partition Coefficients and Density Distributions from Molecular Dynamics Simulations. *J. Phys. Chem. C* **2011**, *115* (28), 13786−13795.
(315) Zimmerman, A. R.; Chorover, J.; Goyne, K. W.; Brantley, S. L. Protection of Mesopore-Adsorbed Organic Matter from Enzymatic Degradation. *Environ. Sci. Technol.* **2004**, *38* (17), 4542−4548.
(316) Ferreira, D. R.; Schulthess, C. P.; Kabengi, N. J. Calorimetric Evidence in Support of the Nanopore Inner Sphere Enhancement Theory on Cation Adsorption. *Soil Sci. Soc. Am. J.* **2013**, *77* (1), 94−99.
(317) Nelson, J.; Bargar, J. R.; Wasylenki, L.; Brown, G. E.; Maher, K. Effects of Nano-Confinement on Zn(II) Adsorption to Nanoporous Silica. *Geochim. Cosmochim. Acta* **2018**, *240*, 80−97.
(318) Cygan, R. T.; Liang, J. J.; Kalinichev, A. G. Molecular Models of Hydroxide, Oxyhydroxide, and Clay Phases and the Development of a General Force Field. *J. Phys. Chem. B* **2004**, *108* (4), 1255−1266.
(319) Cygan, R. T.; Greathouse, J. A.; Heinz, H.; Kalinichev, A. G. Molecular Models and Simulations of Layered Materials. *J. Mater. Chem.* **2009**, *19* (17), 2470−2481.

https://doi.org/10.1021/acs.chemrev.2c00130
Chem. Rev. 2023, 123, 6413−6544

(320) Greathouse, J. A.; Cygan, R. T. Chapter 3: Molecular Simulation of Clay Minerals. *Dev. Clay Sci.* **2013**, *5*, 405−423.
(321) Mähler, J.; Persson, I. A Study of the Hydration of the Alkali Metal Ions in Aqueous Solution. *Inorg. Chem.* **2012**, *51* (1), 425−438.
(322) Martinek, T.; Duboué-Dijon, E.; Timr, Š.; Mason, P. E.; Baxová, K.; Fischer, H. E.; Schmidt, B.; Pluhařová, E.; Jungwirth, P. Calcium Ions in Aqueous Solutions: Accurate Force Field Description Aided by Ab Initio Molecular Dynamics and Neutron Scattering. *J. Chem. Phys.* **2018**, *148*, 222813.
(323) Willemsen, J. A. R.; Myneni, S. C. B.; Bourg, I. C. Molecular Dynamics Simulations of the Adsorption of Phthalate Esters on Smectite Clay Surfaces. *J. Phys. Chem. C* **2019**, *123* (22), 13624−13636.
(324) Van Der Spoel, D.; Van Maaren, P. J.; Berendsen, H. J. C. A Systematic Study of Water Models for Molecular Simulation: Derivation of Water Models Optimized for Use with a Reaction Field. *J. Chem. Phys.* **1998**, *108* (24), 10220−10230.
(325) Cygan, R. T.; Daemen, L. L.; Ilgen, A. G.; Krumhansl, J. L.; Nenoff, T. M. Inelastic Neutron Scattering and Molecular Simulation of the Dynamics of Interlayer Water in Smectite Clay Minerals. *J. Phys. Chem. C* **2015**, *119* (50), 28005−28019.
(326) Wang, J.; Kalinichev, A. G.; Kirkpatrick, R. J. Effects of Substrate Structure and Composition on the Structure, Dynamics, and Energetics of Water at Mineral Surfaces: A Molecular Dynamics Modeling Study. *Geochim. Cosmochim. Acta* **2006**, *70* (3), 562−582.
(327) Berghout, A.; Tunega, D.; Zaoui, A. Density Functional Theory (DFT) Study of the Hydration Steps of Na+/Mg2+/Ca2+/Sr2+/Ba2+-Exchanged Montmorillonites. *Clays Clay Miner.* **2010**, *58* (2), 174−187.
(328) Malikova, N.; Dubois, E.; Marry, V.; Rotenberg, B.; Turq, P. Dynamics in Clays - Combining Neutron Scattering and Microscopic Simulation. *Z. Phys. Chem.* **2010**, *224* (1-2), 153−181.
(329) Suter, J. L.; Kabalan, L.; Khader, M.; Coveney, P. V. Ab Initio Molecular Dynamics Study of the Interlayer and Micropore Structure of Aqueous Montmorillonite Clays. *Geochim. Cosmochim. Acta* **2015**, *169*, 17−29.
(330) Suter, J. L.; Groen, D.; Coveney, P. V. Chemically Specific Multiscale Modeling of Clay-Polymer Nanocomposites Reveals Intercalation Dynamics, Tactoid Self-Assembly and Emergent Materials Properties. *Adv. Mater.* **2015**, *27* (6), 966−984.
(331) Li, W.; Nan, Y.; Zhang, Z.; You, Q.; Jin, Z. Hydrophilicity/Hydrophobicity Driven CO_2 Solubility in Kaolinite Nanopores in Relation to Carbon Sequestration. *Chem. Eng. J.* **2020**, *398*, 125449.
(332) Szczerba, M.; Kalinichev, A. G.; Kowalik, M. Intrinsic Hydrophobicity of Smectite Basal Surfaces Quantitatively Probed by Molecular Dynamics Simulations. *Appl. Clay Sci.* **2020**, *188*, 105497.
(333) Wu, D.; Navrotsky, A. Small molecule - Silica Interactions in Porous Silica Structures. *Geochim. Cosmochim. Acta* **2013**, *109*, 38−50.
(334) Knight, A. W.; Kalugin, N. G.; Coker, E.; Ilgen, A. G. Water Properties Under Nano-Scale Confinement. *Sci. Rep.* **2019**, *9*, 8246.
(335) Ilgen, A. G.; Kabengi, N.; Leung, K.; Ilani-Kashkouli, P.; Knight, A. W.; Loera, L. Defining Silica-Water Interfacial Chemistry Under Nanoconfinement Using Lanthanides. *Environ. Sci. Nano* **2021**, *8* (2), 432−443.
(336) Metin, C. O.; Lake, L. W.; Miranda, C. R.; Nguyen, Q. P. Stability of Aqueous Silica Nanoparticle Dispersions. *J. Nanoparticle Res.* **2011**, *13* (2), 839−850.
(337) Wang, H. W.; Wesolowski, D. J.; Proffen, T. E.; Vlcek, L.; Wang, W.; Allard, L. F.; Kolesnikov, A. I.; Feygenson, M.; Anovitz, L. M.; Paul, R. L. Structure and Stability of SnO2 Nanocrystals and Surface-Bound Water Species. *J. Am. Chem. Soc.* **2013**, *135* (18), 6885−6895.
(338) Marchioro, A.; Bischoff, M.; Lutgebaucks, C.; Biriukov, D.; Predota, M.; Roke, S. Surface Characterization of Colloidal Silica Nanoparticles by Second Harmonic Scattering: Quantifying the Surface Potential and Interfacial Water Order. *J. Phys. Chem. C* **2019**, *123* (33), 20393−20404.
(339) Le Caër, S.; Pignié, M.-C.; Berrod, Q.; Grzimek, V.; Russina, M.; Carteret, C.; Thill, A.; Zanotti, J.-M.; Teixeira, J. Dynamics in Hydrated Inorganic Nanotubes Studied by Neutron Scattering: Towards Nanoreactors in Water. *Nanoscale Adv.* **2021**, *3* (3), 789−799.
(340) Cyran, J. D.; Donovan, M. A.; Vollmer, D.; Siro Brigiano, F.; Pezzotti, S.; Galimberti, D. R.; Gaigeot, M.-P.; Bonn, M.; Backus, E. H. G. Molecular Hydrophobicity at a Macroscopically Hydrophilic Surface. *Proc. Natl. Acad. Sci. U.S.A.* **2019**, *116*, 1520−1525.
(341) Dalstein, L.; Potapova, E.; Tyrode, E. The Elusive Silica/Water Interface: Isolated Silanols Under Water as Revealed by Vibrational Sum Frequency Spectroscopy. *Phys. Chem. Chem. Phys.* **2017**, *19* (16), 10343−10349.
(342) Duval, Y.; Mielczarski, J. A.; Pokrovsky, O. S.; Mielczarski, E.; Ehrhardt, J. J. Evidence of the Existence of Three Types of Species at the Quartz-Aqueous Solution Interface at pH 0-10: XPS Surface Group Quantification and Surface Complexation Modeling. *J. Phys. Chem. B* **2002**, *106* (11), 2937−2945.
(343) Kubicki, J. D.; Sofo, J. O.; Skelton, A. A.; Bandura, A. V. A New Hypothesis for the Dissolution Mechanism of Silicates. *J. Phys. Chem. C* **2012**, *116* (33), 17479−17491.
(344) Brown, M. A.; Arrigoni, M.; Héroguel, F.; Beloqui Redondo, A.; Giordano, L.; van Bokhoven, J. A.; Pacchioni, G. pH Dependent Electronic and Geometric Structures at the Water-Silica Nanoparticle Interface. *J. Phys. Chem. C* **2014**, *118* (50), 29007−29016.
(345) Carroll, S. A.; Maxwell, R. S.; Bourcier, W.; Martin, S.; Hulsey, S. Evaluation of Silica-Water Surface Chemistry Using NMR Spectroscopy. *Geochim. Cosmochim. Acta* **2002**, *66* (6), 913−926.
(346) Wagner, M.; Meyer, B.; Setvin, M.; Schmid, M.; Diebold, U. Direct Assessment of the Acidity of Individual Surface Hydroxyls. *Nature* **2021**, *592* (7856), 722−725.
(347) Macias-Romero, C.; Nahalka, I.; Okur, H. I.; Roke, S. Optical Imaging of Surface Chemistry and Dynamics in Confinement. *Science* **2017**, *357* (6353), 784−788.
(348) Li, I.; Bandara, J.; Shultz, M. J. Time Evolution Studies of the H2O/Quartz Interface Using Sum Frequency Generation, Atomic Force Microscopy, and Molecular Dynamics. *Langmuir* **2004**, *20* (24), 10474−10480.
(349) Casper, C. B.; Verreault, D.; Adams, E. M.; Hua, W.; Allen, H. C. Surface Potential of DPPC Monolayers on Concentrated Aqueous Salt Solutions. *J. Phys. Chem. B* **2016**, *120* (8), 2043−2052.
(350) Bolt, G. H. Determination of the Charge Density of Silica Sols. *J. Phys. Chem.* **1957**, *61* (9), 1166−1169.
(351) Gouveia, R. F.; Bernardes, J. S.; Ducati, T. R. D.; Galembeck, F. Acid-Base Site Detection and Mapping on Solid Surfaces by Kelvin Force Microscopy (KFM). *Anal. Chem.* **2012**, *84* (23), 10191−10198.
(352) Hunter, R. J. *Zeta Potential in Colloid Science: Principles and Applications*; Academic Press, 2013.
(353) Rodriguez, D.; Marquez, M. D.; Zenasni, O.; Han, L. T.; Baldelli, S.; Lee, R. T. Surface Dipoles Induce Uniform Orientation in Contacting Polar Liquids. *Chem. Mater.* **2020**, *32*, 7832−7841.
(354) Bousse, L.; De Rooij, N. F.; Bergveld, P. The Influence of Counter-Ion Adsorption on the ψ0/pH Characteristics of Insulator Surfaces. *Surf. Sci.* **1983**, *135* (1-3), 479−496.
(355) Kallay, N.; Preočanin, T. Measurement of the Surface Potential of Individual Crystal Planes of Hematite. *J. Colloid Interface Sci.* **2008**, *318* (2), 290−295.
(356) Penners, N.; Koopal, L.; Lyklema, J. Interfacial Electrochemistry of Haematite (α-Fe2O3): Homodisperse and Heterodisperse Sols. *Colloids and surfaces* **1986**, *21*, 457−468.
(357) Chang, H.; Ohno, P. E.; Liu, Y.; Lozier, E. H.; Dalchand, N.; Geiger, F. M. Direct Measurement of Charge Reversal on Lipid Bilayers Using Heterodyne-Detected Second Harmonic Generation Spectroscopy. *J. Phys. Chem. B* **2020**, *124*, 641−649.
(358) Mukamel, S. *Principles of Nonlinear Optical Spectroscopy*; Oxford University Press: Oxford, UK, 1995.
(359) Boyd, R. W. *Nonlinear Optics*, 3rd ed.; Elsevier Academic Press: San Diego, 2008.

https://doi.org/10.1021/acs.chemrev.2c00130
Chem. Rev. 2023, 123, 6413−6544

(360) Shen, Y. R. *The Principles of Nonlinear Optics*; John Wiley & Sons: New York, 1984.
(361) Morita, A. *Theory of Sum Frequency Generation Spectroscopy*; Springer, 2018.
(362) Gurau, M. C.; Lim, S.-M.; Castellana, E. T.; Albertorio, F.; Kataoka, S.; Cremer, P. S. On the Mechanism of the Hofmeister Effect. *J. Am. Chem. Soc.* **2004**, *126* (34), 10522−10523.
(363) Karlsson, M.; Craven, C.; Dove, P. M.; Casey, W. H. Surface Charge Concentrations on Silica in Different 1.0 M Metal-Chloride Background Electrolytes and Implication for Dissolution Rates. *Aquat. Geochem.* **2001**, *7* (1), 13−32.
(364) Piasecki, W.; Zarzycki, P.; Charmas, R. Adsorption of Alkali Metal Cations and Halide Anions on Metal Oxides: Prediction of Hofmeister Series Using 1-Pk Triple Layer Model. *Adsorption* **2010**, *16* (4), 295−303.
(365) Kitamura, A.; Fujiwara, K.; Yamamoto, T.; Nishikawa, S.; Moriyama, H. Analysis of Adsorption Behavior of Cations onto Quartz Surface by Electrical Double-layer Model. *J. Nucl. Sci. Technol.* **1999**, *36* (12), 1167−1175.
(366) Stumm, W.; Morgan, J. J. *Aquatic Chemistry, Chemical Equilibria and Rates in Natural Waters*; 3rd ed.; John Wiley & Sons: New York, 1996.
(367) Müller, B. In *ChemEQL*; 3.0 ed.; EAWAG: Kastanienbaum, Switzerland, 1996.
(368) Ma, E.; Geiger, F. M. Divalent Ion Specific Outcomes on Stern Layer Structure and Total Surface Potential at the Silica:Water Interface. *J. Phys. Chem. A* **2021**, *125* (46), 10079−10088.
(369) Pfeiffer-Laplaud, M.; Gaigeot, M.-P. Adsorption of Singly Charged Ions at the Hydroxylated (0001) a-Quartz/Water Interface. *J. Phys. Chem. C* **2016**, *120*, 4866−4880.
(370) Ohno, P. E.; Wang, H.-f.; Paesani, F.; Skinner, J. L.; Geiger, F. M. Second-Order Vibrational Lineshapes from the Air/Water Interface. *J. Phys. Chem. A* **2018**, *122* (18), 4457−4464.
(371) Lützenkirchen, J.; Scharnweber, T.; Ho, T.; Striolo, A.; Sulpizi, M.; Abdelmonem, A. A Set-Up for Simultaneous Measurement of Second Harmonic Generation and Streaming Potential and Some Test Applications. *J. Colloid Interface Sci.* **2018**, *529*, 294−305.
(372) Bousse, L. J.; Mostarshed, S.; Hafeman, D. Combined Measurement of Surface Potential and Zeta Potential at Insulator/Electrolyte Interfaces. *Sens. Actuators, B* **1992**, *10* (1), 67−71.
(373) Hou, J.; Li, H.; Zhu, H.; Wu, L. Determination of Clay Surface Potential: A More Reliable Approach. *Soil Sci. Soc. Am. J.* **2009**, *73* (5), 1658−1663.
(374) Lützenkirchen, J.; Heberling, F.; Supljika, F.; Preocanin, T.; Kallay, N.; Johann, F.; Weisser, L.; Eng, P. J. Structure-Charge Relationship: The Case of Hematite (001). *Faraday Discuss.* **2015**, *180*, 55−79.
(375) Healy, T. W.; Chan, D.; White, L. R. Colloidal Behaviour of Materials with Ionizable Group Surfaces. *Pure Appl. Chem.* **1980**, *52* (5), 1207−1219.
(376) Bousse, L.; Meindl, J. D. In *Geochemical Processes at Mineral Surfaces*; American Chemical Society, 1987; Vol. 323.
(377) Preočanin, T.; Namjesnik, D.; Brown, M. A.; Lützenkirchen, J. The Relationship Between Inner Surface Potential and Electrokinetic Potential from an Experimental and Theoretical Point of View. *Environ. Chem.* **2017**, *14* (5), 295−309.
(378) Brkljača, Z.; Namjesnik, D.; Lützenkirchen, J.; Předota, M.; Preočanin, T. Quartz/Aqueous Electrolyte Solution Interface: Molecular Dynamic Simulation and Interfacial Potential Measurements. *J. Phys. Chem. C* **2018**, *122* (42), 24025−24036.
(379) Boily, J.-F.; Chatman, S.; Rosso, K. M. Inner-Helmholtz Potential Development At The Hematite (α-Fe2O3) (001) Surface. *Geochim. Cosmochim. Acta* **2011**, *75* (15), 4113−4124.
(380) Hiemstra, T.; De Wit, J. C. M.; Van Riemsdijk, W. H. Multisite Proton Adsorption Modeling at the Solid/Solution Interface of (Hydr)oxides: A New Approach: II. Application to Various Important (Hydr)oxides. *J. Colloid Interface Sci.* **1989**, *133* (1), 105−117.
(381) Hiemstra, T.; Van Riemsdijk, W. H. A Surface Structural Approach to Ion Adsorption: The Charge Distribution (CD) Model. *J. Colloid Interface Sci.* **1996**, *179* (2), 488−508.
(382) Wang, Y.; Persson, P.; Michel, F. M.; Brown Jr, G. E. Comparison of Isoelectric Points of Single-Crystal and Polycrystalline α-Al2O3 and α-Fe2O3 Surfaces. *Am. Mineral.* **2016**, *101* (10), 2248−2259.
(383) Ma, E.; Ohno, P. E.; Kim, J.; Liu, Y.; Lozier, E. H.; Miller, T. F.; Wang, H.-F.; Geiger, F. M. A New Imaginary Term in the Second-Order Nonlinear Susceptibility from Charged Interfaces. *J. Phys. Chem. Lett.* **2021**, *12* (24), 5649−5659.
(384) Diot, J. L.; Joseph, J.; Martin, J. R.; Clechet, P. pH Dependence of the Si/SiO2 Interface State Density for EOS Systems: Quasi-Static and AC Conductance Methods. *J. Electroanal. Chem. Interfacial Electrochem.* **1985**, *193* (1), 75−88.
(385) Bousse, L.; De Rooij, N. F.; Bergveld, P. Operation of Chemically Sensitive Field-Effect Sensors as a Function of the Insulator-Electrolyte Interface. *IEEE Trans. Electron Devices* **1983**, *30* (10), 1263−1270.
(386) Kershner, R. J.; Bullard, J. W.; Cima, M. J. Zeta Potential Orientation Dependence of Sapphire Substrates. *Langmuir* **2004**, *20* (10), 4101−4108.
(387) Yang, D.; Krasowska, M.; Sedev, R.; Ralston, J. The Unusual Surface Chemistry of α-Al2O3 (0001). *Phys. Chem. Chem. Phys.* **2010**, *12* (41), 13724−13729.
(388) de Vos, W. M.; Lindhoud, S. Overcharging and Charge Inversion: Finding the Correct Explanation(S). *Adv. Colloid Interface Sci.* **2019**, *274*, 102040.
(389) Pashley, R. M. Forces Between Mica Surfaces in La3+ and Cr3+ Electrolyte Solutions. *J. Colloid Interface Sci.* **1984**, *102* (1), 23−35.
(390) Raji, F.; Ejtemaei, M.; Nguyen, A. V. Resolving the Mystery of the Second Charge Reversal on Solid Surfaces in the Presence of Divalent Heavy Metal Ions. *Applied Surf. Sci.* **2020**, *529*, 147128.
(391) Legg, B. A.; Baer, M. D.; Chun, J.; Schenter, G. K.; Huang, S.; Zhang, Y.; Min, Y.; Mundy, C. J.; De Yoreo, J. J. Visualization of Aluminum Ions at the Mica Water Interface Links Hydrolysis State-to-Surface Potential and Particle Adhesion. *J. Am. Chem. Soc.* **2020**, *142* (13), 6093−6102.
(392) Lee, S. S.; Koishi, A.; Bourg, I. C.; Fenter, P. Ion Correlations Drive Charge Overscreening and Heterogeneous Nucleation at Solid-Aqueous Electrolyte Interfaces. *Proc. Natl. Acad. Sci. U.S.A.* **2021**, *118*, No. e2105154118.
(393) Siretanu, I.; Ebeling, D.; Andersson, M. P.; Stipp, S. L. S.; Philipse, A.; Stuart, M. C.; van den Ende, D.; Mugele, F. Direct Observation of Ionic Structure at Solid-Liquid Interfaces: A Deep Look into the Stern Layer. *Sci. Rep.* **2014**, *4*, 4956.
(394) Schindler, P. W.; Gamsjäger, H. Acid-Base Reactions of the TiO2 (Anatase) — Water Interface and the Point of Zero Charge of TiO2 Suspensions. *Kolloid-Zeitschrift und Zeitschrift für Polymere* **1972**, *250* (7), 759−763.
(395) Huang, C.-P.; Stumm, W. Specific Adsorption Of Cations on Hydrous γ-Al2O3. *J. Colloid Interface Sci.* **1973**, *43* (2), 409−420.
(396) Parks, G. A.; de Bruyn, P. L. The Zero Point of Charge of Oxides. *J. Phys. Chem.* **1962**, *66*, 967−973.
(397) Yoon, R. H.; Salman, T.; Donnay, G. Predicting Points of Zero Charge of Oxides and Hydroxides. *J. Colloid Interface Sci.* **1979**, *70* (3), 483−493.
(398) Hiemstra, T.; Venema, P.; Van Riemsdijk, W. H. Intrinsic Proton Affinity of Reactive Surface Groups of Metal (Hydr)oxides: The Bond Valence Principle. *J. Colloid Interface Sci.* **1996**, *184*, 680−692.
(399) Livi, K. J. T.; Villalobos, M.; Leary, R.; Varela, M.; Barnard, J.; Villacís-García, M.; Zanella, R.; Goodridge, A.; Midgley, P. Crystal Face Distributions and Surface Site Densities of Two Synthetic Goethites: Implications for Adsorption Capacities as a Function of Particle Size. *Langmuir* **2017**, *33* (36), 8924−8932.

https://doi.org/10.1021/acs.chemrev.2c00130
Chem. Rev. 2023, 123, 6413−6544

(400) Lis, D.; Backus, E. H. G.; Hunger, J.; Parekh, S. H.; Bonn, M. Liquid Flow Along a Solid Surface Reversibly Alters Interfacial Chemistry. *Science* **2014**, *344* (6188), 1138−1142.
(401) Ober, P.; Boon, W. Q.; Dijkstra, M.; Backus, E. H. G.; van Roij, R.; Bonn, M. Liquid Flow Reversibly Creates a Macroscopic Surface Charge Gradient. *Nat. Commun.* **2021**, *12*, 4102.
(402) Ong, S.; Zhao, X.; Eisenthal, K. B. Polarization of Water Molecules at a Charged Interface: Second Harmonic Studies of the Silica/Water Interface. *Chem. Phys. Lett.* **1992**, *191* (3-4), 327−335.
(403) Allen, L. H.; Matijevíc, E.; Meites, L. Exchange of Na+ for the Silanolic Protons of Silica. *Journal of Inorganic and Nuclear Chemistry* **1971**, *33* (5), 1293−1299.
(404) García, D.; Lützenkirchen, J.; Petrov, V.; Siebentritt, M.; Schild, D.; Lefèvre, G.; Rabung, T.; Altmaier, M.; Kalmykov, S.; Duro, L.; et al. Sorption of Eu(III) on Quartz at High Salt Concentrations. *Colloids Surf. A Physicochem. Eng. Asp.* **2019**, *578*, 123610.
(405) Fitts, J. P.; Machesky, M. L.; Wesolowski, D. J.; Shang, X.; Kubicki, J. D.; Flynn, G. W.; Heinz, T. F.; Eisenthal, K. B. Second-Harmonic Generation and Theoretical Studies of Protonation at the Water/α-TiO2 (1 1 0) Interface. *Chem. Phys. Lett.* **2005**, *411* (4-6), 399−403.
(406) Liu, X.; Cheng, J.; Sprik, M.; Lu, X.; Wang, R. Understanding Surface Acidity of Gibbsite with First Principles Molecular Dynamics Simulations. *Geochim. Cosmochim. Acta* **2013**, *120*, 487−495.
(407) Gittus, O. R.; Von Rudorff, G. F.; Rosso, K. M.; Blumberger, J. Acidity Constants of the Hematite-Liquid Water Interface from Ab Initio Molecular Dynamics. *J. Phys. Chem. Lett.* **2018**, *9* (18), 5574−5582.
(408) Hiemstra, T.; Van Riemsdijk, W. H. On the Relationship Between Charge Distribution, Surface Hydration, and the Structure of the Interface of Metal Hydroxides. *J. Colloid Interface Sci.* **2006**, *301* (1), 1−18.
(409) Hiemstra, T. Formation, Stability, and Solubility of Metal Oxide Nanoparticles: Surface Entropy, Enthalpy, and Free Energy of Ferrihydrite. *Geochim. Cosmochim. Acta* **2015**, *158*, 179−198.
(410) Hiemstra, T. Size-Dependent Solubility, Stability, and Nucleation of Ferrihydrite. *Abstracts of Papers of the American Chemical Society* **2015**, *249*.
(411) Mendez, J. C.; Hiemstra, T. Carbonate Adsorption to Ferrihydrite: Competitive Interaction with Phosphate for Use in Soil Systems. *ACS Earth Space Chem.* **2019**, *3* (1), 129−141.
(412) Mendez, J. C.; Hiemstra, T. High and Low Affinity Sites of Ferrihydrite for Metal Ion Adsorption: Data and Modeling of the Alkaline-Earth Ions Be, Mg, Ca, Sr, Ba, and Ra. *Geochim. Cosmochim. Acta* **2020**, *286*, 289−305.
(413) Mendez, J. C.; Hiemstra, T. Surface Area of Ferrihydrite Consistently Related to Primary Surface Charge, Ion Pair Formation, and Specific Ion Adsorption. *Chem. Geol.* **2020**, *532*, 119304.
(414) Leung, K.; Nielsen, I. M. B.; Criscenti, L. J. Elucidating the Bimodal Acid-Base Behavior of the Water-Silica Interface from First Principles. *J. Am. Chem. Soc.* **2009**, *131* (51), 18358−18365.
(415) Tazi, S.; Rotenberg, B.; Salanne, M.; Sprik, M.; Sulpizi, M. Absolute Acidity of Clay Edge Sites from Ab-Initio Simulations. *Geochim. Cosmochim. Acta* **2012**, *94*, 1−11.
(416) Pfeiffer-Laplaud, M.; Gaigeot, M. P.; Sulpizi, M. PKa at Quartz/Electrolyte Interfaces. *J. Phys. Chem. Lett.* **2016**, *7* (16), 3229−3234.
(417) Leung, K.; Criscenti, L. J. Predicting the Acidity Constant of a Goethite Hydroxyl Group from First Principles. *J. Phys.: Condens. Matter* **2012**, *24* (12), 124105.
(418) Stengel, M.; Spaldin, N. A.; Vanderbilt, D. Electric Displacement as the Fundamental Variable in Electronic-Structure Calculations. *Nat. Phys.* **2009**, *5* (4), 304−308.
(419) Zhang, C.; Hutter, J.; Sprik, M. Coupling of Surface Chemistry and Electric Double Layer at TiO2 Electrochemical Interfaces. *J. Phys. Chem. Lett.* **2019**, *10* (14), 3871−3876.
(420) Ingri, N.; Andersson, I.; Pettersson, L.; Yagasaki, A.; Andersson, L.; Holmstrom, K.; et al. LAKE-A Program System for Equilibrium Analytical Treatment of Multimethod Data, Especially Combined Potentiometric and Nuclear Magnetic Resonance Data. *Acta Chem. Scand.* **1996**, *50*, 717−734.
(421) Hiemstra, T.; Rahnemaie, R.; van Riemsdijk, W. H. Surface Complexation of Carbonate on Goethite: IR Spectroscopy, Structure and Charge Distribution. *J. Colloid Interface Sci.* **2004**, *278* (2), 282−290.
(422) Nie, Z.; Finck, N.; Heberling, F.; Pruessmann, T.; Liu, C.; Lützenkirchen, J. Adsorption of Selenium and Strontium on Goethite: EXAFS Study and Surface Complexation Modeling of the Ternary Systems. *Environ. Sci. Technol.* **2017**, *51* (7), 3751−3758.
(423) Rehl, B.; Rashwan, M.; DeWalt-Kerian, E. L.; Jarisz, T. A.; Darlington, A. M.; Hore, D. K.; Gibbs, J. M. New Insights into χ(3) Measurements: Comparing Nonresonant Second Harmonic Generation and Resonant Sum Frequency Generation at the Silica/Aqueous Electrolyte Interface. *J. Phys. Chem. C* **2019**, *123* (17), 10991−11000.
(424) Villalobos, M.; Cheney, M. A.; Alcaraz-Cienfuegos, J. Goethite Surface Reactivity: II. A Microscopic Site-Density Model That Describes its Surface Area-Normalized Variability. *J. Colloid Interface Sci.* **2009**, *336* (2), 412−422.
(425) Hiemstra, T., Surface Complexation at Mineral Interfaces: Multisite and Charge Distribution Approach. Ph.D. Thesis. Wageningen University, 2010.
(426) van Riemsdijk, W. H.; Hiemstra, T. The CD-MUSIC Model as a Framework for Interpreting Ion Adsorption on Metal (Hydr)-oxide Surfaces. In *Interface Science and Technology*; Lützenkirchen, J., Ed.; Elsevier, 2006; Vol. *11*, Chapter 8, pp 251−268.
(427) Boily, J. F.; Song, X. W. Direct Identification of Reaction Sites on Ferrihydrite. *Commun. Chem.* **2020**, *3*, 79.
(428) DelloStritto, M. J.; Kubicki, J.; Sofo, J. O. Density Functional Theory Simulation of Hydrogen-Bonding Structure and Vibrational Densities of States at the Quartz (101)-Water Interface and its Relation to Dissolution as a Function of Solution pH and Ionic Strength. *J. Phys.: Condens. Matter* **2014**, *26*, 244101.
(429) Watts, H. D.; Kubicki, J. D.; Kabengi, N. Connecting Thermodynamics of Alkali Ion Exchange on the Quartz (101) Surface with Density Functional Theory Calculations. *J. Phys. Chem. A* **2022**, *126* (26), 4286−4294.
(430) Kosmulski, M. Isoelectric Points and Points of Zero Charge of Metal (Hydr)oxides: 50 Years After Parks' Review. *Adv. Colloid Interface Sci.* **2016**, *238*, 1−61.
(431) Bompoti, N. M.; Chrysochoou, M.; Machesky, M. L. Assessment of Modeling Uncertainties Using a Multistart Optimization Tool for Surface Complexation Equilibrium Parameters (MUSE). *ACS Earth Space Chem.* **2019**, *3* (4), 473−483.
(432) Boily, J. F.; Lützenkirchen, J.; Balmès, O.; Beattie, J.; Sjöberg, S. Modeling Proton Binding at the Goethite (α-FeOOH)-Water Interface. *Colloids Surf. A Physicochem. Eng. Asp.* **2001**, *179* (1), 11−27.
(433) Dove, P. M. The Dissolution Kinetics of Quartz in Aqueous Mixed Cation Solutions. *Geochim. Cosmochim. Acta* **1999**, *63* (22), 3715−3727.
(434) Torn, M. S.; Trumbore, S. E.; Chadwick, O. A.; Vitousek, P. M.; Hendricks, D. M. Mineral Control of Soil Organic Carbon Storage and Turnover. *Nature* **1997**, *389* (6647), 170−173.
(435) Bompoti, N. M.; Chrysochoou, M.; Machesky, M. L. A Unified Surface Complexation Modeling Approach for Chromate Adsorption on Iron Oxides. *Environ. Sci. Technol.* **2019**, *53* (11), 6352−6361.
(436) Blumberger, J.; Gaigeot, M. P.; Sulpizi, M.; Vuilleumier, R. Frontiers in Molecular Simulation of Solvated Ions, Molecules and Interfaces. *Phys. Chem. Chem. Phys.* **2020**, *22* (19), 10393−10396.
(437) Ilgen, A. G.; Heath, J. E.; Akkutlu, I. Y.; Bryndzia, L. T.; Cole, D. R.; Kharaka, Y. K.; Kneafsey, T. J.; Milliken, K. L.; Pyrak-Nolte, L. J.; Suarez-Rivera, R. Shales at All Scales: Exploring Coupled Processes In Mudrocks. *Earth Sci. Rev.* **2017**, *166*, 132−152.
(438) Limousin, G.; Gaudet, J. P.; Charlet, L.; Szenknect, S.; Barthès, V.; Krimissa, M. Sorption Isotherms: A Review on Physical

https://doi.org/10.1021/acs.chemrev.2c00130
Chem. Rev. 2023, 123, 6413−6544

Bases, Modeling and Measurement. *Appl. Geochem.* **2007**, *22* (2), 249−275.
(439) Farley, K. J.; Dzombak, D. A.; Morel, F. M. M. A Surface Precipitation Model for the Sorption of Cations on Metal Oxides. *J. Colloid Interface Sci.* **1985**, *106* (1), 226−242.
(440) Lützenkirchen, J.; Boily, J.-F.; Lövgren, L.; Sjöberg, S. Limitations of the Potentiometric Titration Technique in Determining the Proton Active Site Density of Goethite Surfaces. *Geochim. Cosmochim. Acta* **2002**, *66* (19), 3389−3396.
(441) Snow, C. L.; Lilova, K. I.; Radha, A. V.; Shi, Q.; Smith, S.; Navrotsky, A.; Boerio-Goates, J.; Woodfield, B. F. Heat Capacity and Thermodynamics of a Synthetic Two-Line Ferrihydrite, $FeOOH{\cdot}0.027H_2O$. *J. Chem. Thermodyn.* **2013**, *58*, 307−314.
(442) Zhao, P.; Begg, J. D.; Zavarin, M.; Tumey, S. J.; Williams, R.; Dai, Z. R.; Kips, R.; Kersting, A. B. Plutonium(IV) and (V) Sorption to Goethite at Sub-Femtomolar to Micromolar Concentrations: Redox Transformations and Surface Precipitation. *Environ. Sci. Technol.* **2016**, *50* (13), 6948−6956.
(443) Stachowicz, M.; Hiemstra, T.; van Riemsdijk, W. H. Arsenic-Bicarbonate Interaction on Goethite Particles. *Environ. Sci. Technol.* **2007**, *41* (16), 5620−5625.
(444) Fendorf, S.; Eick, M. J.; Grossl, P.; Sparks, D. L. Arsenate and Chromate Retention Mechanisms on Goethite. 1. Surface Structure. *Environ. Sci. Technol.* **1997**, *31* (2), 315.
(445) Waychunas, G. A.; Rea, B. A.; Fuller, C. C.; Davis, J. A. Surface Chemistry of Ferrihydrite: Part 1. EXAFS Studies of the Geometry of Coprecipitated and Adsorbed Arsenate. *Geochim. Cosmochim. Acta* **1993**, *57* (10), 2251−2269.
(446) Farquhar, M. L.; Charnock, J. M.; Livens, F. R.; Vaughan, D. J. Mechanisms of Arsenic Uptake from Aqueous Solution by Interaction with Goethite, Lepidocrocite, Mackinawite, and Pyrite: An X-ray Absorption Spectroscopy Study. *Environ. Sci. Technol.* **2002**, *36* (8), 1757−1762.
(447) Sherman, D. M.; Randall, S. R. Surface Complexation of Arsenic(V) to Iron(III) (Hydr)oxides: Structural Mechanism from Ab Initio Molecular Geometries and EXAFS Spectroscopy. *Geochim. Cosmochim. Acta* **2003**, *67* (22), 4223−4230.
(448) Hiemstra, T. Ferrihydrite Interaction with Silicate and Competing Oxyanions: Geometry and Hydrogen Bonding of Surface Species. *Geochim. Cosmochim. Acta* **2018**, *238*, 453−476.
(449) Yin, Z.; Lützenkirchen, J.; Finck, N.; Celaries, N.; Dardenne, K.; Hansen, H. C. B. Adsorption of Arsenic(V) onto Single Sheet Iron Oxide: X-Ray Absorption Fine Structure and Surface Complexation. *J. Colloid Interface Sci.* **2019**, *554*, 433−443.
(450) Morelová, N.; Finck, N.; Lützenkirchen, J.; Schild, D.; Dardenne, K.; Geckeis, H. Sorption of Americium / Europium onto Magnetite Under Saline Conditions: Batch Experiments, Surface Complexation Modelling and X-Ray Absorption Spectroscopy Study. *J. Colloid Interface Sci.* **2020**, *561*, 708−718.
(451) Wang, Z.; Giammar, D. E. Mass Action Expressions for Bidentate Adsorption in Surface Complexation Modeling: Theory and Practice. *Environ. Sci. Technol.* **2013**, *47* (9), 3982.
(452) Lützenkirchen, J.; Finck, N. Treatment of Temperature Dependence of Interfacial Speciation by Speciation Codes and Temperature Congruence of Oxide Surface Charge. *Appl. Geochem.* **2019**, *102*, 26−33.
(453) Benjamin, M. M. Modeling the Mass-Action Expression for Bidentate Adsorption. *Environ. Sci. Technol.* **2002**, *36* (3), 307−313.
(454) Venema, P.; Hiemstra, T.; Weidler, P. G.; van Riemsdijk, W. H. Intrinsic Proton Affinity of Reactive Surface Groups of Metal (Hydr)oxides: Application to Iron (Hydr)oxides. *J. Colloid Interface Sci.* **1998**, *198* (2), 282−295.
(455) Lützenkirchen, J.; Boily, J. F.; Gunneriusson, L.; Lövgren, L.; Sjöberg, S. Protonation of Different Goethite Surfaces-Unified Models for $NaNO_3$ and NaCl Media. *J. Colloid Interface Sci.* **2008**, *317* (1), 155−165.
(456) Gaboriaud, F.; Ehrhardt, J. J. Effects of Different Crystal Faces on the Surface Charge of Colloidal Goethite (α-FeOOH) Particles: An Experimental and Modeling Study. *Geochim. Cosmochim. Acta* **2003**, *67* (5), 967−983.
(457) Ponthieu, M.; Juillot, F.; Hiemstra, T.; van Riemsdijk, W. H.; Benedetti, M. F. Metal Ion Binding to Iron Oxides. *Geochim. Cosmochim. Acta* **2006**, *70* (11), 2679−2698.
(458) Venema, P.; Hiemstra, T.; van Riemsdijk, W. H. Multisite Adsorption of Cadmium on Goethite. *J. Colloid Interface Sci.* **1996**, *183* (2), 515−527.
(459) Stolze, L.; Zhang, D.; Guo, H.; Rolle, M. Surface Complexation Modeling of Arsenic Mobilization from Goethite: Interpretation of an In-Situ Experiment. *Geochim. Cosmochim. Acta* **2019**, *248*, 274−288.
(460) Antelo, J.; Fiol, S.; Pérez, C.; Mariño, S.; Arce, F.; Gondar, D.; López, R. Analysis of Phosphate Adsorption onto Ferrihydrite Using the CD-MUSIC Model. *J. Colloid Interface Sci.* **2010**, *347* (1), 112−119.
(461) Barrón, V.; Torrent, J. Surface Hydroxyl Configuration of Various Crystal Faces of Hematite and Goethite. *J. Colloid Interface Sci.* **1996**, *177* (2), 407−410.
(462) Livi, K. J.; Schaffer, B.; Azzolini, D.; Seabourne, C. R.; Hardcastle, T. P.; Scott, A. J.; Hazen, R. M.; Erlebacher, J. D.; Brydson, R.; Sverjensky, D. A. Atomic-Scale Surface Roughness of Rutile and Implications for Organic Molecule Adsorption. *Langmuir* **2013**, *29* (23), 6876−6883.
(463) Villalobos, M. The Role of Surface Edge Sites in Metal(loid) Sorption to Poorly-Crystalline Birnessites. In *Advances in the Environmental Biogeochemistry of Manganese Oxides*; ACS Symposium Series; American Chemical Society, 2015; Vol. *1197*, pp 65−87.
(464) Villalobos, M.; Bargar, J.; Sposito, G. Mechanisms of Pb(II) Sorption on a Biogenic Manganese Oxide. *Environ. Sci. Technol.* **2005**, *39* (2), 569−576.
(465) Kwon, K. D.; Refson, K.; Sposito, G. Surface Complexation of Pb(II) by Hexagonal Birnessite Nanoparticles. *Geochim. Cosmochim. Acta* **2010**, *74* (23), 6731−6740.
(466) Kwon, K. D.; Refson, K.; Sposito, G. Understanding the Trends in Transition Metal Sorption by Vacancy Sites in Birnessite. *Geochim. Cosmochim. Acta* **2013**, *101*, 222−232.
(467) Manceau, A.; Steinmann, S. N. Nature of High-and Low-Affinity Metal Surface Sites on Birnessite Nanosheets. *ACS Earth Space Chem.* **2021**, *5* (1), 66−76.
(468) Li, Y.; Zhao, X.; Wu, J.; Gu, X. Surface Complexation Modeling of Divalent Metal Cation Adsorption on Birnessite. *Chem. Geol.* **2020**, *551*, 119774.
(469) Hass, K. C.; Schneider, W. F.; Curioni, A.; Andreoni, W. The Chemistry of Water on Alumina Surfaces: Reaction Dynamics from First Principles. *Science* **1998**, *282* (5387), 265−268.
(470) Mason, S. E.; Iceman, C. R.; Tanwar, K. S.; Trainor, T. P.; Chaka, A. M. Pb(II) Adsorption on Isostructural Hydrated Alumina and Hematite (0001) Surfaces: A DFT Study. *J. Phys. Chem. C* **2009**, *113* (6), 2159−2170.
(471) Mason, S. E.; Iceman, C. R.; Trainor, T. P.; Chaka, A. M. Density Functional Theory Study of Clean, Hydrated, and Defective Alumina ($1\bar{1}$ 02) surfaces. *Phys. Rev. B* **2010**, *81* (12), 125423.
(472) Mason, S. E.; Trainor, T. P.; Chaka, A. M. Hybridization-Reactivity Relationship in Pb(II) Adsorption on α-Al_2O_3-Water Interfaces: A DFT Study. *J. Phys. Chem. C* **2011**, *115* (10), 4008−4021.
(473) Bargar, J. R.; Towle, S. N.; Brown, G. E.; Parks, G. A. Outer-Sphere Pb(II) Adsorbed at Specific Surface Sites on Single Crystal α-Alumina. *Geochim. Cosmochim. Acta* **1996**, *60*, 3541−3547.
(474) Bargar, J. R.; Brown, G. E.; Parks, G. A. Surface Complexation of Pb(II) at Oxide-Water Interfaces: I. XAFS and Bond-Valence Determination of Mononuclear and Poly Nuclear Pb(II) Sorption Products on Aluminum Oxides. *Geochim. Cosmochim. Acta* **1997**, *61*, 2617−2637.
(475) Bargar, J. R.; Trainor, T. P.; Fitts, J. P.; Chambers, S. A.; Brown, G. E. In Situ Grazing-Incidence Extended X-ray Absorption Fine Structure Study of Pb(II) Chemisorption on Hematite (0001) and (1-102) Surfaces. *Langmuir* **2004**, *20* (5), 1667−1673.

https://doi.org/10.1021/acs.chemrev.2c00130
Chem. Rev. 2023, 123, 6413−6544

(476) Brown, G., Jr.; Calas, G. Mineral−Aqueous Solution Interfaces and Their Impact on the Environment Abstra. *Geochem. Perspect.* **2012**, *1*, 483−742.
(477) Davis, J. A.; Kent, D. B. Chapter 5. Surface Complexation Modeling in Aqueous Geochemistry. In *Mineral−Water Interface Geochemistry*; Hochella, M.; White, A., Eds.; De Gruyter: Berlin, Boston, 1990; pp 177−260.
(478) Bargar, J. R.; Brown, G. E.; Parks, G. A. Surface Complexation of Pb(II) at Oxide-Water Interfaces: II. XAFS and Bond-Valence Determination of Mononuclear Pb(II) Sorption Products and Surface Functional Groups on Iron Oxides. *Geochim. Cosmochim. Acta* **1997**, *61*, 2639−2652.
(479) Aboud, S.; Wilcox, J.; Brown, G. E. Density Functional Theory Investigation of the Interaction of Water with α-Al_2O_3 and α-Fe_2O_3 ($1\bar{1}02$) Surfaces: Implications for Surface Reactivity. *Phys. Rev. B* **2011**, *83* (12), 125407.
(480) Chen, J.; Hope, M. A.; Lin, Z.; Wang, M.; Liu, T.; Halat, D. M.; Wen, Y.; Chen, T.; Ke, X.; Magusin, P. C. M. M.; et al. Interactions of Oxide Surfaces with Water Revealed with Solid-State NMR Spectroscopy. *J. Am. Chem. Soc.* **2020**, *142* (25), 11173−11182.
(481) Catalano, J. G.; Park, C.; Fenter, P.; Zhang, Z. Simultaneous Inner- and Outer-Sphere Arsenate Adsorption on Corundum and Hematite. *Geochim. Cosmochim. Acta* **2008**, *72* (8), 1986−2004.
(482) Schmidt, M. P.; Siciliano, S. D.; Peak, D. Spectroscopic Quantification of Inner- and Outer-Sphere Oxyanion Complexation Kinetics: Ionic Strength and Background Cation Effect on Sulfate Adsorption to Hematite. *ACS Earth Space Chem.* **2020**, *4* (10), 1765−1776.
(483) Xue, M.; Sampath, J.; Gebhart, R. N.; Haugen, H. J.; Lyngstadaas, S. P.; Pfaendtner, J.; Drobny, G. Studies of Dynamic Binding of Amino Acids to TiO_2 Nanoparticle Surfaces by Solution NMR and Molecular Dynamics Simulations. *Langmuir* **2020**, *36* (35), 10341−10350.
(484) Egner, T. K.; Naik, P.; Nelson, N. C.; Slowing, I. I.; Venditti, V. Mechanistic Insight into Nanoparticle Surface Adsorption by Solution NMR Spectroscopy in an Aqueous Gel. *Angew. Chem. Int. Ed.* **2017**, *56* (33), 9802−9806.
(485) Estes, S. L.; Arai, Y.; Becker, U.; Fernando, S.; Yuan, K.; Ewing, R. C.; Zhang, J.; Shibata, T.; Powell, B. A. A Self-Consistent Model Describing the Thermodynamics of Eu(III) Adsorption onto Hematite. *Geochim. Cosmochim. Acta* **2013**, *122*, 430−447.
(486) Trivedi, P.; Dyer, J. A.; Sparks, D. L.; Pandya, K. Mechanistic and Thermodynamic Interpretations of Zinc Sorption onto Ferrihydrite. *J. Colloid Interface Sci.* **2004**, *270* (1), 77−85.
(487) Dyer, J. A.; Trivedi, P.; Scrivner, N. C.; Sparks, D. L. Surface Complexation Modeling of Zinc Sorption onto Ferrihydrite. *J. Colloid Interface Sci.* **2004**, *270* (1), 56−65.
(488) Allen, N.; Machesky, M. L.; Wesolowski, D. J.; Kabengi, N. Calorimetric Study of Alkali and Alkaline-Earth Cation Adsorption and Exchange at the Quartz-Solution Interface. *J. Colloid Interface Sci.* **2017**, *504*, 538−548.
(489) Hawkins, T.; Allen, N.; Machesky, M. L.; Wesolowski, D. J.; Kabengi, N. Ion Exchange Thermodynamics at the Rutile-Water Interface: Flow Microcalorimetric Measurements and Surface Complexation Modeling of Na-K-Rb-Cl-NO_3 Adsorption. *Langmuir* **2017**, *33* (20), 4934−4941.
(490) Allen, N.; Dai, C.; Hu, Y.; Kubicki, J. D.; Kabengi, N. Adsorption Study of Al3+, Cr3+, and Mn2+ onto Quartz and Corundum using Flow Microcalorimetry, Quartz Crystal Microbalance, and Density Functional Theory. *ACS Earth Space Chem.* **2019**, *3* (3), 432−441.
(491) Namayandeh, A.; Kabengi, N. Calorimetric Study of the Influence of Aluminum Substitution in Ferrihydrite on Sulfate Adsorption and Reversibility. *J. Colloid Interface Sci.* **2019**, *540*, 20−29.
(492) Situm, A.; Rahman, M. A.; Allen, N.; Kabengi, N.; Al-Abadleh, H. A. ATR-FTIR and Flow Microcalorimetry Studies on the Initial Binding Kinetics of Arsenicals at the Organic-Hematite Interface. *J. Phys. Chem. A* **2017**, *121* (30), 5569−5579.
(493) Paul, K. W.; Kubicki, J. D.; Sparks, D. L. Sulphate Adsorption at the Fe (Hydr)oxide-H_2O Interface: Comparison of Cluster and Periodic Slab DFT Predictions. *Eur. J. Soil Sci.* **2007**, *58*, 978.
(494) Dzade, N. Y.; de Leeuw, N. H. Density Functional Theory Characterization of the Structures of H_3AsO_3 and H_3AsO_4 Adsorption Complexes on Ferrihydrite. *Environ. Sci.: Process. Impacts* **2018**, *20* (6), 977−987.
(495) Montoya, J. H.; Doyle, A. D.; Nørskov, J. K.; Vojvodic, A. Trends in Adsorption of Electrocatalytic Water Splitting Intermediates on Cubic ABO_3 Oxides. *Phys. Chem. Chem. Phys.* **2018**, *20*, 3813−3818.
(496) Yan, L.; Chan, T.; Jing, C. Arsenic Adsorption on Hematite Facets: Spectroscopy and DFT Study. *Environ. Sci. Nano* **2020**, *7* (12), 3927−3939.
(497) Kubicki, J. D.; Kabengi, N.; Chrysochoou, M.; Bompoti, N. Density Functional Theory Modeling of Chromate Adsorption onto Ferrihydrite Nanoparticles. *Geochem. Trans.* **2018**, *19*, 8.
(498) Sparks, D. L. Advances in Coupling of Kinetics and Molecular Scale Tools to Shed Light on Soil Biogeochemical Processes. *Plant Soil* **2015**, *387*, 1−19.
(499) Sparks, D. *Kinetics of Geochemical Processes*; Springer Netherlands, 2018.
(500) Casey, W. H.; Phillips, B. L.; Nordin, J. Interfacial Kinetics Through the Lens of Solution Chemistry: Hydrolytic Processes at Oxide Mineral Surfaces. In *Mineral−Water Interfacial Reactions*; ACS Symposium Series; American Chemical Society, 1999; Vol. *715*, pp 244−264.
(501) Casey, W. H.; Rustad, J. R. Pathways for Oxygen-Isotope Exchange in Two Model Oxide Clusters. *New J. Chem.* **2016**, *40* (2), 898−905.
(502) Ashida, M.; Sasaki, M.; Kan, H.; Yasunaga, T.; Hachiya, K.; Inoue, T. Kinetics of Proton Adsorption-Desorption at TiO_2-H_2O Interface by Means of Pressure-Jump Technique. *J. Colloid Interface Sci.* **1978**, *67*, 219−225.
(503) Astumian, R. D.; Sasaki, M.; Yasunaga, T.; Schelly, Z. A. Proton Adsorption-Desorption Kinetics on Iron Oxides in Aqueous Suspensions, Using the Pressure-Jump Method. *J. Phys. Chem.* **1981**, *85*, 3832−3835.
(504) Hachiya, K.; Takeda, K.; Yasunaga, T. Pressure-Jump Method to Adsorption-Desorption Kinetics. *Adsorp. Sci. Technol.* **1987**, *4*, 25−44.
(505) Yasunaga, T.; Ikeda, T. Adsorption-Desorption Kinetics at the Metal-Oxide-Solution Interface Studied by Relaxation Methods*Geochemical Processes at Mineral Surfaces*; ACS Symposium Series; American Chemical Society, 1987; Vol. *323*, Chapter 12, pp 230.
(506) Luengo, C.; Brigante, M.; Antelo, J.; Avena, M. Kinetics of Phosphate Adsorption on Goethite: Comparing Batch Adsorption and ATR-IR Measurements. *J. Colloid Interface Sci.* **2006**, *300* (2), 511−518.
(507) Parikh, S. J.; Lafferty, B. J.; Sparks, D. L. An ATR-FTIR Spectroscopic Approach for Measuring Rapid Kinetics at the Mineral/Water Interface. *J. Colloid Interface Sci.* **2008**, *320*, 177−185.
(508) Cuba-Chiem, L. T.; Huynh, L.; Ralston, J.; Beattie, D. A. In Situ Particle Film ATR FTIR Spectroscopy of Carboxymethyl Cellulose Adsorption on Talc: Binding Mechanism, pH Effects, and Adsorption Kinetics. *Langmuir* **2008**, *24*, 8036−8044.
(509) Roonasi, P.; Holmgren, A. An ATR-FTIR Study of Sulphate Sorption on Magnetite; Rate of Adsorption, Surface Speciation, and Effect of Calcium Ions. *J. Colloid Interface Sci.* **2009**, *333*, 27−32.
(510) Tofan-Lazar, J.; Al-Abadleh, H. A. ATR-FTIR Studies on the Adsorption/Desorption Kinetics of Dimethylarsinic Acid on Iron-(Oxyhydr)oxides. *J. Phys. Chem. A* **2012**, *116*, 1596−1604.
(511) Carabante, I.; Grahn, M.; Holmgren, A.; Hedlund, J. In Situ ATR-FTIR Studies on the Competitive Adsorption of Arsenate and Phosphate on Ferrihydrite. *J. Colloid Interface Sci.* **2010**, *351*, 523−531.
(512) Frahm, R. Quick Scanning Exafs: First Experiments. *Nucl. Instrum. Methods Phys. Res. A* **1988**, *270*, 578−581.

https://doi.org/10.1021/acs.chemrev.2c00130
Chem. Rev. 2023, 123, 6413−6544

(513) Briois, V.; La Fontaine, C.; Belin, S.; Barthe, L.; Moreno, T.; Pinty, V.; Carcy, A.; Girardot, R.; Fonda, E. ROCK: The New Quick-EXAFS Beamline at SOLEIL. *J. Phys. Conf. Ser.* **2016**, *712*, 012149.
(514) Bornmann, B.; Kläs, J.; Müller, O.; Lützenkirchen-Hecht, D.; Frahm, R. The Quick EXAFS Setup at Beamline P64 at PETRA III for up to 200 Spectra per Second. *AIP Conf. Proc.* **2019**, *2054*, 040008.
(515) Müller, O.; Lützenkirchen-Hecht, D.; Frahm, R. Quick Scanning Monochromator for Millisecond In Situ and in Operando X-ray Absorption Spectroscopy. *Rev. Sci. Instrum.* **2015**, *86*, 093905.
(516) Ginder-Vogel, M.; Landrot, G.; Fischel, J. S.; Sparks, D. L. Quantification of Rapid Environmental Redox Processes with Quick-Scanning X-Ray Absorption Spectroscopy (Q-XAS). *Proc. Natl. Acad. Sci. U.S.A.* **2009**, *106*, 16124−16128.
(517) Esposito, V.; Castelli, I. E. Metastability at Defective Metal Oxide Interfaces and Nanoconfined Structures. *Adv. Mater. Interfaces* **2020**, *7*, 1902090.
(518) Chahal, S.; Singh, S. S.; Kumar, A.; Kumar, P. Oxygen-deficient Lanthanum Doped Cerium Oxide Nanoparticles for Potential Applications in Spintronics and Photocatalysis. *Vacuum* **2020**, *177*, 109395.
(519) Toulhoat, P. Confinement and Migration of Radionuclides in a Nuclear Waste Deep Repository. *C. R. Phys.* **2002**, *3*, 975−986.
(520) Poinssot, C.; Fillet, C.; Gras, J. M. *Post-Containment Performance of Geological Repository Systems: Source-Term Release and Radionuclide Migration in the Near- and Far-Field Environments*; Elsevier, 2010; Chapter 14, p 421.
(521) Ou, X.; Liu, X.; Liu, W.; Rong, W.; Li, J.; Lin, Z. Surface Defects Enhance the Adsorption Affinity and Selectivity of $Mg(OH)_2$ Towards As(V) and Cr(VI) Oxyanions: A Combined Theoretical and Experimental Study. *Environ. Sci. Nano* **2018**, *5* (11), 2570−2578.
(522) Revellame, E. D.; Fortela, D. L.; Sharp, W.; Hernandez, R.; Zappi, M. E. Adsorption kinetic modeling using pseudo-first order and pseudo-second order rate laws: A review. *Cleaner Eng. Technol.* **2020**, *1*, 100032.
(523) Yiacoumi, S.; Tien, C. Modeling Adsorption of Metal Ions from Aqueous Solutions. I. Reaction-Controlled Cases. *J. Colloid Interface Sci.* **1995**, *175*, 333−346.
(524) Yiacoumi, S.; Tien, C. Modeling Adsorption of Metal Ions from Aqueous Solutions. II. Transport-Controlled Cases. *J. Colloid Interface Sci.* **1995**, *175*, 347−357.
(525) Yiacoumi, S.; Tien, C. *Kinetics of Metal Ion Adsorption from Aqueous Solutions: Models, Algorithms, and Applications*; Springer, 2013.
(526) Cheng, W.; Hanna, K.; Boily, J. F. Water Vapor Binding on Organic Matter-Coated Minerals. *Environ. Sci. Technol.* **2019**, *53* (3), 1252−1257.
(527) Yuan, G.; Cao, Y.; Zan, N.; Schulz, H.; Gluyas, J.; Hao, F.; Jin, Q.; Liu, K.; Wang, Y.; Chen, Z.; et al. Coupled Mineral Alteration and Oil Degradation in Thermal Oil-Water-Feldspar Systems and Implications for Organic-Inorganic Interactions in Hydrocarbon Reservoirs. *Geochim. Cosmochim. Acta* **2019**, *248*, 61−87.
(528) Villalobos, M.; Pérez-Gallegos, A. Goethite Surface Reactivity: A Macroscopic Investigation Unifying Proton, Chromate, Carbonate, and Lead(II) Adsorption. *J. Colloid Interface Sci.* **2008**, *326* (2), 307−323.
(529) Huang, X.; Hou, X.; Song, F.; Zhao, J.; Zhang, L. Ascorbate Induced Facet Dependent Reductive Dissolution of Hematite Nanocrystals. *J. Phys. Chem. C* **2017**, *121* (2), 1113−1121.
(530) Kummert, R.; Stumm, W. The Surface Complexation of Organic Acids on Hydrous γ-Al2O3. *J. Colloid Interface Sci.* **1980**, *75* (2), 373−385.
(531) Biber, M. V.; Stumm, W. An In-Situ ATR-FTIR Study: The Surface Coordination of Salicylic Acid on Aluminum and Iron (III) Oxides. *Environ. Sci. Technol.* **1994**, *28* (5), 763−768.
(532) Kubicki, J. D.; Sykes, D.; Apitz, S. E. Ab Initio Calculation of Aqueous Aluminum and Aluminum-Carboxylate Complex Energetics and ^{27}Al NMR Chemical Shifts. *J. Phys. Chem. A* **1999**, *103* (7), 903−915.
(533) Borowski, S. C.; Biswakarma, J.; Kang, K.; Schenkeveld, W. D. C.; Hering, J. G.; Kubicki, J. D.; Kraemer, S. M.; Hug, S. J. Structure and Reactivity of Oxalate Surface Complexes on Lepidocrocite Derived from Infrared Spectroscopy, DFT-Calculations, Adsorption, Dissolution and Photochemical Experiments. *Geochim. Cosmochim. Acta* **2018**, *226*, 244−262.
(534) Salama, Y.; Chennaoui, M.; Sylla, A.; Mountadar, M.; Rihani, M.; Assobhei, O. Characterization, Structure, and Function of Extracellular Polymeric Substances (EPS) of Microbial Biofilm in Biological Wastewater Treatment Systems: A Review. *Desalin. Water Treat.* **2016**, *57*, 16220−16237.
(535) Kidron, G. J.; Wang, Y.; Herzberg, M. Exopolysaccharides May Increase Biocrust Rigidity and Induce Runoff Generation. *J. Hydrol.* **2020**, *588*, 125081.
(536) Tanaka, N.; Kogo, T.; Hirai, N.; Ogawa, A.; Kanematsu, H.; Takahara, J.; Awazu, A.; Fujita, N.; Haruzono, Y.; Ichida, S.; Tanaka, Y. In-Situ Detection Based on the Biofilm Hydrophilicity for Environmental Biofilm Formation. *Sci. Rep.* **2019**, *9*, 8070.
(537) Shakiba, S.; Hakimian, A.; Barco, L. R.; Louie, S. M. Dynamic Intermolecular Interactions Control Adsorption from Mixtures of Natural Organic Matter and Protein onto Titanium Dioxide Nanoparticles. *Environ. Sci. Technol.* **2018**, *52*, 14158−14165.
(538) Guhra, T.; Ritschel, T.; Totsche, K. U. Formation of Mineral−Mineral and Organo-Mineral Composite Building Units from Microaggregate-Forming Materials Including Microbially Produced Extracellular Polymeric Substances. *Eur. J. Soil Sci.* **2019**, *70* (3), 604−615.
(539) Sit, I.; Sagisaka, S.; Grassian, V. H. Nucleotide Adsorption on Iron(III) Oxide Nanoparticle Surfaces: Insights into Nano-Geo-Bio Interactions through Vibrational Spectroscopy. *Langmuir* **2020**, *36* (51), 15501−15513.
(540) Fry, R. A.; Kwon, K. D.; Komarneni, S.; Kubicki, J. D.; Mueller, K. T. Solid-State NMR and Computational Chemistry Study of Mononucleotides Adsorbed to Alumina. *Langmuir* **2006**, *22* (22), 9281−9286.
(541) Salazar-Camacho, C.; Villalobos, M. Goethite Surface Reactivity: III. Unifying Arsenate Adsorption Behavior Through a Variable Crystal Face - Site Density Model. *Geochim. Cosmochim. Acta* **2010**, *74* (8), 2257−2280.
(542) Cao, S.; Zhang, X.; Huang, X.; Wan, S.; An, X.; Jia, F.; Zhang, L. Insights into the Facet-Dependent Adsorption of Phenylarsonic Acid on Hematite Nanocrystals. *Environ. Sci. Nano* **2019**, *6* (11), 3280−3291.
(543) Zhai, H.; Wang, L. Single-Molecule Determination of the Phase- and Facet-Dependent Adsorption of Alginate on Iron Oxides. *Environ. Sci. Nano* **2020**, *7* (3), 954−962.
(544) Kelkar, A. S.; Dallin, B. C.; Van Lehn, C. Predicting Hydrophobicity by Learning Spatiotemporal Features of Interfacial Water Structure: Combining Molecular Dynamics Simulations with Convolutional Neural Networks. *J. Phys. Chem. B* **2020**, *124*, 9103−9114.
(545) Chuang, I. S.; Maciel, G. E. Probing Hydrogen Bonding and the Local Environment of Silanols on Silica Surfaces Via Nuclear Spin Cross Polarization Dynamics. *J. Am. Chem. Soc.* **1996**, *118*, 401−406.
(546) Smirnov, K. Structure and Sum-Frequency Generation Spectra of Water on Uncharged Q4 Silica Surfaces: A Molecular Dynamics Study. *Phys. Chem. Chem. Phys.* **2020**, *22*, 2033−2045.
(547) Monroe, J. I.; Shell, M. S. Computational Discovery of Chemically Patterned Surfaces that Effect Unique Hydration Water Dynamics. *Proc. Natl. Acad. Sci. U.S.A.* **2018**, *115*, 8093−8098.
(548) Lum, K.; Chandler, D.; Weeks, J. D. Hydrophobicity at Small and Large Length Scales. *J. Phys. Chem. B* **1999**, *103* (22), 4570−4577.
(549) Chandler, D. Interfaces and the Driving Force of Hydrophobic Assembly. *Nature* **2005**, *437* (7059), 640−647.
(550) Davis, J. G.; Gierszal, K. P.; Wang, P.; Ben-Amotz, D. Water Structural Transformation at Molecular Hydrophobic Interfaces. *Nature* **2012**, *491* (7425), 582−585.

(551) Grdadolnik, J.; Merzel, F.; Avbelj, F. Origin of Hydrophobicity and Enhanced Water Hydrogen Bond Strength Near Purely Hydrophobic Solutes. *Proc. Natl. Acad. Sci. U.S.A.* **2017**, *114* (2), 322.
(552) Casillas-Ituarte, N. N.; Allen, H. C. Water, Chloroform, Acetonitrile, and Atrazine Adsorption to the Amorphous Silica Surface Studied by Vibrational Sum Frequency Generation Spectroscopy. *Chem. Phys. Lett.* **2009**, *483* (1-3), 84−89.
(553) Tielens, F.; Folliet, N.; Bondaz, L.; Etemovic, S.; Babonneau, F.; Gervais, C.; Azais, T. Molecular Picture of the Adsorption of Ibuprofen and Benzoic Acid on Hydrated Amorphous Silica through DFT-D Calculations Combined with Solid-State NMR Experiments. *J. Phys. Chem. C* **2017**, *121*, 17339−17347.
(554) Monroe, J. I.; Jiao, S.; Davis, R. J.; Robinson Brown, D.; Katz, L. E.; Shell, M. S. Affinity of Small-Molecule Solutes to Hydrophobic, Hydrophilic, and Chemically Patterned Iinterfaces in Aqueous Solution. *Proc. Natl. Acad. Sci. U. S. A.* **2021**, *118*, e2020205118.
(555) Li, H.; Teppen, B. J.; Johnston, C. T.; Boyd, S. A. Thermodynamics of Nitroaromatic Compound Adsorption from Water by Smectite Clay. *Environ. Sci. Technol.* **2004**, *38* (20), 5433−5442.
(556) Gu, B.; Schmitt, J.; Chen, Z.; Liang, L.; McCarthy, J. F. Adsorption and Desorption of Natural Organic Matter on Iron Oxide: Mechanisms and Models. *Environ. Sci. Technol.* **1994**, *28* (1), 38−46.
(557) Benoit, P.; Hering, J. G.; Stumm, W. Comparative Study of the Adsorption of Organic Ligands on Aluminum Oxide by Titration Calorimetry. *Appl. Geochem.* **1993**, *8* (2), 127−139.
(558) Sabur, M. A.; Goldberg, S.; Gale, A.; Kabengi, N.; Al-Abadleh, H. A. Temperature-Dependent Infrared and Calorimetric Studies on Arsenicals Adsorption from Solution to Hematite Nanoparticles. *Langmuir* **2015**, *31* (9), 2749−2760.
(559) Lin, W.; Walter, J.; Burger, A.; Maid, H.; Hirsch, A.; Peukert, W.; Segets, D. A General Approach to Study the Thermodynamics of Ligand Adsorption to Colloidal Surfaces Demonstrated by Means of Catechols Binding to Zinc Oxide Quantum Dots. *Chem. Mater.* **2015**, *27* (1), 358−369.
(560) Scheutjens, J. M. H. M.; Fleer, G. J. Statistical Theory of the Adsorption of Interacting Chain Molecules. 1. Partition Function, Segment Density Distribution, and Adsorption Isotherms. *J. Phys. Chem.* **1979**, *83* (12), 1619−1635.
(561) Scheutjens, J. M. H. M.; Fleer, G. J. Statistical Theory of the Adsorption of Interacting Chain Molecules. 2. Train, Loop, and Tail Size Distribution. *J. Phys. Chem.* **1980**, *84* (2), 178−190.
(562) Sahai, N. Biomembrane Phospholipid-Oxide Surface Interactions: Crystal Chemical and Thermodynamic Basis. *J. Colloid Interface Sci.* **2002**, *252* (2), 309−319.
(563) Zhou, L.; Martin, S.; Cheng, W.; Lassabatere, L.; Boily, J. F.; Hanna, K. Water Flow Variability Affects Adsorption and Oxidation of Ciprofloxacin onto Hematite. *Environ. Sci. Technol.* **2019**, *53* (17), 10102−10109.
(564) Martin, S.; Shchukarev, A.; Hanna, K.; Boily, J.-F. Kinetics and Mechanisms of Ciprofloxacin Oxidation on Hematite Surfaces. *Environ. Sci. Technol.* **2015**, *49* (20), 12197−12205.
(565) Allmann, S.; Mayer, L.; Olma, J.; Kaina, B.; Hofmann, T. G.; Tomicic, M. T.; Christmann, M. Benzo[A]Pyrene Represses DNA Repair Through Altered E2F1/E2F4 Function Marking an Early Event in DNA Damage-Induced Cellular Senescence. *Nucleic Acids Res.* **2020**, *48*, 12085−12101.
(566) Fleury, G.; Del Nero, M.; Barillon, R. Molecular Fractionation of a Soil Fulvic Acid (FA) and Competitive Sorption of Trace Metals (Cu, Zn, Cd, Pb) in Hematite-Solution Systems: Effect of the FA-to-Mineral Ratio. *RSC Adv.* **2017**, *7* (68), 43090−43103.
(567) Yoon, T. H.; Johnson, S. B.; Musgrave, C. B.; Brown, G. E. Adsorption of Organic Matter at Mineral/Water Interfaces: I. ATR-FTIR Spectroscopic and Quantum Chemical Study of Oxalate Adsorbed at Boehmite/Water and Corundum/Water Interfaces. *Geochim. Cosmochim. Acta* **2004**, *68*, 4505−4518.
(568) Wu, H.; Gonzalez-Pech, N. I.; Grassian, V. H. Displacement Reactions Between Environmentally and Biologically Relevant Ligands on TiO_2 Nanoparticles: Insights into the Aging of Nanoparticles in the Environment. *Environ. Sci. Nano* **2019**, *6* (2), 489−504.
(569) Margenot, A. J.; Sommer, R.; Mukalama, J.; Parikh, S. J. Biological P Cycling is Influenced by the Form of P Fertilizer in an Oxisol. *Biol. Fertil. Soils* **2017**, *53* (8), 899−909.
(570) Parikh, S. J.; Kubicki, J. D.; Jonsson, C. M.; Jonsson, C. L.; Hazen, R. M.; Sverjensky, D. A.; Sparks, D. L. Evaluating Glutamate and Aspartate Binding Mechanisms to Rutile (α-TiO2) via ATR-FTIR Spectroscopy and Quantum Chemical Calculations. *Langmuir* **2011**, *27* (5), 1778−1787.
(571) Xiao, F.; Jin, B.; Golovko, S. A.; Golovko, M. Y.; Xing, B. Sorption and Desorption Mechanisms of Cationic and Zwitterionic Per- and Polyfluoroalkyl Substances in Natural Soils: Thermodynamics and Hysteresis. *Environ. Sci. Technol.* **2019**, *53* (20), 11818−11827.
(572) Shan, X. Q.; Lian, J.; Wen, B. Effect of Organic Acids on Adsorption and Aesorption of Rare Earth Elements. *Chemosphere* **2002**, *47*, 701−710.
(573) Wang, Y.-J.; Chen, J.-H.; Cui, Y.-X.; Wang, S.-Q.; Zhou, D.-M. Effects of Low-Molecular-Weight Organic Acids on Cu(II) Adsorption onto Hydroxyapatite Nanoparticles. *J. Hazard. Mater.* **2009**, *162* (2), 1135−1140.
(574) Rosso, K. M.; Morgan, J. J. Outer-Sphere Electron Transfer Kinetics of Metal Ion Oxidation by Molecular Oxygen. *Geochim. Cosmochim. Acta* **2002**, *66* (24), 4223−4233.
(575) Stumm, W.; Morgan, J. J. *Aquatic Chemistry: Chemical Equilibria and Rates in Natural Waters*; John Wiley & Sons, 2012.
(576) Zachara, J. M.; Fredrickson, J. K.; Li, S.-M.; Kennedy, D. W.; Smith, S. C.; Gassman, P. L. Bacterial Reduction of Crystalline Fe (super 3+) Oxides in Single Phase Suspensions and Subsurface Materials. *Am. Mineral.* **1998**, *83*, 1426−1443.
(577) Newman, D. K.; Kolter, R. A Role for Excreted Quinones in Extracellular Electron Transfer. *Nature* **2000**, *405* (6782), 94−97.
(578) Rosso, K. M.; Smith, D. M.; Wang, Z.; Ainsworth, C. C.; Fredrickson, J. K. Self-Exchange Electron Transfer Kinetics and Reduction Potentials for Anthraquinone Disulfonate. *J. Phys. Chem. A* **2004**, *108* (16), 3292−3303.
(579) Stone, A. T.; Morgan, J. J. Reductive Dissolution of Metal Oxides. In *Aquatic Surface Chemistry: Chemical Processes at the Particle−Water Interface;*; John Wiley and Sons, New York. 1987; pp 221−254.
(580) Felmy, A. R.; Moore, D. A.; Rosso, K. M.; Qafoku, O.; Rai, D.; Buck, E. C.; Ilton, E. S. Heterogeneous Reduction of PuO2 with Fe(II): Importance of the Fe(III) Reaction Product. *Environ. Sci. Technol.* **2011**, *45* (9), 3952−3958.
(581) Skomurski, F. N.; Ilton, E. S.; Engelhard, M. H.; Arey, B. W.; Rosso, K. M. Heterogeneous Reduction of U6+ by Structural Fe2+ from Theory and Experiment. *Geochim. Cosmochim. Acta* **2011**, *75* (22), 7277−7290.
(582) Yanina, S. V.; Rosso, K. M. Linked Reactivity at Mineral−Water Interfaces Through Bulk Crystal Conduction. *Science* **2008**, *320* (5873), 218−222.
(583) Shi, L.; Richardson, D. J.; Wang, Z.; Kerisit, S. N.; Rosso, K. M.; Zachara, J. M.; Fredrickson, J. K. The Roles of Outer Membrane Cytochromes of Shewanella and Geobacter in Extracellular Electron Transfer. *Environ. Microbiol. Rep.* **2009**, *1* (4), 220−227.
(584) Marcus, R. A. On the Theory of Oxidation-Reduction Reactions Involving Electron Transfer. I. *J. Chem. Phys.* **1956**, *24* (5), 966−978.
(585) Marcus, R. A. Electron Transfer Reactions in Chemistry. Theory and Experiment. *Rev. Mod. Phys.* **1993**, *65* (3), 599.
(586) Newton, M. D. Formalisms for Electron-Exchange Kinetics in Aqueous Solution and the Role of Ab Initio Techniques in Their Implementation. *Int. J. Quantum Chem.* **1980**, *18* (S14), 363−391.
(587) Marcus, R. A.; Sutin, N. Electron Transfers in Chemistry and Biology. *Biochim. Biophys. Acta, Rev. Bioenergetics* **1985**, *811* (3), 265−322.

(588) Small, D. W.; Matyushov, D. V.; Voth, G. A. The Theory of Electron Transfer Reactions: What May be Missing? *J. Am. Chem. Soc.* **2003**, *125* (24), 7470−7478.
(589) Wehrli, B. Redox Reactions of Metal Ions at Mineral Surfaces. In *Aquatic Chemical Kinetics: Reaction Rates of Processes in Natural Waters*; Environmental Science and Technology Series; Stumm, W., Ed.; John Wiley & Sons: New York, 1990; pp 311−336.
(590) Rosso, K. M.; Rustad, J. R. Ab Initio Calculation of Homogeneous Outer Sphere Electron Transfer Rates: Application to $M(OH_2)_6^{3+/2+}$ Redox Couples. *J. Phys. Chem. A* **2000**, *104* (29), 6718−6725.
(591) Rosso, K. M.; Smith, D. M.; Dupuis, M. An Ab Initio Model of Electron Transport in Hematite (α-Fe_2O_3) Basal Planes. *J. Chem. Phys.* **2003**, *118* (14), 6455−6466.
(592) Kerisit, S.; Rosso, K. M. Charge Transfer in FeO: A Combined Molecular-Dynamics and Ab Initio Study. *J. Chem. Phys.* **2005**, *123* (22), 224712.
(593) Eggleston, C. M.; Hug, S.; Stumm, W.; Sulzberger, B.; Dos Santos Afonso, M. Surface Complexation of Sulfate by Hematite Surfaces: FTIR and STM Observations. *Geochim. Cosmochim. Acta* **1998**, *62* (4), 585.
(594) Kerisit, S.; Rosso, K. M. Kinetic Monte Carlo Model of Charge Transport in Hematite (alpha-Fe_2O_3). *J. Chem. Phys.* **2007**, *127* (12), 124706.
(595) Breuer, M.; Zarzycki, P.; Blumberger, J.; Rosso, K. M. Thermodynamics of Electron Flow in the Bacterial Deca-Heme Cytochrome MtrF. *J. Am. Chem. Soc.* **2012**, *134* (24), 9868−9871.
(596) Breuer, M.; Rosso, K. M.; Blumberger, J. Electron Flow in Multiheme Bacterial Cytochromes is a Balancing Act Between Heme Electronic Interaction and Redox Potentials. *Proc. Natl. Acad. Sci. U.S.A.* **2014**, *111* (2), 611−616.
(597) Breuer, M.; Rosso, K. M.; Blumberger, J.; Butt, J. N. Multi-Haem Cytochromes in Shewanella Oneidensis MR-1: Structures, Functions and Opportunities. *J. R. Soc. Interface* **2015**, *12* (102), 20141117.
(598) Bylaska, E. J.; Song, D.; Rosso, K. M. Electron Transfer Calculations Between Edge Sharing Octahedra in Hematite, Goethite, and Annite. *Geochim. Cosmochim. Acta* **2020**, *291*, 79−91.
(599) Sherrill, C. D.; Manolopoulos, D. E.; Martínez, T. J.; Michaelides, A. Electronic Structure Software. *J. Chem. Phys.* **2020**, *153* (7), 070401.
(600) Chandler, D. Electron Transfer in Water and Other Polar Environments, How it Happens. In *Classical and Quantum Dynamics in Condensed Phase Simulations*; Berne, B. J., Ciccotti, G., Coker, D. F., Eds.; World Scientific Publishing: London, 1998; pp 25−49.
(601) Warshel, A.; Parson, W. W. Computer Simulations of Electron-Transfer Reactions in Solution and in Photosynthetic Reaction Centers. *Annu. Rev. Phys. Chem.* **1991**, *42* (1), 279−309.
(602) Katz, J. E.; Zhang, X.; Attenkofer, K.; Chapman, K. W.; Frandsen, C.; Zarzycki, P.; Rosso, K. M.; Falcone, R. W.; Waychunas, G. A.; Gilbert, B. Electron Small Polarons and Their Mobility in Iron (Oxyhydr)oxide Nanoparticles. *Science* **2012**, *337* (6099), 1200−1203.
(603) Anderson, N. A.; Lian, T. Ultrafast Electron Transfer at the Molecule-Semiconductor Nanoparticle Interface. *Annu. Rev. Phys. Chem.* **2005**, *56* (1), 491−519.
(604) Yan, C.; Nishida, J.; Yuan, R.; Fayer, M. D. Water of Hydration Dynamics in Minerals Gypsum and Bassanite: Ultrafast 2D IR Spectroscopy of Rocks. *J. Am. Chem. Soc.* **2016**, *138* (30), 9694−9703.
(605) Zarzycki, P.; Kerisit, S.; Rosso, K. M. Molecular Dynamics Study of Fe (II) Adsorption, Electron Exchange, and Mobility at Goethite (α-FeOOH) Surfaces. *J. Phys. Chem. C* **2015**, *119* (6), 3111−3123.
(606) Rosso, K. M.; Dupuis, M. Electron Transfer in Environmental Systems: A Frontier for Theoretical Chemistry. *Theor. Chem. Acc.* **2006**, *116* (1), 124−136.
(607) Rosso, K. M.; Ilton, E. S. Effects of Compositional Defects on Small Polaron Hopping in Micas. *J. Chem. Phys.* **2005**, *122* (24), 244709.
(608) Remsing, R. C.; McKendry, I. G.; Strongin, D. R.; Klein, M. L.; Zdilla, M. J. Frustrated Solvation Structures Can Enhance Electron Transfer Rates. *J. Phys. Chem. Lett.* **2015**, *6* (23), 4804−4808.
(609) Remsing, R. C.; Klein, M. L. Solvation Dynamics in Water Confined Within Layered Manganese Dioxide. *Chem. Phys. Lett.* **2017**, *683*, 478−482.
(610) Bhullar, R. K.; Zdilla, M. J.; Klein, M. L.; Remsing, R. C. Effect of Water Frustration on Water Oxidation Catalysis in the Nano-confined Interlayers of Layered Manganese Oxides Birnessite and Buserite. *J. Mater. Chem. A* **2021**, *9* (11), 6924−6932.
(611) Thenuwara, A. C.; Cerkez, E. B.; Shumlas, S. L.; Attanayake, N. H.; McKendry, I. G.; Frazer, L.; Borguet, E.; Kang, Q.; Remsing, R. C.; Klein, M. L.; et al. Nickel Confined in the Interlayer Region of Birnessite: an Active Electrocatalyst for Water Oxidation. *Angew. Chem. Int. Ed.* **2016**, *55* (35), 10381−10385.
(612) Kang, Q.; Vernisse, L.; Remsing, R. C.; Thenuwara, A. C.; Shumlas, S. L.; McKendry, I. G.; Klein, M. L.; Borguet, E.; Zdilla, M. J.; Strongin, D. R. Effect of Interlayer Spacing on the Activity of Layered Manganese Oxide Bilayer Catalysts for the Oxygen Evolution Reaction. *J. Am. Chem. Soc.* **2017**, *139* (5), 1863−1870.
(613) Ning, J.; Furness, J. W.; Zhang, Y.; Thenuwara, A. C.; Remsing, R. C.; Klein, M. L.; Strongin, D. R.; Sun, J. Tunable Catalytic Activity of Cobalt-Intercalated Layered MnO2 for Water Oxidation Through Confinement and Local Ordering. *J. Catal.* **2019**, *374*, 143−149.
(614) DelloStritto, M. J.; Thenuwara, A. C.; Klein, M. L.; Strongin, D. R. Effect of Interlayer Co2+ on Structure and Charge Transfer in NiFe Layered Double Hydroxides. *J. Phys. Chem. C* **2019**, *123* (22), 13593−13599.
(615) Sanchez, J.; Stevens, M. B.; Young, A. R.; Gallo, A.; Zhao, M.; Liu, Y.; Ramos-Garcés, M. V.; Ben-Naim, M.; Colón, J. L.; Sinclair, R.; et al. Isolating the Electrocatalytic Activity of a Confined NiFe Motif Within Zirconium Phosphate. *Adv. Energy Mater.* **2021**, *11* (20), 2003545.
(616) Augustyn, V.; Gogotsi, Y. 2D Materials with Nanoconfined Fluids for Electrochemical Energy Storage. *Joule* **2017**, *1* (3), 443−452.
(617) Fleischmann, S.; Spencer, M. A.; Augustyn, V. Electrochemical Reactivity Under Confinement Enabled by Molecularly Pillared 2D and Layered Materials. *Chem. Mater.* **2020**, *32* (8), 3325−3334.
(618) Li, Z.; Jeanmairet, G.; Méndez-Morales, T.; Burbano, M.; Haefele, M.; Salanne, M. Confinement Effects on an Electron Transfer Reaction in Nanoporous Carbon Electrodes. *J. Phys. Chem. Lett.* **2017**, *8* (9), 1925−1931.
(619) Rosso, K. M.; Smith, D. M.; Dupuis, M. Aspects of Aqueous Iron and Manganese (II/III) Self-Exchange Electron Transfer Reactions. *J. Phys. Chem. A* **2004**, *108* (24), 5242−5248.
(620) Neal, A. L.; Rosso, K. M.; Geesey, G. G.; Gorby, Y.; Little, B. J. Surface Structure Effects on Direct Reduction of Iron Oxides by Shewanella Oneidensis. *Geochim. Cosmochim. Acta* **2003**, *67*, 4489−4503.
(621) Neal, A. L.; Bank, T. L.; Hochella, M. F.; Rosso, K. M. Cell Adhesion of Shewanella Oneidensis to Iron Oxide Minerals: Effect of Different Single Crystal Faces. *Geochem. Trans.* **2005**, *6*, 77.
(622) Smith, D. M. A.; Rosso, K. M.; Dupuis, M.; Valiev, M.; Straatsma, T. P. Electronic Coupling Between Heme Electron-Transfer Centers and its Decay with Distance Depends Strongly on Relative Orientation. *J. Phys. Chem. B* **2006**, *110*, 15582−15588.
(623) Wigginton, N. S.; Rosso, K. M.; Stack, A. G.; Hochella, M. F., Jr. Long-Range Electron Transfer across Cytochrome- Hematite (α-Fe_2O_3) Interfaces. *J. Phys. Chem. C* **2009**, *113*, 2096−2103.
(624) Gorby, Y. A.; Yanina, S.; McLean, J. S.; Rosso, K. M.; Moyles, D.; Dohnalkova, A.; Beveridge, T. J.; Chang, I. S.; Kim, B. H.; Kim, K. S.; et al. Electrically Conductive Bacterial Nanowires Produced by Shewanella Oneidensis Strain MR-1 and Other Microorganisms. *Proc. Natl. Acad. Sci. U.S.A.* **2006**, *103*, 11358−11363.

https://doi.org/10.1021/acs.chemrev.2c00130
Chem. Rev. 2023, 123, 6413−6544

(625) Gorby, Y.; McLean, J.; Korenevsky, A.; Rosso, K.; El-Naggar, M. Y.; Beveridge, T. J. Redox-Reactive Membrane Vesicles Produced by Shewanella. *Geobiology* **2008**, *6* (3), 232−241.
(626) Stack, A. G.; Rosso, K. M.; Smith, D. M.; Eggleston, C. M. Reaction of Hydroquinone with Hematite: II. Calculated Electron-Transfer Rates and Comparison to the Reductive Dissolution Rate. *J. Colloid Interface Sci.* **2004**, *274* (2), 442−450.
(627) Remucal, C. K.; Ginder-Vogel, M. A Critical Review of the Reactivity of Manganese Oxides with Organic Contaminants. *Environ. Sci.: Process. Impacts* **2014**, *16*, 1247−1266.
(628) Zhang, J.; Stanforth, R. Slow Adsorption Reaction Between Arsenic Species and Goethite (α-FeOOH): Diffusion or Heterogeneous Surface Reaction Control. *Langmuir* **2005**, *21* (7), 2895−2901.
(629) Huang, J.; Zhang, H. Redox Reactions of Iron and Manganese Oxides in Complex Systems. *Front. Environ. Sci. Eng.* **2020**, *14*, 76.
(630) Zhang, H.; Chen, W.-R.; Huang, C.-H. Kinetic Modeling of Oxidation of Antibacterial Agents by Manganese Oxide. *Environ. Sci. Technol.* **2008**, *42*, 5548−5554.
(631) Borch, T.; Kretzschmar, R.; Kappler, A.; Cappellen, P. V.; Ginder-Vogel, M.; Voegelin, A.; Campbell, K. Biogeochemical Redox Processes and Their Impact on Contaminant Dynamics. *Environ. Sci. Technol.* **2010**, *44* (1), 15−23.
(632) Stone, A. T. Reductive Dissolution of Manganese(III/IV) Oxides by Substituted Phenols. *Environ. Sci. Technol.* **1987**, *21*, 979−988.
(633) Stewart, S. M.; Hofstetter, T. B.; Joshi, P.; Gorski, C. A. Linking Thermodynamics to Pollutant Reduction Kinetics by Fe2+ Bound to Iron Oxides. *Environ. Sci. Technol.* **2018**, *52* (10), 5600−5609.
(634) Manning, B. A.; Fendorf, S. E.; Bostick, B.; Suarez, D. L. Arsenic(III) Oxidation and Arsenic(V) Adsorption Reactions on Synthetic Birnessite. *Environ. Sci. Technol.* **2002**, *36* (5), 976−981.
(635) Banerjee, D.; Nesbitt, H. W. Oxidation of Aqueous Cr(III) at Birnessite Surfaces: Constraints on Reaction Mechanism. *Geochim. Cosmochim. Acta* **1999**, *63* (11), 1671−1687.
(636) Stone, A. T.; Morgan, J. J. Reduction and Dissolution of Manganese(III) and Manganese(IV) Oxides by Organics: 1. Reaction with Hydroquinone. *Environ. Sci. Technol.* **1984**, *18* (6), 450−456.
(637) Stone, A. T.; Morgan, J. J. Reduction and Dissolution of Manganese(III) and Manganese(IV) Oxides by Organics: 2. Survey of the Reactivity of Organics. *Environ. Sci. Technol.* **1984**, *18* (8), 617−624.
(638) Laha, S.; Luthy, R. G. Oxidation of Aniline and Other Primary Aromatic Amines by Manganese Dioxide. *Environ.Sci.Technol.* **1990**, *24*, 363−373.
(639) Zhang, H.; Huang, C.-H. Oxidative Transformation of Triclosan and Chlorophene by Manganese Oxides. *Environ. Sci. Technol.* **2003**, *37*, 2421−2430.
(640) Zhang, H.; Huang, C.-H. Oxidative Transformation of Fluoroquinolone Antibacterial Agents and Structurally Related Amines by Manganese Oxide. *Environ. Sci. Technol.* **2005**, *39* (12), 4474−4483.
(641) Zhang, H.; Huang, C.-H. Reactivity and Transformation of Antibacterial N-Oxides in the Presence of Manganese Oxide. *Environ. Sci. Technol.* **2005**, *39*, 593−601.
(642) Zhang, H.; Huang, C.-H. Adsorption and Oxidation of Fluoroquinolone Antibacterial Agents and Structurally Related Amines with Goethite. *Chemosphere* **2007**, *66* (8), 1502−1512.
(643) Lin, K.; Liu, W.; Gan, J. Reaction of Tetrabromobisphenol A (TBBPA) with Manganese Dioxide: Kinetics, Products, and Pathways. *Environ. Sci. Technol.* **2009**, *43* (12), 4480−4486.
(644) Banerjee, D.; Nesbitt, H. W. XPS Study of Reductive Dissolution of Birnessite by Oxalate: Rates and Mechanistic Aspects of Dissolution and Redox Processes. *Geochim. Cosmochim. Acta* **1999**, *63* (19), 3025−3038.
(645) Shaikh, N.; Taujale, S.; Zhang, H.; Artyushkova, K.; Ali, A.-M. S.; Cerrato, J. M. Spectroscopic Investigation of Interfacial Interaction of Manganese Oxide with Triclosan, Aniline, and Phenol. *Environ. Sci. Technol.* **2016**, *50* (20), 10978−10987.
(646) Lin, K.; Liu, W.; Gan, J. Oxidative Removal of Bisphenol A by Manganese Dioxide: Efficacy, Products, and Pathways. *Enviorn. Sci. Technol.* **2009**, *43*, 3860−3864.
(647) Lafferty, B. J.; Ginder-Vogel, M.; Zhu, M.; Livi, K. J. T.; Sparks, D. L. Arsenite Oxidation by a Poorly Crystalline Manganese-Oxide. 2. Results from X-ray Absorption Spectroscopy and X-ray Diffraction. *Environ. Sci. Technol.* **2010**, *44* (22), 8467−8472.
(648) Villalobos, M.; Escobar-Quiroz, I. N.; Salazar-Camacho, C. The Influence of Particle Size and Structure on the Sorption and Oxidation Behavior of Birnessite: I. Adsorption of As(V) and Bxidation of As(III). *Geochim. Cosmochim. Acta* **2014**, *125*, 564−581.
(649) Zhang, H.; Rasamani, K. D.; Zhong, S.; Taujale, S.; Baratta, L. R.; Yang, Z. Dissolution, Adsorption, and Redox Reaction in Ternary Mixtures of Goethite, Aluminum Oxides, and Hydroquinone. *J. Phys. Chem. C* **2019**, *123* (7), 4371−4379.
(650) LaKind, J. S.; Stone, A. T. Reductive Dissolution of Goethite by Phenolic Reductants. *Geochim. Cosmochim. Acta* **1989**, *53* (5), 961−971.
(651) Ying, S. C.; Kocar, B. D.; Fendorf, S. Oxidation and Competitive Retention of Arsenic Between Iron- and Manganese Oxides. *Geochim. Cosmochim. Acta* **2012**, *96*, 294−303.
(652) Xu, L.; Xu, C.; Zhao, M.; Qiu, Y.; Sheng, G. D. Oxidative Removal of Aqueous Steroid Estrogens by Manganese Oxides. *Water Res.* **2008**, *42* (20), 5038−5044.
(653) Zhu, M.-X.; Wang, Z.; Xu, S.-H.; Li, T. Decolorization of Methylene Blue by δ-MnO_2-Coated Montmorillonite Complexes: Emphasizing Redox Reactivity of Mn-Oxide Coatings. *J. Hazard. Mater.* **2010**, *181* (1), 57−64.
(654) Taujale, S.; Zhang, H. Impact of Interactions Between Metal Oxides to Oxidative Reactivity of Manganese Dioxide. *Environ. Sci. Technol.* **2012**, *46*, 2764−2771.
(655) Zhang, H.; Taujale, S.; Huang, J.; Lee, G.-j. Effects of NOM on Oxidative Reactivity of Manganese Dioxide in Binary Oxide Mixtures with Goethite or Hematite. *Langmuir* **2015**, *31*, 2790−2799.
(656) Taujale, S.; Baratta, L. R.; Huang, J.; Zhang, H. Interactions in Ternary Mixtures of MnO2, Al2O3, and Natural Organic Matter (NOM) and the Impact on MnO2 Oxidative Reactivity. *Environ. Sci. Technol.* **2016**, *50* (5), 2345−2353.
(657) Zhang, H.; Rasamani, K. D.; Zhong, S.; Taujale, S.; Baratta, L. R.; Yang, Z. Dissolution, Adsorption, and Redox Reaction in Ternary Mixtures of Goethite, Aluminum Oxides, and Hydroquinone. *J. Phys. Chem. C* **2019**, *123*, 4371−4379.
(658) Jones, A. M.; Collins, R. N.; Rose, J.; Waite, T. D. The Effect of Silica and Natural Organic Matter on the Fe(II)-Catalysed Transformation and Reactivity of Fe(III) Minerals. *Geochim. Cosmochim. Acta* **2009**, *73*, 4409−4422.
(659) Pedersen, H. D.; Postma, D.; Jakobsen, R.; Larsen, O. Fast Transformation of Iron Oxyhydroxides by the Catalytic Action of Aqueous Fe (II). *Geochim. Cosmochim. Acta* **2005**, *69* (16), 3967−3977.
(660) Klausen, J.; Trober, S. P.; Haderlein, S. B.; Schwarzenbach, R. P. Reduction of Substituted Nitrobenzenes by Fe(II) in Aqueous Mineral Suspensions. *Environ. Sci. Technol.* **1995**, *29*, 2396−2404.
(661) Pecher, K.; Haderlein, S. B.; Schwarzenbach, R. P. Reduction of Polyhalogenated Methanes by Surface-Bound Fe(II) in Aqueous Suspensions of Iron Oxides. *Environ. Sci. Technol.* **2002**, *36* (8), 1734−1741.
(662) Handler, R. M.; Beard, B. L.; Johnson, C. M.; Scherer, M. M. Atom Exchange Between Aqueous Fe(II) and Goethite: A Fe Isotope Tracer Study. *Environ. Sci. Technol.* **2009**, *43* (4), 1102−1107.
(663) Gorski, C. A.; Scherer, M. M. Fe2+ Sorption at the Fe Oxide−Water Interface: A Revised Conceptual Framework. In *Aquatic Redox Chemistry*; ACS Symposium Series, Vol. 1071; American Chemical Society, 2011; Vol. *1071*; pp 315−343.
(664) Huang, J.; Jones, A.; Waite, T. D.; Chen, Y.; Huang, X.; Rosso, K. M.; Kappler, A.; Mansor, M.; Tratnyek, P. G.; Zhang, H. Fe(II) Redox Chemistry in the Environment. *Chem. Rev.* **2021**, *121* (13), 8161−8233.

https://doi.org/10.1021/acs.chemrev.2c00130
Chem. Rev. 2023, 123, 6413−6544

(665) Maithreepala, R.; Doong, R.-A. Synergistic Effect of Copper Ion on the Reductive Dechlorination of Carbon Tetrachloride by Surface-Bound Fe(II) Associated with Goethite. *Environ. Sci. Technol.* **2004**, *38* (1), 260−268.
(666) Zhang, H.; Weber, E. J. Elucidating the Role of Electron Shuttles in Reductive Transformations in Anaerobic Sediments. *Environ. Sci. Technol.* **2009**, *43* (4), 1042−1048.
(667) Colón, D.; Weber, E. J.; Anderson, J. L. Effect of Natural Organic Matter on the Reduction of Nitroaromatics by Fe(II) Species. *Environ. Sci. Technol.* **2008**, *42* (17), 6538−6543.
(668) Huang, J.; Wang, Q.; Wang, Z.; Zhang, H. Interactions and Reductive Reactivity in Ternary Mixtures of Fe(II), Goethite, and Phthalic Acid Based on a Combined Experimental and Modeling Approach. *Langmuir* **2019**, *35*, 8220−8227.
(669) Huang, J.; Dai, Y.; Liu, C. C.; Zhang, H. Effects of Second Metal Oxides on Surface-Mediated Reduction of Contaminants by Fe(II) with Iron Oxide. *ACS Earth Space Chem.* **2019**, *3* (5), 680−687.
(670) Gorski, C. A.; Klüpfel, L. E.; Voegelin, A.; Sander, M.; Hofstetter, T. B. Redox Properties of Structural Fe in Clay Minerals: 3. Relationships between Smectite Redox and Structural Properties. *Environ. Sci. Technol.* **2013**, *47* (23), 13477−13485.
(671) Stucki, J. W. Chapter 8: Properties and Behaviour of Iron in Clay Minerals. *Dev. Clay Sci.* **2006**, *1*, 423−475.
(672) Alexandrov, V.; Rosso, K. M. Insights into the Mechanism of Fe(II) Adsorption and Oxidation at Fe-Clay Mineral Surfaces from First-Principles Calculations. *J. Phys. Chem. C* **2013**, *117* (44), 22880−22886.
(673) Neumann, A.; Olson, T. L.; Scherer, M. M. Spectroscopic Evidence for Fe(II)-Fe(III) Electron Transfer at Clay Mineral Edge and Basal Sites. *Environ. Sci. Technol.* **2013**, *47* (13), 6969−6977.
(674) Latta, D. E.; Neumann, A.; Premaratne, W. A. P. J.; Scherer, M. M. Fe(II)-Fe(III) Electron Transfer in a Clay Mineral with Low Fe Content. *ACS Earth Space Chem.* **2017**, *1* (4), 197−208.
(675) Ilgen, A. G.; Kukkadapu, R. K.; Leung, K.; Washington, R. E. Switching On" Iron in Clay Minerals. *Environ. Sci. Nano* **2019**, *6* (6), 1704−1715.
(676) Neumann, A.; Wu, L.; Li, W.; Beard, B. L.; Johnson, C. M.; Rosso, K. M.; Frierdich, A. J.; Scherer, M. M. Atom Exchange Between Aqueous Fe(II) and Structural Fe in Clay Minerals. *Environ. Sci. Technol.* **2015**, *49* (5), 2786−2795.
(677) Schaefer, M. V.; Gorski, C. A.; Scherer, M. M. Spectroscopic Evidence for Interfacial Fe(II)-Fe(III) Electron Transfer in a Clay Mineral. *Environ. Sci. Technol.* **2011**, *45* (2), 540−545.
(678) Jardine, P. M.; Stewart, M. A.; Barnett, M. O.; Basta, N. T.; Brooks, S. C.; Fendorf, S.; Mehlhorn, T. L. Influence of Soil Geochemical and Physical Properties on Chromium(VI) Sorption and Bioaccessibility. *Environ. Sci. Technol.* **2013**, *47*, 11241−11248.
(679) Shahid, M.; Shamshad, S.; Rafiq, M.; Khalid, S.; Bibi, I.; Niazi, N. K.; Dumat, C.; Rashid, M. I. Chromium Speciation, Bioavailability, Uptake, Toxicity and Detoxification in Soil-Plant System: A Review. *Chemosphere* **2017**, *178*, 513−533.
(680) Bibi, I.; Niazi, N. K.; Choppala, G.; Burton, E. Chromium(VI) Removal by Siderite ($FeCO_3$) in Anoxic Aqueous Solutions: An X-Ray Absorption Spectroscopy Investigation. *Sci. Total Environ.* **2018**, *640-641*, 1424−1431.
(681) Amstaetter, K.; Borch, T.; Larese-Casanova, P.; Kappler, A. Redox Transformation of Arsenic by Fe(II)-Activated Goethite (α-FeOOH). *Environ. Sci. Technol.* **2010**, *44*, 102−108.
(682) Perez, J. P. H; Freeman, H. M.; Schuessler, J. A.; Benning, L. G. The Interfacial Reactivity of Arsenic Species with Green Rust Sulfate ($GRSO_4$). *Sci. Total Environ.* **2019**, *648*, 1161−1170.
(683) Charlet, L.; Scheinost, A. C.; Tournassat, C.; Greneche, J. M.; Géhin, A.; Fernández-Martínez, A.; Coudert, S.; Tisserand, D.; Brendle, J. Electron Transfer at the Mineral/Water Interface: Selenium Reduction by Ferrous Iron Sorbed on Clay. *Geochim. Cosmochim. Acta* **2007**, *71*, 5731−5749.
(684) Scheinost, A. C.; Charlet, L. Selenite Reduction by Mackinawite, Magnetite and Siderite: XAS Characterization of Nanosized Redox Products. *Environ. Sci. Technol.* **2008**, *42*, 1984−1989.
(685) Wiramanaden, C. I.E.; Liber, K.; Pickering, I. Selenium Speciation in Whole Sediment Using X-Ray Absorption Spectroscopy and Micro X-Ray Fluorescence Imaging. *Environ. Sci. Technol.* **2010**, *44*, 5389−5394.
(686) Rosenfeld, C. E.; Kenyon, J. A.; James, B. R.; Santelli, C. M. Selenium (IV,VI) Reduction and Tolerance by Fungi in an Oxic Environment. *Geobiology* **2017**, *15*, 441−452.
(687) Fredrickson, J. K.; Zachara, J. M.; Kennedy, D. W.; Dong, H.; Onstott, T. C.; Hinman, N. W.; Li, S. M. Biogenic Iron Mineralization Accompanying the Dissimilatory Reduction of Hydrous Ferric Oxide by a Groundwater Bacterium. *Geochim. Cosmochim. Acta* **1998**, *62*, 3239−3257.
(688) Williams, A. G. B.; Scherer, M. Kinetics of Cr(VI) Reduction by Carbonate Green Rust. *Environ. Sci. Technol.* **2001**, *35*, 3488−3494.
(689) Usman, M.; Byrne, J. M.; Chaudhary, A.; Orsetti, S.; Hanna, K.; Ruby, C.; Kappler, A.; Haderlein, S. B. Magnetite and Green Rust: Synthesis, Properties, and Environmental Applications of Mixed-Valent Iron Minerals. *Chem. Rev.* **2018**, *118*, 3251−3304.
(690) Fendorf, S.; Wielinga, B. W.; Hansel, C. M. Chromium Transformations in Natural Environments: The Role of Biological and Abiological Processes in Chromium(vi) Reduction. *Int. Geol. Rev.* **2000**, *42*, 691−701.
(691) Dhal, B.; Thatoi, H. N.; Das, N. N.; Pandey, B. D. Chemical and Microbial Remediation of Hexavalent Chromium from Contaminated Soil and Mining/Metallurgical Solid Waste: A review. *J. Hazard. Mater.* **2013**, *250-251*, 272−291.
(692) Pettine, M.; D'Ottone, L.; Campanella, L.; Millero, F. J.; Passino, R. The Reduction of Chromium (VI) by Iron (II) in Aqueous Solutions. *Geochim. Cosmochim. Acta* **1998**, *62*, 1509−1519.
(693) Pettine, M.; Millero, F. J.; Passino, R. Reduction of Chromium (VI) with Hydrogen Sulfide in NaCl Media. *Mar. Chem.* **1994**, *46*, 335−344.
(694) Hug, S. J.; Laubscher, H. U.; James, B. R. Iron(III) Catalyzed Photochemical Reduction of Chromium(VI) by Oxalate and Citrate in Aqueous Solutions. *Environ. Sci. Technol.* **1997**, *31*, 160−170.
(695) Deng, B.; Stone, A. T. Surface-Catalyzed Chromium(VI) Reduction: The TiO2-CrVI-Mandelic Acid System. *Environ. Sci. Technol.* **1996**, *30*, 463−472.
(696) Peterson, M. L. P; White, A. F.; Brown, G. E.; Parks, G. A. Surface Passivation of Magnetite by Reaction with Aqueous Cr(VI): XAFS and TEM Results. *Environ. Sci. Technol.* **1997**, *31*, 1573−1576.
(697) Loyaux-Lawniczak, S.; Refait, P.; Ehrhardt, J. J.; Lecomte, P.; Génin, J. M. R. Trapping of Cr by Formation of Ferrihydrite During the Reduction of Chromate Ions by Fe(II)-Fe(III) Hydroxysalt Green Rusts. *Environ. Sci. Technol.* **2000**, *34*, 438−443.
(698) Lovley, D. R. Dissimilatory Metal Reduction. *Annu. Rev. Microbiol.* **1993**, *47*, 263−290.
(699) Lovley, D. R.; Phillips, E. J. P.; Gorby, Y. A.; Landa, E. R. Microbial Reduction of Uranium. *Nature* **1991**, *350*, 413−416.
(700) James, B. R.; Bartlett, R. J. Behavior of Chromium in Soils: V. Fate of Organically Complexed Cr(III) Added to Soil. *J. Environ. Qual.* **1983**, *12*, 169−172.
(701) Brauer, S. L.; Hneihen, A. S.; McBride, J. S.; Wetterhahn, K. E. Chromium(VI) Forms Thiolate Complexes with γ-Glutamylcysteine, N-Acetylcysteine, Cysteine, and the Methyl Ester of N-Acetylcysteine. *Inorg. Chem.* **1996**, *35*, 373−381.
(702) Lay, P. A.; Levina, A. Kinetics and Mechanism of Chromium(III) Reduction to Chromium(III) by L-Cysteine in Neutral Aqueous Solutions. *Inorg. Chem.* **1996**, *35*, 7709−7717.
(703) Sherman, D. M. Electronic Structures of Iron (III) and Manganese (IV)(Hydr) Oxide Minerals: Thermodynamics of Photochemical Reductive Dissolution in Aquatic Environments. *Geochim. Cosmochim. Acta* **2005**, *69* (13), 3249−3255.
(704) Hochella, M. F.; Lower, S. K.; Maurice, P. A.; Penn, R. L.; Sahai, N.; Sparks, D. L.; Twining, B. S. Nanominerals, Mineral Nanoparticles, and Earth Systems. *Science* **2008**, *319* (5870), 1631.

https://doi.org/10.1021/acs.chemrev.2c00130
Chem. Rev. 2023, 123, 6413−6544

(705) Miller, W. L.; King, D. W.; Lin, J.; Kester, D. R. Photochemical Redox Cycling of Iron in Coastal Seawater. *Mar. Chem.* **1995**, *50* (1-4), 63−77.
(706) Wigginton, N. S.; Haus, K. L.; Hochella, M. F., Jr Aquatic Environmental Nanoparticles. *J. Environ. Monit.* **2007**, *9* (12), 1306−1316.
(707) Voelker, B. M.; Morel, F. M.; Sulzberger, B. Iron Redox Cycling in Surface Waters: Effects of Humic Substances and Light. *Environ. Sci. Technol.* **1997**, *31* (4), 1004−1011.
(708) Borer, P.; Sulzberger, B.; Hug, S. J.; Kraemer, S. M.; Kretzschmar, R. Photoreductive Dissolution of Iron (III)(hydr)oxides in the Absence and Presence of Organic Ligands: Experimental Studies and Kinetic Modeling. *Environ. Sci. Technol.* **2009**, *43* (6), 1864−1870.
(709) Boyd, P. W.; Ellwood, M. J. The Biogeochemical Cycle of Iron in the Ocean. *Nat. Geosci.* **2010**, *3* (10), 675−682.
(710) Sunda, W.; Huntsman, S.; Harvey, G. Photoreduction of Manganese Oxides in Seawater and its Geochemical and Biological Implications. *Nature* **1983**, *301* (5897), 234−236.
(711) Siffert, C.; Sulzberger, B. Light-Induced Dissolution of Hematite in the Presence of Oxalate. A Case Study. *Langmuir* **1991**, *7* (8), 1627−1634.
(712) Jickells, T.; An, Z.; Andersen, K. K.; Baker, A.; Bergametti, G.; Brooks, N.; Cao, J.; Boyd, P.; Duce, R.; Hunter, K. Global Iron Connections Between Desert Dust, Ocean Biogeochemistry, and Climate. *Science* **2005**, *308*, 67−71.
(713) Zong, M.; Song, D.; Zhang, X.; Huang, X.; Lu, X.; Rosso, K. M. Facet-Dependent Photodegradation of Methylene Blue by Hematite Nanoplates in Visible Light. *Environ. Sci. Technol.* **2021**, *55* (1), 677−688.
(714) Huang, X.; Chen, Y.; Walter, E.; Zong, M.; Wang, Y.; Zhang, X.; Qafoku, O.; Wang, Z.; Rosso, K. M. Facet-Specific Photocatalytic Degradation of Organics by Heterogeneous Fenton Chemistry on Hematite Nanoparticles. *Environ. Sci. Technol.* **2019**, *53* (17), 10197−10207.
(715) Byrne, J. M.; Klueglein, N.; Pearce, C.; Rosso, K. M.; Appel, E.; Kappler, A. Redox Cycling of Fe (II) and Fe (III) in Magnetite by Fe-Metabolizing Bacteria. *Science* **2015**, *347* (6229), 1473−1476.
(716) Liao, P.; Carter, E. A. Testing Variations of the GW Approximation on Strongly Correlated Transition Metal Oxides: Hematite (α-Fe_2O_3) as a Benchmark. *Phys. Chem. Chem. Phys.* **2011**, *13* (33), 15189−15199.
(717) Ergönenc, Z.; Kim, B.; Liu, P.; Kresse, G.; Franchini, C. Converged G W Quasiparticle Energies for Transition Metal Oxide Perovskites. *Phys. Rev. Mater.* **2018**, *2* (2), 024601.
(718) Schleife, A.; Varley, J.; Fuchs, F.; Rödl, C.; Bechstedt, F.; Rinke, P.; Janotti, A.; Van de Walle, C. Tin Dioxide from First Principles: Quasiparticle Electronic States and Optical Properties. *Phys. Rev. B* **2011**, *83* (3), 035116.
(719) Ping, Y.; Rocca, D.; Galli, G. Optical Properties of Tungsten Trioxide from First-Principles Calculations. *Phys. Rev. B* **2013**, *87* (16), 165203.
(720) Perdew, J. P.; Yang, W.; Burke, K.; Yang, Z.; Gross, E. K.; Scheffler, M.; Scuseria, G. E.; Henderson, T. M.; Zhang, I. Y.; Ruzsinszky, A.; et al. Understanding Band Gaps of Solids in Generalized Kohn-Sham Theory. *Proc. Natl. Acad. Sci. U.S.A.* **2017**, *114*, 2801−2806.
(721) McClain, J.; Sun, Q.; Chan, G. K.-L.; Berkelbach, T. C. Gaussian-Based Coupled-Cluster Theory for the Ground-State and Band Structure of Solids. *J. Chem. Theory Comput.* **2017**, *13* (3), 1209−1218.
(722) Gao, Y.; Sun, Q.; Yu, J. M.; Motta, M.; McClain, J.; White, A. F.; Minnich, A. J.; Chan, G. K.-L. Electronic Structure of Bulk Manganese Oxide and Nickel Oxide from Coupled Cluster Theory. *Phys. Rev. B* **2020**, *101*, 165138.
(723) Rosso, K. M.; Dupuis, M. Reorganization Energy Associated with Small Polaron Mobility in Iron Oxide. *J. Chem. Phys.* **2004**, *120* (15), 7050−7054.
(724) Alexandrov, V.; Rosso, K. M. Electron Transport in Pure and Substituted Iron Oxyhydroxides by Small-Polaron Migration. *J. Chem. Phys.* **2014**, *140* (23), 234701.
(725) Ahart, C. S.; Blumberger, J.; Rosso, K. M. Polaronic Structure of Excess Electrons and Holes for a Series of Bulk Iron Oxides. *Phys. Chem. Chem. Phys.* **2020**, *22* (19), 10699−10709.
(726) Di Valentin, C.; Selloni, A. Bulk and Surface Polarons in Photoexcited Anatase TiO2. *J. Phys. Chem. Lett.* **2011**, *2* (17), 2223−2228.
(727) Selcuk, S.; Selloni, A. Facet-Dependent Trapping and Dynamics of Excess Electrons at Anatase TiO_2 Surfaces and Aqueous Interfaces. *Nat. Mater.* **2016**, *15* (10), 1107−1112.
(728) Wen, B.; Yin, W.-J.; Selloni, A.; Liu, L.-M. Defects, Adsorbates, and Photoactivity of Rutile TiO2 (110): Insight by Frst-Principles Calculations. *J. Phys. Chem. Lett.* **2018**, *9* (18), 5281−5287.
(729) Franchini, C.; Reticcioli, M.; Setvin, M.; Diebold, U. Polarons in Materials. *Nat. Rev. Mater.* **2021**, *6*, 560−586.
(730) Zarzycki, P.; Rosso, K. M. Energetics and the Role of Defects in Fe (II)-Catalyzed Goethite Recrystallization from Molecular Simulations. *ACS Earth Space Chem.* **2019**, *3* (2), 262−272.
(731) Remsing, R. C.; Bates, J. E. Effective Mass Path Integral Simulations of Quasiparticles in Condensed Phases. *J. Chem. Phys.* **2020**, *153* (12), 121104.
(732) Rego, L. G.; Batista, V. S. Quantum Dynamics Simulations of Interfacial Electron Transfer in Sensitized TiO2 Semiconductors. *J. Am. Chem. Soc.* **2003**, *125* (26), 7989−7997.
(733) Duncan, W. R.; Prezhdo, O. V. Theoretical Studies of Photoinduced Electron Transfer in Dye-Sensitized TiO2. *Annu. Rev. Phys. Chem.* **2007**, *58*, 143−184.
(734) Oliboni, R. S.; Yan, H.; Fan, H.; Abraham, B.; Avenoso, J. P.; Galoppini, E.; Batista, V. S.; Gundlach, L.; Rego, L. G. Vibronic Effects in the Ultrafast Interfacial Electron Transfer of Perylene-Sensitized TiO2 Surfaces. *J. Phys. Chem. C* **2019**, *123* (20), 12599−12607.
(735) Akimov, A. V.; Neukirch, A. J.; Prezhdo, O. V. Theoretical Insights into Photoinduced Charge Transfer and Catalysis at Oxide Interfaces. *Chem. Rev.* **2013**, *113* (6), 4496−4565.
(736) Zhang, L.; Chu, W.; Zhao, C.; Zheng, Q.; Prezhdo, O. V.; Zhao, J. Dynamics of Photoexcited Small Polarons in Transition-Metal Oxides. *J. Phys. Chem. Lett.* **2021**, *12* (9), 2191−2198.
(737) Abuabara, S. G.; Rego, L. G.; Batista, V. S. Influence of Thermal Fluctuations on Interfacial Electron Transfer in Functionalized TiO2 Semiconductors. *J. Am. Chem. Soc.* **2005**, *127* (51), 18234−18242.
(738) Torres, A.; Oliboni, R. S.; Rego, L. G. Vibronic and Coherent Effects on Interfacial Electron Transfer Dynamics. *J. Phys. Chem. Lett.* **2015**, *6* (24), 4927−4935.
(739) Limo, M. J.; Sola-Rabada, A.; Boix, E.; Thota, V.; Westcott, Z. C.; Puddu, V.; Perry, C. C. Interactions Between Metal Oxides and Biomolecules: From Fundamental Understanding to Applications. *Chem. Rev.* **2018**, *118*, 11118−11193.
(740) Mudunkotuwa, I. A.; Minshid, A. A.; Grassian, V. H. ATR-FTIR Spectroscopy as a Tool to Probe Surface Adsorption on Nanoparticles at the Liquid-Solid Interface in Environmentally and Biologically Relevant Media. *Analyst* **2014**, *139* (5), 870−881.
(741) Mudunkotuwa, I. A.; Grassian, V. H. Biological and Environmental Media Control Oxide Nanoparticle Surface Composition: The Roles of Biological Components (Proteins and Amino Acids), Inorganic Oxyanions and Humic Acid. *Environ. Sci. Nano* **2015**, *2* (5), 429−439.
(742) Cai, P.; Lin, D.; Peacock, C. L.; Peng, W.; Huang, Q. EPS Adsorption to Goethite: Molecular Level Adsorption Mechanisms Using 2D Correlation Spectroscopy. *Chem. Geol.* **2018**, *494*, 127−135.
(743) Wang, G.; Chen, L.; Weng, D.; Wang, J. Role of Extracellular Polymeric Substances in the Adhesion Interaction of Streptococcus Mutans on TiO2 and SiO2 Surfaces with Different Wettability. *Colloid Interface Sci. Commun.* **2020**, *39*, 100315.

https://doi.org/10.1021/acs.chemrev.2c00130
Chem. Rev. 2023, 123, 6413−6544

(744) Xu, Z.; Grassian, V. H. Bovine Serum Albumin Adsorption on TiO_2 Nanoparticle Surfaces: Effects of pH and Coadsorption of Phosphate on Protein-Surface Interactions and Protein Structure. *J. Phys. Chem. C* **2017**, *121* (39), 21763−21771.
(745) Givens, B. E.; Diklich, N. D.; Fiegel, J.; Grassian, V. H. Adsorption of Bovine Serum Albumin on Silicon Dioxide Nanoparticles: Impact of pH on Nanoparticle-Protein Interactions. *Biointerphases* **2017**, *12* (2), 02D404.
(746) Givens, B. E.; Xu, Z.; Fiegel, J.; Grassian, V. H. Bovine Serum Albumin Adsorption on SiO_2 and TiO_2 Nanoparticle Surfaces at Circumneutral and Acidic pH: A Tale of two Nano-Bio Surface Interactions. *J. Colloid Interface Sci.* **2017**, *493*, 334−341.
(747) Sit, I.; Xu, Z.; Grassian, V. H. Plasma Protein Adsorption on TiO_2 Nanoparticles: Impact of Surface Adsorption on Temperature-Dependent Structural Changes. *Polyhedron* **2019**, *171*, 147−154.
(748) Vallee, A.; Humblot, V.; Pradier, C. M. Peptide Interactions with Metal and Oxide Surfaces. *Acc. Chem. Res.* **2010**, *43* (10), 1297−1306.
(749) Ustunol, I. B.; Gonzalez-Pech, N. I.; Grassian, V. H. pH-Dependent Adsorption of α-Amino Acids, Lysine, Glutamic Acid, Serine and Glycine, on TiO_2 Nanoparticle Surfaces. *J. Colloid Interface Sci.* **2019**, *554*, 362−375.
(750) Srinivasu, B. Y.; Bose, B.; Mitra, G.; Kurpad, A. V.; Mandal, A. K. Adsorption Induced Changes of Human Hemoglobin on Ferric Pyrophosphate Nanoparticle Surface Probed by Isotope Exchange Mass Spectrometry: An Implication on Structure-Function Correlation. *Langmuir* **2017**, *33* (32), 8032−8042.
(751) Buijs, J.; Ramstrom, M.; Danfelter, M.; Larsericsdotter, H.; Hakansson, P.; Oscarsson, S. Localized Changes in the Structural Stability of Myoglobin upon Adsorption onto Silica Particles, as Studied with Hydrogen/Deuterium Exchange Mass Spectrometry. *J. Colloid Interface Sci.* **2003**, *263*, 441−448.
(752) Schmidt, M. P.; Martínez, C. E. Ironing Out Genes in the Environment: An Experimental Study of the DNA-Goethite Interface. *Langmuir* **2017**, *33* (34), 8525−8532.
(753) Sampath, J.; Kullman, A.; Gebhart, R.; Drobny, G.; Pfaendtner, J. Molecular Recognition and Specificity of Biomolecules to Titanium Dioxide from Molecular Dynamics Simulations. *NPJ. Comput. Mater.* **2020**, *6*, 34.
(754) Borcherding, J.; Baltrusaitis, J.; Chen, H.; Stebounova, L.; Wu, C. M.; Rubasinghege, G.; Mudunkotuwa, I. A.; Caraballo, J. C.; Zabner, J.; Grassian, V. H.; et al. Iron Oxide Nanoparticles Induce Pseudomonas Aeruginosa Growth, Induce Biofilm Formation, and Inhibit Antimicrobial Peptide Function. *Environ. Sci. Nano* **2014**, *1* (2), 123−132.
(755) Marques, M. R. C.; Loebenberg, R.; Almukainzi, M. Simulated Biological Fluids with Possible Application in Dissolution Testing. *Dissolut. Technol.* **2011**, *18* (3), 15−28.
(756) Zhu, Y.; Yang, Q.; Lu, T.; Qi, W.; Zhang, H.; Wang, M.; Qi, Z.; Chen, W. Effect of Phosphate on the Adsorption of Antibiotics onto Iron Oxide Minerals: Comparison Between Tetracycline and Ciprofloxacin. *Ecotox. Environ. Safe.* **2020**, *205*, 111345.
(757) Gadd, G. M. Metals, Minerals and Microbes: Geomicrobiology and Bioremediation. *Microbiology* **2010**, *156*, 609−643.
(758) Fomina, M.; Gadd, G. M. Biosorption: Current Perspectives on Concept, Definition and Application. *Bioresour. Technol.* **2014**, *160*, 3−14.
(759) Dong, H. Clay-Microbe Interactions and Implications for Environmental Mitigation. *Elements* **2012**, *8* (2), 113−118.
(760) Dong, H. Mineral−Microbe Interactions: A Review. *Front. Earth Sci. China* **2010**, *4*, 127−147.
(761) Hong, Z.; Chen, W.; Rong, X.; Cai, P.; Dai, K.; Huang, Q. The Effect of Extracellular Polymeric Substances on the Adhesion of Bacteria to Clay Minerals and Goethite. *Chem. Geol.* **2013**, *360-361*, 118−125.
(762) Hong, Z.-N.; Jiang, J.; Li, J.-Y.; Xu, R.-K. Preferential Adhesion of Surface Groups of Bacillus Subtilis on Gibbsite at Different Ionic Strengths and pHs Revealed by ATR-FTIR Spectroscopy. *Colloids Surf. B Biointerfaces* **2018**, *165*, 83−91.
(763) Roberts, J. A. Inhibition and Enhancement of Microbial Surface Colonization: The Role of Silicate Composition. *Chem. Geol.* **2004**, *212* (3), 313−327.
(764) Kendall, T. A.; Lower, S. K. Forces Between Minerals and Biological Surfaces in Aqueous Solution. *Adv. Agron.* **2004**, *82*, 1−54.
(765) Carniello, V.; Peterson, B. W.; van der Mei, H. C.; Busscher, H. J. Physico-Chemistry from Initial Bacterial Adhesion to Surface-Programmed Biofilm Growth. *Adv. Colloid Interface Sci.* **2018**, *261*, 1−14.
(766) Flemming, H. C.; Wingender, J.; Szewzyk, U.; Steinberg, P.; Rice, S. A.; Kjelleberg, S. Biofilms: An Emergent Form of Bacterial Life. *Nat. Rev. Microbiol.* **2016**, *14*, 563−575.
(767) Li, Y.-H.; Tian, X. Quorum Sensing and Bacterial Social Interactions in Biofilms. *Sensors* **2012**, *12*, 2519−2538.
(768) Palmer, J.; Flint, S.; Brooks, J. Bacterial Cell Attachment, The Beginning of a Biofilm. *J. Ind. Microbiol. Biotechnol.* **2007**, *34*, 577−588.
(769) Huang, Q.; Wu, H.; Cai, P.; Fein, J. B.; Chen, W. Atomic Force Microscopy Measurements of Bacterial Adhesion and Biofilm Formation onto Clay-Sized Particles. *Sci. Rep.* **2015**, *5*, 16857.
(770) Lower, S. K.; Hochella, M. F.; Beveridge, T. J. Bacterial Recognition of Mineral Surfaces: Nanoscale Interactions Between Shewanella and α-FeOOH. *Science* **2001**, *292*, 1360−1363.
(771) Ruan, B.; Wu, P.; Liu, J.; Jiang, L.; Wang, H.; Qiao, J.; Zhu, N.; Dang, Z.; Luo, H.; Yi, X. Adhesion of Sphingomonas sp. GY2B onto Montmorillonite: A Combination Study by Thermodynamics and the Extended DLVO Theory. *Colloids Surf. B: Biointerfaces* **2020**, *192*, 111085.
(772) Dorobantu, L. S.; Bhattacharjee, S.; Foght, J. M.; Gray, M. R. Analysis of Force Interactions Between AFM Tips and Hydrophobic Bacteria Using DLVO Theory. *Langmuir* **2009**, *25*, 6968−6976.
(773) Pawlowska, A.; Sadowski, Z. Effect of Schwertmannite Surface Modification by Surfactants on Adhesion of Acidophilic Bacteria. *Microorganisms* **2020**, *8*, 1725.
(774) Elzinga, E. J.; Huang, J. H.; Chorover, J.; Kretzschmar, R. ATR-FTIR Spectroscopy Study of the Influence of pH and Contact Time on the Adhesion of Shewanella Putrefaciens Bacterial Cells to the Surface of Hematite. *Environ. Sci. Technol.* **2012**, *46*, 12848−12855.
(775) Huang, J. H.; Elzinga, E. J.; Brechbuehl, Y.; Voegelin, A.; Kretzschmar, R. Impacts of Shewanella Putrefaciens Strain CN-32 Cells and Extracellular Polymeric Substances on the Sorption of As(V) and As(III) on Fe(III)-(Hydr)oxides. *Environ. Sci. Technol.* **2011**, *45*, 2804−2810.
(776) Banfield, J. F.; Barker, W. W.; Welch, S. A.; Taunton, A. Biological Impact on Mineral Dissolution: Application of the Lichen Model to Understanding Mineral Weathering in the Rhizosphere. *Proc. Natl. Acad. Sci. U.S.A.* **1999**, *96*, 3404−3411.
(777) Vaughan, D.; Lloyd, J. R. Mineral−Organic-Microbe Interactions: Environmental Impacts from Molecular to Macroscopic Scales. *C. R. Geosci.* **2011**, *343*, 140−159.
(778) Allison, D. G.; Sutherland, I. W. The Role of Exopolysaccharides in Adhesion of Freshwater Bacteria. *J. Gen. Microbiol.* **1987**, *133*, 1319−1327.
(779) Costerton, J. W.; Lewandowski, Z.; Caldwell, D. E.; Korber, D. R.; Lappin-Scott, n. H. M. Microbial Biofilms. *Annu. Rev. Microbiol.* **1995**, *49*, 711−745.
(780) Geesey, G. G.; Mutch, R.; Costerton, J. W.; Green, R. B. Sessile Bacteria: An Important Component of the Microbial Population in Small Mountain Streams. *Limnol. Oceanogr.* **1978**, *23*, 1214−1223.
(781) Ha, M.; Wu, M.; Tomer, M. D.; Gassman, P. W.; Isenhart, T. M.; Arnold, J. G.; White, M. J.; Parish, E. S.; Comer, K. S.; Belden, B. Biomass Production with Conservation Practices for Two Iowa Watersheds. *J. Am. Water Resour. Assoc.* **2020**, *56* (6), 1030−1044.
(782) Marshall, K. C. Biofilms : An Overview of Bacterial Adhesion, Activity, and Control at Surfaces. *Am. Soc. Microbiol. News.* **1992**, *58*, 202−207.

https://doi.org/10.1021/acs.chemrev.2c00130
Chem. Rev. 2023, 123, 6413−6544

(783) Ferris, F. G.; Fyfe, W. S.; Beveridge, T. J. Bacteria as Nucleation Sites for Authigenic Minerals in a Metal-Contaminated Lake Sediment. *Chem. Geol.* **1987**, *63*, 225−232.
(784) Ferris, F. G.; Schultze, T.; Witten, T. C.; Fyfe, W. S.; Beveridge, T. J. Metal Interactions with Microbial Biofilms in Acidic and Neutral pH Environments. *Appl. Environ. Microbiol.* **1989**, *55*, 1249−1257.
(785) Southam, G.; Ferris, F. G.; Beveridge, T. J. Mineralized Bacterial Biofilms in Sulphide Tailings and in Acid Mine Drainage Systems. In *Microbial Biofilms*; Lappin-Scott, H. M., Costerton, J. W., Eds.; Biotechnology Research, Cambridge University Press: Cambridge, 1995; pp 148−170.
(786) Geesey, G.G.; Jang, L.K. Extracellular Polymers for Metal Binding. In *Microbial Mineral Recovery*; Brierley, C., Ehrlich, H., Eds.; McGraw-Hill: NY, 1990; pp 223−249.
(787) Kellems, B. L.; Lion, L. W. Effect of Bacterial Exopolymer on Lead (II) Adsorption by γAl2O3 in Seawater. *Estuar. Coast. Shelf Sci.* **1989**, *28*, 443−457.
(788) Rudd, T.; Sterritt, R. M.; Lester, J. N. Complexation of Heavy Metals by Extracellular Polymers in the Activated Sludge Process. *J. Water Pollut. Control Fed.* **1984**, *56*, 1260−1268.
(789) Ha, J.; Gélabert, A.; Spormann, A. M.; Brown, G. E. Role of Extracellular Polymeric Substances in Metal Ion Complexation on Shewanella Oneidensis: Batch Uptake, Thermodynamic Modeling, ATR-FTIR, and EXAFS Study. *Geochim. Cosmochim. Acta* **2010**, *74*, 1−15.
(790) Beveridge, T. J.; Murray, R. G. E. Sites of Metal Deposition in the Cell Wall of Bacillus Subtilis. *J. Bacteriol.* **1980**, *141*, 876−887.
(791) Fein, J. B.; Daughney, C. J.; Yee, N.; Davis, T. A. A Chemical Equilibrium Model for Metal Adsorption onto Bacterial Surfaces. *Geochim. Cosmochim. Acta* **1997**, *61* (16), 3319−3328.
(792) Daughney, C. J.; Fein, J. B. F. The Effect of Ionic Strength on the Adsorption of H+, Cd2+, Pb2+ and Cu2+ by Bacillus Subtilis and Bacillus Licheniformis: A Surface Complexation Model. *J. Colloid Interface Sci.* **1998**, *198*, 53−77.
(793) Jiang, W.; Saxena, A.; Song, B.; Ward, B. B.; Beveridge, T. J.; Myneni, S. C. B. Elucidation of Functional Groups on Gram-Positive and Gram-Negative Bacterial Surfaces Using Infrared Spectroscopy. *Langmuir* **2004**, *20* (26), 11433−11442.
(794) Busch, P. L.; Stumm, W. Chemical Interactions in the Aggregation of Bacteria Bioflocculation in Waste Treatment. *Environ. Sci. Technol.* **1968**, *2*, 49−53.
(795) Collins, Y. E.; Stotzky, G. Heavy Metals Alter the Electrokinetic Properties of Bacteria, Yeasts, and Clay Minerals. *Appl. Environ. Microbiol.* **1992**, *58*, 1592−1600.
(796) Urrutia, M. M.; Beveridge, T. J. Formation of Short-Range Ordered Aluminosilicates in the Presence of a Bacterial Surface (Bacillus Subtilis) and Organic Ligands. *Geoderma* **1995**, *65*, 149−165.
(797) Fortin, D.; Beveridge, T. J. Role of the Bacterium Thiobacillus in the Formation of Silicates in Acidic Mine Tailings. *Chem. Geol.* **1997**, *141*, 235−250.
(798) Schultze-Lam, S.; Harauz, G.; Beveridge, T. J. Participation of a Cyanobacterial S Layer in Fine-Grain Mineral Formation. *J. Bacteriol.* **1992**, *174*, 7971−7981.
(799) Warren, L. A.; Ferris, F. G. Continuum Between Sorption and Precipitation of Fe(III) on Microbial Surfaces. *Environ. Sci. Technol.* **1998**, *32*, 2331−2337.
(800) Beveridge, T. J.; Meloche, J. D.; Fyfe, W. S.; Murray, R. G. E. Diagenesis of Metals Chemically Complexed to Bacteria: Laboratory Formation of Metal Phosphates, Sulfides, and Organic Condensates in Artificial Sediments. *Appl. Environ. Microbiol.* **1983**, *45*, 1094−1108.
(801) Brydie, J. R.; Wogelius, R. A.; Merrifield, C. M.; Boult, S.; Gilbert, P.; Allison, D.; Vaughan, D. J. The μ2M Project on Quantifying the Effects of Biofilm Growth on Hydraulic Properties of Natural Porous Media and on Sorption Equilibria: An Overview. *Geol. Soc. Spec. Publ.* **2005**, *249*, 131−144.
(802) Brydie, J. R.; Wogelius, R. A.; Boult, S.; Merrifield, C. M.; Vaughan, D. J. Model System Studies of the Influence of Bacterial Biofilm Formation on Mineral Surface Reactivity. *Biofouling* **2009**, *25*, 463−472.
(803) Neihof, R.; Loeb, G. Dissolved Organic Matter in Seawater and the Electric Charge of Immersed Surfaces. *J. Mar. Res.* **1974**, *32*, 5−12.
(804) Davis, J. A. Complexation of Trace Metals by Adsorbed Natural Organic Matter. *Geochim. Cosmochim. Acta* **1984**, *48*, 679−691.
(805) Tang, M.; Cziczo, D. J.; Grassian, V. H. Interactions of Water with Mineral Dust Aerosol: Water Adsorption, Hygroscopicity, Cloud Condensation, and Ice Nucleation. *Chem. Rev.* **2016**, *116* (7), 4205−4259.
(806) *Summary for Policymakers of the Scientific Review of the Impact of Climate Change on Plant Pests—A Global Challenge to Prevent and Mitigate Plant Pest Risks in Agriculture, Forestry and Ecosystems*; Food and Agriculture Organization of the United Nations2021; On behalf of the IPPC Secretariat.
(807) Saidou Chaibou, A. A.; Ma, X.; Sha, T. Dust Radiative Forcing and its Impact on Surface Energy Budget Over West Africa. *Sci. Rep.* **2020**, *10*, 12236.
(808) Boucher, O.; Randall, D.; Artaxo, P.; Bretherton, C.; Feingold, G.; Forster, P.; Kerminen, V.-M.; Kondo, Y.; Liao, H.; Lohmann, U.; Rasch, P.; Satheesh, S.K.; Sherwood, S.; Stevens, B.; Zhang, X.Y. Clouds and Aerosols. In *Climate Change 2013: The Physical Science Basis. Contribution of Working Group I to the Fifth Assessment Report of the Intergovernmental Panel on Climate Change*; Stocker, T.F., Qin, D., Plattner, G.-K., Tignor, M., Allen, S.K., Boschung, J., Nauels, A., Xia, Y., Bex, V., Midgley, P.M., Eds.; Cambridge University Press: Cambridge, UK, 2013; pp 571−636.
(809) Dwivedi, D.; Tang, J.; Bouskill, N.; Georgiou, K.; Chacon, S. S.; Riley, W. J. Abiotic and Biotic Controls on Soil Organo-Mineral Interactions: Developing Model Structures to Analyze Why Soil Organic Matter Persists. *Rev. Mineral. Geochem.* **2019**, *85* (1), 329−348.
(810) Hoschen, C.; Hoschen, T.; Mueller, C. W.; Lugmeier, J.; Elgeti, S.; Rennert, T.; Kogel-Knabner, I. Novel Sample Preparation Technique To Improve Spectromicroscopic Analyses of Micrometer-Sized Particles. *Environ. Sci. Technol.* **2015**, *49* (16), 9874−9880.
(811) Chen, C. L.; Qi, J. H.; Zuckermann, R. N.; DeYoreo, J. J. Engineered Biomimetic Polymers as Tunable Agents for Controlling CaCO3Mineralization. *J. Am. Chem. Soc.* **2011**, *133* (14), 5214−5217.
(812) Lukas, M.; Schwidetzky, R.; Kunert, A. T.; Pöschl, U.; Fröhlich-Nowoisky, J.; Bonn, M.; Meister, K. Electrostatic Interactions Control the Functionality of Bacterial Ice Nucleators. *J. Am. Chem. Soc.* **2020**, *142* (15), 6842−6846.
(813) Abdelmonem, A.; Backus, E. H. G.; Hoffmann, N.; Sánchez, M. A.; Cyran, J. D.; Kiselev, A.; Bonn, M. Surface-Charge-Induced Orientation of Interfacial Water Suppresses Heterogeneous Ice Nucleation on α-Alumina (0001). *Atmos. Chem. Phys.* **2017**, *17* (12), 7827−7837.
(814) Anim-Danso, E.; Zhang, Y.; Dhinojwala, A. Surface Charge Affects the Structure of Interfacial Ice. *J. Phys. Chem. C* **2016**, *120* (7), 3741−3748.
(815) Glatz, B.; Sarupria, S. The Surface Charge Distribution Affects The Ice Nucleating Efficiency of Silver Iodide. *J. Chem. Phys.* **2016**, *145* (21), 211924.
(816) Kiselev, A.; Bachmann, F.; Pedevilla, P.; Cox, S. J.; Michaelides, A.; Gerthsen, D.; Leisner, T. Active Sites in Heterogeneous Ice Nucleation—The Example of K-Rich Feldspars. *Science* **2017**, *355*, 367−371.
(817) Di Biagio, C.; Balkanski, Y.; Albani, S.; Boucher, O.; Formenti, P. Direct Radiative Effect by Mineral Dust Aerosols Constrained by New Microphysical and Spectral Optical Data. *Geophys. Res. Lett.* **2020**, *47*, No. e2019GL086186.
(818) Li, P.; Li, X.; Meng, X.; Li, M.; Zhang, Y. Appraising Groundwater Quality and Health Risks from Contamination in a Semiarid Region of Northwest China. *Exposure and Health* **2016**, *8* (3), 361−379.

https://doi.org/10.1021/acs.chemrev.2c00130
Chem. Rev. 2023, 123, 6413−6544

(819) Mathis, J. T.; Cross, J. N.; Bates, N. R. The Role of Ocean Acidification in Systemic Carbonate Mineral Suppression in the Bering Sea. *Geophys. Res. Lett.* **2011**, *38*, 2011GL048884.
(820) Cwiertny, D. M.; Baltrusaitis, J.; Hunter, G. J.; Laskin, A.; Scherer, M. M.; Grassian, V. H. Characterization and Acid-Mobilization Study of Iron-Containing Mineral Dust Source Materials. *J. Geophys. Res. Atmos.* **2008**, *113*, 2007JD009332.
(821) Journet, E.; Desboeufs, K. V.; Caquineau, S.; Colin, J. L. Mineralogy as a Critical Factor of Dust Iron Solubility. *Geophys. Res. Lett.* **2008**, *35*, 2007GL031589.
(822) Rubasinghege, G.; Lentz, R. W.; Scherer, M. M.; Grassian, V. H. Simulated Atmospheric Processing of Iron Oxyhydroxide Minerals at Low pH: Roles of Particle Size and Acid Anion in Iron Dissolution. *Proc. Natl. Acad. Sci. U.S.A.* **2010**, *107* (15), 6628−6633.
(823) Jun, Y. S.; Giammar, D. E.; Werth, C. J. Impacts of Geochemical Reactions on Geologic Carbon Sequestration. *Environ. Sci. Technol.* **2013**, *47* (1), 3−8.
(824) Shao, H. B.; Ray, J. R.; Jun, Y. S. Dissolution and Precipitation of Clay Minerals under Geologic CO_2 Sequestration Conditions: CO_2-Brine-Phlogopite Interactions. *Environ. Sci. Technol.* **2010**, *44* (15), 5999−6005.
(825) Kate, J. M.; Gokhale, C. S. A Simple Method to Estimate Complete Pore Size Distribution of Rocks. *Eng. Geol.* **2006**, *84* (1-2), 48−69.
(826) Franzluebbers, A. J. Achieving Soil Organic Carbon Sequestration with Conservation Agricultural Systems in the Southeastern United States. *Soil Sci. Soc. Am. J.* **2010**, *74* (2), 347−357.
(827) Cordell, D.; Drangert, J. O.; White, S. The Story of Phosphorus: Global Food Security and Food for Thought. *Glob. Environ. Change* **2009**, *19* (2), 292−305.
(828) Jaffer, Y.; Clark, T. A.; Pearce, P.; Parsons, S. A. Potential Phosphorus Recovery by Struvite Formation. *Water Res.* **2002**, *36* (7), 1834−1842.
(829) Martí, N.; Pastor, L.; Bouzas, A.; Ferrer, J.; Seco, A. Phosphorus Recovery by Struvite Crystallization in WWTPs: Influence of the Sludge Treatment Line Operation. *Water Res.* **2010**, *44* (7), 2371−2379.
(830) Mehta, C. M.; Batstone, D. J. Nucleation and Growth Kinetics of Struvite Crystallization. *Water Res.* **2013**, *47* (8), 2890−2900.
(831) Kim, D.; Moore, J.; McCoy, C. P.; Irwin, N. J.; Rimer, J. D. Engaging a Battle on Two Fronts: Dual Role of Polyphosphates as Potent Inhibitors of Struvite Nucleation and Crystal Growth. *Chem. Mater.* **2020**, *32* (19), 8672−8682.
(832) Tansel, B.; Lunn, G.; Monje, O. Struvite Formation and Decomposition Characteristics for Ammonia and Phosphorus Recovery: A Review of Magnesium-Ammonia-Phosphate Interactions. *Chemosphere* **2018**, *194*, 504−514.
(833) Kim, D.; Lee, B.; Thomopoulos, S.; Jun, Y.-S. The Role of Confined Collagen Geometry in Decreasing Nucleation Energy Barriers to Intrafibrillar Mineralization. *Nat. Commun.* **2018**, *9*, 962.
(834) Tan, A. X.; Michalski, E.; Ilavsky, J.; Jun, Y.-S. Engineering Calcium-Bearing Mineral/Hydrogel Composites for Effective Phosphate Recovery. *ACS ES&T Eng.* **2021**, *1* (11), 1553−1564.
(835) Zhang, H.; Waychunas, G. A.; Banfield, J. F. Molecular Dynamics Simulation Study of the Early Stages of Nucleation of Iron Oxyhydroxide Nanoparticles in Aqueous Solutions. *J. Phys. Chem. B* **2015**, *119* (33), 10630−10642.
(836) Zhu, M.; Frandsen, C.; Wallace, A. F.; Legg, B.; Khalid, S.; Zhang, H.; Mørup, S.; Banfield, J. F.; Waychunas, G. A. Precipitation Pathways for Ferrihydrite Formation in Acidic Solutions. *Geochim. Cosmochim. Acta* **2016**, *172*, 247.
(837) Johnston, C. P.; Chrysochoou, M. Mechanisms of Chromate, Selenate, and Sulfate Adsorption on Al-Substituted Ferrihydrite: Implications for Ferrihydrite Surface Structure and Reactivity. *Environ. Sci. Technol.* **2016**, *50* (7), 3589−3596.
(838) Neil, C. W.; Lee, B.; Jun, Y. S. Different Arsenate and Phosphate Incorporation Effects on the Nucleation and Growth of Iron(III) (Hydr)oxides on Quartz. *Environ. Sci. Technol.* **2014**, *48* (20), 11883−11891.
(839) Rose, J.; Flank, A. M.; Masion, A.; Bottero, J. Y.; Elmerich, P. Nucleation and Growth Mechanisms of Fe Oxyhydroxide in the Presence of PO4 Ions. 2. P K-Edge EXAFS Study. *Langmuir* **1997**, *13* (6), 1827−1834.
(840) Xiao, F.; Yi, P.; Pan, X. R.; Zhang, B. J.; Lee, C. Comparative Study of the Effects of Experimental Variables on Growth Rates of Aluminum and Iron Hydroxide Flocs During Coagulation and Their Structural Characteristics. *Desalination* **2010**, *250* (3), 902−907.
(841) Waychunas, G. A.; Davis, J. A.; Fuller, C. C. Geometry of Sorbed Arsenate on Ferrihydrite and Crystalline FeOOH: Re-Evaluation of EXAFS Results and Topological Factors in Predicting Sorbate Geometry, and Evidence for Monodentate Complexes. *Geochim. Cosmochim. Acta* **1995**, *59* (17), 3655−3661.
(842) Eusterhues, K.; Wagner, F. E.; Häusler, W.; Hanzlik, M.; Knicker, H.; Totsche, K. U.; Kögel-Knabner, I.; Schwertmann, U. Characterization of Ferrihydrite-Soil Organic Matter Coprecipitates by X-Ray Diffraction and Mössbauer Spectroscopy. *Environ. Sci. Technol.* **2008**, *42* (21), 7891−7897.
(843) Richmond, W. R.; Loan, M.; Morton, J.; Parkinson, G. M. Arsenic Removal from Aqueous Solution via Ferrihydrite Crystallization Control. *Environ. Sci. Technol.* **2004**, *38* (8), 2368−2372.
(844) Angelico, R.; Ceglie, A.; He, J. Z.; Liu, Y. R.; Palumbo, G.; Colombo, C. Particle Size, Charge and Colloidal Stability of Humic Acids Coprecipitated with Ferrihydrite. *Chemosphere* **2014**, *99*, 239−247.
(845) Cismasu, A. C.; Michel, F. M.; Tcaciuc, A. P.; Tyliszczak, T.; Brown, G. E., Jr. Composition et Propriétés Structurales des Ferrihydrites Naturelles. *C.R. Geosci.* **2011**, *343*, 210−218.
(846) Edzwald, J. K. Coagulation in Drinking Water Treatment: Particles, Organics and Coagulants. *Water Sci. Technol.* **1993**, *27* (11), 21−35.
(847) Hering, J. G.; Katsoyiannis, I. A.; Theoduloz, G. A.; Berg, M.; Hug, S. J. Arsenic Removal from Drinking Water: Experiences with Technologies and Constraints in Practice. *J. Environ. Eng.* **2017**, *143*, 03117002.
(848) Neil, C. W.; Ray, J. R.; Lee, B.; Jun, Y. S. Fractal Aggregation and Disaggregation of Newly Formed Iron(III) (Hydr)oxide Nanoparticles in the Presence of Natural Organic Matter and Arsenic. *Environ. Sci. Nano* **2016**, *3* (3), 647−656.
(849) Epsztein, R.; DuChanois, R. M.; Ritt, C. L.; Noy, A.; Elimelech, M. Towards Single-Species Selectivity of Membranes with Subnanometre Pores. *Nat. Nanotechnol.* **2020**, *15* (6), 426−436.
(850) Sujanani, R.; Landsman, M. R.; Jiao, S.; Moon, J. D.; Shell, M. S.; Lawler, D. F.; Katz, L. E.; Freeman, B. D. Designing Solute-Tailored Selectivity in Membranes: Perspectives for Water Reuse and Resource Recovery. *ACS Macro Lett.* **2020**, *9* (11), 1709−1717.
(851) Park, H. B.; Kamcev, J.; Robeson, L. M.; Elimelech, M.; Freeman, B. D. Maximizing the Right Stuff: The Trade-Off Between Membrane Permeability and Selectivity. *Science* **2017**, *356*, eaab0530.
(852) Werber, J. R.; Osuji, C. O.; Elimelech, M. Materials for Next-Generation Desalination and Water Purification Membranes. *Nat. Rev. Mater.* **2016**, *1*, 16018.
(853) Antony, A.; Low, J. H.; Gray, S.; Childress, A. E.; Le-Clech, P.; Leslie, G. Scale Formation and Control in High Pressure Membrane Water Treatment Systems: A review. *Journal of Membrane Science* **2011**, *383* (1-2), 1−16.
(854) Tong, T.; Wallace, A. F.; Zhao, S.; Wang, Z. Mineral Scaling in Membrane Desalination: Mechanisms, Mitigation Strategies, and Feasibility of Scaling-Resistant Membranes. *Journal of Membrane Science* **2019**, *579*, 52−69.
(855) Ray, J. R.; Wong, W.; Jun, Y.-S. Antiscaling Efficacy of $CaCO_3$ and $CaSO_4$ on Polyethylene Glycol (PEG)-Modified Reverse Osmosis Membranes in the Presence of Humic Acid: Interplay of Membrane Surface Properties and Water Chemistry. *Phys. Chem. Chem. Phys.* **2017**, *19* (7), 5647−5657.
(856) Chen, M.; Ma, J.; Wang, Z.; Zhang, X.; Wu, Z. Insights into Iron Induced Fouling of Ion-Exchange Membranes Revealed by a Quartz Crystal Microbalance with Dissipation Monitoring. *RSC Adv.* **2017**, *7* (58), 36555−36561.

https://doi.org/10.1021/acs.chemrev.2c00130
Chem. Rev. 2023, 123, 6413−6544

(857) Gonzalez-Gil, G.; Behzad, A. R.; Farinha, A. S. F.; Zhao, C.; Bucs, S. S.; Nada, T.; Das, R.; Altmann, T.; Buijs, P. J.; Vrouwenvelder, J. S. Clinical Autopsy of a Reverse Osmosis Membrane Module. *Front. Chem. Eng.* **2021**, *3*, 683379.
(858) Warsinger, D. M.; Swaminathan, J.; Guillen-Burrieza, E.; Arafat, H. A.; Lienhard V, J. H. Scaling and Fouling in Membrane Distillation for Desalination Applications: A Review. *Desalination* **2015**, *356*, 294−313.
(859) Landsman, M. R.; Sujanani, R.; Brodfuehrer, S. H.; Cooper, C. M.; Darr, A. G.; Davis, R. J.; Kim, K.; Kum, S.; Nalley, L. K.; Nomaan, S. M.; et al. Water Treatment: Are Membranes the Panacea? *Annu. Rev. Chem. Biomol. Eng.* **2020**, *11*, 559−585.
(860) Tong, T.; Zhao, S.; Boo, C.; Hashmi, S. M.; Elimelech, M. Relating Silica Scaling in Reverse Osmosis to Membrane Surface Properties. *Environ. Sci. Technol.* **2017**, *51* (8), 4396−4406.
(861) Lu, K. G.; Huang, H. Dependence of Initial Silica Scaling on the Surface Physicochemical Properties of Reverse Osmosis Membranes During Bench-Scale Brackish Water Desalination. *Water Res.* **2019**, *150*, 358−367.
(862) Lu, K. G.; Li, M.; Huang, H. Silica Scaling of Reverse Osmosis Membranes Preconditioned by Natural Organic Matter. *Sci. Total Environ.* **2020**, *746*, 141178.
(863) Quay, A. N.; Tong, T.; Hashmi, S. M.; Zhou, Y.; Zhao, S.; Elimelech, M. Combined Organic Fouling and Inorganic Scaling in Reverse Osmosis: Role of Protein-Silica Interactions. *Environ. Sci. Technol.* **2018**, *52* (16), 9145−9153.
(864) Chen, Y.; Teng, J.; Liao, B. Q.; Li, R.; Lin, H. Molecular Insights into the Impacts of Iron(III) Ions on Membrane Fouling by Alginate. *Chemosphere* **2020**, *242*, 125232.
(865) Melliti, E.; Touati, K.; Van der Bruggen, B.; Elfil, H. Effect of Fe2+ Ions on Gypsum Precipitation During Bulk Crystallization of Reverse Osmosis Concentrates. *Chemosphere* **2021**, *263*, 127866.
(866) Maher, K.; Bargar, J. R.; Brown, G. E. Environmental Speciation of Actinides. *Inorg. Chem.* **2013**, *52* (7), 3510−3532.
(867) Bernier-Latmani, R.; Veeramani, H.; Vecchia, E. D.; Junier, P.; Lezama-Pacheco, J. S.; Suvorova, E. I.; Sharp, J. O.; Wigginton, N. S.; Bargar, J. R. Non-Uraninite Products of Microbial U(VI) Reduction. *Environ. Sci. Technol.* **2010**, *44* (24), 9456−9462.
(868) Wang, Z.; Lee, S. W.; Kapoor, P.; Tebo, B. M.; Giammar, D. E. Uraninite Oxidation and Dissolution Induced by Manganese Oxide: A Redox Reaction Between Two Insoluble Minerals. *Geochim. Cosmochim. Acta* **2013**, *100*, 24−40.
(869) Catalano, J. G.; McKinley, J. P.; Zachara, J. M.; Heald, S. M.; Smith, S. C.; Brown, G. E. Changes in Uranium Speciation Through a Depth Sequence of Contaminated Hanford Sediments. *Environ. Sci. Technol.* **2006**, *40* (8), 2517−2524.
(870) Singer, D. M.; Zachara, J. M.; Brown, G. E. Uranium Speciation as a Function of Depth in Contaminated Hanford Sediments - A Micro-XRF, Micro-XRD, and Micro- and Bulk-XAFS Study. *Environ. Sci. Technol.* **2009**, *43* (3), 630−636.
(871) Wan, J.; Tokunaga, T. K.; Kim, Y.; Wang, Z.; Lanzirotti, A.; Saiz, E.; Serne, R. J. Effect of Saline Waste Solution Infiltration Rates on Uranium Retention and Spatial Distribution in Hanford Sediments. *Environ. Sci. Technol.* **2008**, *42* (6), 1973−1978.
(872) Wan, J.; Tokunaga, T.; Dong, W.; Denham, M.; Hubbard, S. Persistent Source Influences on the Trailing Edge of a Groundwater Plume, and Natural Attenuation Timeframes: The F-Area Savannah River Site. *Environ. Sci. Technol.* **2012**, *46*, 4490−4497.
(873) Kersting, A. B.; Zavarin, M. Colloid-Facilitated Transport of Plutonium at the Nevada Test Site, NV, USA. In *Actinide Nanoparticle Research*; Kalmykov, S. N., Denecke, M. A., Eds.; Springer: Berlin, Heidelberg, 2011; pp 399−412.
(874) Kersting, A. B. Plutonium Transport in the Environment. *Inorg. Chem.* **2013**, *52* (7), 3533−3546.
(875) Zänker, H.; Hennig, C. Colloid-Borne Forms of Tetravalent Actinides: A Brief Review. *J. Contam. Hydrol.* **2014**, *157*, 87−105.
(876) Bierman, M. J.; Jin, S. Potential Applications of Hierarchical Branching Nanowires in Solar Energy Conversion. *Energy Environ. Sci.* **2009**, *2* (10), 1050−1059.
(877) Li, D.; Soberanis, F.; Fu, J.; Hou, W.; Wu, J.; Kisailus, D. Growth Mechanism of Highly Branched Titanium Dioxide Nanowires via Oriented Attachment. *Cryst. Growth Des.* **2013**, *13* (2), 422−428.
(878) Ruan, L. Y.; Ramezani-Dakhel, H.; Lee, C.; Li, Y. J.; Duan, X. F.; Heinz, H.; Huang, Y. A Rational Biomimetic Approach to Structure Defect Generation in Colloidal Nanocrystals. *ACS Nano* **2014**, *8* (7), 6934−6944.
(879) Suyatin, D. B.; Sun, J.; Fuhrer, A.; Wallin, D.; Froberg, L. E.; Karlsson, L. S.; Maximov, I.; Wallenberg, L. R.; Samuelson, L.; Xu, H. Q. Electrical Properties of Self-Assembled Branched InAs Nanowire Junctions. *Nano Lett.* **2008**, *8* (4), 1100−1104.
(880) Boles, M. A.; Engel, M.; Talapin, D. V. Self-Assembly of Colloidal Nanocrystals: From Intricate Structures to Functional Materials. *Chem. Rev.* **2016**, *116* (18), 11220−11289.
(881) Geim, A. K.; Grigorieva, I. V. Van der Waals Heterostructures. *Nature* **2013**, *499* (7459), 419−425.
(882) Davis, M. E. Ordered Porous Materials for Emerging Applications. *Nature* **2002**, *417* (6891), 813−821.
(883) Dinca, M.; Long, J. R. Introduction: Porous Framework Chemistry. *Chem. Rev.* **2020**, *120* (16), 8037−8038.
(884) Gower, L. B. Biomimetic Model Systems for Investigating the Amorphous Precursor Pathway and its Role in Biomineralization. *Chem. Rev.* **2008**, *108* (11), 4551−4627.
(885) Wolf, S. E.; Gower, L. B. Challenges and Perspectives of the Polymer-Induced Liquid-Precursor Process: The Pathway from Liquid-Condensed Mineral Precursors to Mesocrystalline Products. In *New Perspectives on Mineral Nucleation and Growth: From Solution Precursors to Solid Materials*; Van Driessche, A. E. S., Kellermeier, M., Benning, L. G., Gebauer, D., Eds.; Springer International: Cham, 2017; pp 43−75.
(886) Herman, I.; Yeo, J.; Hong, S.; Lee, D.; Nam, K. H.; Choi, J.; Hong, W.; Lee, D.; Grigoropoulos, C. P.; Ko, S. H. Hierarchical Weeping Willow Nano-Tree Growth and Effect of Branching on Dye-Sensitized Solar Cell Efficiency. *Nanotechnology* **2012**, *23* (19), 194005.
(887) Lowenstam, H. A.; Weiner, S. *On Biomineralization*; Oxford University Press, 1989.
(888) Burke, E. M.; Guo, Y.; Colon, L.; Rahima, M.; Veis, A.; Nancollas, G. H. Influence of Polyaspartic Acid and Phosphophoryn on Octacalcium Phosphate Growth Kinetics. *Colloid Surf. B-Biointerfaces* **2000**, *17* (1), 49−57.
(889) Mann, S. *Biomineralization: Principles and Concepts in Bioinorganic Materials Chemistry*; Oxford University Press: Oxford, UK, 2001.
(890) Dove, P. M.; De Yoreo, J. J.; Weiner, S. *Biomineralization*; Mineralogical Society of America: Washington, DC, 2003.
(891) Sollner, C.; Burghammer, M.; Busch-Nentwich, E.; Berger, J.; Schwarz, H.; Riekel, C.; Nicolson, T. Control of Crystal Size and Lattice Formation by Starmaker in Otolith Biomineralization. *Science* **2003**, *302* (5643), 282−286.
(892) Mao, C. B.; Solis, D. J.; Reiss, B. D.; Kottmann, S. T.; Sweeney, R. Y.; Hayhurst, A.; Georgiou, G.; Iverson, B.; Belcher, A. M. Virus-Based Toolkit for the Directed Synthesis of Magnetic and Semiconducting Nanowires. *Science* **2004**, *303* (5655), 213−217.
(893) Fu, G.; Valiyaveettil, S.; Wopenka, B.; Morse, D. E. $CaCO_3$ Biomineralization: Acidic 8-kDa Proteins Isolated from Aragonitic Abalone Shell Nacre Can Specifically Modify Calcite Crystal Morphology. *Biomacromolecules* **2005**, *6* (3), 1289−1298.
(894) Meldrum, F. C.; Ludwigs, S. Template-Directed Control of Crystal Morphologies. *Macromol. Biosci.* **2007**, *7* (2), 152−162.
(895) Olszta, M. J.; Cheng, X. G.; Jee, S. S.; Kumar, R.; Kim, Y. Y.; Kaufman, M. J.; Douglas, E. P.; Gower, L. B. Bone Structure and Formation: A New Perspective. *Mater. Sci. Eng. R-Rep.* **2007**, *58* (3-5), 77−116.
(896) Estroff, L. A. Introduction: Biomineralization. *Chem. Rev.* **2008**, *108* (11), 4329−4331.
(897) Xu, A. W.; Antonietti, M.; Yu, S. H.; Colfen, H. Polymer-Mediated Mineralization and Self-Similar Mesoscale-Organized

https://doi.org/10.1021/acs.chemrev.2c00130
Chem. Rev. 2023, 123, 6413−6544

Calcium Carbonate with Unusual Superstructures. *Adv. Mater.* **2008**, *20* (7), 1333.
(898) Metzler, R. A.; Evans, J. S.; Killian, C. E.; Zhou, D.; Churchill, T. H.; Appathurai, N. P.; Coppersmith, S. N.; Gilbert, P. U. P. A. Nacre Protein Fragment Templates Lamellar Aragonite Growth. *J. Am. Chem. Soc.* **2010**, *132* (18), 6329−6334.
(899) Fang, P. A.; Conway, J. F.; Margolis, H. C.; Simmer, J. P.; Beniash, E. Hierarchical Self-Assembly of Amelogenin and the Regulation of Biomineralization at the Nanoscale. *Proc. Natl. Acad. Sci. U.S.A.* **2011**, *108* (34), 14097−14102.
(900) Weiner, S.; Addadi, L. Crystallization Pathways in Biomineralization. *Annu. Rev. Mater. Res.* **2011**, *41*, 21−40.
(901) Giuffre, A. J.; Hamm, L. M.; Han, N.; De Yoreo, J. J.; Dove, P. M. Polysaccharide Chemistry Regulates Kinetics of Calcite Nucleation Through Competition of Interfacial Energies. *Proc. Natl. Acad. Sci. U.S.A.* **2013**, *110* (23), 9261−9266.
(902) Addadi, L.; Weiner, S. Biomineralization: Mineral Formation by Organisms. *Phys. Scripta* **2014**, *89*, 098003.
(903) Hamm, L. M.; Giuffre, A. J.; Han, N.; Tao, J.; Wang, D.; De Yoreo, J. J.; Dove, P. M. Reconciling Disparate Views of Template-Directed Nucleation Through Measurement of Calcite Nucleation Kinetics and Binding Energies. *Proc. Natl. Acad. Sci. U.S.A.* **2014**, *111* (4), 1304−1309.
(904) Vidavsky, N.; Addadi, S.; Mahamid, J.; Shimoni, E.; Ben-Ezra, D.; Shpigel, M.; Weiner, S.; Addadi, L. Initial Stages of Calcium Uptake and Mineral Deposition in Sea Urchin Embryos. *Proc. Natl. Acad. Sci. U.S.A.* **2014**, *111* (1), 39−44.
(905) Gal, A.; Weiner, S.; Addadi, L. A Perspective on Underlying Crystal Growth Mechanisms in Biomineralization: Solution Mediated Growth Versus Nanosphere Particle Accretion. *CrystEngComm* **2015**, *17* (13), 2606−2615.
(906) Smeets, P. J. M.; Cho, K. R.; Kempen, R. G. E.; Sommerdijk, N. A. J. M.; De Yoreo, J. J. Calcium Carbonate Nucleation Driven by Ion Binding in a Biomimetic Matrix Revealed by In Situ Electron Microscopy. *Nat. Mater.* **2015**, *14* (4), 394−399.
(907) Liu, Z. M.; Zhang, Z. S.; Wang, Z. M.; Jin, B.; Li, D. S.; Tao, J. H.; Tang, R. K.; De Yoreo, J. J. Shape-Preserving Amorphous-to-Crystalline Transformation of CaCO3 Revealed by In Situ TEM. *Proc. Natl. Acad. Sci. U.S.A.* **2020**, *117* (7), 3397−3404.
(908) Eiriksdottir, E. S.; Gislason, S. R.; Oelkers, E. H. Direct Evidence of the Feedback Between Climate and Nutrient, Major, and Trace Element Transport to the Oceans. *Geochim. Cosmochim. Acta* **2015**, *166*, 249−266.
(909) Luttge, A.; Arvidson, R. S.; Fischer, C.; Kurganskaya, I. Kinetic Concepts for Quantitative Prediction of Fluid-Solid Interactions. *Chem. Geol.* **2019**, *504*, 216−235.
(910) Erlandsson, M.; Oelkers, E. H.; Bishop, K.; Sverdrup, H.; Belyazid, S.; Ledesma, J. L. J.; Kohler, S. J. Spatial and Temporal Variations of Base Cation Release from Chemical Weathering on a Hillslope Scale. *Chem. Geol.* **2016**, *441*, 1−13.
(911) Li, X. D.; Wang, Q. Q.; Shen, X. D.; Pedrosa, E. T.; Luttge, A. Multiscale Investigation of Olivine (010) Face Dissolution from a Surface Control Perspective. *Applied Surf. Sci.* **2021**, *549*, 149317.
(912) Eyring, H. The Activated Complex in Chemical Reactions. *J. Chem. Phys.* **1935**, *3*, 107.
(913) Fischer, C.; Luttge, A. Beyond the Conventional Understanding of Water-Rock Reactivity. *Earth Planet. Sci. Lett.* **2017**, *457*, 100−105.
(914) Gin, S.; Jégou, C.; Frugier, P.; Minet, Y. Theoretical Consideration on the Application of the Aagaard-Helgeson Rate Law to the Dissolution of Silicate Minerals and Glasses. *Chem. Geol.* **2008**, *255* (1-2), 14−24.
(915) Lasaga, A. C. *Kinetic Theory in the Earth Sciences*; Princeton University Press, 1998.
(916) Corkhill, C. L.; Myllykylä, E.; Bailey, D. J.; Thornber, S. M.; Qi, J.; Maldonado, P.; Stennett, M. C.; Hamilton, A.; Hyatt, N. C. Contribution of Energetically Reactive Surface Features to the Dissolution of CeO_2 and ThO_2 Analogues for Spent Nuclear Fuel Microstructures. *ACS Appl. Mater. Interfaces* **2014**, *6* (15), 12279−12289.
(917) Davis, M. C.; Wesolowski, D. J.; Rosenqvist, J.; Brantley, S. L.; Mueller, K. T. Solubility and Near-Equilibrium Dissolution Rates of Quartz in Dilute NaCl Solutions at 398-473 K Under Alkaline Conditions. *Geochim. Cosmochim. Acta* **2011**, *75* (2), 401−415.
(918) Gong, L.; Rimstidt, J. D.; Zhang, Y. L.; Chen, K. Y.; Zhu, C. Unidirectional Kaolinite Dissolution Rates at Near-Equilibrium and Near-Neutral pH Conditions. *Appl. Clay Sci.* **2019**, *182*, 105284.
(919) Zhu, G.; Sushko, M. L.; Loring, J. S.; Legg, B. A.; Song, M.; Soltis, J. A.; Huang, X.; Rosso, K. M.; De Yoreo, J. J. Self-Similar Mesocrystals Form Via Interface-Driven Nucleation and Assembly. *Nature* **2021**, *590* (7846), 416−422.
(920) Hellmann, R.; Tisserand, D. Dissolution Kinetics as a Function of the Gibbs Free Energy of Reaction: An Experimental Study Based on Albite Feldspar. *Geochim. Cosmochim. Acta* **2006**, *70* (2), 364−383.
(921) Xu, J.; Fan, C.; Teng, H. H. Calcite Dissolution Kinetics in View of Gibbs Free Energy, Dislocation Density, and pCO 2. *Chem. Geol.* **2012**, *322-323*, 11−18.
(922) Brantley, S. L. *Kinetics of Mineral Dissolution*; Springer: New York, 2008.
(923) Nagy, K. L.; Lasaga, A. C. Dissolution and Precipitation Kinetics of Gibbsite at 80°C and pH 3: The Dependence on Solution Saturation State. *Geochim. Cosmochim. Acta* **1992**, *56* (8), 3093−3111.
(924) Berger, G.; Cadore, E.; Schott, J.; Dove, P. M. Dissolution Rate of Quartz in Lead and Sodium Electrolyte Solutions Between 25 and 300°C: Effect of the Nature of Surface Complexes and Reaction Affinity. *Geochim. Cosmochim. Acta* **1994**, *58* (2), 541−551.
(925) Burch, T. E.; Nagy, K. L.; Lasaga, A. C. Free Energy Dependence of Albite Dissolution Kinetics at 80°C and pH 8.8. *Chem. Geol.* **1993**, *105* (1-3), 137−162.
(926) Schott, J.; Oelkers, E. H. Dissolution and Crystallization Rates of Silicate Minerals as a Function of Chemical Affinity. *Pure Appl. Chem.* **1995**, *67* (6), 903−910.
(927) Devidal, J. L.; Dandurand, J. L.; Schott, J. Dissolution and Precipitation Kinetics of Kaolinite as a Function of Chemical Affinity 93 (T = 150 °C, pH = 2 and 7.8). In *International Symposium on Water−Rock Interaction*; Kharaka, Y.K., Maest, A.S., Eds., Balkema: Rotterdam, 1992; Vol. *1*, pp 93−96.
(928) Nagy, K. L.; Blum, A. E.; Lasaga, A. C. Dissolution and Precipitation Kinetics of Kaolinite at 80°C and pH 3: The Dependence on Solution Saturation State. *Am. J. Sci.* **1991**, *291* (7), 649−686.
(929) Arvidson, R. S.; Luttge, A. Mineral Dissolution Kinetics as a Function of Distance from Equilibrium - New Experimental Results. *Chem. Geol.* **2010**, *269* (1-2), 79−88.
(930) DelloStritto, M. J.; Kubicki, J. D.; Sofo, J. O. Effect of Ions on H-Bond Structure and Dynamics at the Quartz(101)-Water Interface. *Langmuir* **2016**, *32* (44), 11353−11365.
(931) Dove, P. M.; Crerar, D. A. Kinetics of Quartz Dissolution in Electrolyte Solutions Using a Hydrothermal Mixed Flow Reactor. *Geochim. Cosmochim. Acta* **1990**, *54* (4), 955−969.
(932) Rimstidt, J. D.; Zhang, Y. L.; Zhu, C. Rate Equations for Sodium Catalyzed Amorphous Silica Dissolution. *Geochim. Cosmochim. Acta* **2016**, *195*, 120−125.
(933) Dove, P. M.; Han, N.; De Yoreo, J. J. Mechanisms of Classical Crystal Growth Theory Explain Quartz and Silicate Dissolution Behavior. *Proc. Natl. Acad. Sci. U.S.A.* **2005**, *102* (43), 15357−15362.
(934) Dove, P. M.; Han, N. Kinetics of Mineral Dissolution and Growth as Reciprocal Microscopic Surface Processes Across Chemical Driving Force. *AIP Conf. Proc.* **2007**, *916*, 215−234.
(935) Chernov, A. A. *Modern Crystallography III*; Springer: Berlin, Heidelberg, 1984.
(936) Malkin, A. I.; Chernov, A. A.; Alexeev, I. V. Growth of Dipyramidal Face of Dislocation-Free ADP Crystals; Free Energy of Steps. *J. Cryst. Growth* **1989**, *97* (3-4), 765−769.

https://doi.org/10.1021/acs.chemrev.2c00130
Chem. Rev. 2023, 123, 6413−6544

(937) Stumm, W. Reactivity at the Mineral−Water Interface: Dissolution and Inhibition. *Colloids Surf. A Physicochem. Eng. Asp.* **1997**, *120* (1-3), 143−166.
(938) Homoky, W. B.; Conway, T. M.; John, S. G.; Konig, D.; Deng, F. F.; Tagliabue, A.; Mills, R. A. Iron Colloids Dominate Sedimentary Supply to the Ocean Interior. *Proc. Natl. Acad. Sci. U.S.A.* **2021**, *118*, e2016078118.
(939) Cervini-Silva, J.; Sposito, G. Steady-State Dissolution Kinetics of Aluminum-Goethite in the Presence of Desferrioxamine-B and Oxalate Ligands. *Environ. Sci. Technol.* **2002**, *36*, 337−342.
(940) Suter, D.; Siffert, C.; Sulzberger, B.; Stumm, W. Catalytic Dissolution of Iron(III)(hydr)oxides by Oxalic Acid in the Presence of Fe(II). *Naturwissenschaften* **1988**, *75*, 571−573.
(941) Torres, M. A.; Paris, G.; Adkins, J. F.; Fischer, W. W. Riverine Evidence for Isotopic Mass Balance in the Earth's Early Sulfur Cycle. *Nat. Geosci.* **2018**, *11* (9), 661−664.
(942) Cheah, S. F.; Kraemer, S. M.; Cervini-Silva, J.; Sposito, G. Steady-State Dissolution Kinetics of Goethite in the Presence of Desferrioxamine B and Oxalate Ligands: Implications for the Microbial Acquisition of Iron. *Chem. Geol.* **2003**, *198* (1-2), 63−75.
(943) Wang, Z.; Schenkeveld, W. D. C.; Kraemer, S. M.; Giammar, D. E. Synergistic Effect of Reductive and Ligand-Promoted Dissolution of Goethite. *Environ. Sci. Technol.* **2015**, *49* (12), 7236−7244.
(944) Kubicki, J. D.; Blake, G. A.; Apitz, S. E. Ab Initio Calculations on Aluminosilicate Q3 Species: Implications for Atomic Structures of Mineral Surfaces and Dissolution Mechanisms of Feldspars. *Am. Mineral.* **1996**, *81* (7-8), 789−799.
(945) Meskhidze, N.; Volker, C.; Al-Abadleh, H. A.; Barbeau, K.; Bressac, M.; Buck, C.; Bundy, R. M.; Croot, P.; Feng, Y.; Ito, A. Perspective on Identifying and Characterizing the Processes Controlling Iron Speciation and Residence Time at the Atmosphere-Ocean Interface. *Mar. Chem.* **2019**, *217*, 103704.
(946) Ding, Y.; Ye, Q. T.; Liu, M. Q.; Shi, Z. Q.; Liang, Y. Z. Reductive Release of Fe Mineral−Associated Organic Matter Accelerated by Oxalic Acid. *Sci. Total Environ.* **2021**, *763*, 142937.
(947) Chen, K. Y.; Bocknek, L.; Manning, B. Oxidation of Cr(III) to Cr(VI) and Production of Mn(II) by Synthetic Manganese(IV) Oxide. *Crystals* **2021**, *11*, 443.
(948) Pedersen, H. D.; Postma, D.; Jakobsen, R. Release of Arsenic Associated with the Reduction and Transformation of Iron Oxides. *Geochim. Cosmochim. Acta* **2006**, *70* (16), 4116−4129.
(949) Jones, A. M.; Collins, R. N.; Waite, T. D. Redox Characterization of the Fe(II)-Catalyzed Transformation of Ferrihydrite to Goethite. *Geochim. Cosmochim. Acta* **2017**, *218*, 257−272.
(950) Frierdich, A. J.; Helgeson, M.; Liu, C.; Wang, C.; Rosso, K. M.; Scherer, M. M. Iron Atom Exchange Between Hematite and Aqueous Fe(II). *Environ. Sci. Technol.* **2015**, *49* (14), 8479−8486.
(951) Schenkeveld, W. D. C.; Wang, Z.; Giammar, D. E.; Kraemer, S. M. Synergistic Effects Between Biogenic Ligands and a Reductant in Fe Acquisition from Calcareous Soil. *Environ. Sci. Technol.* **2016**, *50* (12), 6381−6388.
(952) Frierdich, A. J.; Catalano, J. G. Fe(II)-Mediated Reduction and Repartitioning of Structurally Incorporated Cu, Co, and Mn in Iron Oxides. *Environ. Sci. Technol.* **2012**, *46* (20), 11070−11077.
(953) Yuan, Z.; Ma, X.; Wu, X.; Wang, X.; Wang, S.; Jia, Y. Effect of Hydroquinone-Induced Iron Reduction on the Stability of Fe(III)-As(V) Co-Precipitate and Arsenic Mobilization. *Appl. Geochem.* **2018**, *97*, 1−10.
(954) Frierdich, A. J.; Scherer, M. M.; Bachman, J. E.; Engelhard, M. H.; Rapponotti, B. W.; Catalano, J. G. Inhibition of Trace Element Release During Fe(II)-Activated Recrystallization of Al-, Cr-, and Sn-Substituted Goethite and Hematite. *Environ. Sci. Technol.* **2012**, *46* (18), 10031−10039.
(955) Latta, D. E.; Bachman, J. E.; Scherer, M. M. Fe Electron Transfer and Atom Exchange in Goethite: Influence of Al-Substitution and Anion Sorption. *Environ. Sci. Technol.* **2012**, *46* (19), 10614.
(956) Williams, A. G. B.; Scherer, M. M. Spectroscopic Evidence for Fe(II)-Fe(III) Electron Transfer at the Iron Oxide-Water Interface. *Environ. Sci. Technol.* **2004**, *38* (18), 4782−4790.
(957) Elzinga, E. J. Reductive Transformation of Birnessite by Aqueous Mn(II). *Environ. Sci. Technol.* **2011**, *45* (15), 6366−6372.
(958) Cruz-Hernandez, Y.; Villalobos, M.; Marcus, M. A.; Pi-Puig, T.; Zanella, R.; Martinez-Villegas, N. Tl(I) Sorption Behavior on Birnessite and its Implications for Mineral Structural Changes. *Geochim. Cosmochim. Acta* **2019**, *248*, 356−369.
(959) Wick, S.; Peña, J.; Voegelin, A. Thallium Sorption onto Manganese Oxides. *Environ. Sci. Technol.* **2019**, *53* (22), 13168−13178.
(960) Zhao, H.; Zhu, M.; Li, W.; Elzinga, E. J.; Villalobos, M.; Liu, F.; Zhang, J.; Feng, X.; Sparks, D. L. Redox Reactions Between Mn(II) and Hexagonal Birnessite Change Its Layer Symmetry. *Environ. Sci. Technol.* **2016**, *50* (4), 1750−1758.
(961) Tu, S.; Racz, G. J.; Goh, T. B. Transformations of Synthetic Birnessite as Affected by pH and Manganese Concentration. *Clays Clay Miner.* **1994**, *42* (3), 321−330.
(962) Ruiz-Garcia, M.; Villalobos, M.; Voegelin, A.; Pi-Puig, T.; Martínez-Villegas, N.; Göttlicher, J. Transformation of Hexagonal Birnessite upon Reaction with Thallium(I): Effects of Birnessite Crystallinity, pH, and Thallium Concentration. *Environ. Sci. Technol.* **2021**, *55* (8), 4862−4870.
(963) Jung, H.; Taillefert, M.; Sun, J.; Wang, Q.; Borkiewicz, O. J.; Liu, P.; Yang, L.; Chen, S.; Chen, H.; Tang, Y. Redox Cycling Driven Transformation of Layered Manganese Oxides to Tunnel Structures. *J. Am. Chem. Soc.* **2020**, *142* (5), 2506−2513.
(964) Frey, C. E.; Wiechen, M.; Kurz, P. Water-Oxidation Catalysis by Synthetic Manganese Oxides-Systematic Variations of the Calcium Birnessite Theme. *Dalton Trans.* **2014**, *43* (11), 4370−4379.
(965) Thenuwara, A. C.; Shumlas, S. L.; Attanayake, N. H.; Cerkez, E. B.; McKendry, I. G.; Frazer, L.; Borguet, E.; Kang, Q.; Zdilla, M. J.; Sun, J.; et al. Copper-Intercalated Birnessite as a Water Oxidation Catalyst. *Langmuir* **2015**, *31* (46), 12807−12813.
(966) Alves Ribeiro, I. D.; Gazolla Volpiano, C.; Kayser Vargas, L.; Eichelberger Granada, C.; Brito Lisboa, B.; Pereira Passaglia, L. M. Use of Mineral Weathering Bacteria to Enhance Nutrient Availability in Crops: A Review. *Front. Plant Sci.* **2020**, *11*, 590774.
(967) Lu, A. H.; Li, Y.; Liu, F. F.; Liu, Y. W.; Ye, H.; Zhuang, Z. Y.; Li, Y. Z.; Ding, H. R.; Wang, C. Q. The Photogeochemical Cycle of Mn Oxides on the Earth's Surface. *Mineral. Mag.* **2021**, *85* (1), 22−38.
(968) Li, Z. M.; Cornelis, J. T.; Vander Linden, C.; Van Ranst, E.; Delvaux, B. Neoformed Aluminosilicate and Phytogenic Silica are Competitive Sinks in the Silicon Soil-Plant Cycle. *Geoderma* **2020**, *368*, 114308.
(969) Gerrits, R.; Pokharel, R.; Breitenbach, R.; Radnik, J.; Feldmann, I.; Schuessler, J. A.; von Blanckenburg, F.; Gorbushina, A. A.; Schott, J. How the Rock -Inhabiting Fungus K. Petricola A95 Enhances Olivine Dissolution Through Attachment. *Geochim. Cosmochim. Acta* **2020**, *282*, 76−97.
(970) Rim, G.; Marchese, A. K.; Stallworth, P.; Greenbaum, S. G.; Park, A. H. A. 29Si Solid State MAS NMR Study on Leaching Behaviors and Chemical Stability of Different Mg-Silicate Structures for CO_2 Sequestration. *Chem. Eng. J.* **2020**, *396*, 125204.
(971) Sattler, T.; Pomberger, R.; Schimek, J.; Vollprecht, D. Mineral Wool Waste in Austria, Associated Health Aspects and Recycling Options. *Detritus* **2020**, *9*, 174−180.
(972) Sahai, N.; Schoonen, M. A. A.; Skinner, H. C. W. The Emergent Field of Medical Mineralogy and Geochemistry. *Rev. Mineral. Geochem.* **2006**, *64*, 1−4.
(973) Kaur, J.; Rickman, D.; Schoonen, M. A. Reactive Oxygen Species (ROS) Generation by Lunar Simulants. *Acta Astronaut.* **2016**, *122*, 196−208.
(974) Barly, S. H. Q.; Okhrimenko, D. V.; Solvang, M.; Yue, Y. Z.; Stipp, S. L. S. Dissolution of Stone Wool Fibers with Phenol-urea-formaldehyde Binder in a Synthetic Lung Fluid. *Chem. Res. Toxicol.* **2019**, *32* (12), 2398−2410.

(975) Hettiarachchi, E.; Paul, S.; Cadol, D.; Frey, B.; Rubasinghege, G. Mineralogy Controlled Dissolution of Uranium from Airborne Dust in Simulated Lung Fluids (SLFs) and Possible Health Implications. *Environ. Sci. Technol. Lett.* **2019**, *6* (2), 62−67.
(976) Van Pelt, R. S.; Shekhter, E. G.; Barnes, M. A. W.; Duke, S. E.; Gill, T. E.; Pannell, K. H. Spatial and Temporal Patterns of Heavy Metal Deposition Resulting from a Smelter in El Paso, Texas. *J. Geochem. Explor.* **2020**, *210*, 106414.
(977) Padilla, M. A.; Elobeid, M.; Ruden, D. M.; Allison, D. B. An Examination of the Association of Selected Toxic Metals with Total and Central Obesity Indices: NHANES 99-02. *Int. J. Environ. Res. Public Health* **2010**, *7* (9), 3332−3347.
(978) Zhong, L. J.; Yu, Y. L.; Lian, H. Z.; Hu, X.; Fu, H. M.; Chen, Y. J. Solubility of Nano-Sized Metal Oxides Evaluated by using In Vitro Simulated Lung and Gastrointestinal Fluids: Implication for Health Risks. *J. Nanoparticle Res.* **2017**, *19*, 375.
(979) Liu, N. M.; Miyashita, L.; Maher, B. A.; McPhail, G.; Jones, C. J. P.; Barratt, B.; Thangaratinam, S.; Karloukovski, V.; Ahmed, I. A.; Aslam, Z.; Grigg, J. Evidence for the Presence of Air Pollution Nanoparticles in Placental Tissue Cells. *Sci. Total Environ.* **2021**, *751*, 142235.
(980) Kim, H. N.; Lee, S. K. Atomic Structure and Dehydration Mechanism of Amorphous Silica: Insights from 29Si and 1H Solid-State MAS NMR Study of SiO2 Nanoparticles. *Geochim. Cosmochim. Acta* **2013**, *120*, 39−64.
(981) Dove, P. M.; Han, N.; Wallace, A. F.; De Yoreo, J. J. Kinetics of Amorphous Silica Dissolution and the Paradox of the Silica Polymorphs. *Proc. Natl. Acad. Sci. U.S.A.* **2008**, *105* (29), 9903−9908.
(982) Bandstra, J. Z.; Brantley, S. L. Understanding the Mechanisms of Solid-Water Reactions Through Analysis of Surface Topography. *Phys. Rev. E* **2015**, *92*, 062114.
(983) Gibbs, G. V. Molecules as Models for Bonding in Silicates. *Am. Mineral.* **1982**, *67*, 421−450.
(984) Gratz, A. J.; Bird, P. Quartz Dissolution: Theory of Rough and Smooth Surfaces. *Geochim. Cosmochim. Acta* **1993**, *57* (5), 977−989.
(985) Yang, Y.; Min, Y.; Jun, Y.-S. A Mechanistic Understanding of Plagioclase Dissolution Based on Al Occupancy and T-O Bond Length: From Geologic Carbon Sequestration to Ambient Conditions. *Phys. Chem. Chem. Phys.* **2013**, *15* (42), 18491−18501.
(986) Yang, Y.; Min, Y.; Lococo, J.; Jun, Y.-S. Effects of Al/Si Ordering on Feldspar Dissolution: Part I. Crystallographic Control on the Stoichiometry of Dissolution Reaction. *Geochim. Cosmochim. Acta* **2014**, *126*, 574−594.
(987) Yang, Y.; Min, Y.; Jun, Y.-S. Effects of Al/Si Ordering on Feldspar Dissolution: Part II. The pH Dependence of Plagioclases' Dissolution Rates. *Geochim. Cosmochim. Acta* **2014**, *126*, 595−613.
(988) Jung, H.; Lee, B.; Lengyel, M.; Axelbaum, R.; Yoo, J.; Kim, Y. S.; Jun, Y. S. Nanoscale In Situ Detection of Nucleation and Growth of Li Electrodeposition at Various Current Densities. *J. Mater. Chem. A* **2018**, *6* (11), 4629−4635.
(989) Jun, Y.-S.; Kim, D.; Neil, C. W. Heterogeneous Nucleation and Growth of Nanoparticles at Environmental Interfaces. *Acc. Chem. Res.* **2016**, *49* (9), 1681−1690.
(990) Jun, Y.-S.; Zhu, Y.; Wang, Y.; Ghim, D.; Wu, X.; Kim, D.; Jung, H. Classical and Nonclassical Nucleation and Growth Mechanisms for Nanoparticle Formation. *Annu. Rev. Phys. Chem.* **2022**, *73* (1), 453−477.
(991) De Yoreo, J. J. A Holistic View of Nucleation and Self-Assembly. *MRS Bull.* **2017**, *42* (7), 525−536.
(992) Henzler, K.; Fetisov, E. O.; Galib, M.; Baer, M. D.; Legg, B. A.; Borca, C.; Xto, J. M.; Pin, S.; Fulton, J. L.; Schenter, G. K.; et al. Supersaturated Calcium Carbonate Solutions are Classical. *Sci. Adv.* **2018**, *4*, No. eaao6283.
(993) Cölfen, H.; Mann, S. Higher-Order Organization by Mesoscale Self-Assembly and Transformation of Hybrid Nanostructures. *Angew. Chem. Int. Ed.* **2003**, *42* (21), 2350−2365.
(994) De Yoreo, J. J.; Gilbert, P. U. P. A.; Sommerdijk, N. A. J. M.; Penn, R. L.; Whitelam, S.; Joester, D.; Zhang, H.; Rimer, J. D.; Navrotsky, A.; Banfield, J. F.; Wallace, A. F.; Michel, F. M.; Meldrum, F. C.; Cölfen, H.; Dove, P. M. Crystallization by Particle Attachment in Synthetic, Biogenic, and Geologic Environments. *Science* **2015**, *349* (6247), aaa6760.
(995) Lukić, M. J.; Gebauer, D.; Rose, A. Nonclassical Nucleation Towards Separation and Recycling Science: Iron and Aluminium (Oxy)(hydr)oxides. *Curr. Opin. Colloid In.* **2020**, *46*, 114−127.
(996) Jun, Y.-S.; Kendall, T. A.; Martin, S. T.; Friend, C. M.; Vlassak, J. J. Heteroepitaxial Nucleation and Oriented Growth of Manganese Oxide Islands on Carbonate Minerals under Aqueous Conditions. *Environ. Sci. Technol.* **2005**, *39* (5), 1239−1249.
(997) De Yoreo, J. J.; Vekilov, P. G. Principles of Crystal Nucleation and Growth. *Rev. Mineral. Geochem.* **2003**, *54* (1), 57−93.
(998) Kalikmanov, V. *Nucleation Theory*; Springer, 2013.
(999) Lasaga, A. C. *Kinetic Theory in the Earth Sciences*; Princeton University Press, 2014.
(1000) Baumgartner, J.; Dey, A.; Bomans, P. H. H.; Le Coadou, C.; Fratzl, P.; Sommerdijk, N. A. J. M.; Faivre, D. Nucleation and Growth of Magnetite from Solution. *Nat. Mater.* **2013**, *12* (4), 310−314.
(1001) Navrotsky, A. Energetic Clues to Pathways to Biomineralization: Precursors, Clusters, and Nanoparticles. *Proc. Natl. Acad. Sci. U.S.A.* **2004**, *101* (33), 12096−12101.
(1002) Hu, Q.; Nielsen, M. H.; Freeman, C. L.; Hamm, L. M.; Tao, J.; Lee, J. R. I.; Han, T. Y. J.; Becker, U.; Harding, J. H.; Dove, P. M.; De Yoreo, J. J. The Thermodynamics of Calcite Nucleation at Organic Interfaces: Classical vs. Non-Classical Pathways. *Faraday Discuss.* **2012**, *159*, 509−523.
(1003) Fernandez-Martinez, A.; Hu, Y.; Lee, B.; Jun, Y.-S.; Waychunas, G. A. In Situ Determination of Interfacial Energies between Heterogeneously Nucleated $CaCO_3$ and Quartz Substrates: Thermodynamics of CO_2 Mineral Trapping. *Environ. Sci. Technol.* **2013**, *47* (1), 102−109.
(1004) Li, Q.; Fernandez-Martinez, A.; Lee, B.; Waychunas, G. A.; Jun, Y.-S. Interfacial Energies for Heterogeneous Nucleation of Calcium Carbonate on Mica and Quartz. *Environ. Sci. Technol.* **2014**, *48* (10), 5745−5753.
(1005) De Yoreo, J. J.; Waychunas, G. A.; Jun, Y.-S.; Fernandez-Martinez, A. In Situ Investigations of Carbonate Nucleation on Mineral and Organic Surfaces. *Rev. Mineral. Geochem.* **2013**, *77* (1), 229−257.
(1006) Vehkamäki, H. *Classical Nucleation Theory in Multicomponent Systems*; Springer Science & Business Media, 2006.
(1007) Nielsen, A. E. *Kinetics of Precipitation*; Pergamon Press Oxford, 1964.
(1008) Li, Q.; Jun, Y.-S. The Apparent Activation Energy and Pre-Exponential Kinetic Factor for Heterogeneous Calcium Carbonate Nucleation on Quartz. *Comm. Chem.* **2018**, *1*, 56.
(1009) Wu, X.; Lee, B.; Jun, Y.-S. Interfacial and Activation Energies of Environmentally Abundant Heterogeneously Nucleated Iron(III) (Hydr)oxide on Quartz. *Environ. Sci. Technol.* **2020**, *54* (19), 12119−12129.
(1010) Wallace, A. F.; DeYoreo, J. J.; Dove, P. M. Kinetics of Silica Nucleation on Carboxyl-and Amine-Terminated Surfaces: Insights for Biomineralization. *J. Am. Chem. Soc.* **2009**, *131* (14), 5244−5250.
(1011) Habraken, W. J. E. M.; Tao, J.; Brylka, L. J.; Friedrich, H.; Bertinetti, L.; Schenk, A. S.; Verch, A.; Dmitrovic, V.; Bomans, P. H. H.; Frederik, P. M. Ion-Association Complexes Unite Classical and Non-Classical Theories for the Biomimetic Nucleation of Calcium Phosphate. *Nat. Commun.* **2013**, *4*, 1507.
(1012) Alexander, B.; Daulton, T. L.; Genin, G. M.; Lipner, J.; Pasteris, J. D.; Wopenka, B.; Thomopoulos, S. The Nanometre-Scale Physiology of Bone: Steric Modelling and Scanning Transmission Electron Microscopy of Collagen-Mineral Structure. *J. R. Soc., Interface* **2012**, *9* (73), 1774−1786.
(1013) Landis, W. J.; Jacquet, R. Association of Calcium and Phosphate Ions with Collagen in the Mineralization of Vertebrate Tissues. *Calcif. Tissue Int.* **2013**, *93* (4), 329−337.
(1014) Landis, W. J.; Song, M. J.; Leith, A.; McEwen, L.; McEwen, B. F. Mineral and Organic Matrix Interaction in Normally Calcifying Tendon Visualized in Three Dimensions by High-Voltage Electron

https://doi.org/10.1021/acs.chemrev.2c00130
Chem. Rev. 2023, 123, 6413−6544

Microscopic Tomography and Graphic Image Reconstruction. *J. Struct. Biol.* **1993**, *110* (1), 39−54.
(1015) Nair, A. K.; Gautieri, A.; Chang, S.-W.; Buehler, M. J. Molecular Mechanics of Mineralized Collagen Fibrils in Bone. *Nat. Commun.* **2013**, *4*, 1724.
(1016) Li, D.; Nielsen, M. H.; Lee, J. R. I.; Frandsen, C.; Banfield, J. F.; De Yoreo, J. J. Direction-Specific Interactions Control Crystal Growth by Oriented Attachment. *Science* **2012**, *336* (6084), 1014−1018.
(1017) Nielsen, M. H.; Aloni, S.; De Yoreo, J. J. In Situ TEM Imaging of $CaCO_3$ Nucleation Reveals Coexistence of Direct and Indirect Pathways. *Science* **2014**, *345* (6201), 1158−1162.
(1018) Nudelman, F.; Pieterse, K.; George, A.; Bomans, P. H. H.; Friedrich, H.; Brylka, L. J.; Hilbers, P. A. J.; de With, G.; Sommerdijk, N. A. J. M. The Role of Collagen in Bone Apatite Formation in the Presence of Hydroxyapatite Nucleation Inhibitors. *Nat. Mater.* **2010**, *9* (12), 1004−1009.
(1019) Zhou, J.; Yang, Y.; Yang, Y.; Kim, D. S.; Yuan, A.; Tian, X.; Ophus, C.; Sun, F.; Schmid, A. K.; Nathanson, M.; et al. Observing Crystal Nucleation in Four Dimensions using Atomic Electron Tomography. *Nature* **2019**, *570* (7762), 500−503.
(1020) Jun, Y. S.; Lee, B.; Waychunas, G. A. In Situ Observations of Nanoparticle Early Development Kinetics at Mineral−Water Interfaces. *Environ. Sci. Technol.* **2010**, *44*, 8182−8189.
(1021) Cho, K. S.; Talapin, D. V.; Gaschler, W.; Murray, C. B. Designing PbSe Nanowires and Nanorings Through Oriented Attachment of Nanoparticles. *J. Am. Chem. Soc.* **2005**, *127* (19), 7140−7147.
(1022) Boneschanscher, M. P.; Evers, W. H.; Geuchies, J. J.; Altantzis, T.; Goris, B.; Rabouw, F. T.; van Rossum, S. A. P.; van der Zant, H. S. J.; Siebbeles, L. D. A.; Van Tendeloo, G.; et al. Long-Range Orientation and Atomic Attachment of Nanocrystals in 2D Honeycomb Superlattices. *Science* **2014**, *344* (6190), 1377−1380.
(1023) Olszta, M. J. *A New Paradigm for Biomineral Formation: Mineralization via an Amorphous Liquid-Phase Precursor Process*. Ph.D. Dissertation. University of Florida, Gainesville, FL, 2004.
(1024) Cao, K.; Biskupek, J.; Stoppiello, C. T.; McSweeney, R. L.; Chamberlain, T. W.; Liu, Z.; Suenaga, K.; Skowron, S. T.; Besley, E.; Khlobystov, A. N.; et al. Atomic Mechanism of Metal Crystal Nucleus Formation in a Single-Walled Carbon Nanotube. *Nat. Chem.* **2020**, *12* (10), 921−928.
(1025) De Yoreo, J. J.; Legg, B. A. What Atoms Do when They Get Together. *Nat. Chem.* **2020**, *12* (10), 883−885.
(1026) Gary, D. C.; Terban, M. W.; Billinge, S. J. L.; Cossairt, B. M. Two-Step Nucleation and Growth of InP Quantum Dots Via Magic-Sized Cluster Intermediates. *Chem. Mater.* **2015**, *27* (4), 1432−1441.
(1027) Ma, X.; Zhang, S.; Jiao, F.; Newcomb, C. J.; Zhang, Y. L.; Prakash, A.; Liao, Z. H.; Baer, M. D.; Mundy, C. J.; Pfaendtner, J.; et al. Tuning Crystallization Pathways Through Sequence Engineering of Biomimetic Polymers. *Nat. Mater.* **2017**, *16*, 767.
(1028) Galkin, O.; Chen, K.; Nagel, R. L.; Hirsch, R. E.; Vekilov, P. G. Liquid-Liquid Separation in Solutions of Normal and Sickle Cell Hemoglobin. *Proc. Natl. Acad. Sci. U.S.A.* **2002**, *99* (13), 8479−8483.
(1029) Maes, D.; Vorontsova, M. A.; Potenza, M. A. C.; Sanvito, T.; Sleutel, M.; Giglio, M.; Vekilov, P. G. Do Protein Crystals Nucleate Within Dense Liquid Clusters? *Acta Crystallogr. F* **2015**, *71*, 815−822.
(1030) Vekilov, P. G. Two-Step Mechanism for the Nucleation of Crystals from Solution. *J. Cryst. Growth* **2005**, *275* (1-2), 65−76.
(1031) Rimer, J. D.; Tsapatsis, M. Nucleation of Open Framework Materials: Navigating the Voids. *MRS Bull.* **2016**, *41* (5), 393−398.
(1032) Van Driessche, A. E. S.; Van Gerven, N.; Bomans, P. H. H.; Joosten, R. R. M.; Friedrich, H.; Gil-Carton, D.; Sommerdijk, N. A. J. M.; Sleutel, M. Molecular Nucleation Mechanisms and Control Strategies for Crystal Polymorph Selection. *Nature* **2018**, *556* (7699), 89−94.
(1033) Gebauer, D.; Colfen, H. Prenucleation Clusters and Non-Classical Nucleation. *Nano Today* **2011**, *6* (6), 564−584.
(1034) Gebauer, D.; Kellermeier, M.; Gale, J. D.; Bergstrom, L.; Colfen, H. Pre-Nucleation Clusters as Solute Precursors in Crystallisation. *Chem. Soc. Rev.* **2014**, *43* (7), 2348−2371.
(1035) Kumar, S.; Wang, Z.; Penn, R. L.; Tsapatsis, M. A Structural Resolution Cryo-TEM Study of the Early Stages of MFI Growth. *J. Am. Chem. Soc.* **2008**, *130*, 17284.
(1036) Lupulescu, A. I.; Rimer, J. D. In Situ Imaging of Silicalite-1 Surface Growth Reveals the Mechanism of Crystallization. *Science* **2014**, *344* (6185), 729−732.
(1037) Houben, L.; Weissman, H.; Wolf, S. G.; Rybtchinski, B. A Mechanism of Ferritin Crystallization Revealed by Cryo-STEM Tomography. *Nature* **2020**, *579*, 540.
(1038) Loh, N. D.; Sen, S.; Bosman, M.; Tan, S. F.; Zhong, J.; Nijhuis, C. A.; Kral, P.; Matsudaira, P.; Mirsaidov, U. Multistep Nucleation of Nanocrystals in Aqueous Solution. *Nat. Chem.* **2017**, *9* (1), 77−82.
(1039) Wallace, A. F.; Hedges, L. O.; Fernandez-Martinez, A.; Raiteri, P.; Gale, J. D.; Waychunas, G. A.; Whitelam, S.; Banfield, J. F.; De Yoreo, J. J. Microscopic Evidence for Liquid-Liquid Separation in Supersaturated $CaCO_3$ Solutions. *Science* **2013**, *341* (6148), 885−889.
(1040) Zou, Z. Y.; Habraken, W. J. E. M.; Bertinetti, L.; Politi, Y.; Gal, A.; Weiner, S.; Addadi, L.; Fratzl, P. On the Phase Diagram of Calcium Carbonate Solutions. *Adv. Mater. Interfaces* **2017**, *4*, 1600076.
(1041) Cheng, Y.; Tao, J.; Zhu, G.; Soltis, J. A.; Legg, B. A.; Nakouzi, E.; De Yoreo, J. J.; Sushko, M. L.; Liu, J. Near Surface Nucleation and Particle Mediated Growth of Colloidal Au Nanocrystals. *Nanoscale* **2018**, *10* (25), 11907−11912.
(1042) Deng, N.; Stack, A. G.; Weber, J.; Cao, B.; De Yoreo, J. J.; Hu, Y. D. Organic-Mineral Interfacial Chemistry Drives Heterogeneous Nucleation of Sr-Rich (Ba-x, Sr1-x)SO_4 from Undersaturated Solution. *Proc. Natl. Acad. Sci. U.S.A.* **2019**, *116* (27), 13221−13226.
(1043) Ocaña, M.; Morales, M. P.; Serna, C. J. The Growth Mechanism of α-Fe_2O_3 Ellipsoidal Particles in Solution. *J. Colloid Interface Sci.* **1995**, *171* (1), 85−91.
(1044) Penn, R. L.; Banfield, J. F. Imperfect Oriented Attachment: Dislocation Generation in Defect-Free Nanocrystals. *Science* **1998**, *281* (5379), 969−971.
(1045) Penn, R. L.; Banfield, J. F. Oriented Attachment and Growth, Twinning, Polytypism, and Formation of Metastable Phases: Insights from Nanocrystalline TiO_2. *Am. Mineral.* **1998**, *83* (9-10), 1077−1082.
(1046) Yuwono, V. M.; Burrows, N. D.; Soltis, J. A.; Penn, R. L. Oriented Aggregation: Formation and Transformation of Mesocrystal Intermediates Revealed. *J. Am. Chem. Soc.* **2010**, *132* (7), 2163−2165.
(1047) Choi, J. J.; Bealing, C. R.; Bian, K. F.; Hughes, K. J.; Zhang, W. Y.; Smilgies, D. M.; Hennig, R. G.; Engstrom, J. R.; Hanrath, T. Controlling Nanocrystal Superlattice Symmetry and Shape-Anisotropic Interactions through Variable Ligand Surface Coverage. *J. Am. Chem. Soc.* **2011**, *133* (9), 3131−3138.
(1048) Song, M.; Zhou, G.; Lu, N.; Lee, J.; Nakouzi, E.; Wang, H.; Li, D. Oriented Attachment Induces Fivefold Twins by Forming and Decomposing High-Energy Grain Boundaries. *Science* **2020**, *367* (6473), 40−45.
(1049) Kuno, M. An Overview of Solution-Based Semiconductor Nanowires: Synthesis and Optical Studies. *Phys. Chem. Chem. Phys.* **2008**, *10* (5), 620−639.
(1050) Liao, H. G.; Shao, Y. Y.; Wang, C. M.; Lin, Y. H.; Jiang, Y. X.; Sun, S. G. TEM Study of Fivefold Twined Gold Nanocrystal Formation Mechanism. *Mater. Lett.* **2014**, *116*, 299−303.
(1051) Yuk, J. M.; Park, J.; Ercius, P.; Kim, K.; Hellebusch, D. J.; Crommie, M. F.; Lee, J. Y.; Zettl, A.; Alivisatos, A. P. High-Resolution EM of Colloidal Nanocrystal Growth Using Graphene Liquid Cells. *Science* **2012**, *336* (6077), 61−64.
(1052) Davis, T. M.; Drews, T. O.; Ramanan, H.; He, C.; Dong, J. S.; Schnablegger, H.; Katsoulakis, M. A.; Kokkoli, E.; McCormick, A. V.; Penn, R. L.; et al. Mechanistic Principles of Nanoparticle Evolution to Zeolite Crystals. *Nat. Mater.* **2006**, *5* (5), 400−408.

https://doi.org/10.1021/acs.chemrev.2c00130
Chem. Rev. 2023, 123, 6413−6544

(1053) Burrows, N. D.; Hale, C. R. H.; Penn, R. L. Effect of pH on the Kinetics of Crystal Growth by Oriented Aggregation. *Cryst. Growth Des.* **2013**, *13* (8), 3396−3403.
(1054) Cölfen, H. In *Handbook of Biomineralization: Biological Aspects and Structure Formation*; Bauerlein, E., Ed.; Wiley-VCHWeinheim, Germany, 2008.
(1055) Nielsen, M. H.; Li, D. S.; Zhang, H. Z.; Aloni, S.; Han, T. Y. J.; Frandsen, C.; Seto, J.; Banfield, J. F.; Colfen, H.; De Yoreo, J. J. Investigating Processes of Nanocrystal Formation and Transformation via Liquid Cell TEM. *Microsc. Microanal.* **2014**, *20* (2), 425−436.
(1056) Penn, R. L. Kinetics of Oriented Aggregation. *J. Phys. Chem. B* **2004**, *108* (34), 12707−12712.
(1057) Raju, M.; van Duin, A. C. T.; Fichthorn, K. A. Mechanisms of Oriented Attachment of TiO_2 Nanocrystals in Vacuum and Humid Environments: Reactive Molecular Dynamics. *Nano Lett.* **2014**, *14* (4), 1836−1842.
(1058) Zhang, H. Z.; De Yoreo, J. J.; Banfield, J. F. A Unified Description of Attachment-Based Crystal Growth. *ACS Nano* **2014**, *8* (7), 6526−6530.
(1059) Mirabello, G.; Ianiro, A.; Bomans, P. H. H.; Yoda, T.; Arakaki, A.; Friedrich, H.; de With, G.; Sommerdijk, N. Crystallization by Particle Attachment is a Colloidal Assembly Process. *Nat. Mater.* **2020**, *19* (4), 391−396.
(1060) Gal, A.; Kahil, K.; Vidavsky, N.; DeVol, R. T.; Gilbert, P. U. P. A.; Fratzl, P.; Weiner, S.; Addadi, L. Particle Accretion MechanismUnderlies Biological Crystal Growth from an Amorphous Precursor Phase. *Adv. Funct. Mater.* **2014**, *24* (34), 5420−5426.
(1061) Bard, A. B.; Zhou, X. Z.; Xia, X. J.; Zhu, G. M.; Lim, M. B.; Kim, S. M.; Johnson, M. C.; Kollman, J. M.; Marcus, M. A.; Spurgeon, S. R.; et al. A Mechanistic Understanding of Nonclassical Crystal Growth in Hydrothermally Synthesized Sodium Yttrium Fluoride Nanowires. *Chem. Mater.* **2020**, *32* (7), 2753−2763.
(1062) Burkett, S. L.; Davis, M. E. Mechanism of Structure Direction in the Synthesis of Si-Zsm-5 - an Investigation by Intermolecular H-1-Si-29 Cp Mas Nmr. *J. Phys. Chem.* **1994**, *98* (17), 4647−4653.
(1063) Chen, J. J.; Zhu, E. B.; Liu, J.; Zhang, S.; Lin, Z. Y.; Duan, X. F.; Heinz, H.; Huang, Y.; De Yoreo, J. J. Building Two-Dimensional Materials One Row at a Time: Avoiding the Nucleation Barrier. *Science* **2018**, *362* (6419), 1135−1139.
(1064) Aabdin, Z.; Lu, J. Y.; Zhu, X.; Anand, U.; Loh, N. D.; Su, H. B.; Mirsaidov, U. Bonding Pathways of Gold Nanocrystals in Solution. *Nano Lett.* **2014**, *14* (11), 6639−6643.
(1065) Frandsen, C.; Legg, B. A.; Comolli, L. R.; Zhang, H. Z.; Gilbert, B.; Johnson, E.; Banfield, J. F. Aggregation-Induced Growth and Transformation of b-FeOOH Nanorods to Micron-Sized a-Fe_2O_3 Spindles. *CrystEngComm* **2014**, *16* (8), 1451−1458.
(1066) Su, H.; Bomans, P. H. H.; Friedrich, H.; Xu, Y. F.; Sommerdijk, N. Crystallization Via Oriented Attachment of Nanoclusters with Short-Range Order in Solution. *J. Phys. Chem. C* **2021**, *125* (1), 1143−1149.
(1067) Zhang, H. Z.; Banfield, J. F. Energy Calculations Predict Nanoparticle Attachment Orientations and Asymmetric Crystal Formation. *J. Phys. Chem. Lett.* **2012**, *3* (19), 2882−2886.
(1068) Zhang, H. Z.; Banfield, J. F. Interatomic Coulombic Interactions as the Driving Force for Oriented Attachment. *CrystEngComm* **2014**, *16* (8), 1568−1578.
(1069) Li, D.; Chun, J.; Xiao, D.; Zhou, W.; Cai, H.; Zhang, L.; Rosso, K. M.; Mundy, C. J.; Schenter, G. K.; De Yoreo, J. J. Trends in Mica-Mica Adhesion Reflect the Influence of Molecular Details on Long-Range Dispersion Forces Underlying Aggregation and Coalignment. *Proc. Natl. Acad. Sci. U.S.A.* **2017**, *114* (29), 7537−7542.
(1070) Liu, L.; Nakouzi, E.; Sushko, M. L.; Schenter, G. K.; Mundy, C. J.; Chun, J.; De Yoreo, J. J. Connecting Energetics to Dynamics in Particle Growth by Oriented Attachment Using Real-Time Observations. *Nat. Commun.* **2020**, *11*, 1045.
(1071) Wu, Z. G.; Chun, J. H.; Chatterjee, S.; Li, D. S. Fabrication of Oriented Crystals as Force Measurement Tips Via Focused Ion Beam and Microlithography Methods. *Surf. Interface Anal* **2018**, *50* (1), 117−122.
(1072) Kerisit, S. N.; De Yoreo, J. J. Effect of Hydrophilicity and Interfacial Water Structure on Particle Attachment. *J. Phys. Chem. C* **2020**, *124* (9), 5480−5488.
(1073) Zhang, X.; He, Y.; Sushko, M. L.; Liu, J.; Luo, L.; De Yoreo, J. J.; Mao, S. X.; Wang, C.; Rosso, K. M. Direction-Specific Van der Waals Attraction Between Rutile TiO_2 Nanocrystals. *Science* **2017**, *356* (6336), 434−437.
(1074) Zhang, X.; Shen, Z.; Liu, J.; Kerisit, S. N.; Bowden, M. E.; Sushko, M. L.; De Yoreo, J. J.; Rosso, K. M. Direction-Specific Interaction Forces Underlying Zinc Oxide Crystal Growth by Oriented Attachment. *Nat. Commun.* **2017**, *8*, 835.
(1075) Li, D. S.; Wang, H. L.; Xiao, D. D.; Song, M.; Legg, B.; Chun, J. Investigating the Magnitude and Source of Orientation-Dependent InteractionsBetween TiO2 Crystal Surfaces. *Nanoscale* **2017**, *9* (29), 10173−10177.
(1076) Prelesnik, J. L.; Alberstein, R. G.; Zhang, S.; Pyles, H.; Baker, D.; Pfaendtner, J.; De Yoreo, J. J.; Tezcan, F. A.; Remsing, R. C.; Mundy, C. J. Ion-Dependent Protein-Surface Interactions from Intrinsic Solvent Response. *Proc. Natl. Acad. Sci. U.S.A.* **2021**, *118*, No. e2025121118.
(1077) Ho, T. A.; Criscenti, L. J. Molecular-Level Understanding of Gibbsite Particle Aggregation in Water. *J. Colloid Interface Sci.* **2021**, *600*, 310−317.
(1078) O'Carroll, D.; English, N. J. Self-Ordering Water Molecules at TiO2 Interfaces: Advances in Structural Classification. *J. Chem. Phys.* **2020**, *153*, 064502.
(1079) Uhlig, M. R.; Martin-Jimenez, D.; Garcia, R. Atomic-Scale Mapping of Hydrophobic Layers on Graphene and Few-Layer MoS2 and WSe2 in Water. *Nat. Commun.* **2019**, *10*, 2606.
(1080) Yin, Z.-W.; Betzler, S. B.; Sheng, T.; Zhang, Q.; Peng, X.; Shangguan, J.; Bustillo, K. C.; Li, J.-T.; Sun, S.-G.; Zheng, H. Visualization of Facet-Dependent Pseudo-Photocatalytic Behavior of TiO_2 Nanorods for Water Splitting Using In Situ Liquid Cell TEM. *Nano Energy* **2019**, *62*, 507−512.
(1081) Nakouzi, E.; Soltis, J. A.; Legg, B. A.; Schenter, G. K.; Zhang, X.; Graham, T. R.; Rosso, K. M.; Anovitz, L. M.; De Yoreo, J. J.; Chun, J. Impact of Solution Chemistry and Particle Anisotropy on the Collective Dynamics of Oriented Aggregation. *ACS Nano* **2018**, *12* (10), 10114−10122.
(1082) Li, T. D.; Chiu, H. C.; Ortiz-Young, D.; Riedo, E. Nanorheology by Atomic Force Microscopy. *Rev. Sci. Instrum.* **2014**, *85* (12), 123707.
(1083) Zhu, Y. X.; Granick, S. Viscosity of Interfacial Water. *Phys. Rev. Lett.* **2001**, *87*, 096104.
(1084) Lin, G. H.; Chee, S. W.; Raj, S.; Kral, P.; Mirsaidov, U. Linker-Mediated Self-Assembly Dynamics of Charged Nanoparticles. *ACS Nano* **2016**, *10* (8), 7443−7450.
(1085) Liu, L. L.; Song, D.; Jin, B.; Sinnwell, M. A.; Liu, J.; De Yoreo, J. J.; Sushko, M. L. Role of the Solvent-Surfactant Duality of Ionic Liquids in Directing Two-Dimensional Particle Assembly. *J. Phys. Chem. C* **2020**, *124* (44), 24215−24222.
(1086) Yang, J.; Zeng, Z.; Kang, J.; Betzler, S.; Czarnik, C.; Zhang, X.; Ophus, C.; Yu, C.; Bustillo, K.; Pan, M.; et al. Formation of Two-Dimensional Transition Metal Oxide Nanosheets with Nanoparticles as Intermediates. *Nat. Mater.* **2019**, *18* (9), 970−976.
(1087) Putnis, A.; Putnis, C. V. The Mechanism of Re-equilibration of Solids in the Presence of a Fuid Phase. *Journal of Solid State Chemistry* **2007**, *180* (5), 1783−1786.
(1088) Putnis, A. Mineral Replacement Reactions. *Rev. Mineral. Geochem.* **2009**, *70* (1), 87−124.
(1089) Putnis, C. V.; Tsukamoto, K.; Nishimura, Y. Direct Observations of Pseudomorphism: Compositional and Textural Evolution at a Fluid-Solid Interface. *Am. Mineral.* **2005**, *90* (11-12), 1909−1912.
(1090) Jun, Y.-S.; Martin, S. T. Microscopic Observations of Reductive Manganite Dissolution Under Oxic Conditions. *Environ. Sci. Technol.* **2003**, *37* (11), 2363−2370.

https://doi.org/10.1021/acs.chemrev.2c00130
Chem. Rev. 2023, 123, 6413−6544

(1091) Altree-Williams, A.; Pring, A.; Ngothai, Y.; Brugger, J. Textural and Compositional Complexities Resulting from Coupled Dissolution-Reprecipitation Reactions in Geomaterials. *Earth Sci. Rev.* **2015**, *150*, 628−651.
(1092) Cardew, P. T.; Davey, R. J. The Kinetics of Solvent-Mediated Phase Transformations. *Proceedings of the Royal Society of London. A* **1985**, *398*, 415−428.
(1093) Songen, H.; Marutschke, C.; Spijker, P.; Holmgren, E.; Hermes, I.; Bechstein, R.; Klassen, S.; Tracey, J.; Foster, A. S.; Kuhnle, A. Chemical Identification at the Solid-Liquid Interface. *Langmuir* **2017**, *33* (1), 125−129.
(1094) Putnis, C. V.; Ruiz-Agudo, E. The Mineral−Water Interface: Where Minerals React with the Environment. *Elements* **2013**, *9* (3), 177−182.
(1095) Ruiz-Agudo, E.; Putnis, C. V.; Putnis, A. Coupled Dissolution and Precipitation at Mineral−Fluid Interfaces. *Chem. Geol.* **2014**, *383*, 132−146.
(1096) Jun, Y.-S.; Martin, S. T. Cobalt Alters The Growth of a Manganese Oxide Film. *Langmuir* **2006**, *22* (5), 2235−2240.
(1097) Putnis, C. V.; Wang, L.; Ruiz-Agudo, E.; Ruiz-Agudo, C.; Renard, F. In *Crystallization via Nonclassical Pathways Vol. 2: Aggregation, Biomineralization, Imaging & Application*; American Chemical Society, 2021; Vol. *1383*.
(1098) Dove, P. M.; Hochella, M. F. Calcite Precipitation Mechanisms and Inhibition by Orthophosphate: In situ Observations by Scanning Force Microscopy. *Geochim. Cosmochim. Acta* **1993**, *57* (3), 705−714.
(1099) Ruiz- Agudo, E.; Putnis, C. V. Direct Observations of Mineral Fluid Reactions Using Atomic Force Microscopy: The Specific Example of Calcite. *Mineral. Mag.* **2012**, *76*, 227−253.
(1100) Zhong, J.; Yan, J. Seeing is Believing: Atomic Force Microscopy Imaging for Nanomaterial Research. *RSC Adv.* **2016**, *6* (2), 1103−1121.
(1101) Matter, J. M.; Stute, M.; Snæbjörnsdottir, S.; Oelkers, E. H.; Gislason, S. R.; Aradottir, E. S.; Sigfusson, B.; Gunnarsson, I.; Sigurdardottir, H.; Gunnlaugsson, E.; et al. Rapid Carbon Mineralization for Permanent Disposal of Anthropogenic Carbon Dioxide Emissions. *Science* **2016**, *352* (6291), 1312−1314.
(1102) Hövelmann, J.; Putnis, C. V.; Ruiz-Agudo, E.; Austrheim, H. Direct Nanoscale Observations of CO2 Sequestration During Crucite [Mg(OH)2] Dissolution. *Environ. Sci. Technol.* **2012**, *46* (9), 5253−5260.
(1103) Di Lorenzo, F.; Ruiz-Agudo, C.; Ibañez-Velasco, A.; Gil-San Millán, R.; Navarro, J.; Ruiz-Agudo, E.; Rodriguez-Navarro, C. The Carbonation of Wollastonite: A model Reaction to Test Natural and Biomimetic Catalysts for Enhanced CO_2 Sequestration. *Minerals* **2018**, *8*, 209.
(1104) Knoll, A. Biomineralization and Evolutionary History. *Rev. Mineral. Geochem.* **2003**, *54* (1), 329−356.
(1105) Konhauser, K. O. Bacterial Iron Biomineralisation in Nature. *FEMS Microbiology Reviews* **1997**, *20* (3-4), 315−326.
(1106) Duckworth, O. W.; Bargar, J. R.; Sposito, G. Coupled Biogeochemical Cycling of Iron and Manganese as Mediated by Microbial Siderophores. *BioMetals* **2009**, *22* (4), 605−613.
(1107) Kim, D.; Lee, B.; Marshall, B.; Thomopoulos, S.; Jun, Y.-S. Cyclic Strain Enhances the Early Stage Mineral Nucleation and the Modulus of Demineralized Bone Matrix. *Biomaterials Science* **2021**, *9*, 5907.
(1108) Kim, D.; Lee, B.; Marshall, B. P.; Jang, E.; Thomopoulos, S.; Jun, Y.-S. Pulsed Electrical Stimulation Enhances Body Fluid Transport for Collagen Biomineralization. *ACS Appl. Bio Mater.* **2020**, 3 (2), 902−910.
(1109) Kim, D.; Lee, B.; Thomopoulos, S.; Jun, Y. S. In Situ Evaluation of Calcium Phosphate Nucleation Kinetics and Pathways during Intra and Extrafibrillar Mineralization of Collagen Matrices. *Cryst. Growth Des.* **2016**, *16* (9), 5359−5366.
(1110) Beniash, E.; Metzler, R. A.; Lam, R. S. K.; Gilbert, P. U. P. A. Transient Amorphous Calcium Phosphate in Forming Enamel. *J. Struct. Biol.* **2009**, *166* (2), 133−143.
(1111) Fincham, A. G.; Moradianoldak, J.; Diekwisch, T. G. H.; Lyaruu, D. M.; Wright, J. T.; Bringas, P.; Slavkin, H. C. Evidence for Amelogenin Nanospheres as Functional Components of Secretory-Stage Enamel Matrix. *J. Struct. Biol.* **1995**, *115* (1), 50−59.
(1112) Mahamid, J.; Sharir, A.; Addadi, L.; Weiner, S. Amorphous Calcium Phosphate is a Major Component of the Forming Fin Bones of Zebrafish: Indications for an Amorphous Precursor Phase. *Proc. Natl. Acad. Sci. U.S.A.* **2008**, *105* (35), 12748−12753.
(1113) Mahamid, J.; Sharir, A.; Gur, D.; Zelzer, E.; Addadi, L.; Weiner, S. Bone Mineralization Proceeds Through Intracellular Calcium Phosphate Loaded Vesicles: A Cryo-Electron Microscopy Study. *J. Struct. Biol.* **2011**, *174* (3), 527−535.
(1114) Weiner, S.; Traub, W.; Wagner, H. D. Lamellar Bone: Structure-Function Relations. *J. Struct. Biol.* **1999**, *126* (3), 241−255.
(1115) Weiner, S.; Dove, P. M. An Overview of Biomineralization Processes and the Problem of the Vital Effect. *Rev. Mineral. Geochem.* **2003**, *54* (1), 1−29.
(1116) Schenk, A. S.; Albarracin, E. J.; Kim, Y. Y.; Ihli, J.; Meldrum, F. C. Confinement Stabilises Single Crystal Vaterite Rods. *Chem. Commun.* **2014**, *50* (36), 4729−4732.
(1117) Stephens, C. J.; Ladden, S. F.; Meldrum, F. C.; Christenson, H. K. Amorphous Calcium Carbonate is Stabilized in Confinement. *Adv. Funct. Mater.* **2010**, *20* (13), 2108−2115.
(1118) Wang, Y. W.; Christenson, H. K.; Meldrum, F. C. Confinement Leads to Control over Calcium Sulfate Polymorph. *Adv. Funct. Mater.* **2013**, *23* (45), 5615−5623.
(1119) Tester, C. C.; Whittaker, M. L.; Joester, D. Controlling Nucleation in Giant Liposomes. *Chem. Commun.* **2014**, *50* (42), 5619−5622.
(1120) Xu, Y.; Nudelman, F.; Eren, E. D.; Wirix, M. J. M.; Cantaert, B.; Nijhuis, W. H.; Hermida-Merino, D.; Portale, G.; Bomans, P. H. H.; Ottmann, C.; et al. Intermolecular Channels Direct Crystal Orientation in Mineralized Collagen. *Nat. Commun.* **2020**, *11*, 5068.
(1121) Xu, Y.; Sommerdijk, N. Aragonite Formation in Confinements: A Step Toward Understanding Polymorph Control. *Proc. Natl. Acad. Sci. U.S.A.* **2018**, *115* (34), 8469−8471.
(1122) Hedges, L. O.; Whitelam, S. Patterning a Surface so as to Speed Nucleation from Solution. *Soft Matter* **2012**, *8* (33), 8624−8635.
(1123) Sun, C. Y.; Stifler, C. A.; Chopdekar, R. V.; Schmidt, C. A.; Parida, G.; Schoeppler, V.; Fordyce, B. I.; Brau, J. H.; Mass, T.; Tambutté, S.; et al. From Particle Attachment to Space-Filling Coral Skeletons. *Proc. Natl. Acad. Sci. U.S.A.* **2020**, *117* (48), 30159−30170.
(1124) Kahil, K.; Varsano, N.; Sorrentino, A.; Pereiro, E.; Rez, P.; Weiner, S.; Addadi, L. Cellular Pathways of Calcium Transport and Concentration Toward Mineral Formation in Sea Urchin Llarvae. *Proc. Natl. Acad. Sci. U.S.A.* **2020**, *117* (49), 30957−30965.
(1125) Branson, O.; Bonnin, E. A.; Perea, D. E.; Spero, H. J.; Zhu, Z.; Winters, M.; Honisch, B.; Russell, A. D.; Fehrenbacher, J. S.; Gagnon, A. C. Nanometer-Scale Chemistry of a Calcite Biomineralization Template: Implications for Skeletal Composition and Nucleation. *Proc. Natl. Acad. Sci. U.S.A.* **2016**, *113* (46), 12934−12939.
(1126) Geerken, E.; de Nooijer, L. J.; van Dijk, I.; Reichart, G. J. Impact of Salinity on Element Incorporation in Two Benthic Foraminiferal Species with Contrasting Magnesium Contents. *Biogeosciences* **2018**, *15* (7), 2205−2218.
(1127) Cadmus, P.; Clements, W. H.; Williamson, J. L.; Ranville, J. F.; Meyer, J. S.; Gutiérrez Ginés, M. J. The Use of Field and Mesocosm Experiments to Quantify Effects of Physical and Chemical Stressors in Mining-Contaminated Streams. *Environ. Sci. Technol.* **2016**, *50* (14), 7825−7833.
(1128) Marie, T.; Mélanie, A.; Lenka, B.; Julien, I.; Isabelle, K.; Christine, P.; Elise, M.; Catherine, S.; Bernard, A.; Ester, A.; et al. Transfer, Transformation, and Impacts of Ceria Nanomaterials in Aquatic Mesocosms Simulating a Pond Ecosystem. *Environ. Sci. Technol.* **2014**, *48* (16), 9004−9013.
(1129) Prather, K. A.; Bertram, T. H.; Grassian, V. H.; Deane, G. B.; Stokes, M. D.; DeMott, P. J.; Aluwihare, L. I.; Palenik, B. P.; Azam, F.;

https://doi.org/10.1021/acs.chemrev.2c00130
Chem. Rev. 2023, 123, 6413−6544

Seinfeld, J. H.; et al. Bringing the Ocean into the Laboratory to Probe the Chemical Complexity of Sea Spray Aerosol. *Proc. Natl. Acad. Sci. U.S.A.* **2013**, *110* (19), 7550−7555.
(1130) Stebounova, L. V.; Guio, E.; Grassian, V. H. Silver Nanoparticles in Simulated Biological Media: A Study of Aggregation, Sedimentation, and Dissolution. *J. Nanoparticle Res.* **2011**, *13* (1), 233−244.
(1131) Rakovan, J. Word to the Wise: Solid Solution. *Rocks Miner.* **2005**, *80* (6), 449−450.
(1132) Noel, J. D.; Wang, Y.; Giammar, D. E. Effect of Water Chemistry on the Dissolution Rate of the Lead Corrosion Product Hydrocerussite. *Water Res.* **2014**, *54*, 237−246.
(1133) Schock, M. R.; Lytle, D. A.; Sandvig, A. M.; Clement, J.; Harmon, S. M. Replacing Polyphosphate with Silicate to Solve Lead, Copper, and Source Water Iron Problems. *J. Am. Water Works Assoc.* **2005**, *97* (11), 84−93.
(1134) Xie, Y.; Giammar, D. E. Effects of Flow and Water Chemistry on Lead Release Rates from Pipe Scales. *Water Res.* **2011**, *45* (19), 6525−6534.
(1135) Peng, C.-Y.; Korshin, G. V.; Valentine, R. L.; Hill, A. S.; Friedman, M. J.; Reiber, S. H. Characterization of Elemental and Structural Composition of Corrosion Scales and Deposits Formed in Drinking Water Distribution Systems. *Water Res.* **2010**, *44* (15), 4570−4580.
(1136) Jurgens, B. C.; Parkhurst, D. L.; Belitz, K. Assessing the Lead Solubility Potential of Untreated Groundwater of the United States. *Environ. Sci. Technol.* **2019**, *53* (6), 3095−3103.
(1137) Zhu, Y.; Huang, B.; Zhu, Z.; Liu, H.; Huang, Y.; Zhao, X.; Liang, M. Characterization, Dissolution and Solubility of the Hydroxypyromorphite-Hydroxyapatite Solid Solution $[(Pb_xCa_{1-x})_5(PO_4)_3OH]$ at 25° C and pH 2-9. *Geochem. Trans.* **2016**, *17*, 2.
(1138) Zhao, Y.; Jia, X.; Waterhouse, G. I.; Wu, L. Z.; Tung, C. H.; O'Hare, D.; Zhang, T. Layered Double Hydroxide Nanostructured Photocatalysts for Renewable Energy Production. *Adv. Energy Mater.* **2016**, *6* (6), 1501974.
(1139) Guo, X.; Zhang, F.; Evans, D. G.; Duan, X. Layered Double Hydroxide Films: Synthesis, Properties and Applications. *Chem. Commun.* **2010**, *46* (29), 5197−5210.
(1140) Chen, H.; Hu, L.; Chen, M.; Yan, Y.; Wu, L. Nickel-Cobalt Layered Double Hydroxide Nanosheets for High-Performance Supercapacitor Electrode Materials. *Adv. Funct. Mater.* **2014**, *24* (7), 934−942.
(1141) Song, F.; Hu, X. Ultrathin Cobalt-Manganese Layered Double Hydroxide is an Efficient Oxygen Evolution Catalyst. *J. Am. Chem. Soc.* **2014**, *136* (47), 16481−16484.
(1142) Fan, G.; Li, F.; Evans, D. G.; Duan, X. Catalytic Applications of Layered Double Hydroxides: Recent Advances and Perspectives. *Chem. Soc. Rev.* **2014**, *43* (20), 7040−7066.
(1143) Mishra, G.; Dash, B.; Pandey, S. Layered Double Hydroxides: A Brief Review from Fundamentals to Application as Evolving Biomaterials. *Appl. Clay Sci.* **2018**, *153*, 172−186.
(1144) Liang, X.; Zang, Y.; Xu, Y.; Tan, X.; Hou, W.; Wang, L.; Sun, Y. Sorption of Metal Cations on Layered Double Hydroxides. *Colloids Surf. A Physicochem. Eng. Asp.* **2013**, *433*, 122−131.
(1145) Siebecker, M. G.; Li, W.; Sparks, D. L. The Important Role of Layered Double Hydroxides in Soil Chemical Processes and Remediation: What We Have Learned over the Past 20 Years. *Adv. Agron.* **2018**, *147*, 1−59.
(1146) Wang, Q.; O'Hare, D. Recent Advances in the Synthesis and Application of Layered Double Hydroxide (LDH) Nanosheets. *Chem. Rev.* **2012**, *112* (7), 4124−4155.
(1147) Ma, L.; Wang, Q.; Islam, S. M.; Liu, Y.; Ma, S.; Kanatzidis, M. G. Highly Selective and Efficient Removal of Heavy Metals by Layered Double Hydroxide Intercalated with the MoS42-Ion. *J. Am. Chem. Soc.* **2016**, *138* (8), 2858−2866.
(1148) Gong, J.; Liu, T.; Wang, X.; Hu, X.; Zhang, L. Efficient Removal of Heavy Metal Ions from Aqueous Systems with the Assembly of Anisotropic Layered Double Hydroxide Nanocrystals@Carbon Nanosphere. *Environ. Sci. Technol.* **2011**, *45* (14), 6181−6187.
(1149) Gu, P.; Zhang, S.; Li, X.; Wang, X.; Wen, T.; Jehan, R.; Alsaedi, A.; Hayat, T.; Wang, X. Recent Advances in Layered Double Hydroxide-Based Nanomaterials for the Removal of Radionuclides from Aqueous Solution. *Environ. Pollut.* **2018**, *240*, 493−505.
(1150) Li, R.; Wang, J. J.; Zhou, B.; Awasthi, M. K.; Ali, A.; Zhang, Z.; Gaston, L. A.; Lahori, A. H.; Mahar, A. Enhancing Phosphate Adsorption by Mg/Al Layered Double Hydroxide Functionalized Biochar with Different Mg/Al Ratios. *Sci. Total Environ.* **2016**, *559*, 121−129.
(1151) Guo, Y.; Zhu, Z.; Qiu, Y.; Zhao, J. Adsorption of Arsenate on Cu/Mg/Fe/La Layered Double Hydroxide from Aqueous Solutions. *J. Hazard. Mater.* **2012**, *239*, 279−288.
(1152) Goh, K.-H.; Lim, T.-T.; Dong, Z. Application of Layered Double Hydroxides for Removal of Oxyanions: A Review. *Water Res.* **2008**, *42* (6-7), 1343−1368.
(1153) Trainor, T. P.; Brown Jr, G. E.; Parks, G. A. Adsorption and Precipitation of Aqueous Zn (II) on Alumina Powders. *J. Colloid Interface Sci.* **2000**, *231* (2), 359−372.
(1154) Forano, C.; Hibino, T.; Leroux, F.; Taviot-Guého, C. Layered Double Hydroxides. *Dev. Clay Sci.* **2006**, *1*, 1021−1095.
(1155) Rojas, R. Layered Double Hydroxides Applications as Sorbents for Environmental Remediation. In *Hydroxides: Synthesis, Types and Applications*; Calixto Carillo, A., Analiz Griego, D., Eds.; Nova Science Publishers 2012; pp 40−73.
(1156) Sasai, R.; Sato, H.; Sugata, M.; Fujimura, T.; Ishihara, S.; Deguchi, K.; Ohki, S.; Tansho, M.; Shimizu, T.; Oita, N.; et al. Why Do Carbonate Anions Have Extremely High Stability in the Interlayer Space of Layered Double Hydroxides? Case Study of Layered Double Hydroxide Consisting of Mg and Al (Mg/Al = 2). *Inorg. Chem.* **2019**, *58* (16), 10928−10935.
(1157) Elzinga, E. J. Formation of Layered Fe(II)-Al(III)-Hydroxides during Reaction of Fe(II) with Aluminum Oxide. *Environ. Sci. Technol.* **2012**, *46* (9), 4894−4901.
(1158) Thompson, H. A.; Parks, G. A.; Brown, G. E. Dynamic Interactions of Dissolution, Surface Adsorption, and Precipitation in an Aging Cobalt(II)-Clay-Water System. *Geochim. Cosmochim. Acta* **1999**, *63* (11), 1767−1779.
(1159) Eick, M. J.; Fendorf, S. E. Reaction Sequence of Nickel (II) with Kaolinite: Mineral Dissolution and Surface Complexation and Precipitation. *Soil Sci. Soc. Am. J.* **1998**, *62* (5), 1257−1267.
(1160) Ford, R. G.; Sparks, D. L. The Nature of Zn Precipitates Formed in the Presence of Pyrophyllite. *Environ. Sci. Technol.* **2000**, *34* (12), 2479−2483.
(1161) Scheidegger, A. M.; Lamble, G. M.; Sparks, D. L. Investigation of Ni Sorption on Pyrophyllite: An XAFS Study. *Environ. Sci. Technol.* **1996**, *30* (2), 548−554.
(1162) Li, W.; Livi, K. J.; Xu, W.; Siebecker, M. G.; Wang, Y.; Phillips, B. L.; Sparks, D. L. Formation of Crystalline Zn-Al Layered Double Hydroxide Precipitates on γ-alumina: The Role of Mineral Dissolution. *Environ. Sci. Technol.* **2012**, *46* (21), 11670−11677.
(1163) He, X.; Qiu, X.; Hu, C.; Liu, Y. Treatment of Heavy Metal Ions in Wastewater using Layered Double Hydroxides: A Review. *J. Dispers. Sci. Technol.* **2018**, *39* (6), 792−801.
(1164) Ma, B.; Fernandez-Martinez, A.; Grangeon, S.; Tournassat, C.; Findling, N.; Carrero, S.; Tisserand, D.; Bureau, S.; Elkaïm, E.; Marini, C.; et al. Selenite Uptake by Ca-Al LDH: A Description of Intercalated Anion Coordination Geometries. *Environ. Sci. Technol.* **2018**, *52*, 1624−1632.
(1165) Livi, K. J.; Senesi, G. S.; Scheinost, A. C.; Sparks, D. L. Microscopic Examination of Nanosized Mixed Ni- Al Hydroxide Surface Precipitates on Pyrophyllite. *Environ. Sci. Technol.* **2009**, *43* (5), 1299−1304.
(1166) Nachtegaal, M.; Sparks, D. L. Nickel Sequestration in a Kaolinite-Humic Acid Complex. *Environ. Sci. Technol.* **2003**, *37* (3), 529−534.

https://doi.org/10.1021/acs.chemrev.2c00130
Chem. Rev. 2023, 123, 6413−6544

(1167) Du, Q.; Freysz, E.; Shen, Y. R. Surface Vibrational Spectroscopic Studies of Hydrogen Bonding and Hydrophobicity. *Science* **1994**, *264* (5160), 826−828.
(1168) Dewan, S.; Yeganeh, M. S.; Borguet, E. Experimental Correlation Between Interfacial Water Structure and Mineral Reactivity. *J. Phys. Chem. Lett.* **2013**, *4* (11), 1977−1982.
(1169) Fukuma, T.; Higgins, M. J.; Jarvis, S. P. Direct Imaging of Individual Intrinsic Hydration Layers on Lipid Bilayers at Angstrom Resolution. *Biophys. J.* **2007**, *92* (10), 3603−3609.
(1170) Fukuma, T.; Jarvis, S. P. Development of Liquid-Environment Frequency Modulation Atomic Force Microscope with Low Noise Deflection Sensor for Cantilevers of Various Dimensions. *Rev. Sci. Instrum.* **2006**, *77*, 043701.
(1171) Kilpatrick, J. I.; Loh, S. H.; Jarvis, S. P. Directly Probing the Effects of Ions on Hydration Forces at Interfaces. *J. Am. Chem. Soc.* **2013**, *135* (7), 2628−2634.
(1172) Loh, S. H.; Jarvis, S. P. Visualization of Ion Distribution at the Mica-Electrolyte Interface. *Langmuir* **2010**, *26* (12), 9176−9178.
(1173) Herruzo, E. T.; Asakawa, H.; Fukuma, T.; Garcia, R. Three-Dimensional Quantitative Force Maps in Liquid with 10 Piconewton, Angstrom and Sub-Minute Resolutions. *Nanoscale* **2013**, *5* (7), 2678−2685.
(1174) Martin-Jimenez, D.; Chacon, E.; Tarazona, P.; Garcia, R. Atomically Resolved Three-Dimensional Structures of Electrolyte Aqueous Solutions Near a Solid Surface. *Nat. Commun.* **2016**, *7*, 12164.
(1175) Fukuma, T.; Reischl, B.; Kobayashi, N.; Spijker, P.; Canova, F. F.; Miyazawa, K.; Foster, A. S. Mechanism Of Atomic Force Microscopy Imaging of Three-Dimensional Hydration Structures at a Solid-Liquid Interface. *Phys. Rev. B* **2015**, *92*, 155412.
(1176) Schaefer, J.; Backus, E. H. G.; Bonn, M. Evidence for Auto-Catalytic Mineral Dissolution from Surface-Specific Vibrational Spectroscopy. *Nat. Commun.* **2018**, *9*, 3316.
(1177) Kubicki, J. D. Self-Consistent Reaction Field Calculations of Aqueous Al3+, Fe3+, and Si4+: Calculated Aqueous-Phase Deprotonation Energies Correlated with Experimental ln(Ka) and pKa. *J. Phys. Chem. A* **2001**, *105* (38), 8756−8762.
(1178) Duckworth, O. W.; Martin, S. T. Role of Molecular Oxygen in the Dissolution of Siderite and Rhodochrosite. *Geochim. Cosmochim. Acta* **2004**, *68* (3), 607−621.
(1179) Samson, S. D.; Stillings, L. L.; Eggleston, C. M. The Depletion and Regeneration of Dissolution-Active Sites at the Mineral−Water Interface: I. Fe, Al, and in Sesquioxides. *Geochim. Cosmochim. Acta* **2000**, *64* (20), 3471−3484.
(1180) Schott, J.; Pokrovsky, O. S.; Oelkers, E. H. The Link Between Mineral Dissolution/Precipitation Kinetics and Solution Chemistry. *Rev. Mineral. Geochem.* **2009**, *70*, 207−258.
(1181) Pearce, C. R.; Jones, M. T.; Oelkers, E. H.; Pradoux, C.; Jeandel, C. The Effect of Particulate Dissolution on the Neodymium (Nd) Isotope and Rare Earth Element (Ree) Composition of Seawater. *Earth Planet. Sci. Lett.* **2013**, *369-370*, 138−147.
(1182) Jones, M. T.; Gislason, S. R.; Burton, K. W.; Pearce, C. R.; Mavromatis, V.; Pogge von Strandmann, P. A. E.; Oelkers, E. H. Quantifying the Impact of Riverine Particulate Dissolution in Seawater on Ocean Chemistry. *Earth Planet. Sci. Lett.* **2014**, *395*, 91−100.
(1183) Beal, L.; Senison, J.; Banner, J.; Musgrove, M. L.; Yazbek, L.; Bendik, N.; Herrington, C.; Reyes, D. Stream and Spring Water Evolution in a Rapidly Urbanizing Watershed, Austin, TX. *Water Resour. Res.* **2020**, *56*, e2019WR025623.
(1184) Gaillardet, J.; Viers, J.; Dupré, B. 7.7 Trace Elements in River Waters. *Treatise on Geochemistry* **2014**, 195−235.
(1185) Hinkle, M. A. G.; Wang, Z.; Giammar, D. E.; Catalano, J. G. Interaction of Fe(II) With Phosphate and Sulfate on Iron Oxide Surfaces. *Geochim. Cosmochim. Acta* **2015**, *158*, 130−146.
(1186) Gräfe, M.; Donner, E.; Collins, R. N.; Lombi, E. Speciation of Metal(Loid)S in Environmental Samples by X-Ray Absorption Spectroscopy: A Critical Review. *Anal. Chim. Acta* **2014**, *822*, 1−22.
(1187) Laborda, F.; Bolea, E.; Cepriá, G.; Gómez, M. T.; Jiménez, M. S.; Pérez-Arantegui, J.; Castillo, J. R. Detection, Characterization and Quantification of Inorganic Engineered Nanomaterials: A Review of Techniques and Methodological Approaches for the Analysis of Complex Samples. *Anal. Chim. Acta* **2016**, *904*, 10−32.
(1188) Kraemer, S. M.; Butler, A.; Borer, P.; Cervini-Silva, J. Siderophores and the Dissolution of Iron-Bearing Minerals in Marine Systems. *Rev. Mineral. Geochem.* **2005**, *59* (1), 53−84.
(1189) Cornell, R. M.; Schwertmann, U. *Iron Oxides : Structure, Properties, Reactions, Occurences and Uses* 2nd ed.; Wiley-VCH: Weinheim, 2003.
(1190) González-Davila, M.; Santana-Casiano, J. M.; Millero, F. J. Oxidation of Iron (Ii) Nanomolar with H2o2 in Seawater. *Geochim. Cosmochim. Acta* **2005**, *69* (1), 83−93.
(1191) Mao, Y.; Pham, A. N.; Rose, A. L.; Waite, T. D. Influence of Phosphate on the Oxidation Kinetics of Nanomolar Fe(II) in Aqueous Solution at Circumneutral pH. *Geochim. Cosmochim. Acta* **2011**, *75* (16), 4601−4610.
(1192) King, D. W.; Lounsbury, H. A.; Millero, F. J. Rates and Mechanism of Fe(II) Oxidation at Nanomolar Total Iron Concentrations. *Environ. Sci. Technol.* **1995**, *29* (3), 818−824.
(1193) Wiederhold, J. G.; Kraemer, S. M.; Teutsch, N.; Borer, P. M.; Halliday, A. N.; Kretzschmar, R. Iron Isotope Fractionation During Proton-Promoted, Ligand-Controlled, and Reductive Dissolution of Goethite. *Environ. Sci. Technol.* **2006**, *40* (12), 3787−3793.
(1194) Kraemer, S. M. Iron Oxide Dissolution and Solubility in the Presence Of Siderophores. *Aquat. Sci.* **2004**, *66* (1), 3−18.
(1195) Kang, K.; Schenkeveld, W. D. C.; Biswakarma, J.; Borowski, S. C.; Hug, S. J.; Hering, J. G.; Kraemer, S. M. Low Fe(II) Concentrations Catalyze the Dissolution of Various Fe(III)(hydr)-oxide Minerals in the Presence of Diverse Ligands and over a Broad pH Range. *Environ. Sci. Technol.* **2019**, *53* (1), 98−107.
(1196) Biswakarma, J.; Kang, K.; Borowski, S. C.; Schenkeveld, W. D. C.; Kraemer, S. M.; Hering, J. G.; Hug, S. J. Fe(II)-Catalyzed Ligand-Controlled Dissolution of Iron(hydr)oxides. *Environ. Sci. Technol.* **2019**, *53* (1), 88−97.
(1197) Marsili, E.; Baron, D. B.; Shikhare, I. D.; Coursolle, D.; Gralnick, J. A.; Bond, D. R. Shewanella Secretes Flavins That Mediate Extracellular Electron Transfer. *Proc. Natl. Acad. Sci. U.S.A.* **2008**, *105* (10), 3968−3973.
(1198) Michelson, K.; Alcalde, R. E.; Sanford, R. A.; Valocchi, A. J.; Werth, C. J. Diffusion-Based Recycling of Flavins Allows Shewanella Oneidensis MR-1 to Yield Energy from Metal Reduction Across Physical Separations. *Environ. Sci. Technol.* **2019**, *53* (7), 3480−3487.
(1199) Herting, D. L.; Reynolds, J. G.; Barton, W. B. Conversion of Coarse Gibbsite Remaining in Hanford Nuclear Waste Tank Heels to Solid Sodium Aluminate $[NaAl(OH)_4 \cdot 1.5H_2O]$. *Ind. Eng. Chem. Res.* **2014**, *53* (36), 13833−13842.
(1200) McGinnis, C. P.; Welch, T. D.; Hunt, R. D. Caustic Leaching of High-Level Radioactive Tank Sludge: A Critical Literature Review. *Sep. Sci. Technol.* **1999**, *34*, 1479−1494.
(1201) Colburn, H. A.; Peterson, R. A. A History of Hanford Tank Waste, Implications for Waste Treatment, and Disposal. *Environ. Prog. Sustain. Energy* **2021**, *40*, No. e13567.
(1202) Gephart, R. E. A Short History of Waste Management at the Hanford Site. *Phys. Chem. Earth* **2010**, *35* (6-8), 298−306.
(1203) Hill, R. P.; Reynolds, J. G.; Rutland, P. L. A Comparison of Hanford and Savannah River Site High-Level Wastes. In *Proceedings of the 13th International High-Level Waste Management Conference*, 2011; p 114−117.
(1204) Reynolds, D. A.; Reynolds, J. G. In *Annual Waste Management Conference*; WM Symposia: Phoenix, AZ, 2018.
(1205) Zhang, X.; Zhang, X.; Graham, T. R.; Pearce, C. I.; Mehdi, B. L.; N'Diaye, A. T.; Kerisit, S.; Browning, N. D.; Clark, S. B.; Rosso, K. M. Fast Synthesis of Gibbsite Nanoplates and Process Optimization Using Box-Behnken Experimental Design. *Cryst. Growth Des.* **2017**, *17* (12), 6801−6808.
(1206) Hu, J. Z.; Zhang, X.; Jaegers, N. R.; Wan, C.; Graham, T. R.; Hu, M.; Pearce, C. I.; Felmy, A. R.; Clark, S. B.; Rosso, K. M.

Transitions in Al Coordination During Gibbsite Crystallization Using High-Field ^{27}Al and ^{23}Na MAS NMR Spectroscopy. *J. Phys. Chem. C* **2017**, *121* (49), 27555−27562.
(1207) Zhang, X.; Huestis, P. L.; Pearce, C. I.; Hu, J. Z.; Page, K.; Anovitz, L. M.; Aleksandrov, A. B.; Prange, M. P.; Kerisit, S.; Bowden, M. E.; et al. Boehmite and Gibbsite Nanoplates for the Synthesis of Advanced Alumina Products. *ACS Appl. Nano Mater.* **2018**, *1*, 7115−7128.
(1208) Zhang, X.; Cui, W.; Page, K. L.; Pearce, C. I.; Bowden, M. E.; Graham, T. R.; Shen, Z.; Li, P.; Wang, Z.; Kerisit, S.; et al. Size and Morphology Controlled Synthesis of Boehmite Nanoplates and Crystal Growth Mechanisms. *Cryst. Growth Des.* **2018**, *18*, 3596−3606.
(1209) Zhang, X.; Cui, W.; Hu, J. Z.; Wang, H.-W.; Prange, M. P.; Wan, C.; Jaegers, N. R.; Zong, M.; Zhang, H.; Pearce, C. I.; et al. Transformation of Gibbsite to Boehmite in Caustic Aqueous Solution at Hydrothermal Conditions. *Cryst. Growth Des.* **2019**, *19*, 5557−5567.
(1210) Wang, S.; Zhang, X.; Graham, T. R.; Zhang, H.; Pearce, C. I.; Wang, Z.; Clark, S. B.; Jiang, W.; Rosso, K. M. Two-Step Route to Size and Shape Controlled Gibbsite Nanoplates and the Crystal Growth Mechanism. *CrystEngComm* **2020**, *22* (15), 2555−2565.
(1211) Shen, Z.; Kerisit, S. N.; Stack, A. G.; Rosso, K. M. Free-Energy Landscape of the Dissolution of Gibbsite at High pH. *J. Phys. Chem. Lett.* **2018**, *9* (7), 1809−1814.
(1212) Chen, X. Y.; Huh, H. S.; Lee, S. W. Hydrothermal Synthesis of Boehmite (γ-AlOOH) Nanoplatelets and Nanowires: pH-Controlled Morphologies. *Nanotechnology* **2007**, *18* (28), 285608.
(1213) Gong, X.; Nie, Z.; Qian, M.; Liu, J.; Pederson, L. A.; Hobbs, D. T.; McDuffie, N. G. Gibbsite to Boehmite Transformation in Strongly Caustic and Nitrate Environments. *Ind. Eng. Chem. Res.* **2003**, *42* (10), 2163−2170.
(1214) Mathieu, Y.; Lebeau, B.; Valtchev, V. Control of the Morphology and Particle Size of Boehmite Nanoparticles Synthesized Under Hydrothermal Conditions. *Langmuir* **2007**, *23* (18), 9435−9442.
(1215) Graham, T. R.; Han, K. S.; Dembowski, M.; Krzysko, A. J.; Zhang, X.; Hu, J.; Clark, S. B.; Clark, A. E.; Schenter, G. K.; Pearce, C. I.; Rosso, K. M. 27Al Pulsed Field Gradient, Diffusion-NMR Spectroscopy of Solvation Dynamics and Ion Pairing in Alkaline Aluminate Solutions. *J. Phys. Chem. B* **2018**, *122*, 10907−10912.
(1216) Pouvreau, M.; Dembowski, M.; Clark, S. B.; Reynolds, J. G.; Rosso, K. M.; Schenter, G. K.; Pearce, C. I.; Clark, A. E. Ab Initio Molecular Dynamics Reveal Spectroscopic Siblings and Ion Pairing as New Challenges for Elucidating Prenucleation Aluminum Speciation. *J. Phys. Chem. B* **2018**, *122* (29), 7394−7402.
(1217) Dembowski, M.; Snyder, M. M.; Delegard, C. H.; Reynolds, J. G.; Graham, T. R.; Wang, H.-W.; Leavy, I. I.; Baum, S. R.; Qafoku, O.; Fountain, M. S.; et al. Ion-Ion Interactions Enhance Aluminum Solubility in Alkaline Suspensions of Nano-Gibbsite (A-Al (OH) 3) With Sodium Nitrite/Nitrate. *Phys. Chem. Chem. Phys.* **2020**, *22*, 4368−4378.
(1218) Dembowski, M.; Graham, T. R.; Reynolds, J. G.; Clark, S. B.; Rosso, K. M.; Pearce, C. I. Influence of Soluble Oligomeric Aluminum on Precipitation in the Al-KOH-H 2 O System. *Phys. Chem. Chem. Phys.* **2020**, *22* (42), 24677−24685.
(1219) Pouvreau, M.; Martinez-Baez, E.; Dembowski, M.; Pearce, C. I.; Schenter, G. K.; Rosso, K. M.; Clark, A. E. Mechanisms of Al3+ Dimerization in Alkaline Solutions. *Inorg. Chem.* **2020**, *59* (24), 18181−18189.
(1220) Cui, W.; Zhang, X.; Pearce, C. I.; Chen, Y.; Zhang, S.; Liu, W.; Engelhard, M. H.; Kovarik, L.; Zong, M.; Zhang, H.; et al. Cr (III) Adsorption by Cluster Formation on Boehmite Nanoplates in Highly Alkaline Solution. *Environ. Sci. Technol.* **2019**, *53*, 11043−11055.
(1221) Cui, W.; Zhang, X.; Pearce, C. I.; Engelhard, M. H.; Zhang, H.; Wang, Y.; Heald, S. M.; Zheng, S.; Zhang, Y.; Clark, S. B.; et al. Effect of Cr (III) Adsorption on the Dissolution of Boehmite Nanoparticles in Caustic Solution. *Environ. Sci. Technol.* **2020**, *54*, 6375−6384.
(1222) Antelo, J.; Fiol, S.; Carabante, I.; Arroyo, A.; Lezama-Pacheco, J. S.; Josevska, N.; Protopapa, C.; Kumpiene, J. Stability of Naturally Occurring AMD-Schwertmannite in the Presence of Arsenic and Reducing Agents. *J. Geochem. Explor.* **2021**, *220*, 106677.
(1223) Schoepfer, V. A.; Burton, E. D.; Johnston, S. G.; Kraal, P. Phosphate Loading Alters Schwertmannite Transformation Rates and Pathways During Microbial Reduction. *Sci. Total Environ.* **2019**, *657*, 770−780.
(1224) Sánchez-Andrea, I.; Sanz, J. L.; Bijmans, M. F. M.; Stams, A. J. M. Sulfate Reduction at Low pH to Remediate Acid Mine Drainage. *J. Hazard. Mater.* **2014**, *269*, 98−109.
(1225) Alcobé, X.; Bassas, J.; Tarruella, I.; Roca, A.; Viñals, J. Structural Characterization of Synthetic Beudantite-Type Phases by Rietveld Refinement. *Mater. Sci. Forum* **2001**, *378-381* (II), 671−676.
(1226) Baron, D.; Palmer, C. D. Solid-Solution Aqueous-Solution Reactions Between Jarosite (Kfe3(SO4)2(OH)6) and its Chromate Analog. *Geochim. Cosmochim. Acta* **2002**, *66* (16), 2841−2853.
(1227) Savage, K. S.; Bird, D. K.; O'Day, P. A. Arsenic Speciation in Synthetic Jarosite. *Chem. Geol.* **2005**, *215*, 473−498.
(1228) Gräfe, M.; Beattie, D. A.; Smith, E.; Skinner, W. M.; Singh, B. Copper and Arsenate Co-Sorption at the Mineral−Water Interfaces of Goethite and Jarosite. *J. Colloid Interface Sci.* **2008**, *322* (2), 399−413.
(1229) Forray, F. L.; Smith, A. M. L.; Navrotsky, A.; Wright, K.; Hudson-Edwards, K. A.; Dubbin, W. E. Synthesis, Characterization and Thermochemistry of Synthetic Pb-As, Pb-Cu And Pb-Zn Jarosites. *Geochim. Cosmochim. Acta* **2014**, *127*, 107−119.
(1230) Aguilar-Carrillo, J.; Villalobos, M.; Pi-Puig, T.; Escobar-Quiroz, I. N.; Romero, F. M. Synergistic Arsenic(V) and Lead(Ii) Retention on Synthetic Jarosite. I. Simultaneous Structural Incorporation Behaviour and Mechanism. *Environ. Sci. Process. Impacts* **2018**, *20* (2), 354−369.
(1231) Jönsson, J.; Persson, P.; Sjöberg, S.; Lövgren, L. Schwertmannite Precipitated from Acid Mine Drainage: Phase Transformation, Sulphate Release and Surface Properties. *Appl. Geochem.* **2005**, *20* (1), 179−191.
(1232) Bigham, J. M.; Schwertmann, U.; Traina, S. J.; Winland, R. L.; Wolf, M. Schwertmannite and the Chemical Modeling of Iron in Acid Sulfate Waters. *Geochim. Cosmochim. Acta* **1996**, *60* (12), 2111−2121.
(1233) Veil, J. *Produced Water Volumes and Management Practices in 2017*; Groundwater Research & Education Foundation, 2020.
(1234) Khan, H. J.; Spielman-Sun, E.; Jew, A. D.; Bargar, J.; Kovscek, A.; Druhan, J. L. A Critical Review of the Physicochemical Impacts of Water Chemistry on Shale in Hydraulic Fracturing Systems. *Environ. Sci. Technol.* **2021**, *55* (3), 1377−1394.
(1235) Li, Q.; Jun, Y.-S. Salinity-Induced Reduction of Interfacial Energies and Kinetic Factors During Calcium Carbonate Nucleation on Quartz. *J. Phys. Chem. C* **2019**, *123* (23), 14319−14326.
(1236) Thyne, G.; Brady, P. Evaluation of Formation Water Chemistry and Scale Prediction: Bakken Shale. *Appl. Geochem.* **2016**, *75*, 107−113.
(1237) Langmuir, D. *Aqueous Environmental Geochemistry*; Prentice Hall: Upper Saddle River, N.J, 1997.
(1238) Zhao, Y.; Dai, Z.; Wang, X.; Dai, C.; Paudyal, S.; Ko, S.; Kan, A. T.; Tomson, M. Evaluation of Silica and Related Matrix Ion Effects on Common Scale Inhibitors. *Energy Fuels* **2021**, *35* (3), 2144−2152.
(1239) Suzuki, Y.; Duran, H.; Steinhart, M.; Kappl, M.; Butt, H.-J.; Floudas, G. Homogeneous Nucleation of Predominantly Cubic Ice Confined in Nanoporous Alumina. *Nano Lett.* **2015**, *15* (3), 1987−1992.
(1240) Monnier, V.; Sanz, N.; Botzung-Appert, E.; Bacia, M.; Ibanez, A. Confined Nucleation and Growth of Organic Nanocrystals in Sol-Gel Matrices. *J. Mater. Chem.* **2006**, *16* (15), 1401−1409.
(1241) Jiang, Q.; Ward, M. D. Crystallization Under Nanoscale Confinement. *Chem. Soc. Rev.* **2014**, *43* (7), 2066−2079.
(1242) Stack, A. G.; Fernandez-Martinez, A.; Allard, L. F.; Bañuelos, J. L.; Rother, G.; Anovitz, L. M.; Cole, D. R.; Waychunas, G. A. Pore-

https://doi.org/10.1021/acs.chemrev.2c00130
Chem. Rev. 2023, 123, 6413−6544

Size-Dependent Calcium Carbonate Precipitation Controlled by Surface Chemistry. *Environ. Sci. Technol.* **2014**, *48* (11), 6177−6183.
(1243) Massa, M. V.; Lee, M. S. M.; Dalnoki-Veress, K. Crystal Nucleation of Polymers Confined to Droplets: Memory Effects. *J. Polym. Sci. B Polym. Phys.* **2005**, *43* (23), 3438−3443.
(1244) Whittaker, M. L.; Dove, P. M.; Joester, D. Nucleation on Surfaces and in Confinement. *MRS Bull.* **2016**, *41* (5), 388−392.
(1245) Zhu, Y.; Derami, H. G.; Gupta, P.; Gupta, R.; Singamaneni, S.; Jun, Y.-S. Ionic Surface Propensity Controls pH in Nanopores. *Chem* **2022**, *8*, 3081−3095.
(1246) Placencia-Gómez, E.; Kerisit, S. N.; Mehta, H. S.; Qafoku, O.; Thompson, C. J.; Graham, T. R.; Ilton, E. S.; Loring, J. S. Critical Water Coverage during Forsterite Carbonation in Thin Water Films: Activating Dissolution and Mass Transport. *Environ. Sci. Technol.* **2020**, *54* (11), 6888−6899.
(1247) Thompson, C. J.; Loring, J. S.; Wang, Z.; Joly, A. G.; Rosso, K. M.; Felmy, A. R. In Situ Infrared Spectroscopic Study of the Reactivity of Forsterite, Antigorite, and Lizardite in Dry to Water-Saturated Supercritical CO_2. *Prep. Pap.-Am. Chem. Soc., Div. Fuel Chem.* **2011**, *56* (1), 280−281.
(1248) Miller, Q. R. S.; Kaszuba, J. P.; Kerisit, S. N.; Schaef, H. T.; Bowden, M. E.; McGrail, B. P.; Rosso, K. M. Emerging Investigator Series: Ion Diffusivities in Nanoconfined Interfacial Water Films Contribute to Mineral Carbonation Thresholds. *Environ. Sci.: Nano* **2020**, *7* (4), 1068−1081.
(1249) Daval, D.; Martinez, I.; Corvisier, J.; Findling, N.; Goffe, B.; Guyot, F. Carbonation of Ca-Bearing Silicates, the Case of Wollastonite: Experimental Investigations and Kinetic Modeling. *Chem. Geol.* **2009**, *265* (1), 63−78.
(1250) Daval, D.; Martinez, I.; Guigner, J.-M.; Hellmann, R.; Corvisier, J.; Findling, N.; Dominici, C.; Goffe, B.; Guyot, F. Mechanism of Wollastonite Carbonation Deduced From Micro- to Nanometer Length Scale Observations. *Am. Mineral.* **2009**, *94* (11-12), 1707−1726.
(1251) Felmy, A. R.; Qafoku, O.; Arey, B. W.; Hu, J. Z.; Hu, M.; Schaef, H. T.; Ilton, E. S.; Hess, N. J.; Pearce, C. I.; Feng, J.; Rosso, K. M. Reaction of Water-Saturated Supercritical CO2 with Forsterite: Evidence for Magnesite Formation at Low Temperatures. *Geochim. Cosmochim. Acta* **2012**, *91*, 271−282.
(1252) Fricker, K. J.; Park, A.-H. A. Effect of H_2O on $Mg(OH)_2$ Carbonation Pathways for Combined CO2 Capture and Storage. *Chem. Eng. Sci.* **2013**, *100* (0), 332−341.
(1253) Hur, T.-B.; Baltrus, J. P.; Howard, B. H.; Harbert, W. P.; Romanov, V. N. Carbonate Formation in Wyoming Montmorillonite Under High Pressure Carbon Dioxide. *Int. J. Greenhouse Gas Control* **2013**, *13* (0), 149−155.
(1254) Kwak, J. H.; Hu, J. Z.; Turcu, R. V. F.; Rosso, K. M.; Ilton, E. S.; Wang, C.; Sears, J. A.; Engelhard, M. H.; Felmy, A. R.; Hoyt, D. W. The role of H_2O in the Carbonation of Forsterite in Supercritical CO2. *Int. J. Greenhouse Gas Control* **2011**, *5* (4), 1081−1092.
(1255) Lin, H.; Fujii, T.; Takisawa, R.; Takahashi, T.; Hashida, T. Experimental Evaluation of Interactions in Supercritical CO_2/Water/Rock Minerals System Under Geologic CO_2 Sequestration Conditions. *J. Mater. Sci.* **2008**, *43* (7), 2307−2315.
(1256) Loring, J. S.; Thompson, C. J.; Wang, Z.; Joly, A. G.; Sklarew, D. S.; Schaef, H. T.; Ilton, E. S.; Rosso, K. M.; Felmy, A. R. In Situ Infrared Spectroscopic Study of Forsterite Carbonation in Wet Supercritical CO_2. *Environ. Sci. Technol.* **2011**, *45* (14), 6204−6210.
(1257) Loring, J. S.; Thompson, C. J.; Zhang, C.; Wang, Z.; Schaef, H. T.; Rosso, K. M. In Situ Infrared Spectroscopic Study of Brucite Carbonation in Dry to Water-Saturated Supercritical Carbon Dioxide. *J. Phys. Chem. A* **2012**, *116* (19), 4768−4777.
(1258) McGrail, B. P.; Schaef, H. T.; Glezakou, V. A.; Dang, L. X.; Owen, A. T. Water Reactivity in the Liquid and Supercritical CO_2 Phase: Has Half the Story Been Neglected? *Energy Procedia* **2009**, *1* (1), 3415−3419.
(1259) Miller, Q. R. S.; Kaszuba, J. P.; Schaef, H. T.; Bowden, M. E.; McGrail, B. P. Impacts of Organic Ligands on Forsterite Reactivity in Supercritical CO_2 Fluids. *Environ. Sci. Technol.* **2015**, *49* (7), 4724−4734.
(1260) Miller, Q. R. S.; Thompson, C. J.; Loring, J. S.; Windisch, C. F.; Bowden, M. E.; Hoyt, D. W.; Hu, J. Z.; Arey, B. W.; Rosso, K. M.; Schaef, H. T. Insights into Silicate Carbonation Processes in Water-Bearing Supercritical CO_2 Fluids. *Int. J. Greenhouse Gas Control* **2013**, *15* (0), 104−118.
(1261) Qafoku, O.; Hu, J.; Hess, N. J.; Hu, M. Y.; Ilton, E. S.; Feng, J.; Arey, B. W.; Felmy, A. R. Formation of Submicron Magnesite During Reaction of Natural Forsterite in H_2O-Saturated Supercritical CO_2. *Geochim. Cosmochim. Acta* **2014**, *134* (0), 197−209.
(1262) Qafoku, O.; Kovarik, L.; Kukkadapu, R. K.; Ilton, E. S.; Arey, B. W.; Tucek, J.; Felmy, A. R. Fayalite Dissolution and Siderite Formation in Water-Saturated Supercritical CO_2. *Chem. Geol.* **2012**, *332-333* (0), 124−135.
(1263) Schaef, H. T.; Windisch Jr, C. F.; McGrail, B. P.; Martin, P. F.; Rosso, K. M. Brucite [$Mg(OH_2)$] Carbonation in Wet Supercritical CO_2: An In Situ High Pressure X-Ray Diffraction Study. *Geochim. Cosmochim. Acta* **2011**, *75* (23), 7458−7471.
(1264) Shao, H.; Ray, J. R.; Jun, Y.-S. Effects of Salinity and the Extent of Water on Supercritical CO_2-Induced Phlogopite Dissolution and Secondary Mineral Formation. *Environ. Sci. Technol.* **2011**, *45* (4), 1737−1743.
(1265) Schaef, H. T.; McGrail, B. P.; Loring, J. L.; Bowden, M. E.; Arey, B. W.; Rosso, K. M. Forsterite [Mg_2SiO_4)] Carbonation in Wet Supercritical CO2: An In Situ High-Pressure X-Ray Diffraction Study. *Environ. Sci. Technol.* **2013**, *47*, 174−181.
(1266) Wang, X.; Alvarado, V.; Swoboda-Colberg, N.; Kaszuba, J. P. Reactivity of Dolomite in Water-Saturated Supercritical Carbon Dioxide: Significance for Carbon Capture and Storage and for Enhanced Oil and Gas Recovery. *Energy Convers. Manage.* **2013**, *65* (0), 564−573.
(1267) Whitfield, P. S.; Mitchell, L. D. In Situ Laboratory X-Ray Powder Diffraction Study of Wollastonite Carbonation Using a High-Pressure Stage. *Appl. Geochem.* **2009**, *24* (9), 1635−1639.
(1268) Min, Y.; Jun, Y. S. Wollastonite Carbonation in Water-bearing CO_2: Effects of Water Saturation Condition, Temperature, and Pressure. *Chem. Geol.* **2018**, *483*, 239−246.
(1269) Saraji, S.; Goual, L.; Piri, M.; Plancher, H. Wettability of Supercritical Carbon Dioxide/Water/Quartz Systems: Simultaneous Measurement of Contact Angle and Interfacial Tension at Reservoir Conditions. *Langmuir* **2013**, *29* (23), 6856−6866.
(1270) Wehrli, B.; Friedl, G.; Manceau, A. Reaction Rates and Products of Manganese Oxidation at the Sediment-Water Interface. In *Aquatic Chemistry*; Advances in Chemistry; American Chemical Society, 1995; Vol. *244*, pp 111−134.
(1271) Morgan, J. J. Kinetics of Reaction Between O_2 and Mn (II) Species in Aqueous Solutions. *Geochim. Cosmochim. Acta* **2005**, *69* (1), 35−48.
(1272) Francis, C. A.; Co, E.-M.; Tebo, B. M. Enzymatic Manganese (II) Oxidation by a Marine A-Proteobacterium. *Appl. Environ. Microbiol.* **2001**, *67*, 4024−4029.
(1273) Hansel, C. M.; Francis, C. A. Coupled Photochemical and Enzymatic Mn (II) Oxidation Pathways of a Planktonic Roseobacter-Like Bacterium. *Appl. Environ. Microbiol.* **2006**, *72* (5), 3543−3549.
(1274) Learman, D.; Voelker, B.; Vazquez-Rodriguez, A.; Hansel, C. Formation of Manganese Oxides by Bacterially Generated Superoxide. *Nat. Geosci.* **2011**, *4* (2), 95−98.
(1275) Learman, D.; Wankel, S.; Webb, S.; Martinez, N.; Madden, A.; Hansel, C. Coupled Biotic-Abiotic Mn (II) Oxidation Pathway Mediates the Formation and Structural Evolution of Biogenic Mn Oxides. *Geochim. Cosmochim. Acta* **2011**, *75* (20), 6048−6063.
(1276) Jung, H.; Chadha, T. S.; Kim, D.; Biswas, B.; Jun, Y. S. Photochemically-Assisted Fast Oxidation of Manganese and Formation of δ-MnO2 Nanosheets in Nitrate Solution. *Chem. Commun.* **2017**, *53*, 4445−4448.
(1277) Jung, H.; Chadha, T. S.; Min, Y.; Biswas, P.; Jun, Y. S. Photochemically-Assisted Synthesis of Birnessite Nanosheets and

https://doi.org/10.1021/acs.chemrev.2c00130
Chem. Rev. 2023, 123, 6413−6544

Their Structural Alteration in the Presence of Pyrophosphate. *ACS Sustain. Chem. Eng.* **2017**, *5* (11), 10624−10632.
(1278) Gao, Z.; Liu, J.; Skurie, C.; Zhu, Y.; Jun, Y.-S. Photochemical Reactions of Dissolved Organic Matter and Bromide Ions Facilitate Abiotic Formation of Manganese Oxide Solids. *Water Res.* **2022**, *222*, 118831.
(1279) Gao, Z.; Skurie, C.; Jun, Y.-S. Reactive Halogen Radicals in Saline Water Promote Photochemically-Assisted Formation of Manganese Oxide Nanosheets. *Environ. Sci. Nano* **2022**, *9* (10), 3756−3765.
(1280) Grahame, D. C. The Electrical Double Layer and the Theory of Electrocapillarity. *Chem. Rev.* **1947**, *41* (3), 441−501.
(1281) Pezzotti, S.; Galimberti, D. R.; Shen, Y. R.; Gaigeot, M. P. What the Diffuse Layer (DL) Reveals in Non-Linear SFG Spectroscopy. *Minerals* **2018**, *8*, 305.
(1282) Pfeiffer-Laplaud, M.; Gaigeot, M. P. Electrolytes at the Hydroxylated (0001) alpha-Quartz/Water Interface: Location and Structural Effects on Interfacial Silanols by DFT-Based MD. *J. Phys. Chem. C* **2016**, *120* (26), 14034−14047.
(1283) Ma, E.; Kim, J.; Chang, H.; Ohno, P. E.; Jodts, R. J.; Miller, T. F.; Geiger, F. M. Stern and Diffuse Layer Interactions during Ionic Strength Cycling. *J. Phys. Chem. C* **2021**, *125* (32), 18002−18014.
(1284) Gonella, G.; Lutgebaucks, C.; de Beer, A. G. F.; Roke, S. Second Harmonic and Sum-Frequency Generation from Aqueous Interfaces Is Modulated by Interference. *J. Phys. Chem. C* **2016**, *120* (17), 9165−9173.
(1285) Schaefer, J.; Gonella, G.; Bonn, M.; Backus, E. H. G. Surface-Specific Vibrational Spectroscopy of the Water/Silica Interface: Screening and Interference. *Phys. Chem. Chem. Phys.* **2017**, *19* (25), 16875−16880.
(1286) Dobrotvorskaia, A. N.; Kolomiitsova, T. D.; Petrov, S. N.; Shchepkin, D. N.; Smirnov, K. S.; Tsyganenko, A. A. Effect of Resonance Dipole-Dipole Interaction on Spectra of Adsorbed SF6Molecules. *Spectrochim. Acta A Mol. Biomol. Spectrosc.* **2015**, *148*, 271−279.
(1287) Al-Abadleh, H. A.; Mifflin, A. L.; Bertin, P. A.; Nguyen, S. T.; Geiger, F. M. Control of Carboxylic Acid and Ester Groups on Chromium (VI) Binding to Functionalized Silica/Water Interfaces Studied by Second Harmonic Generation. *J. Phys. Chem. B* **2005**, *109* (19), 9691−9702.
(1288) Berland, K.; Cooper, V. R.; Lee, K.; Schröder, E.; Thonhauser, T.; Hyldgaard, P.; Lundqvist, B. I. Van der Waals Forces in Density Functional Theory: A Review of the vdW-DF Method. *Rep. Prog. Phys.* **2015**, *78* (6), 066501.
(1289) Klimeš, J.; Michaelides, A. Perspective: Advances and Challenges in Treating Van der Waals Dispersion Forces in Density Functional Theory. *J. Chem. Phys.* **2012**, *137* (12), 120901.
(1290) Priezjev, N. V.; Darhuber, A. A.; Troian, S. M. Slip Behavior in Liquid Films on Surfaces of Patterned Wettability: Comparison Between Continuum and Molecular Dynamics Simulations. *Phys. Rev. E* **2005**, *71* (4), 041608.
(1291) Ortiz-Young, D.; Chiu, H.-C.; Kim, S.; Voïtchovsky, K.; Riedo, E. The Interplay Between Apparent Viscosity and Wettability in Nanoconfined Water. *Nat. Commun.* **2013**, *4*, 2482.
(1292) Kendall, T. A.; Na, C.; Jun, Y. S.; Martin, S. T. Electrical Properties of Mineral Surfaces for Increasing Water Sorption. *Langmuir* **2008**, *24* (6), 2519−2524.
(1293) Byrd, T. L.; Walz, J. Y. Interaction Force Profiles between Cryptosporidium parvum Oocysts and Silica Surfaces. *Environ. Sci. Technol.* **2005**, *39* (24), 9574−9582.
(1294) Lee, W. J.; Kubicki, J. D. Molecular Dynamics Simulations of Periclase Crystallization. *Geophys. Res. Lett.* **1993**, *20* (19), 2103−2106.
(1295) Matsumoto, M.; Saito, S.; Ohmine, I. Molecular Dynamics Simulation of the Ice Nucleation and Growth Process Leading to Water Freezing. *Nature* **2002**, *416* (6879), 409−413.
(1296) Giberti, F.; Salvalaglio, M.; Parrinello, M. Metadynamics Studies of Crystal Nucleation. *IUCrJ.* **2015**, *2* (2), 256−266.
(1297) Réocreux, R.; Girel, E.; Clabaut, P.; Tuel, A.; Besson, M.; Chaumonnot, A.; Cabiac, A.; Sautet, P.; Michel, C. Reactivity of Shape-Controlled Crystals and Metadynamics Simulations Locate the Weak Spots of Alumina in Water. *Nat. Commun.* **2019**, *10*, 3139.
(1298) Piaggi, P. M.; Valsson, O.; Parrinello, M. Enhancing Entropy and Enthalpy Fluctuations to Drive Crystallization in Atomistic Simulations. *Phys. Rev. Lett.* **2017**, *119* (1), 015701.
(1299) Wang, L.; Ruiz-Agudo, E.; Putnis, C. V.; Menneken, M.; Putnis, A. Kinetics of Calcium Phosphate Nucleation and Growth on Calcite: Implications for Predicting the Fate of Dissolved Phosphate Species in Alkaline Soils. *Environ. Sci. Technol.* **2012**, *46* (2), 834−842.
(1300) Miller, Q. R.; Kaszuba, J. P.; Schaef, H. T.; Bowden, M. E.; McGrail, B. P.; Rosso, K. M. Anomalously Low Activation Energy of Nanoconfined Mgco 3 Precipitation. *Chem. Commun.* **2019**, *55* (48), 6835−6837.
(1301) Zhou, K.; Xu, Z. Renormalization of Ionic Solvation Shells in Nanochannels. *ACS Appl. Mater. Interfaces* **2018**, *10* (33), 27801−27809.
(1302) French, R. H.; Parsegian, V. A.; Podgornik, R.; Rajter, R. F.; Jagota, A.; Luo, J.; Asthagiri, D.; Chaudhury, M. K.; Chiang, Y. M.; Granick, S.; et al. Long Range Interactions in Nanoscale Science. *Rev. Mod. Phys.* **2010**, *82* (2), 1887−1944.
(1303) Wang, Y.; Bryan, C.; Xu, H.; Gao, H. Nanogeochemistry: Geochemical Reactions and Mass Transfers in Nanopores. *Geology* **2003**, *31* (5), 387−390.
(1304) Li, Q.; Steefel, C. I.; Jun, Y.-S. Incorporating Nanoscale Effects into a Continuum-Scale Reactive Transport Model for CO_2-Deteriorated Cement. *Environ. Sci. Technol.* **2017**, *51* (18), 10861−10871.
(1305) Dethlefsen, F.; Haase, C.; Ebert, M.; Dahmke, A. Uncertainties of Geochemical Modeling During CO_2 Sequestration Applying Batch Equilibrium Calculations. *Environ. Earth Sci.* **2012**, *65* (4), 1105−1117.
(1306) Haase, C.; Dahmke, A.; Ebert, M.; Schäfer, D.; Dethlefsen, F. Suitability of Existing Numerical Model Codes and Thermodynamic Databases for the Prognosis of Calcite Dissolution Processes in Near-Surface Sediments Due to a CO2 Leakage Investigated by Column Experiments. *Aquat. Geochem.* **2014**, *20* (6), 639−661.
(1307) Qin, F. Q.; Beckingham, L. E. The Impact of Mineral Reactive Surface Area Variation on Simulated Mineral Reactions and Reaction Rates. *Appl. Geochem.* **2021**, *124*, 104852.
(1308) Bourg, I. C.; Beckingham, L. E.; DePaolo, D. J. The Nanoscale Basis of CO2 Trapping for Geologic Storage. *Environ. Sci. Technol.* **2015**, *49* (17), 10265−10284.
(1309) Beckingham, L. E.; Winningham, L. Critical Knowledge Gaps for Understanding Water-Rock-Working Phase Interactions for Compressed Energy Storage in Porous Formations. *ACS Sustain. Chem. Eng.* **2020**, *8* (1), 2−11.
(1310) Bensinger, J.; Beckingham, L. E. CO2 Storage in the Paluxy Formation at the Kemper County CO2 Storage Complex: Pore Network Properties and Simulated Reactive Permeability Evolution. *Int. J. Greenhouse Gas Control* **2020**, *93*, 102887.
(1311) Pourret, O.; Bollinger, J.-C.; van Hullebusch, E. D. On the Difficulties of Being Rigorous in Environmental Geochemistry Studies: Some Recommendations for Designing an Impactful Paper. *Environ. Sci. Pollut. R.* **2020**, *27* (2), 1267−1275.
(1312) Greczynski, G.; Hultman, L. Reliable Determination of Chemical State in X-Ray Photoelectron Spectroscopy Based on Sample-Work-Function Referencing to Adventitious Carbon: Resolving the Myth of Apparent Constant Binding Energy of the C 1s Peak. *Applied Surf. Sci.* **2018**, *451*, 99−103.
(1313) Bandura, A. V.; Kubicki, J. D.; Sofo, J. O. Periodic Density Functional Theory Study of Water Adsorption on the α-Quartz (101) Surface. *J. Phys. Chem. C* **2011**, *115* (13), 5756−5766.
(1314) Eriksson, M.; Hansson, A.; Leemann, S.; Lindgren, L.-J.; Sjostrom, M.; Wallén, E.; Rivkin, L.; Streun, A. Using Multi-bend Achromats in Synchrotron Radiation Sources. In *EPAC 2008 - Contributions to the Proceedings*, Genoa, Italy, 2008; pp 2007−2009.

https://doi.org/10.1021/acs.chemrev.2c00130
Chem. Rev. 2023, 123, 6413−6544

(1315) Bostedt, C.; Boutet, S.; Fritz, D. M.; Huang, Z.; Lee, H. J.; Lemke, H. T.; Robert, A.; Schlotter, W. F.; Turner, J. J.; Williams, G. J. Linac Coherent Light Source: The First Five Years. *Rev. Mod. Phys.* **2016**, *88* (1), 015007.
(1316) Al Hassan, A.; Lähnemann, J.; Leake, S.; Küpers, H.; Niehle, M.; Bahrami, D.; Bertram, F.; Lewis, R.; Davtyan, A.; Schuelli, T. Spatially-Resolved Luminescence and Crystal Structure of Single Core-Shell Nanowires Measured in the As-Grown Geometry. *Nanotechnology* **2020**, *31*, 214002.
(1317) Nahalka, I.; Zwaschka, G.; Campen, R. K.; Marchioro, A.; Roke, S. Mapping Electrochemical Heterogeneity at Gold Surfaces: A Second Harmonic Imaging Study. *J. Phys. Chem. C* **2020**, *124* (37), 20021−20034.
(1318) Shah, S. A.; Baldelli, S. Chemical Imaging of Surfaces With Sum Frequency Generation Vibrational Spectroscopy. *Acc. Chem. Res.* **2020**, *53* (6), 1139−1150.
(1319) Yeh, C.-H.; Tan, C.-Z.; Cheng, C.-h. A.; Hung, J.-T.; Chen, S.-Y. Improving Resolution of Second Harmonic Generation Microscopy Via Scanning Structured Illumination. *Biomed. Opt. Express* **2018**, *9* (12), 6081−6081.
(1320) Jinschek, J. R. Advances in the Environmental Transmission Electron Microscope (ETEM) for Nanoscale In Situ Studies of Gas-Solid Interactions. *Chem. Commun.* **2014**, *50* (21), 2696−2706.
(1321) Wu, J.; Shan, H.; Chen, W.; Gu, X.; Tao, P.; Song, C.; Shang, W.; Deng, T. In Situ Environmental TEM in Imaging Gas and Liquid Phase Chemical Reactions for Materials Research. *Adv. Mater.* **2016**, *28* (44), 9686−9712.
(1322) Luo, L.; Su, M.; Yan, P.; Zou, L.; Schreiber, D. K.; Baer, D. R.; Zhu, Z.; Zhou, G.; Wang, Y.; Bruemmer, S. M.; et al. Atomic Origins of Water-Vapour-Promoted Alloy Oxidation. *Nat. Mater.* **2018**, *17* (6), 514−518.
(1323) Wise, M. E.; Biskos, G.; Martin, S. T.; Russell, L. M.; Buseck, P. R. Phase Transitions of Single Salt Particles Studied Using a Transmission Electron Microscope with an Environmental Cell. *Aerosol Sci. Technol.* **2005**, *39* (9), 849−856.
(1324) Wang, B. B.; Knopf, D. A.; China, S.; Arey, B. W.; Harder, T. H.; Gilles, M. K.; Laskin, A. Direct Observation of Ice Nucleation Events on Individual Atmospheric Particles. *Phys. Chem. Chem. Phys.* **2016**, *18* (43), 29721−29731.
(1325) de Jonge, N.; Ross, F. M. Electron Microscopy of Specimens in Liquid. *Nat. Nanotechnol.* **2011**, *6* (11), 695−704.
(1326) De Yoreo, J. J.; Sommerdijk, N. A. J. M. Investigating Materials Formation with Liquid-Phase and Cryogenic TEM. *Nat. Rev. Mater.* **2016**, *1*, 16035.
(1327) Ross, F. M. Opportunities and Challenges in Liquid Cell Electron Microscopy. *Science* **2015**, *350*, aaa9886.
(1328) Ross, F. M. *Liquid Cell Electron Microscopy*; Cambridge University Press: New York, 2017.
(1329) Klein, K. L.; Anderson, I. M.; De Jonge, N. Transmission Electron Microscopy with a Liquid Flow Cell. *J. Microsc.* **2011**, *242* (2), 117−123.
(1330) Nielsen, M. H.; De Yoreo, J. J. In *New Perspectives on Mineral Nucleation and Growth: From Solution Precursors to Solid Materials*; van Driessche, A. E. S., Kellermeier, M., Benning, L. G., Gebauer, D., Eds.; Springer, 2016.
(1331) Zhu, G.; Reiner, H.; Colfen, H.; De Yoreo, J. J. Addressing Some of the Technical Challenges Associated with Liquid Phase S/TEM Studies of Particle Nucleation, Growth and Assembly. *Micron* **2019**, *118*, 35−42.
(1332) Radisic, A.; Vereecken, P. M.; Hannon, J. B.; Searson, P. C.; Ross, F. M. Quantifying Electrochemical Nucleation and Growth of Nanoscale Clusters Using Real-Time Kinetic Data. *Nano Lett.* **2006**, *6* (2), 238−242.
(1333) Radisic, A.; Vereecken, P. M.; Searson, P. C.; Ross, F. M. The Morphology and Nucleation Kinetics of Copper Islands During Electrodeposition. *Surf. Sci.* **2006**, *600* (9), 1817−1826.
(1334) Wang, C. M.; Liao, H. G.; Ross, F. M. Observation of Materials Processes in Liquids by Electron Microscopy. *MRS Bull.* **2015**, *40* (1), 46−52.
(1335) Williamson, M. J.; Tromp, R. M.; Vereecken, P. M.; Hull, R.; Ross, F. M. Dynamic Microscopy of Nanoscale Cluster Growth at the Solid-Liquid Interface. *Nat. Mater.* **2003**, *2* (8), 532−536.
(1336) Beker, A. F.; Sun, H.; Lemang, M.; van Omme, J. T.; Spruit, R. G.; Bremmer, M.; Basak, S.; Perez Garza, H. H. In Situ Electrochemistry Inside a TEM with Controlled Mass Transport. *Nanoscale* **2020**, *12* (43), 22192−22201.
(1337) Huang, J. Y.; Zhong, L.; Wang, C. M.; Sullivan, J. P.; Xu, W.; Zhang, L. Q.; Mao, S. X.; Hudak, N. S.; Liu, X. H.; Subramanian, A.; et al. In Situ Observation of the Electrochemical Lithiation of a Single SnO_2 Nanowire Electrode. *Science* **2010**, *330* (6010), 1515−1520.
(1338) Kassal, I.; Whitfield, J. D.; Perdomo-Ortiz, A.; Yung, M. H.; Aspuru-Guzik, A. Simulating Chemistry Using Quantum Computers. *Annu. Rev. Phys. Chem.* **2011**, *62*, 185−207.
(1339) O'Malley, P. J. J.; Babbush, R.; Kivlichan, I. D.; Romero, J.; McClean, J. R.; Barends, R.; Kelly, J.; Roushan, P.; Tranter, A.; Ding, N.; et al. Scalable Quantum Simulation of Molecular Energies. *Phys. Rev. X* **2016**, *6*, 031007.
(1340) Kandala, A.; Mezzacapo, A.; Temme, K.; Takita, M.; Brink, M.; Chow, J. M.; Gambetta, J. M. Hardware-Efficient Variational Quantum Eigensolver for Small Molecules and Quantum Magnets. *Nature* **2017**, *549* (7671), 242−246.
(1341) Nam, Y.; Chen, J.-S.; Pisenti, N. C.; Wright, K.; Delaney, C.; Maslov, D.; Brown, K. R.; Allen, S.; Amini, J. M.; Apisdorf, J.; et al. Ground-State Energy Estimation of the Water Molecule on a Trapped-Ion Quantum Computer. *npj Quantum Inf.* **2020**, *6*, 33.
(1342) Villalonga, B.; Lyakh, D.; Boixo, S.; Neven, H.; Humble, T. S.; Biswas, R.; Rieffel, E. G.; Ho, A.; Mandra, S. Establishing the Quantum Supremacy Frontier with a 281 Pflop/S Simulation. *Quantum Sci. Technol.* **2020**, *5*, 034003.
(1343) Hammes-Schiffer, S.; Galli, G. Integration of Theory and Experiment in the Modelling of Heterogeneous Electrocatalysis. *Nat. Energy* **2021**, *6* (7), 700−705.
(1344) Schneider, P. E.; Tao, Z.; Pavosevic, F.; Epifanovsky, E.; Feng, X. T.; Hammes-Schiffer, S. Transition States, Reaction Paths, and Thermochemistry Using the Nuclear-Electronic Orbital Analytic Hessian. *J. Chem. Phys.* **2021**, *154*, 054108.
(1345) Pavošević, F.; Tao, Z.; Hammes-Schiffer, S. Multicomponent Coupled Cluster Singles and Doubles with Density Fitting: Protonated Water Tetramers with Quantized Protons. *J. Phys. Chem. Lett.* **2021**, *12* (6), 1631−1637.
(1346) Pavosevic, F.; Hammes-Schiffer, S. Multicomponent Unitary Coupled Cluster and Equation-of-Motion for Quantum Computation. *J. Chem. Theory Comput.* **2021**, *17* (6), 3252−3258.
(1347) Kühne, T. D.; Iannuzzi, M.; Del Ben, M.; Rybkin, V. V.; Seewald, P.; Stein, F.; Laino, T.; Khaliullin, R. Z.; Schütt, O.; Schiffmann, F.; et al. CP2K: An Electronic Structure and Molecular Dynamics Software Package-Quickstep: Efficient and Accurate Electronic Structure Calculations. *J. Chem. Phys.* **2020**, *152*, 194103.
(1348) Menzeleev, A. R.; Ananth, N.; Miller, T. F., III Direct Simulation of Electron Transfer Using Ring Polymer Molecular Dynamics: Comparison with Semiclassical Instanton Theory and Exact Quantum Methods. *J. Chem. Phys.* **2011**, *135* (7), 074106.
(1349) Menzeleev, A. R.; Bell, F.; Miller, T. F., III Kinetically Constrained Ring-Polymer Molecular Dynamics for Non-Adiabatic Chemical Reactions. *J. Chem. Phys.* **2014**, *140* (6), 064103.
(1350) Kenion, R. L.; Ananth, N. Direct Simulation of Electron Transfer in the Cobalt Hexammine (II/III) Self-Exchange Reaction. *Phys. Chem. Chem. Phys.* **2016**, *18* (37), 26117−26124.
(1351) Duke, J. R.; Ananth, N. Mean Field Ring Polymer Molecular Dynamics for Electronically Nonadiabatic Reaction Rates. *Faraday Discuss.* **2016**, *195*, 253−268.
(1352) Pfalzgraff, W. C.; Kelly, A.; Markland, T. E. Nonadiabatic Dynamics in Atomistic Environments: Harnessing Quantum-Classical Theory with Generalized Quantum Master Equations. *J. Phys. Chem. Lett.* **2015**, *6* (23), 4743−4748.
(1353) Kreysing, M.; Keil, L.; Lanzmich, S.; Braun, D. Heat Flux Across an Open Pore Enables the Continuous Replication and

https://doi.org/10.1021/acs.chemrev.2c00130
Chem. Rev. 2023, 123, 6413−6544

Selection of Oligonucleotides Towards Increasing Length. *Nat. Chem.* **2015**, *7* (3), 203−208.
(1354) Craven, G. T.; He, D.; Nitzan, A. Electron-Transfer-Induced Thermal and Thermoelectric Rectification. *Phys. Rev. Lett.* **2018**, *121* (24), 247704.
(1355) Craven, G. T.; Nitzan, A. Electron Transfer Across a Thermal Gradient. *Proc. Natl. Acad. Sci. U.S.A.* **2016**, *113* (34), 9421−9429.
(1356) Keith, J. A.; Vassilev-Galindo, V.; Cheng, B.; Chmiela, S.; Gastegger, M.; Müller, K.-R.; Tkatchenko, A. Combining Machine Learning and Computational Chemistry for Predictive Insights Into Chemical Systems. *Chem. Rev.* **2021**, *121* (16), 9816−9872.
(1357) Zhong, S.; Zhang, K.; Bagheri, M.; Burken, J. G.; Gu, A.; Li, B.; Ma, X.; Marrone, B. L.; Ren, Z. J.; Schrier, J.; et al. Machine Learning: New Ideas and Tools in Environmental Science and Engineering. *Environ. Sci. Technol.* **2021**, *55*, 12741−12754.
(1358) Mueller, T.; Hernandez, A.; Wang, C. H. Machine learning for Interatomic Potential Models. *J. Chem. Phys.* **2020**, *152*, 050902.
(1359) Cusentino, M. A.; Wood, M. A.; Thompson, A. P. Explicit Multielement Extension of the Spectral Neighbor Analysis Potential for Chemically Complex Systems. *J. Phys. Chem. A* **2020**, *124* (26), 5456−5464.
(1360) Thompson, A. P.; Swiler, L. P.; Trott, C. R.; Foiles, S. M.; Tucker, G. J. Spectral Neighbor Analysis Method for Automated Generation of Quantum-Accurate Interatomic Potentials. *J. Comput. Phys.* **2015**, *285*, 316−330.
(1361) Wood, M. A.; Thompson, A. P. Extending the Accuracy of the SNAP Interatomic Potential Form. *J. Chem. Phys.* **2018**, *148* (24), 241721.
(1362) Calegari Andrade, M. F.; Ko, H. Y.; Zhang, L. F.; Car, R.; Selloni, A. Free Energy of Proton Transfer at the Water-Tio2 Interface from Ab Initio Deep Potential Molecular Dynamics. *Chem. Sci.* **2020**, *11*, 2335−2341.
(1363) Alimohammadi, M.; Fichthorn, K. A. Molecular Dynamics Simulation of the Aggregation of Aqueous Tio2 Nanocrystals. *Geochim. Cosmochim. Acta* **2010**, *74* (12), A13−A13.
(1364) Yang, Y.; Chen, B.; Hower, J.; Schindler, M.; Winkler, C.; Brandt, J.; Di Giulio, R.; Ge, J. P.; Liu, M.; Fu, Y. H. Discovery and Ramifications of Incidental Magneli Phase Generation and Release from Industrial Coal-Burning. *Nat. Commun.* **2017**, *8*, 194.
(1365) Cheng, L. X.; Welborn, M.; Christensen, A. S.; Miller, T. F. A Universal Density Matrix Functional from Molecular Orbital-Based Machine Learning: Transferability Across Organic Molecules. *J. Chem. Phys.* **2019**, *150*, 131103.
(1366) Husch, T.; Sun, J. C.; Cheng, L. X.; Lee, S. J. R.; Miller, T. F. Improved Accuracy and Transferability of Molecular-Orbital-Based Machine Learning: Organics, Transition-Metal Complexes, Non-Covalent Interactions, and Transition States. *J. Chem. Phys.* **2021**, *154*, 064108.
(1367) Secor, M.; Soudackov, A. V.; Hammes-Schiffer, S. Artificial Neural Networks as Mappings between Proton Potentials, Wave Functions, Densities, and Energy Levels. *J. Phys. Chem. Lett.* **2021**, *12* (9), 2206−2212.
(1368) Magdau, I. B.; Miller, T. F. Machine Learning Solvation Environments in Conductive Polymers: Application to ProDOT-2Hex with Solvent Swelling. *Macromolecules* **2021**, *54* (7), 3377−3387.
(1369) Kubillus, M.; Kubař, T.; Gaus, M.; Řezáč, J.; Elstner, M. Parameterization of the DFTB3Method for Br, Ca, Cl, F, I, K, and Na in Organic and Biological Systems. *J. Chem. Theory Comput.* **2015**, *11* (1), 332−342.
(1370) Elstner, M.; Porezag, D.; Jungnickel, G.; Elsner, J.; Haugk, M.; Frauenheim, T.; Suhai, S.; Seifert, G. Self-Consistent-Charge Density-Functional Tight-Binding Method for Simulations of Complex Materials Properties. *Phys. Rev. B* **1998**, *58*, 7260−7268.
(1371) Cui, Q.; Elstner, M. Density Functional Tight Binding: Values of Semi-Empirical Methods in an Ab Initio Era. *Phys. Chem. Chem. Phys.* **2014**, *16* (28), 14368−14377.
(1372) Nishizawa, H.; Nishimura, Y.; Kobayashi, M.; Irle, S.; Nakai, H. Three Pillars for Achieving Quantum Mechanical Molecular Dynamics Simulations of Huge Systems: Divide-and-Conquer, Density-Functional Tight-Binding, and Massively Parallel Computation. *J. Comput. Chem.* **2016**, *37* (21), 1983−1992.
(1373) Nishimoto, Y.; Fedorov, D. G.; Irle, S. Density-Functional Tight-Binding Combined with the Fragment Molecular Orbital Method. *J. Chem. Theory Comput.* **2014**, *10* (11), 4801−4812.
(1374) Goyal, P.; Qian, H. J.; Irle, S.; Lu, X.; Roston, D.; Mori, T.; Elstner, M.; Cui, Q. Molecular Simulation of Water and Hydration Effects in Different Environments: Challenges and Developments for DFTB Based Models. *J. Phys. Chem. B* **2014**, *118* (38), 11007−11027.
(1375) Gruden, M.; Andjeklovic, L.; Jissy, A. K.; Stepanović, S.; Zlatar, M.; Cui, Q.; Elstner, M. Benchmarking Density Functional Tight Binding Models for Barrier Heights and Reaction Energetics of Organic Molecules. *J. Comput. Chem.* **2017**, *38* (25), 2171−2185.
(1376) Ito, S.; Fedorov, D. G.; Okamoto, Y.; Irle, S. Implementation of Replica-Exchange Umbrella Sampling in GAMESS. *Comput. Phys. Commun.* **2018**, *228*, 152−162.
(1377) Ito, S.; Irle, S.; Okamoto, Y. Implementation of Replica-Exchange Umbrella Sampling in the DFTB+ Semiempirical Quantum Chemistry Package. *Comput. Phys. Commun.* **2016**, *204*, 1−10.
(1378) Yuan, K.; Rampal, N.; Fenter, P.; Kubicki, J. D.; Stack, A. G.; Irle, S. Density Functional Tight-Binding Simulations Reveal the Presence of Surface Defects on the Quartz (101)-Water Interface. *J. Phys. Chem. C* **2021**, *125* (29), 16246−16255.
(1379) Machesky, M. L.; Predota, M.; Wesolowski, D. J.; Vlcek, L.; Cummings, P. T.; Rosenqvist, J. R.; Ridley, M. K.; Kubicki, J. D.; Bandura, A. V.; Kumar, N.; Solo, J. O. Surface Protonation at the Rutile (110) Interface: Explicit Incorporation of Solvation Structure Within the Refined MUSIC Model Framework. *Langmuir* **2008**, *24*, 12331−12339.
(1380) Dentz, M.; Le Borgne, T.; Englert, A.; Bijeljic, B. Mixing, Spreading And Reaction in Heterogeneous Media: A Brief Review. *J. Contam. Hydrol.* **2011**, *120-121*, 1−17.
(1381) Steefel, C. I.; Appelo, C. A. J.; Arora, B.; Jacques, D.; Kalbacher, T.; Kolditz, O.; Lagneau, V.; Lichtner, P. C.; Mayer, K. U.; Meeussen, J. C. L.; et al. Reactive Transport Codes for Subsurface Environmental Simulation. *Comput. Geosci.* **2015**, *19* (3), 445−478.
(1382) Gasperino, D.; Yeckel, A.; Olmsted, B. K.; Ward, M. D.; Derby, J. J. Mass Transfer Limitations at Crystallizing Interfaces in an Atomic Force Microscopy Fluid Cell: A Finite Element Analysis. *Langmuir* **2006**, *22* (15), 6578−6586.
(1383) Georget, F.; Prevost, J. H.; Huet, B. Reactive Transport Modelling of Cement Paste Leaching in Brines. *Cem. Concr. Res.* **2018**, *111*, 183−196.
(1384) Surasani, V. K.; Li, L.; Ajo-Franklin, J. B.; Hubbard, C.; Hubbard, S. S.; Wu, Y. Bioclogging and Permeability Alteration by L-mesenteroides in a Sandstone Reservoir: A Reactive Transport Modeling Study. *Energy Fuels* **2013**, *27* (11), 6538−6551.
(1385) Kolditz, O.; Bauer, S.; Bilke, L.; Böttcher, N.; Delfs, J. O.; Fischer, T.; Görke, U. J.; Kalbacher, T.; Kosakowski, G.; McDermott, C. I.; et al. OpenGeoSys: An Open-Source Initiative for Numerical Simulation of Thermo-Hydro-Mechanical/Chemical (THM/C) Processes in Porous Media. *Environ. Earth Sci.* **2012**, *67* (2), 589−599.
(1386) *Pore Scale Geochemical Processes*; Steefel, C. I., Emmanuel, S., Anovitz, L., Eds.; De Gruyter, 2015; Vol. *80*.
(1387) *Reactive Transport in Natural and Engineered Systems*; Druhan, J., Tournassat, C., Eds.; De Gruyter: Berlin, 2020; Vol. *85*.
(1388) Steefel, C. I. 1. Reactive Transport at the Crossroads. In *Reactive Transport in Natural and Engineered Systems*; Reviews in Mineralogy & Geochemistry; Druhan, J., Tournassat, C., Eds.; De Gruyter, 2019; Vol. *85*; pp 1−26.
(1389) Franz, C.; Saubert, S.; Wendl, A.; Haslbeck, F. X.; Soltwedel, O.; Jochum, J. K.; Spitz, L.; Kindervater, J.; Bauer, A.; Boni, P.; Pfleiderer, C. MIEZE Neutron Spin-Echo Spectroscopy of Strongly Correlated Electron Systems. *J. Phys. Soc. Jpn.* **2019**, *88* (8), 081002.

https://doi.org/10.1021/acs.chemrev.2c00130
Chem. Rev. 2023, 123, 6413−6544

Supplemental Information

Oxide- and Silicate-Water Interfaces and Their Roles in Technology and the Environment

José Leobardo Bañuelos,[1] Eric Borguet,[*2] Gordon E. Brown, Jr.,[3] Randall T. Cygan,[4] James J. DeYoreo,[5] Patricia M. Dove,[6] Marie-Pierre Gaigeot,[7] Franz M. Geiger,[8] Julianne M. Gibbs,[*9] Vicki H. Grassian,[10] Anastasia G. Ilgen,[*11] Young-Shin Jun,[*12] Nadine Kabengi,[*13] Lynn Katz,[14] James D. Kubicki,[*15] Johannes Lützenkirchen,[16] Christine V. Putnis,[17] Richard C. Remsing,[18] Kevin M. Rosso,[19] Gernot Rother,[20] Marialore Sulpizi,[21] Mario Villalobos,[22] Huichun Zhang[23]

TABLE OF CONTENTS

1. Overview of Techniques for Probing Oxide- and Silicate-Water Interfaces

Since Brown et al.,[1] advances in oxide-water interface chemistry have benefited from developments in advanced instrumentation and computational chemistry. Surface and interfacial imaging and spectroscopy of oxide-water systems have become available. Especially significant are the advances in X-ray and neutron sources [2-4] and the development of multiple synchrotron facilities for diffraction, reflectivity, absorption, scattering, and related spectroscopies.[5-9] Brighter X-ray sources and improved particle accelerators have provided improved energies, coherence, and resolutions for diffraction, scattering, imaging, tomographic, spectroscopies, and other techniques. Upgrades and projects for major international accelerator facilities that are upcoming were compiled in a recent report sponsored by the European Physical Society Accelerator Group.[10] The techniques that enabled discoveries reported in our review are summarized in **Table S1.**

Surface-specific analytical spectroscopies such as sum-frequency generation, SFG, [11-13] and second harmonic generation, SHG,[14-16] atomic force and interfacial force microscopies,[1,17-19] and high-resolution reflectivity,[8] crystal truncation rod (CTR) methods,[6,7] and other advanced X-ray techniques [20] have played a leading role in moving our understanding forward. Current advancements allow for smaller samples for difficult to synthesize nanoparticles as well as the ability to study different adsorbates.

Software based on molecular orbital (MO) and density functional theories (DFT) have leapt forward. The latest codes utilize on convenient graphical interfaces (GUIs) for submitting computational jobs and post-processing analysis. Quantum mechanics codes based on DFT allow simulation of chemical systems of 1000s of atoms, typically employing periodic boundaries for simulating crystalline materials, surfaces and interfacial systems. Molecular simulations using classical-based energy force fields (or interatomic potentials – IAPs) that are typically parametrized from experimental data and quantum calculations, allow modelling millions of

atoms.[21] Use of both deterministic (e.g., molecular dynamics - MD) and stochastic (e.g., Monte Carlo - MC) approaches allow quantum and classical computing methods to supplement the experimental and spectroscopic work on the oxide-water systems. [22-24]

In parallel with the experimental innovations, there have been significant developments in computational platforms and user-friendly software. Micro-processing power and computer hardware have advanced to provide users with outstanding computational power to address aspects of oxide-water chemistry. High-performance computing (HPC) methods using massively-parallel supercomputers have evolved to allow advance quantum-based approaches to become accessible to many researchers.[25] Exascale (10^{18} floating point operations per second – FLOPS) computing is expected soon for distributed and massively parallel supercomputers.[26] However, integrating simulation with experiment is essential for studying metal oxide-water interfaces.[27]

To further introduce recent advanced experimental analytical techniques, the following section will provide summaries of recent advances most relevant to the main manuscript content. However, it is not intended to encompass all advanced analytical techniques.

2. Experimental Analytical Techniques

2.1 Synchrotron-based techniques

The development of synchrotron radiation (SR) sources in the early 1970's and more recently has revolutionized the way X-ray science is done in many disciplines, including interfacial chemistry, environmental chemistry/geochemistry, materials science, and protein crystallography, all of which require atomic-level characterization studies. The key reason is that SR provides continuum vacuum ultraviolet (VUV) and X-ray radiation with about 13 orders of magnitude greater average brightness from 3rd generation sources than from standard sealed or rotating anode X-ray tubes (**Figure S1**). Fourth generation SR sources, such as the Linac Coherent Light Source

(LCLS) at SLAC National Accelerator Laboratory (Stanford University), provide about 30 orders of magnitude greater peak brightness than sealed X-ray tubes. These enormous increases in X-ray brightness have led to the development of many new atomic-level characterization methods and new discoveries about chemical processes in many fields of science, particularly those involving interfacial chemistry.

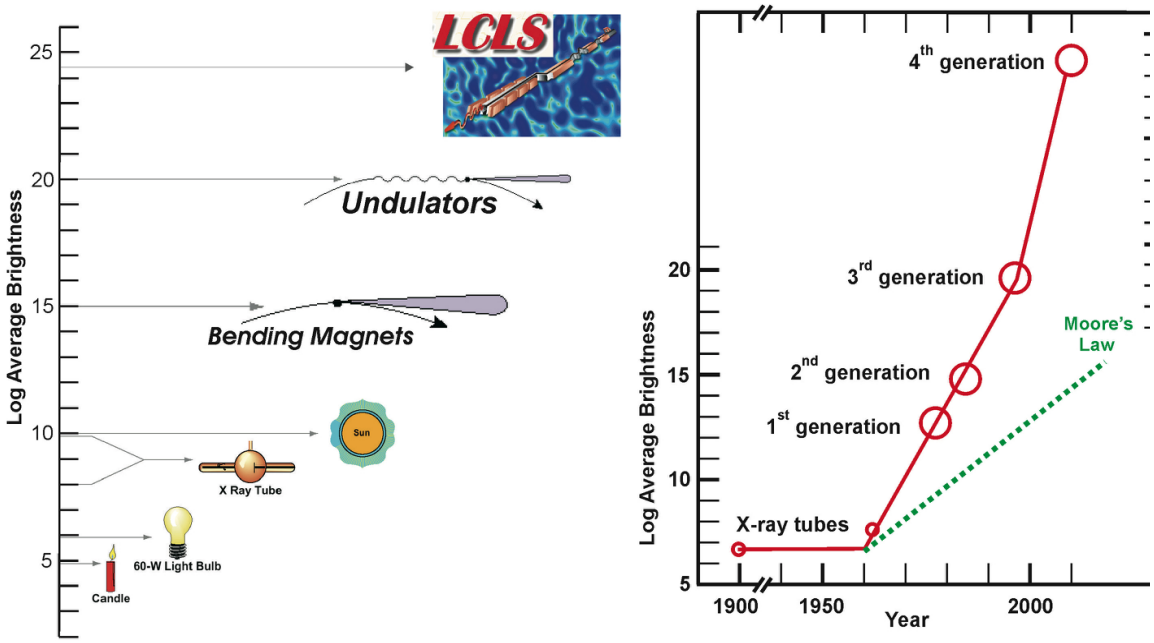

Figure S1. Comparison of average and peak brightness of synchrotron radiation sources and laboratory X-ray sources. The rate of increase of the number of transistors on a microchip doubling every two years (Moore's Law – green dashed line) is less than the rate of increase of the average brightness of synchrotron radiation sources (red solid line) (after J. Stohr, Stanford Synchrotron Radiation Lightsource (SSRL), personal comm.).

X-ray scattering offers benefits for exploring structural, dynamical and energetic properties of nanoscale mineral-water interface interactions. X-ray fluorescence, diffraction, absorption, microtomography, standing wave, emission, and reflectivity have been reviewed,[20] with a presentation of seminal works applying these experimental approaches to geochemistry and environmental science problems. The high intensity of synchrotron sources now allows unprecedented high spatial and time resolution measurements of evolving nanostructures both *in*

situ and over a wide range of conditions. Elastic scattering techniques including X-ray reflectivity (XRR), small-angle X-ray scattering, and X-ray micro-computed tomography (X-ray μCT) represent an important subset of methods of value to the study of oxide- and silicate-water interfaces.

2.1.1. Extended X-ray Absorption Fine Structure (EXAFS) Spectroscopy

The first SR experiments relevant to interfacial chemistry/geochemistry and environmental science, although not performed on Earth or environmental materials, were extended X-ray absorption fine structure (EXAFS) spectroscopy measurements on amorphous and crystalline germanium oxide conducted on the SPEAR storage ring at the Stanford Synchrotron Radiation Project in 1971 by Dale Sayers, Farrel Lytle, and Edward Stern.[28,29] Prior to the availability of SR in the hard X-ray energy range (> 5 keV), EXAFS spectroscopy measurements were impractical because of the high X-ray flux required and the need for a continuously tunable range of X-ray energies extending up to 1000 eV above the absorption threshold of the element of interest. In the 50 years since these synchrotron-based EXAFS measurements, this method has been applied to materials ranging from metalloproteins and catalysts to silicate liquids at high temperatures, cation complexes in aqueous and hydrothermal solutions, and complex environmental samples containing heavy metal and metalloid contaminants and pollutants, just to name a few.

The most widely used synchrotron-based analytical methods characterized samples of importance in low temperature geochemistry and environmental science is EXAFS spectroscopy. Early applications of EXAFS spectroscopy to these fields as well as to mineralogy are reviewed by Brown et al.[30] XAFS spectroscopy measures the absorption of X-rays by a selected element in a sample at and above that element's characteristic absorption edge energy. Such measurements are typically feasible only with X-rays from a synchrotron radiation source, particularly if the

element of interest is at low concentration (< 1 wt.%). Absorption edges correspond to excitation of deep core electrons to valence or continuum levels of an atom and occur at unique energies for each element. The X-ray absorption near edge structure (XANES) spectrum is sensitive to the valence state of the atom and the geometry and types of surrounding atoms, whereas the extended X-ray absorption fine structure (EXAFS) spectrum provides quantitative information on the distances between absorbing atoms and surrounding atoms (out to a radial distance of about 5 Å), the atomic number of surrounding atoms, and their relative disorder (both positional and thermal). Because EXAFS spectroscopy is a local probe, it does not require the long-range order of a crystalline sample and is one of the few methods that can provide quantitative structural information about the local environments around cations and anions in amorphous materials, such as silicate glasses and silicate melts, or in aqueous solutions, hydrothermal/supercritical fluids, or complex environmental samples. X-ray or neutron scattering can provide this information in cases where the pair correlations of interest are separable from all other pair correlations contributing to a radial distribution function. Synchrotron-based differential anomalous scattering can probe the medium-range structure around selected elements in amorphous and poorly crystalline materials by combining the element selectivity of EXAFS spectroscopy with the high *k*-range of X-ray scattering. Also, because EXAFS spectroscopy is element specific, it can be quite sensitive to the surface of a sample in which the element of interest occurs only at or near the surface. This feature allows one to determine the geometry, composition, and mode of attachment of a range of adsorbate ions at mineral/water interfaces.[31]

Examples of the application of EXAFS spectroscopy for determining the surface complexation geometries of heavy metals and actinides at ferric hydroxide (FeOX)/aqueous solution interfaces are shown in **Table 1** from Waychunas et al.[32] In addition to EXAFS

spectroscopy methods, synchrotron-based micro-X-ray fluorescence spectroscopy and synchrotron X-ray diffraction methods are now commonly used in studies of Earth materials, environmental materials, and technological materials. Other synchrotron-based analytical methods include VUV and soft X-ray photoemission spectroscopy, X-ray standing waves, X-ray reflectivity measurements, small angle X-ray scattering, X-ray microtomography, X-ray microscopy measurements, photoelectron diffraction, and synchrotron infrared spectroscopy. Each of these methods is beginning to provide useful, and in many cases, unique information about Earth and environmental materials and their interactions with aqueous fluids, atmospheric gases, organic matter, microbial organisms, plant roots, and environmental contaminants. The potential of many of these methods, particularly those that require high brightness (μEXAFS, μXRD, X-ray reflectivity, X-ray standing waves, X-ray microtomography, and X-ray microscopy), could not be fully realized prior to the availability of third-generation synchrotron radiation sources in the mid-1990's. The review by Brown and Sturchio [5], although a bit dated, discusses these and other synchrotron-based analytical methods that are routinely used to characterize sorption complexes of metals at metal oxide- and silicate-aqueous solution interfaces. A more up-to-date summary of the applications of synchrotron-based analytical methods to environmental science is given by Brown and Calas.[33]

2.1.2. X-ray reflectivity (XRR)

The theoretical foundations, experimental considerations, and progress on using fluid XRR in mineral interface research has been highlighted in a comprehensive review.[20] Thin film and transmission sample cell geometries for "environmental" setups are described, along with the necessary experimental corrections that must be considered in order to extract quantitative molecular and nanoscale information for comparison with simulation. Special attention is given to

the importance of model calculations of the mineral surface termination and the formalism is extended to a large molecule adsorption example of a stearate monolayer on calcite. XRR is able to distinguish between adsorbed water on a mineral surface and full hydration water environment normal to a flat mineral surface. Mineral defect structures and dissolution reactions may be followed in real-time using XRR. Elemental sensitivity may be obtained by choosing probe energies near an element's X-ray absorption edge. The increased brilliance of synchrotron sources also offers new opportunities to use microbeams to study small crystals, or adsorption/desorption, complex formation kinetics on millisecond time scales or less. A recent example can be found in Lee et al. [34] who combined resonant anomalous X-ray reflectivity (RAXR) with classical MD simulations to study high salt (RbCl) concentrations at the (001) muscovite mica surface. These authors observed charge overscreening and heterogeneous nucleation to address non-classical EDL behavior. They conclude

"*The observed transition from classical Langmuir-type full charge compensation by adsorbed ions to non-classical charge overscreening is controlled by positional correlations between adsorbed ions rather than chemical complexations (e.g., ion pair formation) that are generally assumed in current physicochemical theories*."

Studies such as this could be extended to other minerals and salt compositions [35] at higher T and P to obtain data more directly applicable to environmental conditions.

2.1.3. Small-Angle X-ray Scattering (SAXS)

Transmission and grazing incidence small angle X-ray scattering (SAXS & GISAXS) for the study of nanomaterials and nanoscale interfaces have been recently reviewed.[36] The development of *in situ* sample environments allows application of fluid flow, controlled humidity, electrochemical studies, and other natural and engineered interface environments. Using an

environmental setup to utilize synchrotron-based SAXS/GISAXS, Jun et al. obtained initial stage nucleation rates and critical nucleus sizes for both homogeneous and heterogeneous nucleation, changes in mineral surface area, interfacial energies, and activation energies in aqueous systems. [37-42] Mineral phases were also identified by transmission and grazing incidence mode wide angle X-ray scattering (WAXS/GIWAXS). Using these capabilities, nucleation mechanisms and kinetics of environmentally important nanoporous systems and nanoparticles have been studied.

The critical nucleus size was also determined for highly amorphous Fe(hydr)oxide. This *in situ* approach also provided size, volume, surface area and particle distributions of evolving Fe-(hydr)oxide nanoparticles in the presence of ubiquitous cations such as Al^{3+} [43] and anions (NO_3^-, Cl^-, SO_4^{2-}, PO_4^{3-}, and AsO_4^{3-}[38,44] and natural organic matter. [45] Notably, in the presence of Cl^-, the Fe-oxy(hydr)oxides undergo faster Ostwald ripening than those for other anions. [38] This approach also elucidates how mineral substrates significantly affect the heterogeneous Fe-oxy(hydr)oxide nucleation and growth.[46]

Other applications include understanding nucleation and growth rates of $CaCO_3$, [39-41,47,48] Ca-phosphates, [49-52] and Mn-oxy(hydr)oxide, [53,54] which enable the quantification of interfacial free energies of these systems. In $CaCO_3$ nucleation systems, an intriguing finding is that salinity can affect the heterogeneous nucleation of $CaCO_3$ on quartz and the interfacial energies significantly.[41] High salinity lowers the interfacial energy of the system and facilitates $CaCO_3$ nucleation on quartz.

2.1.4. Neutron Diffraction/X-Ray Diffraction/Pair Distribution Function Analysis

The combined use of X-ray and neutron diffraction is a recognized approach to obtaining structural information at the scale of nearest atomic neighbors, including ion solvation shell

composition and coordination numbers and nanoparticle/nanoporous material surface/defect structure. However, the decreased size of a nanoparticle makes phase identification problematic due to diminishing long-range periodicity and consequent broadening of diffraction peaks. In such situations, standard crystal refinement tools fail and instead the measurement of diffraction data over a wide range of momentum is necessary for the application of pair distribution function (PDF) analysis. In this method, the full diffraction pattern is Fourier transformed to obtain the real-space correlation function of the system.[55] Open source structure refinement programs allow an experimenter, most often through a reverse Monte Carlo approach,[56] to obtain a structural model that is consistent with the data. With the aid of chemically realistic computational models, another option is to compare directly the experimentally obtain *G(r)* functions corresponding correlation functions obtain via theory and simulation.

Atom-atom correlations may modulate in some cases by employing neutron diffraction with isotopic substitution (NDIS) in combination with X-ray PDF (e.g., arsenic in gypsum and calcite). Extreme environments are also accessible due to the penetrating power of neutrons that allow robust sample containers. Examples of studies include ion-water coordination near an ion, solvation of simple organic molecules and NDIS to obtain solute-solvent and solute-solute structure (e.g., clay-phenol-water structural data, structure of water in clays (with implications to mechanical and chemical strength, and cation exchange dynamics). High T and P experiments revealed the structural changes giving rise to reversible hydration/dehydration reactions under geological conditions.

Hoeher et al. (2019) utilized mixed-flow reactors (MFRs) and X-ray scattering to obtain pair distribution functions (PDFs) *in situ* structures of Ca-phosphate and Ca-carbonate amorphous nanoparticles in solution.[57] Because the Ostwald Step Rule often leads to the formation of poorly

crystalline metastable phases before the more crystalline and stable phase grows, observing the initial nanoparticle formation process is a key to developing predictive kinetic models of natural aqueous systems (e.g., ferrihydrite formation before goethite or hematite growth).[58] Extension of this technique to study metal oxide and silicate precipitation would shed light on this grey area in our knowledge where small particle size and high disorder lead to poor X-ray diffraction results. When complemented by molecular simulations of the nucleation process, unseen details of the nucleation can be obtained that will allow for better control of solid-phase formation from aqueous solutions.

2.1.5 Ambient Pressure X-ray Photoelectron Spectroscopy (APXPS)

Distinguishing signals from the interfacial region from the bulk solid and solution can be problematic. Qian et al. (2020) addressed this using APXPS for a well-defined system of KBr in aqueous solution in contact with gold. Their approach included prediction of the spectra via *ab initio* MD and DFT calculations to create an analytical model and an *ab initio* constructed spectrum.[59] These authors constrained conditions under which surface and solution Br^- could be detected. A similar approach on other substrates and solutions is worth investigating to determine when it will be possible to gain insights into interfacial chemistry with APXPS.

2.1.6. μ-XRF and μ-XANES

Phosphorous behavior in soils is important (**Section 4.2.3**) because it is a key nutrient for plants but can lead to the water pollution problem known as 'eutrophication'. Soil scientists have long relied upon sequential extraction techniques to identify various types of P, but the information gained may not be quantitative depending upon extraction efficiency, and it does not supply spatial information on the location of the P within the soil texture. Gamble et al. (2020) applied μ-XRF and μ -XANES to obtain details on the types and distribution of P in soils. P soil biogeochemistry

is complex because P can be in biological compounds, adsorbed to minerals and form its own phases. Gamble et al. found that

"*Combined* μ*-XRF and* μ*-XANES analysis was useful for identifying Ca phosphate, Fe phosphate, Al-sorbed P, and Fe-sorbed P species in heterogeneous soil samples. X-ray fluorescence maps were valuable to distinguish Al-oxide sorbed P from Fe-oxide sorbed P species*." [60]

Microscopic maps of P distributions and mineral associations can be used to connect analyses of single-mineral studies to the more complex soil system. Similar methods can be used to study cement reactions that are crucial in applications such as the growing geothermal energy industry.[61]

2.1.7 Nano-XRF

One consequence of mineral growth from natural solutions is compositional zoning as solution composition changes with time. Analysis of this zonation can provide information on the conditions under which a crystal formed and have implications for how the crystal will dissolve with time. An excellent example of the use of nano-XRF to study mineral zonation is found in Ling et al. (2018).[62] These authors utilized the Hard X-ray Nanoprobe (HXN) beamline at the National Synchrotron Light Source II (NSLS-II) to map out Sr and As in barite ($BaSO_4$). The Multilayer Laue Lenses (MLL) provide the specificity, resolution, and sensitivity to map trace element concentrations at 15 nm pixel sizes. Changes in growth can be discerned and the effect of crystal surface on the incorporation of trace elements. Since the types of surfaces present can also influence isotope incorporation,[63] the ability to interpret isotopic signatures of minerals also requires reconstructing crystallization histories. As with other recent advancements, performing experiments on well-controlled and characterized samples in combination with analyses of real-

world samples will better allow the deconstructionist approach to provide information that can be scaled to more complex systems.

2.1.8. Radiography and Computed Tomography

X-ray computed tomography allows the visualization of precipitation/dissolution phenomena with resolution ranging from microns (μ-CT) down to 10's of nm (nano-CT; [64]). The two modes typically implemented are absorption and phase contrast modes. High speed X-ray radiographic imaging captures processes with μs-scale time resolution.[65] Three-dimensional reconstructions require the collection multiple radiographs as a function of sample rotation about a precisely defined axis and thus decrease the achievable frame rates compared to radiography. Recent developments in transmission X-ray microscopes (TXM) now allow fast (85 min) sub-10 nm spatial resolution 3D nano-computed-tomography.[64] As this full-field, high-resolution technique pushes the limits of resolution towards the domain of electron-based imaging methods, the merging, segmentation, and processing of vast datasets also requires advancements in machine learning-based algorithms to reduce processing bottlenecks.[66] Neutron imaging is ideal for dynamic imaging of the transport of H-rich fluids through geologic media due to the penetrating power of neutrons deep into geological materials combined with the large neutron cross-section of H (which attenuates the beam), thus providing bulk information with 50-100 μm scale resolution of samples with cm-scale dimensions.[67,68]

TXM experiments have shown that the presence of Pb^{2+} ions in static acidic solutions decreases the overall dissolution rates of calcite by half compared to Pb-free solutions, and resolved the accompanying increase in surface roughness and micropyramid formation primarily near acute edges of calcite crystals.[69] Variations in micropyramid morphology and spatially-resolved dissolution rates were also observed over time. In another example, fracturing of olivine

upon carbonation at 13 MPa and 200 °C has been observed using *in situ* time-resolved X-ray microtomography.[70]

Water transport through bentonite engineered barriers for radioactive waste disposal has been studied using neutron radiography.[67] Neutron tomography with a 42 μm voxel size has been used to study water dynamics during curing of cements containing superabsorbent polymers.[71] The construction of new neutron imaging facilities are expected to achieve resolutions < 15 μm with a field of view up to 20 x 20 cm^2 [72]. Advances in detector technologies are enabling energy-resolved neutron imaging [73] to allow spatially-resolved elemental composition for some elements; this concept has been demonstrated in real time crystal growth studies [74] and microstructure studies of crystalline materials. [75] One example highlighting the elemental sensitivity and non-destructive nature of neutron imaging is a recent study that tracked in real time the transport of water, iodine and uranium through concrete.[76] These advances now make it possible to carry out 4-D (3D+spectral) neutron tomography.[77]

2.2. Neutron Scattering

As a probe that interacts primarily with atomic nuclei, neutrons have high sample penetration power, sensitivity to light elements such as H, isotope sensitivity, and have no selection rules in comparison to photon-based spectroscopies. Neutron techniques for mineral-water interfaces have been reviewed in Rinaldi, 2009 and references therein.[78] The principles and use of deep inelastic scattering (INS), quasi-elastic neutron scattering (QENS), combined with DFT and MD simulations to study water on metal oxide nanoparticle surfaces are discussed.

2.2.1. Inelastic Scattering (INS)

INS is not restricted by selection rules or hampered by optical opacity and sample absorption as with Raman and IR spectroscopies. INS is useful for studying the speed-up and slow-

down of dynamics, shifts in glass transition and crystallization temperature induced by confinement.[79] For example, vibrational spectroscopy of water on nano-forsterite with the (010) face dominant with 0.5, 1, and 2 monolayers of water demonstrates the distinct dynamics and thermodynamics between the first layer of adsorbed water and water located farther from the surface.

2.2.2. Quasi-Elastic Neutron Scattering (QENS)

Diffusional and rotational molecular motions with energy transfers of μV to mV and timescales nanoseconds to picoseconds are observed with QENS. QENS and MD are linked by the intermediate scattering function resulting from the incoherent scattering of H nuclei. The ISF is obtained from the time-space trajectories of MD simulations, making the two approaches complementary. Combined INS and QENS to study the dynamics of water on mineral oxide nanoparticle surfaces, is demonstrated in a series of studies.[80] Using QENS and classical MD, precise water exchange rates at a mineral surface have been obtained. Measurements of the impact on water dynamics due to ion type and electrolyte concentration in a pore-confined system affect can provide information on pore confined dissolution and precipitation reaction rates.[81] Studies of SnO_2 destabilization upon thermal removal of inner layer adsorbed water demonstrate how the first few hydration layers are important to a nanoparticle (NP) and should be considered an intrinsic part of the NP itself.

2.3. Neutron Spin Echo (NSE)

The Neutron Spin Echo (NSE) technique may enable slow diffusion dynamics (characteristic of the innermost hydration layer) to time scales of 1 to 100s of nanoseconds. Because it may achieve longer relaxation times in comparison to QENS, NSE has been employed to study the dynamics of water confined in natural and synthetic clays.[82-85]

2.3. Vibrational Spectroscopic Methods

2.3.1. Attenuated Total-Reflectance Fourier-Transform Infrared (ATR FTIR) and Synchrotron IR

Hao et al. examined organic-mineral interactions over scales of nanometers to 100's of microns using a combination of ATR FTIR spectroscopy and synchrotron-based IR nano-spectroscopy.[86] The combination allows for mapping organic-mineral distributions over relevant length scales for applications such as hydraulic fracturing and CO_2 sequestration while collecting compositional information at the nano-scale. A large radius Ge hemi-spherical crystal as the internally reflective element in the ATR FTIR instrument significantly improved the spatial resolution. Hao et al. identified selective mineral-organic associations and gas-phase absorbents. Coordination of simpler, laboratory studies with analyses of real rocks and sediments will go a long way towards addressing problems of scaling, complexity and heterogeneity. Such information will be invaluable in connecting molecular data and simulation results with reactive transport models.[87]

2.3.2 Sum Frequency Generation (SFG)

Sum Frequency Generation (SFG), is a surface-specific vibrational probe that is well-suited to studying buried interfaces and was used to study the Al_2O_3(0001)-H_2O interface.[88] By incorporating a flexible polarizability model which accounted for local dipole interactions within both the surface and solvent molecules, this study identified that two distinct H stretching peaks were due to independent solvent and surface modes, instead of from H_2O modes as was previously believed. Recently, Kroutil et al. showed that SFG spectra may be calculated at low computational cost by using classical molecular dynamics (CMD) simulations in combination with simple non-polarizable force fields (FFs).[89] The computation of the SFG spectra is achieved by using velocity−velocity autocorrelation functions that are weighted by parameterized Raman and atomic

polar tensors. This methodology yields good qualitative agreement with experiment and avoids the use of costly *ab initio* molecular dynamics (AIMD) simulations or CMD simulations with computationally demanding FFs and opens the possibility to study larger systems for long time periods. Environmentally relevant processes, such as electric double-layer formation at interfaces with mM ionic concentrations, can be characterized by combined theoretical CMD and SFG spectroscopy. SFG studies benefit from interpretation with DFT-MD simulations.[89-93]

2.3.3. Raman Spectroscopy

In situ, fluid-cell Raman spectroscopy has been used to obtain real-time information of reaction and transport processes in a borosilicate glass undergoing aqueous corrosion.[94] In this study, which supports an interface-coupled dissolution–reprecipitation process for surface alteration layer (SAL) formation, a micrometer-scale water-rich zone between SALs and the glass, interpreted as an interface solution, was detected. Gradients in pH at the glass surface and within the SAL were also identified. This experimental tool opens the possibility of *in situ*, real-time studies of processes in solid–water reactions by using stable isotopes.[94] The use of Raman spectroscopy for mineral phase identification and chemistry, including describing crystallinity and crystallographic orientation has been recently reviewed.[95] The incorporation of isotopic tracers to provide kinetic information on isotope substitution and the potential to gain insights on mineral replacement processes using Raman spectroscopy is described therein. Furthermore, the Raman scattering intensity of molecules adsorbed on a metal surface, such as gold or silver nanostructures, is greatly enhanced, a phenomenon called surface-enhanced Raman scattering (SERS).[96,97] By utilizing SERS with plasmonic gold nanorods, Zhu et al. detected the pH and ion concentrations in nanopores *in situ* and with high resolution.[98]

2.4. Nuclear Magnetic Resonance-Based Techniques (NMR)

Pulsed-field gradient nuclear magnetic resonance (PFG NMR) techniques collect spectrally-resolved diffusion data of adsorbed complex molecules. In diffusion-ordered spectroscopy (DOSY) NMR, a two-dimensional map of chemical shift information and diffusion coefficient is obtained.[99] The observed translational diffusion coefficients of molecular species give information of effective sizes and shapes of molecular species. NMR relaxometry[100] can also be used to obtain molecular translational diffusion coefficients and is effective in obtaining desorption activation energies (ΔE_{desorb}) of molecular species in porous materials.[101]

Quantitative continuous wave Overhauser effect dynamic nuclear polarization (cw ODNP) NMR technique measures dipolar cross-relaxation between the electron spins and the ^{1}H nuclear spins at X-band frequencies.[102] To realize this technique, an NMR probe head must be inserted into a continuous wave ESR instrument. This technique selectively measures the translational mobility of water within a volume extending 0.5-1.5 nm outward from a nitroxide radical spin probe that is attached to a targeted site of a macromolecule. This mode allows the study of dynamics of water that hydrates or permeates the surface or interior of proteins, lipid membrane vesicles, and other interfaces. Because ODNP measures the coupling factor, it exhibits a better selectivity for high-frequency (typically translational) motions of the solvent than an NMR relaxometry measurement that measures the self-relaxivity of the water in the presence of the spin probe. The cw ODNP method allows studying water dynamics within the first 0.5 to 1.5 nm of an interface and time scales of 10 ps to 1 ns. It can distinguish between bulk translational diffusion of water and first-layer surface-bound water.[102] Single-sided NMR can provide concentration gradient depth profiles of NMR active solvents on surfaces[103] and mobile version of this technique has been developed.[104] Many of the aforementioned NMR techniques focus on understanding

water dynamics at interfaces; the insights of these methods help to inform mass transport properties of solutes to interfaces that impact inner-sphere complexation processes near mineral interfaces. Furthermore, advanced NMR methods can be coupled with machine-learning approaches to provide accurate atomic structures.[105]

2.5. Atomic Force Microscopy, Scanning Tunneling Microscopy, Optical Techniques

2.5.1. Atomic Force Microscopy (AFM)

Real-time imaging of dynamic interfacial processes is enabled by environmental atomic force microscopy (AFM). AFM is an indispensable tool obtain quantitative descriptions of mineral precipitation and dissolution processes with crystal facet specificity; a few such processes include molecular step advancement, etch pit formation, and toxic element sequestration. Examples include *in situ* nanoscale thin film oxide formation on environmentally abundant mineral surfaces, which observed interfacial reactions in real-time using fluid-cell AFM.[106-108] Complex phenomena including coupled dissolution of a parent phase with new product phases in environmental mineral interfaces may also be identified.[109] The structural information obtained from these methods tests current theories of heterogeneous nucleation, growth and dissolution, and is amenable to comparisons with results from various computational approaches.

5.2.2. Transmission Electron and Scanning Electron Microscopy (TEM & SEM)

TEM and SEM are no longer limited to high vacuum sample environments and the need for special sample coatings. Environmental TEM (E-TEM), which introduces a gas into the TEM sample chamber, is becoming a standard technique at several large facilities, many of which allow access to a larger community of scientists worldwide. E-TEM is routinely used to investigate mineral substrates under humid atmosphere. Moreover, by lowering the T below the dew point, the formation of liquid water and ice films on mineral substrates can be imaged.

The advent of *in sit*u, liquid-phase TEM (LP-TEM) and SEM (LP-SEM) in microfabricated Si/SiN cells and sandwiched graphene films has enabled direct observation of mineral particles in solution, including their nucleation, growth, interaction dynamics, aggregation and fusion. Microfabricated TEM cells can include capabilities for fluid flow, mixing of reagents, heating to near 100°C and application of electric fields. In situ LP-TEM and -SEM has led to numerous discoveries about the behavior of mineral systems in aqueous electrolytes. For example, a recent study from Zhu et al. provided an explanation for the formation of self-similar hematite mesocrystals from ferrihydrite suspensions, which has significant consequences for understanding the structural and chemical heterogeneity at mineral-water interfaces.[110] The authors found that, when $Na_2C_2O_4$ is added to ferrihydrite suspensions heated to 80°C, isolated hematite particles rarely appear in the solution, but once formed, interfacial gradients at the oxalate-covered surfaces drive hematite particles to nucleate about 2 nm from those surfaces to which they then attach, thereby generating the mesocrystals.

2.5.3. Atomic Probe Tomography (APT)

One of the most interesting observations of mineral-water chemistry in the last 20 years was the observation by Williams and Scherer that $^{56}Fe/^{57}Fe$ exchange could occur between goethite and aqueous solutions containing isotopically-concentrated $^{57}Fe^{2+}(aq)$. [111] Complete isotopic exchange was observed while the particles did not change their habits, so explaining this observation required further study. One method for addressing this and other longer-term mineral-water kinetics related to exchange, dissolution and precipitation is atom probe tomography (APT). Atom probe tomography (APT) provides three-dimensional compositional mapping with sub-nanometre resolution in the range of parts per million concentrations of all elements.[112] Taylor et al. used APT on goethite and hematite and found evidence for heterogeneous atom exchange fronts

several nanometers deep into the particles consistent with exchange along microstructural domain boundaries.[113] Because Fe-oxy(hydr)oxides and other minerals often form via aggregation of smaller, metastable particles (e.g., ferrihydrite in this case), the original grain-to-grain contact boundaries may leave defects within the re-crystallized particles. The defects are critical for the long-term behavior of minerals in the environment. Diffusion along these defects may be 4 orders of magnitude faster than through the bulk crystal,[114] diffusivities are likely to be further enhanced by exposure to radiation.[115] Studies such as these are complemented by DFT calculations modeling the structures and diffusion mechanisms. These new reaction pathways must be explored in the Fe-oxy(hydr)oxide-water and other mineral systems because they have been neglected.

2.5.4. Spatially-Resolved Mass Spectrometry (FT-ICRMS & TOF SIMS)

Organic-mineral associations are critical for soil health and consequently biological productivity (**Section 3.3**). Connecting detailed molecular-level studies with soils is problematic due to the general simplicity of the former and complexity of the latter. An excellent technique for dealing with this is Fourier-transform ion cyclotron resonance mass spectrometry (FTICR MS) because it can be used to distinguish individual compounds from complex mixtures with high resolution. Bahureksa et al. critically reviewed progress in this area and highlighted the potential applications of this method.[116] For example, FT-ICRMS combined with electrospray ionization has been used to examine fractionation of dissolved organic matter at several mineral-water interfaces.[117] Time-of-flight secondary ion mass spectrometry (TOF SIMS) allows the construction of spatially resolved (<100 nm lateral resolution) 3-D composition maps with high mass resolution.[118] Needs for parallel spectroscopic studies, unified sample preparation methods and database repositories are examples of why more integrated studies of mineral-water interfacial chemistry are necessary.

2.5.5. Vertical Scanning and Phase Shift Interferometry

Vertical scanning interferometry (VSI), atomic force microscopy, and other techniques were combined with kinetic Monte Carlo (kMC) calculations to analyze surface topography and kinetic of interface alteration and obtain insights into reaction mechanisms of molecular-scale interfaces due to changes in the physicochemical environment.[119] VSI and phase shift interferometry (PSI) can resolve large surfaces with high resolution normal to the surface over a broad size range. VSI was also used to study the material flux to and from a solid surface resulting from fluid-solid reactions.[120] They obtained spatially resolved rate maps that revealed rhythmic pulses of the material flux from the crystal surface. Fluctuations of the reactive surface site density and oscillations in the fluid saturation imply spatial and temporal variability in surface reaction rates. Understanding this variability could help upscale microscopic rates and predict reactive transport in porous media. Other interesting phenomena related to variability in crystal surface reactivity and enabled by VSI/PSI based methods is discussed in Fischer et al.[121]

Table S1. Summary of analytical and experimental approaches.

Technique	Measured Property
AFM	Surface morphological changes
AFM-FFM	Atomic scale force mapping
AFM-IR Spectroscopy	Nanoscopic vibrational spectroscopy, chemical speciation during atomic scale imaging
APT	Functional group identification, sorption kinetics
AP (ambient pressure) XPS	Binding and oxidation information of samples under ambient conditions
ATR-FTIR Spectroscopy	Functional group identification, sorption kinetics, useful for sorption information in liquid
CTR	Surface diffraction. atomic structure alteration at the surface
Environmental TEM	Atomic scale imaging under vacuum and humid atmosphere
Focused ion beam TEM	Atomic scale imaging of samples with elemental analysis
FT-ICR MS	High mass resolution analysis of complex organic mixtures
GISAXS	Nucleated particle size, shape, and their distribution on substrates
HD-SFG	Absolute molecular orientation at the interface
INS (Neutron spectroscopy)	Vibrations and H-bonding using inelastic scattering
Synchrotron-based IR nano-spectroscopy	High resolution IR
Kelvin Probe microscopy	Electronic properties on surface
Microcalorimetry	Heats/energetics and enthalpies of reactions
NDIS (Neutron diffraction)	Solute-solvent and solute-solute structures
NMR	Surface species, dynamics, reactive sites
NSE (Neutron spectroscopy)	Slow diffusion dynamics, useful for water dynamics in confined spaces.
QENS (Neutron spectroscopy)	Water dynamics using quasi-elastic neutron scattering
Raman	Functional groups, water structure, mineral phase identification
SERS	High resolution detection of functional group, water structure, and mineral phase identification
RAXR	Ion distribution at mineral-water surfaces
SAXS/USAXS/WAXS	Nucleated particle size, shape, phase, and aggregation
SHG	Total surface potential, in situ binding
SFG	Water structure, in situ binding, vibrational lifetimes
TOF SIMS	3D composition map (< 100 nm) with high mass resolution analysis of surface compositions
TXM	High resolution (<10 nm) three-dimensional sample structure
VSI/PSI	Surface topology analysis for large surfaces
EXAFS (μ-EXAFS)	Local coordination environment, interatomic distances, coordination numbers.
XANES (μ-XANES)	Oxidation state and in some cases bond angles.
XPCS	
X-ray PDF	Short range order of nanomaterials, phase identification
XPS	Surface potential, oxidation state
XRF (μ-XRF and nano-XRF)	Mapping of elemental distribution
X-ray CT (μ-CT and nano-CT)	Three-dimensional reconstruction of samples, dissolution and precipitation in porous media,
XRD (μ-XRD)	Lattice structure.
XRR	Vertical water and ion structure at mineral-water interfaces

References

(1) Brown, G. E.; Henrich, V. E.; Casey, W. H.; Clark, D. L.; Eggleston, C.; Felmy, A.; Goodman, D. W.; Grätzel, M.; Maciel, G.; McCarthy, M. I. et al. Metal Oxide Surfaces and Their Interactions with Aqueous Solutions and Microbial Organisms. *Chem. Rev.* **1999,** *99* (1), 77.

(2) Faraone, A.; Fratini, E.; Todea, A. M.; Krebs, B.; Miiller, A.; Baglioni, P. Dynamics of Water in Voids Between Well-Defined and Densely Packed Spherical Nanocages Acting as Polyprotic Inorganic Acids. *J. Phys. Chem. C* **2009,** *113* (20), 8635.

(3) Malikova, N.; Dubois, E.; Marry, V.; Rotenberg, B.; Turq, P. Dynamics in Clays - Combining Neutron Scattering and Microscopic Simulation. *Z. Phys. Chem.* **2010,** *224* (1-2), 153.

(4) Cygan, R. T.; Daemen, L. L.; Ilgen, A. G.; Krumhansl, J. L.; Nenoff, T. M. Inelastic Neutron Scattering and Molecular Simulation of the Dynamics of Interlayer Water in Smectite Clay Minerals. *J. Phys. Chem. C* **2015,** *119* (50), 28005.

(5) Brown, G. E.; Sturchio, N. C. An Overview of Synchrotron Radiation Applications to Low Temperature Geochemistry and Environmental Science. *Rev. Mineral. Geochem.* **2002,** *49* (1), 1.

(6) Fenter, P. A.; Rivers, M. L.; Sturchio, N. C.; Sutton, S. R. Applications of Synchrotron Radiation in Low-Temperature Geochemistry and Environmental Science. *Geochemical Society and Mineralogical Society of America* **2002**, DOI:10.1515/9781501508882 10.1515/9781501508882, 564.

(7) Fenter, P.; Sturchio, N. C. Mineral-Water Interfacial Structures Revealed by Synchrotron X-ray Scattering. *Prog. Surf. Sci.* **2004,** *77* (5-8), 171.

(8) Fenter, P.; Lee, S. S. Hydration Layer Structure at Solid-Water Interfaces. *MRS Bulletin* **2014,** *39* (12), 1056.

(9) Catlow, C. R. A. Synchrotron Radiation Techniques in Materials and Environmental Science. *Philos. Trans. R. Soc. A* **2015,** *373* (2036).

(10) Chautard, F. "Particle Accelerator Projects and Upgrades," 2020.

(11) Hopkins, A. J.; McFearin, C. L.; Richmond, G. L. Investigations of the Solid-Aqueous Interface with Vibrational Sum-Frequency Spectroscopy. *Curr. Opin. Solid State Mater. Sci.* **2005,** *9* (1-2), 19.

(12) Shen, Y. R.; Ostroverkhov, V. Sum-Frequency Vibrational Spectroscopy on Water Interfaces: Polar Orientation of Water Molecules at Interfaces. *Chem. Rev.* **2006,** *106* (4), 1140.

(13) Tian, C. S.; Shen, Y. R. Recent Progress on Sum-Frequency Spectroscopy. *Surf. Sci. Rep.* **2014,** *69* (2-3), 105.

(14) Eisenthal, K. B. Second Harmonic Spectroscopy of Aqueous Nano- and Microparticle Interfaces. *Chem. Rev.* **2006,** *106* (4), 1462.

(15) Malin, J. N.; Hayes, P. L.; Geiger, F. M. Interactions of Ca, Zn, and Cd Ions at Buried Solid/Water Interfaces Studied by Second Harmonic Generation. *J. Phys. Chem. C* **2009,** *113* (6), 2041.

(16) Gomez, S. A. S.; Geiger, F. M. Precipitates of Al(III), Sc(III), and La(III) at the Muscovite-Water Interface. *J. Phys. Chem. A* **2014,** *118* (46), 10974.

(17) Butt, H. J.; Cappella, B.; Kappl, M. Force Measurements with the Atomic Force Microscope: Technique, Interpretation and Applications. *Surf. Sci. Rep.* **2005,** *59* (1-6), 1.

(18) Dove, P. M.; Han, N.; De Yoreo, J. J. Mechanisms of Classical Crystal Growth Theory Explain Quartz and Silicate Dissolution Behavior. *Proc. Natl. Acad. Sci. U.S.A* **2005,** *102* (43), 15357.
(19) Zhang, X.; He, Y.; Liu, J.; Bowden, M. E.; Kovarik, L.; Mao, S. X.; Wang, C.; De Yoreo, J. J.; Rosso, K. M. Accessing Crystal–Crystal Interaction Forces with Oriented Nanocrystal Atomic Force Microscopy Probes. *Nat. Protoc.* **2018,** *13* (9), 2005.
(20) Fenter, P. A. X-ray Reflectivity as a Probe of Mineral-Fluid Interfaces: A User Guide. *Rev. Mineral. Geochem.* **2002,** *49* (1), 149.
(21) Suter, J. L.; Kabalan, L.; Khader, M.; Coveney, P. V. Ab Initio Molecular Dynamics Study of the Interlayer and Micropore Structure of Aqueous Montmorillonite Clays. *Geochim. Cosmochim. Acta* **2015,** *169*, 17.
(22) Cygan, R. T. Molecular Modeling in Mineralogy and Geochemistry. *Rev. Mineral. Geochem.* **2001,** *42* (1), 1.
(23) Woodley, S. M.; Catlow, C. R. A. High-Performance Computing in the Chemistry and Physics of Materials. *Proc. R. Soc. A: Math. Phys. Eng. Sci.* **2011,** *467* (2131), 1880.
(24) *Molecular Modeling of Geochemical Reactions: An Introduction*; Wiley, 2016.
(25) De Jong, W. A.; Bylaska, E.; Govind, N.; Janssen, C. L.; Kowalski, K.; Müller, T.; Nielsen, I. M. B.; Van Dam, H. J. J.; Veryazov, V.; Lindh, R. Utilizing high performance computing for chemistry: Parallel computational chemistry. *Phys. Chem. Chem. Phys.* **2010,** *12* (26), 6896.
(26) Richard, R. M.; Bertoni, C.; Boschen, J. S.; Keipert, K.; Pritchard, B.; Valeev, E. F.; Harrison, R. J.; De Jong, W. A.; Windus, T. L. Developing a Computational Chemistry Framework for the Exascale Era. *Comput. Sci. Eng.* **2019,** *21* (2), 48.
(27) Hammes-Schiffer, S.; Galli, G. Integration of theory and experiment in the modelling of heterogeneous electrocatalysis. *Nat. Energy* **2021,** *6* (7), 700.
(28) Sayers, D. E.; Stern, E. A.; Lytle, F. W. New Technique for Investigating Noncrystalline Structures: Fourier Analysis of the Extended X-Ray---Absorption Fine Structure. *Phys. Rev. Lett.* **1971,** *27* (18), 1204.
(29) Sayers, D. E.; Lytle, F. W.; Stern, E. A. Structure determination of amorphous Ge, GeO2 and GeSe by fourier analysis of extended x-ray absorption fine structure (EXAFS). *J. Non-Cryst. Solids* **1972,** *8-10*, 401.
(30) Brown, G. E.; Calas, G.; Waychunas, G. A.; Petiau, J.; Hawthorne, F. C., Ed.; De Gruyter, 1988, DOI:doi:10.1515/9781501508974-013 doi:10.1515/9781501508974-013.
(31) Hayes, K. F.; Roe, A. L.; Brown, G. E.; Hodgson, K. O.; Leckie, J. O.; Parks, G. A. In Situ X-ray Absorption Study of Surface Complexes: Selenium Oxyanions on α-FeOOH. *Science* **1987,** *238* (4828), 783.
(32) Waychunas, G.; Trainor, T.; Eng, P.; Catalano, J.; Brown, G.; Davis, J.; Rogers, J.; Bargar, J. Surface complexation studied via combined grazing-incidence EXAFS and surface diffraction: arsenate an hematite (0001) and (10-12). *Anal. Bioanal. Chem.* **2005,** *383* (1), 12.
(33) Brown, G.; Calas, G. Mineral-Aqueous solution interfaces and their impact on the environment. *Geochem. Perspect.* **2012,** *1* (4-5), 483.
(34) Lee, S. S.; Koishi, A.; Bourg, I. C.; Fenter, P. Ion correlations drive charge overscreening and heterogeneous nucleation at solid–aqueous electrolyte interfaces. *Proc. Natl. Acad. Sci.* **2021,** *118* (32), e2105154118.

(35) de Oca-Palma, R. M.; Solache-Rios, M.; Jimenez-Reyes, M.; Garcia-Sanchez, J. J.; Almazan-Sanchez, P. T. Adsorption of cobalt by using inorganic components of sediment samples from water bodies. *Int. J. Sediment Res.* **2021,** *36* (4), 524.
(36) Jun, Y. S.; Kim, D.; Neil, C. W. Heterogeneous Nucleation and Growth of Nanoparticles at the Environmental Interfaces. *Acc. Chem. Res.* **2016,** *49* (9), 1681.
(37) Jun, Y. S.; Lee, B.; Waychunas, G. A. In situ observations of nanoparticle early development kinetics at mineral-water interfaces. *Environ. Sci. Technol.* **2010,** *44*, 8182.
(38) Hu, Y.; Lee, B.; Bell, C.; Jun, Y. S. Environmentally Abundant Anions Influence the Nucleation, Growth, Ostwald Ripening, and Aggregation of Hydrous Fe(III) Oxides. *Langmuir* **2012,** *28* (20), 7737.
(39) Li, Q.; Fernandez-Martinez, A.; Lee, B.; Waychunas, G. A.; Jun, Y. S. Interfacial Energies for Heterogeneous Nucleation of Calcium Carbonate on Mica and Quartz Substrates. *Environ. Sci. Technol.* **2014,** *48* (10), 5745.
(40) Li, Q.; Jun, Y.-S. The apparent activation energy and pre-exponential kinetic factor for heterogeneous calcium carbonate nucleation on quartz. *Commun. Chem.* **2018,** *1* (1), 56.
(41) Li, Q.; Jun, Y.-S. Salinity-Induced Reduction of Interfacial Energies and Kinetic Factors during Calcium Carbonate Nucleation on Quartz. *J. Phys. Chem. C* **2019,** *123* (23), 14319.
(42) Wu, X.; Lee, B.; Jun, Y.-S. Interfacial and Activation Energies of Environmentally Abundant Heterogeneously Nucleated Iron(III) (Hydr)oxide on Quartz. *Environ. Sci. Technol.* **2020,** *54* (19), 12119.
(43) Hu, Y.; Li, Q.; Lee, B.; Jun, Y. S. Aluminum Affects Heterogeneous Fe(III) (Hydr)oxide Nucleation, Growth, and Ostwald Ripening. *Environ. Sci. Technol.* **2014,** *48* (1), 299.
(44) Neil, C. W.; Lee, B.; Jun, Y. S. Different Arsenate and Phosphate Incorporation Effects on the Nucleation and Growth of Iron(III) (Hydr)oxides on Quartz. *Environ. Sci. Technol.* **2014,** *48* (20), 11883.
(45) Neil, C. W.; Ray, J. R.; Lee, B.; Jun, Y. S. Fractal aggregation and disaggregation of newly formed iron(III) (hydr)oxide nanoparticles in the presence of natural organic matter and arsenic. *Environ. Sci. Nano* **2016,** *3* (3), 647.
(46) Hu, Y.; Neil, C. W.; Lee, B.; Jun, Y. S. Control of Heterogeneous Fe (III) (Hydr)oxide Nucleation and Growth by Interfacial Energies and Local Saturations. *Environ. Sci. Technol.* **2013,** *47*, 9198.
(47) Fernandez-Martinez, A.; Hu, Y.; Lee, B.; Jun, Y. S.; Waychunas, G. A. *In situ* determination of interfacial energies between heterogeneously nucleated $CaCO_3$ and quartz substracts: Thermodynamics of CO_2 mineral trapping. *Environ. Sci. Technol.* **2013,** *47* (1), 102.
(48) Zhu, Y.; Li, Q.; Kim, D.; Min, Y.; Lee, B.; Jun, Y.-S. Sulfate-controlled Heterogeneous $CaCO_3$ Nucleation and Its Non-linear Interfacial Energy Evolution. *Environ. Sci. Technol.* **2021**, DOI:10.1021/acs.est.1c02865 10.1021/acs.est.1c02865
(49) Kim, D.; Lee, B.; Marshall, B.; Thomopoulos, S.; Jun, Y.-S. Cyclic strain enhances the early stage mineral nucleation and the modulus of demineralized bone matrix. *Biomater. Sci.* **2021**, DOI:10.1039/D1BM00884F 10.1039/D1BM00884F.
(50) Kim, D.; Lee, B.; Marshall, B. P.; Jang, E.; Thomopoulos, S.; Jun, Y.-S. Pulsed Electrical Stimulation Enhances Body Fluid Transport for Collagen Biomineralization. *ACS Appl. Bio Mater.* **2020,** *3* (2), 902.

(51) Kim, D.; Lee, B.; Thomopoulos, S.; Jun, Y. S. In Situ Evaluation of Calcium Phosphate Nucleation Kinetics and Pathways during Intra and Extrafibrillar Mineralization of Collagen Matrices. *Cryst. Growth Des.* **2016,** *16* (9), 5359.
(52) Kim, D.; Lee, B.; Thomopoulos, S.; Jun, Y.-S. The role of confined collagen geometry in decreasing nucleation energy barriers to intrafibrillar mineralization. *Nat. Commun.* **2018,** *9* (1), 1.
(53) Jung, H.; Lee, B.; Jun, Y. S. Structural Match of Heterogeneously Nucleated $Mn(OH)_2$ (s) Nanoparticles on Quartz under Various pH Conditions. *Langmuir* **2016,** *32* (41), 10735.
(54) Jung, H. S.; Jun, Y. S. Ionic Strength-Controlled Mn (Hydr)oxide Nanoparticle Nucleation on Quartz: Effect of Aqueous $Mn(OH)_2$. *Environ. Sci. Technol.* **2016,** *50* (1), 105.
(55) Egami, T.; Billinge, S. *Underneath the Bragg Peaks - Structural Analysis of Complex Materials*; 2 ed., 2012.
(56) Soper, A. K.; Edler, K. J. Coarse-grained empirical potential structure refinement: Application to a reverse aqueous micelle. *Biochim. Biophys. Acta - General Subjects* **2017,** *1861*, 1652.
(57) Hoeher, A.; Mergelsberg, S.; Borkiewicz, O. J.; Dove, P. M.; Michel, F. M. A new method for in situ structural investigations o nano-sized amorphous and crystalline materials using mixed-now reactors. *Acta Crystallogr. A* **2019,** *75*, 758.
(58) Funnell, N. P.; Fulford, M. F.; Inoue, S.; Kletetschka, K.; Michel, F. M.; Goodwin, A. L. Nanocomposite structure of two-line ferrihydrite powder from total scattering. *Commun. Chem.* **2020,** *3* (1).
(59) Qian, J.; Baskin, A.; Liu, Z.; Prendergast, D.; Crumlin, E. J. Addressing the sensitivity of signals from solid/liquid ambient pressure XPS (APXPS) measurement. *J. Chem. Phys.* **2020,** *153* (4).
(60) Gamble, A. V.; Northrup, P. A.; Sparks, D. L. Elucidation of soil phosphorus speciation in mid-Atlantic soils using synchrotron-based microspectroscopic techniques. *J. Environ. Qual.* **2020,** *49* (1), 184.
(61) Elbakhshwan, M. S.; Gill, S. K.; Rod, K. A.; Bingham, E. B.; McKinney, A. L.; Huerta, N.; Lopano, C. L.; Kutchko, B. G.; Chen-Wiegart, Y. C. K.; Zhao, C. H.et al. Structural and chemical changes from CO_2 exposure to self-healing polymer cement composites for geothermal wellbores. *Geothermics* **2021,** *89*.
(62) Ling, F. T.; Hunter, H. A.; Fitts, J. P.; Peters, C. A.; Acerbo, A. S.; Huang, X. J.; Yan, H. F.; Nazaretski, E.; Chu, Y. S. Nanospectroscopy Captures Nanoscale Compositional Zonation in Barite Solid Solutions. *Sci. Rep.* **2018,** *8*.
(63) Harouaka, K.; Kubicki, J. D.; Fantle, M. S. Effect of amino acids on the precipitation kinetics and Ca isotopic composition of gypsum. *Geochim. Cosmochim. Acta* **2017,** *218*, 343.
(64) De Andrade, V.; Nikitin, V.; Wojcik, M.; Deriy, A.; Bean, S.; Shu, D.; Mooney, T.; Peterson, K.; Kc, P.; Li, K.et al. Fast X-ray Nanotomography with Sub-10 nm Resolution as a Powerful Imaging Tool for Nanotechnology and Energy Storage Applications. *Adv. Mater.* **2021,** *33* (21), 2008653.
(65) Tan, D.; Lee, T. L.; Khong, J. C.; Connolley, T.; Fezzaa, K.; Mi, J. High-Speed Synchrotron X-ray Imaging Studies of the Ultrasound Shockwave and Enhanced Flow during Metal Solidification Processes. *Metall. Mater. Trans. A* **2015,** *46* (7), 2851.

(66) Torbati-Sarraf, H.; Niverty, S.; Singh, R.; Barboza, D.; De Andrade, V.; Turaga, P.; Chawla, N. Machine-Learning-based Algorithms for Automated Image Segmentation Techniques of Transmission X-ray Microscopy (TXM). *JOM* **2021,** *73* (7), 2173.
(67) McFarlane, J.; Anovitz, L. M.; Cheshire, M. C.; DiStefano, V. H.; Bilheux, H. Z.; Bilheux, J.-C.; Daemen, L. L.; Hale, R. E.; Howard, R. L.; Ramirez-Cuesta, A.et al. Water Migration and Swelling in Engineered Barrier Materials for Radioactive Waste Disposal. *Nucl. Technol.* **2021,** *207* (8), 1237.
(68) Ott, F.; Loupiac, C.; Désert, S.; Hélary, A.; Lavie, P. IMAGINE: A Cold Neutron Imaging Station at the Laboratoire Léon Brillouin. *Phys. Procedia* **2015,** *69*, 67.
(69) Yuan, K.; Starchenko, V.; Lee, S. S.; De Andrade, V.; Gursoy, D.; Sturchio, N. C.; Fenter, P. Mapping Three-Dimensional Dissolution Rates of Calcite Microcrystals: Effects of Surface Curvature and Dissolved Metal Ions. *ACS Earth Space Chem.* **2019,** *3* (5), 833.
(70) Zhu, W.; Fusseis, F.; Lisabeth, H.; Xing, T.; Xiao, X.; De Andrade, V.; Karato, S.-I. Experimental Evidence of Reaction-Induced Fracturing During Olivine Carbonation. *Geophys. Res. Lett.* **2016,** *43* (18), 9535.
(71) Snoeck, D.; Goethals, W.; Hovind, J.; Trtik, P.; Van Mullem, T.; Van den Heede, P.; De Belie, N. Internal Curing of Cement Pastes by Means of Superabsorbent Polymers Visualized by Neutron Tomography. *Cem. Concr. Res.* **2021,** *147*, 106528.
(72) Bilheux, H.; Herwig, K.; Keener, S.; Davis, L. Overview of the Conceptual Design of the Future VENUS Neutron Imaging Beam Line at the Spallation Neutron Source. *Phys. Procedia* **2015,** *69*, 55.
(73) Kockelmann, W.; Minniti, T.; Pooley, D. E.; Burca, G.; Ramadhan, R.; Akeroyd, F. A.; Howells, G. D.; Moreton-Smith, C.; Keymer, D. P.; Kelleher, J.et al. Time-of-Flight Neutron Imaging on IMAT@ISIS: A New User Facility for Materials Science. *J. Imaging* **2018,** *4* (3).
(74) Tremsin, A. S.; Perrodin, D.; Losko, A. S.; Vogel, S. C.; Bourke, M. A. M.; Bizarri, G. A.; Bourret, E. D. Real-time Crystal Growth Visualization and Quantification by Energy-Resolved Neutron Imaging. *Sci. Rep.* **2017,** *7* (1), 46275.
(75) Tremsin, A. S.; Sokolova, A. V.; Salvemini, F.; Luzin, V.; Paradowska, A.; Muransky, O.; Kirkwood, H. J.; Abbey, B.; Wensrich, C. M.; Kisi, E. H. Energy-Resolved Neutron Imaging Options at a Small Angle Neutron Scattering Instrument at the Australian Center for Neutron Scattering. *Rev. Sci. Instrum.* **2019,** *90* (3), 035114.
(76) Losko, A. S.; Daemen, L.; Hosemann, P.; Nakotte, H.; Tremsin, A.; Vogel, S. C.; Wang, P.; Wittmann, F. H. Separation of Uptake of Water and Ions in Porous Materials Using Energy Resolved Neutron Imaging. *JOM* **2020,** *72* (9), 3288.
(77) Tran, K. V.; Woracek, R.; Kardjilov, N.; Markötter, H.; Hilger, A.; Kockelmann, W.; Kelleher, J.; Puplampu, S. B.; Penumadu, D.; Tremsin, A. S. et al. Spectral Neutron Tomography. *Mater. Today Adv.* **2021,** *9*, 100132.
(78) Rinaldi, R.; Liang, L.; Schober, H., 2009, DOI:10.1007/978-0-387-09416-8_1 10.1007/978-0-387-09416-8_1.
(79) Trofymluk, O.; Levchenko, A. A.; Navrotsky, A. Interfacial Effects on Vitrification of Confined Glass-Forming Liquids. *J. Chem. Phys.* **2005,** *123* (19), 194509.
(80) Mamontov, E.; Vlcek, L.; Wesolowski, D. J.; Cummings, P. T.; Wang, W.; Anovitz, L. M.; Rosenqvist, J.; Brown, C. M.; Sakai, V. G. Dynamics and Structure of Hydration

Water on Rutile and Cassiterite Nanopowders Studied by Quasielastic Neutron Scattering and Molecular Dynamics Simulations. *J. Phys. Chem. C* **2007,** *111* (11), 4328.
(81) Kruteva, M. Dynamics studied by Quasielastic Neutron Scattering (QENS). *Adsorption* **2021**, DOI:10.1007/s10450-020-00295-4 10.1007/s10450-020-00295-4.
(82) Malikova, N.; Cadéne, A.; Marry, V.; Dubois, E.; Turq, P.; Zanotti, J. M.; Longeville, S. Diffusion of Water in Clays - Microscopic Simulation and Neutron Scattering. *Chem. Phys.* **2005,** *317*, 226.
(83) Malikova, N.; Cadène, A.; Marry, V.; Dubois, E.; Turq, P. Diffusion of Water in Clays on the Microscopic Scale: Modeling and Experiment. *J. Phys. Chem. B* **2006,** *110*, 3206.
(84) Malikova, N.; Cadènea, A.; Dubois, E.; Marry, V.; Durand-Vidal, S.; Turq, P.; Breu, J.; Longeville, S.; Zanotti, J. M. Water Diffusion in a Synthetic Hectorite Clay Studied by Quasi-Elastic Neutron Scattering. *J. Phys. Chem. C* **2007,** *111*, 17603.
(85) Swenson, J.; Bergman, R.; Longeville, S. A Neutron Spin-Echo Study of Confined Water. *J. Chem. Phys.* **2001,** *115*, 11299.
(86) Hao, Z.; Bechtel, H. A.; Kneafsey, T.; Gilbert, B.; Nico, P. S. Cross-Scale Molecular Analysis of Chemical Heterogeneity in Shale Rocks. *Sci. Rep.* **2018,** *8*.
(87) Beckingham, L. E.; Winningham, L. Critical Knowledge Gaps for Understanding Water–Rock–Working Phase Interactions for Compressed Energy Storage in Porous Formations. *ACS Sustain. Chem. Eng.* **2020,** *8* (1), 2.
(88) Tuladhar, A.; Dewan, S.; Kubicki, J. D.; Borguet, E. Spectroscopy and Ultrafast Vibrational Dynamics of Strongly Hydrogen Bonded OH Species at the α-Al_2O_3(112-0)/H_2O Interface. *J. Phys. Chem. C* **2016,** *120* (29), 16153.
(89) Kroutil, O.; Pezzotti, S.; Gaigeot, M. P.; Předota, M. Phase-Sensitive Vibrational SFG Spectra from Simple Classical Force Field Molecular Dynamics Simulations. *J. Phys. Chem. C* **2020,** *124* (28), 15253.
(90) Sulpizi, M.; Salanne, M.; Sprik, M.; Gaigeot, M. P. Vibrational Sum Frequency Generation Spectroscopy of the Water Liquid-Vapor Interface from Density Functional Theory-Based Molecular Dynamics Simulations. *J. Phys. Chem. Lett.* **2013,** *4* (1), 83.
(91) DelloStritto, M.; Sofo, J. Bond Polarizability Model for Sum Frequency Generation at the Al_2O_3(0001)-H_2O Interface. *J. Phys. Chem. A* **2017,** *121* (16), 3045.
(92) DelloStritto, M.; Piontek, S. M.; Klein, M. L.; Borguet, E. Relating Interfacial Order to Sum Frequency Generation with Ab Initio Simulations of the Aqueous Al_2O_3(0001) and (11(2)over-bar0) Interfaces. *J. Phys. Chem. C* **2018,** *122* (37), 21284.
(93) Pezzotti, S.; Galimberti, D. R.; Gaigeot, M. P. Deconvolution of BIL-SFG and DL-SFG Spectroscopic Signals Reveals Order/Disorder of Water at the Elusive Aqueous Silica Interface. *Phys. Chem. Chem. Phys.* **2019,** *21* (40), 22188.
(94) Geisler, T.; Dohmen, L.; Lenting, C.; Fritzsche, M. B. K. Real-time in Situ Observations of Reaction and Transport Phenomena During Silicate Glass Corrosion by Fluid-Cell Raman Spectroscopy. *Nat. Mater.* **2019,** *18*, 342.
(95) King, H. E.; Geisler, T. Tracing Mineral Reactions using Confocal Raman Spectroscopy. *Minerals* **2018,** *8* (4).
(96) Langer, J.; Jimenez de Aberasturi, D.; Aizpurua, J.; Alvarez-Puebla, R. A.; Auguié, B.; Baumberg, J. J.; Bazan, G. C.; Bell, S. E. J.; Boisen, A.; Brolo, A. G.et al. Present and Future of Surface-Enhanced Raman Scattering. *ACS Nano* **2020,** *14* (1), 28.
(97) Willets, K. A.; Van Duyne, R. P. Localized Surface Plasmon Resonance Spectroscopy and Sensing. *Annu. Rev. Phys. Chem.* **2007,** *58* (1), 267.

(98) Zhu, Y.; Derami, H. G.; Gupta, P.; Gupta, R.; Singamaneni, S.; Jun, Y.-S. Ionic Surface Propensity Controls pH in Nanopores. *Chem* **2022**, DOI:https://doi.org/10.1016/j.chempr.2022.07.021 https://doi.org/10.1016/j.chempr.2022.07.021.
(99) Pagès, G.; Gilard, V.; Martino, R.; Malet-Martino, M. Pulsed-Field Gradient Nuclear Magnetic Resonance Measurements (PFG NMR) for Diffusion Ordered Spectroscopy (DOSY) Mapping. *Analyst* **2017,** *142*, 3771.
(100) Meier, R.; Herrmann, A.; Kresse, B.; Privalov, A. F.; Kruk, D.; Fujara, F.; Rössler, E. A. Long-time Diffusion in Polymer Melts Revealed by ^{1}H NMR Relaxometry. *ACS Macro Lett.* **2013,** *2*, 96.
(101) D'Agostino, C.; Mitchell, J.; Mantle, M. D.; Gladden, L. F. Interpretation of NMR Relaxation as a Tool for Characterising the Adsorption Strength of Liquids Inside Porous Materials. *Chem. Eur. J.* **2014,** *20*, 13009.
(102) Franck, J. M.; Pavlova, A.; Scott, J. A.; Han, S. Quantitative cw Overhauser Effect Dynamic Nuclear Polarization for the Analysis of Local Water Dynamics. *Prog. Nucl. Magn. Reson. Spectrosc.* **2013,** *74*, 33.
(103) Ulrich, K.; Centeno, S. A.; Arslanoglu, J.; Del Federico, E. Absorption and Diffusion Measurements of Water in Acrylic Paint Films by Single-sided NMR. *Prog. Org. Coat.* **2011,** *71*, 283.
(104) Blümich, B.; Perlo, J.; Casanova, F. Mobile Single-sided NMR. *Prog. Nucl. Magn. Reson. Spectrosc.* **2008,** *52*, 197.
(105) Haghighatlari, M.; Li, J.; Heidar-Zadeh, F.; Liu, Y. C.; Guan, X. Y.; Head-Gordon, T. Learning to Make Chemical Predictions: The Interplay of Feature Representation, Data, and Machine Learning Methods. *Chem* **2020,** *6* (7), 1527.
(106) Jun, Y.-S.; Martin, S. T. Microscopic Observations of Reductive Manganite Dissolution under Oxic Conditions. *Environ. Sci. Technol.* **2003,** *37* (11), 2363.
(107) Jun, Y.-S.; Kendall, T. A.; Martin, S. T.; Friend, C. M.; Vlassak, J. J. Heteroepitaxial Nucleation and Oriented Growth of Manganese Oxide Islands on Carbonate Minerals under Aqueous Conditions. *Environ. Sci. Technol.* **2005,** *39* (5), 1239.
(108) Jun, Y.-S.; Martin, S. T. Cobalt Alters The Growth of a Manganese Oxide Film. *Langmuir* **2006,** *22* (5), 2235.
(109) Wang, L.; Putnis, C. V. Dissolution and Precipitation Dynamics at Environmental Mineral Interfaces Imaged by in Situ Atomic Force Microscopy. *Acc. Chem. Res.* **2020,** *53* (6), 1196.
(110) Zhu, G.; Sushko, M. L.; Loring, J. S.; Legg, B. A.; Song, M.; Soltis, J. A.; Huang, X.; Rosso, K. M.; De Yoreo, J. J. Self-similar Mesocrystals form via Interface-driven Nucleation and Assembly. *Nature* **2021,** *590* (7846), 416.
(111) Williams, A. G. B.; Scherer, M. M. Spectroscopic Evidence for Fe(II)-Fe(III) Electron Transfer at the Iron Oxide-Water Interface. *Environ. Sci. Technol.* **2004,** *38* (18), 4782.
(112) Gault, B.; Moody, M. P.; Cairney, J. M.; Ringer, S. P. *Atom Probe Microscopy*; Springer New York, NY, 2012.
(113) Taylor, S. D.; Liu, J.; Zhang, X.; Arey, B. W.; Kovarik, L.; Schreiber, D. K.; Perea, D. E.; Rosso, K. M. Visualizing the Iron Atom Exchange Front in the Fe(II)-Catalyzed Recrystallization of Goethite by Atom Probe Tomography. *Proc. Natl. Acad. Sci. U.S.A* **2019,** *116* (8), 2866.

(114) Kaspar, T. C.; Taylor, S. D.; Yano, K. H.; Lach, T. G.; Zhou, Y. D.; Zhu, Z. H.; Kohnert, A. A.; Still, E. K.; Hosemann, P.; Spurgeon, S. R.et al. Bulk and Short-Circuit Anion Diffusion in Epitaxial Fe_2O_3 Films Quantified Using Buried Isotopic Tracer Layers. *Adv. Mater. Interfaces* **2021,** *8* (9).
(115) Yano, K. H.; Kohnert, A. A.; Banerjee, A.; Edwards, D. J.; Holby, E. F.; Kaspar, T. C.; Kim, H.; Lach, T. G.; Taylor, S. D.; Wang, Y. Q. et al. Radiation-Enhanced Anion Transport in Hematite. *Chem. Mater.* **2021,** *33* (7), 2307.
(116) Bahureksa, W.; Tfaily, M. M.; Boiteau, R. M.; Young, R. B.; Logan, M. N.; McKenna, A. M.; Borch, T. Soil Organic Matter Characterization by Fourier Transform Ion Cyclotron Resonance Mass Spectrometry (FTICR MS): A Critical Review of Sample Preparation, Analysis, and Data Interpretation. *Environ. Sci. Technol.* **2021,** *55* (14), 9637.
(117) Lv, J.; Zhang, S.; Wang, S.; Luo, L.; Cao, D.; Christie, P. Molecular-Scale Investigation with ESI-FT-ICR-MS on Fractionation of Dissolved Organic Matter Induced by Adsorption on Iron Oxyhydroxides. *Environ. Sci. Technol.* **2016,** *50*, 2328.
(118) Kubicek, M.; Holzlechner, G.; Opitz, A. K.; Larisegger, S.; Hutter, H.; Fleig, J. A Novel ToF-SIMS Operation Mode for Sub 100 nm Lateral Resolution: Application and Performance. *Appl. Surf. Sci.* **2014,** *289*, 407.
(119) Luttge, A.; Arvidson, R. S. Reactions at Surfaces: A New Approach Integrating Interferometry and Kinetic Simulations. *J. Am. Ceram. Soc.* **2010,** *93*, 3519.
(120) Fischer, C.; Luttge, A. Pulsating Dissolution of Crystalline Matter. *Proc. Natl. Acad. Sci. U.S.A* **2018,** *115* (5), 897.
(121) Fischer, C.; Kurganskaya, I.; Schäfer, T.; Lüttge, A. Variability of Crystal Surface Reactivity: What Do We Know? *Appl. Geochem.* **2014,** *43*, 132.